



## Proceedings of the 21st Annual Wisconsin Space Conference



# SEEING FARTHER FROM SPACE

August 18-19, 2011  
University of Wisconsin-La Crosse  
La Crosse, Wisconsin

Proceedings of the 21st Annual  
Wisconsin Space Conference

Seeing Farther From Space

2011



For information about the programs of the Wisconsin Space Grant Consortium, contact the Program Office or any of the following individuals:

**Wisconsin Space Grant Consortium**

University of Wisconsin-Green Bay  
2420 Nicolet Drive  
Green Bay, WI 54311-7001  
Tel: (920)465-2108; Fax: (920)465-2376  
www.uwgb.edu/wsgc

**Director**

R. Aileen Yingst  
University of Wisconsin-Green Bay  
(920)465-2327; yingsta@uwgb.edu

**Program Manager/Associate Director for Outreach**

Sharon D. Brandt  
University of Wisconsin-Green Bay  
(920)465-2941; brandts@uwgb.edu

**Chair, WSGC Advisory Council and Institutional Representative**

Karen Valley  
Wisconsin Department of Transportation  
(608)266-8166; karen.valley@dot.state.wi.us

**WSGC Associate Director for Scholarships/Fellowships**

Steven Dutch  
University of Wisconsin-Green Bay  
(920)465-2246; dutchs@uwgb.edu

**WSGC Associate Director for Student Satellite Programs**

William Farrow  
Milwaukee School of Engineering  
(414)277-2241; faroww@msoe.edu

**WSGC Associate Director for Research Infrastructure**

Gubbi R. Sudhakaran  
University of Wisconsin-La Crosse  
(608)785-8431; sudhakar.gubb@uwlax.edu

**WSGC Associate Director for Higher Education**

John Borg  
Marquette University  
(414)288-7519; john.borg@marquette.edu

**WSGC Associate Director for Special Initiatives**

Thomas Bray  
Milwaukee School of Engineering  
(414)277-7416; brayt@msoe.edu

**WSGC Associate Director for Industry Program**

Eric Rice  
Orbital Technologies Corporation  
(608)827-5000; ricee@orbitec.com

## WSGC Members and Institutional Representatives

### Lead Institution

#### University of Wisconsin-Green Bay

Scott Ashmann

### Affiliates

**Aerogel Technologies, LLC**  
Stephen Steiner

**AIAA - Wisconsin Section**  
Marty Gustafson

**Alverno College**  
Paul Smith

**Astronautics Corporation of America**  
Steven Russek

**BioPharmaceutical Technology Center Institute**  
Karin Borgh

**Carroll University**  
Damon Resnick

**Carthage College**  
Kevin Crosby

**College of Menominee Nation**  
Kathy Denor

**Experimental Aircraft Association (EAA)**  
Lee Siudzinski

**Great Lakes Spaceport Education Fdn.**  
Carol Lutz

**Lawrence University**  
Megan Pickett

**Marquette University**  
Christopher Stockdale

**Medical College of Wisconsin**  
Danny A. Riley

**Milwaukee School of Engineering**  
William Farrow

**Orbital Technologies Corporation**  
Eric E. Rice

**PLANET LLC**  
Thomas Crabb

**Ripon College**  
Mary Williams-Norton

**Saint Norbert College**  
Terry Jo Leiterman

**Space Education Initiatives**  
Jason Marcks

**Space Explorers, Inc.**  
George French

**Spaceflight Fundamentals, LLC**  
Bradley Staats

**University of Wisconsin-Fox Valley**  
Martin Rudd

**University of Wisconsin-La Crosse**  
Eric Barnes

**University of Wisconsin-Madison**  
Gerald Kulcinski

**University of Wisconsin-Milwaukee**  
Ronald Perez

**University of Wisconsin-Oshkosh**  
Nadejda Kaltcheva

**University of Wisconsin-Parkside**  
David Bruning

**University of Wisconsin-River Falls**  
Glenn Spiczak

**University of Wisconsin-Sheboygan**  
Harald Schenk

**University of Wisconsin-Stout**  
John Rompala

**University of Wisconsin-Superior**  
Richard Stewart

**University of Wisconsin-Whitewater**  
Rex Hanger

**Western Technical College**  
Michael LeDocq

**Wisconsin Aerospace Authority**  
Tom Crabb

**Wisconsin Association of CESA Administrators**  
Robert Kellogg

**Wisconsin Department of Public Instruction**  
Shelley A. Lee

**Wisconsin Department of Transportation**  
Nicole Wiessinger

**Wisconsin Lutheran College**  
Kerry Kuehn

*See [www.uwgb.edu/wsgc](http://www.uwgb.edu/wsgc) for up-to-date contact information*

# SEEING FARTHER FROM SPACE

**21<sup>st</sup> Annual Wisconsin Space Conference**

**August 18-19, 2011**

**Host: University of Wisconsin-La Crosse**

**La Crosse, Wisconsin**



---

**Edited by:** R. Aileen Yingst, Director, Wisconsin Space Grant Consortium  
Sharon D. Brandt, Program Manager, Wisconsin Space Grant Consortium  
Martin Rudd, Associate Professor, UW-Fox Valley

**Cover by:** Mao Vang, Student Assistant, Wisconsin Space Grant Consortium

**Layout by:** Brittany Luedtke, Office Coordinator, Wisconsin Space Grant Consortium

**Published by:** Wisconsin Space Grant Consortium  
University of Wisconsin-Green Bay

Copyright c 2011 Wisconsin Space Grant Consortium  
Wisconsin Space Grant Consortium  
University of Wisconsin - Green Bay  
Green Bay, WI 54311

Pp. + Illustrated

December, 2011



## **Preface and Acknowledgements**

We as a species are coming of age in our Solar System. With due respect to Carl Sagan, I'm not sure I can agree that we're ready to come of age in the Milky Way, but the Solar System — that's another story. We are in a great age of exploration, in which whole planets and systems are being revealed for the first time; spacecraft are discovering moons not every ten years, but by the dozen every year; and our robotic avatars roll across worlds that just a few years ago were only blurry disks in the most powerful telescopes.

Just this year alone, we have seen the second largest asteroid in the asteroid belt go from a few pixels in a Hubble Space Telescope image to a geologic world in its own right, thanks to the Dawn spacecraft. Cassini continues its historic mission to Saturn and its many moons, revealing shepherd moons, methane atmospheres, and ice volcanoes on worlds where the Sun shines barely brighter than the background stars. And at the end of the year, NASA plans to launch the largest autonomous roving vehicle in history to Mars, where its primary mission is measured, not in days, but in years. What intensely exciting times we live in!

This issue of our Conference Proceedings represents the “coming of age” of our Wisconsin Space Conference as well – we are now 21! I'm not sure if our insurance rates will go down or not, but we've certainly grown by leaps and bounds in the past 21 years. We've gone from perhaps a one day conference with mostly plenary sessions, to two packed days with several session “streams,” a student poster competition, two guest speakers, a devoted student satellite session and more participants than we ever could have imagined 21 years ago when we started. That's a pretty impressive success, and there is plenty of “thanks” to spread around for it.

For these proceedings, we in the Wisconsin Space Grant Consortium office especially want to thank our host, the University of Wisconsin—LaCrosse, starting with Conference lead Dr. Eric Barnes and his staff of helpful volunteers. We always find hospitality and excellent management at UW-LaCrosse and we are grateful to Eric, to Associate Director Dr. Gubbi Sudhakaran, and to everyone who made our conference run so smoothly. Thanks must go to our session moderators and our poster judges for their conscientious work and their strong support for our students. Our keynote speakers are also to be thanked for adding so much to our conference: Dr. Jonathan P. Gardner, Chief of the Observational Cosmology Lab, NASA's Goddard Space Flight Center and Deputy Senior Project Scientist for the James Webb Space Telescope and Dr. Robert D. Gehrz, Professor of Physics and Astronomy, and Department of Astronomy Chair, University of Minnesota-Twin Cities. And ultimately, I especially appreciate all the scientists, engineers, students, educators and others, who contributed papers to this volume.

Forward!

R. Aileen Yingst, Ph.D.  
Director

# *Wisconsin Space Grant Consortium*

## *Programs for 2011*

### **Student Programs**

- Undergraduate Scholarship
- Undergraduate Research
- Graduate Fellowship
- Dr. Laurel Salton Clark Memorial Graduate Fellowship
- University Sounding Rocket Team Competition
- Student High-Altitude Balloon Launch
- Student High-Altitude Balloon Payload
- Student High-Altitude Balloon Instrument Development
- Industry Member Internships
- NASA ESMD Internships
- NASA Academy Leadership Internships
- NASA Centers/JPL Internships
- NASA Reduced/Gravity Team Launches
- Relevant Student Travel

(see detailed descriptions on next page)

### **Research**

The Research Infrastructure Program provides Research Seed Grant Awards to faculty and staff from WSGC Member and Affiliate Member colleges and universities to support individuals interested in starting or enhancing space- or aerospace-related research program(s).

### **Higher Education**

The Higher Education Incentives Program is a seed-grant program inviting proposals for innovative, value-added, higher education teaching/training projects related to space science, space engineering, and other space- or aerospace-related disciplines. The Student Satellite Program including Balloon and Rocket programs is also administered under this program.

### **Industry Program**

The WSGC Industry Program is designed to meet the needs of Wisconsin Industry member institutions in multiple ways including:

- 1) the Industry Member Internships (listed under students above),
- 2) the Industry/Academic Research Seed Program designed to provide funding and open an avenue for member academia and industry researchers to work together on a space-related project, and
- 3) the Industrial Education and Training Program designed to provide funding for industry staff members to keep up-to-date in NASA-relevant fields.

### **Aerospace Outreach Program**

The Aerospace Outreach Program provides grant monies to promote outreach programs and projects that disseminate aerospace and space-related information to the general public, and support the development and implementation of aerospace and space-related curricula in Wisconsin classrooms. In addition, this program supports NASA-trained educators in teacher training programs.

### **Special Initiatives**

The Special Initiatives Program is designed to provide planning grants and program supplement grants for ongoing or new programs which have space or aerospace content and are intended to encourage, attract, and retain under-represented groups, especially women, minorities and the developmentally challenged, in careers in space- or aerospace-related fields.

### **Wisconsin Space Conference**

The Wisconsin Space Conference is an annual conference featuring presentations of students, faculty, K-12 educators and others who have received grants from WSGC over the past year. The Conference allows all to share their work with others interested in Space. It also includes keynote addresses, and the announcement of award recipients for the next year.

### **Regional Consortia**

WSGC is a founding member of the Great Midwest Regional Space Grant Consortia. The Consortia consists of eight members, all Space Grants from Midwest and Great Lakes States.

### **Communications**

WSGC web site [www.uwgb.edu/wsgc](http://www.uwgb.edu/wsgc) provides information about WSGC, its members and programs, and links to NASA and other sites.

### **Contact Us**

Wisconsin Space Grant Consortium  
University of Wisconsin–Green Bay  
2420 Nicolet Drive, ES 301  
Green Bay, Wisconsin 54311-7001  
Phone: (920) 465-2108  
Fax: (920) 465-2376  
E-mail: [wsgc@uwgb.edu](mailto:wsgc@uwgb.edu)  
Website: [www.uwgb.edu/wsgc](http://www.uwgb.edu/wsgc)



# *Wisconsin Space Grant Consortium*

## *Student Programs for 2011*

### **Undergraduate Scholarship Program**

Supports outstanding undergraduate students pursuing aerospace, space science, or other space-related studies or research.

### **Undergraduate Research Awards**

Supports qualified students to create and implement a small research study of their own design during the summer or academic year that is directly related to their interests and career objectives in space science, aerospace, or space-related studies.

### **Graduate Fellowships**

Support outstanding graduate students pursuing aerospace, space science, or other interdisciplinary space-related graduate research.

### **Dr. Laurel Salton Clark Memorial Graduate Fellowship**

In honor of Dr. Clark, Columbia Space Shuttle astronaut and resident of Wisconsin, this award supports a graduate student pursuing studies in the fields of environmental or life sciences, whose research has an aerospace component.

### **University Sounding Rocket Team Competition**

Provides an opportunity and funding for student teams to design and fly a rocket that excels at a specific goal that is changed annually.

### **High School Sounding Rocket Team Competition**

For high school students. This program is in its initial stages. It mimics the university competition.

### **Student High-Altitude Balloon Instrument Development**

Students participate in this instrument development program through engineering or science teams. Working models created by the students will be flown on high-altitude balloons.

### **Student High-Altitude Balloon Payload/Launch Program**

The Elijah Project is a high-altitude balloon program in which science and engineering students work in integrated science and engineering teams, to design, construct, launch, recover and analyze data from a high-altitude balloon payload. These balloons travel up to 100,000 ft., considered "the edge of space." Selected students will join either a launch team or a payload design team.

### **Industry Member Internships**

Supports student internships in space science or engineering for the summer or academic year at WSGC Industry members co-sponsored by WSGC and Industry partners.

### **NASA ESMD Internships**

Supports student internships at NASA centers or WSGC industry members that tie into NASA's Exploration Systems Mission Directorates.

### **NASA Academy Leadership Internships**

This summer internship program at NASA Centers promotes leadership internships for college juniors, seniors and first-year graduate students and is co-sponsored by participating state Space Grant Consortia.

### **NASA Centers/JPL Internships**

Supports WSGC students for research internships at NASA Centers or JPL.

### **NASA Reduced Gravity Program**

Operated by the NASA Johnson Space Center, this program provides the unique "weightless" environment of space flight for test and training purposes. WSGC student teams submit reduced gravity experiments to NASA and, if selected, get to perform their experiments during a weightless environment flight with the support of WSGC.

### **Relevant Student Travel**

Supports student travel to present their WSGC-funded research.

# 21st Annual Conference

## TABLE OF CONTENTS

### Preface

#### Part 1: Student Satellite Program: High Altitude Balloon

##### **Balloon Payload Team:**

Amber Bakkum, Carthage College  
Tyler Capek, University of Wisconsin- River Falls  
Patrick Johnson, Carroll University  
Aleysha Kobiske, Carroll University  
Paul Nurczyk, Milwaukee School of Engineering  
Richard Oliphant, Milwaukee School of Engineering

##### **Balloon Launch Team:**

Michael Czech, University of Wisconsin-Milwaukee  
Patrick Johnson, Carroll University  
Tyler Van Fossen, University of Wisconsin-Milwaukee  
Kelly Westphal, Milwaukee School of Engineering

#### Part 2: Student Satellite Program: Rocket Design Competition

##### **1<sup>st</sup> Place – Non Engineering**

**Team Falcon One**, University of Wisconsin-River Falls  
Wesley Barnes  
Joey DeCarlo  
Charlotte Evans  
Glen Gregerson

##### **1<sup>st</sup> Place – Engineering**

**Team Jarts**, Milwaukee School of Engineering  
Ryan May  
Jacob Rice  
Cameron Schulz  
Jordan Wagner

##### **2<sup>nd</sup> Place - Engineering**

**Team Rally Axe**, University of Wisconsin-Madison  
Tyler Van Fossen  
Alex Gonring

##### **3<sup>rd</sup> Place - Engineering**

**Team Rocket Power**, Milwaukee School of Engineering  
Brandon Jackson  
Jonathon Slightam  
Ben Steffes

**Part 3: NASA Reduced Gravity Program**

*Modal Evaluation of Fluid Volume in Spacecraft Propellant Tanks*, Stephanie Finnvik, Steven Metallo, John Robinson, Kevin M. Crosby, Rudy Werlink, Undergraduate Students, Carthage College

*Electric Capacitance Volumetric Tomography ECVT for Fuel Gauging Under Zero Gravity*, Benjamin Butler, Paul Pezzi, Undergraduate Students, University of Wisconsin-Madison

**Part 4: Senior Design**

*In-Situ Resource Utilization: Investigation of Melted Lunar Regolith Simulant JSC-1A*, Matthew Kallerud, Brian Nguyen, Tim Paladin, Anthony Wilson, Undergraduate Students, Milwaukee School of Engineering

**Part 5: Biology and Medical Sciences**

*Optimization of Lipid Accumulation for Biofuel Production Using the Single-celled Alga *Chlamydomonas Reinhardtii**, David Higgs, Department of Biological Sciences, University of Wisconsin-Parkside

*Preserving Muscle Length Requires Simultaneous Stretch and Contraction*, Jonathan M. Van Dyke, Graduate Student, Medical College of Wisconsin

**Part 6: Engineering**

*FeatherSail 2: The Next Generation of Sailcraft*, Collin Bezrouk, University of Wisconsin Madison

*Characterization of Zinc Oxide Nanolaminate Films*, B.J. Oleson, Seth King, Department of Physics, University of Wisconsin-La Crosse

*The Effect of Magnetization Defects on DW Motion in Ferromagnetic Nanowires*, Kyle Kimminau, Physics Department, Marquette University

*Compression After Impact: Damage Characterization of Multi-Directional 10-Ply Carbon-Epoxy Prepreg Laminates Subject to Quasi-Static Impact Force*, Marco Lo Ricco, Graduate Student, University of Wisconsin-Milwaukee

*Experimental Determination of Flow and Heat Transfer Correlations for Passive Regenerators*, Stefanie Knauf, Graduate Student, University of Wisconsin-Madison

*Symbolic Computation Tools in Spacecraft Design Methods*, Capri Pearson, Undergraduate Student, University of Wisconsin-Madison

*Modeling Complex Dynamics with Symbolic Computation Software*, Collin Bezrouk, Undergraduate Student, University of Wisconsin-Madison

*A Tool to Create Stories About Software Evolution*, Mark Mahoney, Carthage College

*Experimentation for Diagnostic Algorithm Benchmarking*, Callie Kwiatkowski, Undergraduate Student, University of Wisconsin-Milwaukee

## **Part 7: Physics and Astronomy**

*Structure and Behavior of AWM and MKW Clusters*, Michael Ramuta, Undergraduate Student, University of Wisconsin-Madison

*Big Bang Blackbody Simulator*, Sara Stanchfield, Undergraduate Student, University of Wisconsin-Madison

*Cancellation of Space-Based Interference in Radio Telescopes*, Lou Nigra, Graduate Student, University of Wisconsin-Madison

*Detection of Non-Einsteinian Gravitational Waves Using a Pulsar Timing Array*, Sydney J. Chamberlin, Graduate Student, University of Wisconsin-Milwaukee

*Extracting Equation of State Parameters from Black Hole-Neutron Star Mergers*, Benjamin D. Lackey, Graduate Student, University of Wisconsin-Milwaukee

*Towards a Better Understanding of Dark Matter Halo Structures Around Galaxies*, Melissa Wheeler, Undergraduate Student, University of Wisconsin-La Crosse

*Identification of Crystallized Ice on Kuiper Belt Objects*, Victoria Hartwick, Undergraduate Student, University of Wisconsin-Madison

*Using Networking Algorithms to Assess the Environment of Galaxy Groups*, Ali M. Bramson, Undergraduate Student, University of Wisconsin-Madison

*Magnetohydrodynamic Turbulence at High-Latitude Regions of the Milky Way*, Nickolas Pingel, Undergraduate Student, University of Wisconsin-Madison

*Studying Interstellar Shells in our Milky Way Galaxy*, Shauna Sallmen, Department of Physics, University of Wisconsin-La Crosse

*Studying in Neutral Hydrogen Shells in the Interstellar Medium*, Elizabeth M. Tennyson, Department of Physics, University of Wisconsin-La Crosse

**Part 8: Education and Public Outreach**

*Round 2: Flight, Floating, and Mars Courses*, Sarah Desotell, Department of Physics, Ripon College

*A Celebration of Life!*, Barbara Bielec, BioPharmaceutical Technology Center Institute

*Biotechnology Teacher Training*, Barbara Bielec, BioPharmaceutical Technology Center Institute

*Spaceflight Academy for CESA District #5*, Brad Staats, Spaceflight Fundamentals, LLC

*Promoting the Computation Science Initiative (ProCSI) Summer Program*, Dan Melanz, Undergraduate Student, University of Wisconsin-Madison

*Rocket Science for Educators; K-12 Techniques for Science Technology Engineering and Mathematics*, Todd H. Treichel, American Institute of Aeronautics and Astronautics and Orbital Technologies Corporation

*Teaching Teachers about Astronomy*, Coggin Heeringa, Crossroads at Big Creek

*Spanish Translation for Astronomy Outreach*, James M. Lattis, UW Space Place, University of Wisconsin-Madison

**Appendix A: 21<sup>st</sup> Annual Conference 2011 Program**

# **21st Annual Conference Part One**

Student Satellite Program  
High Altitude Balloon

# WSGC Elijah High Altitude Balloon 2011 Summer Payload Team

## Final Report

August 17, 2011

Amber Bakkum<sup>1</sup>, Tyler Capek<sup>2</sup>, Patrick Johnson<sup>3</sup>, Aleysha Kobiske<sup>3</sup>, Paul Nurczyk<sup>4</sup>, Richard Oliphant<sup>4</sup>, William Farrow<sup>4</sup>

<sup>1</sup>Carthage College, <sup>2</sup>University of Wisconsin-River Falls, <sup>3</sup>Carroll University, <sup>4</sup>Milwaukee School of Engineering

### Abstract

The payload team brainstormed several experiment ideas to be sent in a high altitude balloon. Once the team settled on three experiments - an experiment to determine payload orientation using photodiodes, an experiment to explore the functionality of a Stirling engine in the upper atmosphere, and an experiment to measure ion density as a function of altitude - research and fabrication began. The team learned how to machine parts, solder and re-solder wires and how to budget money and time. The launch was successful though only two experiments were flown and one recovered. The internship taught the team members skills to be better scientists and engineers through experience and mistake.

### Introduction

**Beginnings.** This past summer will be remembered by the payload team for many reasons, but none more than the experience we gained and the friendships we forged. Though the final product of our hard work did not culminate into success, it would be foolish to say that we did not have a successful summer. The valuable amount of experience that we gained coupled with the skills each one of us learned not only strengthened us as individuals, but it instilled a passion for the sciences in each of us. The following report details what we set out to do, and reflects upon our experiences during the summer.

The first few weeks of the program centered around research and getting to know each of our teammates. Dr. William Farrow, our team advisor, had developed multiple team building exercises as ice breakers. We did not complain, because most of these exercises entailed playing with Legos. We were also charged with the task of researching possible experiments. These experiments could either look at some sort of natural phenomena, or it could be an experiment designed to improve technology and the payload. Overall, we came up with over 20 ideas. After more research we were able to concentrate on three experiments, based on our interests and the

feasibility of each experiment. These three experiments were the ion density counter(Paul and Amber), Solar Orientation(Aleysha and Richard), and a Stirling Engine(Patrick and Tyler).

**Finale.** Since we launched during the week, and the Launch Team was unavailable, the Payload Team was presented with an excellent opportunity. We were tasked with launching and tracking the balloon. Though all is well did not end well, as we watched the payload fall out of the sky in two pieces. Upon retrieving the payload, we eventually found that all of the battery packs along with the Arduino in charge of taking data for the solar tracking system had fallen out of the payload. Unfortunately, there was not enough data gathered, even for ion counter (whose Arduino miraculously stayed aboard). Though it was tough to swallow such a defeat, the summer was still a success do to the great learning experience that we all had.

### Stirling Engine Experiment

**Theory.** The idea to build a Stirling Engine stems from the idea that Stirling engines become more efficient as the altitude increases. Theoretically this would make them supremely efficient in a near space environment. To understand this, it is better to first look at how a Stirling Engine operates. A Stirling Engine uses the idea of the Stirling Cycle in output work. A four step process, the Stirling Cycle is visually represented in Figure 1. The following steps are provided by Dr. James Senft in his book *Ringbom Stirling Engines* (Figure 1):

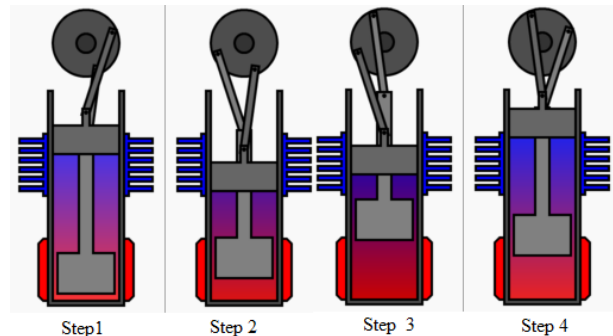


Figure 1: Each of the steps for the Stirling Cycle Engine

1. In the first step of the ideal Stirling Cycle, the displacer remains stationary all the way into the hot end of the cylinder. Virtually all of the air is in the cold space adjacent to the piston. The piston is made to move inward, compressing the air. Ideally this will take place at the temperature at the cold end. Typically, the volume is reduced half, and the energy required to carry out the compression is usually supplied by a rotating flywheel through a linkage.
2. In the second step of the Stirling cycle, the piston is held stationary and the displacer is moved right up to the piston. During the movement, engine air flows around the displacer and ends up in the hot space of the cylinder where its temperature and pressure rise. This is the transfer stroke and it effects the heating of the engine air. The mechanical energy required for the displacer movement is relatively small and again is usually supplied from the flywheel.
3. With the engine air now at a higher pressure, work can be extracted by letting the piston be pushed outward. The displacer moves outward right along with the piston. This keeps the engine air completely in the hot space during the expansion, keeping pressure as high as possible. Ideally, the expansion process of the Stirling is isothermal. The isothermal expansion takes place until the piston reaches its original outermost position.
4. In the final step of the Stirling cycle, the displacer moves into the hot end to transfer the air back to the cold side. Again the piston is stationary during this transfer stroke and the

only effect is the cooling of the engine gas. Since the displacer rod is usually made very small in diameter compared to the piston, the volume of the engine air is essentially constant during both of the transfer strokes. At the end of the cooling transfer stroke, the displacer is all the way into the hot end and the piston is at its outer extreme, which is the starting point of the compression stroke, so a complete cycle has been described.

A traditional engine often requires that some form of combustion be present within the engine. In order for combustion to happen, you need three things: a fuel source (often gasoline or oil), some sort of spark (spark plug), and oxygen. However, in high altitudes such as near space, there is little to no oxygen present. Thus, the traditional engine becomes less efficient to the point that it will not work at certain altitudes. A Stirling Engine on the other hand, does not need combustion of any sort. Actually, because there is less air in the upper echelon of our atmosphere, there is less air resistance on the Stirling Engines moving parts. This means that it would theoretically become more efficient as altitude increases, provided that the engine had an adequate heat source of course. Building an adequate Stirling Engine that would hold up in such an environment would not be as clear cut.

**Process.** The plans for the Stirling Engine we decided to use were derived from an online source. The engine (Figure 2), dubbed The Jan Ridders LTD Stirling Engine, seemed to be a simple yet adequate design for us to use. Being ambitious, we decided it was possible to fabricate all of the parts in the Machine Shop upstairs. After making every piece Patrick discovered that some of them were slightly disproportionate, and he had to re-fabricate them. An even bigger problem arose when our 'air tight' silicon glue turned out to be less air tight than advertised and very difficult to use. While Patrick was dealing with the Stirling Engine and its parts, Tyler worked on the Secondary systems for the experiment. This entailed three main components: electrical, heat sink creation, and the start motor. The electrical interface centered around an Arduino Micro-controller. With the Arduino, not only was it possible to supply power to all of the sensors and log the resulting data, but we could also control a starter motor and provide a consistent heat source. Along with the Arduino, the electrical components also included a CNY70 Reflective Optical Sensor with Transistor, two LM35CAZ Precision Centigrade Sensor, and an AMS 5812 absolute pressure sensor. The purpose of the optical sensor was to sense when the engine's flywheel made a complete rotation. From there, with the help of a little bit of computer code, we would be able to determine the engine's revolutions per minute. We needed the pressure sensor to determine how much air was producing drag on the engine. Last, the temperature sensors were an important tool for determining how warm our heat sink needed to be at any given moment. Finding an adequate heat source to produce our heat sink was quite possibly the most frustrating part of the entire summer. We decided that heating foils would provide the best source of heat. We ended up burning up two of our heating foils trying to get the Stirling Engine to start (with an input of 40 volts when the heating foils are rated for 115



Figure 2: Stirling Engine

volts). The possibility of the Stirling Engine stopping while in flight was another problem we had to plan for. In order to restart the Stirling, which was not self starting, we needed some sort of kick-start motor that would only engage when the Stirling Engine stopped operating. Using Arduino Code, it was possible to hook such a motor up to a Servo Motor. The code would tell the Servo to move the motor into position, and then the code would initiate the kick-start motor until the Stirling was operating again.

**Results.** Despite every effort made by Patrick in order to get the Stirling Engine operational, we were not able to get it up in the air. We definitely approached this experiment in a way that was way too ambitious for our skill set at the time. Though this left a bitter taste in our mouths, the experience gained coming out of this opportunity was life changing. However, knowing what we know now about how we approached our experiment, we would take the ambitious path every single time. Even if we knew it wasn't going to work out how we planned. Our goal was to learn and become better because of it, and where is the learning in taking the easy path. Some of the skills we learned never would have come to fruition had we not taken the path less traveled.

### **Solar Orientation Experiment**

The payload team had interest in using solar equipment from the beginning of the brainstorming sessions at the start of the summer. After tossing ideas around it was decided that using some sort of an array of solar sensors on the outside of the payload to track the orientation of the payload in relation to the sun would be pursued.

To start, we explored different types of solar sensing components: photo-resistors, photo-transistors, and photo-diodes. Understanding that the payload would be climbing to high altitude, very low pressure, and sub-zero temperatures, we were able to determine that photo-diodes would be best. Not only is their behavior very stable throughout these conditions, but their reaction time is among the quickest. From watching other projects' flight videos we expected our payload to behave similarly. Meaning, sometimes, the payload would be swinging and spinning wildly. We knew the photo-sensors would have to be able to react very quickly in order to accurately tell us the behavior of the payload.

The next step was to find a photo-diode to work with. We narrowed the search by size and price, looking for small size and mid-price photo-diodes. After this process we ordered seven that met our criteria and began running tests to find which was best suited for this project. Using Matlab and a LabJack to read several analog inputs we ran tests to see which photo-diode had the best reaction time, most stable readings in sunlight, and sensitivity to sunlight. At the start of these tests we discovered that the photo-diodes were not very directional, meaning they would react to light incident from the side and not just directly above them. For this project we needed a much more direction-specific sensor. Placing a short (about an inch long) black tube over the photo-

diode we were able to block any light from the sides and made the photo-diodes react very accurately to the change in light directly above them. After exploring different tubing, we found that *Panera Bread* drinking straws are black and fit snugly over the photo-diode casing. We thank them for their donation of several drinking straws.

The next obstacle was saturation. The photo-diodes worked well indoors and in outdoor ambient light, but when pointed directly at the sun on a clear day they would come close to reaching their maximum, or saturation. We were warned, too that once above the cloud layer the sun's rays are even more intense. Therefore, we needed some kind of filter. We tried white printer paper and found that it worked just swimmingly. It was placed inside the black tube just a millimeter above the photo-diode. It reduced the amount of light incident on the active area of the photo-diode and provided more travel in the photo-diode's range before saturation.

We finished testing all of the photo-diodes and were able to make the final decision of which to go with. The results from our tests favored one photo-diode highly above the others so we ordered 26 more of them.

Usually, the high-altitude balloon payload is a simple box shape made of 2-inch foam. We decided however that we needed a spherical shaped payload. Using the same pink insulating foam we designed a spherical payload that would be constructed by cutting disks of differing sizes and stacking them. First, a small model of about six inch diameter was made using only ½ inch thick foam. We learned about cutting the foam with a hot-wire cutter and using course



sandpaper to smooth the edges. The result looked promising so we pursued a full-size payload of 23-inch diameter. This soon became quite a task and time consuming. We cut squares out from the middle four disks to create a box for the experiments. With the finished product we weighed it and were alarmed to see it tip the scale at 5.8 pounds! With a six pound limit this was problematic so we set to work enlarging the inside box and scraping and cutting foam away where we could. These efforts brought the weight down to 3.5 pounds which was decent but not low enough. The other experiments plus batteries were

going to bring the total weight well over the six pound limit. We decided to take the knowledge gained from constructing this foam sphere to make another smaller, more efficient sphere and much quicker this time. The new foam spherical payload was finished in three days (versus the two weeks for the first) and only weighed in at 1.5 pounds.

By this time, the 26 selected photo-diodes had arrived and we needed to leave the LabJack behind because it only could read four analog inputs. We moved on to using a multiplex board that can read up to 48 analog inputs through an Arduino microprocessor. To record data a data logging add-on board was also utilized. This board stores data collected by the Arduino to an SD card and gives each entry a time stamp. The picture at the right shows the Arduino, multiplex, and data logger boards stacked from bottom to top.



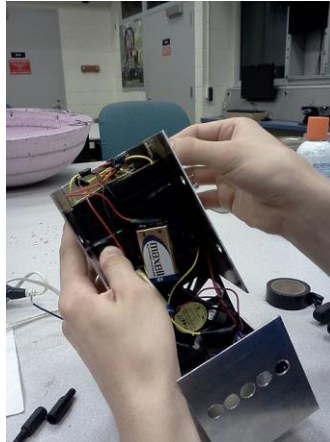
Earlier in the summer we had been directed to use an operational amplifier with our photo-diodes. We weren't very experienced with electronics and circuits and so after a lot of trial and error and internet searches and frustration we went to the MSOE technical help desk. They helped us find our misunderstandings and discover the proper circuitry for our photo-diodes. From this experience we also realized that we would not be able to power all 26 photo-diodes from the 5 volt source that the Arduino provides.

Once we figured out a circuit that worked for us we began soldering. We had a battery pack for every six diodes, resulting in a total of four battery packs. Each battery pack had five batteries which supplied a total of seven and half volts. Since we needed a five volt supply we had to use a voltage regulator. We were able to get some helpful assistance from the electrical engineering department at MSOE with the voltage regulator and in perfecting our circuit. While working on our circuit there were times we would solder everything, desolder it all, and then resolder it again. From this we were able to gain some expertise in soldering. To connect wires to the diodes we twisted them together and then secured them with heat shrink tubing. We didn't want to solder them for fear of over heating the diode with the soldering gun. Then in order to secure the twenty-four diodes in holes around the payload we used Great Stuff. This was the last step in our construction so we then began our three hour test. During the three hour test we wanted to make sure the batteries lasted and the data didn't show any irregularities. However after the three hours were up we looked at the data only to find twelve seconds of data. After we found the cause of this and fixed it we ran another test. This test we only ran for an hour but the data we got looked promising.

When it finally came time to launch we secured everything in place and watched it take off. When the payload was descending we noticed that the lid had separated from the payload. After finding the payload in a cornfield we noticed a lot of our equipment missing. At some point during the launch the Velcro holding the lid to the payload failed and all five of our battery packs, arduino, multiplex board, data logger with SD card, and circuits had fallen back to Earth. Therefore we had no data to analyze. It was estimated that we would have had approximately 1.1 million data points to analyze so losing the data wasn't the worse thing, however it was still



be held at ground. Perforated circuit board was used for the circuit connecting the electronic components. We ran into an issue with the aluminum screening, as solder does not adhere to aluminum, however we overcame this by using brass screening. After constructing the aluminum housing, we assembled the circuit inside the housing and closed it and tested the switches and “pull before flight” pins.



*The assembly of the ion counter into the aluminum housing.*

Once the ion counter was assembled we began ground tests to establish the functionality of the device. We began by measuring the readout at ground level. This provided us with a different voltage than the Scientific American article cited for ground level. Our voltage hovered around 0.7 Volts in the lab, when we were supposed to get numbers closer to 0.1 millivolts. During ground testing, we held a flame near the intake fan to provide a spike in ion density. The measurement quickly rose to approximately 3 Volts, due to the flame. The Arduino microprocessor only reads positive voltages, so we had to keep the switch at negative 5 Volts. Since the ion counter was working, despite our voltages being higher than those cited in the article, we could correlate the voltage to altitude. We would be unable to learn the exact ion density, but we would learn how the density changed based on altitude.

We then tested the ion counter in a vacuum bell jar and saw that the voltage fell as more air was extracted. The bell jar has a minimum pressure of around half an atmosphere and the voltage was approximately halved, we saw that the relationship between ion density and pressure is linear inside the bell jar. Finally, we did a three-hour endurance test to ensure the device would function for the entire flight. After the three-hour test, the test data revealed fairly constant voltages and lasting batteries.



*The ion counter in the vacuum bell jar with a voltmeter to monitor changes.*

To prepare for the flight, we attached the ion counter to the payload using Velcro and rope. The Arduino microprocessor was soldered to the output wires and was programmed to record voltage every half second. This was due to the speed of the balloon during ascent, as we wanted as many data points as possible. When assembling the balloon, we turned on the switches, but the “pull before flight” pins did not allow the circuit to be closed until the very last moment.

The payload was recovered just outside our launch site. We retrieved the ion density data since its Arduino microprocessor stayed inside the payload. The data suggested that about an hour into the flight the ion counter was switched off by something inside the payload that had detached. Despite the setback, the data showed some variations. The voltage did decrease as it gained altitude, but there was a range of altitudes (7000-20500 feet) where the voltage spiked and it peaked at five volts at 11000 feet. Approximately 25 minutes into the flight, the voltage started to approach zero and for the remaining time that we collected data it approached zero. Although it did not reach to the peak of the flight, the data collection was successful as we did see a correlation and it was not a linear relationship.

## **Arduino**

**Basics.** An Arduino is a microprocessor that is not only able to process information sent out by various sensors, but it is also used for controlling motors, LED arrays, and more! In order to use the Arduino, it is imperative to learn the Arduino Programming Code. This form of computer code was mostly based on the C programming language, with just a few unique quirks allowing it to operate with the Arduino.

**Implementing Arduinos.** Playing around with the Arduino ended up being one of the most intriguing portions of the entire summer. Since the Solar Orientation Experiment demanded more than twenty inputs, we were in need of a multiplex board. The multiplex board, which you can find at Mayhew Labs website, allows for 48 inputs for data taking. The code for the Multiplex was pretty complex, but Richard charged through it in order to get a final product for the Solar Orientation Experiment. Since both SD loggers had certain digital inputs/outputs that were used by each of their respective boards, there was a challenge to find where we could hook up all of the auxiliary systems. For the ion detector and the Stirling Engine’s sensors, it was easy enough to hook up each of those to the analog input. The temperature sensors, pressure sensor, and the ion detector all had pretty straight forward codes which read the voltage signal coming out of each. The Solar Orientation experiment used the same sort of idea, with the exception of the implementation of the Multiplex boards unique features. Both the signal coming from the temperature sensor and the pressure sensor had to be manipulated in order to get the correct reading as well. The rpm counting optical sensor required a different approach. The reflective photo-sensor had a similar voltage output as the others, however much more code manipulation was needed in order to get the revolutions per minute of the Stirling Engine. In order to get this to work, the sensor had to be reading data constantly. Every time the voltage would go below a set parameter, it would log it as a revolution. Finally, a *while loop* was used to count up the number of revolutions over a set period of time. The longer the period of time, the better the resolution for this reading. Overall, the Arduinos were a very exciting venture for us to take up.

## References

### Stirling

1. "Action of a Beta Type Stirling Engine." *Wikipedia*. Web. 16 Aug 2011. <[http://en.wikipedia.org/wiki/Stirling\\_Engine](http://en.wikipedia.org/wiki/Stirling_Engine)>. (Figure 1)
2. Senft, James. *Ringbom Stirling Engines*. New York: Oxford University Press, USA, 1993. 15-20. Print.
3. Ridder, Jan. "Low Temperature Stirling." *Jan Ridders Modelbouw*. N/A, 15 04 2009. Web. 16 Aug 2011. <<http://www.machinistblog.com/downloads/LTD%20Stirling.pdf>>.
4. Vishay, . "Reflective Optical Sensor with Transistor Output." *Vishay Semiconductors*. N/A, 11-Mar-11. Web. 16 Aug 2011. <<http://www.vishay.com/docs/83751/cny70.pdf>>.
5. Nation Semiconductor, . "Reflective Optical Sensor with Transistor Output." *LM35 Precision Centigrade Temperature Sensors*. N/A, November 2000. Web. 16 Aug 2011. <<http://www.national.com/ds/LM/LM35.pdf>>.
6. Servoflo, . "AMS 5812 Amplified pressure sensor with an analog and I<sup>2</sup>C output." *AMSYS*. N/A, November 2008. Web. 16 Aug 2011. <<http://www.servoflo.com/downloads/ams5812.pdf>>.

### Arduino

1. ARDX, . "Arduino Experimentation Kit." *OOMLOUT*. N.p., n.d. Web. 16 Aug 2011. <<http://www.oomlout.com/a/products/ardx/>>.
2. Adafruit, . "Adafruit GPS logger shield kit - v1.1." *Adafruit*. N.p., n.d. Web. 16 Aug 2011. <<http://adafruit.com/products/98>>.
3. Adafruit, . "Adafruit Data logging shield for Arduino - v1.0." *Adafruit*. N.p., n.d. Web. 16 Aug 2011. <<http://adafruit.com/products/243>>.
4. Mayhew Labs, . "Mux Shield." *Mayhew Labs*. N.p., n.d. Web. 16 Aug 2011. <<http://mayhewlabs.com/products/arduino-mux-shield>>.

### Ion Density

1. Carlson, Shawn. "Counting Atmospheric Ions." *Scientific American* 19 Sept. 1999

## Elijah Project Balloon Launch Team

### Balloon Tracking Methods

Mike Czech (UW-Milwaukee) Tyler Van Fossen (UW-Madison)

Patrick Johnson (Carroll University) Kelly Westphal (MSOE)<sup>1</sup>



#### **Abstract**

The Elijah Project provides students with the opportunity to develop and conduct experiments in the near-space environment of Earth's atmosphere via high-altitude weather balloons. The balloons reach altitudes up to and sometimes exceeding 100,000 feet before bursting. The Launch Team is responsible for overseeing the successful launch, tracking, and recovery of the balloon and science payloads, along with generating flight path predictions. Much of the Launch Team's job is to coordinate launch sites with desired landing zones based on the weather, along with identifying recovery obstacles. Using MapPoint software, the experienced flight path can be plotted on a map by receiving the GPS location of the balloon during flight. Chase vehicles are equipped with receiving antennae, which allows the team to ideally meet the descending payload at the landing site.

---

<sup>1</sup> A special thanks to the Wisconsin Space Grant Consortium and the National Space Grant College and Fellowship Program for funding the program. Additional thanks to the team's leader, Dr. William Farrow of MSOE.

## Elijah Project Overview

For nearly a decade, the Elijah Project has sent a variety of science payloads into the near-space environment of Earth's atmosphere via high-altitude weather balloons. The program is sponsored by the Wisconsin Space Grant Consortium (WSGC) and the National Space Grant College and Fellowship Program (NASA). The student-run experiments are meant to investigate the phenomena of the stratosphere at altitudes up to and sometimes exceeding 100,000 feet. Past experiments include efficiency of solar panels, buildup of static charge, quantification of atmospheric mercury, and many more. Payloads must comply with FAA regulation to qualify for a permit-free launch.

Launches are conducted a few times each year for different payload groups; Payload Team, Instrument Development Team, and other WSGC affiliated teams. This paper focuses strictly on the responsibilities of the Launch Team, which are as follows:

- Identify potential launch sites
- Determine desired landing locations
- Monitor weather for available launch windows
- Predict flight path to coordinate launch site with landing zone
- Prepare the balloon, tracking payloads, and attachments for launch
- Track balloon from chase vehicles
- Safely recover the payload

## Determination of the Launch Site

Launch sites are chosen based on the weather conditions for the selected launch date and the resulting flight path prediction (see Weather Tracking for Flight Prediction). Usually a



Figure 1: Map of Wisconsin launch sites.

smaller town in Western Wisconsin is selected due to the prevailing westward winds of the region to avoid Lake Michigan. There must be a free wireless hot spot nearby (typically McDonald's) for a final check on the weather to ensure that a safe landing zone will be achieved. Additionally, a large public field is required with minimal obstructions to the rising balloon. These fields are typically located via the satellite feature of Google Maps. Previous launch sites meeting all of these requirements are shown in Figure 1 to the left, which include Mount Horeb, Fennimore, Reedsburg and Chippewa Falls. Preference is given to sites that are closest to Milwaukee, since that is where the team is stationed, but weather ultimately determines the site.

## Preferred Landing Zones

Selection of the launch site is an iterative process to land the payload in a desired landing zone. Besides the obvious avoidances of water bodies, areas with high population densities, or government restricted areas, obstacles that obstruct the chase vehicles' lines of sight to the pod are also a problem. Therefore, regions with rolling hills or excessive trees are also avoided. No zone guarantees successful recovery, but by avoiding high-risk areas, we can increase the probability. The remaining landscapes that are most desired are typically farmland or countryside. Additional preference is given to areas in Southeastern Wisconsin for time and fuel efficiency, since the team is based in Milwaukee. **Error! Reference source not found.** below shows the avoidance areas as darkly shaded, with the preferred landing zones as lightly shaded.

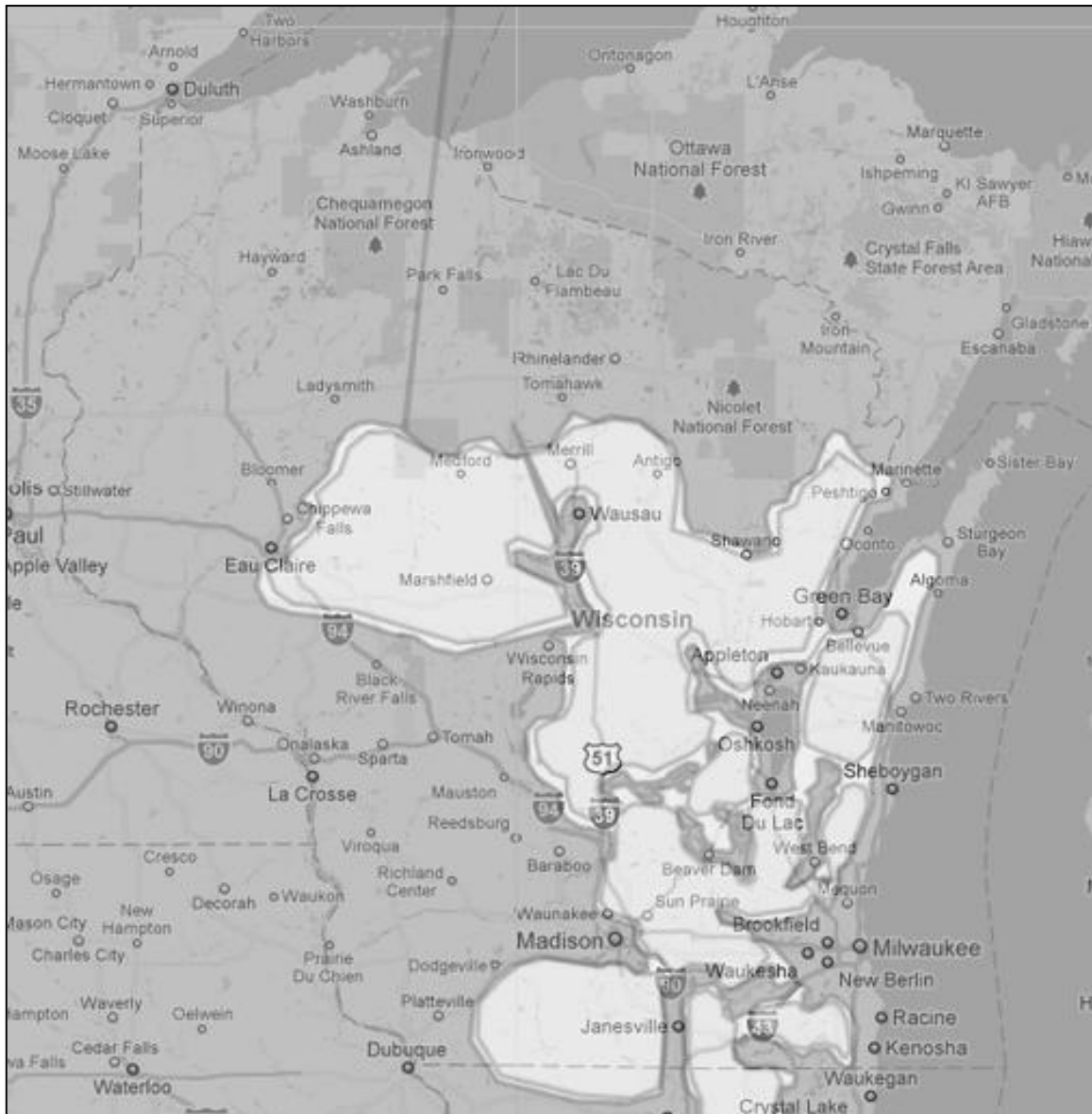


Figure 2: Map of Wisconsin showing avoidance areas (dark) and preferred landing zones (light).

## Weather Tracking for Flight Path Prediction

Weather and balloon tracking is done online via Near Space Ventures, Inc.'s web page. The site requires inputs of date, time, location, elevation, anticipated balloon performance, and the nearest weather station. The site then predicts and generates a map of the flight path of the balloon based on predicted wind patterns throughout the atmosphere generated by that weather station's measurements. Shown in Figure below is one of the outputted flight path predictions.

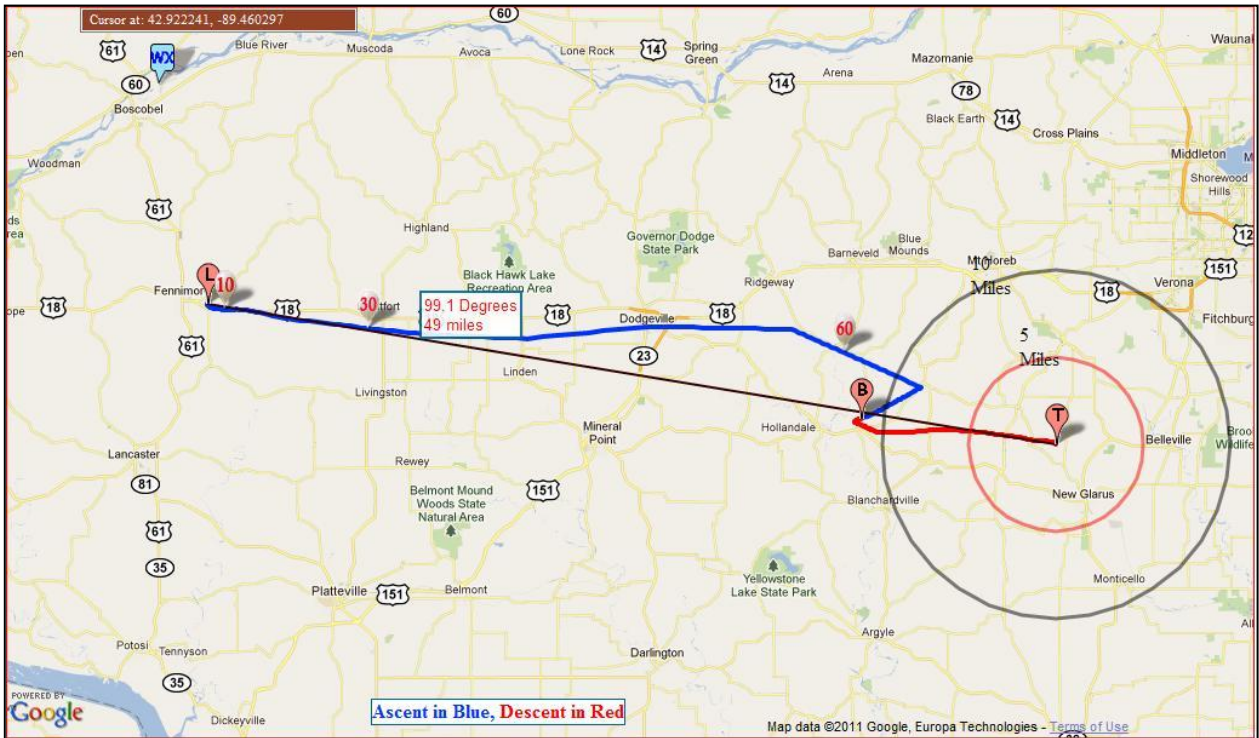


Figure 3: Example of a flight-path prediction generated by Near Space Ventures Inc.'s online tool.

Starting one week before a launch, the analysis is run daily for each potential launch site to track any pattern changes. If none of the existing launch sites predict the payload landing in a desired area (see Preferred Landing Zones), a new site is selected. On the morning of the launch, a final balloon tracking prediction is run as a last-minute check.

Additionally, jet stream analyses are used to determine upper-atmospheric conditions. The grey areas in Figure represent strong jet stream activity, which affects the payload with violent winds and turbulence. The payload may be damaged and/or the balloon will travel a great distance making tracking difficult. When strong jet stream activity is present within the launching region, launches should be postponed until activity subsides.

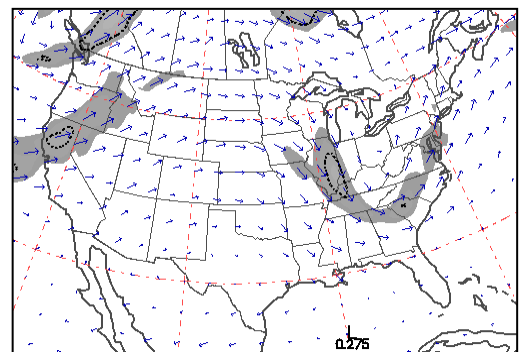


Figure 4: Map of US jet stream activity.

## Launch Day Preparation and Setup

The balloon setup consists of a parachute, the science payload, a tracking pod, and a secondary tracking pod (in that order). The parachute is secured approximately 20 feet below the balloon, and slows the descent rate to around 1500 fpm. This speed minimizes the risk of impact damage to the payload while preventing excessive travel during descent. The primary and backup tracking pods are purchased from StratoStar Systems and are secured a few feet below the parachute. Heavy-duty snap swivels shown in Figure 5 to the right and 50-pound-test fishing line are used as the connecting hardware.



Figure 5: Snap swivels are used as the connection points between components.

When all components have been prepped and are ready for flight, the balloon is filled with helium. The amount of helium is dependent on the weight of the tracking pods and science payload, but needs to provide at least 1.5 times the amount of lift as the total weight of the system. Lift is measured with either a fish scale or a bucket of pre-weighed dead weight. More lift ascends the balloon more rapidly, but reduces the peak altitude achieved. This is a more desirable result, however, than to under-inflate the balloon and have it travel great distances. When handling the balloon, the team must wear gloves because the oils from human skin start to degrade the latex and can cause pinhole leaks, which cause the balloon to rise to excessive altitudes before bursting. Higher altitudes typically relate to farther tracking distances.

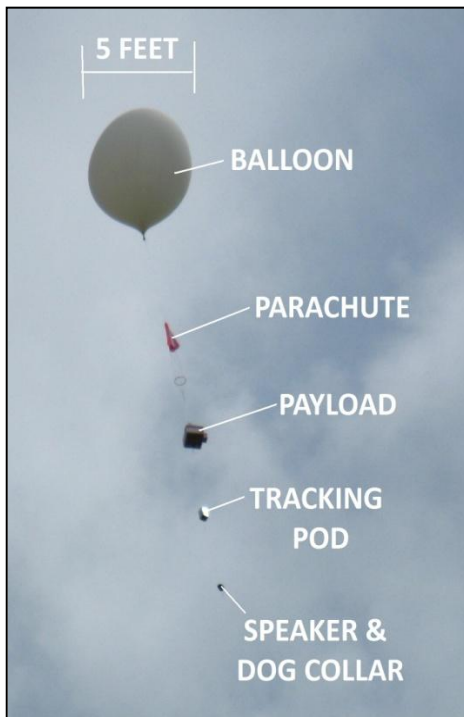


Figure 6: The 2010 balloon setup shown to depict approximate spacing.

To depict the approximate spacing of the components, Figure 6 to the left shows last year's setup, which utilized a speaker and dog collar as the secondary tracking components. The order of the components has also been altered since last year. When the balloon is launched, it is approximately 5 feet in diameter with the entire setup extending roughly 40 feet below that. An interesting fact is that by the time the balloon bursts, it will have expanded to nearly 40 feet in diameter.

## Tracking Methods

Once in flight, the primary tracking pod pings out a GPS coordinate along with its speed and direction of motion every 30 seconds or so. The signal is received by antennae secured to the chase vehicles and plotted on a map using MapPoint software. It is the job of the Launch Team to coordinate the actual flight path with the predicted one, and hopefully meet the payload at the landing site. If the team is too far away from the payload when it lands, the line of sight will be broken and the final coordinates will be from when the balloon was still in flight. If this is the case, interpolation of the MapPoint path offers an approximate landing location. For a “second opinion” the secondary tracking pod’s signal is received by ham radio (amateur radio) receivers and recorded online; accessible in the field via Smartphones.

## Recovery Methods

Several methods exist to recover the payload from less than ideal situations. A majority of the time the recovery effort will experience at least one of these conditions: disrupted line of sight causing the final GPS point received to be above the ground, landing in trees, or landing on private property. The third situation is handled by simply asking permission of the landowner to avoid trespassing charges. Most often this will solve the problem. However, the first two complications require more complicated solutions and are discussed in detail below.

**Interpolation of flight path.** When line of site is broken between the tracking pod and the receiving antennae of the chase vehicles, the final resting location of the payload is unknown. However, the rate of descent can be easily calculated based on the difference in altitudes and time interval between pings. Likewise, the horizontal speed can be obtained, so that we know the full velocity vector. The time remaining between the last ping and touchdown is calculated using Equation 1, where  $y$  is the elevation of the landing site,  $y_0$  is the last known altitude,  $v$  is the descent rate,  $t$  is time, and  $a$  is the acceleration of the descent (zero).

$$(1) \quad y = y_0 + v * t - \frac{1}{2} * a * t^2$$

Solving for time, the horizontal distance traveled in the direction the payload was traveling during the last ping can be approximated using the same equation. However,  $y$  becomes the horizontal distance traveled since the last ping,  $y_0$  is the starting horizontal position (zero), and  $v$  is the horizontal speed. An extension line on the MapPoint map is then drawn to predict the final resting location of the payload. This interpolation method substantially reduces the guesswork involved by narrowing down the search area.

**Recovering the payload from tress.** One of the greatest obstacles when recovering a payload exists when trees are present. Because the payload is traveling with both horizontal and vertical speed, the likelihood of tree landings increases and simply cannot be avoided other than

ruling out landing zones with high tree density. The launch team acknowledges the high probability of tree landings and is prepared in the following ways:

- *Bean bags*. When the payload is stuck at a lower height, a bean bag with a rope tied to it can be thrown over the payload or branch in attempt to dislodge it.
- *Slingshot*. Similar to the bean bag approach, a slingshot can be used for greater heights. A moderately-sized fishing weight with a string tied to it is launched around the branch in which the payload is lodged. The small string is tied to a rope so that the rope can be fed up to the branch for greater leverage.
- *Chainsaw*. If the branch is too large to pull down with the rope, a manual chain saw can be fed up to the branch via the rope. The back and forth motion of the chain across the branch slowly cuts down the payload.

### **Conclusion**

The Elijah Project Balloon Launch Team utilizes existing methods to successfully launch, track, and recover balloon science payloads. Tracking pods are available from StratoStar Systems and are compatible with MapPoint software, while weather tracking and flight prediction software is available through Near Space Ventures, Inc. Two of the greatest assets of the Launch Team are organization and communication to ensure that they are prepared for a variety of situations that may arise on launch day. After all, having the appropriate materials for a launch is crucial. In short, the Elijah Project is an extremely beneficial program in that it enables students to develop their professional careers with a unique hands-on work experience.

# **21st Annual Conference Part Two**

Student Satellite Program  
Rocket Design Competition

## **Flight of the Falcon**

Glen Gregerson

Department of Physics  
University of Wisconsin-River Falls

Charlotte Evans

Department of Physics  
University of Wisconsin-River Falls

Joey DeCarlo

Department of Physics  
University of Wisconsin-River Falls

Wesley Barnes

Department of Physics  
University of Wisconsin-River Falls

### **Abstract**

Team Falcon One competed in NASA's Wisconsin Space Grant Consortium (WSGC) sponsored Collegiate Rocket Competition, earning first place in the non-engineering category. The rocket contained a radio-controlled parafoil deployed from side-bay doors in order to land as closely as possible to a target flag on the ground.

### **Competition Parameters**

The mission for the 2011 Wisconsin Space Grant Consortium's student rocket design competition was to create a rocket that reached a minimum altitude of 2000 ft with a controlled descent that allowed the rocket to land as close to a designated area as possible. Team Falcon One, from the University of Wisconsin-River Falls, constructed a 5.5" diameter, nine foot tall rocket with a radio-controlled parafoil that was released with side deployment doors. The main parachute will be deployed, via the onboard flight computer, at apogee and will be manipulated by remote control to land the rocket at the designated landing area. The WSGC provided a \$1000 grant to fund construction.

### **Design**

**Concept.** The success of this competition relied on a rocket that not only reached an altitude of 2000 feet, but also allow for a controlled descent such that the rocket would land in a designated area and considered in re-launch-able condition. Team Falcon One designed a rocket that utilized a parafoil as its main parachute, allowing the rocket to be flown to its designated landing area. The control of the main chute was handled by an FM radio control transmitter. To accomplish stable flight, side deployment of the chute was selected. By using this method the rocket remained intact during descent, minimizing swaying which in turn increased stability, and allowed for a horizontal landing. The main parachute bay door deployment was initiated via radio controlled release of locking pins, allowing the spring-loaded doors to open and for passive

deployment of the chute upon contact with the airstream. The rocket was also designed with future mission viability in mind. It had three independent and separable sections; the forward electronics section, mid-ship side-door parachute bay, and the rear engine/fin section. As an added measure of safety, a backup parachute system was included in the design.

**Nose Cone.** The nose cone was made of heavy duty, blow molded, polypropylene with a parabolic shape purchased from LOC Precision. It was 26" long, with an inner diameter of 5.38", shoulder length of 5.0" and weighed only 22 oz. The nose cone was selected for the maximum aerodynamic efficiency while protecting the inner components in the rocket and minimizing weight.

**Body Tube.** The nearly 8' body tube housed and protected the internal components. The body tube was purchased from Discount Rocketry. This body tube had a 5.38" inner diameter and an outer diameter of 5.54" and was made of heavy duty kraft fiber tubing with glassine finish. To further strengthen the body tube, a fiberglass overlay was applied. This body tube was selected because of its lightweight, yet durable strength with a diameter that allowed for the parafoil and other components to safely fit without leaving excess room.

**Internal Framework.** The internal wood framework was designed on AutoCAD and was sent to AK-Models Inc. to be laser cut onto 1/4" and 1/8" aircraft grade birch plywood. This internal framework spanned the entire length of the body tube to reinforce its strength and also took the place of couplers. This framework is shown in figure 1.



Figure 1. The internal framework outside of the body tube. After the pieces were assembled, they were later slid down into the body tube to be secured with glue.

**Electronics Bay.** The electronics bay held the electronics that were used to analyze and control portions of the flight. The electronics were mounted on a piece of 1/4" plywood that slid out of the bay through the forward end when the nose cone was removed. The electronics

mounted in the bay were the Arduino Uno, Remote Control receiver, altimeter and various batteries for power supply. The on-board flight computer, Arduino Uno, was an open source programmable microprocessor equipped with an accelerometer, barometer, GPS module and data logging capabilities. The accelerometer is used primarily as a G-switch to start the program sequence upon sensing launch. The barometer is used to log the altitude. To guarantee proper connections upon assembly at the launch site, all wires leading from the electronics tray to the rocket were connected via a single connector plug.

**Main Parachute Bay.** The main parachute bay held the remote-controlled parafoil that steered the rocket to a successful and accurate landing. The parafoil was a 2.5 meter dual line control stunt kite converted to a four riser parachute. It was steered by two metal-gear, high torque Blue Bird servos from RC-Mart. The parafoil was released when two side, spring-loaded doors opened upon release of a locking mechanism.

**Reserve Parachute Compartment.** Behind the main parachute bay was the reserve parachute compartment. This 60” round silk chute, purchased from Aerocon Systems, was deployed traditionally using black powder charges and rocket section separation. It was deployed via remote control command during our first launch attempt when, after apogee, the main chute did not deploy because of a jammed locking pin. This was also used during our second launch as an air brake to reduce over shooting the landing zone.

**Tail Engine/Fin Section.** The powerful K-513 engine powered this rocket. The fins, which gave the rocket stability during ascent, were laser cut from ¼” birch plywood. They were sized and shaped trapezoidal based on OpenRocket simulations. The fins were slotted into the centering rings that also held the engine in place. These centering rings allowed for maximum strength and stability in the fin section of the rocket. The motor was held in place by an AeroPack Retainer bolted to the engine mount tube, and the other piece simply screwed over the top after the rocket motor was inserted into the rocket. It was made from aircraft-grade aluminum. To further reinforce the rear section, all cavities were filled with spray foam.

**Rail Buttons.** Rail buttons allowed the rocket to utilize a rail launch rod and lift off the pad as straight as possible. The rail buttons were mounted mid-way between the fins and at the forward bulkhead of the parachute bay. They were purchased from Apogee Rockets.

**Remote Control.** The remote control allowed for ground control of the main parachute and deployment of the reserve parachute. The remote control was a HiTech six-channel FM transmitter/receiver. The control operator had independent control of the right-turn and left-turn servos. This also allowed for pitch control by applying the same directional control to both servos at the same time.

**Diagram of Rocket.** A diagram of the rocket’s features is shown in figure 2. The actual rocket is shown in figure 3.

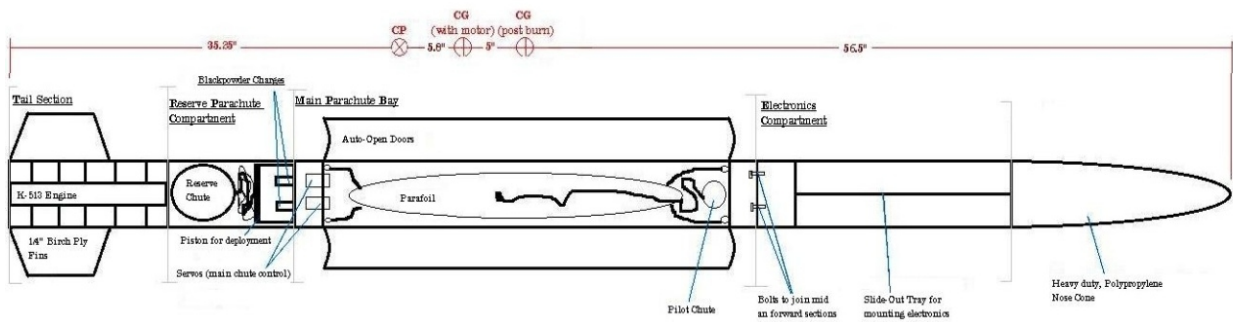


Figure 2: Detailed diagram of the rocket explaining its different features and components. The CP, CG<sub>1</sub> and CG<sub>2</sub> are all clearly identified.



Figure 3: The finished rocket prior to launch.

## Performance

The results of the flight during key aspects are described below.

**Launch.** Both flights had successful launches. On our first launch we were told by the range safety officer to leave the launch rail vertical. Our simulations showed that given our stability we should angle into the wind roughly  $1^\circ$  from vertical for every 1 mph wind speed in the 3-10 mph range, consistent with predicted wind speeds that day. The rocket ascended with a gentle arc into the wind, consistent with our calculated caliber of stability margin making it marginally over stable rocket, giving it a tendency to weathercock into the wind. Reviewing the on-board flight video showed a slow  $\sim 1$  Hz spin during ascent, likely due to a slight warp in the plywood fins.

For our second launch we were allowed to launch roughly  $8^\circ$  from vertical, though not quite at our ideal angle considering the wind speed was at 12 mph, but because of flag location there was concern that this would aim a little too close to the crowd. The rocket started with a small wobble at the initial low speeds but quickly stabilized and flew similarly to the first flight,

except for the lower angle trajectory as aimed. This initial instability was likely due to a slight misalignment of the airframe that occurred at a field repaired joint.

**Side Bay Doors Open.** A key component of our recovery system and controlled descent is the ability to remotely open the parafoil bay doors near apogee. On our first flight, the bay doors failed to open due to an overheated micro servo that actuates the locking mechanism on the spring-loaded doors. Although this worked fine just after the parafoil was packed before heading to the launch tower, once the rocket was on the tower we double-checked the orientation of the line control servo drums using the remote control, and upon reclosing in this vertical position something was binding against the mechanism, causing the micro servo to heat up. Then, just as we started the countdown, a plane and helicopter flew on opposite sides overhead, delaying launch for a few minutes. Upon recovery, we noticed the servo had overheated long enough to melt its plastic housing, a clear indication of the failure. To avoid this problem on the subsequent flight, the door locking mechanism was field modified to use a full sized, high torque, metal gear servo. With this improvement, the bay doors opened flawlessly on the second flight.

**Parafoil Deployment.** The parafoil deployment utilized passive release of a pilot chute. On the first flight, the parafoil was not deployed due to the inoperable door mechanism. On the second flight the doors opened and released the pilot chute, pulling the parafoil out of the bay. Unfortunately, some parafoil control lines initially entangled on the rocket fins. This was most likely due to the passive deployment system that allowed the airflow to push the pilot chute too close to the fins. Our vertical drop tests for parafoil deployment did not mimic this precise airflow. An active ejection device to get the pilot chute quickly away from the airframe would have helped. Nonetheless, the lines ultimately pulled free as the servos wound the control lines and the parafoil fully inflated.

**Controllable Descent Achieved.** Control of the main parafoil relies on two servo-controlled drums that reel in control lines connected to the parafoil. On the first flight, we did not have the opportunity to try this due to the door jam. On the second flight, the servo drums reeled in the control lines until they pulled free of the fins. However, by the time the parafoil was fully inflated it was too low to establish directional control in time to turn significantly toward the flag, but the viability of the control system was proven.

**Reserve Parachute Deployment.** Due to the experimental and innovative nature of our parafoil deployment system, a reserve parachute system was included in the airframe as a failsafe and final brake, if needed, upon nearing the flag. During the first flight, the rocket fell nearly 2000 feet after apogee while attempts were made to open the bay doors. As the rocket approached the ground, charges were blown which ejected the chute almost immediately. The reserve chute opened rapidly, slowing descent to give us a recoverable rocket. During the second flight, the reserve chute was used again, but only as a brake deployed at around 200 feet to supplement the main parafoil drag.

**Recovered and Determined to be in Flyable Condition.** Both flights were recovered and determined to be in varying degrees of flyable condition. The first flight had a hard landing under only the reserve chute, leaving a fractured inner coupling between two sections of the airframe. But, the segmented design allowed for re-joining any damaged seam with an external

coupling. A collar was fashioned out of a larger diameter body tube and epoxied over the fractured joint. This joint was a known weak point and was not designed to handle the hard angled side impact of the first flight. After the second flight, the rocket was recovered completely unharmed.

### Performance Analysis

	Predicted	Actual
Maximum Altitude (ft)	3065	2397
Peak Acceleration (ft/s <sup>2</sup> )	237	231.84
<b>Distance from Target Flag (ft)</b>	0	596

Table 1: Flight performance comparison of second flight (nearest to flag)

**Altitude Difference.** The predicted altitude, given by OpenRocket, was 668 ft (28%) too high for our second flight. However, we did not expect this simulated altitude since the simulation assumed a vertical launch under perfect conditions. According to Sampo Niskanen’s paper “OpenRocket technical documentation”, OpenRocket overestimates apogee from 7-16%, depending on the engine & rocket (2010-04-06 pp. 85-86). A 16% reduction brings the predicted value down to 2575 feet, only 178 feet (7.4%) higher than our actual apogee (and 2.5% below our actual first flight maximum of 2640 ft). The increased drag of the misting rain, field repair collar, door seams, launch angle, airframe misalignment and warping of the fins reasonably accounts for the remaining difference. Figure 4 shows the predicted versus actual values of altitude as a function of time. The predicted descent rate shown was expected to be faster than actual since our parafoil has reduced drag and lift relative to the round chute used in the simulation.

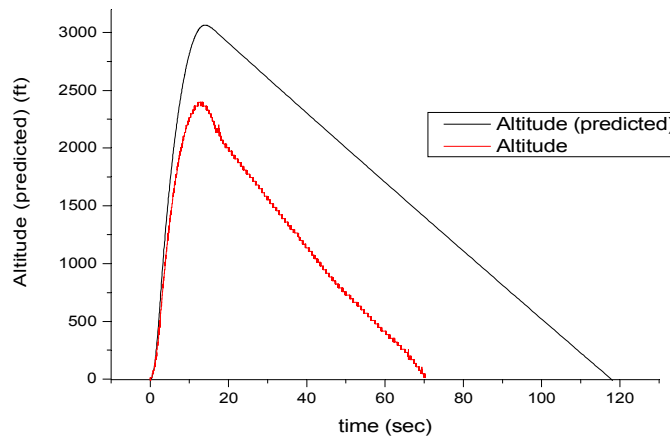


Figure 4: Altitude prediction vs. measured value as a function of time.

**Acceleration Difference.** The acceleration values provided by the R-DAS are in very good agreement with the values predicted by OpenRocket, with the simulated peak acceleration only 2.2% above actual. This lower actual acceleration is consistent with the lower actual maximum altitude. One point of interest on figure 5 is the difference between the decelerations

of the parafoil deployment at approximately 16-17 seconds. The actual values show a sharp, rapid deceleration then a second spike. This second spike is due to bouncing of the shock cords used on the main parafoil riser lines.

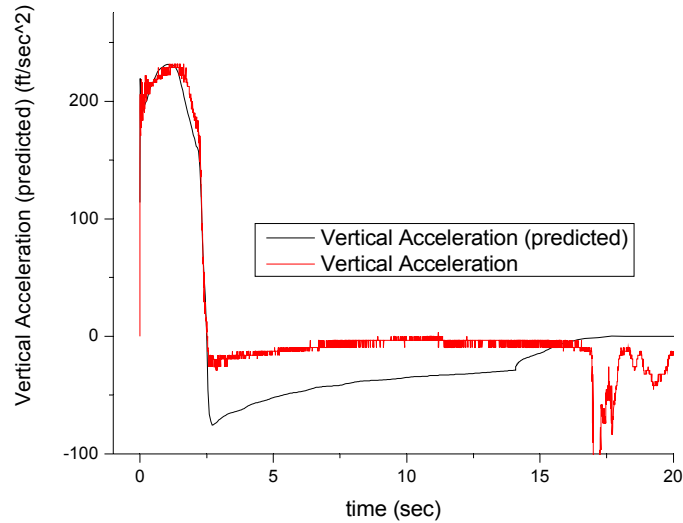


Figure 5: Acceleration prediction vs. measured value as a function of time.

### Conclusions

With two successful flights we proved and improved our rocket design. The side deployment technique worked but could benefit from a positive deployment device for the pilot chute. The servo drums proved to be functional and useful for parafoil control. On comparison of pre and post flight values, OpenRocket was shown to be a reliable simulator, albeit somewhat optimistic on altitude. Most of all, we proved the need for redundancy and the benefits of preparation and testing. A team photo with the recovered rocket after the successful landing of the second launch is shown in figure 6.



Figure 6: Team photo with rocket after the successful flight and landing.

Through this competition, made possible by NASA and the Wisconsin Space Grant Consortium, we were able to challenge ourselves in teamwork and innovative design. Now that this year's competition is over, we have learned a lot about high powered rocketry and are anxiously looking forward to next year's competition.

## **References**

Niskanen, Sampo. *OpenRocket technical documentation*. For OpenRocket version 1.1.6.  
7/18/2011. <http://openrocket.sourceforge.net/techdoc.pdf>

## Team Jarts Rocket Design

Ryan May, Jake Rice, Cameron Schulz, Jordan Wagner

Milwaukee School of Engineering

### Abstract

The objective of the 2011 Wisconsin Space Grand Consortium collegiate rocket competition was to construct a rocket capable of a controlled descent towards a designated area after having reached an altitude of 2,000 ft. or greater.<sup>1</sup>

The airframe of the rocket was designed to provide a proper balance between simplistic and a low weight design. This main chute has two scenarios for its deployment; one involves a remote controlled manual deployment, and the other is an automatic elevation triggered deployment which will serve as a failsafe to ensure the rocket has a safe landing. A numerical simulation in MATLAB was used to predict the performance of the rocket. The maximum predicted acceleration is **454 ft/s<sup>2</sup>**, and the maximum predicted altitude is **2735.9 feet**. The actual flight results varied from the prediction with the maximum predicted acceleration is **541.4 ft/s<sup>2</sup>**, and the maximum predicted altitude is **3645 feet**. The rocket design and analysis of these discrepancies are below.

### Design Features of the Rocket

#### General Design of the Rocket

The airframe for the rocket was constructed out of Quantum tubing with a diameter of 2.68 inches. Quantum tubing was used because it provided the best balance between high strength and low weight available.<sup>2</sup> Another advantage of Quantum tubing is its resilience in that it is capable of deforming under force only to return to its original shape which helps to make the rocket more robust especially when it comes in contact with the ground. The Tubing is also resistant to zipping which is not a large concern but the rocket is descending a little over 1500 feet before the main chute is deployed with only the drogue chute to slow it down. These characteristics all combined formulate the reason for why Quantum tube was chosen over phenolic tubing which is less expensive. The rocket was designed to utilize a 2.68 inch in diameter airframe which when during modeling was to use a total of 44 inches of tubing have enough space to accommodate the internals while placing the CG and CP in proper relation to one another. With the addition of the nose cone and the boat tail the total rocket length is a total of 61.25 inches. The launch weight of the rocket (including the airframe, boat tail, recovery system, motor mount and motor) was 6.35 pounds.

The rocket uses three clipped delta fiberglass fins evenly spaced around the bottom of the rocket's airframe. The specific shape of the fins provide sufficient manipulation of the Center of

---

<sup>1</sup> [http://www.uwgb.edu/WSGC/students/announcements/ssp\\_sr.aspx](http://www.uwgb.edu/WSGC/students/announcements/ssp_sr.aspx) (5/15/2011)

<sup>2</sup> <https://www.publicmissiles.com/secure/> (5/15/2011)

Special thanks to the WSGC for making this competition possible through their dedication and support.

Pressure so as to eliminate the need for a fourth fin which reduces of any unnecessary drag on the rocket while maintaining a stable flight with the CP lower than the CG.

### **Recovery System**

A main parachute with a variable diameter of 18, 24, or 30 inches, drogue parachute with a diameter of 18 inches, 0.5 inch wide high strength climbing webbing, and two flame retardant cloths are used to serve as the recovery system of the rocket. When the thrust from the motor has ended, the rocket will continue gaining altitude until apogee, at which point the first ejection charge will be automatically triggered to separate the upper portion of the rocket from the center electronics bay and lower portion. This will also deploy the drogue parachute, which will bring the rocket into a rapid but controlled descent. While observing the descent, Team Jarts will have the ability manually trigger the deployment sooner via radio control system. However should there be a system failure in the remote control the main parachute will also be connected to a programmable altimeter deployment system to deploy the primary parachute at the preset altitude of 500 feet. This aspect of the design required versatile parachute deployment electronics. The system needed to be capable of deploying at least two parachutes independently and at different portions of the flight. This system would also be ideally filed programmable and easy to use so that the team has the ability to tailor the recovery system to the conditions that are experienced on the date of the launch such as being able to modify the deployment altitude depending on the strength of the wind. The deployment of the primary parachute is a result of a second ejection charge that will separate the bottom section of the rocket from the center electronics bay, leaving the electronics bay tethered between the top and bottom sections as shown in Figure 1.

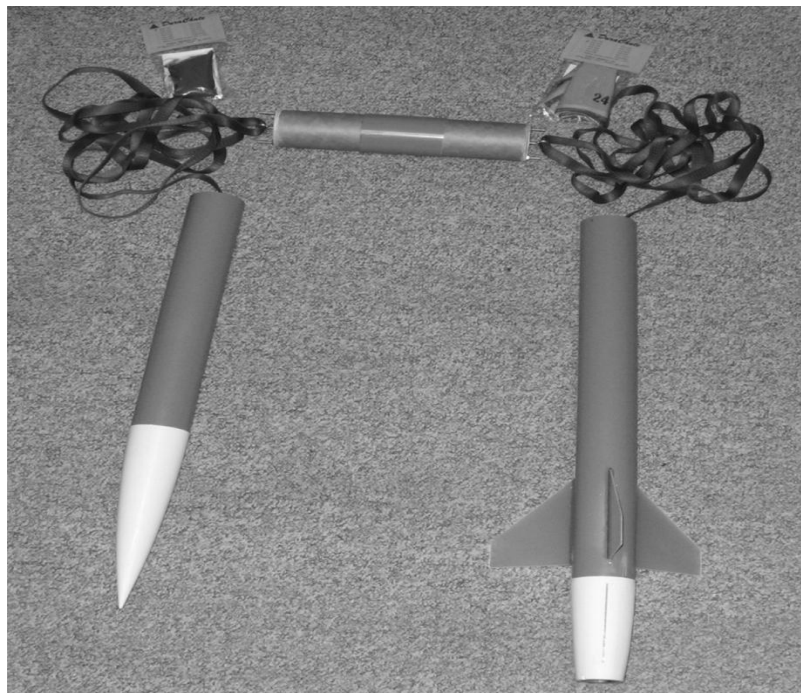


Figure 1: Rocket Disassembled showing the Placement of the Parachutes

## Electronics/ Electronics storage

The center section of the rocket is used to house all of the electronics and was constructed using a portion of coupling tubing that was approximately 12 inches long, with a shorter section of Quantum airframe centered and epoxied around it as shown in Figure 2.



Figure 2: Electronics Bay with the Eye-Hook Connections and Threaded Rod Mounting Rails

This left approximately 4 inches of exposed coupling tube on each end on the center section to fit into both the top and bottom sections of the rocket airframe, connecting all three pieces. The electronic bay was capped on both ends by bulk plates, and these bulk plates are held to the electronic bay tube by a pair of threaded rods that run the full length of the bay. Each bulk plate also had an eye-bolt attached through it to allow webbing to tether the electronics bay between the upper and lower sections of the rocket as shown in Figure 1 above.

The altimeter used in the rocket is a MARS454 programmable parachute deployment system. This particular system was selected due because of its multiple ejection channels, 4 of them, it is also field programmable and it provides a plethora of data from each flight. This combination of characteristics makes this system ideal for the simple controlled descent system that is being implemented.<sup>3</sup> The fact that this system satisfies the design parameters for the controlled decent is added to by the use of a suite of sensors on onboard analysis to provide the team with extremely accurate flight data which will be very useful in the post flight report. This is all accomplished in a simple to use and small device that is shown in Figure 3.

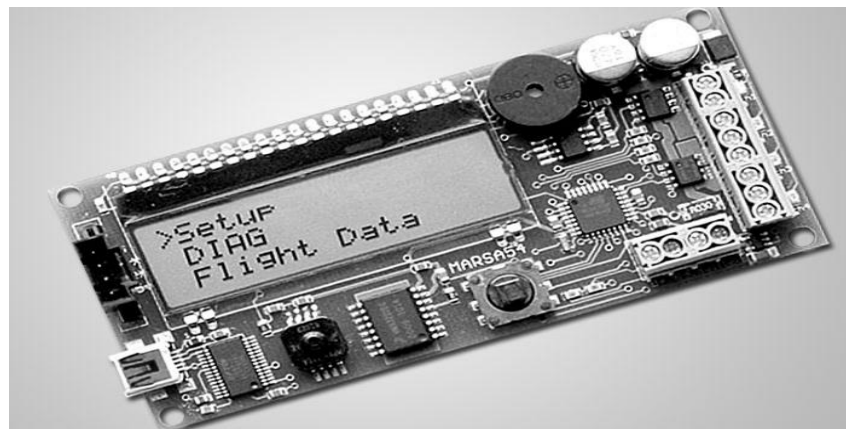


Figure 3: MARS454 Parachute Deployment System

Source: <http://www.rocketryplanet.com/content/view/3541/29/#axzz1KVksSdHZ> (4/20/2011)

<sup>3</sup> [http://mars4.com/jmla/index.php?option=com\\_content&view=article&id=48&Itemid=53](http://mars4.com/jmla/index.php?option=com_content&view=article&id=48&Itemid=53) (5/14/2011)

The controlled recovery system that was devised for this competition uses a combination of the MARS54 shown in Figure 3 and a remote deployment system. The ability to deploy the main parachute at any point during the decent between apogee and the failsafe deployment floor is made possible using a modified remote system. A DX5e 5 channel airplane remote was selected because it was affordable, available, and could be easily adapted to be used in the design.<sup>4</sup> The specific characteristic that is being used is the auxiliary channel which depending on the used input produces one of two different pulsed signals. This signal is converted to an on/off signal using a Pololu RC Switch board.<sup>5</sup> This system will be run in parallel to the fail safe deployment found on the MARS54. Depending on the conditions observed during the launch the designated operator will decide at what point during the decent the main parachute will be deployed. This system is also very small and light so that very little of the analysis was affected by the inclusion of this subsystem. The major components used can be seen in Figure 4 with a quarter used as a size reference.

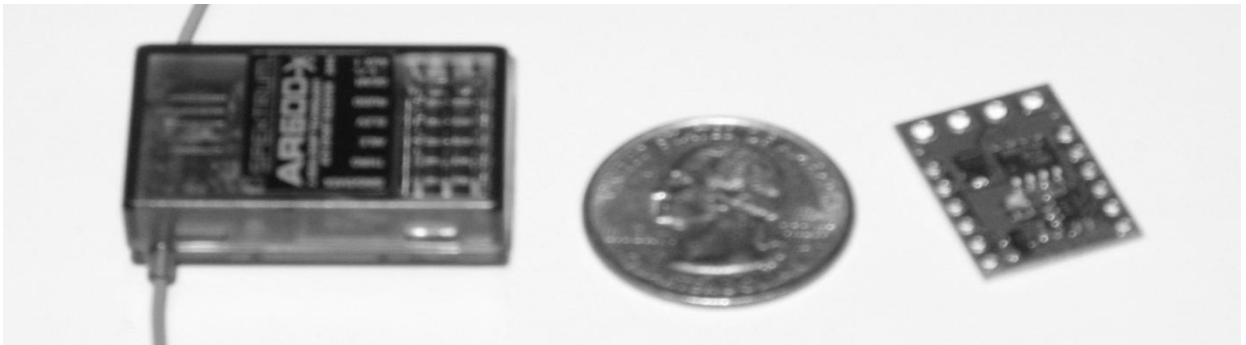


Figure 4: Remote Controlled Parachute Deployment System (Quarter used for Size Reference)

These systems are joined by the competition an R-DAS altimeter used to record flight data. All of these components that are found in the electronics bay are mounted to a Plexiglas tray in the electronics bay using stand-offs and screws. This tray has two tubes mounted to it to hold it in place on the mounting rails to ensure that the electronics remain in the proper position and do not move around or break during the flight. This system makes the electronics easy to access by simply undoing a few nuts any component in the e-bay can be accessed or programmed

### **Center of Pressure/ Center of Gravity**

The locations for the center of gravity and the center of pressure were determined by constructing a sample model in RockSim. The rocket construction analysis found in RockSim allowed for the modeling of every component of the design while enabling the designer to make adjustments to find the ideal dimensions. The result of the analysis can be seen in Figure 5 which shows the layout of the rocket design and the resulting calculations for the placement of the Center of Gravity and the Center of Pressure. The analysis also provides how these two points relate to each in producing a stable rocket. The CP must be located approximately 1-2 airframe diameters below the CG to make the rocket stable. If this distance is greater than that it will cause the rocket to be over stable and cause the rocket to wobble on ascent sacrificing altitude. Should the CP be located above the CG the rocket would be considered under stable and would

<sup>4</sup> <http://www.spektrumrc.com/products/default.aspx?prodid=spm5500> (5/15/2011)

<sup>5</sup> <http://www.pololu.com/catalog/product/1211> (5/14/2011)

veer erratically during flight costing altitude as well.<sup>6</sup> This is why when a motor is present in the rocket designed the ratio of distance over diameter for this particular design is approximately 1.5.

Length: 60.4500 In., Diameter: 2.7000 In., Span diameter: 10.6800 In.  
 Mass: 74.0813 Oz., Selected stage mass: 74.0813 Oz.  
 CG: 34.0992 In., CP: 43.7141 In., Margin: 3.56 Overstable  
 Shown without engines.

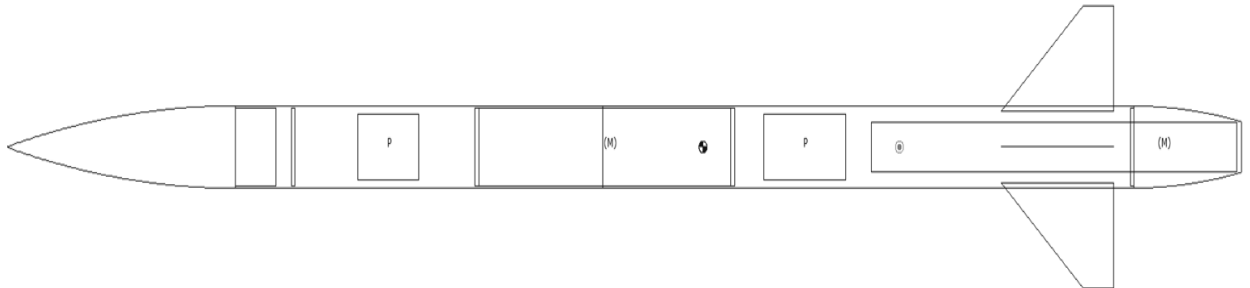


Figure 5: RockSim Construction Analysis

$CP_{\text{Rocket}} = 18.4''$  from bottom of rocket

$CG_{\text{Rocket}} = 22.5''$  from bottom of rocket **with motor**

$CG_{\text{Rocket}} = 27.7''$  from bottom of rocket **after burnout**

**Stability Ratio = 1.53**

### Analysis of the Anticipated Performance

The maximum acceleration and height at apogee was predicted by using Newton's Second Law and a numerical algorithm. To do this, several assumptions had to be made.

### Assumptions

1. Weight was assumed to be constant throughout the flight.

$$w_{\text{rocket}} = 6.35 \text{ lbs}$$

2. The density of air was assumed to be constant throughout the entire portion of the flight.

$$\rho_{\text{air}} = 0.0023 \text{ slug / ft}^3$$

3. Thrust was assumed to be constant during the first **1.5 seconds** of flight.<sup>7</sup>

$$= 62.2 \text{ lbf}$$

4. Gravity was assumed to be constant.

$$g = 32.2 \text{ ft/s}^2$$

5. The drag force due to air resistance was assumed to be proportional to the square of the velocity. The drag force was calculated using Equation 1:

<sup>6</sup> <http://exploration.grc.nasa.gov/education/rocket/rktstabc.html> (5/14/2011)

<sup>7</sup> <http://www.thrustcurve.org/simfilesearch.jsp?id=938> (5/15/2011)

$$F_D = \frac{1}{2} \rho C_D A v^2 \quad (1)$$

Where:  $\rho$  = density of air  
 $C_D$  = coefficient of drag

$A$  = cross sectional area of the rocket  
 $v$  = instantaneous velocity of the rocket

6. The coefficient of drag was assumed to be constant.

$$C_D = 0.6$$

### Predicted Velocity History

Two distinct portions of the flight are present. *First is the thrust portion of the flight.* During this phase, the rocket is accelerated upward from the ground to the point when the thrust ends. Thrust is maintained throughout this entire phase. *The second phase of the flight is when the motor finishes providing thrust and the rocket decelerates until apogee.* During this portion, the rocket continues to fly as a projectile. There is no thrust during the second phase.

**Phase I:** Motor Accelerating Rocket ( $0 < \text{time} < 1.5$  seconds)

The velocity can be predicted using Newton's second Law and a numerical algorithm. Newton's second Law says that the sum of the forces is equal to the product of mass and acceleration.

$$\sum F = ma \quad (2)$$

When applied to the rocket, Equation 2 becomes:

$$-\frac{1}{2} \rho C_D A v^2 - mg + T = ma \quad (3)$$

A numerical method (Euler's Method) is applied and this becomes:

$$-\frac{1}{2} \rho C_D A v_i^2 - mg + T = m \frac{v_{i+1} - v_i}{\Delta t} \quad (4)$$

Equation 4 can be rearranged as follows:

$$v_{i+1} = v_i + \left( \frac{-\frac{1}{2} \rho C_D A v_i^2}{m} - g + \frac{T}{m} \right) \Delta t \quad (4)$$

Equation 4 was scripted in a MATLAB code (Appendix 1) from the time of launch ( $t=0$  sec) until the thrust ends ( $t=1.5$  sec). A plot of this equation can be seen in Figure 6.

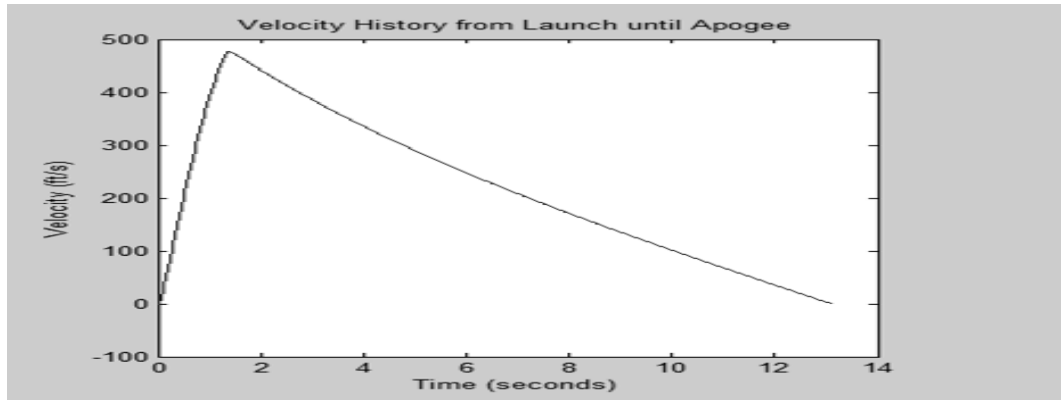


Figure 6: Velocity History Plot of the Rocket Produce by MATLAB

### Predicted Acceleration History

The acceleration of the rocket was predicted by applying a numerical differentiation model on the predicted velocity data. The acceleration was calculated as follows:

$$a_i = \frac{v_i - v_{i-1}}{\Delta t} \quad (5)$$

Equation 9 was scripted in a MATLAB code (Appendix 1). This algorithm was applied from the time of launch until apogee was achieved. A plot showing the acceleration data can be seen in Figure 7.

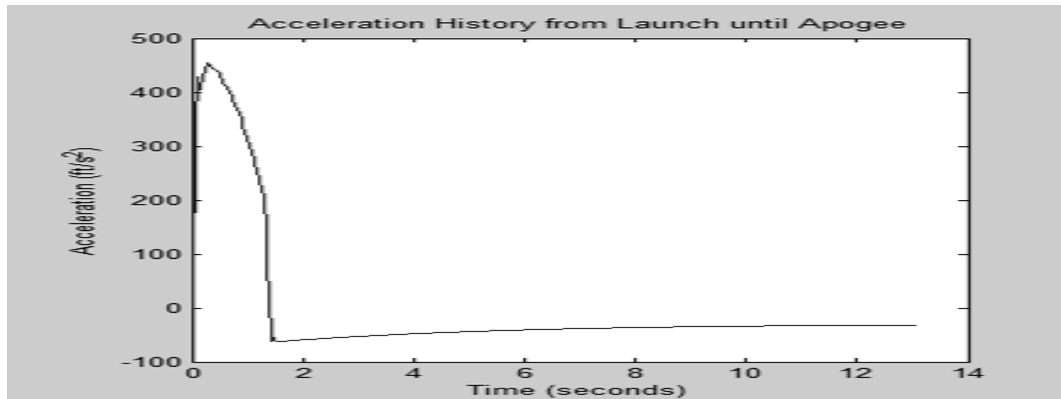


Figure 7: Acceleration History Plot of the Rocket Produce by MATLAB

It is anticipated that acceleration is initially positive since thrust is applied. The acceleration decreases during this phase because the drag force is increasing. Acceleration is negative after thrust ends because the rocket is slowing down. It should be noted that the maximum acceleration achieved in the flight is **454 ft/s<sup>2</sup>**.

### Predicted Altitude History

The altitude history of the flight was also predicted using a numerical model. This was calculated by applying the trapezoid rule to find the area under the velocity curve. The equation used to calculate the height above Earth's surface (altitude) is as follows:

$$h_{i+1} = h_i + \frac{(v_{i+1} - v_i)}{2} \Delta t \quad (6)$$

Equation 10 was scripted in a MATLAB code (Appendix 1). This algorithm was applied from the time of launch until apogee was achieved. A plot showing the predicted altitude history can be seen in Figure 8. The maximum altitude achieved was **2735.9 feet**.

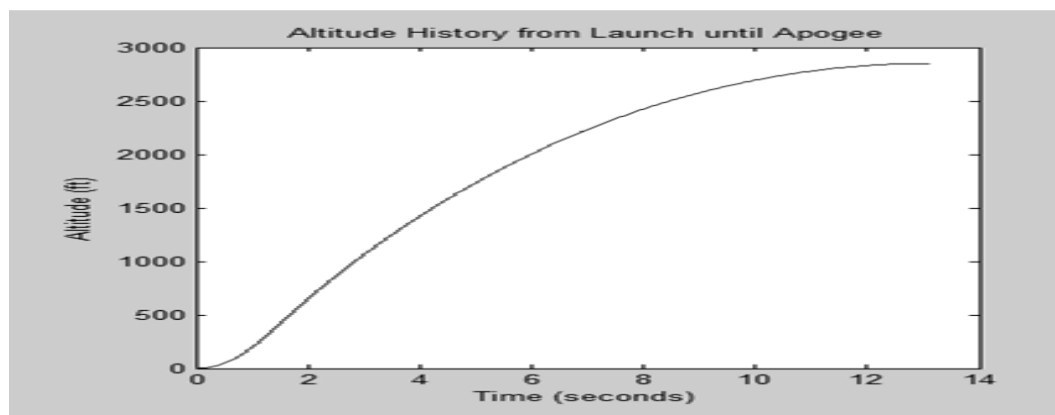


Figure 8: Anticipated Altitude Projection Plot of the Rocket Produce by MATLAB

### Summary of Flight Performance

Maximum Acceleration	<b>454 ft/s<sup>2</sup></b>
Maximum Altitude	<b>2735.9 feet</b>
Time at Apogee	<b>13.47 seconds</b>

Table 1: Pre-Flight Analysis Predictions of Results

### Flight Comparative Analysis:

The pre-flight analysis above was for the I-284 rocket motor. This analysis was performed to understand the flight of the rocket that was designed and built by Team Jarts. The deviation of the predicted values from the experimental result is unfortunately rather large. The reason for this is that the analysis in the design report was performed under the assumption that the teams were guaranteed the motor type that was requested for the competition flight. The motor that Team Jarts selected was the I-285 for which the analysis in the design report was performed. The analysis contained in this post-flight report is for the I-284 motor which was provided to Team Jarts at the time of competition.

The table below has three distinct columns of values that were obtained from different sources. The “Predicted” Column contains the values that were determined from the MATLAB model that Team Jarts constructed of the rocket used for completion. The “Official” Column contains the values that were measured using the equipment provided by competition officials. The “Team Recorded” Column has the values that were determined using the team’s hardware (MARSA4) to monitor the rocket’s flight.

Flight		Predicted	Predicted	Official	Team
Maximum Altitude [ft]		3869.2	3489	-----	3645
Peak Acceleration [ft/s^2]		475.9	458	-----	541.4
Distance from the Target Flag		796.9	-----	384	1058.6

Table 2: Summary of both Predicted and Measured Results for Analytical Comparison

The reason why there is no ‘Official’ altitude or acceleration was a result of the competition R-Das malfunctioning and therefore not providing any retrievable data. The ‘Official’ distance measurement is a result of the GPS coordinates that were obtained from following the directions of a competition official to obtain the distance between the rocket’s landing site and the target flag. Due to the fact that there was no acceleration or altitude officially measured the measurements that were recorded by Team Jarts’ altimeter were used for analysis. The other issue is the distance from the flag. This value is different because it appeared that the location at which the rocket landed was not where it is officially recorded to be. The listed “Team Recorded” value was a result of a team member that was part of the collection team noting the landing site and the target flag to determine the distance that the rocket landed from the target. The origin of this discrepancy was undeterminable during the review of the launch proceedings but the need to bring this to light was apparent during the post-flight analysis.

**Altitude:**

The results of the analysis and the recorded flight data when compared with each other serve to confirm the analysis method that was used. The small disparity between the predicted altitude and the recorded altitude are such that the percent difference is only 6.1% for the RockSIM and only 4.3% for the MATLAB analysis. This level of deviation could have been a result of additional friction on the rail during launch or due to unexpected conditions in the atmosphere or wind patterns during flight. The fact that the two methods of analysis produce a window of potential altitudes that the system will achieve and the launch was right in the middle confirms the analysis.

**Acceleration:**

The comparison of the acceleration values yields a larger variation. However this could very well be the result of the time resolution of the measurements that was used was not fine enough. One solution would be to launch again to obtain measurements with a higher time resolution which could eliminate this artifact and therefore yield the same level of accuracy that was seen in the comparison of the acceleration values. The discrepancy in the MATLAB analysis shown in Figure 7 could be a result of having used a conservatively high coefficient of drag.

**Distance to the Target:**

The final value of the distance from the target also has a larger than anticipated deviation between the expected maximum and the recorded value. This could be the result of unforeseen winds or a variation in the angle of the launch rail from what was calculated. Another possibility is that the wind speed that was taken into account that would affect the rocket during the descent is not constant as the analysis assumes which could cause the system to deviate in the manner seen from the predicted values.

**Conclusion**

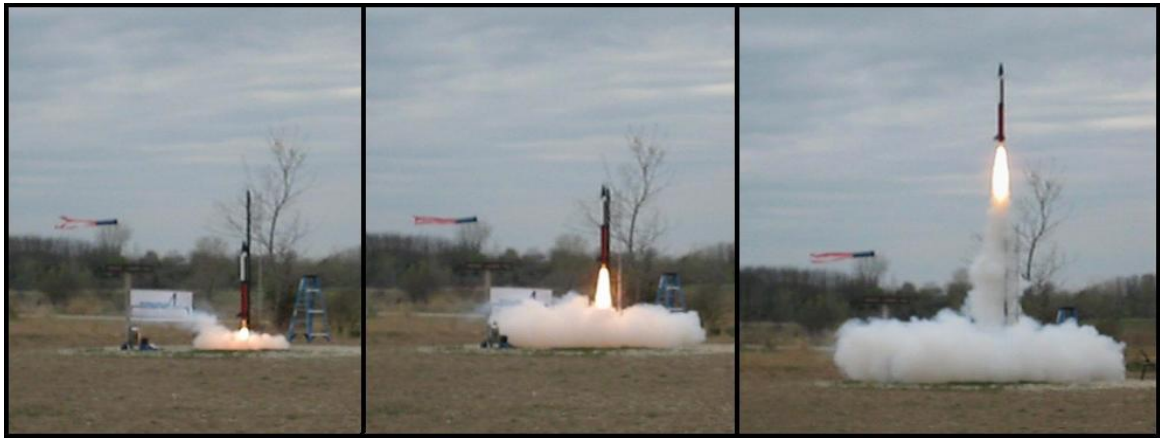
Team Jarts confidence in their rocket to meet the completion performance criteria and its ability to perform in such a way as to field repairable were validated at competition. Although, the numerical simulation predicted were not correct in the pre-flight analysis the post-flight analysis was able to identify potential sources for these errors. The conclusion that was reached as a result of the post flight analysis was that the MATLAB model that was designed and used by Team Jarts to perform the analysis produces reliable predictions of how the design rocket will operate. The small deviation of only 6.1% for the altitude and explainable differences between the predicted and actual accelerations and distance from the target validates the analytical model used. This allows Team Jarts to see their design, analysis, and execution of this project as an engineering achievement.

## Collegiate Rocket Design Competition

### Team Rally Axe

Alex Gonring & Tyler Van Fossen<sup>1</sup>

Engineering Mechanics & Astronautics  
University of Wisconsin-Madison



### Abstract

The objective of the 2011 Rocket Design Competition was to launch a rocket to a minimum of 1500 feet at apogee, then control the descent to land closest to a designated target. As a second year team, Rally Axe continued its philosophy of making their rocket by hand as much as possible, with only a few manufactured components. A PVC body tube was used, which features two separation points to deploy both a drogue parachute and parafoil as the controlled recovery device. The lower stage deploys the drogue at apogee to slow the rocket during descent. This stage also contains the AeroTech K550 motor. The upper stage stores the parafoil, which is deployed at 1000 feet by a smaller drogue parachute sewn directly to it. The center of pressure was found using Barrowman Equations, while the centers of gravity of both the fully-loaded rocket and the rocket after burnout were found experimentally. Both margins were made to be sufficiently close to one, thus enabling stable flight. The analysis of the expected performance of the rocket was calculated using MATLAB's ode45 function to solve the equation of motion, which depends on changing mass, temperature and pressure. The rocket was successfully flown during two competition flights, averaging 2395 feet at apogee, 7.3 G's of acceleration, and landing 953 feet and 686 feet from the target. In comparison to the predicted values, the rocket's performance confirmed the overall effectiveness of the construction and flight-prediction methods.

---

<sup>1</sup> A special thanks to the Wisconsin Space Grant Consortium and the National Space Grant College and Fellowship Program for funding the competition.

## Competition Objective

The objective of the 2011 Collegiate Rocket Design Competition was to launch a rocket to at least 2000 feet at apogee, then control the descent to land closest to a designated target. The first decision was to select an appropriate engine, which dictated the final weight of the rocket. Rally Axe selected the AeroTech K550; capable of sending a 23 pound rocket 2600 feet into the sky. The rocket had to be safely recovered in flyable condition to earn the most points. Along with the competition flight, competitors were required to perform outreach, submit a design report, give a formal presentation to a panel of judges, and submit a post-flight analysis demonstrating an understanding between any differences in expected and actual flight performance.

## Design Features of the Rocket

Simply put, Team Rally Axe's rocket is a unique entry to the 2011 Collegiate Rocket Competition. A majority of the components are custom designs and hand-crafted from common, durable materials. Its 4.5 inch outer-diameter body is constructed of PVC with thick pine bulkheads secured through the body tube for extra strength. The overall length is 6 feet, which separates into three pieces during the recovery phase, shown below in Figure 1. Besides being the only team to utilize the low cost and durability of PVC, much of the uniqueness of the design lies in the recovery system; two drogue chutes and a remote-controlled (RC) parafoil.

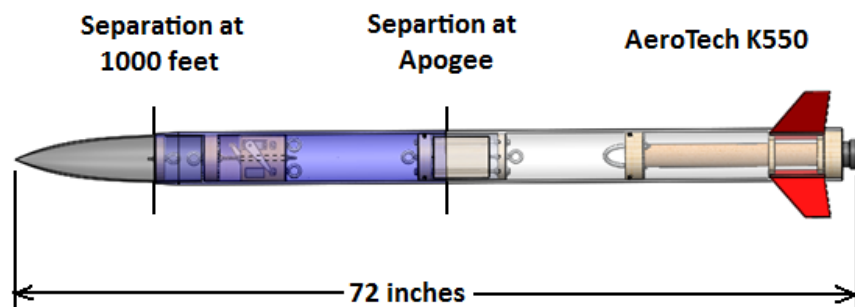


Figure 1: SolidWorks model of the rocket showing the separation points.

**Thru-Wall Construction of Fin and Motor Mount.** Two wood mounts are used to radially constrain the motor tube and secure the fins. The motor is vertically constrained by a bulkhead and retainer on either end. The mounts are similar to the bulkheads used in the rest of the rocket, but are thinner, only 0.75 inches thick, and have a hole through them for the motor mount tube and three equally spaced slits for the fins. Both the fins and the bulkhead are secured through the body tube for extra strength of the lower stage, shown on the next page in Figure 2.

To help with the distribution of weight to maintain stability is one pound of dead weight, comprised of lead shot wrapped in strands of duct tape for safety. Though not pictured in Figure 2, the strands of weight were wrapped around the motor tube and sandwiched between the upper

motor mount and the bulkhead. The lower section was the last to be constructed, so the exact location of the weight could be determined to manipulate the center of gravity as needed.

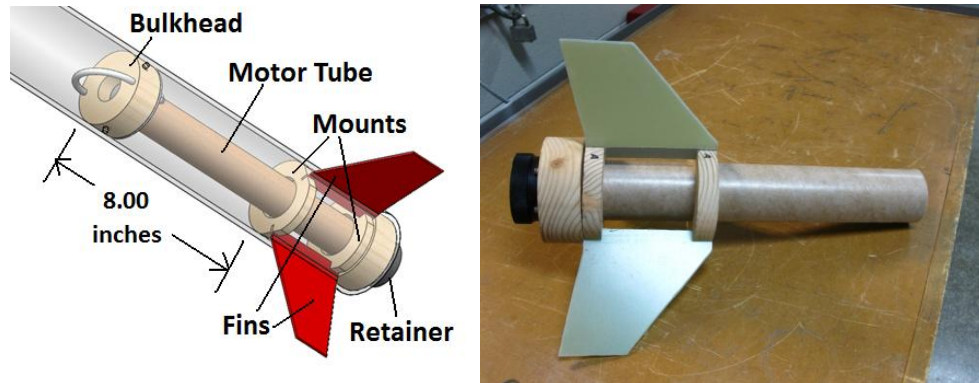


Figure 2: The left image shows the SolidWorks representation of the lower stage of the rocket, while the right shows the constructed innards of the lower stage without the motor or motor bulkhead.

**Dual Deployment, Tri-Chute Recovery System.** The ability to maneuver and safely land the descending rocket was crucial in this year's competition. To do so, a user-operated, remote-controlled parafoil was implemented. RC systems can only be effectively operated when the object is within visual range, so the parafoil will not be deployed at apogee, but rather a lower, more visible altitude. To achieve this, a dual-deployment recovery system was designed. The recovery system consists of a large drogue chute deployed at apogee, and a small drogue and 6 foot parafoil deployed at 1000 feet. The large drogue is a necessary component, for if it were absent, the rocket would be descending far too quickly for the parafoil to eject without causing catastrophic failure. Figure 3 (next page) depicts the recovery system after parafoil deployment. Most parafoils require an already-opened deployment with initial forward motion to inflate its cells. To get by this unfortunate technique, the small drogue has multiple lines attached to the top surface of parafoil so that tension on the strings forces the parafoil to open and inflate its cells.

**Accessible Electronics Bay as a Coupler.** The electronics bay conveniently serves as both an easily-accessible housing for the altimeters, as well as a coupler tube to join the upper and lower stages of the rocket. The bay shown in Figure 4 (next page), is 7.5 inches long and has a detachable cover and removable mounting board. Two threaded rods support the tensile stresses caused from the shock cords pulling on either eye-bolt. Just over 5 inches of the coupler protrudes into the lower tube for stability. The electronics bay houses two altimeters: AIM USB by Apogee Components, and the required RDAS competition altimeter. The AIM USB controls the two ejection charges. Both altimeters measure the approximate altitude based on the surrounding air pressure of the rocket. For this reason, three 0.125 inch vent holes are required for an equivalent "cabin pressure".

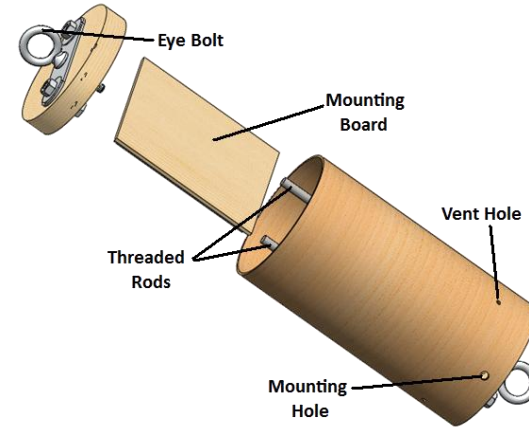
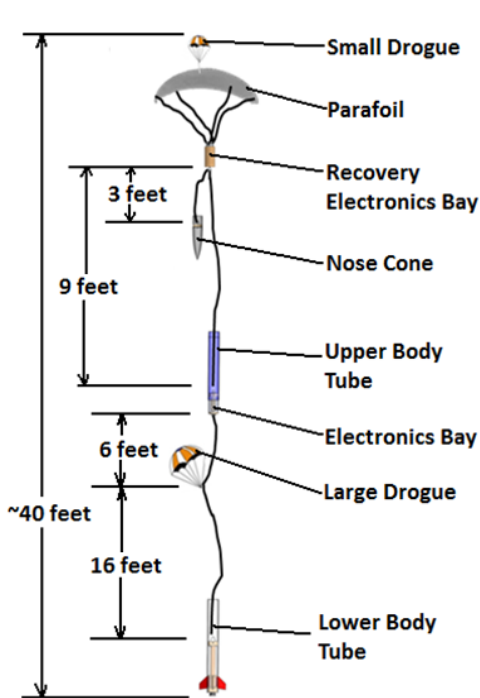


Figure 3 (Left): The large drogue is deployed at apogee, while the small drogue and parafoil are ejected at 1000 feet in the final recovery configuration.

Figure 4 (Above): The electronics bay houses two easily-accessible altimeters and connects the upper and lower halves of the rocket.

**Custom-Built Recovery Electronics and Steering Pod.** The parafoil is controlled by strings attached to servo motors within the rocket. Controlled remotely from the ground, these motors pull down on the left or right lines to steer the parafoil and rocket in the direction of the ground target. Two ultra-torque HiTec servos (HS-645MG) were used as the parafoil's steering mechanism. These metal-gearred motors are capable of delivering 107 oz-in of torque, which is equivalent to 3.34 pounds of force at a 2 inch distance from the center point. The setup, shown

in Figure 5, allows the desired inner-turn string to be pulled 1.38 inches, coupled with the outer-turn string to be loosened 1.69 inches. The total difference in string length of approximately 3 inches does not allow for aerobatics during descent, but at least allow necessary gradual turns.

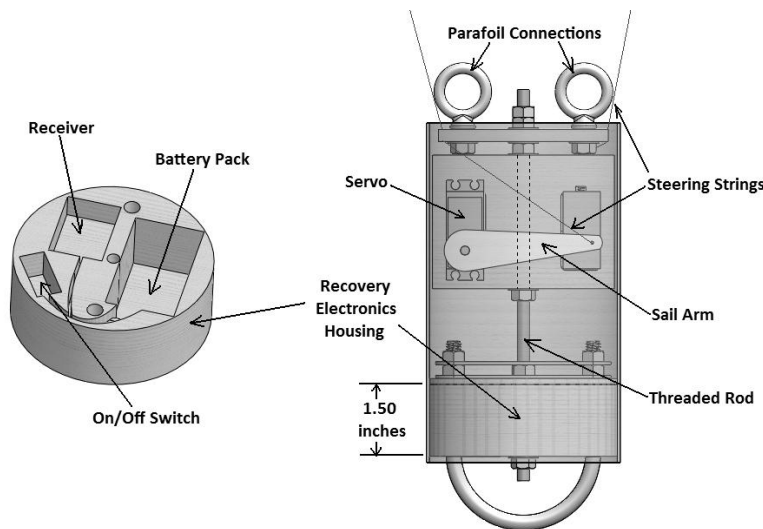


Figure 5: The recovery electronics bay houses two servo motors used to alter the steering strings' lengths

The components used to power the servos are housed in the recovery electronics

bay, including the RC receiver, power supply, and on/off switch. The receiver selected is the Futaba R2004GF, a 2.4 GHz radio system with frequency-hopping technology. Simply put, the system eliminates radio interference to ensure complete control for up to one mile. Four NiMH (nickel-metal hydride) batteries power the receiver and both servos. The housing was designed to transmit the force around these vital electronic components through a network of metal rods and plates.

### Critical Stability Points

In order for a rocket to endure a stable flight, the static margin needs to be close to one. This is the same as saying that the difference between the locations of the center of pressure (CP) and the center of gravity (CG) should be about one body tube diameter.

The location of the center of pressure does not effectively change during flight, but the center of gravity does. The CG changes because two pounds of propellant weight is lost during the burn phase, shifting it forward. Because of this, both the CG before launch and after burnout must be found to ensure stability during both stages. Therefore, when designing the rocket, the weight should be distributed such that the average CG is one body tube diameter in front of the CP. Using this location ensures that the two extreme locations of the center of gravity will be equally close to one caliber above the center of pressure to produce maximum stability.

To find the locations of the CP and CG, an iterative process was used. The first step was to use Barrowman Equations to calculate an initial CP. These equations factor in the geometry of the rocket, including body tube and transition diameters, lengths of components, and proposed fin dimensions.

Once construction was complete with a ballpark location of the center of gravity in mind, the fully assembled rocket was weighed and balanced to experimentally determine the location of the CG without the motor. Since the weight and CG of the motor were known, along with the location of the motor in the rocket, the CG of the fully-loaded rocket could be easily calculated.

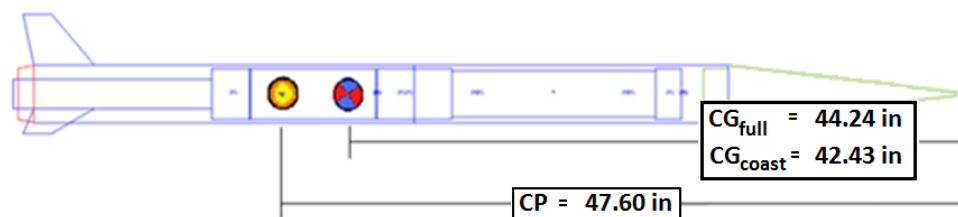


Figure 6: Locations of the centers of gravity and pressure.

As shown in Figure 6, it was found that the center of gravity of the fully-loaded rocket is 44.24 inches from the nose tip, while the CG of the burned out rocket is 42.43 inches from the same

location. The two centers of gravity did not line up perfectly with the ideal CG from the proposed center of pressure, so the fin shape was modified.

The fin dimensions in the model were iterated in the Barrowman Equations to manipulate the location of the center of pressure, so that the average of the experimental CG's (43.33 inches from the nose) was approximately one caliber in front of the CP. The selected position for the center of pressure, as determined by the fin shape, is 47.60 inches from the nose, which is shown in Figure 6. As one final effort to ensure stability, one pound of dead weight was left to be positioned in the final construction process to manipulate the center of gravity as needed.

### Flight Dynamics Modeled in MATLAB

The rocket's performance was simulated by finding the associated second-order differential equation of motion (EOM) and using numerical methods to solve. The calculation was done in MATLAB with the fourth and fifth-order Runge-Kutta method, ode45. The code was structured such that known design parameters were the inputs, while the anticipated altitude, velocity, and acceleration of the rocket were the outputs. Since there is a desired value for the altitude output (1500 foot minimum plus 500 feet for safe measure), the code required iteration within the design to achieve this altitude. The easiest design parameter to manipulate was weight, so that was the primary design constraint.

The derivation of the EOM begins with a simple free-body diagram to balance the forces of weight and drag with thrust, as shown in Figure 7. Note that this derivation assumes a perfectly vertical and windless flight, which is an unrealistic, but practical simplifying assumption. Since high winds strongly affect over-stable rockets, extra emphasis has been put on rocket stability to mitigate the error in this assumption. Additionally, over 500 were added to the target apogee as a safety net. The balance of forces from the free-body diagram in the vertical direction yields Equation 1:

$$(1) \text{ mass} \times \text{acceleration} = \text{thrust} - \text{weight} - \text{drag}$$

All terms in the above equation are ultimately dependent on time, which makes it much more difficult to solve than one would expect. For starters, the overall mass decreases at an assumed linear rate throughout the burn stage with the loss of solid propellant. Second, the thrust of the engine is inconsistent and in fact varies substantially throughout the 3.4 second burn region. Weight, like mass, decreases over the burn period, and drag depends on several changing factors as well. Equation 2 shows the linear decrease in mass throughout the burn, while thrust and drag are covered later on.

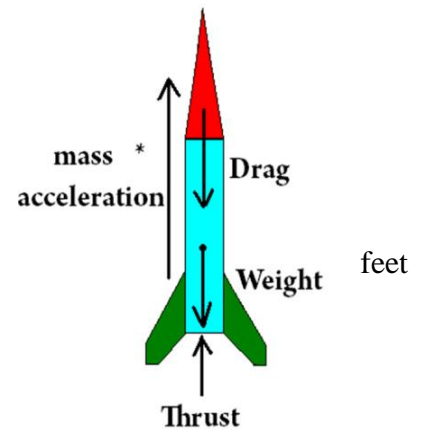


Figure 7: Free body diagram with both the body forces and inertial forces shown. Balancing these forces yields the equation of motion.

$$(2) \quad mass = mass_{total} - \frac{0.889}{3.356} \times time \quad [\text{kg}]$$

The variable  $mass_{total}$  is the initial mass of the rocket, which loses 0.889 kg of propellant over the 3.356 second burn period.

Equation 3 is the drag equation, where  $density$  is that of air,  $area$  is the frontal area of the rocket (what is seen when looking straight down at the rocket), and  $c_d$  is the coefficient of drag, an experimental parameter that we assumed to be 0.75 based on typical rocket values.

$$(3) \quad drag = \frac{1}{2} \times density \times velocity^2 \times area \times c_d \quad [\text{N}]$$

The  $density$  term depends on both temperature and pressure, which are both dependent upon the altitude of the rocket, which has a time-dependence. Additionally,  $velocity$  is the time derivative of the altitude. As you can see, the equation becomes very difficult to solve by hand, which is why numerical methods were used. Expanding the density term as a function of pressure,  $P(y)$ , and temperature,  $T(y)$ , yields Equation 4, where  $R$  is the universal gas constant. The updated EOM is then shown in Equation 5.

$$(4) \quad density = \frac{P(y)}{R \times T(y)} \quad [\text{kg/m}^3]$$

$$(5) \quad \left( mass_{total} - \frac{0.889}{3.356} \times time \right) \left( \frac{d^2 y}{dt^2} \right) = thrust - \dots$$

$$\left( mass_{total} - \frac{0.889}{3.356} \times time \right) \times g - \frac{\left( \frac{dy}{dt} \right)^2 \times c_d \times A \times P(y)}{2 \times R \times T(y)}$$

By substituting in functions of altitude for both pressure and temperature, the final equation of motion can be obtained. Equation 6 (Lide, 1996) and Equation 7 (Hurt, 1965) represent these respective relationships, where Equation 8 is the final result after substitution.

$$(6) \quad P(y) = 100 \times \left( \frac{44331.514 - y}{11880.516} \right)^{5.255966} \quad [\text{Pa}]$$

$$(7) \quad T(y) = (initial_{temp} - 0.002 \times y) \quad [\text{K}]$$

$$(8) \quad \left( \frac{d^2 y}{dt^2} \right) = \frac{thrust}{\left( mass_{total} - \frac{0.889}{3.356} \times t \right)} - g - \dots$$

$$\frac{\left( \frac{dy}{dt} \right)^2 \times c_d \times A \times 100 \times \left( \frac{44331.514 - y}{11880.516} \right)^{5.255966}}{2 \times R \times (initial_{temp} - 0.002 \times y) \times \left( mass_{total} - \frac{0.889}{3.356} \times t \right)}$$

Once the solution to the EOM is obtained, plotting is fairly straightforward. The ode45 method outputs the time, altitude and velocity for each thrust region, so it is as easy as plotting all regions onto one grid. The acceleration plot is similarly constructed after substituting in the altitude and velocity solutions into the original EOM to obtain the acceleration for each thrust region.

It would be incorrect to say that this method of analysis tells us the exact position and velocity of the rocket at any given time, since the ode45 method solves with an inconsistent time step. However, the varying time step is dependent on the rate of change in the EOM, so it is still extremely accurate. With the results shown in Figures 8-10, one would be able to interpolate the altitude, velocity, and acceleration of the rocket at any given time.

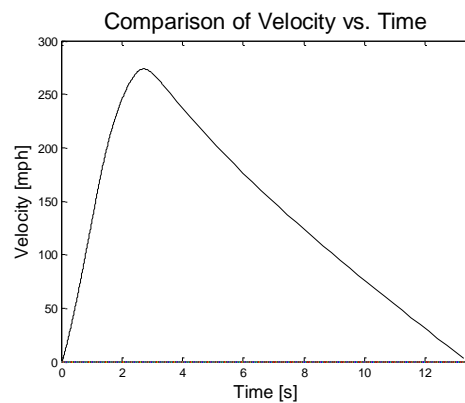
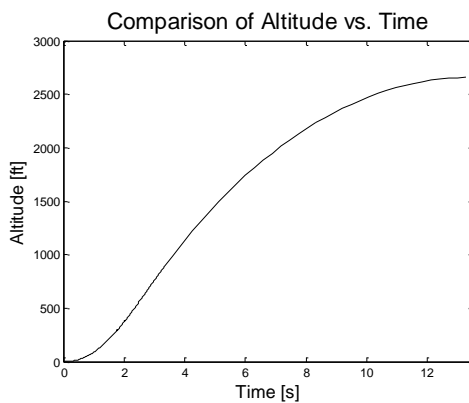


Figure 8 (Top left): The altitude increases rapidly through the burn stage, followed by a parabolically decreasing rate through the coast stage. A maximum altitude of 2657 feet is anticipated.

Figure 9 (Top right): Velocity is the derivative of the position, so it is logical that the velocity peaks at the inflection point of the altitude curve in Figure 8. The expected top speed of the rocket is 274 mph.

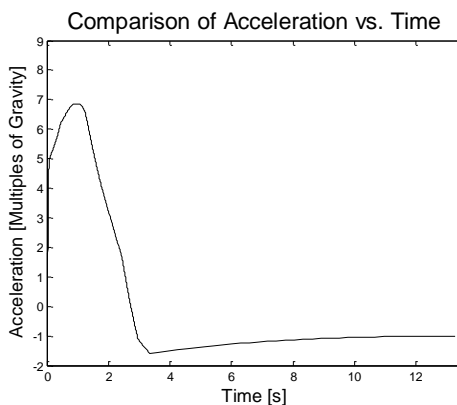


Figure 10 (Bottom Left): Acceleration is the derivative of the velocity, so higher accelerations occur when the velocity curve is steeply increasing. After burnout, the acceleration quickly falls to a greater-than gravity value, due to drag. A maximum acceleration of 6.84 G's is expected.

Note that the slope of the altitude is the velocity and the slope of the velocity is the acceleration. Also, acceleration becomes negative slightly before the coast stage, because the thrust force is not strong enough to overcome gravitational and drag forces in the last few milliseconds before burnout. As a check, the acceleration during the entirety of the coast stage should be approximately the value of gravity, which is true. There is a slightly stronger negative acceleration right after the burnout because the rocket is traveling around 270 mph, which causes

a significant amount of drag. The pertinent numbers of anticipated performance are a flight time of 13.3 seconds, 2657 feet at apogee, 274 mph top speed, and 6.84 G's maximum acceleration.

### Comparison of Anticipated Values with Actual Performance

**Comparison of Accelerations.** The anticipated peak acceleration was 6.84 multiples of gravity. Since the R-DAS altimeter records resting acceleration as “zero”, the predicted value on the same scale is 7.84 G's. This value over-predicts the experienced accelerations of 7.5 G's and 7.1 G's by 4.5% and 10.4%, respectively. Figure 11 shows the predicted and experimental values of acceleration over time during ascent. Although the predicted peak acceleration is higher than what was experienced and drops off more quickly, all three curves follow very similar paths. Since both flights produced nearly identical plots, the variances cannot be attributed to motor-to-motor fluctuation.

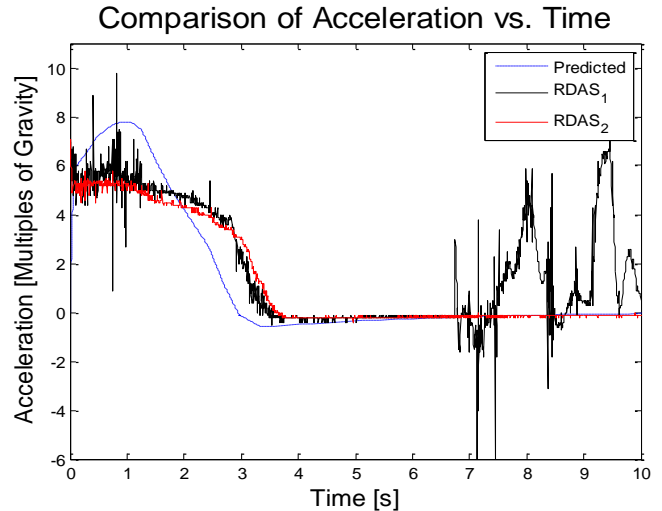


Figure 11: Predicted Versus Actual Acceleration

**Comparison of Altitudes.** The altitude at apogee of the first flight was recorded at 2444 feet, which is 6.4% lower than the predicted altitude of 2600 feet. The second flight was 99 feet lower, but does not offer a valid comparison to the predicted value since the second flight was launched at an acute angle, unlike the first flight or the calculations. Altitude estimations were markedly improved this year over last, and the predicted altitude over time closely matches the recorded straight-flight curve shown in Figure 12. The only significant difference between the plots is that apogee occurred much sooner than expected.

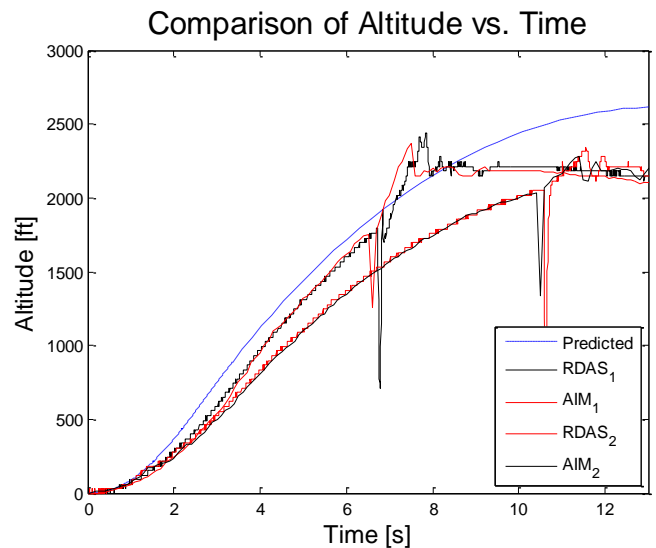


Figure 12: Predicted Versus Actual Altitude.

**Comparison of Times to Apogee.** The most notable error between our anticipated performance and experienced values was the time to apogee. This is a direct result of how the values were calculated using MATLAB's ode45 internal solver. Though very useful, this Runge-Kutta method tends to have a time-delay. In the absence of this shift, the projected altitude over time would have compared more favorably to the experienced rate. Additionally, with the over-estimated peak acceleration and altitude, the rocket was flying at a lower speed than what was anticipated, so the time to apogee was affected by that as well.

**General Flight Observations.** A more subjective look at each of the flight paths of the rocket validates the design calculations. Both rockets experienced relatively straight flights to apogee, confirming that the calculated margins were stable throughout ascent. Both flights had moderately successful deployment of the recovery system. However, the chutes received some burn damage during the first flight due to poor packing of the Nomex blanket, and had some tangled lines. Full deployment was achieved regardless, with successful drogue parachute and parafoil ejections from the body tube. The steering strings were unfortunately severed during ejection in the first flight, and overlooked during the rushed preparation for the second launch. This means that we were unable to effectively control the parafoil on either launch. In both cases though, the rocket clearly survived ground impact because of a design which maximized strength. It was thus determined that Team Rally Axe accomplished two successful launches.

## **Conclusion**

In its second year in the competition, Team Rally Axe was confident in its design and construction of custom-made components from common materials. With two separation points and a controlled recovery system to design, several engineering challenges were presented to maintain the required durability, but were creatively solved. Key features of the rocket included wood bulkheads secured through the PVC body tube, a parafoil descent, and an electronics bay coupler. The team's confidence that the design was safe to fly, strong enough to survive adverse conditions, and powerful enough to reach the minimum altitude requirement was validated when all three hypotheses were tested and confirmed through two competition launches, and a second place finish was achieved.

## **References**

Hurt, Hugh H. *Aerodynamics for Naval Aviator*. [Washington, D.C.]: Office of the Chief of Naval Operations, Aviation Training Division, 1965. Print.

Lide, David R. *CRC Handbook of Chemistry and Physics: A Ready-reference Book of Chemical and Physical Data*. Boca Raton: CRC, 1996. Print.

# Team Rocket Power Design Report

2011 WSGC Collegiate Rocket Competition

Milwaukee School of Engineering

Brandon Jackson

Ben Steffes

Jonathon Slightam

## Executive Summary

The objective of the 2011 Wisconsin Space Grant Consortium Collegiate Rocket competition is to design and build a single-stage rocket that is controlled during decent to land close to a predetermined target under operating parachute(s). The rocket must reach a minimum altitude of 2000 feet and deploy its parachute(s) electronically. Upon recovery, the rocket must be determined to be in a flyable condition to be determined a successful recovery consider the recovery successful. The winner of the competition will be the rocket which lands closest to the landing target while meeting the previously stated criteria.<sup>1</sup>

After running preliminary simulations of performance, Team Rocket Power chose to utilize a 5.5-in diameter body tube along with the K513 motor. The guidance system for recovery consists of a steerable parachute which will be controlled from the ground through FM radio transmission. Upon reaching apogee, the rocket will descend under drogue chute until reaching an altitude of 1200 ft. At this altitude, a second, controllable parachute will be deployed for the final descent. Redundant flight altimeters will be utilized to ensure chute deployment.

Included in the report are detailed design decisions based on the competition parameters, governing physics, and the anticipated flight performance of the rocket. This report also includes photos of the construction process and a detailed budget.

## 1. Recovery Method Selection

Several potential recovery methods were generated, and the overall advantages and drawbacks of each option were assessed. A decision matrix (Table 1) was generated ranking each concept in several categories. From this decision matrix, Design 2 was then selected.

Table 1: Decision Matrix for Recovery Methods

Design	Risk	Cost	Complexity	Totals
1. Autonomous Control Parachute	1	2	1	4
2. Radio Control Parachute from Ground	2	3	3	8
3. Winged	2	2	1	5

Legend: 1-least beneficial 2-average 3-most beneficial

The radio controlled Parachute system would incorporate an R/C controller intended for model airplanes which would control two servo motors onboard the rocket. By controlling the deflection of the break lines for a square ram-air parachute, steering is obtainable.

Typical range for 72 MHz RC controls is limited to approximately 2000 feet. Since the direct path between rocket at apogee and the controller would exceed this distance, it was decided the rocket would descend under drogue chute until approximately 1200 feet where it would be within range of the controller. At this altitude, the altimeters will deploy the main parachute. Details of the development of the control system necessary for this recovery will be further discussed in Section: 3. Control System on Page 7.

## **2. Rocket Design and Construction**

Based on the parameters of the competition, the focus of the design was on the recovery method for the rocket. As a result, the rocket was designed around accommodating this feature. The following subsections will detail the process of motor selection and airframe design.

### **2.1 Motor Selection**

The competition parameters limit the motor selection to eight motor ranging from classes I to K. Teams were then challenged to select a motor which would sufficiently meet the requirements of the competition based on their design.

A decision was made to create a MATLAB program to simulate the performance of each motor across a range of weights given an anticipated rocket geometry and drag coefficient. For the previous year's competition, one team member wrote a simulation program which agreed well with commercially available software and measured flight results. This code was modified for this year's competition to include the ability to run multiple simulations across a range of weight classes and report peak altitude, acceleration, and velocities for each.

The code written took account of the following factors when determining the performance of the rocket:

- Aerodynamic drag
- Mass change of the rocket due to propellant loss
- Gravitational forces.

The following assumptions were made regarding the rocket geometry and launch conditions:

- Body tube diameter of 5.5"
- $C_D = 0.50$
- Standard temperature and pressure

It should be noted that factors such as wind, stability, and deviation from vertical flight could not be accounted for. As a result, these rough predictions are likely over estimates of the probable flight performance. To account for this uncertainty a buffer of 500 feet was added to the minimum required altitude for motor selection. This height buffer was decided from experience in previous year's competitions. The results of this simulation are shown in Figure 1.

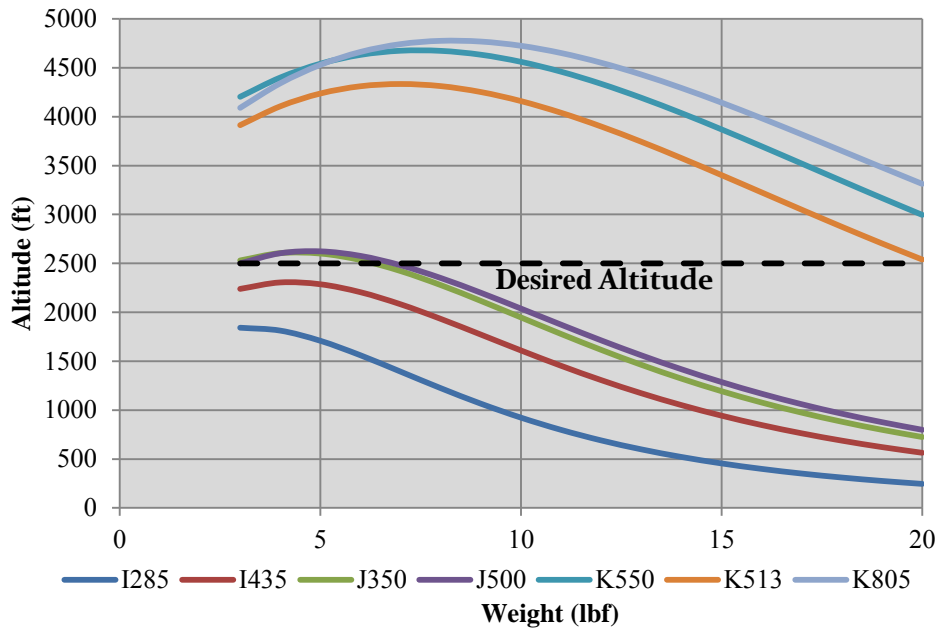


Figure 1: Motor Performance Results Across Potential Weights

The mass of desired components was assessed to obtain a predicted final weight of 10 lbf. With addition of the motors, the takeoff weight was predicted to be between 12 and 15 lbf. From constraint criteria, the K513 motor was selected.

## 2.2 Airframe Design

Simulations were run on various body tube diameters to determine their effect on overall performance, shown in Figure 2. Based on this simulation and the need for space for housing the internal components, it was decided that the 5.5-in diameter body tube would best meet the requirements for this competition and design.

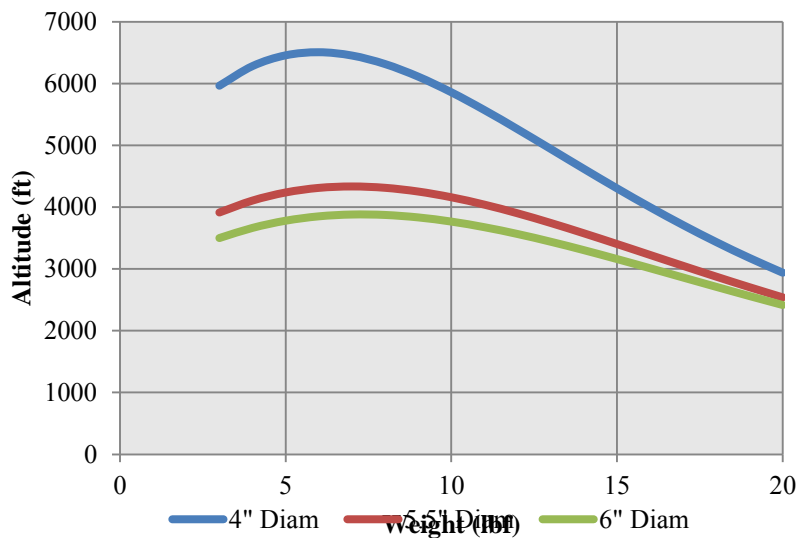


Figure 2: Effects of Body Tube Diameter on Overall Altitude

The primary challenge for this competition was the design of the control system for the rocket. As a result, the overall design of the rocket was aimed to be as simple as possible. A simple two stage rocket utilizing high density, high strength cardboard was decided upon. A cost analysis was performed on the components necessary to construct the design from individual parts from reputable vendors. This total cost was compared against that of purchasing an existing kit and modifying to fit our needs. It was determined that the most cost effective way to construct the rocket would be to modify an existing kit. The HyperLOC 1600 was purchased and modified for the design. These modifications will be discussed further in the subsequent sections. The overall design of the rocket is shown in Figure 3.

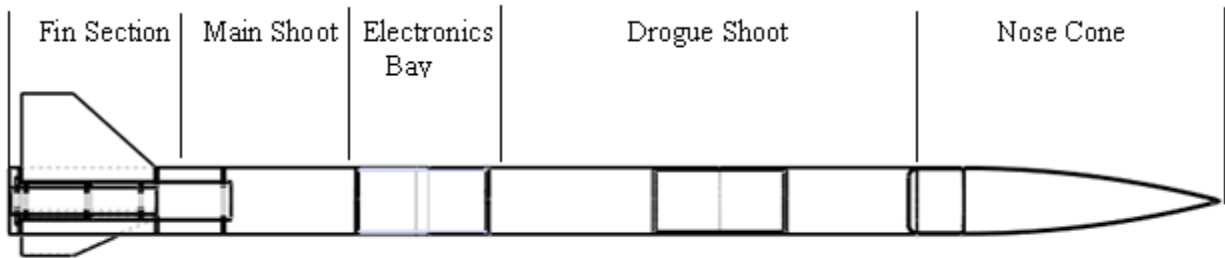


Figure 3: Rocket Schematic

### 2.2.1 Center of Gravity (CG) and Center of Pressure (CP)

The relationship between the center of pressure and center of gravity is one of the most important relationships in high powered rocketry. The center of pressure is defined as the point at which the aerodynamic forces on the rocket are centered. The center of gravity is the location at which the whole weight of the rocket can be considered to act. The relationship between these two locations can be used to predict the stability of the rocket during flight. Generally, the center of gravity must be at least one body-tube diameter forward of the center of pressure. The NFPA 1171: Code for High Powered Rocketry requires that the flyer must be capable of providing the location of the CG and CP prior to launch.

The center of pressure was determined analytically through the use of Barrowman's theory.<sup>ii</sup>

The following assumptions were made during the derivation of this theory:

1. The flow over the rocket is potential flow.
2. The point of the nose is sharp.
3. Fins are thin flat plates.
4. The angle of attack is near zero.
5. The flow is steady and subsonic.
6. The rocket is a rigid body.
7. The rocket is axially symmetric.

The rocket design presented in this paper did not violate any of these assumptions; therefore, this theory was utilized. Detail into the equations used can be found in **Error! Reference source not found.**

Using modeling software, the location of the CG was estimated. This estimate was used to determine the location of the desired center of pressure. The exact center of gravity was later determined through balancing the rocket on a wooden dowel and noting the point where the rocket remained balanced. This was performed with and without the propellant mass to obtain the stability before and after burnout.

The results obtained from Barrowman's Theory were compared against those generated through the simulation software. These results yielded similar results.

The overall location and of the CP and CG are shown in Table 2:

**Table 2: Location of CP and CG (In Inches)\***

	<b>Center of Gravity (CG)</b>	<b>Center of Pressure (CP)</b>	<b>Stability (Caliber)</b>
<b>Ignition</b>	70.5	76	1
<b>Motor Burn Out</b>	67	76	1.65

\* Distance from nose tip.

### 2.2.2 Fin Design

The design of the fins is the most important factor in determining the location of the center of pressure and stability of the rocket. Even at small angles of attack, fins provide high restoring forces to correct any imbalances. Using an iterative approach and Barrowman's Theory, several potential fin geometries were analyzed. The final fin design, shown in Figure 4, utilizes three fins which are equally spaced.

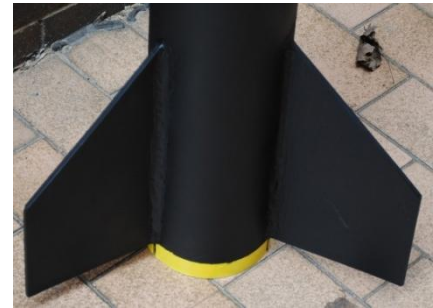


Figure 4: Fin Design

Fins were constructed using five-ply 1/4in. plywood. G10 fiberglass is often preferred over plywood; however, plywood was selected due to availability, and ease of use. To account for this weakness, through-the-wall fin construction with adhesive fillets on all contact surfaces was used for the construction.

### 2.2.3 Pressure Relief

Barometric altimeters must have proper venting to outside air during flight to account for pressure changes, which are used to determine altitude. This is critical since both RRC2 and R-DAS altimeters use barometric pressure sensor. Improperly sized static port holes can result in early or late parachute deployment.<sup>iii</sup> To determine the proper size of the static port holes for rapid pressure equalization, the following equations were used:<sup>iv</sup>

$$D_{\text{single}} = 2\sqrt{(r^2)(4.908 \times 10^{-4})}$$

$$D_{\text{hole}} = \sqrt{\left(\frac{D_{\text{single}}^2}{n}\right)}$$

Where:

$D_{\text{single}}$  is the diameter of the static port hole

$r$  is the radius of the bay (~2.5 inches)

$l$  is the length of the bay (~10 inches)

$n$  number of holes

$D_n$  diameter of  $n$  holes

It was decided to use three static port holes equally spaced around the electronics bay to reduce the likelihood that a wind gust would result in the altimeter detecting apogee and firing the ejection charges prematurely. The resulting minimum diameter for the port holes was 0.22 inches.

### **2.3 Electronics Bay**

The electronics bay, which serves as a coupler for the top and bottom sections of the rocket, houses both the parachute altimeters in addition to: the WSGC RDAS altimeter, servos, FM receiver, and batteries. To insulate the electronics from ejection-charge gases, a standard design was employed which utilized bulkheads above and below a tube coupler. Threaded steel rods were passed through the bay to which the electronics board was attached. Finally, holes were drilled in the tube coupler to allow for wires to be passed through, thus allowing the altimeters to be armed while the rocket is on the launch rail.

The front and back sides of the electronics board are shown in Figure 5 and Figure 6, respectively.



Figure 5: Electronics Board (Front)

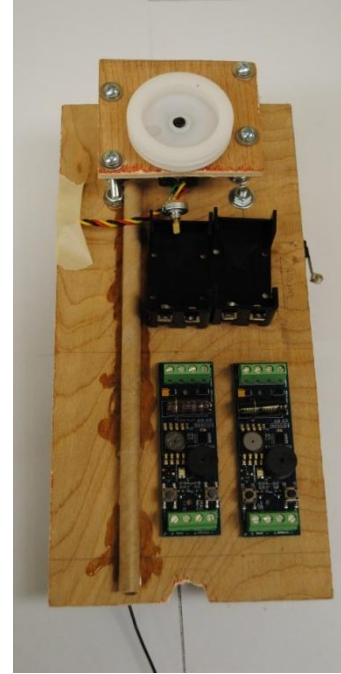


Figure 6: Electronics Bay (Back)

### 3. Control System

The control system was designed to guide the rocket to a designated landing site using a steerable ram-air parachute. The goal was to use two servos to control the two control lines on the parachute. As a result of the relatively large weight of the rocket these servos needed to handle high torque to control the parachute and allow continuous rotation.

Initially, two options of control were considered. The first option was to use XBee modules and an Arduino microcontroller board to drive the servos. This option would allow the rocket to be controlled by a ground based PC using digital RF data transfer and would allow an operable range of over a mile. The only recognized problems with this method were our lack of digital RF data transfer experience, high cost, and the use of a keyboard rather than a controller.

The second option was to use a FM transmitter and receiver pair designed for R/C aircraft control. This option would offer a more standard approach to aircraft control and come at a lower cost than the Arduino based control. The main drawback of this method was relatively short range of approximately 2000ft (conservative). This drawback could easily be resolved by using a drogue chute to drop the rocket to a lower altitude within range of the transmitter before deploying the main chute and turning on the receiver.

The decision was made to use the FM transmitter and receiver pair. This approach required that the receiver be turned on only when within range of the transmitter to prevent unwanted motion of the servos which resulted when the receiver neared the edge of its range. This was resolved using a contact switch which, when released, supplies power to the receiver. This contact switch was placed so that it would be released when the body tube separates from the equipment bay at the deployment of the main chute.

The transmitter used was the HiTEC Laser 6 FM which operates in the 72MHz range. The selected receiver was the HiTEC Supreme 8 FM with auto-shift. The channels were arranged on the controller so that both servos could be controlled from one control stick and rotate at equal angular velocities in opposite directions.

The control components are shown in Figure 7.

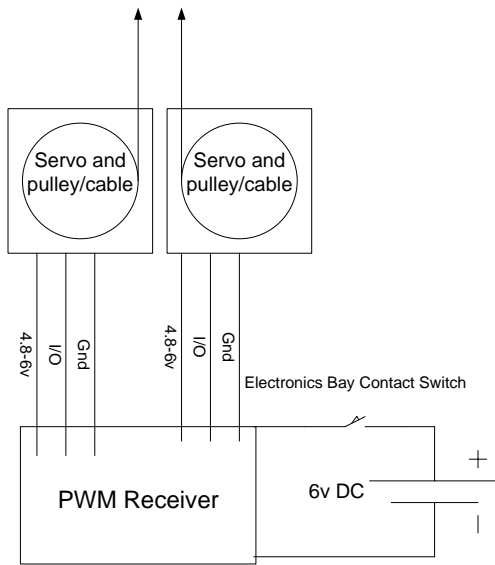


Figure 7: Diagram of Control System



Figure 8: HQ Series Symphony Beach (1.7 m)<sup>v</sup>

### 3.1 Servo Modification

Standard servos provide position control, thus allowing a specific angular deflection of the shaft to be controlled. In this application, the servos need to operate continuously where an angular velocity of the output shaft is controlled. Doing this required modifying servos by removing a mechanical stop (pin) in the servo gearing and moving the internal potentiometer to outside of the servo housing. This potentiometer was then used to set the neutral control stick position to a zero velocity of the servos.

The servos purchased and modified for the control of the parachute were HiTEC HS645MG Ultra Torque servo motors. These servos provide a rated torque of 106.93 oz-in. at 4.8v and 133.31 oz-in. at 6v. Based on an estimated 13 lb rocket weight, these servos will be sufficient in supplying the required torque to deflect the parachute and control the descent.

### 3.2 Parachute Design

The primary recovery method for the rocket utilized a HQ Series Symphony Beach stunt kite (Figure 8). The geometry of this kite is very similar to that of a ram-air parachute, allowing it to be easily adapted for this design. Ram-air parachutes can obtain directional control can be obtained through deflecting one side of the parachute using a break lines. For integration into the rocket design, high torque servos control by a FM transmitter on the ground will produce the deflection necessary for directional control.

Unlike traditional round-parachutes, which generate no lift, ram-air parachutes are designed for lift generation. As a result, the proper decent rate for such a design is difficult to obtain without a great deal of testing. In attempt to estimate the descent rate for the rocket, the parachute was approximated as a square chute. The resulting terminal velocity for the rocket was 22 ft/s. This is on the high end of preferred decent rates; however, this does not account for lift generation of the airfoil, contributions of the drogue chute, or drag on the actual rocket body itself.

### 3.3 Other Control Considerations

It should be noted that the selected control method requires that the antennas of both the receiver and the transmitter be matched either horizontally or vertically for optimal range. Also, to avoid interference, the controller should in the possession of the launch coordinators until the rocket is to be launched.

## 4. Anticipated Performance

Two simulation programs were used to design and estimate the performance of the rocket. The programs used to simulated performance were RASAero and a program written using MATLAB by a team member. The results from both simulations will be combined to predict the performance of the rocket. The overall weight of each assembly/components was measured and is shown in Table 3.

Table 3: Component Weights

<b>Part</b>	<b>Weight (oz)</b>
Nose Cone	22.96
Top Section	41.37
Base Section	65.99
Electronics Bay	35.76
Main Parachute	6.60
Recovery Harness	9.88
Drogue chute	1.23
2x RRC-2 Altimeters, RDAS, Receiver	4.23
Batteries and Holders	9.77
Ballast	0
Motor Casing & Nozzle	23.74
Total (w/o propellant):	221.53

### 4.1 Motor Thrust Curve

The motor thrust profile for the AeroTech K513 is shown in Figure 9. From the thrust curve, the weight of the propellant at any given time can be approximated as being equal to the area under unburned portion of the thrust time curve relative to the total area, which is then multiplied by the initial propellant mass.

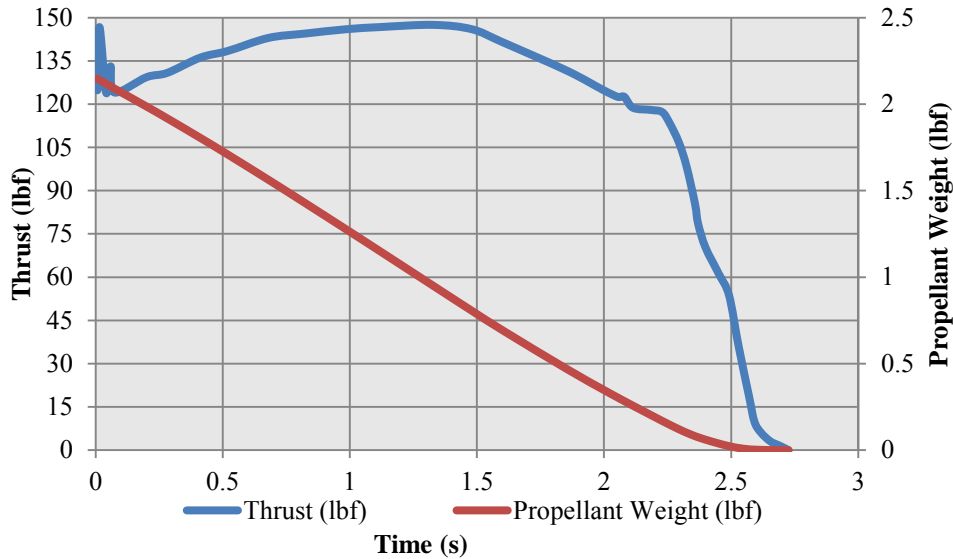


Figure 9: Motor Thrust and Propellant Weight Profile

The average thrust of this motor is approximately 125 lbf, yielding a thrust to weight ratio of 10:1 for the rocket, well above the minimum 5:1 ratio.

#### 4.2 Limitations and Assumptions

The primary assumptions made were that the rocket would be launched vertically and that the rocket would follow a vertical flight path.

#### 4.3 MATLAB Simulation

The MATLAB simulation was designed to be a basic simulation program used in addition to RASAero. This program was originally developed and used in the 2010 WSGC competition and compared closely with flight data. The program was designed to perform the following functions:

- Load thrust data obtained from ThrustCurve.org
- Interpolate thrust curve for more discrete steps
- Calculate change in mass resulting from burnt propellant
- Calculate velocity from the combined impulse from drag, gravity, and thrust
- Calculate altitude and acceleration from velocity
- Determine maximum altitude, velocity while leaving the launch rail, and landing velocity
- Export all data to excel for graphical analysis

The velocity of the rocket was determined from the previous momentum plus the impulse. This relationship is shown in Eq. 1:

$$m_i v_i + F_i \Delta t = m_{i+1} v_{i+1} \quad [1]$$

Where  $F_i$  is the net force acting on the rocket and  $\Delta t$  is the time step between calculations. The net force acting on the rocket during ascent is expressed in Eq. 2:

$$\begin{aligned}
F_{net} &= F_{grav} + F_{drag} + F_{thrust} \\
&= m_i g + \frac{1}{2} \rho v_i^2 C_d A + T_i
\end{aligned}
\tag{2}$$

Where:

$\rho$  is the density of air

$C_d$  is the coefficient of drag

$A$  is the frontal cross sectional area of the rocket

$T_i$  is force from the motor

Substituting Eq. 2 into Eq. 1 and solving for  $v_{i+1}$  yields:

$$v_{i+1} = \frac{1}{m_{i+1}} \left[ v_i m_i + \frac{1}{\Delta t} (T_i - m_i g - k v_i^2) \right]
\tag{3}$$

Where:

$$k = \frac{1}{2} C_d A$$

Acceleration was calculated using Newton's second law which is expressed in Eq. 4:

$$a_i = \frac{F_i}{m_i}
\tag{4}$$

The trapezoidal method for approximating the area under a curve was used to calculate the altitude of the rocket during the flight.

From the acceleration, velocity, and position data the maximum altitude, peak acceleration, and velocity while leaving the launch rail were determined. These results will be discussed in the subsequent section.

It should be noted that this simulation was not able to account for variables such as wind speed and direction, launch altitude, the effects of stability on flight, and flights other than perfectly vertical.

#### 4.4 RASAero

RASAero is a free, open source, software similar in function to RockSim. It is capable of calculating acceleration, velocity, and position data while accounting for variables including: elevation, wind speed, and the effects of individual components such as surface roughness and leading edge fin radii on drag and stability. For the simulation performed for this analysis, wind speeds were set to 12-mi/hr. This speed is an estimate of the average wind speed in May for south-eastern Wisconsin by NOAA.

### 4.5 Flight Prediction

Altitude, acceleration, and velocity predictions are compared between the MATLAB and RASAero simulations Figure 10.

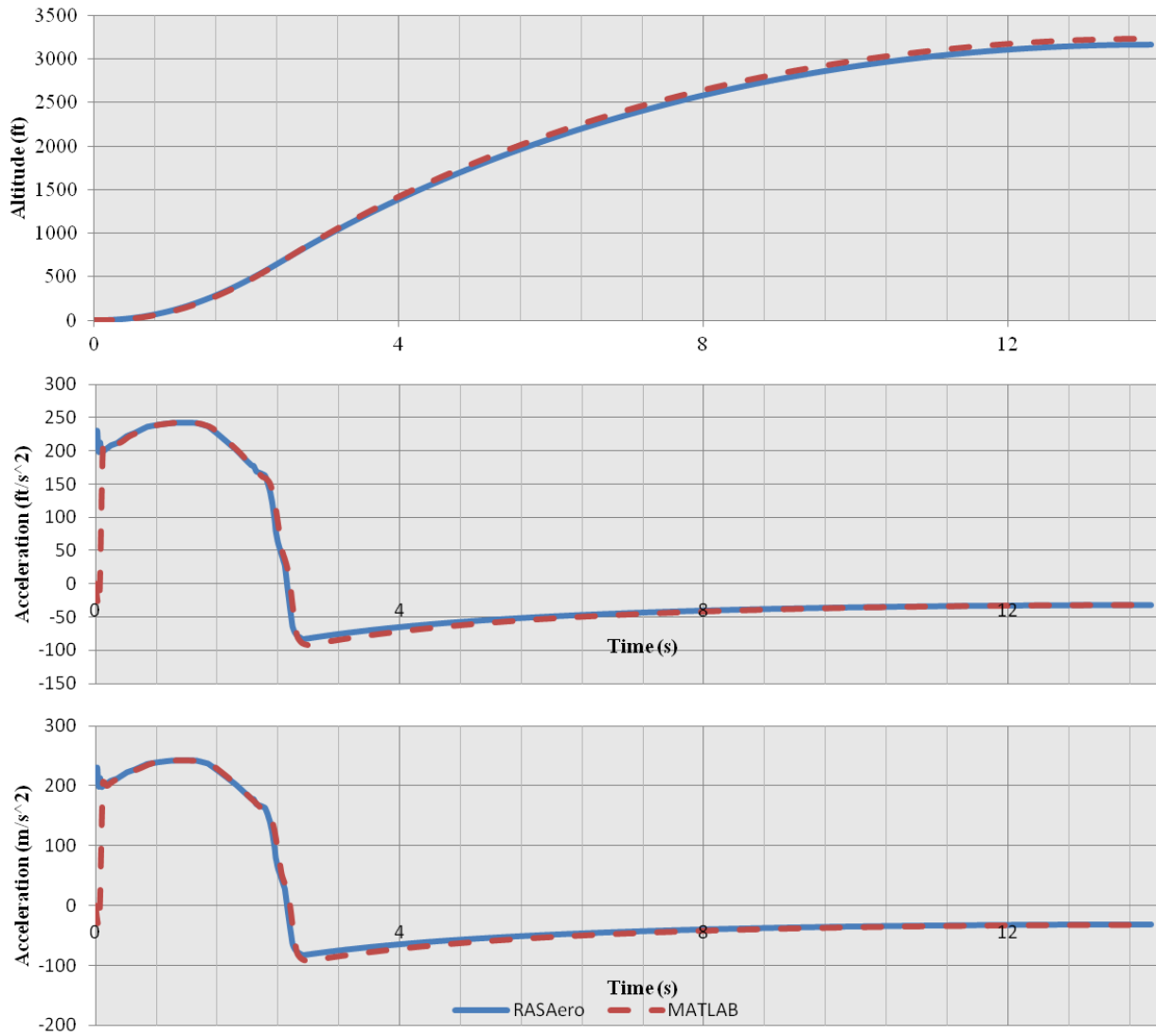


Figure 10: Simulated Flight Performance

Simulated peak altitude, acceleration, and velocity for each simulation method are compared in Table 4.

Table 4: Simulation Result Comparison

	RASAero	MATLAB	% Diff
<b>Altitude (ft)</b>	3164	3230	2.06
<b>Acceleration (ft/s<sup>2</sup>)</b>	243	243	0.12
<b>Velocity (ft/s)</b>	515	539	4.64

## 5. Conclusion

This design will provide a safe and effective flight in which the goals set by the WSGC are achieved. The rocket is expected to climb to an altitude of approximately 3000 ft where it will then descent by drogue chute to approximately 1200 ft. At this altitude, a ram-air parachute controlled by servo motors will be used to steer the rocket to the desired landing site.

---

<sup>i</sup> WSGC 2011 Collegiate Rocket Competition Handbook

<sup>ii</sup> Barrowman, James. "The Theoretical Predictions of the Center of Pressure." (1966). Apogee Rockets. Web. 13 Apr. 2011. <[http://www.apogeerockets.com/education/downloads/barrowman\\_report.pdf](http://www.apogeerockets.com/education/downloads/barrowman_report.pdf)>.

<sup>iii</sup> Canepa, Mark B. "Chapter 8 - High-Powered Electronics." *Modern High-power Rocketry*. Victoria, B.C.: Trafford, 2005. E-Book.

<sup>iv</sup> Missile Works. "RR2 User Manual and Instructions."

[http://www.missileworks.com/user\\_downloads/RRC2X\\_RevC.pdf](http://www.missileworks.com/user_downloads/RRC2X_RevC.pdf)

<sup>v</sup> S. Friswold, Amazon.com: Customer Image; [http://www.amazon.com/gp/customer-media/product-gallery/B0015KAMS4/ref=cm\\_ciu\\_pdp\\_images\\_0?ie=UTF8&index=0](http://www.amazon.com/gp/customer-media/product-gallery/B0015KAMS4/ref=cm_ciu_pdp_images_0?ie=UTF8&index=0)

# **21st Annual Conference Part Three**

NASA Reduced Gravity Program

# Modal evaluation of fluid volume in spacecraft propellant tanks

Stephanie Finnvik<sup>1</sup>, Steven Metallo<sup>1</sup>, John Robinson<sup>1</sup>, Kevin M. Crosby<sup>1,†</sup>, Rudy Werlink<sup>2</sup>

<sup>1</sup>Carthage College, Kenosha, WI, USA

<sup>2</sup>NASA Kennedy Space Center, Florida, USA (rudy.werlink-1@nasa.gov)

<sup>†</sup>Corresponding author: kcrosby@carthage.edu

## Abstract

A novel, real-time method of determining the volume of propellant present in a spacecraft tank in reduced gravity is presented. In the experiment reported here, modal analysis techniques are applied to detect shifts in resonant mode frequencies of a fluid-loaded tank as fluid is drained from the tank. These experiments are conducted in the weightless environment of parabolic flights through participation in the NASA Systems Engineering Exploration Discovery (SEED) program. Ground testing of the experimental methods is compared with the flight data, and the resolution of the analysis is estimated to be better than 10% of actual fill-fraction. Comparison with existing direct and indirect techniques for assessing propellant volume in reduced gravity suggests that the modal analysis method may prove to be more cost effective and afford better resolution than existing methods.

## Introduction

Direct measurement of fluid volume in spacecraft propellant tanks is a significant challenge in microgravity environments [Fortescue et al., 2003]. In reduced gravity, traditional buoyancy or level-based techniques for fuel gauging are not useful, necessitating the use of indirect methods such as those based on equations of state (for pressurized propellant systems), impulse-response measurements of spacecraft motion, and even careful bookkeeping of thruster burn times to estimate total fuel consumption. Many of these methods require additional hardware for tank pressurization or additional propellant burns to monitor spacecraft dynamics in order to infer mass. With launch costs reaching \$10,000 per pound, uncertainty in fuel consumption is an extremely important consideration in the economics of spaceflight [Peters, 2004].

In the study reported here, we employ experimental modal analysis (EMA) to infer fluid volume in a model tank over a range of fill levels. Structural resonant frequencies shift with fluid loading as the effective mass and/or the stiffness of the structure is affected by the presence of fluid. These shifts in resonant frequency can be measured and monitored using standard techniques of EMA.

## Background

Modal analysis techniques involve the application of acoustic forces to test structures. The input forces can be in the form of point sources such as impact hammers or can be presented as continuous, broad spectrum excitations such as noise or chirp functions. Natural resonances of the test structure will be excited by particular frequencies present in the the applied force, and sensors affixed to the structure record the amplitude of the acoustic response across the range of resonating frequencies.

Typically, EMA involves the computation of frequency response functions (FRF) to determine the resonant frequencies present at each sensor location. The FRF is computed as the ratio of the Fourier Transform of an output sensor to the Fourier Transform of the input signal. In this way, the FRF shows peaks at the frequencies where the sensor records a strong resonance that is not present in the spectrum of the input signal. In practice the Fourier Transforms are calculated using Fast Fourier Transform (FFT) algorithms. Modal techniques can therefore be used as real-time diagnostics of structural properties. In practice, a “monitor sensor” is positioned near the actuator to record the driver signal produced by the actuator, and is used instead of the input signal to construct the FRFs. Additional sensors are placed at different locations on the test item as discussed in Research Objectives below.

Mathematically, we denote the time series recorded by the monitor sensor as  $x_0(t)$ , and the time series recorded by the  $i$ -th ( $i = 1, 2, \dots, n$ ) sensor as  $x_i(t)$ . The Fourier transforms of these voltage signals in frequency-space are denoted by  $X_i(\omega)$ . In terms of the transforms, the FRF of the  $i$ -th sensor data is computed according to

$$H_i(\omega) = \frac{X_i(\omega)}{X_0(\omega)}. \quad (1)$$

$H_i(\omega)$  is a complex valued function, but here we consider only its real part which provides the information on resonance amplitudes. Data from multiple sensors ( $n \geq 2$ ) can be used to reconstruct geometric properties of the tank. In our case, we are less interested in the known geometric properties of the tank than in tracking frequency shifts of the primary modes.

EMA has long been used to infer the existence, location, and extent of physical defects such as fractures in a load-bearing column or beam [Pandey et al., 1991]. These techniques are also widely used in the component design process in the automotive and aerospace industries. More recently, modal techniques have been successfully used in the characterization of fluid-filled structures such as water tanks subject to the shear forces associated with earthquakes [Malhotra et al., 2000].

## Research Objectives

The central objective of the present study is to demonstrate the feasibility of real-time, non-invasive modal analysis to determine propellant volume contained in a model spacecraft tank subject to sloshing in a zero-g environment. Fluid in a container may have two opposing influences on the

structural resonances of the container. In some cases, it is possible that fluid loading of structures serves to increase the effective stiffness of the structure, an effect that would result in an increase in the structure's resonant frequencies. It is also possible that fluid loading will increase the effective mass of the loaded structure, resulting in a decrease in the structure's resonant frequencies. Whether fluid in a tank serves to increase or decrease structural resonant frequencies is determined by the coupling of fluid properties and the elastic moduli of the tank material. Extensive ground-testing performed on the tank in this study and on other tanks at NASA KSC suggests that the dominant effect of fluid loading with water and other propellant simulants is to increase the effective structural mass, thereby decreasing resonant mode frequencies.

The zero-g data was obtained through participation in NASA's Systems Engineering Exploration Discovery (SEED) student microgravity parabolic flight program. In order to assess the feasibility of modal techniques in this application, we have established preliminary estimates of the resolution of the technique in 1-g, and carried out a statistical analysis of zero-g modal data at several fill fractions. Our working hypothesis for this project is that the effective mass of the tank is correlated most closely with the total contact area between fluid and tank wall surface (provided a minimum thickness of the fluid layer). The sloshing and swirling of the fluid in reduced gravity will result in variation of total contact area between fluid and tank walls, and therefore in a fluctuation of the resonant frequencies around the corresponding flat-surface 1-g values obtained in lab testing. We therefore expect to have to average over time windows that are much longer than the typical slosh periods. For our tank, we estimate slosh periods on the order of one second, so that our FRF time averaging will need to take place over multiple 1.0-sec. windows.

Finally, we identify experimental modes present in our data using the structural shell theory of Soedel [Soedel, 1981]. Identification of experimental modes in terms of shell theory is necessary in order to study the influence of structural artifacts such as mounting brackets and weld seams on the tank's modal response. Mode identification is also necessary to understand the optimal placement of sensors because each mode represents the unique superposition of longitudinal (wave propagation up and down the length of tank) and radial vibrations. For this reason, transverse modes are typically identified by two mode numbers referencing each of the two characteristics.

## **Experimental Design**

Our experimental rig consists of a cylindrical steel tank of diameter 15.3 cm, and total length including two (approximately) hemispherical end caps of 48.3 cm. The tank has a capacity of two gallons, and has six FPT ports to which are attached pressure gauges, drain and fill valves, and a pressure-release valve. The tank has two welded feet for attachment to a support structure. Fig. 1 shows the tank in schematic. In the experiments reported here, the tank is oriented vertically.

Affixed to the tank are three PZT-based MFC sensors and an actuator of identical design [Smart Materials, 2011]. The actuator is driven with a white noise acoustic signal generated in LabView software from a random function sampled at 24kB/sec, amplified and biased over the voltage range -100 to 350V [National Instruments, 2011]. The actuator is capable of faithfully reproducing the driver signal over the frequency range 0-10kHz with average power generation of

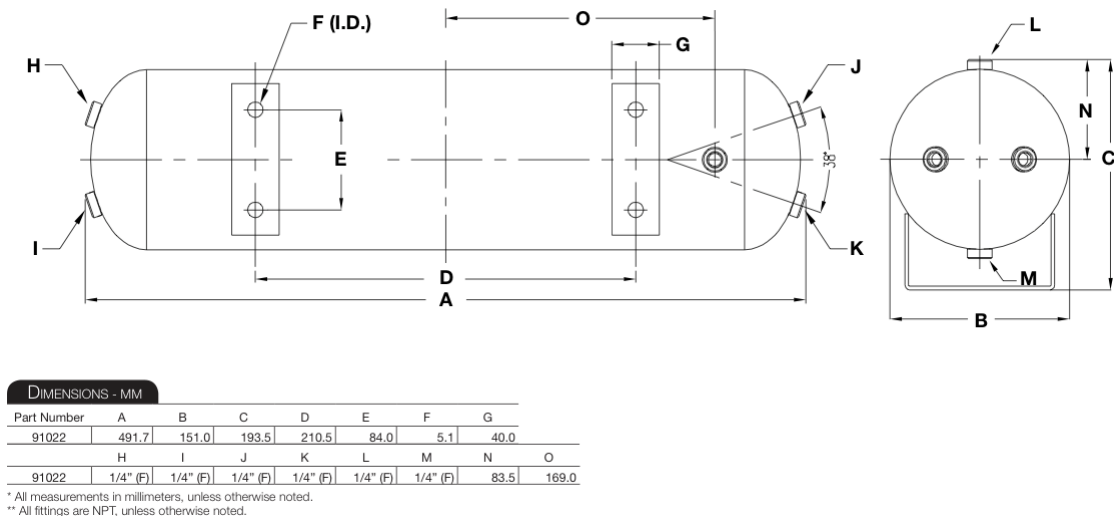


Figure 1: Schematic of experimental tank [Viar, 2011].

20W. A single sensor placed adjacent to the actuator responds directly to the actuator signal and is identified as the monitor sensor. Two additional sensors placed at empirically determined anti-nodal positions on the tank convert structural response vibrations to proportional voltage signals for processing in a data acquisition rig. The two response sensors and the monitor sensor comprise the data stream for the experiment, and their signals are sampled by a data acquisition box at 16kB/sec to ensure that the Nyquist frequency lies well above the upper end of the frequency range of interest, 0-5kHz. The schematic relationship of electronic components in the experimental rig is illustrated in Fig. 2.

Our team designed a custom software interface for the automated acquisition of data through the use of LabView. The interface allows for the control of data file generation and storage, pump and valve control, and DAQ settings. Design of the interface was complicated by the need to ensure that operators could manage the experiment in the challenging environment of weightlessness. Simple interface operations such as pushing buttons and typing commands that are taken for granted in lab are exceedingly difficult in zero-g environments.

In flight configuration, the experimental tank is initially 70% full with water. A software-triggered solenoid valve opens to drain a fixed amount of fluid from the tank into a reservoir through a small pump. We chose to keep the same fill-level for a minimum of five consecutive parabolas before draining down to next targeted fill-level. In this way, we obtained enough data at each fill-level to ensure reasonable statistical validity of the resonant frequency shifts. Fill levels are monitored by means of a flow-rate meter and post-flight calculations based on the volume of fluid contained in the reservoir tank.

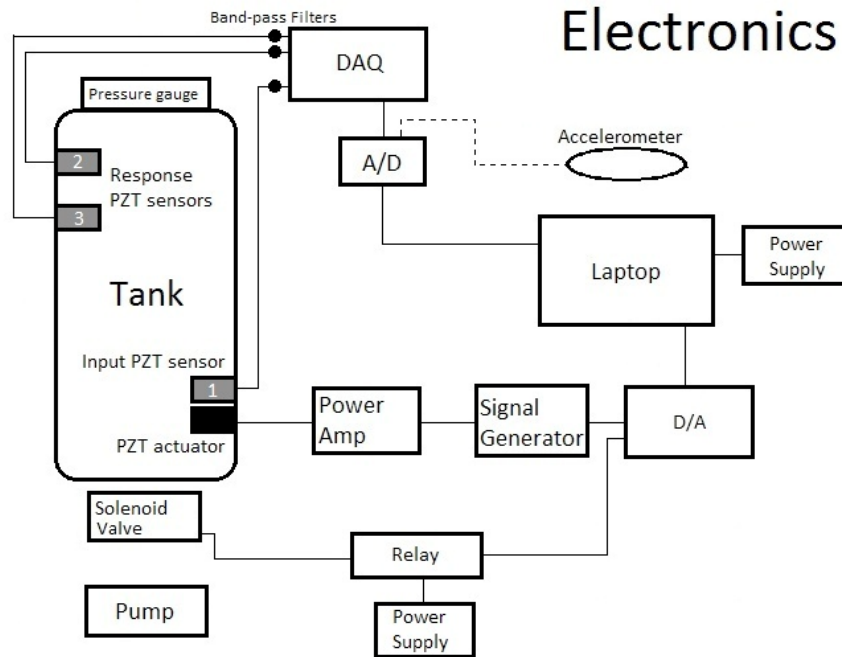


Figure 2: Data acquisition schematic.

## Results

Fig. 3 shows a typical FRF spectrum recorded for the empty tank in 1-g lab testing. Several prominent resonances are present, with the fundamental mode at 740 Hz. The data were acquired with a 1 second window at a sampling rate of 16kB/sec. The frequency resolution is 1.0 Hz. As sensor positions are varied along the length of the tank, the fundamental resonance at 740 Hz varies significantly in amplitude, disappearing entirely at nodal locations.

In Fig. 4, FRFs are recorded across several representative fill fractions with the fluid in equilibrium under 1-g lab testing. The frequency of each of the primary resonances decreases with increasing fill fraction from 0 to 70%. These data confirm that the dominant role played by the fluid is one of mass-loading. The structure's effective mass increases with fluid load, resulting in a continuous decrease in the frequencies of the primary resonances of the tank. It is also important to note that the amplitude of the fundamental resonance (inset of Fig. 4) does not decrease with increasing fill fraction.

In the reduced gravity of the parabolic flight, fluid instabilities cause the fluid to swirl and slosh throughout the tank for periods that exceed the 30 second parabola time. The fluid is therefore in constant motion, and the sloshing results in continual variation of the contact area between fluid and tank wall. As a result, the frequencies of resonant modes will shift with periods on the order of the average slosh period of 1-2 seconds. To obtain reliable average peak positions at each fill-fraction, we choose to average multiple 1.0 second windows of FRF data to obtain average peak positions. A set of sample averaged FRFs is shown in Fig. 5. The effect of the sloshing is evident

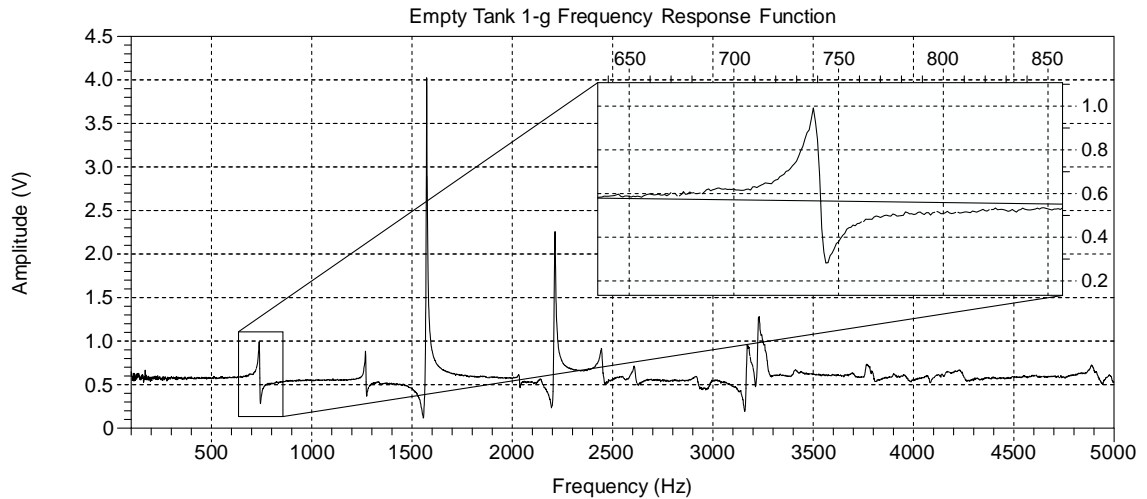


Figure 3: Empty Tank Frequency Response Function. Inset shows blow-up of fundamental mode.

in the increased noise and reduced amplitude of the mode peaks in Fig. 5.

To address the central question of the feasibility of the modal analysis technique for establishing the fluid volume in the tank, we extract the positions of the fundamental mode at each known fill-fraction. These data for both ground and flight data are presented in Fig. 6. The flight data in Fig. 6 have been averaged over between 5-20 1.0-second windows, resulting in a frequency resolution that is better than 10% in fill fraction. The resolution of the method may in fact exceed the 10% we estimate, but flight data was only obtained for four different fill fractions; a better assessment of mode shift resolution will require additional flight data.

### Comparison with Shell Theory

To identify the modes present in the FRF data, we turn to Soedel's theory of shell vibrations [Soedel, 1981]. In the context of this theory, we consider a simply supported thin, cylindrical shell, open at both ends, and simply supported at its ends. The free vibrations of a simply supported shell can be characterized by three mode numbers,  $(l, m, n)$ . Here  $l$  references the oscillation type (transverse, in-plane). We consider the  $l = 0$  modes where transverse component of oscillations dominates as these modes are an order of magnitude lower than the higher-order (shear and in-plane)  $l$  modes. These higher order modes are not observed in the experimental data. The mode number  $m$  characterizes the longitudinal vibrations that propagate along the length of the cylinder, while  $n$  characterizes the circumferential vibrations. Therefore, we are interested in the  $f_{lmn}$  modes for comparison with our experimental modes.

For the material and geometric properties of our tank, we find the theoretical modes associated with the equivalent open, simply supported cylinder to be slightly lower than the empty tank modes determined experimentally. The set of theoretical modes for the open cylinder and the closest matching experimental empty-tank modes are shown in Fig. 7.

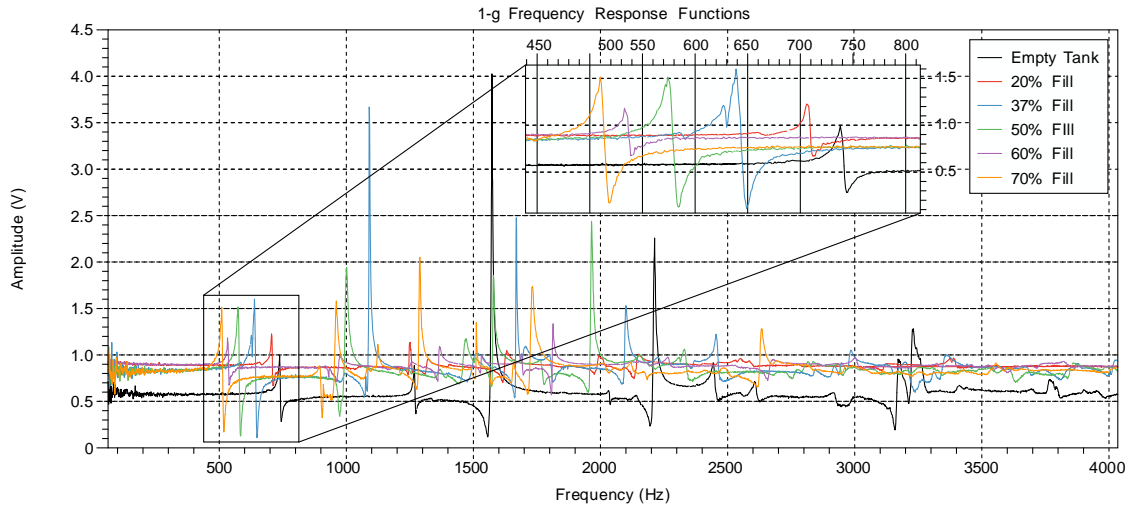


Figure 4: 1-g Frequency Response Functions recorded for fluid in equilibrium with tank in vertical position. Inset shows blow-up of fundamental mode and demonstrates the decrease of mode frequency with increasing fill-fraction.

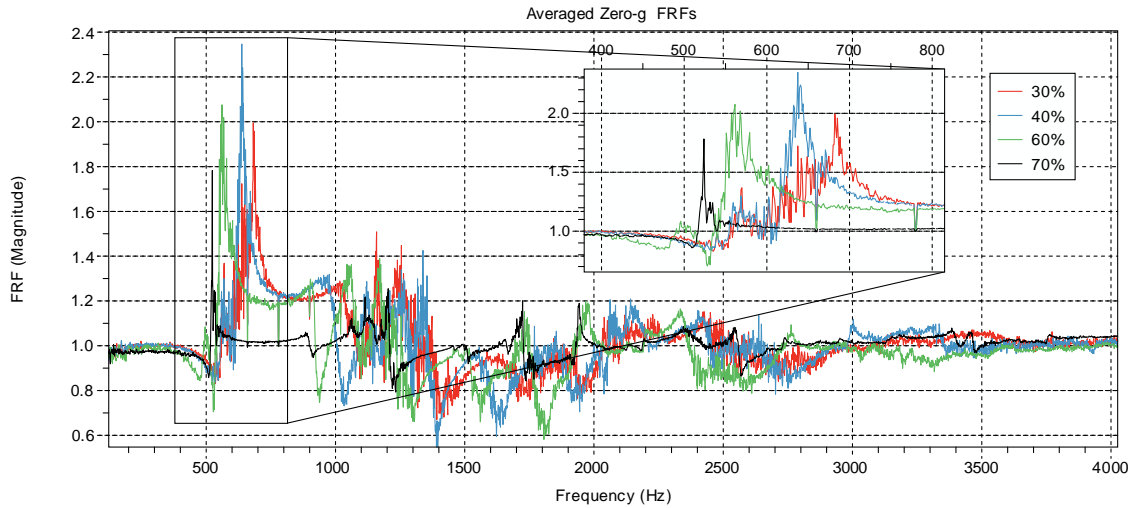


Figure 5: Zero-g Frequency Response Functions recorded for fluid with tank in vertical position. FRFs are averaged over multiple 1.0 second windows. Inset shows blow-up of fundamental mode and demonstrates the decrease of mode frequency with increasing fill-fraction.

While there is reasonable agreement between the lowest experimentally determined modes and the theoretical values for  $f_{112}$ ,  $f_{113}$ , and  $f_{114}$ , these open cylinder modes are generally lower in frequency than the equivalent modes for a tank with end caps. We have verified this by taking FRF data with a model PVC tank with removable end caps. Further, the result is easily understood in terms of the clamping boundary condition provided by the end caps. Such clamping generates fixed nodes that should increase the resonant frequencies. Additionally, there are several modes present in the experimental cylinder that do not appear in the theoretical mode spectrum of Soedel.

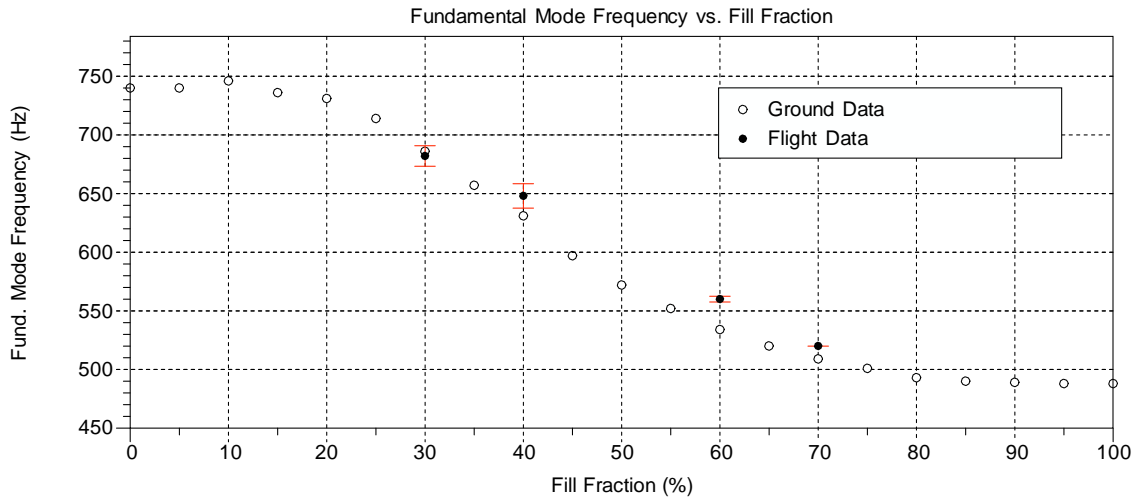


Figure 6: Variation of fundamental mode frequency with fill fraction for both 1-g equilibrium fluid configurations and zero-g slosh-averaged fluid. Error bars on the flight data represent standard error in the data, while error bars for the 1.0g data are not depicted, but would be smaller than data symbol.

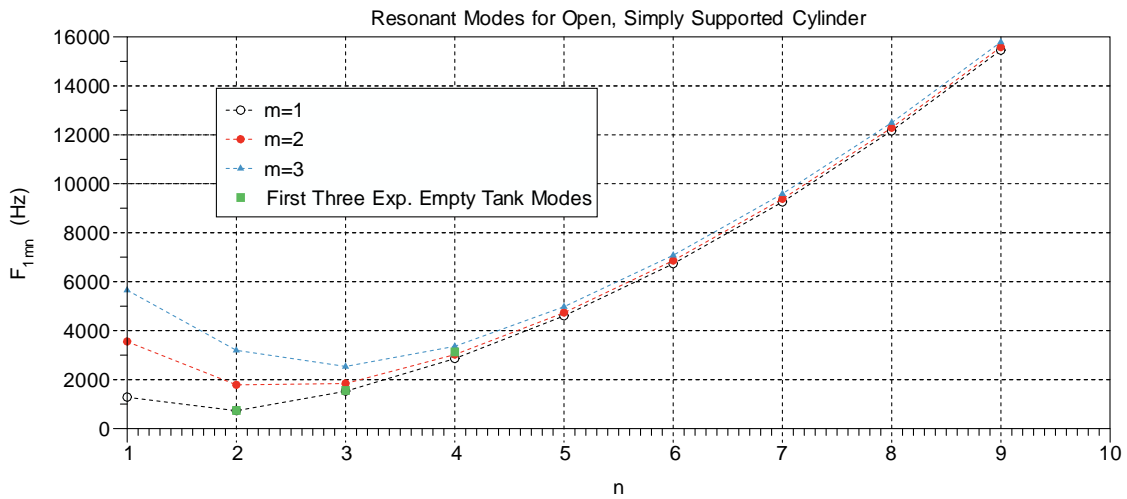


Figure 7: Theoretical modes for the open-ended, simply supported cylinder as derived from Soedel's theory. Also shown are the closest matching experimental modes for the empty tank.

These are likely due to the nodes introduced by mounting hardware, ports, and end-cap resonances.

The key observations associated with Fig. 7 are that (a), the fundamental frequency is not associated with the lowest  $n = 1$  breathing mode, but is in fact an  $n = 2$  mode, and (b) the lowest modes observed and tracked in our experiment are associated with the  $m = 1$  longitudinal mode.

## **Discussion**

The central objective of the study reported here was to determine the feasibility of using modal analysis to evaluate the fluid load in a spacecraft tank in a reduced gravity environment. Our 1-g ground experiments with fluid in static equilibrium revealed the basic mechanism associated with fluid-loading. In these experiments, we determined that the primary effect of fluid loading on the tank was to increase its effective mass rather than its effective stiffness. This is evidenced in the marked reduction of resonant frequency with fill-level. In the 1-g testing, we conclude that modal estimation of fluid volume can achieve a resolution of 5% or better in the cylindrical portion of the tank. We further determined that the effect of fluid loading on resonant mode shifts was most strongly correlated with the total contact area between fluid and tank wall. We investigated this hypothesis by comparing the mode shifts for a tank in the vertical orientation to those in a tank experiencing equivalent fluid volume changes in the horizontal orientation. Effective contact area changes are smaller for equivalent fluid volume changes in the horizontal orientation, and corresponding mode shifts are reduced as well.

In the reduced gravity environment provided by the parabolic flights, sloshing of the fluid produces continuous variation in effective surface wetting, and so resonant modes are not fixed in this dynamic environment in which the fluid never has time to reach its zero-g free surface configuration. The central question in this case was whether the mode shifts would be large enough to reduce the resolution of the modal analysis technique below the threshold of viability. Our experiments suggest that even in the dynamic sloshing environment of parabolic flight, mode shifts can be averaged over to produce fluid volume estimates with relatively low standard errors.

We have demonstrated that EMA is a viable technique for the real-time, non-invasive estimation of fluid volumes in propellant tanks in microgravity environments. The data presented here suggests that the EMA technique may produce fluid volume resolutions that match or exceed those of existing methods. Given that EMA methods are relatively inexpensive to implement, do not require modification of tank structures, and can provide real-time monitoring of fluid volume in propellant tanks, further studies seem warranted to probe the potential of the methods for addressing the significant and expensive problem of propellant volume gauging in microgravity.

## **Acknowledgments**

The authors gratefully acknowledge the Wisconsin Space Grant Consortium for financial support, and the Reduced Gravity Office at NASA Johnson Space Center for support of the Systems Engineering Educational Discovery (SEED) program. The authors also acknowledge the useful contributions made by Prof. Douglas Arion. The Carthage Microgravity Team student members who worked on this project include KelliAnn Anderson, Amber Bakkum, Stephanie Finnvik, Erin Gross, Cecilia Grove, Steven Mathe, Kimberly Schultz, and Danielle Weiland.

## References

- [Fortescue et al., 2003] Fortescue, P., Stark, J. & Swinderd, G. (Eds.). (2003). Spacecraft Systems Engineering, 3rd Ed.. Wiley.
- [Malhotra et al., 2000] Malhotra, P., Wenk, T. & Wieland, M. (2000). Simple Procedure for Seismic Analysis of Liquid-Storage Tanks. Structural Engineering International 3, 197-201.
- [National Instruments, 2011] National Instruments, Inc., Austin, TX.
- [Pandey et al., 1991] Pandey, A.K., Biswas, M., & Samman, M.M. (1991). Damage detection from changes in curvature mode shapes. Journal of Sound and Vibration, 145(2), 321-332.
- [Peters, 2004] Peters, J. (2004). Spacecraft Systems Design and Operations. Kendall Hunt Publishing.
- [Smart Materials, 2011] Smart Materials, Inc., Sarasota, FL.
- [Soedel, 1981] Soedel, W. (1981). Vibrations of Shells and Plates. Marcel Dekker Inc.
- [Viar, 2011] Viar, Inc., Irvine, CA.

# **Electric Capacitance Volumetric Tomography ECVT for Fuel Gauging Under Zero Gravity**

ZeroG Team  
University of Wisconsin-Madison  
1500 Engineering Dr.  
Madison, WI 53706

Principal Investigator  
Dr. Manohar Deshpande  
Manohr.d.deshpande@nasa.gov

Student Team Contact  
Paul Pezzi  
Paul.pezzi@gmail.com

Written/Edited By  
Benjamin Butler  
Btbutler@wisc.edu

## **Project Summary**

To better allow for measurement of liquids, such as propellant, in microgravity, the University of Wisconsin – Madison ZeroG Team conducted an experiment using electric capacitance and volumetric tomography. This procedure allowed for 3D computer imaging of the internal contents of a reservoir to determine the volume of substance inside. For this experiment, polypropylene spheres were used to eliminate the hazards of having fuel inside the cabin of the aircraft. Full analysis of the flight procedures can be seen below.

## **Experimental Background**

Proper measurements of propellants in microgravity were vital to mission optimization. Currently there is not a proven method for accurately measuring the amount of propellant in real time. Because of this, spacecraft must carry extra fuel to compensate for this uncertainty, reducing the payload capacity. One method being studied to determine fuel volume is electric capacitance volumetric tomography (ECVT).

As seen with recent experiments [3], ECVT allows the user to acquire three-dimensional volumetric images. In the case put forth, ECVT has allowed the imaging of dielectric within thermal protection system tiles on the Space Shuttle which can not only tell that there is moisture present that could be potentially harmful but also how much there is and its location, thereby saving money and time as to which tiles need to be replaced.

In other cases, such as mass metering for cryogenic fluids [2], and the TPS case the ECVT technique can be configured to a shape that is helpful to the task at hand. For example, in

measuring the cryogenic fluid, the sensor can fit over the span of the tank and receive the required measurements while the ECVT equipment for the TPS tiles can be fit to match the tile size and square shape to collect the images needed.

ECVT technology shows promising potential for spaceflight applications; not only could ECVT acquire images of rocket fuel or another fluid inside an expensive or dangerous piece of equipment for NASA, but this method could be applied to many other fields where nonintrusive analysis is key, such as medical areas [1]. However, research on this imaging and measuring technique in microgravity has not been extensively studied.

### **Experimental Description**

This experiment investigated the accuracy of the ECVT technology in microgravity. During the flight, polypropylene spheres were placed inside the sensor, and the ECVT sensor took record the dielectric distribution. Polypropylene was chosen because its dielectric constant is close to that of fuel, and provides a safer alternate to using actual fuel in the experiment. This data was to be outputted to the data acquisition device, and was to be processed after the flight to estimate the volume of polypropylene spheres in the sensor by creating a three dimensional image inside the sensor. The volume of the spheres was known, and will be compared to the volume obtained experimentally to determine the accuracy of the ECVT measurement technique. On each flight different sized spheres were used to determine if sphere size affects accuracy.

### **Structural Verification**

This experiment was designed to comply with all NASA and ZeroG Corporation loading configurations. The center of mass of the experiment was found, and then the structure was analyzed under each loading configuration. Four straps provided by the RGO (5000lb rated) will be used to secure the experiment to the floor. Analysis on both the straps and the bolts connecting to the straps to the floor has been performed. This analysis, as well as the analysis performed on other key structural members can be found in the attached appendix.

### **Electrical Analysis**

Schematic

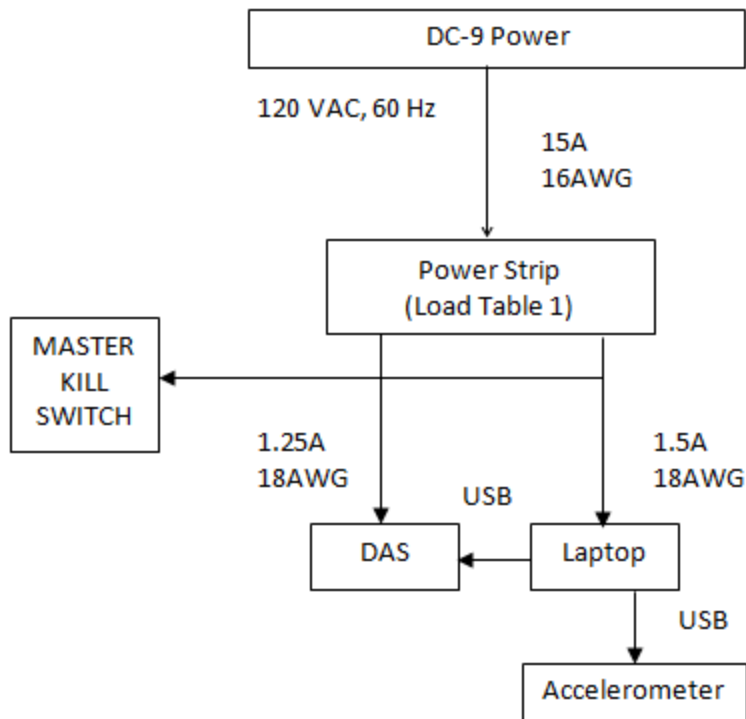


Figure 1: Schematic of electrical system

## Team

Fritz, Marcus	Flyer	Fritz, Marcus
Marron, Samuel	Flyer	marron@wisc.edu
Pezzi, Paul	Flyer	paul.pezzi@gmail.com
Weiss, Kevin	Flyer	kjweiss2@wisc.edu
Wong, Nathan	Flyer	nwong@wisc.edu
Bolyard, Craig	Flyer	cbolyard@wisc.edu
Mackstutis, Kevin	Ground Crew	mackstutis@wisc.edu
Bersch, Patrick	Ground Crew	bersch@wisc.edu
Butler, Benjamin	Ground Crew	btbutler@wisc.edu
Kainz, Nathaniel	Ground Crew	nokainz@wisc.edu
Lange, Benjamin	Ground Crew	bjlange@wisc.edu

## Experimental Procedures

### Equipment Shipment

The experiment was shipped to Ellington Field the week of March 23<sup>rd</sup>, 2011 so that it will arrive before our arrival in Houston. The experiment came in one package completely assembled and ready for flight.

## **Ground Operations**

Before the flight, it was pertinent to do some standard checks:

1. Check the physical condition of the experiment, and ensure all components were functioning.
2. Check that the Matlab program and other software being used (i.e. for the accelerometer) were working properly and ready to receive data by performing ground testing.
3. Check all bolts and fasteners to ensure that the experiment was structurally secure.

## **Loading/Stowing**

The experiment required the forklift to be loaded through the side of the airplane. Once loaded, two members moved the experiment into position for the flight.

## **Pre-Flight**

The data acquisition system was calibrated again to account for any environmental changes from previous days of ground testing.

## **Take-Off/Landing**

No special procedures were needed at this time.

## **In-Flight**

The sensor and computer were turned on and prepared for performing the experiment. The accelerometer was activated at this point and recorded data throughout the flight. Data from the ECVT system was recorded in 3 sets; approximately at 10 parabola intervals. These data sets stored in Matlab data files for later analysis.

## **Off-Loading**

A forklift was needed to offload the experiment, and it was shipped back to the University of Wisconsin-Madison.

## Supplementary materials and references:

### Reference Information

Principal Investigator: Dr. Manohar Deshpande

Contact Information: manohar.d.deshpande@nasa.gov

Experiment Title: Electric Capacitance Volumetric Tomography ECVT for fuel gauging under zero gravity

Work Breakdown Structure (WBS): N/A

Flight Dates: March 31, 2011-April 9, 2011

Overall Assembly Weight (lbs): 40.3lbs.

Assembly Dimensions (L x W x H): 15in. x 15in. x 27in

Equipment Orientation Requests: None, experiment is square.

Proposed Floor Mounting Strategy: Straps

Gas Cylinder Requests: None

Overboard Vent Requests: None

Power Requirements: 120VAC Single Phase

Free Float Experiment: No

Flyer Names for Each Proposed Flight Day:

- Day 1: Paul Pezzi, Kevin Weiss, Nathan Wong
- Day 2: Samuel Marron, Marcus Fritz, Dr. Manohar Deshpande

Camera Pole and/or Video Support: Camera Mount

### References

[1] Fan, L (2009) *Electrical Capacitance Volume Tomography*. Columbus, OH: Department of Chemical and Biomolecular Engineering.

[2] Mark A. Nuge, R. Y. (2003, May 4). *Capacitance Based Mass Metering for Cryogenic Fluids*. Retrieved February 8, 2011, from Science Direct: [www.elsevier.com/locate/cryogenics](http://www.elsevier.com/locate/cryogenics)

[3] Nurge M. A. (2007). Electrical Capacitance Volume Tomography with High Contrast Dielectrics Using Cuboid Sensor Geometry. *Measurement Science and Technology*, 1511-1515.

# **21st Annual Conference Part Four**

Senior Design

# **In-Situ Resource Utilization: Investigation of Melted Lunar Regolith Simulant JSC-1A**

Matthew Kallerud, Brian Nguyen, Timothy Paladin, Anthony Wilson

Department of Mechanical Engineering; Milwaukee School of Engineering, Milwaukee, WI

This study focused on the importance of in-situ resource utilization in the pursuit of space exploration. Experimentation focused on lunar regolith simulant JSC-1A, of which the mechanical properties of melted JSC-1A were to be explored. Specific properties that were tested included compression strength, hardness, density, magnetic properties, and the capability to drill and tap melted regolith. Results showed the compressive strength being greater than that of granite, higher densities in melted regolith versus settled JSC-1A powder, as well as inconclusive hardness and magnetic property testing.

## **Background**

The 2009 Augustine Commission, a group that reviewed the human spaceflight plans of the United States, concluded that “the ultimate goal of human exploration is to chart a path for human expansion into the solar system.” It is well known that this exploration and expansion will come at a significant energy cost. Supplying the required energy by transporting material and equipment for power production from Earth’s surface to orbit is very costly due to Earth’s gravity well. Because of the high costs, utilizing space resources is economically desirable. The utilization of space materials for space exploration is referred to as in-situ resource utilization (ISRU). It is well known in the space exploration community that this concept is the key to an economically feasible expansive human presence in space. ISRU can also reduce the risk of space exploration by reducing the number of necessary Earth launches.

Initially, it was proposed that a study be performed on an energy collection or storage device that can be manufactured in space using in-situ materials found on near-Earth-asteroids (NEA), concentrating specifically on the relevant material properties that lunar and asteroidal materials may have. Early on, the concept of manufacturing an energy collection or storage device using in situ resources was explored. The device that held the most promise, a solar PV cell, was designed. The material that was expected to compose 100% of the cell was to be that of an S-type asteroid, which is composed mostly of olivine and pyroxene. Once the design had been completed and analyzed, it was determined that the system was far too complex to recoup the costs that it would require in order to set the infrastructure in place. In addition to this, the system relied too heavily on controlled environments, similar to Earth in the aspect of requiring gravity and an atmosphere.

The main concept of ISRU was reexamined and it was realized that material for any structures or parts could be processed and developed using in-situ resources. Based on this theory, the new focus was on the properties of the lunar & asteroidal regolith found in space. Upon exploration of lunar simulants, a simulant that was developed specifically for NASA and specialized projects such as this was discovered. The goal would be to perform material property testing of Orbitec’s lunar regolith simulant JSC-1A. Because the simulant is intended to mimic the properties of real lunar regolith, the concept of simplistic ISRU was able to be explored.

Funding provided by Wisconsin Space Grant Consortium

Advised by: Professor Michael Swedish, Milwaukee School of Engineering  
Dr. Peter Curreri, Marshall Space Flight Center  
Dr. Vito Gervasi, Milwaukee School of Engineering

Despite previous complexities and difficulties encountered with ISRU processing, a new attempt to take advantage of the benefits gained with ISRU was envisioned using a simplified concept. This concept was to avoid any unnecessary processing while also producing something useful. In addition, current research suggested that material property testing on melted and formed simulant does not currently exist. In order to determine if the regolith would be a suitable material for a variety of purposes, material testing needed to be completed to quantify the material properties of JSC-1A.

Currently, asteroid regolith simulant is not readily available. Previous studies indicated that the S-type (siliceous) asteroid examined (99942 Apophis) has an estimated composition of “70% olivine, 22% orthopyroxene, and 8% clinopyroxene,” which is very similar to that of the moon (Binzel, et al., 2009). Based on the availability of lunar regolith simulant, it was determined that this was a feasible way in which to pursue the new project focus.

**Refocus on Use of JSC-1A in Space.** The decision to use lunar regolith simulant JSC-1A was based on the expertise that manufacturing company Orbitec has with the material. It is produced not only for independent projects such as this, but also for NASA’s purposes. Based on these criteria, it was deemed to be a suitable material to use.

JSC-1A is produced through the milling and sieving of volcanic ash that is mined from the Merriam Crater of the San Francisco volcano, which is located near Flagstaff Arizona. It is sieved until a particle size of less than 1 mm is achieved, which is important for certain tests as well as for reproducing the nature of real lunar regolith.

The approximate chemical composition can also be seen below in Figure 1. It is important to note that all of the elements are listed in the oxidation state and do not necessarily accurately represent the actual phase or minerals in the simulant.

Major Element Composition	CAS #	% by Wt.
Silicon Dioxide (SiO <sub>2</sub> )	14808-60-7	46-49
Titanium Dioxide (TiO <sub>2</sub> )	13463-67-7	1-2
Aluminum Oxide (Al <sub>2</sub> O <sub>3</sub> )	1344-28-1	14.5 – 15.5
Ferric Oxide (Fe <sub>2</sub> O <sub>3</sub> )	1309-37-1	3-4
Iron Oxide (FeO)	1332-37-2	7 – 7.5
Magnesium Oxide (MgO)	1309-48-4	8.5 – 9.5
Calcium Oxide (CaO)	1305-78-8	10 – 11
Sodium Oxide (Na <sub>2</sub> O)	1313-59-3	2.5 – 3
Potassium Oxide (K <sub>2</sub> O)	12136-45-7	0.75 – 0.85
Manganese Oxide (MnO)	1344-43-0	0.15 – 0.20
Chromium III Oxide (Cr <sub>2</sub> O <sub>3</sub> )	1308-38-9	0.02 – 0.06
Diphosphorus Pentoxide (P <sub>2</sub> O <sub>5</sub> )	1314-56-3	0.6 – 0.7

Figure 1 - Chemical Composition of Lunar Regolith Simulant JSC-1A

**Use of Melted Regolith as a Structural Component.** The concept of using the regolith from either asteroids or the moon as a structural component was envisioned because of the mass involved with structural components. Previously, the production of solar PV cells was thought to be very useful, but the complexity and relative mass of a PV cell negated the majority of benefits of ISRU. Looking on the opposite side of the spectrum, structural components tend to be high in mass and are needed to hold most other important components in place. Based on this observation, it was determined that the use of regolith for structural purposes would yield much higher mass cost savings as compared to the production of PV cells.

**Intent of Melting Material & Material Property Testing.** There is more to bring into consideration aside from the mass penalty benefits when considering regolith for use as a structural material. This includes the mechanical properties of it once melted; specifically the tensile and compressive strength, hardness, impact strength, the ability to machined/formed, and other material properties. These properties will determine first and foremost, what the material is capable of withstanding, as well as give insight as to what uses this might have, either structural or otherwise.

**Material Testing to be Performed.** Material property testing is needed in order to classify and utilize the melted samples properly. There is a variety of tests that are usually performed on samples in order to measure and quantify these properties. When the JSC-1A is melted it is expected to perform in a similar fashion to a ceramic, as the chemical composition is highly comprised of the ceramic material silicon dioxide (SiO<sub>2</sub>). As such, the mechanical property testing was tailored for a ceramic material.

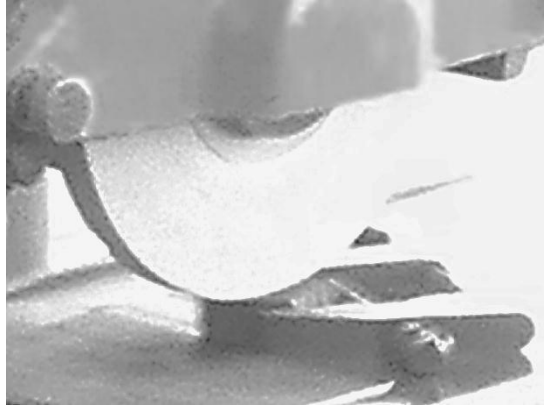
*Rockwell Hardness Test.* Hardness is defined as a means to specify the resistance of a material to deformation, scratching, and erosion. Hardness is a key attribute of ceramics. The test is based on indenting the sample with a hard indenter. Hardness of the ceramic is important for characterizing ceramic cutting tools, wear and abrasion resistant parts, prosthetic hip joint balls and sockets, optical lens glasses, ballistic armor, molds and die and valves and seals (Quinn, 2003).

Hardness characterizes the resistance of the ceramic to deformation, densification, displacement, and fracture. Densification is important because “it relates to the microporosity that is often present in sintered ceramics” (Quinn, 2003).

Though Rockwell indenters are rarely used for ceramics, they were used in this experiment because they are the only hardness testing capability MSOE had available. About 5% of published values use the Rockwell indenter, usually the HRA or superficial HR45N scales. The scale used in this experiment was superficial HR45N. The sample size must be leveled and at least 1/2” thick and 3/4” round or squared.

*Uniaxial Compression Test.* Compression loads occur in a wide variety of material applications. Unlike tension tests, compression tests are not limited by necking. Additionally, compression test specimens are simpler in shape and do not require threads or special ends for gripping. Since the melted samples for this project are difficult to machine, compression test samples are easier to obtain than tension test samples. Samples for compression testing can be obtained by slicing a cylinder section into coin shapes, which can be ground flat on both sides as, shown in *Figure 2*.

Precautions must be taken in order to ensure useful information about failure is obtained, including buckling prevention. Analyses



cited in the ASM Handbook Volume 8 predict that specimens with a length-to-diameter ratio less than 5.0 are safe from buckling and can be used for compression testing of brittle materials. When using parallel plates, care must be taken to ensure that the plates are parallel to prevent eccentric loading. For the samples used in this experiment, the length to diameter ratio was less than 1.0, well within the recommended ratio.

Figure 2 - Grinding of Sample A1

$$\frac{L}{D} = \frac{0.625in}{1.48in} = 0.422 < 5.0$$

“In compression of a brittle... material, fracture occurs catastrophically by shear. The failure either occurs either along one large shear plane, leading to complete separation, or at several sites around the specimen, leading to crushing of the material. In either case, the load-carrying capacity of the material comes to an abrupt halt, and the fracture strength of the material is easily defined as the load at that point divided by the cross-sectional area...in brittle materials the ultimate compressive strength occurs at fracture” (Kuhn, 2003).

*Drilling/Tapping Capability.* As stated earlier, the melted form of regolith has potential for structural application in space. To fully utilize the regolith as a structural tool, the capability of connecting and interlocking members together is an important aspect that should not be overlooked. A study would be conducted to determine the possibility to drill and install a self-tapping screw in the melted JSC-1A.

## **Procedure**

Compared to metals, most ceramics are brittle in nature with higher hardness and lower ductility. They have great wear resistance and thermal insulation. Due to the physical property of ceramics, careful selection of sectioning, mounting, grinding, and etching procedures are required in-order to achieve the desired shape for testing.

**Separating Regolith from Crucibles.** One of the biggest problems with melting JSC-1A was its high melting temperature. In order to melt the regolith, the container must be able to withstand temperatures of over 1500C. Another problem was getting the sample out of the crucible without damaging the sample once it was melted and cooled. This would be a challenge considering that the wetting characteristic of the melted regolith was unknown. To ease the removal of the sample from the crucibles, graphite powder was considered as a possible lining to prevent the JSC-1A from bonding to the crucible walls. This would be tested in run 1 by the use of the clay/ graphite jeweler's crucible. Another idea was to machine the crucible off the sample using the MSOE machine shop facility. This method would be dependent on the hardness of the crucible. The final idea was to carefully create small fractures and chips in the crucible using a hammer and a chisel, and then slowly remove pieces of the crucibles off the sample.

**Cutting and Sectioning Sample.** Generally, ceramics are cut with a lubricated (water or a special cutting fluid), rotating diamond cutting wheel. The cutting speed is dependent on the ceramic type as well as the desired surface finish. The quality of cut is dependent on the cutting speed: low-speed (25 to 500 rpm) and high speed (500 to 5000 rpm) (Taffner, Carle, & Schafer, 2004). Typically a slow cutting speed and low cut pressure produces less cutting and surface damage for most ceramics. The cutting wheel plays a large role in cutting ceramics as well. The higher the contact stress on each of the abrasive particle results in a higher cutting rate. For this reason, low abrasive concentrated blades are used.

Another method for cutting ceramics would be the use of a water jet. Using water and occasionally a garnet abrasive, the fluid is pressurized to 20,000-60,000 psi and forced through a small orifice. This fluid's high velocity thin stream is capable of cutting through much harder materials without generating heat and mechanical stresses (Staff, 2011).

**Grinding and Polishing.** Once cut, it is important for the both sides of the samples to be leveled. To do this a grinding machine would be used. MSOE's grinding machine was utilized to level all the samples for compression testing. It should be noted that MSOE's grinding machine is not water cooled, so great care while grinding the samples must be taken to prevent fractures.

## **Results**

**Density Testing.** Mass density is a measure of the mass per unit volume of a material. It is an important property to this particular project due the compacting nature of the regolith simulant. Mass can be calculated using a simple scale and an accurate way to measure volume is through displacement of water.

Density was calculated for several samples from each run. Mass was measured using a digital scale. Propagation of error was performed on each density calculation and graphed against the reported density for JSC-1A according to its MSDS. The density measurements are summarized in Figure 3.

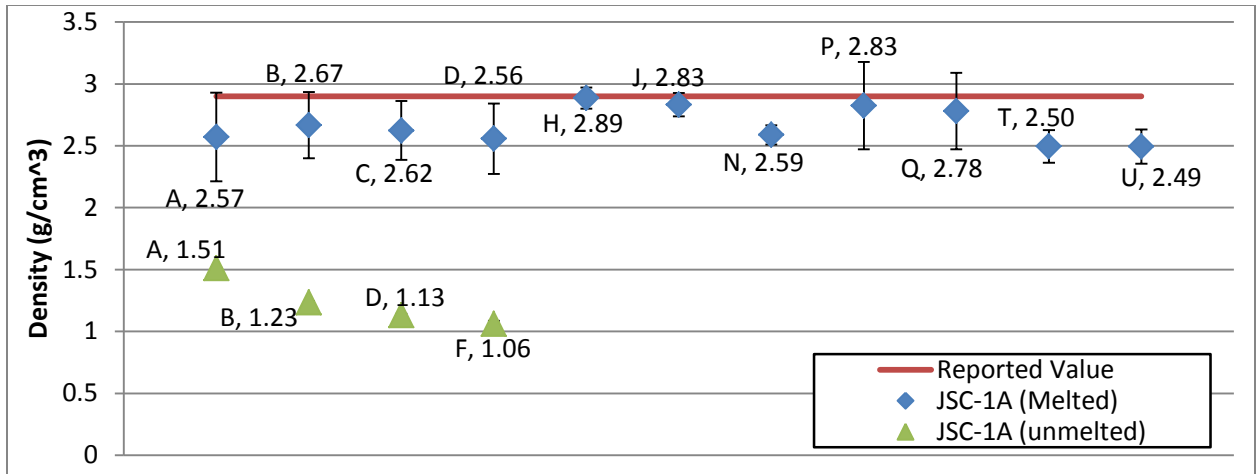


Figure 3 - Density Measurement Summary

The melted samples shown in Figure 3 are from a variety of runs. The MSDS reported value for density is also shown. Select non-melted sample densities are also shown. The accepted value is within the density range for samples B, H, J, P, and Q.

**Magnetic Property Testing.** Magnetism is a material property that results in having a response to a magnetic field. It is important in many applications, such as use in magnetic, low or no friction bearings. Magnetism of all melted samples was tested qualitatively, with a 0-3 scale created on which to rate the relative attraction to a magnet. The number 0 represented no reaction to a powerful magnet and 3 represented a strong reaction. These data are summarized in Table 1.

Table 1 - Magnetism Summary

Run	Sample	(0=none, 1=weak, 2=med, 3=strong)						
1	A:	1	B:	1	C:	1	D:	1
	E:	0.5	F:	0.5	G:	0		
2	H:	0	I:	0.5				
3	J:	0.5	K:	0	L:	1	M:	0
4	N:	1	O:	0.5	P:	1	Q:	1

All but one sample from Run 1 exhibited some level of magnetism. All samples from Run 4 exhibited magnetism. Overall, 4 of 17 samples did not exhibit any level of magnetism. The magnetism was not consistent among samples in the same run, but each sample came from a different crucible.

**Compression Testing.** Two coin shaped samples from the A crucible of the first melt, A1 and A2, were tested to fracture in a Tinius-Olsen hydraulic tester. The samples were placed between two parallel plates one at a time and loaded until fracture. The first sample, A1, showed failure primarily on one side. The second sample, A2, was similarly placed between the two steel plates and loaded to fracture. This sample took significantly more load to fracture, and failed uniformly across the sample, crushing the sample.

The Tinius-Olsen machine recorded the fracture load on a load curve. Since the fracture load required was unknown prior to testing, scales were changed during the test. Scales of 12,000, 60,000 and 120,000 pounds were used. Sample A1 fractured at around 66,000 pounds and sample A2 fractured at around 98,000 pounds. Samples H3 and H4 from the second run were also tested to failure under compression in the same way. They were pulverized at 67,500 and 48,600 pounds force respectively.

The area of each sample was calculated from the measured diameters, and the ultimate compressive strength of each sample was found. The ultimate compressive strength of the sample is the load at fracture divided by the area of the sample.

The values for diameter and load were measured in inches and pounds-force but were converted to meters and Newtons for calculations. Propagation of error was also performed based on the error in the load and diameter measurements. The error and the calculated ultimate compressive strengths are shown in Figure 4.

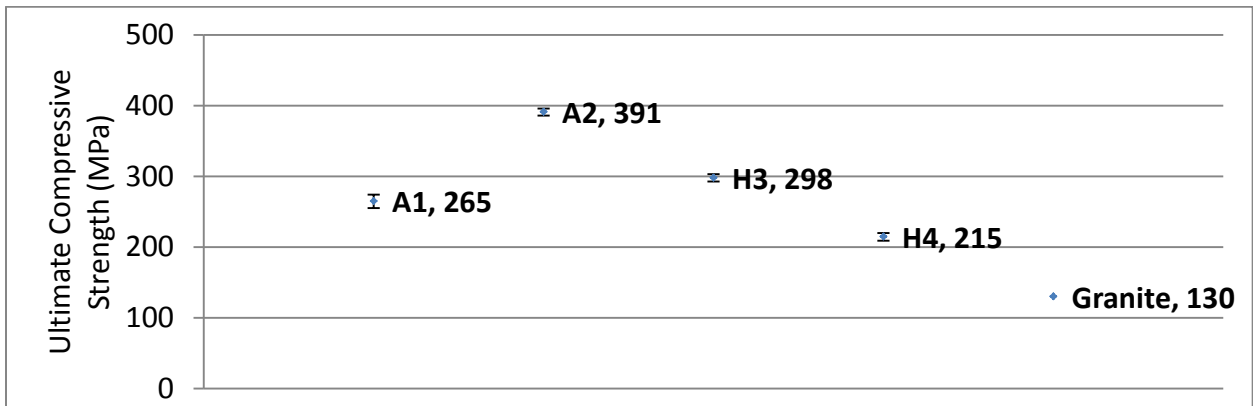


Figure 4 - Ultimate Compressive Strength of Melted JSC-1A Samples

The results indicate relatively low error but immeasurable error exists due to geometry imperfection and the non-homogenous nature of the melt. These errors are hard to quantify and are not reflected in the error analysis. However, the data show that the ultimate compressive strength of the melted JSC-1A is considerably higher than that of granite, which suggests possible application as a structural material.

**Hardness Testing.** The scale used in this experiment was superficial HR45N. Four samples were tested 10 times each on the same side. The results are summarized in Table 2.

Table 2 - HR45N Hardness Test Summary

Test	H1a	H1b	A1	A2
1	-66.8	2.7	-11.7	47.5
2	9.0	-35.7	-40.9	-12.7
3	25.6	-12.2	-13.5	18.6
4	-20.4	8.0	19.9	34.3
5	63.0	-5.9	23.2	7.8

6	-20.3	14.8	-39	-60.1
7	26.2	24.6	36.7	37.7
8	-18.2	-43.1	17.5	13.1
9	48.3	-23.1	-	-10.6
10	13.7	-35.0	-	-

The data show significantly inconsistent results; values range from -66.8 to 63.0 on sample H1a. The inconsistency of the data may be attributed to the Rockwell indenter or the poor surface quality of the samples. Indentation cracking due to the hardness testing load applied as well as the non-uniform porosity at the surface could have contributed to the inconsistency. A Vickers or Knoop test, better suited to ceramics, should be performed to characterize the hardness of melted and solidified JSC-1A.

**Drilling Testing.** Being able to drill and tap into materials is an important requirement for fastening materials together or to other materials. After initial difficulty with drilling into the melted JSC-1A samples, three specialty drill bits were acquired. The bits are all ¼ inch: a Vermont American rotary masonry drill bit, a Bosch glass & tile drill bit, and a RIGID diamond tile drill bit. The bits were used to drill into various samples with varying success. The results are summarized in Table 3.

Table 3 - Drilling/Tapping Summary

Sample	Drill? (Yes/No)	Tap? (Yes/No)	Bit
C	Yes	N/A	Diamond Tip
C	Yes	N/A	Glass/Tile
H2	Yes	N/A	Diamond Tip
H2	Yes	N/A	Glass/Tile
B	Yes	N/A	Masonry
H2	Yes. Through? No	N/A	Diamond Tip
H1	Yes. Through? No	N/A	Diamond Tip
A	Yes	N/A	Glass/Tile

All of the samples tested were successfully drilled by at least one of the bits. Qualitatively, the diamond tip drill bit provided the cleanest and quickest cut. Samples H1 and H2 were fractured during drilling, shown in

Figure 55. Other samples were drilled successfully, shown in Figure 6.



Figure 5 - Sample H1 Fracture during Drilling

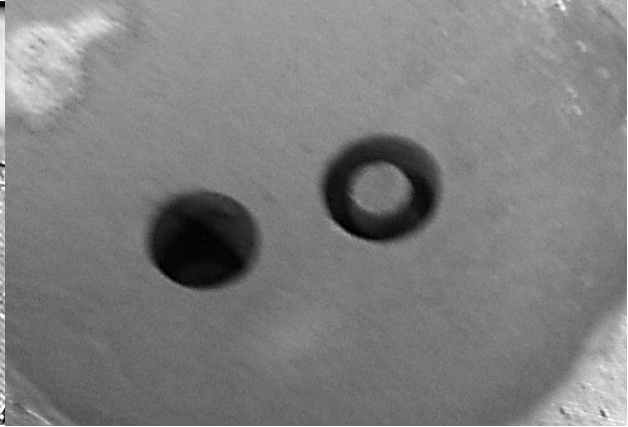


Figure 6 - Successfully Drilled Sample

None of the samples were tested for tapping to this point. Three hex head screws, 2 of 5/16 inch diameter and 1 of 1/4 inch diameter were acquired for thread testing of the holes. The ability to drill into the samples creates flexibility in using the material, but the ability to tap will determine if screws or bolts would be used. Also, the best performing drill bit, the diamond tile drill bit, required active water cooling, which would be difficult and unlikely to work in space environments.

## Conclusions

**Potential Applications of Melted In-Situ Resources Based on Observations of Melted JSC-1A.** Based on the material property testing that was accomplished, along with the observations made along the way, it is certain that there are constructive space applications for in-situ resources similar to simulant JSC-1A. One application that had initially sparked interest in the testing of JSC-1A was its use as a structural material. In an attempt to lower the mass penalty of shuttle launches, parts or structural members that undergo high compressive forces can be manufactured or replaced while in space, rather than needing to bring them along.

Planetary and space based habitats are also a target market for this concept. Rather than needing to bring all of the structural material along to begin or continue human expansion into space, these habitats can be built and expanded in space through ISRU of lunar or asteroidal material. If roads are involved, such as on a planetary habitat, the observed compressive properties of JSC-1A suggest that ISRU would be an appropriate option in the construction of these roads.

Alternative to structural uses, these materials can potentially be used for radiation protection. Many of the samples that were manufactured had glossy or glasslike finishes, and therefore can help reflect or redirect electromagnetic waves. Additionally, the material can act as a particle shield to protect from the various micrometeorites and similar threats found in space.

Downsides to the application of ISRU of lunar or asteroidal material based on JSC-1A include the relatively high temperatures required to melt and form it, the brittleness that

was observed in a variety of property tests, and the difficulty involved in machining and forming it into the desired product.

**Future Testing.** If this project was allotted time and resources for further testing, it would be beneficial to explore other material properties of the simulant JSC-1A. Two of the more important tests would be tensile testing and 3-point bending testing, to further evaluate its potential use as a structural material. Additionally, more accurate hardness testing via the Vickers or Knoop methods would help in evaluating the potential failure modes of the material when it might affect mission safety. Further exploration of the magnetic capabilities could prove beneficial for use in low friction magnetic bearings or electric generators. Lastly, microstructural analysis of the various phases of the melted material could help determine which phase would be best in each application, be it structural, shielding, or other.

**Limitations.** Given that this project was intended to explore the properties of regolith simulant JSC-1A in the hopes of better understanding lunar and asteroidal material properties, there exist several fundamental limitations on what can properly be tested. In the tests performed, the induction furnace used requires a medium through which the heat can be transferred. Additionally, the medium that was used was standard Earth air, which has a specific chemical composition that can allow for chemical reactions that may not occur in open space where there is no atmosphere.

Another fundamental limitation encountered was the gravity applied on the samples by the Earth. In space there is a variety of gravitational forces but most are very faint or practically non-existent. That said, the formation of the samples was capable only in an environment with gravity. Low or no gravity environments will require a closed system to form the material into the desired product, which can require complex mechanical systems.

## References

- Binzel, R. P., Rivkin, A. S., Thomas, C. A., Vernazza, P., Burbine, T. H., DeMeo, F. E., et al. (2009). Spectral properties and composition of potentially hazardous Asteroid (99942) Apophis. *Elsevier Icarus*, 400-485.
- Kuhn, H. A. (2003). Uniaxial Compression Testing. *Vol. 8 ASM Handbooks*, 8.
- Lawrenz, A., Manning, B., Kilroy, K., & Larson, P. (2010). *Engineered Compact Lunar Interchangeable Power Systems*. Milwaukee: Team ECLIPS.
- Price, S., Phillips, T., & Knier, G. (2001, March 21). *Staying Cool on the ISS*. Retrieved November 7, 2010, from NASA Science: Science News: [http://science.nasa.gov/science-news/science-at-nasa/2001/ast21mar\\_1/](http://science.nasa.gov/science-news/science-at-nasa/2001/ast21mar_1/)
- Quinn, G. (2003). Indentation Hardness Testing of Ceramics. *Vol 8. ASM Handbook*, 8.
- Shapiro, E. (2003). Three-Point and Four-Point Bend Tests. *Vol.8 ASM Handbook*, 640-647.
- Staff. (2011). *waterjet.org*. Retrieved May 24, 2011, from Joomla: <http://www.webcitation.org/5nWaNTDGA>
- Taffner, U., Carle, V., & Schafer, U. (2004). Preparation and Microstructural Analysis of High-Performance Ceramics. *Vol. 9 ASM Handbook*, 1057-1066.

**21st Annual Conference  
Part Five**

Biology and Medical Sciences

# Optimization of Lipid Accumulation for Biofuel Production using the Single-celled Alga *Chlamydomonas reinhardtii*

David C. Higgs<sup>1\*</sup> and Matthew Effinger<sup>2</sup>

<sup>1</sup>Department of Biological Sciences and <sup>2</sup>Department of Chemistry, University of Wisconsin-Parkside, Kenosha, WI

## Abstract

The use of biofuels as renewable energy sources has grown in recently years. As a renewable biofuel, algal biodiesel has potential of being an important renewable fuel that is sustainable and reduces total CO<sub>2</sub> emission, and thus has potential to ameliorate climate change. Stressful growth environments cause some algae to accumulate lipids in the form of Triacylglycerols (TAGs). TAGs can be extracted and treated to produce fatty acid methyl esters that make fuel-grade biodiesel. Using the alga *Chlamydomonas reinhardtii* in a laboratory setting, growth conditions were tested to determine which induced high TAG accumulation to maximize biodiesel. Algae grown for three days at 23°C, in high light (248 μE/m<sup>2</sup>/sec) and low nitrogen (< 0.1 mM) had the highest TAG accumulation, as measured by Nile Red fluorescence. These conditions resulted in high TAG in both a wild-type strain and a cell wall-less mutant, but wild-type cells accumulated the highest amount.

## Introduction

The use and awareness of plant-based biofuels as viable alternatives to the petroleum-based fossil fuels has grown considerably in recent years, and the capability and production of plant biofuels has increased (Durrett *et al.*, 2008; Greenwell *et al.*, 2010; Hu *et al.*, 2008). Interest in biofuels has increased, in part, because of the growing awareness of environmental issues from non-renewable fossil fuels as well as concerns of long-term availability of fossil fuels. Biofuels are produced from high-energy carbon compounds synthesized by plants and algae. Biodiesel is a high-energy biofuel that is formed when plant Triacylglycerols (TAGs) are chemically converted to fatty acid methyl esters (FAMES). The usefulness of TAGs for biodiesel production is demonstrated by the fact that TAGs from plants, mostly soybeans, are currently being converted to biodiesel and sold to consumers as blends of biodiesel and petroleum-based diesel. Biodiesel is of high fuel-grade quality and compliant with the strict industry specifications set by the American Standards and Testing and Materials (ASTM D6751). Furthermore, biofuels have been registered with the Environmental Protection Agency and are compliant with the 1990 Clean Air Act amendments with regard to emissions (Durrett *et al.*, 2008). Throughout the United States, a small but growing number of retail filling stations sell biodiesel as an alternative fuel, with the highest concentration in the Midwestern states, including Wisconsin (National Biodiesel Board, 2011).

Through photosynthesis, all carbon atoms in biofuels originate from atmosphere CO<sub>2</sub>, and this fixed carbon is incorporated into high-energy molecules, including cellulose, starch and lipids. In both plants and algae, TAGs are common high-energy lipids that can accumulate to high

\* Special thanks to the Wisconsin Space Grant Consortium (WSGC) for a Research Infrastructure Seed Grant award and the University of Wisconsin-Parkside for additional financial support.

amount. TAGs contain three fatty acid chains, usually 16 or 18 carbons in length, covalently attached to the 3-carbon glycerol backbone via ester bonds (Durrett *et al.*, 2008). As compared to starch or cellulose, the inherent energy in TAG lipids is 2.3 times higher (Buchanan *et al.*, 2000). To be a useable biofuel, the high-energy photosynthetic products must be extracted from plants or algae and chemically converted to fuels such as ethanol or biodiesel. For any biofuel to be carbon neutral, the refining and transportation processes must be efficient and require fuel inputs significantly lower than the inherent energy in the final biofuel.

Algal biodiesel has gained more interest and attention due mostly to the high efficiency by which algae convert sunlight energy into high-energy carbon compounds useful for biodiesel production. Depending on the growth conditions and species, microalgae can accumulate 20 – 50% of cellular biomass as TAGs (Hu *et al.*, 2008). Although algae have high potential for biodiesel production, the infrastructure and culturing systems for this purpose have some unique challenges as compared to the culturing and production of traditional plants. Two general growth systems have been tested for algal biodiesel, shallow open ponds, which are exposed directly to the environment, or closed bioreactors. Pending geographical location and weather, each of the culturing methods has value.

Algae have some advantages over plants for biofuel production. Single-celled algae grow very rapidly and unlike plants do not dedicate energy or carbon to supportive structures such as roots or stems. Algae also require less input materials (water and fertilizer) than that needed for “land plants” grown using traditional agricultural methods (Greenwell *et al.*, 2010). Together, these characteristics contribute to the ability of algae to accumulate 10 – 100 times more energy-rich chemicals per land area, as compared to plants (Greenwell *et al.*, 2010). The predominant high-energy compounds that algae accumulate are TAGs that are concentrated in lipid bodies within the algal cells. Depending on algal species and growth conditions, TAGs can accumulate to 20 – 50% of the dry cell weight (DCW) of the cell (Hu, *et al.*, 2008). In contrast, soybean, one of the most commonly used plants for biodiesel production, accumulates TAGs to only 8% DCW in seed. Further, it takes a full growing season to produce the seeds, but the remainder of the plant is left behind. Soybeans require significant amounts of fuel for the nutrient-intensive farming, and they are grown on high-quality agricultural land that could be used for food production (Greenwell *et al.*, 2010; Durrett *et al.*, 2008).

Before algal biodiesel can become an efficient renewable biofuel, there remains critical biological questions as well as the refining and distribution issues that need to be resolved (Greenwell *et al.*, 2010; Hu *et al.*, 2008). These include identifying the optimal culturing conditions to maximize lipid accumulation in algae, knowing how culturing and lipid accumulation vary between species or strains of algae, and determining which growth system (bioreactor or open pond) is most appropriate (Greenwell *et al.*, 2010). In addition, understanding the underlying biological factors that control TAG accumulation will help maximize biodiesel production. These include identifying key genes that control and limit accumulation of TAGs. Identifying such genes would allow for genetic-based strategies to maximize biofuel production while minimizing necessary resources to grow the algae. Genetic strategies might also allow the improvement of biofuel quality so that the resulting FAMES have the best fuel properties (Durrett *et al.*, 2008).

Fortunately, there is a history of research on algae as a source of renewal energy. Most notable, was the U.S. Department of Energy's National Renewable Energy Laboratory (NREL) Aquatic Species Program that conducted numerous studies on different algal species, growth conditions and energy quality assessments (Sheehan *et al.*, 1998). The NREL closing report is a "landmark" publication that summarizes many of the advantages of algal-based biodiesels while also describing key limitations and aspects that require further investigation in order for algae biodiesel production to be ecologically and economically feasible. One key recommendation in the NREL summary was for more basic studies in well-developed genetic systems (organisms) to help understand ways to improve the efficiency of lipid productivity and the genes that associate with this process (Sheehan *et al.*, 1998). It was suggested that for basic research, laboratory-sized small scale analysis would be useful to optimize lipid induction, through physiochemical and other environmental conditions and to understand the fundamental genetics of lipid production in algae. The NREL report also concluded that of the many different classes of microalgae, the green algae group (Chlorophyceae) is one of the most promising for biofuel production (Sheehan *et al.*, 1998).

The single-celled eukaryotic green alga *Chlamydomonas reinhardtii* is among the Chlorophyceae and is widely considered the best studied algae. The nuclear, chloroplast and mitochondrial genomes have been sequenced, and this alga can be genetically manipulated to alter genes and their encoded protein products (Merchant *et al.*, 2007). Furthermore, extensive work on general growth conditions and media has been done (Harris, 2010). For this study, *C. reinhardtii* was used to evaluate optimal growth conditions that maximize accumulation of TAGs. The results presented here establish conditions and methods that will allow us to begin molecular genetic studies to identify *C. reinhardtii* genes that control TAG accumulation. Knowledge gained about growth conditions and genetic factors that control TAG accumulation in *C. reinhardtii* may prove relevant to many microalgae used for biofuel production.

## Methods

A wild-type strain (P17) and a cell wall-less mutant (cc406) of *C. reinhardtii* were grown in standard Tris-Acetate-Phosphate (TAP) media unless otherwise stated (Harris, 2009). Cells were grown in 50 ml of media in 250 ml Erlenmeyer flasks and passaged to fresh media weekly to maintain cultures. For TAG-accumulation growth studies, 1 ml of an actively growing culture ( $1 \times 10^7$  cells / ml) was transferred to 50 ml of fresh TAP media and grown for three days with constant agitation using a stir plate and magnetic bar (200 rpm) at 23°C under standard light intensity (100  $\mu\text{E}/\text{m}^2/\text{sec}$ ). To control for rise in culture temperature due to heat from the stir plate motor, a plastic Petri plate was used as a thermal barrier to isolate the flask from contacting the stir plate. Cells were then transferred to the experimental conditions and allowed to grow an addition three days under constant stirring using the thermal barrier.

Algae were grown for three days under different growth treatments in a light and temperature controlled incubator. Light treatments included high (248  $\mu\text{E}/\text{m}^2/\text{sec}$ ) and low (58  $\mu\text{E}/\text{m}^2/\text{sec}$ ) light. Nitrogen treatments included standard TAP medium with either 28 mM nitrogen or a low nitrogen (< 0.1 mM) treatment that was TAP medium containing only nitrogen from Trace Elements plus residual nitrogen from the transferred cells. After three days, cultures were collected and cell densities determined using a hemocytometer microscopic analysis (Harris,

2009). Cultures were immediately frozen and stored  $-20^{\circ}\text{C}$  until TAG abundance was measured. Relative abundance of TAG was determined using Nile Red fluorescence, as previously described (Lee *et al.*, 1998). Fluorescence was measured using a fluorometric spectrophotometer with 490 nm excitation and 585 nm emission wavelengths. The relative fluorescence for each culture was standardized per cell density to control for differences in cell growth. The final standardized relative fluorescence is presented as “TAG Fluorescence / million cells.” Three independently grown and treated cultures were analyzed for each treatment, and data from all three are shown to demonstrate the reproducibility in the measured TAG accumulation.

## Results

Rapid and reliable quantification of TAGs in algal cells was performed by employing the fluorescent stain Nile Red. This method has previously been used to measure TAG in algae, including *C. reinhardtii* (Lee *et al.*, 1998; Moellering and Benning, 2010; Wang *et al.*, 2009). Nile Red is known to stain TAGs and can be used for both microscopic and spectrophotometric analysis. To test if Nile Red staining of TAG was sufficiently reproducible, independently grown cultures of wild-type (WT) and cell wall-less strains were analyzed by Nile Red fluorescence and standardized per cell density (TAG fluorescence per million cells). The results across three independently grown control experiments revealed that the Nile Red fluorescence was highly reproducible (data not shown). Nile Red fluorescence provides a rapid and reliable way to quantify TAG accumulation. These initial control experiments also allowed us to test if freezing and storing cultures at  $-20^{\circ}\text{C}$  for extended periods of time (months) interfered with TAG quantification, which it does not. The ability to safely store algal cultures at  $-20^{\circ}\text{C}$  makes it possible to collect and freeze cultures grown at different times and analyze independently grown samples together, saving time and reducing variables due to independent TAG analyses.

To optimize growth conditions that maximize TAG accumulation per cell, both WT and cell wall-less strains were grown for three days in standard growth conditions. Cells were then changed to different environmental conditions and grown another three days under treatment. The treatments included high (HL) and low (LL) light and presence (N+) or absence (N-) of nitrogen. After the three-day treatment, cells were tested for cell density and TAG accumulation in three independently grown cultures (Figure 1). The Control growth condition (standard media, nitrogen and light) accumulated a relatively low level of TAG. Cultures treated with high light and with nitrogen (HL, N+) had a significantly higher level of TAG than that in the Control, while a low light with standard nitrogen (LL, N+) did not increase TAG accumulation as compared to the Control. Growth in low nitrogen (N-) resulted in a significant increase in TAG accumulation, either in low light (Figure 1) or when light was left at standard level (data not shown). The combination of high light and low nitrogen (HL, N-) resulted in the highest level of TAG accumulation, indicating that both environmental stresses contribute additively to increase TAG accumulation.

Wild type and the cell wall-less strains were analyzed to test if different strains accumulated different amounts of TAG. The cell wall-less strain has reduced cell wall material and this could impact carbon allocation such that TAG might accumulate to higher amounts. Furthermore, a cell wall-less strain might be useful for easier TAG extraction than from a

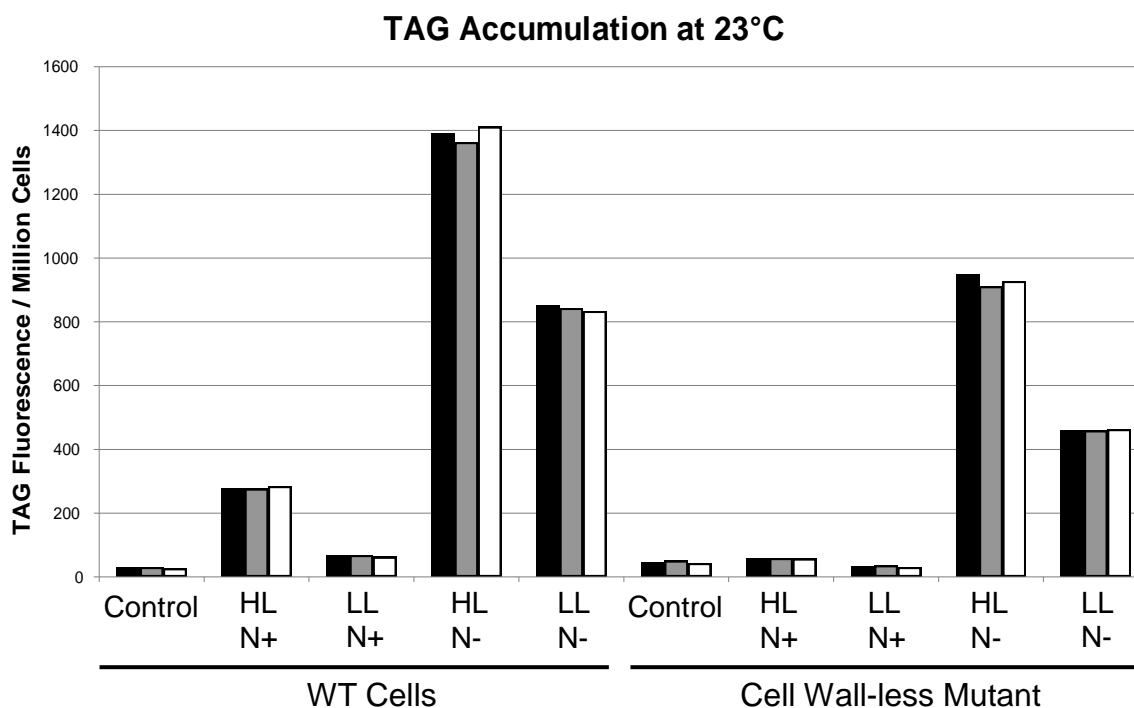


**Figure 1.** Accumulation of Triacylglycerols (TAGs) in two strains, wild type (WT) and Cell Wall-less mutant, of *C. reinhardtii* after three day at 23°C and different treatments related to light and nitrogen. Treatments were standard growth conditions (Control) or combinations of high light (HL), low light (LL), standard nitrogen amounts (N+), and nitrogen starvation (N-). TAG accumulation was determined using Nile Red fluorescence standardized to cell density, and the relative fluorescence is presented as “TAG Fluorescence / Million Cells.” Each environmental treatment was tested in three independently replicated cultures grown at different times, and each column represents TAG data from one replication.

walled strain, such as WT. The rank order of TAG accumulation in response to growth conditions was the same in both strains (Figure 1). For both strains the highest TAG accumulation was observed when cells were grown in high light and low nitrogen (HL, N-). However, under these conditions, WT accumulated more TAG and the maximum amount of TAG in the cell wall-less strain was less than the maximum amount in WT. Similar results were observed when cell wall-less cells were grown in low light and low nitrogen.

Interestingly, high light stress alone did not have a significant impact on TAG accumulation in the cell wall-less strain when grown in the presence of nitrogen (Figure 1). TAG accumulation when grown in high or low light but with nitrogen was not significantly different from the Control for cell wall-less strain. As previously mentioned, there was a significant difference in TAG for WT when treated with high light stress alone (HL, N+).

Both WT and cell wall-less strains were tested for differences in TAG accumulation when grown at different temperatures. Three-day treatments of cells grown at low (19°C) and high (27°C) temperatures were tested, and both conditions greatly reduced the rate of cell growth, as measured by cell density (data not shown). The very low rate of growth limited our ability to

accurately quantify TAG accumulation. TAG amounts per million cells were highly variable between independently grown samples in the same environmental conditions. Thus, the data were inclusive for quantifying TAG amounts.

## **Conclusions**

We tested different growth conditions to determine which results in the highest accumulation of TAGs in *C. reinhardtii*, on a per cell basis. Nile Red fluorescence proved useful as a rapid and reliable method to quantify TAGs in these algal cultures. Independently, high light and low nitrogen treatments resulted in significantly higher TAGs in cells as compared to the standard growth condition (Control) for *C. reinhardtii*. Combined, these stress treatments caused the algae to accumulate even higher amounts of TAG. The highest TAG accumulation was observed when cells were grown in high light plus low nitrogen for three days, and this was the case for both WT and the cell wall-less mutant. The second highest TAG accumulation occurred when cells were grown in low light plus low nitrogen. High light by itself, when nitrogen was included in the medium, led to a significant increase in TAG in WT, but the amount was less than that observed when the high light treatment was combined with low nitrogen. Low light by itself, when nitrogen was present, did not result in a significant increase in TAG accumulation in either WT or cell wall-less cells. Others have reported that low nitrogen can induce TAG accumulation in algae (Moellering and Benning, 2010; Wang *et al.*, 2008). However, we have not seen reports using the combination of high light and low nitrogen to induce even higher levels of TAG.

The additive effect of high light and low nitrogen treatments on TAG accumulation could be caused by two different mechanisms. Often in biology, when two different stimuli cause an additive effect, it is due to each stimuli acting through distinct cellular pathways (Herrara *et al.*, 2010). For TAG accumulation in response to low nitrogen and high light, this might be due to these treatments each inducing a different cellular processes that independently causes higher amounts of TAG to accumulate. Together, both are able to function, leading to a higher TAG amount as compared to either individual treatment. Alternatively, both treatments could induce TAG accumulation through the same cellular process such that both cause a quantitative increase in this same process. The data presented here do not distinguish between the two mechanisms. Identifying the underlying cellular process that increases TAG accumulation would be needed before a distinction could be determined.

There were differences between WT and the cell wall-less mutant with regard to TAG accumulation in response to different treatments. The rank order of TAG accumulation per cell in response to growth conditions was the same in both algal strains, but WT cells had a quantitatively greater increase in TAG accumulation as compared to the cell wall-less strain. The biological cause for the different TAG amounts between the two strains is not known. It could be due to either direct or indirect physiological effects that result from a weaker cell wall in the mutant as compared to WT. This may result in differences in cellular water and osmotic potentials. Alternatively, there might be genetic differences between the two strains independent of the cell wall gene mutation, and these additional genetic differences might contribute to differences in TAG accumulation in response to the growth treatments. Independent of the cause, it is clear that the cell wall-less strain does not accumulate higher

TAG, as initially hypothesized based on the concept of less carbon allocation to cell wall material might lead to more carbon being used in TAG synthesis.

In summary, we have identified different growth conditions that lead to progressively higher accumulation of TAGs. In order from lowest to highest accumulation of TAGs per cell, WT cells can be grown using: standard growth condition, high light stress, low light plus low nitrogen stress, and high light plus low nitrogen stress. These growth conditions result in increasing amounts of TAG and can be used in future genetic studies to better understand TAG synthesis and degradation. By correlating gene expression with quantitative changes in TAG accumulation, genes with the largest impact on TAG accumulation could be identified. Those genes that control TAG accumulation may prove useful in manipulating algae genetically for more and better forms of biodiesel.

## References

- Buchanan, B., Gruissem, W., and Jones, R. (2000) *Biochemistry and Molecular Biology of Plants*, The American Society of Plant Physiologists Press.
- Durrett, T.P., Benning, C., and Ohrogge, J. (2008) Plant triacylglycerols as feedstocks for the production of biofuels. *Plant Journal*, 54: 593-607.
- Greenwell, H.C., Laurens, L.M., Shields, R.J., Lovitt, R.W., and Flynn, K.J. (2010) Placing microalgae on the biofuels priority list: a review of the technological challenges. *J. Royal. Society Interface*, 7: 703-726.
- Harris, E.H. (2009) *The Chlamydomonas Sourcebook, 2<sup>nd</sup> Edition: Volume 1: Introduction to Chlamydomonas and its Laboratory Use*. Academic Press.
- Herrera, R., Krier, C., Lalanne, C., Ba el, H.M., Stokes, A., Salin, F., Fourcaud, T., Claverol, S., and Plomion, C. (2010) (Not) keeping the stem straight: a proteomic analysis of maritime pine seedlings undergoing phototropism and gravitropism. *BMC Plant Biol.* 10: 217-228.
- Hu, Q., Sommerfield, M., Jarvis, E., Ghirardi, M., Posewitz, M., Seibert, M., and Darzins, A. (2008) Microalgal triacylglycerols as feedstocks for biofuel production: perspectives and advances. *Plant Journal*, 54: 621-639.
- Lee, S.J., Byung-Dae, Y., and Oh, H.-M. (1998) Rapid method for the determination of lipid from the green alga *Botryococcus braunii*. *Biotechnology Techniques*, 12: 553-556.
- Merchant, S.S., Prochnik, S.E., Vallon, O., Harris, E.H., Karpowicz, S.J., Witman, G.B., Terry, A., Salamov, A., Fritz-Laylin, L.K., Marechal-Drouard, L., Marshall, W.F., Qu, L.-H., Nelson, D.R., Sanderfoot, A.A., Spalding, M.H., Kapitonov, V.V., Ren, Q., Ferris, P., Lindquist, E., Shapiro, H., *et al.* (2007). The *Chlamydomonas* genome reveals the evolution of key animal and plant functions. *Science* 318: 245-250.
- Moellering, E.R. and Benning, C. (2010) RNA interference silencing of a major lipid droplet protein affects lipid droplet size in *Chlamydomonas reinhardtii*. *Eukaryotic Cell*, 9: 97-106.
- National Biodiesel Board, Jefferson City, MO, [www.biodiesel.org](http://www.biodiesel.org).
- Sheehan, J., Dunahay, T., Benemann, J., and Roessler, P.G. (1998) A Look Back at the U.S. Department of Energy's Aquatic Species Program—Biodiesel from Algae. National Renewable Energy Laboratory Report. U.S. Department of Energy's Office of Fuels Development.
- Riekhof, W.R. and Benning, C. (2009) Glycerolipid Biosynthesis. In *The Chlamydomonas Sourcebook 2<sup>nd</sup> Edition Volume 2: Organellar and Metabolic Processes*, Edited by David Stern. Academic Press.
- Wang, Z.T., Ullrich, N., Joo, S., Waffenschmidt, S., and Goodenough, U. (2009) Algal lipid bodies: stress induction, purification, and biochemical characterization in wild-type and starchless *Chlamydomonas reinhardtii*. *Eukaryotic Cell*, 8: 1856-1868.

# Preserving Muscle Length Requires Simultaneous Stretch and Contraction

Jonathan Van Dyke

Department of Cell Biology, Neurobiology & Anatomy  
Medical College of Wisconsin, Milwaukee, WI 53226

## ABSTRACT

Humans unloaded by microgravity or chronic bedrest exhibit muscle shortening and loss of muscle extensibility within 7 days. Prolonged unloading of the musculoskeletal system by microgravity leads to posture changes that ultimately trigger the adaptation of the muscles to new joint angles. Upon return to Earth gravity, many of these muscles are maladapted and are too short resulting in reduced performance and increased susceptibility of muscles to injury when returned to weightbearing activity. Stretch is a therapy traditionally thought to preserve range of motion and slow muscle atrophy at the clinical level; however, the type of stretch best suited for achieving this preservation is disputed and the mechanisms by which stretch exerts its effect on muscle are poorly understood. This study uses a rat tenotomy model to simulate the muscle unloading experienced by astronauts in orbit. Two stretch protocols (passive stretch and stretch+contraction) are used to prevent unloading induced muscle shortening maladaptation. While 20 minutes of daily passive stretch does not prevent unloading induced shortening maladaptation, the combination of contraction and stretch partially prevents shortening of the soleus muscle and activates protein kinase B (Akt) and ribosomal subunit S6 kinase (p70<sup>S6K</sup>), signaling molecules well known to be related to protein synthesis and muscle growth. Passive stretch does not activate Akt or p70<sup>S6K</sup>. These findings indicate that passive stretch alone is not likely a useful counter to microgravity induced muscle shortening in astronauts but that contraction of the lengthened muscles would be far more effective.

## BACKGROUND AND SIGNIFICANCE

Astronauts/cosmonauts returning to the 1-G gravitational environment of Earth often complain of muscle weakness, reduced range of motion, and delayed-onset muscle soreness following spaceflight. These symptoms are indicative of muscle cell shortening which manifests during long exposure to microgravity (7+ days). Short adapted muscles are often strained and damaged when astronauts return from space reloading their muscles with the weight of the body.

Skeletal muscle is a remarkably adaptable tissue that optimizes its functional, biochemical and structural properties to perform work demands efficiently throughout our lifetime. The weightless environment of space reduces and/or alters the work demands of muscle leading to atrophy (loss of muscle strength) and postural changes in the astronauts which often lead to a shortening maladaptation of muscle working range. Maladapted muscle is no longer optimized for work in normal gravity. Muscle shortening maladaptation occurs through the subtraction of sarcomeres (the smallest functional unit of organization in a muscle cell) at the ends of muscle fibers [1, 2]. Muscle held in a shortened position has a reduced average sarcomeric length and is thought to subtract sarcomeres to restore normal resting length to the remaining sarcomeres.

An example of shortening of range of motion can be observed in the ankle joint of astronauts as plantarflexion posture (downward pointing of the foot) in which the resting ankle joint opens from 90° to 100° in astronauts/cosmonauts exposed to as little as 7 days of microgravity [3, 4]. This ankle posture shortens the calf muscles and persists for the duration of spaceflight. Adaptation to this shortened state predisposes the muscles to injury when it is reloaded with the weight of the body upon return to 1-G. Force falls because of reduced overlap and crossbridge

formation between thick filaments (force generating myosin) and thin filaments (actin filaments) [5, 6]. In unloaded rat models, prolonged unloading of the primary antigravity muscle of the lower leg, the soleus, has been shown to produce a significant shortening of length, loss of mass and weakening of muscle fibers [7, 8].

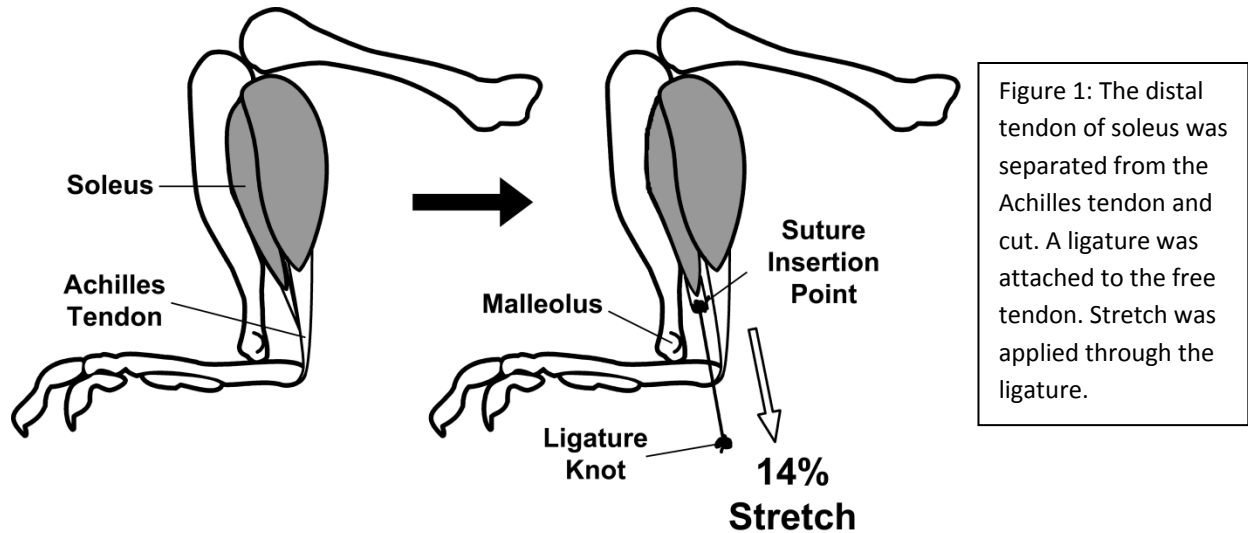
In an attempt to reduce muscle atrophy in astronauts during spaceflight, the flight surgeon prescribes ~2.5 hours daily of daily exercise. However, these exercise regimens focus chiefly on preventing the loss of muscle strength (transverse atrophy) rather than muscle shortening (longitudinal atrophy) because the loss of range of motion is often less appreciated than loss of muscle mass when discussing muscle atrophy. As a result, the subcellular signaling that drives the shortening or lengthening adaptation of muscle to a new shortened or lengthened state is incompletely understood. Stretch, a long standing therapy, is often prescribed to preserve and/or return range of motion in patients suffering from a wide range of neural and musculoskeletal injuries and illnesses. Stretch could potentially be used in combination with existing countermeasures to prevent the muscle shortening maladaptation and range of motion loss in astronauts.

Previously, I focused on passive stretch, a long-standing physical therapy during which the relaxed muscle is held in a lengthened state. I found that passive stretch, while able to prevent some muscle fiber breakdown, was unable to prevent the shortening adaptation in unloaded and hypershortened soleus (Van Dyke et al. 2011, in review). This was surprising because other studies have concluded that passive stretch produces significant preservation of range of motion and muscle mass [9-12]. Following an in-depth review of the literature to understand this discrepancy, it became evident that in those studies, stretch was applied to conscious animals which allowed voluntary muscle contractions [9, 11, 12]. Active contractions during stretch is in stark contrast to our tenotomy + passive stretch approach which is designed specifically to isolate the effects of passive mechanical force from those due to active muscle force generation. In animals, true passive stretch is achieved when the animal is anesthetized. Since passive stretch alone is not sufficient to prevent shortening adaptation, it is important to determine whether adding muscle contractile activity to a lengthened muscle will preserve muscle mass and length. Further indication that stretch + active contraction is necessary for length regulation comes from the clinical therapy regimen termed proprioceptive neuromuscular facilitation (PNF) stretch [13-15]. Essentially, PNF means that the muscle is actively contracted when at a stretched length. PNF therapy reportedly increases range of motion and flexibility better than passive stretch [15-19]. While active stretch is a promising approach, there is insufficient basic science data to substantiate that PNF stretch directly influences muscle length and what the mechanism might be. Without these data it is premature to recommend PNF as a countermeasure for preventing human plantarflexion posture.

The purpose of this study was to investigate the effects of stretch in combination with controlled contraction on the muscles of fully anesthetized rats. I hypothesized that the addition of contractile activity prevents the shortening maladaptation of the tenotomized soleus and increases the activation of signaling proteins responsible for triggering synthesis of sarcomeric proteins [20-22].

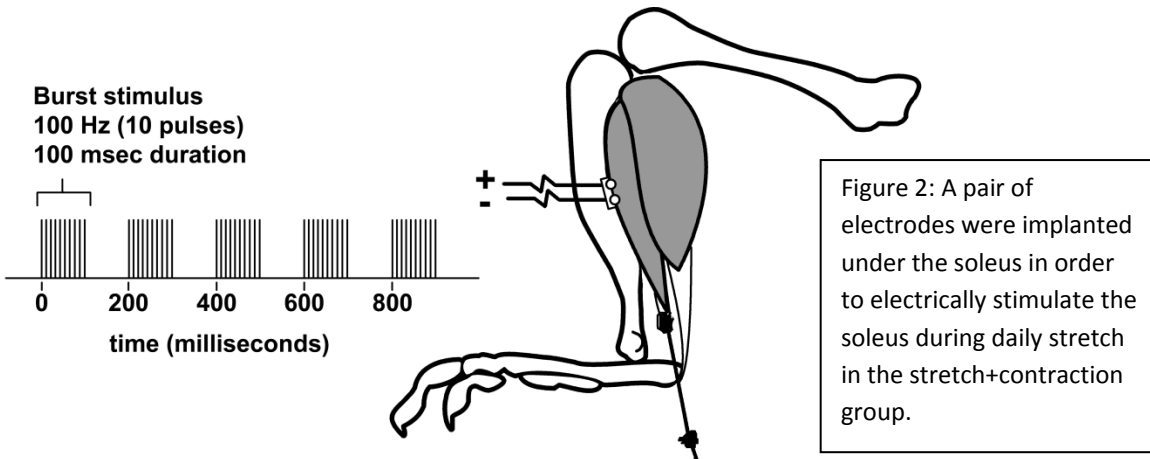
## RESEARCH EFFORTS AND FINDINGS

Using a tenotomy unloading model, I tested the ability of passive stretch alone and the combination of stretch+contraction to prevent the muscle shortening adaptation. Tenotomy is the transection of a tendon resulting in the loss of resting muscle tension and freeing the muscle to shorten. It is a surgical manipulation used clinically in the treatment of multiple injury and disease states affecting the tendon and muscle imbalance at a joint. In animal models, it mimics tendon rupture and subsequent shortening of the muscle [23]. Persistent shortening of the muscle results in rapid contractile protein breakdown and reduction in muscle length, and therefore, tenotomy is an appropriate model for studying shortening adaptation [23].



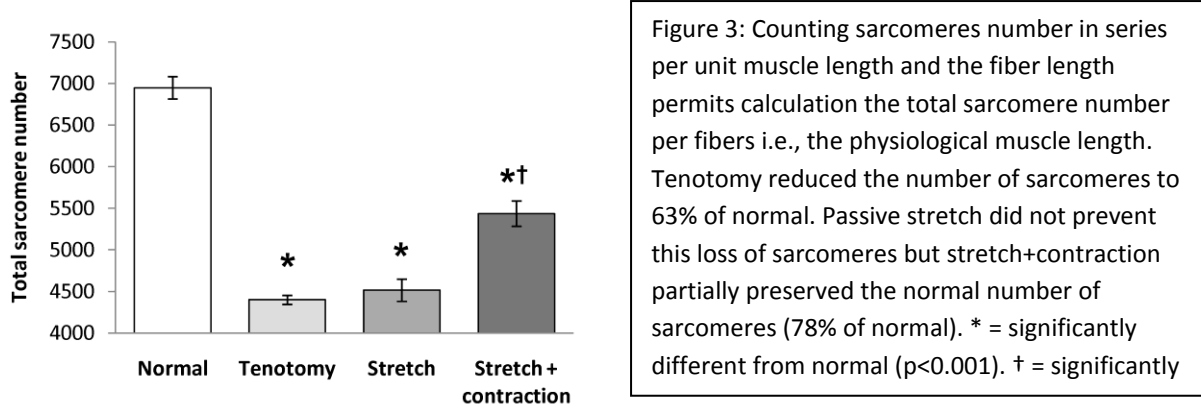
Briefly, my tenotomy plus stretch protocol was as follows: both legs of a fully anesthetized rat were tenotomized. One leg had an inelastic monofilament line attached to the distal tendon of the soleus. This monofilament line was used to connect the soleus to a lengthening apparatus through which the muscle was lengthened 14% beyond the resting muscle length when the ankle was held at 90° (Fig. 1). The stretch was applied for 20 minutes daily. The rat was fully anesthetized during this daily stretch in order to eliminate motor nerve impulses and muscle contraction i.e., the result was pure passive stretch.

In the group treated with a combination of stretch+contraction, the leg to be stretched was implanted with an electrode pair and allowed to heal. Ten days later, right and left solei were tenotomized, and one muscle had the monofilament line attached to the tendon of the soleus implanted with the electrodes. During the stretch+contraction treatment, the rats were fully anesthetized, and the soleus was stretched and held lengthened 14% while stimulated continuously with 5 Hz bursts of biphasic impulses for 20 min (Fig. 2)



**Stretch+Contraction Prevents Shortening Adaptation.**

Tenotomy resulted in a dramatic decrease in soleus length (number of sarcomeres in series) after 4 days. The tenotomized muscles were 63% of normal length (Fig 3). Daily passive stretch of the tenotomized solei for 4 days did not prevent the shortening adaptation and resulted in muscles that were 65% of normal length. Stretch+contraction however, partially prevented shortening. Solei treated with stretch+contraction for 20 min daily were 78% of normal length after 4 days, a significant improvement over stretch alone ( $p < 0.001$ ) (Fig 3). Based on these findings, I conclude that stretch alone is not sufficient to prevent shortening maladaptation in tenotomized muscle but contraction of the lengthened muscle is required.



**Contraction and Length Dependant Activation of Protein Synthetic Pathways.**

Exercise has been shown to activate protein kinase B (Akt), a factor directly linked to protein synthetic signaling during muscle hypertrophy (growth and increase in potential force generation). This activation occurs by upstream kinases that phosphorylate Akt's primary activation site: threonine 308 (P-Akt<sup>T308</sup>). Twenty minutes of passive stretch alone did not increase the amount of P-Akt<sup>T308</sup> as determined by immunoblotting (Fig 4). The Akt signaling cascade is upstream of another enzyme called ribosomal S6 kinase (p70<sup>S6K</sup>). p70<sup>S6K</sup> has been shown to be indispensable for muscle hypertrophy. Activation of Akt during exercise generally results in activation of p70<sup>S6K</sup>. As Akt was not activated by passive stretch, it was not surprising to find that there was no significant increase in activated p70<sup>S6K</sup> (P- p70<sup>S6K</sup>) with passive stretch alone (Fig 5).

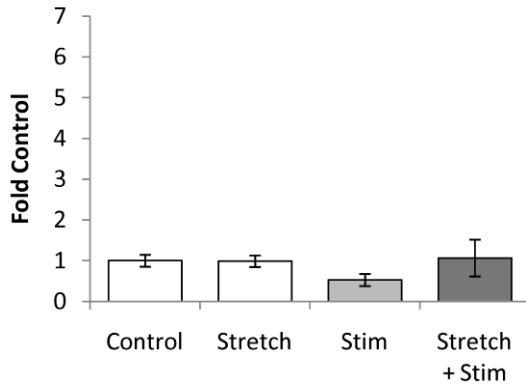


Figure 4: P-Akt<sup>T308</sup> levels were measured and normalized to the control. Stretch alone, stimulation (Stim) alone, and the combination of stretch+stimulation had no effect on the activation of Akt at T308. Error bars = standard error of mean.

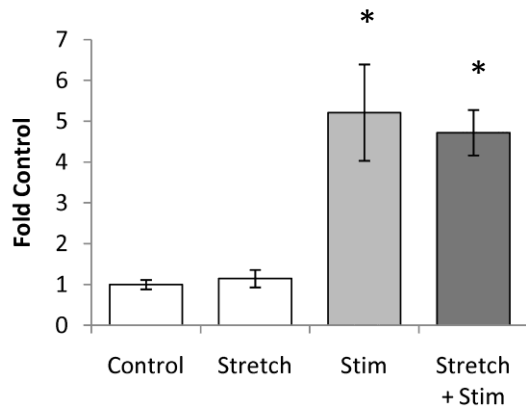


Figure 5: P-p70<sup>S6K</sup> levels were measured and normalized to control. Stretch alone did not increase p70<sup>S6K</sup> activation. Stimulation (Stim) significantly increased P-p70<sup>S6K</sup> to 5.2±1.1-fold of control levels. Stretch+stimulation had a similar effect, increasing P-p70<sup>S6K</sup> to 4.7±0.6-fold of control. \* p<0.001. Error bars = standard error of mean.

Next, I examined the effect of stretch+contraction on Akt and p70<sup>S6K</sup> activation. Twenty minutes of stretch+contraction, surprisingly, also had no significant effect on P-Akt<sup>T308</sup> (Fig 4); however, P-p70<sup>S6K</sup> was increased 4.7±0.6-fold (Fig 5, p<0.001). A secondary activation site exists on Akt at serine 473 (P-Akt<sup>S473</sup>). With passive stretch, P-Akt<sup>S473</sup> was unchanged but stretch+contraction significantly increased P-Akt<sup>S473</sup> by 3.7±1.1-fold (Fig 6, p<0.05). These data suggest that preserving muscle length by increasing protein synthesis requires not just the stretch of muscle but also the contraction of muscle held in the lengthened state.

To test whether contraction alone could account for the activation of Akt<sup>S473</sup> and p70<sup>S6K</sup>, rats implanted with electrodes and tenotomized were stimulated without stretch. The solei of these animals were instead held at -14% of resting muscle length. There was no significant increase in activation of Akt<sup>T308</sup> or Akt<sup>S473</sup> (Fig 4 and 6). There was a significant increase in the activation of p70<sup>S6K</sup> to 5.2±1.1-fold of normal with contraction alone (Fig 5, p<0.05). These data suggest that Akt<sup>S473</sup> is a biomarker for signaling pathways activated only when a muscle is contracted while in a lengthened state.

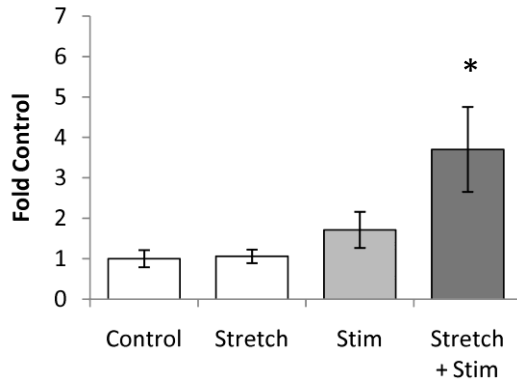


Figure 6: P-Akt<sup>S473</sup> levels were measured and normalized to control. Neither stretch nor stimulation (Stim) alone had significant effect on the activation of Akt at S473. Stretch+stimulation significantly increased P-Akt<sup>S473</sup> levels 3.7±1.1-fold. \* p<0.05. Error bars = standard error of mean.

### IMPLICATIONS AND FUTURE RESEARCH DIRECTIONS

The present findings have significant implications for maintaining the health of astronauts while in orbit as well as applications for clinical and exercise rehabilitation on Earth. Astronauts floating in microgravity develop a foot drop plantarflexion posture within 1 week that persists throughout long term spaceflight [3]. The astronaut solei are likely to be maladapted to a shortened state. Upon return to walking on Earth, the muscles are less functional. Humans in space will benefit from daily stretch+contraction protocols that optimally maintain their muscle lengths suited for function in normal gravity. This preservation of 1 gravity-appropriate muscle length, presumably translates to retained function. For patients on Earth, the combination of stretch+contraction is a more effective and efficient therapy for the rehabilitation of patients recovering from contracture or injury requiring the lengthening of short-adapted muscles. Additionally, in sports medicine, restoration of the range of motion following muscle injury is likely to benefit from stretch+contraction therapy.

While a single daily bout of stretch+contraction prevents some of the shortening maladaptation that results from tenotomy, it does not perfectly maintain normal muscle length. It is likely that multiple bouts of stretch+contraction evenly spaced throughout the day would be more effective countermeasures. Additionally, the duration of daily stretch+contraction may not be optimal for crewmembers with limited time for exercise on orbit. It is possible that shorter bouts of stretch+contraction will prevent the shortening maladaptation just as well as the 20 minutes used in the rat study. It is also possible that the opposite is true and that 20 minutes/session is too brief of stimulus to invoke muscle protein synthesis to achieve full preservation of normal soleus length. Future studies should be performed in rats and then in human with the objectives to optimize the stretch+contraction efficacy pattern.

Finally, the unique combination of signaling patterns observed in this study has identified P-Akt<sup>S473</sup> as a biomarker for the combination of stretch+contraction. Akt<sup>S473</sup> is only activated when stretch and contraction are occurring together. This is a novel and exciting observation that has led our lab to begin investigating other proteins known to interact with Akt in an attempt to identify those that might be involved in a potential muscle length-sensitive growth control signaling pathway. Increasing the understanding of these signaling pathways will promote long term safe human spaceflight by interventional therapies (physical and chemical) that maintain human muscle structure and function in the weightless environment of space.

## REFERENCES

1. Tardieu, C., et al., *Adaptation of Sarcomere Numbers to the Length Imposed on the Muscle*. Advances in Physiological Science, 1980. **24**: p. 99-114.
2. Williams, P.E. and G. Goldspink, *Changes in sarcomere length and physiological properties in immobilized muscle*. J Anat, 1978. **127**(Pt 3): p. 459-68.
3. Clement, G. and F. Lestienne, *Adaptive modifications of postural attitude in conditions of weightlessness*. Exp Brain Res, 1988. **72**(2): p. 381-9.
4. Tengwall, R. and J. Jackson, *Human Posture in Zero Gravity*. Current Anthropology, 1982. **23**(6): p. 657-666.
5. Gordon, A.M., A.F. Huxley, and F.J. Julian, *The variation in isometric tension with sarcomere length in vertebrate muscle fibres*. J Physiol, 1966. **184**(1): p. 170-92.
6. Lieber, R.L. and J. Friden, *Functional and clinical significance of skeletal muscle architecture*. Muscle Nerve, 2000. **23**(11): p. 1647-66.
7. Edgerton, V.R., et al., *Human fiber size and enzymatic properties after 5 and 11 days of spaceflight*. J Appl Physiol, 1995. **78**(5): p. 1733-9.
8. Fitts, R.H., D.R. Riley, and J.J. Widrick, *Functional and structural adaptations of skeletal muscle to microgravity*. J Exp Biol, 2001. **204**(Pt 18): p. 3201-8.
9. Baewer, D.V., et al., *Passive stretch inhibits central corelike lesion formation in the soleus muscles of hindlimb-suspended unloaded rats*. J Appl Physiol, 2004. **97**(3): p. 930-4.
10. Goldspink, D.F., et al., *The effect of hypokinesia and hypodynamia on protein turnover and the growth of four skeletal muscles of the rat*. Pflugers Arch, 1986. **407**(3): p. 333-40.
11. Loughna, P., G. Goldspink, and D.F. Goldspink, *Effect of inactivity and passive stretch on protein turnover in phasic and postural rat muscles*. J Appl Physiol, 1986. **61**(1): p. 173-9.
12. Williams, P.E., *Use of intermittent stretch in the prevention of serial sarcomere loss in immobilised muscle*. Ann Rheum Dis, 1990. **49**(5): p. 316-7.
13. Kabat, H., *Studies on neuromuscular dysfunction; new principles of neuromuscular reeducation*. Perm Found Med Bull, 1947. **5**(3): p. 111-23.
14. Kabat, H. and M. Knott, *Proprioceptive facilitation technics for treatment of paralysis*. Phys Ther Rev, 1953. **33**(2): p. 53-64.
15. Sharman, M.J., A.G. Cresswell, and S. Riek, *Proprioceptive neuromuscular facilitation stretching : mechanisms and clinical implications*. Sports Med, 2006. **36**(11): p. 929-39.
16. Etnyre, B.R. and L.D. Abraham, *Gains in range of ankle dorsiflexion using three popular stretching techniques*. Am J Phys Med, 1986. **65**(4): p. 189-96.
17. Ferber, R., L. Osternig, and D. Gravelle, *Effect of PNF stretch techniques on knee flexor muscle EMG activity in older adults*. J Electromyogr Kinesiol, 2002. **12**(5): p. 391-7.
18. Funk, D.C., et al., *Impact of prior exercise on hamstring flexibility: a comparison of proprioceptive neuromuscular facilitation and static stretching*. J Strength Cond Res, 2003. **17**(3): p. 489-92.
19. Tanigawa, M.C., *Comparison of the hold-relax procedure and passive mobilization on increasing muscle length*. Phys Ther, 1972. **52**(7): p. 725-35.
20. Long, Y.C., U. Widegren, and J.R. Zierath, *Exercise-induced mitogen-activated protein kinase signalling in skeletal muscle*. Proc Nutr Soc, 2004. **63**(2): p. 227-32.
21. Rockl, K.S., C.A. Witzak, and L.J. Goodyear, *Signaling mechanisms in skeletal muscle: acute responses and chronic adaptations to exercise*. IUBMB Life, 2008. **60**(3): p. 145-53.
22. Tidball, J.G., *Mechanical signal transduction in skeletal muscle growth and adaptation*. J Appl Physiol, 2005. **98**(5): p. 1900-8.
23. Jamali, A.A., et al., *Skeletal muscle response to tenotomy*. Muscle Nerve, 2000. **23**(6): p. 851-62.

# **21st Annual Conference Part Six**

Engineering

# FeatherSail 2: The Next Generation of Sailcraft

Collin Bezrouk

*University of Wisconsin – Madison*

William Burns

*Tennessee Technological University*

Katherine Czaplicki

*Rose-Hulman Institute of Technology*

Daniel Goff

*University of Florida*

Mentor: Dean Alhorn

*NASA/MSFC, Huntsville, Alabama, 35812*

## Abstract

Feathersail 2 is the next generation of solar sail satellite following the success of Nanosail-D. It is designed to demonstrate sail attitude control and to conduct solar research out of the ecliptic plane. This satellite uses solar radiation pressure (SRP), or the momentum gained from reflecting photons from the sun, as its primary means of propulsion and attitude control. Three axis attitude control can be obtained by “feathering”, or rotating sections of the sail out of the plane. The use of SRP means that Feathersail’s lifetime is not limited by on-board fuel reserves. Additionally, the small but continuous force from solar radiation pressure allows for more orbital maneuvering than chemical propulsion, which enables many missions that are otherwise infeasible. Feathersail consists of four main components. First, the Detumble stage is an expendable section that provides rigidity and enables attitude control prior to the sail’s deployment. Second, the central hub houses the flight computer, telecommunications and other avionics. Third, there are four pods, which are deployed 12 m from the central hub using ATK’s Coilable boom technology. Each pod then deploys another three 12 m booms and hoists the sail with them. The fully deployed sail is 34 x 34 m, and Feathersail will have an areal density of 50 g/m<sup>2</sup>. The final component is the science boom, which deploys 12 m off of the central hub. The boom supports two magnetometers and four cameras to document successful deployment. Feathersail will leave Earth via chemical propulsion means, and rely on SRP for other orbital maneuvers. After leaving Earth, Feathersail will spiral inwards towards the sun, passing and photographing Venus. Upon reaching 0.5 AU above the sun, it will begin a plane change maneuver out of the ecliptic, which will continue until the end of its lifetime. It will measure the sun’s magnetic field and solar wind activity during the entire mission.

## Abbreviations and Acronyms

ACS	Attitude Control System	PDB	Power Distribution Board
BCR	Battery Control Regulator	RW	Reaction Wheels
CMG	Control Moment Gyro	SMART	Smart Multi-Purpose Advanced
IMU	Inertial Measurement Unit		Reconfigurable Technology
MLI	Multi-layered Insulation	SRP	Solar Radiation Pressure

## Introduction

Feathersail 2 is a design for the next generation of solar sail satellite following the success and lessons learned from Nanosail-D. FeatherSail is about 34 x 34 m when deployed (about 115 times larger than Nanosail) and should have an areal density of about 79 g/m<sup>2</sup>, making it capable of using solar radiation pressure for effective orbital maneuvering. It can rotate sections of its sail out of plane, known as “feathering”, to obtain three axis attitude control. Because FeatherSail uses solar radiation pressure for both attitude and orbital maneuvering, it is completely unhindered by fuel reserves. Additionally, the low and constant thrust makes many missions possible that are not achievable by chemically propelled spacecraft.

## FeatherSail Components and Deployment Strategy

FeatherSail consists of four main modules: Central Hub, Detumble Stage, Science Boom, and Pods. Each module (aside from the Science Boom) has six faces and contains components particular to its specified role in the mission. Throughout the mission, FeatherSail will have one side that is always illuminated and one side that is always in the dark, referred to as sun side and dark side, respectively. The Detumble Stage is attached to the dark side of the Central Hub, and after the sails are all fully deployed, the Detumble Stage will be detached from the system. The Science Boom is attached to the sun side of the Central Hub for the entire mission. There are four Pods attached to the four side faces on the Central Hub. The configuration of the satellite is shown in Figure 1.

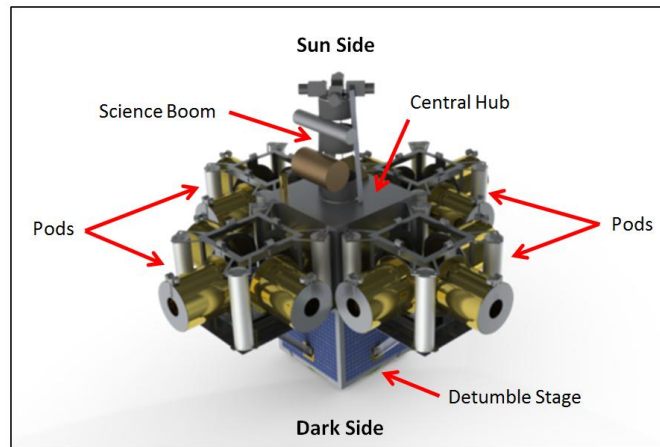


Figure 1: The main modules of FeatherSail.

FeatherSail begins in a stowed configuration for launch and must deploy in space. There are six steps to the deployment, which are numbered in Figure 2. Step 1 shows FeatherSail in its stowed configuration after it releases from the launch vehicle. Step 2 shows the extension of the science boom, which has cameras for documenting the remainder of the deployment. In step 3, the arms that support the pods against launch loads are retracted. In step 4, the pods are deployed from the Central Hub using ATK Coilable booms. These booms rotate the pods  $n + \frac{1}{2}$  revolutions during deployment, which puts the solar panels on the sun side. All of the pods deploy simultaneously so that the rotation from the booms deployment does not induce spin on the spacecraft. Afterwards, in step 5, each pod deploys an additional three booms, all simultaneously. These booms are used to hoist the main sail off of their rolls stored in the four corners of each pod, as seen in step 6. The Detumble Stage detaches off of the dark side, and takes several images of FeatherSail as it backs away. This is to inspect the sail for tears and to verify successful deployment.

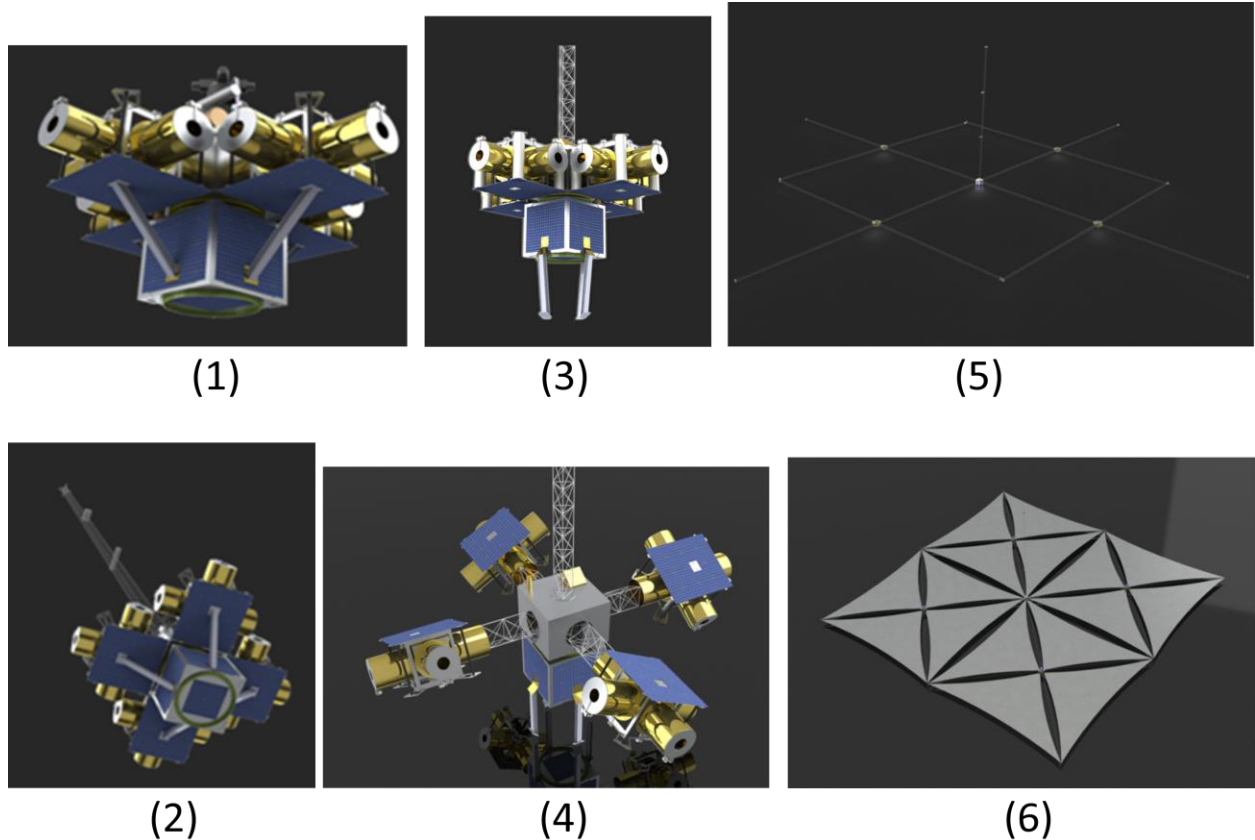


Figure 2: FeatherSails six steps of deployment after it separates from the launch vehicle.

## Solar Sail Propulsion

Solar sail satellites, such as FeatherSail, use the steady stream of photons emitted by the sun as a means of propulsion. While photons are massless, they still have momentum ( $p$ ) proportional to their energy ( $E$ ) by the formula:  $p = E/c$ , where  $c$  is the speed of light in a vacuum. This momentum is transferred to the sail whenever the photon interacts with it, resulting in a pressure called solar radiation pressure (SRP). There are three ways that a photon can interact with a solar sail based on several properties of the material. The coordinate system used to define thrust direction is based on three orthonormal vectors.  $\hat{R}$  is the direction from the center of the sun to FeatherSail,  $\hat{N}$  is the direction normal to the orbit plane, and  $\hat{T}$  is orthogonal to  $\hat{R}$  and  $\hat{N}$ . It is assumed that the sail is flat, the sail is thick enough that light is not transmitted through, and that solar wind effects are negligible at the altitudes the satellite is operating at, typically greater than 0.1 AU [1].

The first interaction occurs when the sail absorbs the energy, effectively bringing the photon to rest and transferring its momentum completely to the sail. The net momentum transfer from absorption is in the direction of incidence, or  $\hat{R}$ . The amount of light that is absorbed as depends on the absorptivity of the sail material at its current temperature. In a steady state thermal environment, the sail rejects all the energy that is absorbed via radiative heat transfer. This rejection of energy results in the second momentum transfer interaction. Energy is emitted diffusely on both sides of the sail, and its amount is dependent on the temperature and emissivity (which is also temperature dependent). Typical sail designs involve a reflective layer on the sun-side and an emissive layer on the dark side for thermal control. Because of this, the momentum from emission is generally stronger on the dark side of the sail, resulting in a small net force opposite to the sail's normal direction ( $\hat{n}$ ).

Finally, there is the interaction where the photon is reflected. The sail can reflect the photon in either a specular (directional) or a diffuse (non-directional) manner. Diffuse reflections act identically to absorption by imparting the photon's momentum to the sail in the  $\hat{R}$  direction. Specular reflection is the preferred interaction because it results in

a net force normal to the sail, as seen in Figure 3. This direction can be controlled by the satellite and makes it possible to perform orbital maneuvers. Because of this, engineers try to design sails to be as specularly reflective as possible.

It is assumed for this paper that the specular reflectivity of FeatherSail results in a force that is significantly higher than the other forces due to absorptivity, diffuse reflection, and emission. Removing those three components, we can derive a simple equation for thrust force produced by SRP. The term in square brackets represents the actual pressure due to solar radiation.

$$\vec{F}_{SRP} = 2 \cdot \left[ \frac{I_{sun}}{c} \cdot \left( \frac{1 \text{ AU}}{r_{AU}} \right)^2 \right] \cdot A_{sail} \cdot \cos^2(\theta) \cdot \hat{n} \quad (1)$$

Where:

$\vec{F}_{SRP}(N)$  is the vector thrust force due to solar radiation pressure.

$I_{sun} (W/m^2)$  is the intensity of light from the sun at 1 AU, or 1366 W/m<sup>2</sup> on average. [2]

$c (m/s)$  is the speed of light in a vacuum, or approximately 300,000,000 m/s.

$r_{AU} (AU)$  is the distance from the center of the sun to FeatherSail, expressed in AU.

$A_{sail} (m^2)$  is the effective reflecting area of the sail.

$\theta$  (deg) is the angle between the  $\hat{n}$  and  $\hat{R}$  directions.

$\hat{n}$  is the unit vector that points normal to the sail.

From this equation, we see that the thrust is both dependent on position and attitude. The force is inversely proportional to the square of the distance to the sun, meaning the closer FeatherSail gets, the more thrust it can produce. Additionally, the thrust is proportional to the square of the cosine of its angle relative to the radial direction. This means that as FeatherSail rotates away from the radial direction the thrust force quickly tapers off. Because the thrust is position and attitude dependent, creating an effective trajectory becomes increasingly difficult.

## Mission Profile

FeatherSail is designed to conduct solar research out of the ecliptic plane, particularly magnetic field and solar wind measurements. Leaving the ecliptic plane requires a large change in velocity, made possible for FeatherSail by SRP's constant thrust. To date, the only spacecraft to perform solar research at high latitudes is NASA/ESA's Ulysses satellite. In its final orbit, however, Ulysses had a semi-major axis of over 3 AU, making its orbital period about 6.2 years. It was also locked at 80.2° inclination. FeatherSail will operate at about 0.5 AU, allowing it to pass over different latitudes at a higher rate. It will also change its inclination slowly over time, providing a complete 3-D view of the sun's magnetic field and solar wind.

## Launch and Earth Eject

FeatherSail will be launched with an Athena II rocket manufactured by Lockheed Martin and ATK. Previously decommissioned, the Athena II has been brought back under the NASA Launch Services (NSL II) contract for \$26 million. This rocket uses the Castor 120 solid rocket motors produced by ATK for its first two stages, and the Castor 30 motor for its upper stage. According to the NSL II performance graphs, Athena II can send a 100 kg payload (a conservative estimate for FeatherSail) on an Earth escape trajectory with an excess energy (C3) of 35 km<sup>2</sup>/s<sup>2</sup>. This maximum performance can be achieved with an inclination of 28.5°. The right ascension of the ascending node ( $\Omega$ ) must be chosen so that FeatherSail's orbit passes through Earth's velocity vector relative to the sun, which is dependent on the launch date. With these defined characteristics, FeatherSail will achieve the maximum possible escape velocity, which will increase its performance during the mission.

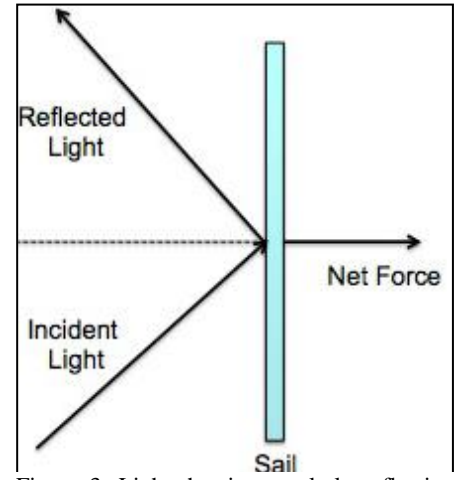


Figure 3: Light that is specularly reflective creates a net force in the sail's normal direction.

Once in orbit and on an escape trajectory, FeatherSail will deploy its main sail. It will orient itself such that the sail's  $\hat{n}$  direction is in the orbit plane, approximately  $35.3^\circ$  away from  $\hat{R}$ , and away from the Earth. This maximizes the thrust in the direction of travel and accelerates FeatherSail towards Earth's sphere of influence. From a heliocentric perspective, this also serves to reduce the semi-major axis.

### Spiraling Inward and Venus Flyby

Once FeatherSail has escaped Earth's gravitational influence, it will begin maneuvers that will allow it to collect data for its primary and secondary science instruments. Because SRP is stronger closer to the sun, the first phase of the mission is to decelerate FeatherSail until it falls to its minimum altitude (0.5 AU). At this altitude, SRP is four times stronger than it was when FeatherSail left Earth. It takes 1 year and 8 months for it to reach it to reach the semi-major axis target, and another 8 months to finish circularizing.

While spiraling inwards towards the sun, FeatherSail will perform a flyby of Venus. Because Venus lies approximately in the ecliptic plane, passing it while enroute to the sun is simply a matter of choosing a launch date such that the spiraling path crosses Venus's orbit at the proper time. Feathersail crosses Venus's orbit five times during its flight inward as seen in Figure 4. Each of these presents an opportunity to flyby the planet and use the onboard multi-spectral imager to collect secondary science data. Table 1 shows a list of possible Earth eject dates and the distance which FeatherSail would approach Venus. Note that these distances were found without any attention put on rendezvousing with Venus, and with slight adjustments to the orbit, these values can easily drop an order of magnitude. Also, a close approach can be obtained with an eject date near 583 days (Venus' synodic period) after the eject dates listed in the table.

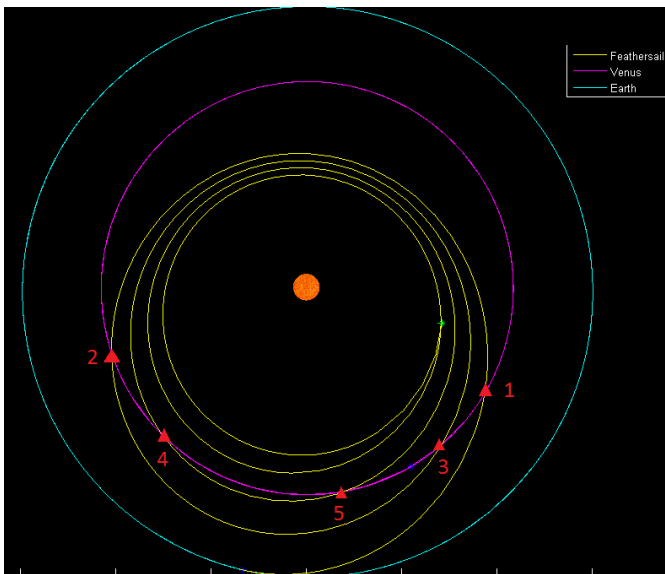


Figure 4: The five crossings that Feathersail (yellow) will make of Venus's orbit (purple). Earth's orbit is shown in blue.

Eject Date	Pass	Min Dist ( $10^6$ km)
October 22, 2015	1	4.60
December 22, 2015	3	7.45
February 28, 2016	2	6.42
May 16, 2016	4	10.65
May 24, 2017	1	7.37
July 20, 2017	3	7.35
October 5, 2017	2	8.86
December 23, 2017	4	9.10

Table 1: Possible Earth eject dates that give FeatherSail a close approach to Venus

### Leaving the Ecliptic Plane

When FeatherSail gets near its 0.5 AU circular orbit, it will begin the second phase where it pitches the sail out of the orbit plane and focuses on increasing its inclination. It is important to note that the two phases of the mission are not mutually exclusive. There is some minor inclination change while FeatherSail is spiraling inwards and vice versa. Because the thrust is higher at lower altitudes, the majority of inclination change occurs after FeatherSail has reached its semi-major axis target. After 10 years from launch, FeatherSail will reach an inclination of  $61.3^\circ$  out of the ecliptic plane and it will reach  $90^\circ$  in approximately 14 years. Figure 5 below shows its trajectory alongside Earth and Venus' orbits.

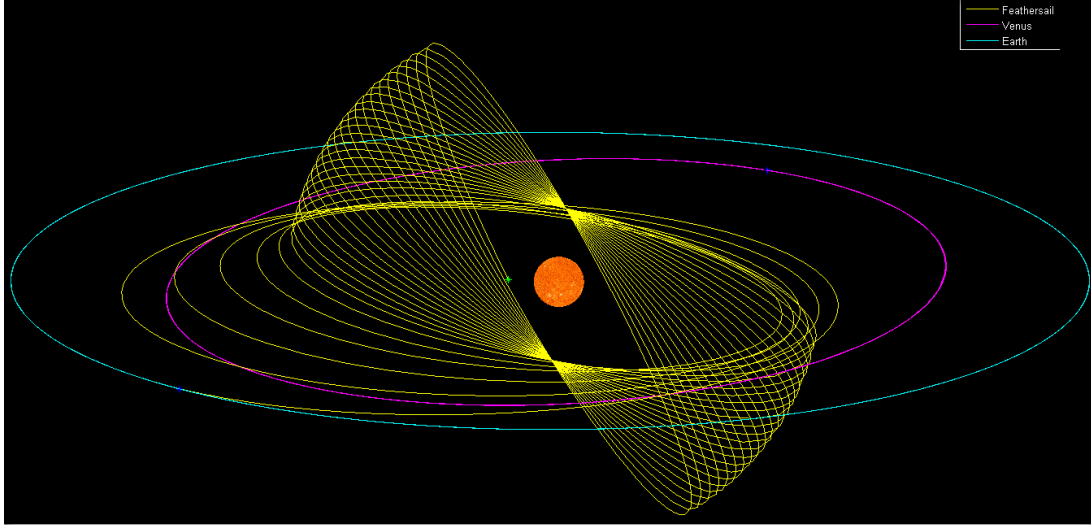


Figure 5: FeatherSail's trajectory (yellow) to achieve maximum inclination. Earth's orbit is shown in blue and Venus' in purple. The sun's size is exaggerated by ten fold.

## Trajectory Optimization

Determining orbital maneuvers that provide an effective trajectory for the mission ultimately involves finding the time history of the yaw angle ( $\alpha$ ) in the orbit plane from the  $\hat{R}$  direction and the pitch angle ( $\beta$ ) out of the orbit plane. To find these angles, we need to find the time history of the direction of thrust that brings about the highest inclination at the end of the mission. Because FeatherSail deals with low and constant thrust, we began by using Lagrange's planetary equations in Gauss' form [1]. These equations show how the three elements we want to change are affected by a perturbing acceleration:  $\vec{a} = [a_R \ a_T \ a_N]$ .

$$\frac{da}{dt} = \frac{2a^2}{h} (e \sin f \ a_R + (p/r) \ a_T) = \frac{2a^2}{h} \begin{bmatrix} e \sin f \\ p/r \\ 0 \end{bmatrix} \cdot \vec{a} = \mathbf{k}_a \cdot \vec{a} \quad (2)$$

$$\frac{de}{dt} = \frac{1}{h} (p \sin f \ a_R + [(p/r) \cos f + re] \ a_T) = \frac{1}{h} \begin{bmatrix} p \sin f \\ r \cos f + re \\ 0 \end{bmatrix} \cdot \vec{a} = \mathbf{k}_e \cdot \vec{a} \quad (3)$$

$$\frac{di}{dt} = \frac{r}{h} \cos(\omega + f) \ a_N = \frac{r}{h} \begin{bmatrix} 0 \\ 0 \\ \cos(\omega + f) \end{bmatrix} \cdot \vec{a} = \mathbf{k}_i \cdot \vec{a} \quad (4)$$

From these three equations, we can see that in order to change any element by its maximum amount, we must apply thrust in its respective  $\mathbf{k}$  direction.

### Weight Factors

It is also apparent from Equations 2-4 that the element rates are coupled and that it is not possible to change all elements by their maximum rate at the same time. For an effective trajectory, weight factors must be introduced to control which element is most important to change at a particular time. For this study, we developed a metric for determining weights based on how effective it would be to adjust an element at the current location versus an optimal location. For a constant set of orbital elements ( $a, e, i, \Omega, \omega$ ), there exists values for the true anomaly that maximizes the rate of that element. Using a Maple worksheet, we derived equations for the magnitude of the rate of each element and observed how they varied with true anomaly ( $f$ ).

Recall that SRP is position dependent and that higher altitudes result in lower thrust. Because of this, the perturbing accelerations are also dependent on  $f$  and this must be accounted for in the weight factor. In the same Maple

worksheet, we factored the  $\left(\frac{1\text{AU}}{r_{\text{AU}}}\right)^2$  term, referred to as the “thrust scale factor”, from the acceleration. Equations for the rate’s magnitudes for the three orbital elements we are controlling are found below, as well as plots (Figure 6) showing how they vary over  $f$ . These equations account for the reduced thrust at higher altitudes.

$$\dot{a} = 2 \sqrt{\frac{(e^2 + 1 + 2 e \cos f) (1 + e \cos f)^4 a^2}{p^4 h^2}} \quad (5)$$

$$\dot{e} = \sqrt{\frac{(2 e \cos^3 f + 3 \cos^2 f + 3 e^2 \cos^2 f + e^2 + 6 e \cos f + 1) (1 + e \cos f)^2}{p^2 h^2}} \quad (6)$$

$$\dot{i} = \sqrt{\frac{(1 + e \cos f)^2 \cos^2(\omega + f)}{p^2 h^2}} \quad (7)$$

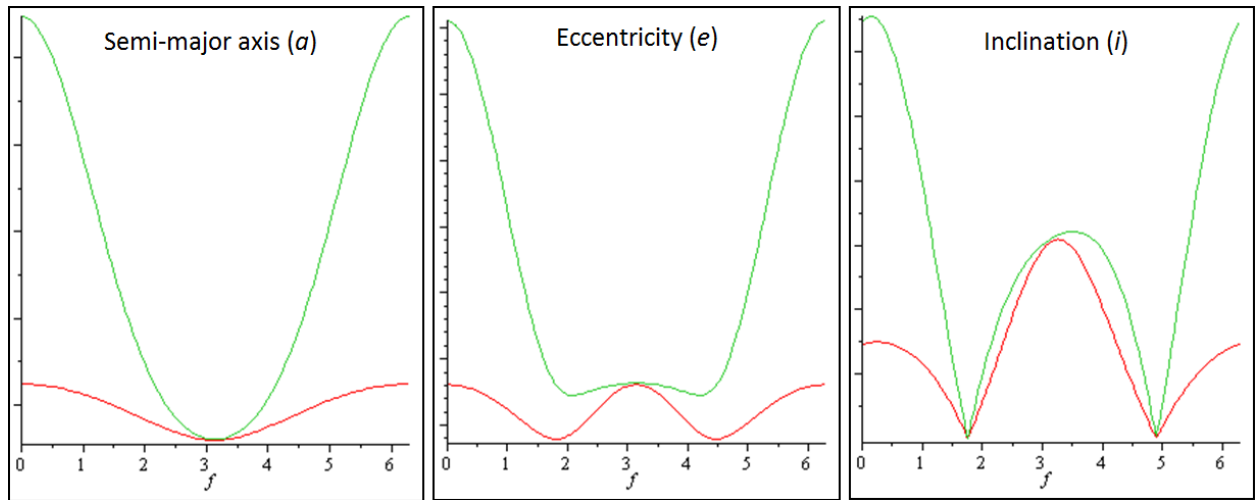


Figure 6: Magnitude of the orbital element rates versus true anomaly. Red shows standard rates and green shows rates using the thrust scale factor.

With these equations, the weights can be calculated. By dividing the magnitude of the element rate at the current  $f$  by the magnitude at an optimal  $f$ , we obtain a weight number (between zero and one), scaled evenly between the three elements.

### Orbit Control Law

A MATLAB script was written to integrate the orbit of FeatherSail and, at each time step, calculate the most effective  $\alpha$  and  $\beta$  angles. First, the initial conditions (Earth escape trajectory with a C3 of  $35 \text{ km}^2/\text{s}^2$ ) are fed into *ode113*, MATLAB’s variable order Runge Kutta integrator. Then all of the instantaneous orbital elements are calculated based on the position and velocity for that time step. Next, the direction of thrust must be determined. This begins by calculating the  $\mathbf{k}$  direction for each element. Then the weights for each element rate are determined as discussed above using Equations 5-7.

At this point, the weights need to be modified to adapt to the problem. If an orbital element is at or beyond its target value, then we don’t want it to change any more, so its weight is set to zero. Additionally, there are points in an orbit where changing one element favorably causes another to change unfavorably. This is due to the fact that FeatherSail’s initial solar orbit is not quasi-circular. For example, at apogee, circularizing the orbit (reducing eccentricity) would increase the semi-major axis of the orbit. Because we don’t want these two elements to duel each other, the control law modifies their weight factors if necessary. It calculates the angle between the  $\mathbf{k}_a$  and  $\mathbf{k}_e$  directions and if it is greater than  $90^\circ$ , then these elements are in opposition. If neither element has reached their target and the perigee altitude is above the altitude limit (0.5 AU), then FeatherSail opts to reduce  $a$  by setting the eccentricity weight to zero. This results in a lower altitude and thus higher thrust for other orbital maneuvers. If the

perigee radius is below the limit, then the semi-major axis weight is set to zero instead, and the control law opts to circularize the orbit by changing  $e$ .

Now that the weights have been appropriately modified, they can be used to determine the optimal thrust direction and the sail angles that can achieve it. The optimal direction is calculated as a weighted sum of the  $k$  directions using the weights calculated. Next, the angles that maximize the thrust in the optimal direction need to be calculated. This is done with MATLAB's *fmincon* function, which uses a Sequential Quadratic Programming algorithm to find the constrained, multivariable input that produces the minimum value for a function. In this case, the inputs are the  $\alpha$  (yaw) and  $\beta$  (pitch) angles. This input is used to form a direction vector by converting the angles from spherical to Cartesian coordinates. Recall that the thrust from SRP is attitude dependent, so the input angles also create a magnitude scalar to account for the  $\cos^2\theta$  term in Equation 1. The magnitude times the direction vector is then dotted onto the optimal thrust direction vector. The function output, which is minimized by *fmincon*, is the negative of this dot product, which means the positive dot product is maximized. MATLAB returns the  $\alpha$  and  $\beta$  angles that maximize thrust in the optimal direction. These angles are recorded for each time step in the integration. The time history of the  $\alpha$  and  $\beta$  angles as well as the resulting time history of the orbital elements can be found in Figure 7 and Figure 8, respectively.

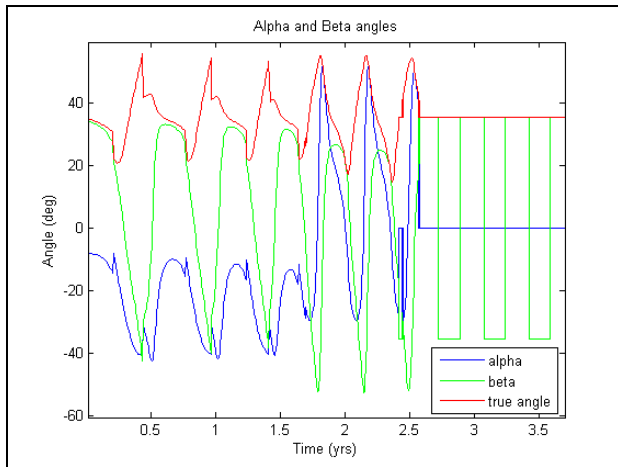


Figure 7: Yaw (alpha) and pitch (beta) angles throughout FeatherSail's mission. The plot stops at 3.5 years because the same pattern repeats for the rest of the mission.

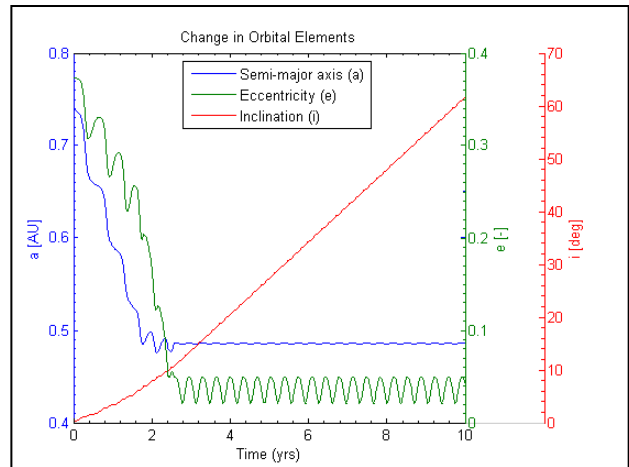


Figure 8: The time history of the orbital elements throughout the mission.

You may notice that at about 2.5 years into the simulation, the  $\alpha$  angle remains locked at zero, but the semi-major axis and eccentricity oscillate. This is due to the fact that orbital elements are calculated based on spacecraft only under the influence of gravity, but FeatherSail always has some radial force on the sail due to SRP. This force counteracts some of the gravity that is holding the satellite in orbit. Therefore, FeatherSail can have the position and speed that a traditional satellite would have in a circular orbit, but because of the gravity offloading, it takes an elliptical path instead.

## Central Hub and Avionics

The Central Hub houses the flight computer, battery, data storage, communications, star tracker, electrostatic analyzer, and multispectral imager. The electrostatic analyzer is used to collect data on solar wind using an electric field to measure charged particles with specific energies. The multispectral imager will be used during the Venus flyby. It takes pictures through different filters yielding pictures which only capture certain wavelengths of light. With these pictures data can be extracted about the surface of Venus that cannot be seen with a normal picture.

## Communications and Data Handling

The most important command and data handling component is the flight computer, which is used to control the entire satellite from the Central Hub. We decided to use the Proton 200K flight computer made by Space Micro, which is included in the Proton-X Box. The Proton-X Box on FeatherSail also contains other boards such as a power

distribution board (PDB), a battery control regulator (BCR) board, a digital IO board, and an analog IO board. A simple block diagram of FeatherSail is shown in Figure 9.

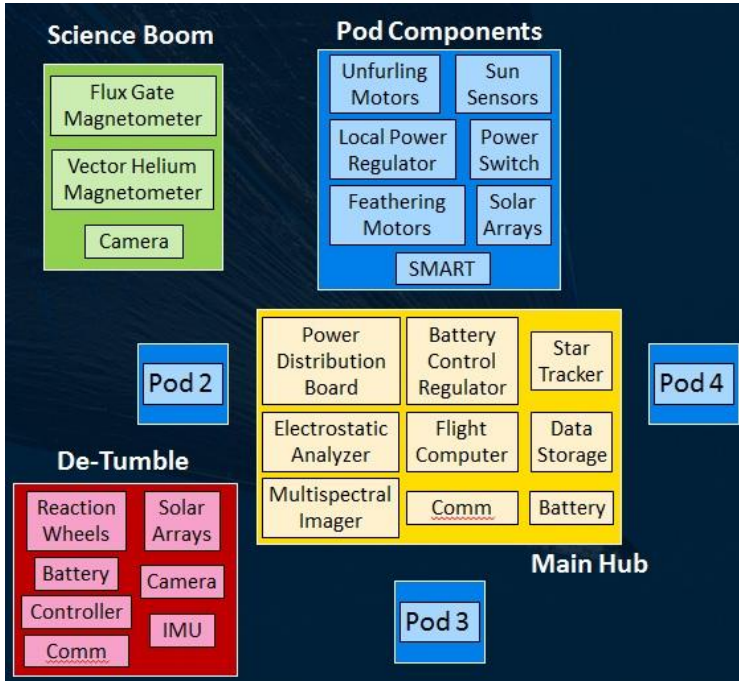


Figure 9: FeatherSail Block Diagram

The flight computer transmits engineering and science data through a three module communication radio. The Modular S band Radio by Comtech Aeroastro includes a transmitter, receiver, and power amplifier that uses software based radio technology. The software based radio technology allows the communication system to change bandwidth frequencies, because it does not require a change in hardware. The advantage of this is avoiding unwanted frequencies. The communication system also needs a high link margin and data rate, which depends on the size of the antenna and the amount of power it can transmit. FeatherSail will be transmitting and receiving data between 0.5 AU and 1.5 AU, so it will also need a high gain directional antenna. As the sailcraft orbits the sun, it gathers scientific and engineering data in a data storage device. Then FeatherSail transmits this data back to Earth when it is orbiting at a minimum distance, which occurs every 277 days.

### Science Boom

The Science Boom is an ATK Coilable boom that is six inches in diameter and twelve meters in length. Attached to it is a flux gate magnetometer at four meters, a vector helium magnetometer at eight meters, and a camera system (described below) at twelve meters. The instruments are at different distances from the Central Hub because the magnetometers, used to measure the magnetic field of the sun, need to be as far from the other electronics as possible so there is no magnetic interference. There are two magnetometers for redundancy and since they use different operating principles, bias in one instrument can be seen by the other. The camera system consists of four cameras pointed at the position the pods will be in after sail deployment, with overlapping views. The four pictures will then be combined to form one big picture of the sail. Using four cameras we are able to get a higher pixel count for the overall picture which means it will have better quality. It also allows for a level of redundancy; even if one of the cameras fails, you will still get images of the rest of the sail. These images will be used to verify successful deployment of the sails and to monitor sail integrity throughout the mission.

### The Pods

There are four identical pods on FeatherSail mounted to the central hub in a single plane. They are cube-shaped and made from grade 162 aluminum beryllium alloy, with a boom on the four side faces. Each side of the pods is covered in multi-layer insulation (MLI) except where solar panels are mounted on the sun-side. The pods are used to unfurl and hold the sails open and for attitude control and propulsion. The sails are opened using ATK Coilable graphite booms that extend from a compressed state to the full length. They are coiled in the compressed state and rotate out to the extended state. Figure 10 shows a fully deployed pod. The pods are launched in a stowed position and are deployed near an altitude of 1100 km. Once deployed, the sails are unfurled and the Detumble stage is

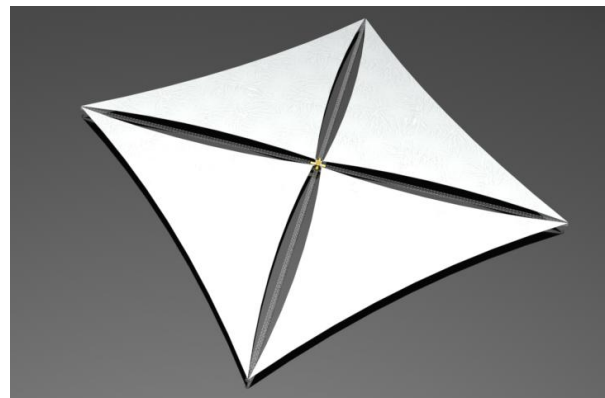


Figure 10: A fully deployed pod. The Central Hub and other three pods are not shown.

ejected. The rotation of the pod creates a moment on the hub that would cause the satellite to spin because the Attitude Control System (ACS) is not strong enough to hold FeatherSail stable as the inertia increases throughout deployment. However, pods on opposite sides of the central hub will be deployed at the same time to prevent the spin.

The deployment of each pod occurs in three steps: the boom connected to the hub deploys, the three other booms deploy, and the sails are unfurled. These steps are shown in Figure 11. The order is necessary so that the booms from different pods do not collide and so that deployment is quick.

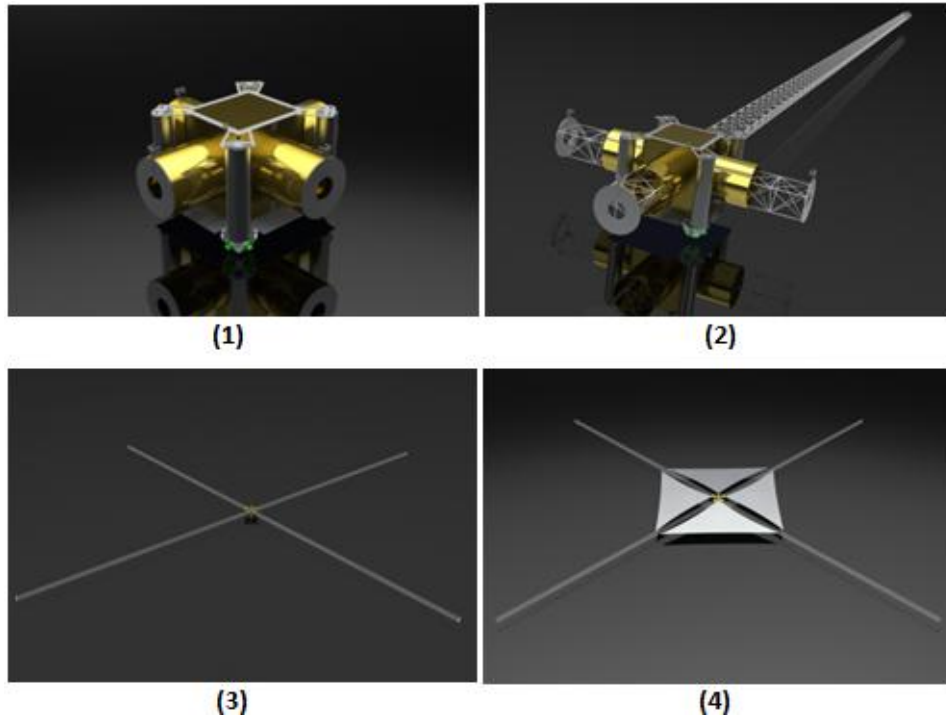


Figure 11: Closed Pod (1), Booms Deploying (2), Booms Deployed (3), Sails Deploying (4)

### Boom Deployment

Each pod has four 8-inch diameter Coilable graphite booms, made by ATK, that are mounted in cans on the outer walls of the pod. The booms consist of longerons, battens and diagonals. The longerons are the long rods that go from one end of the boom to the other. The battens and diagonals support the longerons. Figure 12 shows a section of an extended boom.

Each boom is compressed in a spiral to approximately two percent of its total length into a can. Once released, the stowed strain energy in the boom causes it to deploy. A damper at the end of the boom controls the rate at which the boom deploys.

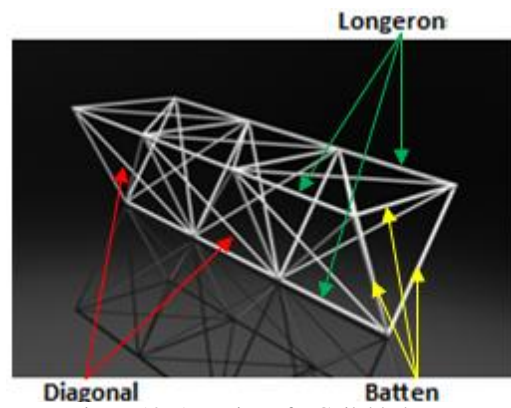
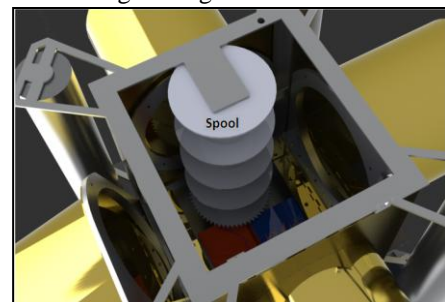


Figure 12: A section of a Coilable boom

### Sail Unfurling

At each corner between the booms on the pod, there is a 12 x 12 m right triangular sail that has been folded like a large accordion and rolled onto a tube. The sails are made of CP1, an aluminized polyimide material with high reflectivity. At each corner of the sails there is a 1.6 mm Kevlar halyard that passes through a ring in the sail.

Any wire can be attached to the longerons with rings, as long as the wire diameter is not greater than the diameter of the longeron. While the boom is



compressed, the halyard is attached to the longerons and passes through a series of Teflon rings, which direct the halyard to the spool in one direction and the sail roll in the other direction. Once the boom deploys, the halyard pops off of the longerons but stays in the rings. The far end of the boom has an end cap, on which two Teflon rings are mounted to aid in unfurling the sail. Figure 11.1 shows a pod before deploying with the end caps at the end of the cans. That prevents the halyards from getting twisted around the booms as they are deployed. For simplicity and to save space, there is only one wire that is wound up on the spool. That wire is swaged in to two wires near the end cap of the boom. Each of the two wires passes through the Teflon rings on the end cap and goes back to the sail rolls. A diagram of the halyards and spool is shown in Figure 14. The halyard motor turns the spool and winds in the halyards, which unfurls the sails off of the rolls.

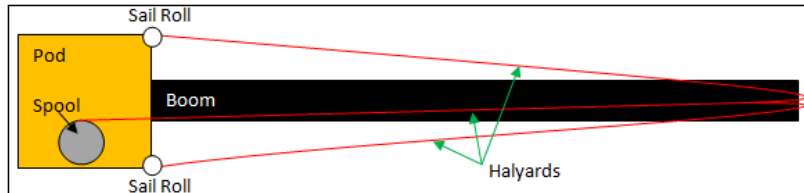


Figure 14: Halyards for a single boom

All halyards are attached to one spool so each sail is unfurled at the same time. The spool is separated in to four sections, one for each halyard. The spool is designed to feed the halyards so they do not get tangled and wrap around the spool evenly. There is a ratchet on one end of the spool so that there will always be tension in the halyards and sails. The halyard motor used is the BS12 brushless motor from Moog. Figure 13 shows the spool in the pod.

### Feathering

On each pod, two booms are capable of “feathering” up to 20° for attitude control. Those two booms are attached to a piano hinge, and there is a linear

actuator and lever for each boom that feathers. The linear actuators are 1200 series actuators from Diamond Motion that travel up to two inches. There were multiple linear actuators capable of completing the task, but the 1200 series is the smallest and lightest one that was capable of moving the booms. As the actuator extends, the lever pushes the boom door outward, angling the sail and boom out of plane. To keep the satellite insulated, MLI will still be placed on the moving side. The insulation will be folded like an accordion to allow it to stretch with the movement of the boom door.

To determine the angle that the boom is at, there is an absolute magnetic encoder attached to the moving part of the hinge. The feedback from the encoder will tell the SMART box when to stop the actuator to achieve a certain angle. The encoder is absolute, so if the power fails the encoder will not zero to determine its location once power is regained. It is an RXM 22 absolute magnetic encoder from Encoder Technology.

FeatherSail is designed to be redundant and lightweight because it increases the life and effectiveness of the mission. Each motor in the pod will actually have two motors. If one motor fails, the second one will be strong enough to overcome the first-failed motor and perform the task required. Since there are four pods, if both motors in one pod fail, the satellite will have additional redundancy in attitude control. If one of the booms on a pod cannot feather, the FeatherSail will not be able to complete either the pitch or yaw maneuver involving that boom. However, with a 90° rotation with the roll maneuver, pitch becomes yaw and vice versa, so FeatherSail still has full maneuverability.

### Pod Avionics

Figure 13: The spool mounted in the pod

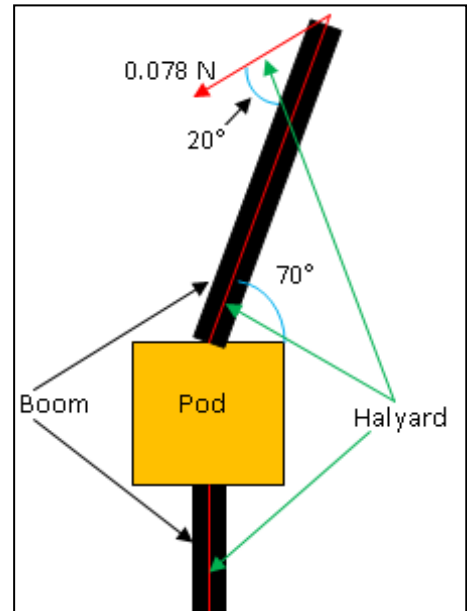


Figure 15: Halyard Force Diagram

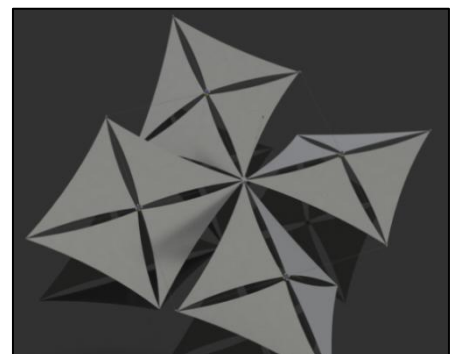


Figure 16: FeatherSail with the sails articulated in a roll maneuver. Sail angle is exaggerated at 35°.

One of the custom avionic components, which is integral to the control of the pods, is the Smart Multi-Purpose Advanced Reconfigurable Technology (SMART) module. SMART is a reprogrammable drive and sensor module. We have included three SMART units, SMART A, B, and C, on each of the pods.

When FeatherSail is deploying the pods, SMART unit A is responsible for the boom release mechanism. Once the boom is extended, SMART unit A is used once again to control the motor that unfurls the sails. Redundancy is built into the system by wiring the boom release mechanism to another SMART unit. The boom release mechanism and unfurling motor are only used once, and the power for those SMART units comes directly from the solar arrays on the pods. Wires carrying power and data run down the boom connecting each pod to the Central Hub.

After the sails deploy and the Detumble stage detaches, the attitude control system changes significantly. The flight computer on the Central Hub continues to process the measurements and give commands, but the system is changed to distributed attitude control at the pods. A Star Tracker on the Central Hub is used along with sun sensors on two of the four pods to provide attitude measurements, and changes in solar pressure on the sails create changes in attitude. FeatherSail uses a sun sensor pyramid made up of five smaller sensors. The sun sensor we chose was the Aeroastro Miniature Sun Sensors, which gives two axis attitude determination. The attitude of FeatherSail can then be determined using the angle measurements from the two pyramids at opposite ends of the satellite. SMART unit B can then read the signal from the sensor and transmit it to the Central Hub. A spread sheet showing the function of each SMART unit is shown in Table 2.

	SMART A	SMART B	SMART C
<b>Drive</b>	Boom Release Prime	Boom Tilt $\alpha$ Prime	Sail Motor Backup
	Boom Release Backup	Boom Tilt $\alpha$ Prime	Boom Tilt $\alpha$ Backup
	Sail Motor Prime	Boom Tilt $\beta$ Prime	Boom Tilt $\alpha$ Backup
	Sail Motor Backup	Boom Tilt $\beta$ Prime	Boom Tilt $\beta$ Backup
<b>Sensor</b>	Boom Release Feedback 1	Boom Tilt Position $\alpha$ Prime	Boom Tilt Position $\alpha$ Prime Backup
	Boom Release Feedback 2	Boom Tilt Position $\beta$ Prime	Boom Tilt Position $\beta$ Prime Backup
	Boom Release Feedback 3	Sun Sensor Prime	Sun Sensor Redundant
	Sail Motor Rate		

Table 2: SMART units and their respective functions in the pods.

Once the attitude of FeatherSail is determined, changes in attitude can be made accordingly. Attitude adjustments are made by altering the angles of the sails to create the roll, pitch, and yaw. SMART unit B is used to control the feathering of the booms by operating in a closed loop circuit with the feathering motors. A signal is sent thorough the wires on the booms from the Central Hub to the pod, and this signal is sent to the SMART unit in the pod specifying an angle for the boom. SMART will then continually check the variations in the angle using an encoder until the motor has rotated to the specified position. Redundancy is again built into the system by wiring two SMART units to the feathering motors.

### Pod Strength

The pod is made out of the aluminum beryllium alloy because of its strength and light weight. The frame is capable of supporting the pod under the four G's experienced during launch. When each boom is in the sail plane, the moment forces on the boom cancel each other out, leaving a compressive force. However, when the boom is feathered, there is a torque at the end of the boom created by the tension in the halyards, as shown in Figure 15. Therefore, the boom must also be strong enough to support that moment.

Each sail is assumed to have 1 psi of stress, to ensure that it is taut and flat. That equates to a tension of 0.039 N in each halyard. The sum of the force perpendicular to the angled boom from the two halyards is 0.027 N. The bending strength of the graphite boom is 4.40 N m. Therefore, each graphite boom is 13.75 times stronger than the moment created by the halyards.

The halyard motor must also be strong enough to overcome friction in the Teflon rings and the torque on the spool from the halyards. The tensional force from each of the four halyards that connect to the spool is 0.078 N. The maximum lever arm distance is 68 mm. The torque created by the halyards is 0.0212 Nm total. The BS12 motor used for the spool has a torque rating that is three times greater than the torque from the halyards.

## Detumble Stage

The Detumble Stage is an expendable stage which is mounted to the Central Hub. It houses the attitude control system (ACS), a camera, a battery, solar arrays, an inertial measurement unit (IMU), three CubeSats, and communications. The ACS (described below) is in the Detumble Stage instead of the Central Hub because it is only needed before the sails are unfurled. Once the sail is fully deployed, FeatherSail will be able to maintain its own attitude by feathering. The camera will be used to verify deployment of the sails as well as check for any tears. The sail will be backlit which will make tears highly visible as the Detumble Stage retreats from the sailcraft.

The Detumble Stage is designed to operate independently once it detaches from FeatherSail. The Detumble Stage uses a PC104 as a controller, which is similar to a flight computer. It also has a Microhard S-band communication system to transmit and receive data. The Detumble stage will be close enough to earth for this small communications device to provide enough power. Once the Detumble stage detaches from Feathersail, it switches to solar arrays and a battery array for the power system, and the reaction wheels and IMU continue to control the orientation.

### Reaction Wheel Attitude Control

An attitude control system (ACS) in the Detumble Stage is needed to stabilize the vehicle before beginning boom deployment and sail unfurling. Several systems were initially considered including hydrazine thrusters, reaction wheels (RW), control moment gyros (CMGs), and magnetic torque rods. We decided against hydrazine thrusters because they provide more torque than we need and overcomplicate the ACS necessary. Magnetic torque rods were not ideal to use because they work best with strong magnetic fields, and the satellite will not be in low earth orbit. To decide between reaction wheels and CMGs, we calculated the inertia of FeatherSail, shown in Table 3. To calculate the inertia, the sails, pods, booms, and avionics were treated as point masses at their centers of gravity. The inertia's affecting each of the maneuver directions are shown below in Figure 17. The reaction wheels only need to control the satellite until the booms and sails are deployed and attitude can be controlled using the sails.

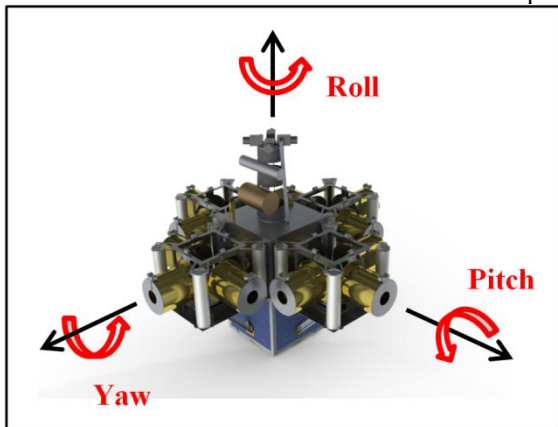


Figure 17: The directions of maneuver for FeatherSail.

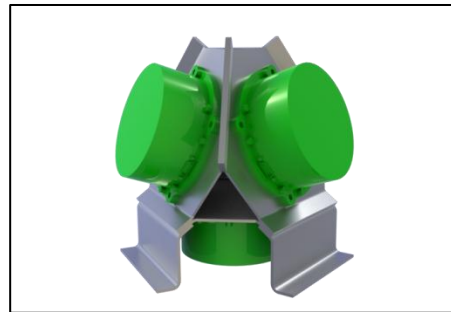


Figure 18: The four RW35 reaction wheels on their tetrahedron mount.

Maneuvers	Inertia (kg m <sup>2</sup> )
Roll	8.4
Pitch	4.4
Yaw	4.4

Table 3: Shows inertias affecting maneuverability.

We selected RW35 reaction wheels from Astro- und Feinwerktechnik Adlershof GmbH because they provided a sufficient amount of torque for their given size to control the satellite. We decided to use four reaction wheels, for redundancy, organized with each one on a face of a tetrahedron mount shown in Figure 18 above. With this organization, one of the reaction wheels can fail and there will still be three-axis attitude control. The IMU, model HG1930 made by Honeywell, is used to measure the wheels are used to change it. The IMU and reaction wheels both receive Hub through the Lightband. Calculations can then be made with the flight computer to continuously check and make modifications to the attitude of the spacecraft.

## Stage Support and Separation

The Central Hub and Detumble Stage need to be rigidly attached so that they can survive launch loads but still be easily separable once in orbit. Each of the booms is attached inside the Central Hub to a mounting plate five inches from the outer face. During launch, each of the pods is a cantilever with a large mass at its end and all of the shear and bending loads being focused through the fragile booms. To solve this problem, we attached support arms going from the Detumble Stage to the bottom of each of the pods. Each of the arms is on a spring hinge at the point of attachment on the Detumble Stage. They are attached to the pod using two Frangibolts made by TiNi Aerospace. Each Frangibolt, as shown below in Figure 19, consists of a notched fastener, an actuator, washers, and a nut. When it is time for the components to separate, the actuator is heated and expands, putting pressure on the fastener until it fractures at its designed fail point. Once the arms detach from the pods, the spring hinge will swing the arms away from the pods to ensure that they do not get in the way of deployment.

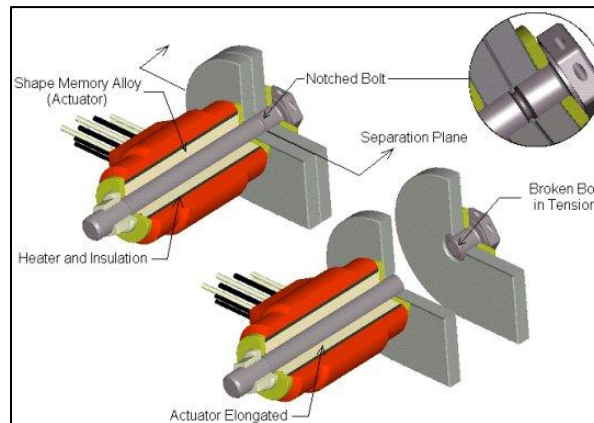


Figure 19: The Frangibolt assembly used to attach support arms.

The Detumble Stage needs to stay firmly attached to and get power from the Central Hub before they are separated. We decided to use a 16 inch Mark II Lightband to attach the two stages [3]. So far 23 light bands have been flown and there has not yet been a failed detachment. This system contains an upper and a lower ring which ensures rigid attachment of the two vehicles, as shown in Figure 20. Before separation the lower ring has “leaves” that press outward on the upper ring. Once the motors are powered, the leaves snap inward freeing the upper and lower rings and the separation springs push the two vehicles apart. The separation mechanism is shown in Figure 21. After the vehicles are separated the Detumble Stage begins to obtain its own power using side-mounted solar panels as it moves away from the Central Hub.

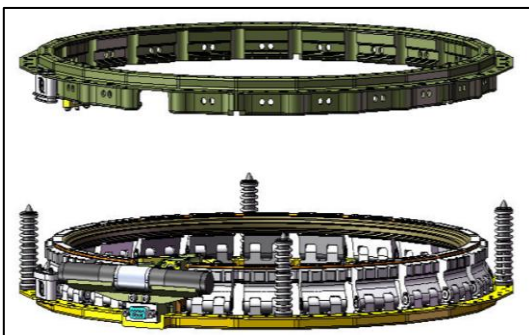


Figure 20: Shows the upper (green) and lower (yellow) light bands.

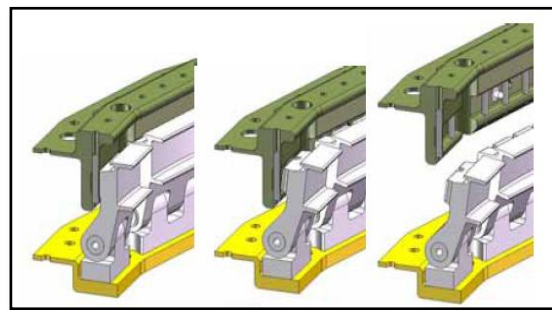


Figure 21: Shows compression of the leaves to allow for stage separation

The solar arrays used to power the Central Hub will be attached to the bottom side of each pod, and until deployment, will not be facing the sun. During boom deployment, the booms will make  $n + \frac{1}{2}$  rotations so that once each boom is fully deployed the solar panels will be facing the sun side. The solar panels will have up to a  $40^\circ$  incidence angle but their combined surface area is large enough that this will still collect enough energy to power the components of the satellite. The Detumble Stage has four main solar panels; each of these is the correct size to

collect enough power for the entire module. There are also two smaller solar panels on the top and bottom of the stage to supply power until the satellite can be rotated to another face.

## **Power System**

The Detumble Stage has four main solar panels; each of these is the correct size to collect enough power for the entire module. There are also two smaller solar panels on the top and bottom of the stage to supply power until the satellite can be rotated to another face. The solar arrays used to power the Central Hub will be attached to the bottom side of each pod, and until deployment, will not be facing the sun. During boom deployment, the booms will make  $n + \frac{1}{2}$  rotations so that once each boom is fully deployed the solar panels will be facing the sun side. FeatherSail uses XTJ space solar panels made by Spectrolab. The solar panels will have up to a  $40^\circ$  incidence angle but their combined surface area is large enough that this will still collect enough energy to power the components of the satellite. A switch is used to reroute the power to the battery on the Central Hub or the components on the pod. Wires run down the booms to the Central Hub to a battery control regulator (BCR), and the BCR switches between charging the array of batteries and providing power to the power distribution board (PDB). FeatherSail will use a standard 28 Volts DC throughout the sail craft, powered by an array of ten batteries located in the Central Hub. The PDB divides the power among the avionic components. A similar device called the local power regulator is located on each pod to power the SMART units.

The power budget includes the peak power budget for the Detumble stage and Feathersail without the Detumble Stage. The peak power for the Detumble Stage is 62.0 Watts, and the peak power for FeatherSail without the Detumble Stage is 244.1 Watts. The 244.1 Watts includes the 168.8 Watts from the combined Halyard motor power used for unfurling the sails. These motors will only be used once, however, and the normal power load that FeatherSail will run at is 75.3 W. The mass of FeatherSail without the Detumble stage is 68.7 kg. The mass of the Detumble Stage is 19.7 kg. With an effective sail area of  $871 \text{ m}^2$  the areal density of FeatherSail is approximately  $79 \text{ g/m}^2$ , which gives it a characteristic acceleration of  $0.15 \text{ mm/s}^2$ .

## **Conclusion and Future Recommendations**

FeatherSail is the next step in solar sail satellites for NASA following the success of Nanosail-D, making it a likely near-term project. The design and analysis discussed in this paper has yielded a near complete pre-phase A design for FeatherSail. It involves solutions to geometric problems, detailed lists of required components, and an outlined mission plan. The designed mechanisms will allow for the deployment of a  $34 \times 34 \text{ m}$  square sail, which can be articulated for three-axis attitude control. Most of the needed avionics have been given specifications and the central hub is designed to house and protect them. A mission plan has been developed that includes all stages from launch to end-of-life. With this work, FeatherSail is nearly ready for a mission proposal and a phase-A design.

There are several areas in the design of FeatherSail that remain incomplete that must be addressed in the phase-A design. A communications system is needed in order for FeatherSail to send data back to Earth. Additionally, a load analysis needs to be done to ensure it can survive launch conditions. FeatherSail is currently too heavy to meet its areal density target. Either the sails must be made larger or weight needs to be cut. Finally, our group has discussed ways of minimizing failure modes during the sail deployment. One that was not implemented was a mechanism that locks the corners of the sail in place when they are fully deployed. That way, a halyard can break after deployment without affecting the sail tension.

## Works Cited

- [1] Dachwald, B., Ohndorf, A., & Wie, B. (August 2006). Solar Sail Trajectory Optimization for the Solar Polar Imager (SPI) Mission. *AIAA/AAS Astrodynamics Specialist Conference and Exhibit*. Keystone, Colorado: AIAA.
- [2] G. Vulpetti, *Solar sails : a novel approach to interplanetary travel*. New York; [Chichester UK]: Copernicus Books; In Association with Praxis Pub., 2008.
- [3] Planetary Systems Corporation. (2009). User's Manual for Mark II Lightband. Silver Spring, MD.

# Characterization of Zinc Oxide Nanolaminate Films

B. J. Oleson, L. M. Bilke, J. S. Krueger, S. T. King

Department of Physics, University of Wisconsin – La Crosse

**Abstract:** This project sought to increase the understanding of fundamental properties of the transparent conducting oxide materials needed to improve solar energy device efficiency. Specifically, this study focused on the development of Cu:ZnO nanolaminate materials where Cu and ZnO form alternating layers on the nanometer scale. Initial results show no intermixing of materials, and suggest that these nanolaminates may be employed as infrared mirrors.

## Introduction

With the earth's current energy supplies dwindling at an accelerating rate, it seems obvious that renewable energy is necessary for the future of mankind. Being abundant and relatively low cost, solar energy may be the most feasible route for clean and renewable energy. It is estimated that the earth's population will double within the next 50 years and create a 1.5-3-fold increase in energy demand [1]. With the population growing, space colonization is a topic receiving more focus. Seeing as solar panels are already used to power crafts in space including the international space station, it is reasonable to believe any colonization efforts will make use of solar energy. Also, it has been proposed that large photovoltaic grids be built in space to harness the energy and transmit it to earth in the form of microwaves. To lower the cost of such a project, thin-film solar cells must be employed.

Although solar cells can be found all around the world, the majority of the sun's energy goes unharnessed. The amount of solar energy reaching the surface of the planet is so vast that in one year it is about twice as much as will ever be obtained from all of the Earth's non-renewable resources [2]. Before solar panels can be employed on a large scale on earth or in space, significant challenges in material physics and chemistry must be overcome. Thin film solar cells require both an absorbing medium as well as a transparent medium with good electrical conductivity to extract electrons. Currently, indium doped tin oxide (ITO) makes up the transparent conducting oxide (TCO) layer. One setback of thin films is that indium is about as rare and expensive as silver. High cost of solar panels make them more popular in wealthier nations such as Europe and North America, which are countries poorly suited for large scale photovoltaic deployment. This project works on replacing indium with a cheaper material so that the cost of these tools can be drastically reduced and the potential of solar panels can better be realized.

Zinc oxide is a safe and inexpensive material that shows great promise for replacing the ITO used in the TCO layer of modern photovoltaic devices [3]. Although ZnO has a large and direct band gap desired for photovoltaic devices, it does not display a sufficiently low resistance for solar cell applications. This project aims to understand and overcome the difficulties ZnO possess and observe the effect annealing has on the material. Specifically it focuses on ZnO/Cu nanolaminate films.

## Experimental Results

The films were grown on Si and micro-glass substrates with via a reactive DC sputter deposition apparatus outfitted with two independently controlled sputter heads. Due to its flexibilities in the control of composition and microstructure, magnetron sputtering is widely employed [4]. One sputter head consisted of an aluminum doped zinc target (Zn:Al/96%:4%) and the other contained a copper metal target (Cu/99.99%). Al is added to the Zn target to add free electrons and ultimately increase its conductivity. Two substrates were used to complement each other and overcome physical properties each substrate possesses that restrain future testing of the thin films. Silicon's high melting point of 1414°C was utilized to study the effects of annealing and the micro-glass grown samples were used to study transparency. Before the substrates were used in the sputter apparatus they were cut into pieces approximately 1 cm x 2.5 cm, ultrasonic cleaned in acetone, ultrasonic cleaned in alcohol, rinsed in alcohol, and dried. The sputter system has a base pressure of  $10^{-5}$  torr which is raised to  $10^{-3}$  torr during deposition. All deposition occurred at an emission current of 20 mA with a 8:1 Argon:O<sub>2</sub> ratio of sputter gasses. Argon was used as a sputter gas because it is inert and will not react with the materials being deposited, but its relatively large mass results in an efficient sputter yield. The preferential amount of oxygen was allowed into the chamber to react with Zn and create ZnO.

Before ZnO/Cu nanolaminate films could be grown and studied, a thick sample of pure ZnO was grown and analyzed with X-ray diffraction (XRD) to confirm its content and purity. As seen in Figure 1 the diffraction pattern shows only ZnO present with no impurities, including zinc metal.

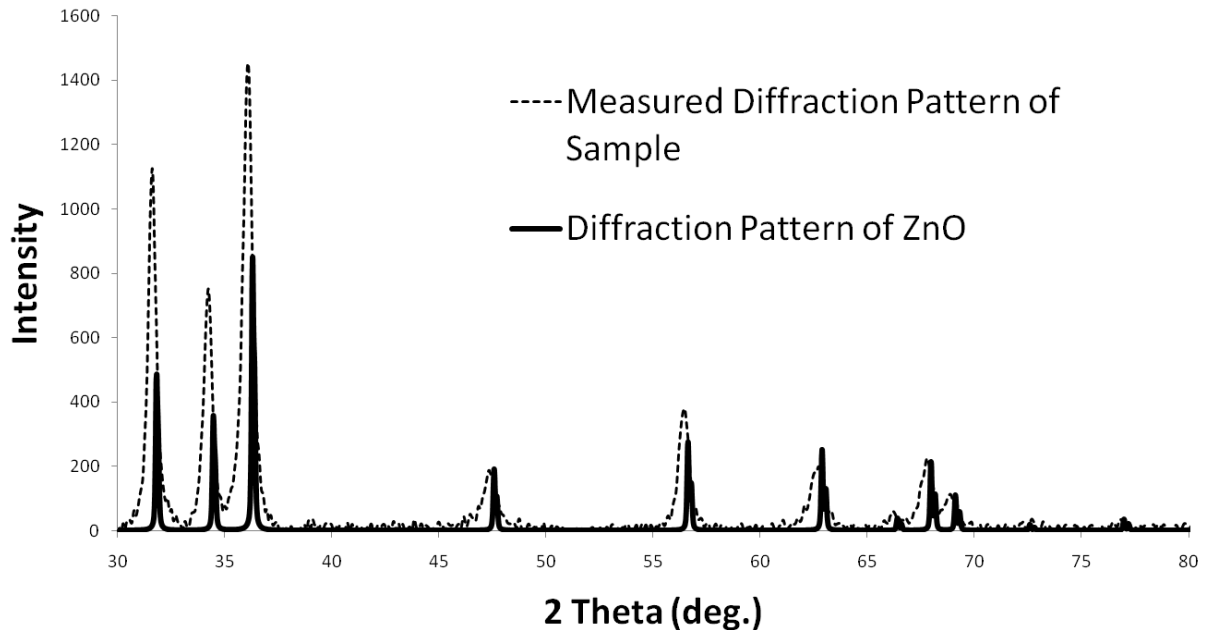


Figure 1. Comparison of XRD patterns, measured and known, reveal a successful growth of ZnO.

After ZnO was successfully grown Cu could be incorporated. A six layer (3 Cu, 3 ZnO) nanolaminate thin film was created by first depositing a Cu layer directly onto the substrate. A layer of ZnO was then put on top of the Cu and the process repeated until the sixth layer was complete. To study the effects the Cu thickness has on the ZnO based film, the ZnO layers in all of the samples were held at 40 nm each, or a total of 120 nm per thin film. The Cu layers contained the same thicknesses within each sample but Cu thicknesses were varied between. XRD performed on the fabricated films confirm the presence of both Cu and ZnO with no evidence of the formation of impurity species (Fig. 2).

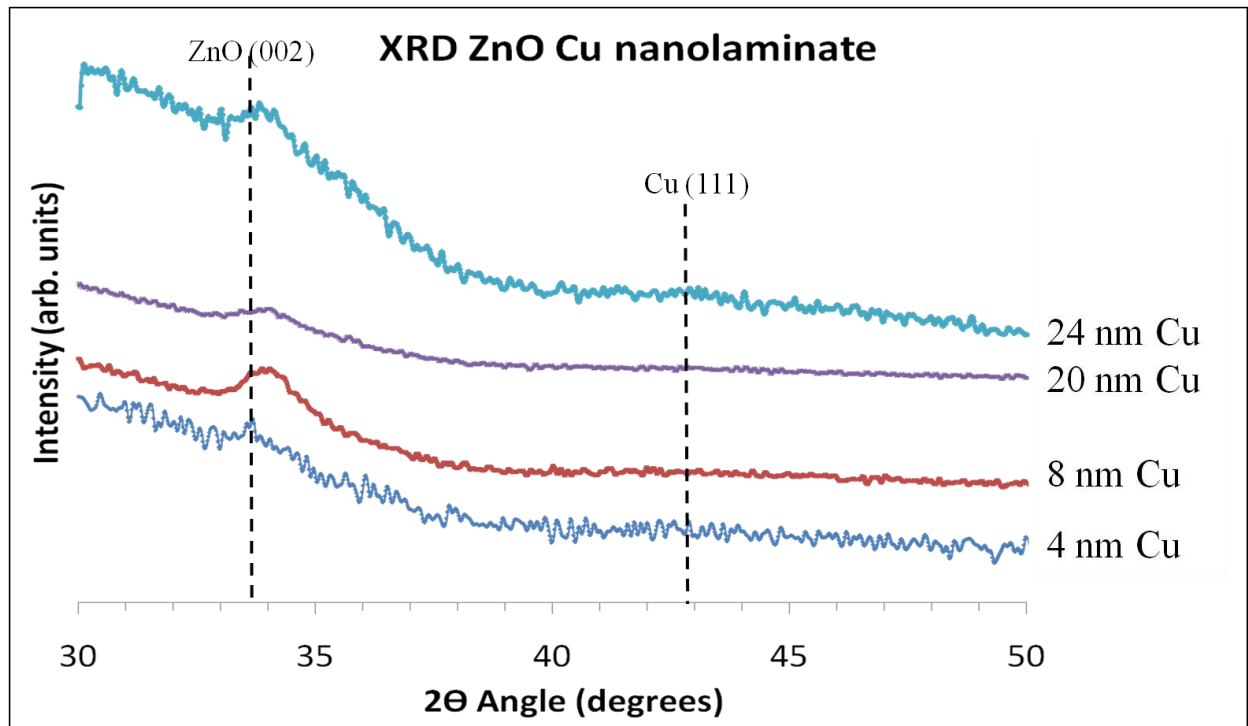


Figure 2. XRD of nanolaminate films shows definite presence of ZnO and possibly Cu in the thicker grown samples.

The plot in Figure 2 shows ZnO is present but it is unclear whether Cu exists within the film. It appears that when the Cu layer is thickest (24 nm) a characteristic Cu diffraction peak can be made out. X-ray fluorescence was used as a complementary technique to confirm elemental make-up of the film. Although Cu presence cannot be confirmed in the thinner films in Figure 2, Figure 3 clearly shows both ZnO and Cu exist within the film.

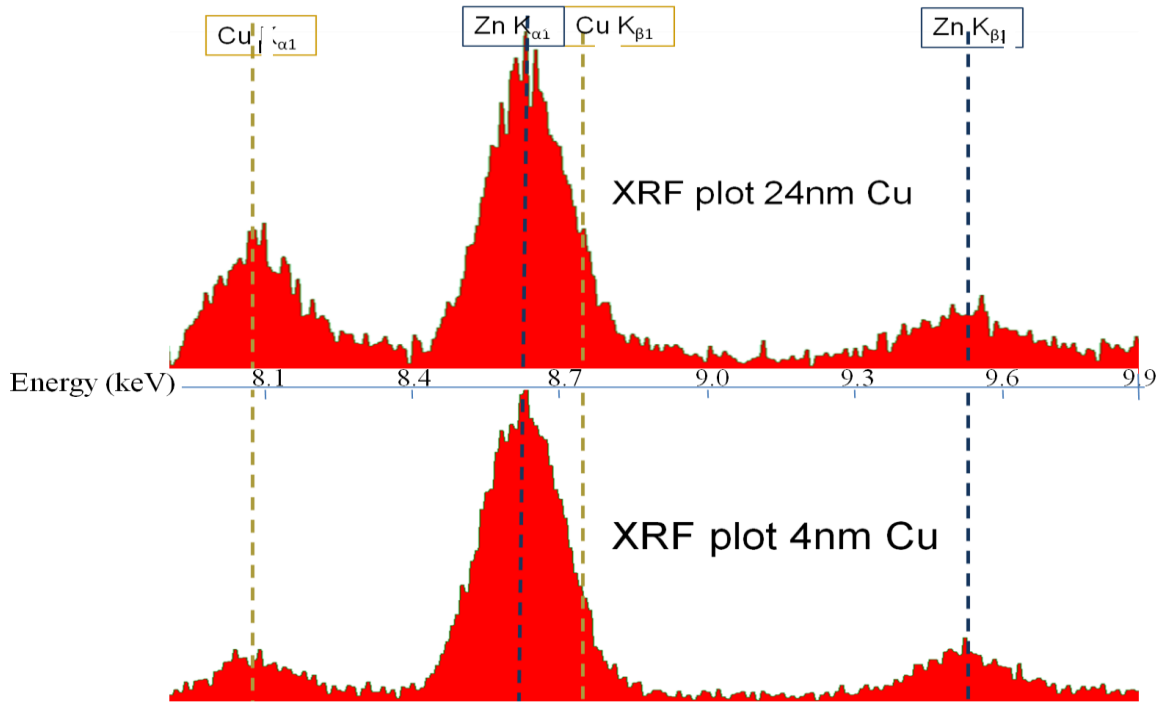


Figure 3. XRF plots of samples with thin and thick layers of Cu are compared.

An important characteristic of a TCO is its transparency. In this study UV-Vis spectroscopy was used to study the transparency for different thicknesses of Cu in the films. Figure 4 shows the amount of light transmitted, within the visible spectrum, through these films. These measurements indicate that the films containing 8 nm and 4 nm of Cu exhibit excellent transparency which is more than adequate for TCO applications.

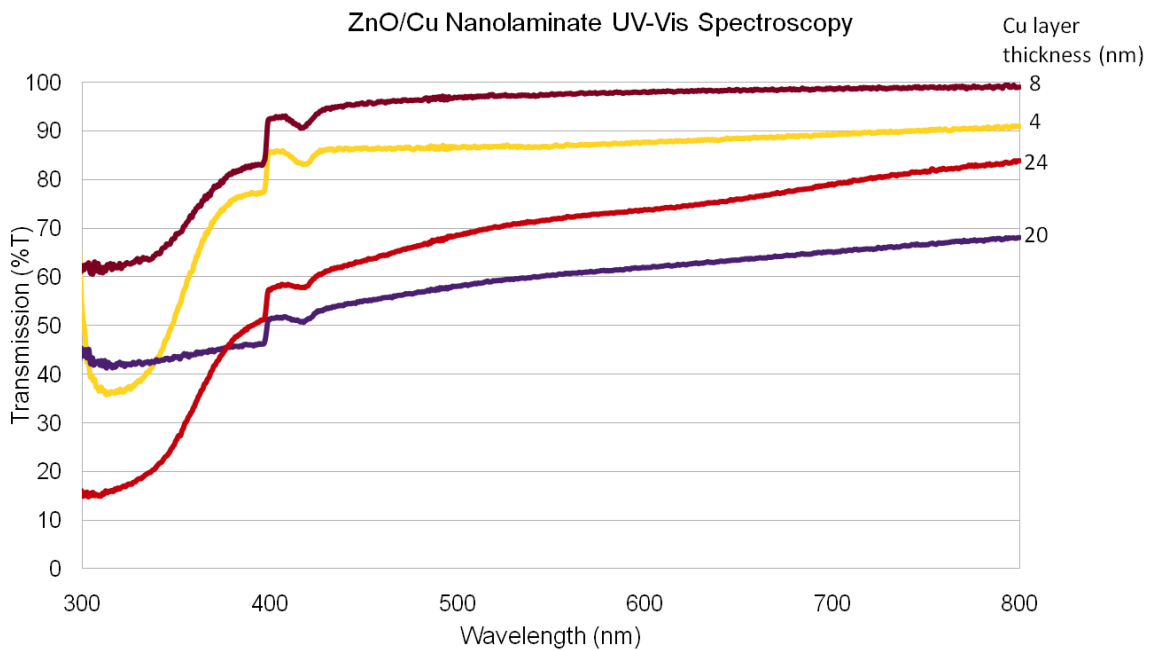


Figure 4. ZnO/Cu nanolaminate UV-Vis Spectroscopy comparing transmission for different thicknesses of Cu.

The next phase of this study required an atomic force microscope (AFM) to study the surface of films and how the surface morphology changes via annealing. Before the nanolaminate films were studied, surface changes of ZnO due to annealing were first explored. The films were heated to 450°C in a tube furnace and evaluated every 30 minutes. The surface didn't change significantly from 0-60 minutes annealed. However, from 60-90 minutes drastic changes were noted as seen in Figure 5.

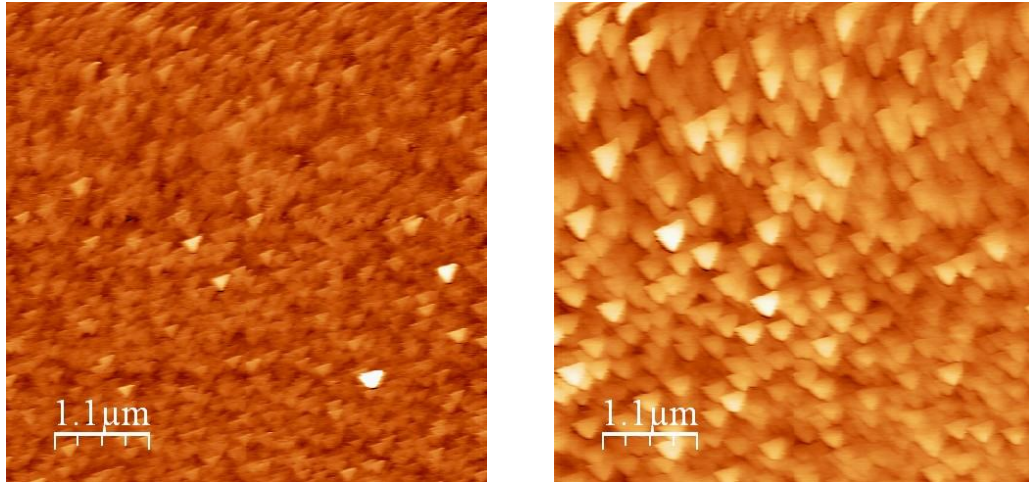


Figure 5. Left: AFM image of ZnO after being annealed 60 minutes. Right: AFM image of ZnO after annealed for 90 minutes.

Arbitrary cross sections are commonly used to evaluate the height and width by taking the average of several of these measurements. Before the large change in surface structure, ZnO exhibits general uniformity of small, fine, triangular grains about 200 nm wide. After annealing for 90 minutes the triangular grains grew to 350 nm wide. It is likely these terraces are growing together to make larger ones. Changes in the surface structure could hold important changes in the optical and electrical properties of the film. These terraces are important because their size is related to the resistivity of the surface. As the films were annealed for longer than 90 minutes the grains continued to grow in size at a much slower rate and the uniformity of the films were lost.

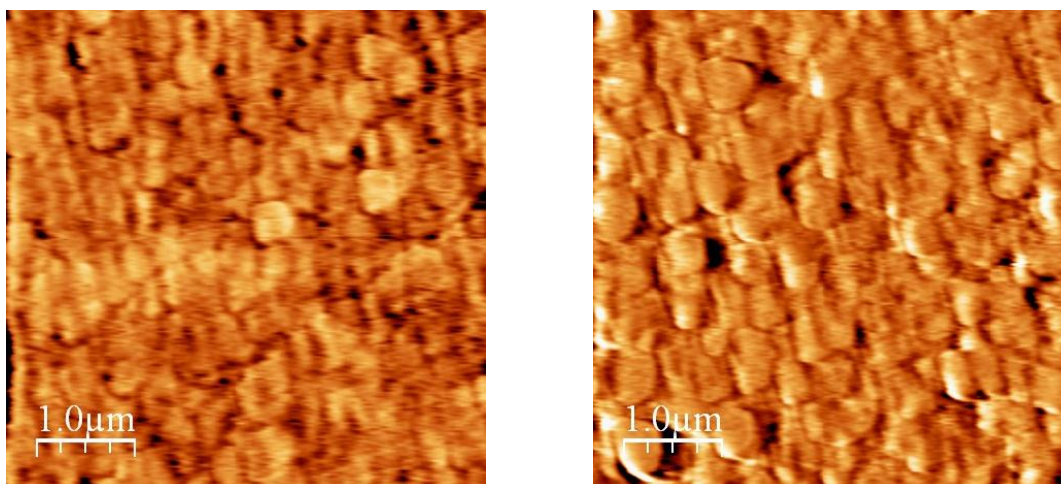


Figure 6. On the left is an AFM image of a ZnO/Cu nanolaminate sample after 60 minutes annealed. On the right is an image of the same sample with an additional 30 minutes annealed.

After the pure ZnO films were analyzed the ZnO/Cu nanolaminate films were annealed and evaluated. The largest change in surface structure occurred over the same time interval as the pure ZnO films. Figure 6 shows the change in the surface from 60 to 90 minutes annealed. As expected, the cross sectional analysis again shows an increase in grain sizes; from 400nm to 550nm in the 30 minutes shown.

## Conclusion

After sputter deposition the thin ZnO film has a surface which may be too rough to be applicable in solar devices. This can be overcome by annealing the sample to create a smoother more compatible surface. The grain sizes are important because their size is related to the resistivity of the surface, a property that is obviously crucial when studying the possibility of implementing into photovoltaic devices. Annealing also increases uniformity, which is ideal for use in semiconductors. As a result, annealing the films for 90 minutes was determined to be the proper amount needed for the desired surface changes. This increase in crystal size should lower the resistance of the film and allow the short circuit current density to increase [5].

The reality of an inexpensive, good electrical conductor with a transparent medium shows the possibility of replacing the TCO layer in photovoltaic devices. With the ability to be produced at a low temperature and its' wide and direct band gap, a ZnO alloy is a prospect worthwhile. Significant visual changes were found in the annealing process of these films. This study will set the ground work in future work to better understand ZnO applications in photovoltaic devices.

## References

- [1] N. Lior, Energy Conv. And Manage. **42**, 1769 (2001)
- [2] <http://gcep.stanford.edu/research/exergycharts.html>
- [3] J. C. Bernède, Y. Berredjem, L. Cattin, and M. Morsli , Appl. Phys. Lett. **92**, 083304 (2008)
- [4] Z. Li and W. Gao, Mat. Lett. **58**, 1363 (2004)
- [5] H.H. Afify, S.H. El-Hefnawi, A.Y. Eliwa, M.M. Abdel-Naby, and N.M. Ahmed, Egypt. J. Solids **28**, 243 (2005)

# The Effect of Magnetization Defects on DW Motion in Ferromagnetic Nanowires

Kyle Kimminau, and Andrew Kunz

Physics Department, Marquette University, Milwaukee, WI

## Abstract

The propagation of domain walls in ferromagnetic nanowires offers the possibility of ultrafast logic devices and high density data storage. The understanding and control of domain wall motion has become more desirable recently as these devices come closer to realization. Domain walls can only be propagated by small magnetic fields or their movement becomes hindered by the precessional motion of the magnetic dipoles, also called the Walker breakdown effect<sup>1</sup>. Through the use of Landau-Lifshitz Gilbert Simulation, we report a method of eliminating the Walker breakdown. This investigation also offers some insight into how these proposed devices might perform in the high energy radiation of space for extended periods of time.

## Introduction

In a ferromagnetic nanowire, it is energetically favorable for the magnetization to be aligned with the length of the wire. Thus, the magnetization lies along the long axis of the wire, with magnetic domains oriented to the left or to the right; the transition region that must exist between these regions is termed a domain wall. The domain wall can be oriented upwards or downwards, and the domains surrounding the domain wall can be oriented head to head or tail to tail. These domain walls can be propagated along the length of the wire by applying an external magnetic field on the sample; a domain with magnetization aligned with the external field will grow at the expense of adjacent domains.

This motion along the wire is smooth and fast for small fields, but fields applied above a certain value, the Walker field limit, cause the dipoles in the domain wall to precess around direction of the external field. This precessional motion, called the Walker breakdown, causes an anti-vortex to nucleate on the edge of the domain wall, and travel across the width of the wire. During this nucleation and movement of the anti-vortex the domain wall itself remains relatively stationary. Following the ejection of the anti-vortex, the wall continues moving smoothly until the next nucleation occurs, creating a periodic behavior and significantly reducing the average speed.

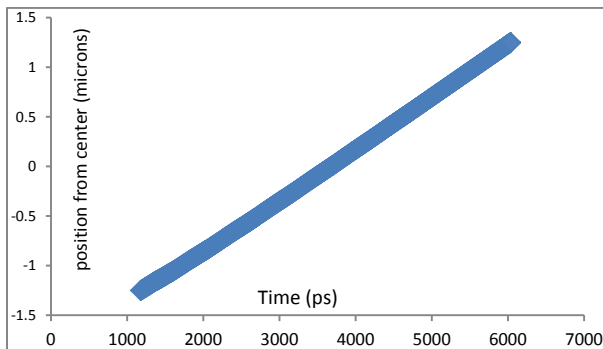


Figure 1: The domain wall is pushed through the wire with an applied field of 15 Oersteds. This causes the wall to move smoothly and quickly along the wire.

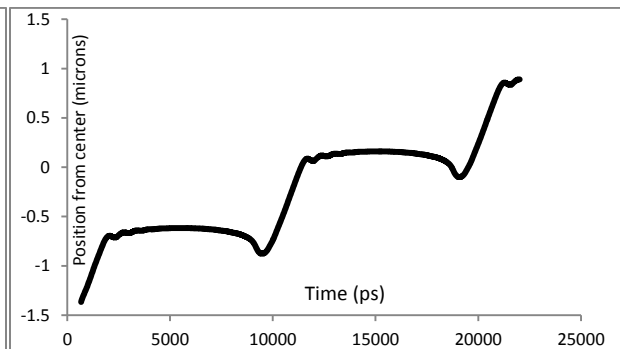


Figure 2: The domain wall is propagated with a field of 30 Oersteds. Instead of smooth fast motion along the wire the motion is periodic and the average speed is very much lower than at fields lower than the Walker limit.

## Micromagnetic Simulation

The LLG Micromagnetic simulator utilizes the Landau-Lifshitz Gilbert equation of motion for magnetic dipoles in order to simulate interactions within magnetic materials<sup>2</sup>. The equation is

$$[1] \quad \frac{\partial \vec{m}_i}{\partial t} = -\gamma(\vec{m}_i \times \vec{H}_i) - \frac{\alpha\gamma}{M_s} \vec{m}_i \times (\vec{m}_i \times \vec{H}_i)$$

such that  $\gamma$  is the gyromagnetic ratio and  $H$  is the sum of the applied external field, the dipole field and an exchange field. The first term on the right hand side of the equation describes how the dipoles precess about the magnetic field. This term is responsible for the Walker breakdown behavior observed at high fields. The second term describes how the dipoles align with the magnetic field, and is why the application of an external magnetic field propagates the domain wall through the wire. At low fields the first term is dominated by the second term, so Walker breakdown does not occur.

The material parameters used in the trials model permalloy with no crystalline anisotropy:  $\alpha=0.008$ , exchange stiffness  $A=1.3 \times 10^{-11}$  J/m, and the saturation magnetization of the material  $M_s=8 \times 10^5$  A/m. The magnetic material is discretized by the program into small blocks of magnetization that act as the dipoles in the system and are usually within 1-10 nm on each side. The blocks used in our trials were 2nm on a side. The program then calculates the motion of every dipole initially and repeats the calculation at time increments, or steps, that are less than a picosecond<sup>2</sup>. The high spatial and temporal resolutions together allow for very detailed investigation into the important phenomena that occur in magnetic interactions.

## Methods

The saturation magnetization has been found to be diminished in magnetic materials if irradiated with certain particles<sup>4</sup>. In order to model the effects of high energy particles colliding with the magnetized sample, we used the program to eliminate random blocks of magnetization in the wire. The density of defects was gradually increased from 0% to 10% density in increments of .5%, and then from 10% to 25% in increments of 2.5%. These defect densities were saved as masks and used for trials over a variation of applied magnetic fields.

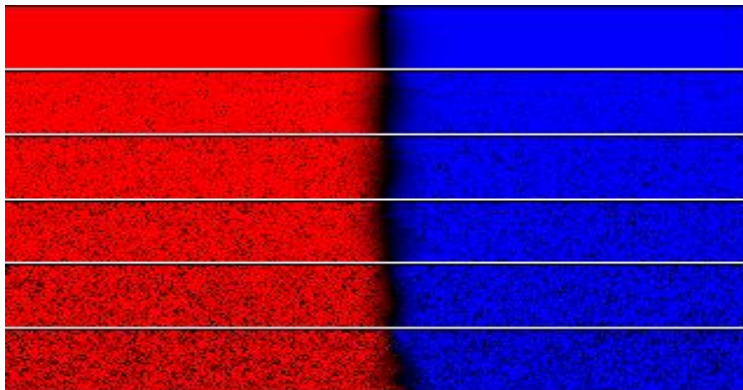


Figure 3: The series of wires have had blocks of magnetization eliminated to model defects from irradiation. The defect densities, from top to bottom, are as follows: 0%, 5%, 10%, 15%, 20%, and 25%. The wire dimensions used were  $5\mu\text{m} \times 100\text{nm} \times 2\text{nm}$ .

## Results

The addition of magnetization defects to the nanowires has two significant effects on domain wall motion. The first effect is an overall decrease in domain wall speed, whether the applied field is below or above the Walker field. When a domain wall is propagated by a field less than the Walker limit the wall speed decreases with increasing defect density, as might be expected. No considerable change in speed occurs until the defect density reaches 10%. The speed of the wall is only lessened by 10% at 10% defect density. However between 10% and 20%, the speed of domain wall pushed by fields less than the Walker limit is halved if it is not stopped altogether. The same effect occurs when the wall is moved with fields greater than the Walker limit, but the speed doesn't begin to decrease until about 10% density. Regardless of field, no domain wall can be propagated in a defect density of 25% or greater.

The second effect observed due to the defects in the magnetization is the elimination of the Walker breakdown effect. In the presence of defects, the motion of a domain wall pushed by fields above the Walker limit becomes more smooth and linear. This effect becomes more prominent as the defect density increases. The domain wall speed reaches its' max at about 10% defect density, and is where the first effect starts to overpower the propagation. At low densities the domain wall continues to nucleate an anti-vortex, and clusters of defects large enough act as pinning sites for these anti-vortices. The Walker breakdown stems from the cross product of the magnetic field, and the moments of the dipoles in the domain wall. If the magnetization were to be perturbed inside the domain wall geometry, the cross product would diminish, causing the first term in the equation of motion to be overpowered. The defects provide these perturbations by forcing the magnetization to form around the area lacking magnetization, thus countering the breakdown effect.

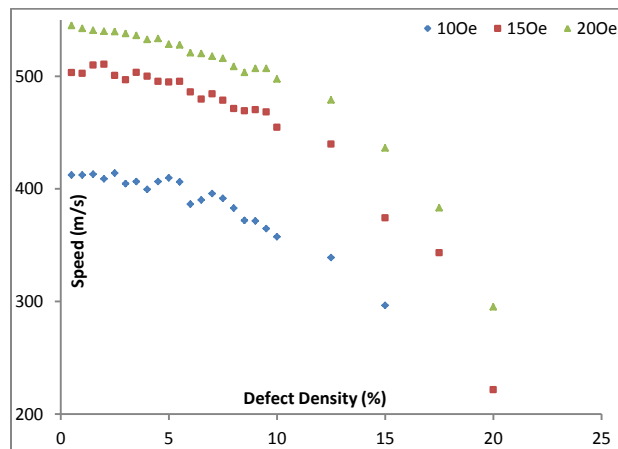


Figure 4: Domain walls with increasing defect densities are propagated with three fields under the Walker field. It can be seen that speeds do not decrease significantly until after 10% defect density.

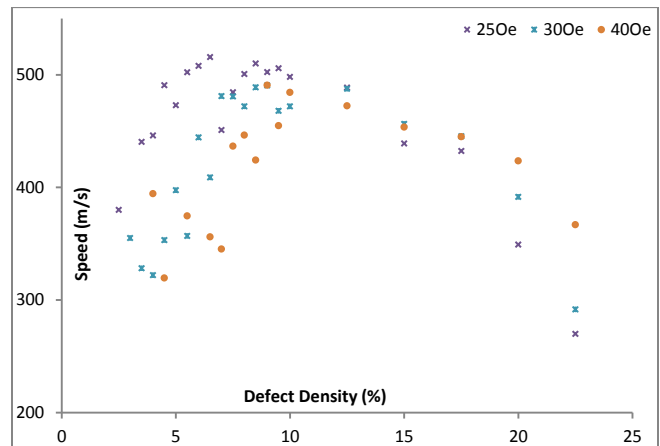


Figure 5: The walls in this graph were moved with three fields above the Walker limit. The wall speed increases with increasing fill until about 10% density for all fields. After 10% the walls act similarly to walls pushed by fields less than the Walker limit

## Conclusions

The proposed magnetic nanowire devices utilize the control of domain walls to store/analyze information. In order to move and control these walls a magnetic field must be applied, but these fields must be under the Walker field limit. Generating such small and precise magnetic fields would prove difficult if not impossible. Therefore the elimination of the Walker breakdown is of importance if the computers of the future will include magnetic devices. We have found that the Walker breakdown is countered if random defects are placed in the wires. However, pinning occurs when an anti-vortex comes in contact with a cluster of defects. A controlled pattern of defects applied during production of the nanowires could eliminate the pinning sites and serve to eliminate the Walker breakdown more effectively.

We have also shown that domain wall speed is not dramatically changed for small defect densities. This could mean that these devices are plausible for use in space, but unfortunately they will inevitably require replacements. The current electronic devices do not face this issue, and could be more desirable even if the magnetic devices are operational under small defect densities, especially considering pinning issues with the lower densities.

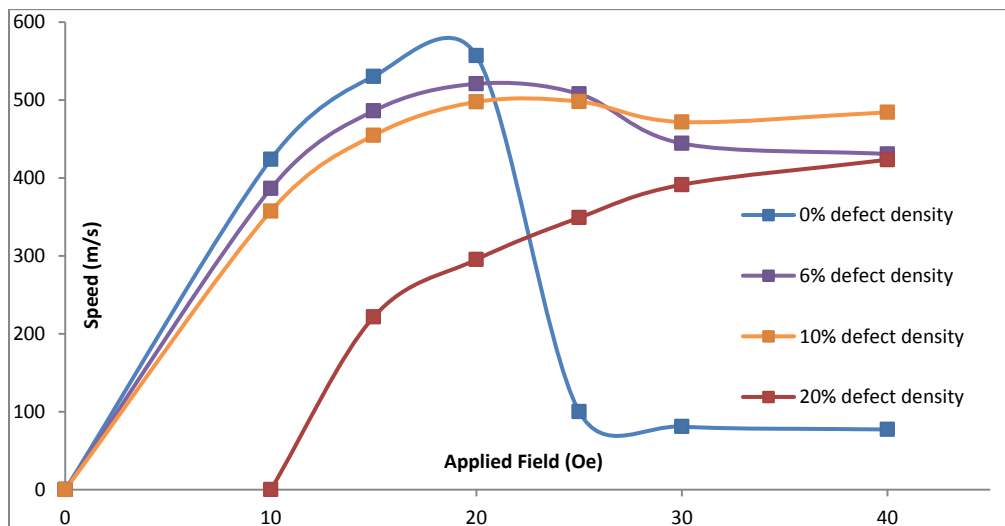


Figure 6: The behavior of domain walls in nanowires with no defects is shown by the blue data; the Walker breakdown occurs just above 20 Oe and the speed decreases significantly. The other sets of data show various defect densities and how the breakdown affects the motion of the walls. The 10% defect density gives the highest speed at higher fields, and at higher densities the wall speed is diminished due to the number of perturbation.

## Future Projects

Defect clusters have been observed to act as pinning sites for anti-vortices. This is of interest if we are to prevent the pinning of domain walls at undesired locations. The energy well created by the defects can most likely be described using a simple magnetic charge model. Magnetic charge is defined as

$$[2] \quad Q_m = -\mu_0 \oint_S \vec{M} \cdot d\vec{S}$$

where  $M$  is the magnetization. By using the LLG simulator we can calculate the charge in each block and map out the charge geometry. By doing this we can investigate the energies of the domain wall and any type of defect that it might interact with. This might lead to defect patterns better suited for eliminating breakdown behavior and avoiding pinning of domain walls.

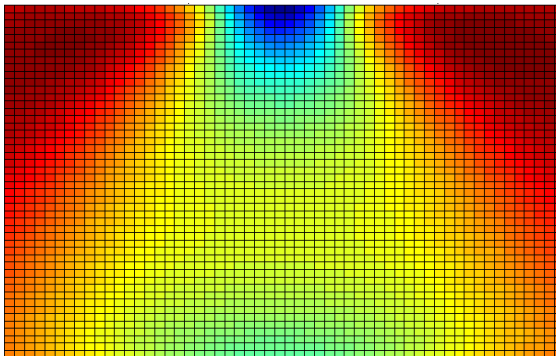


Figure 7: The charge structure of a head to head down domain wall. It seems that the densest area of charge is located at the top of its triangle geometry.

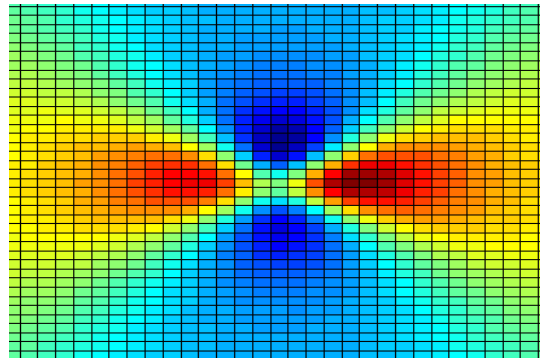


Figure 8: Above is the charge structure for an anti-vortex nucleated from a head to head down domain wall (left). The charge density is high around the core of the anti-vortex. The dynamics could explain the pinning phenomena observed.

## References

- [1] N.L. Schryer, L.R. Walker, “The motion of  $180^\circ$  domain walls in uniform dc magnetic fields”, *JAP* **45**, 5406 (1974).
- [2] LLG Micromagnetics Simulator, LLG Inc.
- [3] J.-Y. Lee, et al., “Dynamic transformation of the internal structure of a moving domain wall in magnetic nanostripes”, *Phys. Rev. B*. **76**, 184408 (2007)
- [4] A. Vogel, S. Wintz, J. Kimling, M. Bolte, “Domain-Wall Pinning and Depinning at Soft Spots in Magnetic Nanowires”, *IEEE Trans. Magn.* **46**, (2010)

# **Compression after Impact: Damage Characterization of Multi-Directional 10-Ply Carbon-Epoxy Prepreg Laminates Subject to Quasi-Static Impact Force**

by Graduate Fellow Marco Lo Ricco, P.E., S.E., and Rani El-Hajjar, P.E., PhD., Assistant Professor, Department of Civil Engineering and Mechanics, University of Wisconsin—Milwaukee

## **Abstract**

During the course of service, aerospace structures inevitably will suffer some form of damage, including the possibility of impact. Two general types of impact damage, either resulting from a quasi-static force or a dynamic impulse force, characterize the nature of impact threats for analysis and experimentation in a lab setting. Using ASTM D7137 Standard Test method for Compressive Residual Strength Properties of Damaged Polymer Matrix Composite, this study subjects multidirectional carbon-fiber/epoxy laminates to Compression After Impact (CAI) tests to determine whether the results may be used to characterize and quantify the effects of impact damage on laminate compressive strength. Characterization of impact damage in regions of a structure subject to high-strain compression could assist decision-making in implementing repairs. In addition, this paper examines the effects of different impacting patterns on the behavior in compression.

## **Executive Summary**

The impacts delivered to the carbon fiber epoxy laminates of this study simulate the two general categories of damage that may occur to aerospace vehicles made of stiff, lightweight composite materials. Quasi-static impacts simulate the damage that may occur when two vehicles collide at low velocities. Low-velocity impact may occur when space vehicles misalign during docking or when airport service vehicles back into a plane on the runway. Dynamic impacts simulate the damage that may occur when debris hits a vehicle in flight. Quasi-static impacts leave visible dents. Low-velocity impacts may leave little visual evidence, but may cause cracking and delaminations hidden between interior plies of the laminate. Both seen and hidden damage may cause a loss of strength in the laminate. This study seeks to quantify and characterize the loss of strength of the laminates when subject to axial compression loads. Understanding how forces redistribute around damage areas may lead to better development of repair methodologies.

## 1. Introduction

Aerospace structures increasingly utilize composite laminate materials to take advantage of the materials' inherent stiffness, strength, and lightweight properties. The high cost of laminate layup and overall investment in high-performance technological aerospace structures has sparked a need to understand the efficacy of different repair options. Inevitably, every vehicle put to use suffers damage.

Many researchers have sought experimental and analytical justification for repairs conducted in composite laminate materials. Commonly developed repair options include ply overlays to damaged sites, where raised surfaces may be accepted.<sup>[1]</sup> Other repairs, known as “scarf” repairs, include tapered cuts that expose individual ply layers for bonding with new layers to achieve a flush repair surface, where preservation of the aerodynamic surface is important.<sup>[2]</sup> Fusions of repair plugs have also been investigated.<sup>[3]</sup>

In all types of repairs, the change in stiffness and load redistribution of the repaired structure becomes an utmost concern, because stresses and strains in the repaired region may vary significantly from the original structure. The longevity of the repair, furthermore, becomes a constant concern for safety. Despite advanced techniques in the analysis and techniques of repairing composite laminates, most repairs fail in modes that differ from the original structure's behavior. This change in behavior, caused by the damage and repair, therefore must be evaluated to determine whether the repair is better or worse for the structure, relative to operating in its damaged state.

Previous research and experimentation of compression behavior in impact-damaged aerospace-grade composite laminates commonly uses one of two compression-after-impact (CAI) test fixtures, the NASA version or the Boeing version.<sup>[4],[5]</sup> Both versions of the tests are similar, but differ in the specimen dimensions. The NASA version tests specimens measuring 10 inches tall by 5 inches wide (254 mm by 127 mm). The Boeing version tests specimens 6 inches tall by 4 inches wide (152 mm by 102 mm), as pictured in *Figure 1*. By virtue of using a smaller specimen size, the Boeing fixture has become more popularly used in industry, and is the fixture specified in ASTM D7137 Standard Test Method for Residual Strength Properties of Damaged Polymer Matrix Composite Plates.

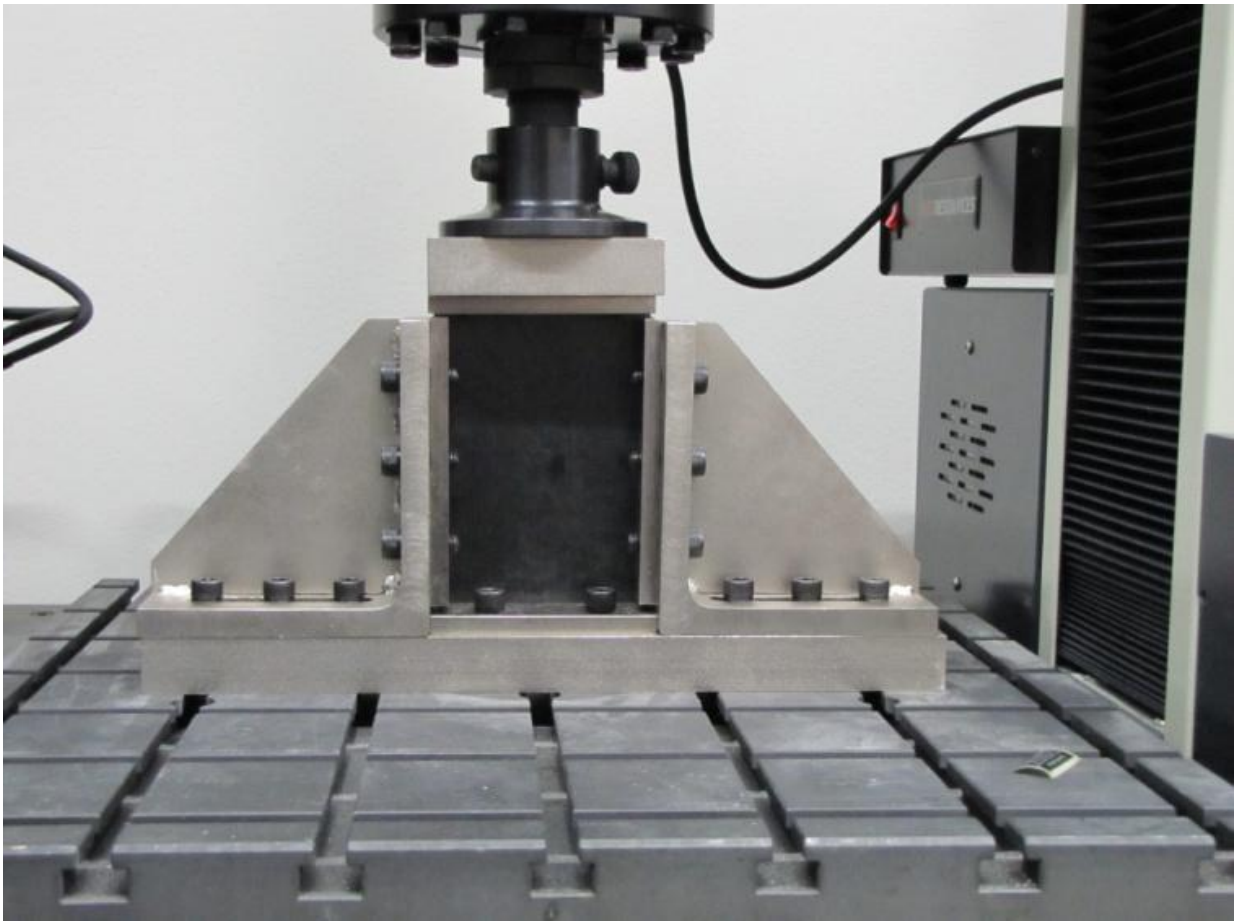


**Figure 1:** Photo of ASTM D7137 Compression Test Apparatus with Carbon/Epoxy Laminate Specimen.

## 2. The Compression After Impact Test

ASTM D7137 refers to two other test standards as acceptable methods for imparting damage, ASTM D6264 *Standard Test Method for Measuring the Damage Resistance of a Fiber-Reinforced Polymer-Matrix Composite to a Concentrated Quasi-Static Indentation Force* and ASTM D7136 *Standard Test Method for Measuring the Damage Resistance of a Fiber-Reinforced Polymer Matrix Composite to a Drop-Weight Impact Event*.<sup>[6], [7]</sup> These two test methods were developed in order to simulate the different effects of two general types of impact damage. Quasi-static indentations might occur when two vehicles collide at a low velocity. Luggage carts backing slowly into a plane fuselage or a space vehicle docking with another might produce damage simulated by the quasi-static indentation force. Small debris colliding with an aircraft or tools dropped by service crew on the vehicle might produce damage simulated

by the drop-weight impact. In the case of the quasi-static impact, damage is visible in the form of a dent. Drop-weight impacts, by contrast, might leave little form of visual evidence. Therefore, non-destructive (NDT) imaging techniques such as ultrasonic testing might be necessary to characterize the full extent of damage that is barely visible.

To advance the knowledge of repair options in lightweight, high-strength fiber-epoxy composites used in aerospace structures, this research aims to develop recommendations regarding testing and quantifying the effects of impact-damaged laminates that must be subsequently subject to high-strain compressive loads. The effects and characterization of the damage may elucidate repair options or direct a plan of action to address the impact damage.

### 3. Experimental Setup

ASTM D7137 sets forth the procedures that form the basis of this test. The ASTM standard lists Recommended Layups for Various Nominal Cured Ply Thicknesses, Unidirectional Tape in *ASTM D7137 Table 1*. The 10-ply carbon/epoxy laminate [0/45/90/-45/0]<sub>s</sub> panels used for this study were selected since they are not currently listed in *Table 1* of the reference standard, though the 10-ply laminates would fill in the gap of data in between the 8 and 16-ply layups that the standard does address. Each of the laminate test panels is made from carbon-fiber/epoxy prepreg unidirectional tape (TORAY T700GC-12K-31E/#2510).<sup>[8]</sup> This material is the subject of previous aerospace research programs to advance industry knowledge and data.

Nominal Cured Ply Thickness		Ply Count	Layup
Minimum, mm [in.]	Maximum, mm [in.]		
0.085 [0.0033]	0.10 [0.004]	48	[45/0/-45/90] <sub>6s</sub>
0.10 [0.004]	0.13 [0.005]	40	[45/0/-45/90] <sub>5s</sub>
0.13 [0.005]	0.18 [0.007]	32	[45/0/-45/90] <sub>4s</sub>
0.18 [0.007]	0.25 [0.010]	24	[45/0/-45/90] <sub>3s</sub>
0.25 [0.010]	0.50 [0.020]	16	[45/0/-45/90] <sub>2s</sub>
0.50 [0.020]	0.75 [0.030]	8	[45/0/-45/90] <sub>s</sub>

#### Actual Laminate Used for Study <sup>[8]</sup>

Cured Laminate thickness                      **10**      **[0/45/90/45/0]<sub>s</sub>**  
1.5 m [0.058 in.]

**Table 1:** Recommended Layups for Various Nominal Cured Ply Thicknesses, Unidirectional Tape, ASTM D 7137.

Plies were assembled by industry standard hand layup techniques. The laminates were cured in a hot press, under controlled pressure and temperature cycles, to solidify panels measuring 356 mm (14 inches) square. The same cure cycle was specified for every panel, and samples placed under the microscope revealed less than 1% porosity in the material. Each panel was cut, using wet saws and sanders, to machine specimens to their final dimensions (102mm by 152 mm or 4 inches by 6 inches) per the ASTM test standard. Thus, each panel yielded a total of 6 specimens. Specimens produced for this study were separated, prior to executing compression tests in the ASTM D7137 test fixture, into three groups:

1. *Quasi-Static Indentation* test group, per ASTM procedure D6264,
2. *Drop-Weight Impact* test group, per ASTM procedure D7136, and
3. Undamaged, new laminate test group.

Damage sustained by the first two test groups was characterized visually and by non-destructive imaging using ultrasonic testing, to determine whether underlying damage undetectable by visual scans existed. To impart damage to *Group 1: Quasi-Static Indentation* specimens, a threaded rod with an interchangeable ball bearing transfer was attached to a standard test machine. A 38 mm (1-½-inch) thick steel plate, measuring 152 mm by 152 mm (6 inches square) with a 51 mm (2-inch) diameter hole in the center, was placed on the test bed, as shown in *Figure 2*. Specimens were placed over the plate and aligned beneath the hemispherical, frictionless impact ball, as shown in *Figure 3*, such that damage was inflicted on the center of each panel. *Figure 4* pictures the dent/depression damage typically pressed into the top, impact face of the plate. Broken fibers on the underside, opposite to the face of impact, are pictured in *Figure 5*.

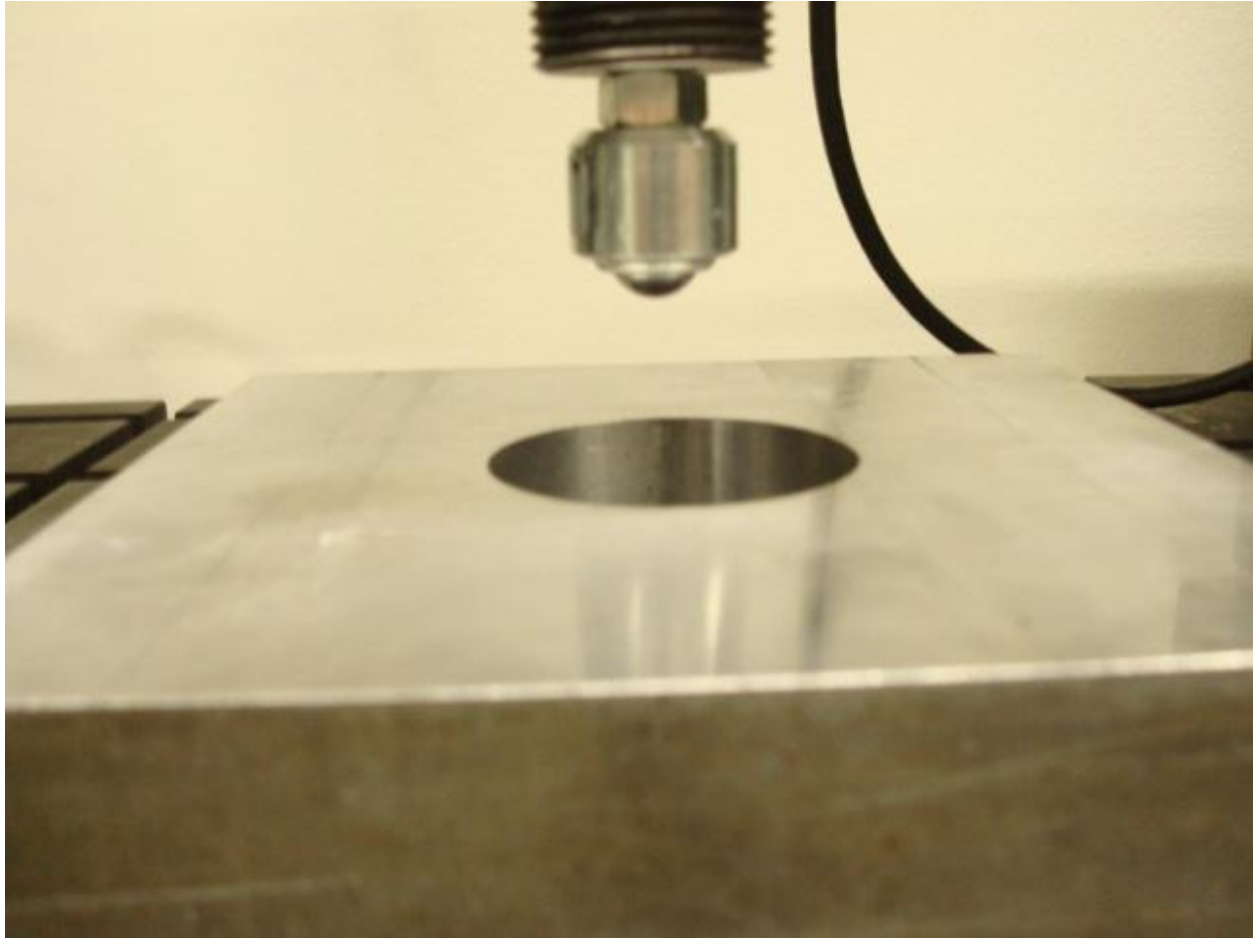


**Figure 2:** Photo of ASTM D6264 Quasi-Static Impact Test Apparatus over Backing Plate with Hole.

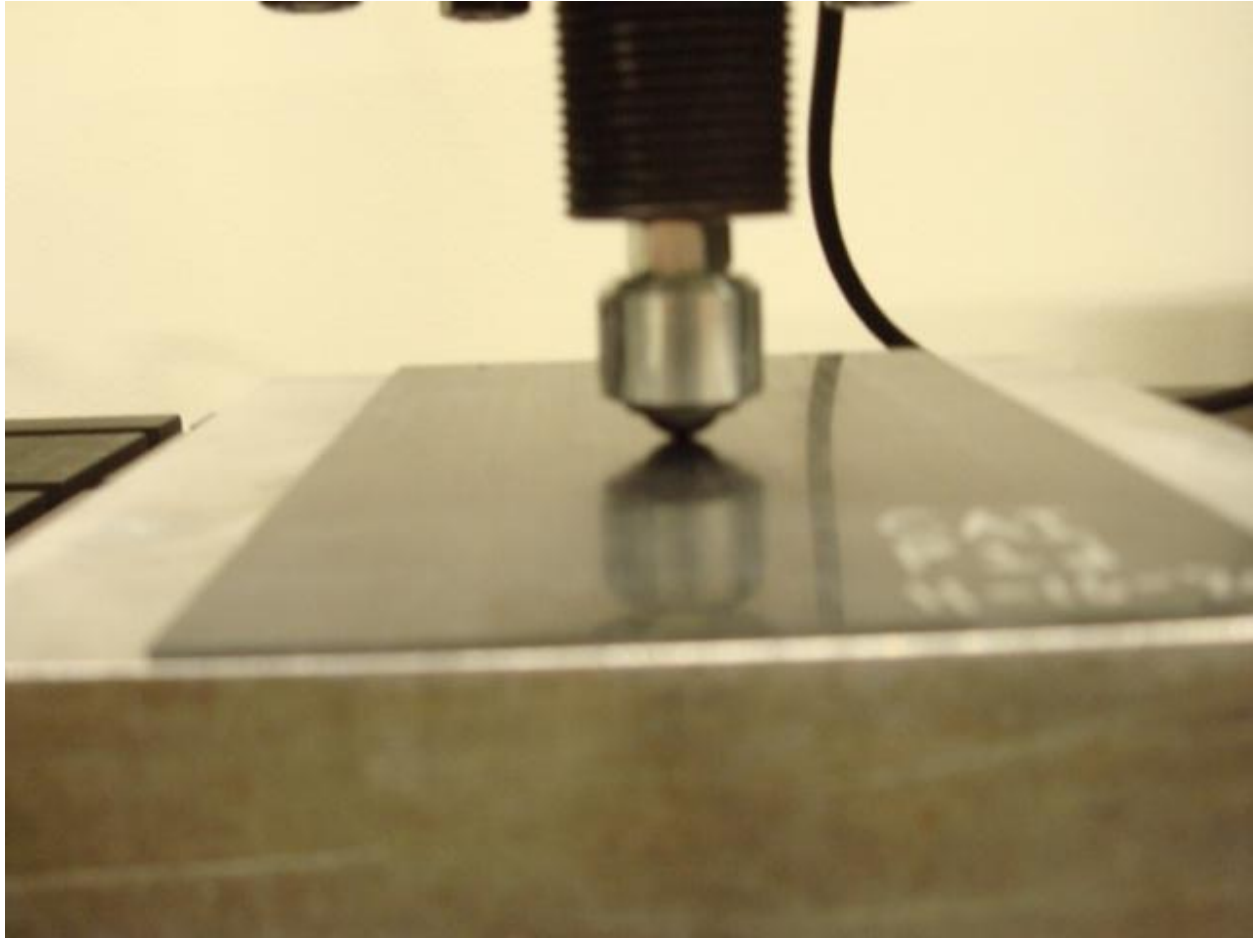


**Figure 3:** Photo of ASTM D6264 Quasi-Static Impact Test Indenter on Carbon/Epoxy Specimen.



**Figure 4:** Photo of Typical Dent/Depression Imparted by Quasi-Static Impact on Top, Impact Face of Plate.



**Figure 5:** Photo of Typical Combined Large Cracks with Fiber Breakage, Indentation/Puncture Imparted by Quasi-Static Impact on Underside, Opposite Impact Face of Plate.

Examples of commonly observed damage modes and the nomenclature presented in the ASTM reference standards are illustrated in *Figure 6*. The load-displacement curves, illustrated in *Figure 7*, correspond to the quasi-static indentation damage of five specimens each impacted with a single central dent. *Table 2* lists the measured out-of-plane quasi-static loads that caused first fiber breakage in each impacted specimen produced for this study. Several of the specimens listed in the table were impacted with multiple dents, to purposefully increase damage levels. Only the data corresponding to the first quasi-static impact dent, in specimens with multiple depressions, was selected for comparisons with specimens containing one standard, central indentation.

<b>Specimen Name</b>	<b>Peak Load lb</b>	<b>Peak Load N</b>
P02b-10m	384.8	1712
P02c-10m	390.8	1738
P03b-10m	434.8	1934
P03c-10m	402.5	1790
P04b-10m	602.2	2679
P04c-10m	553.4	2462
P01a-10m	552.6	2458
P05b-10m	465.8	2072
P05c-10m	570.2	2536
P07b-10m	531.7	2365
P07c-10m	530.3	2359
P06a-10m	267	1188
P06b-10m	318.9	1419
P06d-10m	314.9	1401
P06e-10m	251.3	1118
P06f-10m	275.9	1227

Mean Load = 428 lbs (1900 N)

Standard Sample Deviation = 119 lbs (529 N)

**Table 2:** Load at First Breakage of Carbon Fibers in 10-ply [0/45/90/-45/0]<sub>s</sub> Laminate under Quasi-Static Indentation

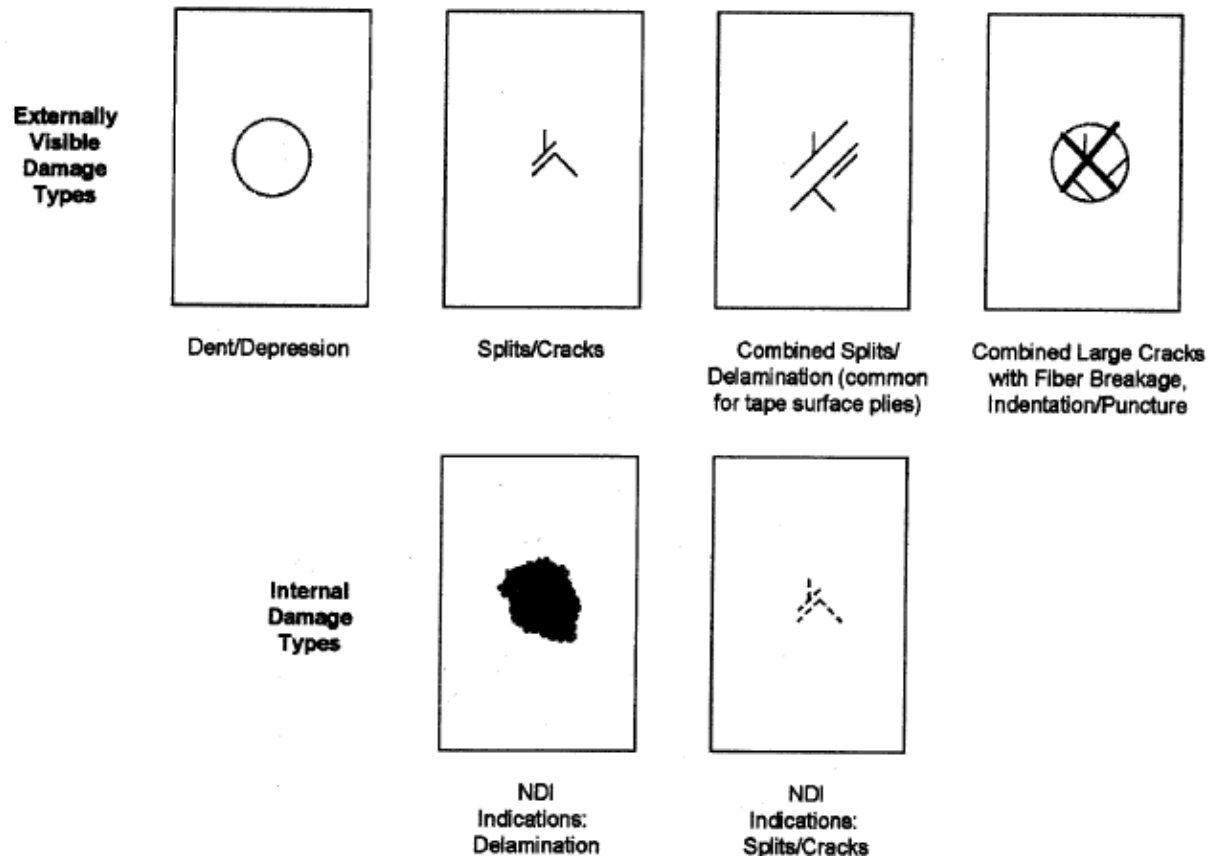


**Figure 6:** Commonly Observed Damage Modes from Out-of-Plane Quasi-Static Indentation and Drop-Weight Impact, listed in ASTM D 7137.

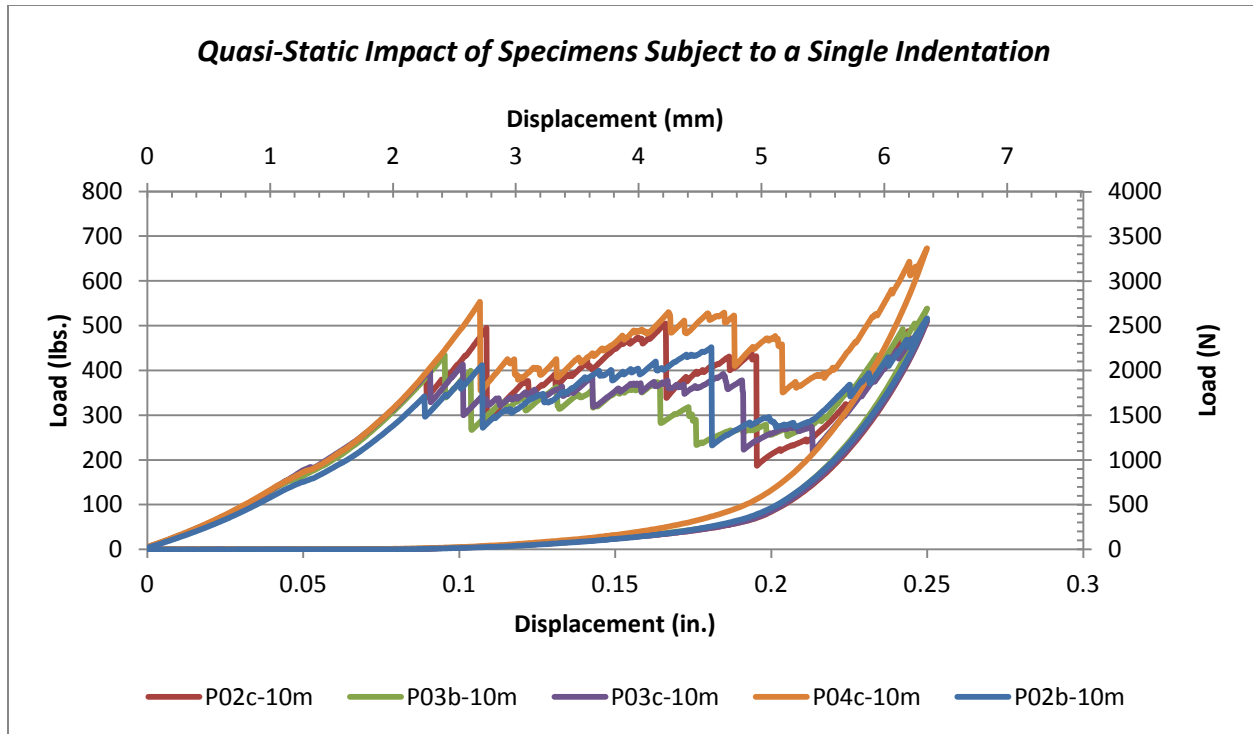


**Figure 7:** Load-Displacement Curves of Six Specimens with Single, Central Quasi-Static Indentation.

In two later test subgroups of *Quasi-Static Indentation* samples, comprising of three specimens each, multiple indentations were inflicted on each panel. Five indentations per specimen were spaced closely about the middle of the panel, in the pattern of a die face. The pattern was repeated, for another test group of three specimens, but at spacing further away from the middle. *Figure 8* depicts the typical five-dent pattern for the widely spaced indentations, with 38 mm (one-and-one-half-inch) clear spacing between depressions. The typical resultant fiber breakage on the backside of a panel is shown in *Figure 9*. The closely spaced pattern had 25 mm (one-inch) clear spacing between depressions, clustering more damage in the center of the specimen. In all cases, load-displacement curves were recorded to quantify the quasi-static impact events. The load-displacement curves of *Figure 10* represent five out-of-plane quasi-static indentations on the specimen pictured in the previous two images. The decision to produce these five-dent specimens, imparting more damage than called for in the standard, was prompted by analysis of initial compression testing discussed in the *Experimental Results* section.



**Figure 8:** Five Quasi-Static-Indentation Pattern Dent/Depression Damage on Top, Impact-Face of Panel.



**Figure 9:** Combined Large Cracks with Fiber Breakage, Indentation/Puncture on Underside, Opposite Face of Impact on Five-Dent Specimen.

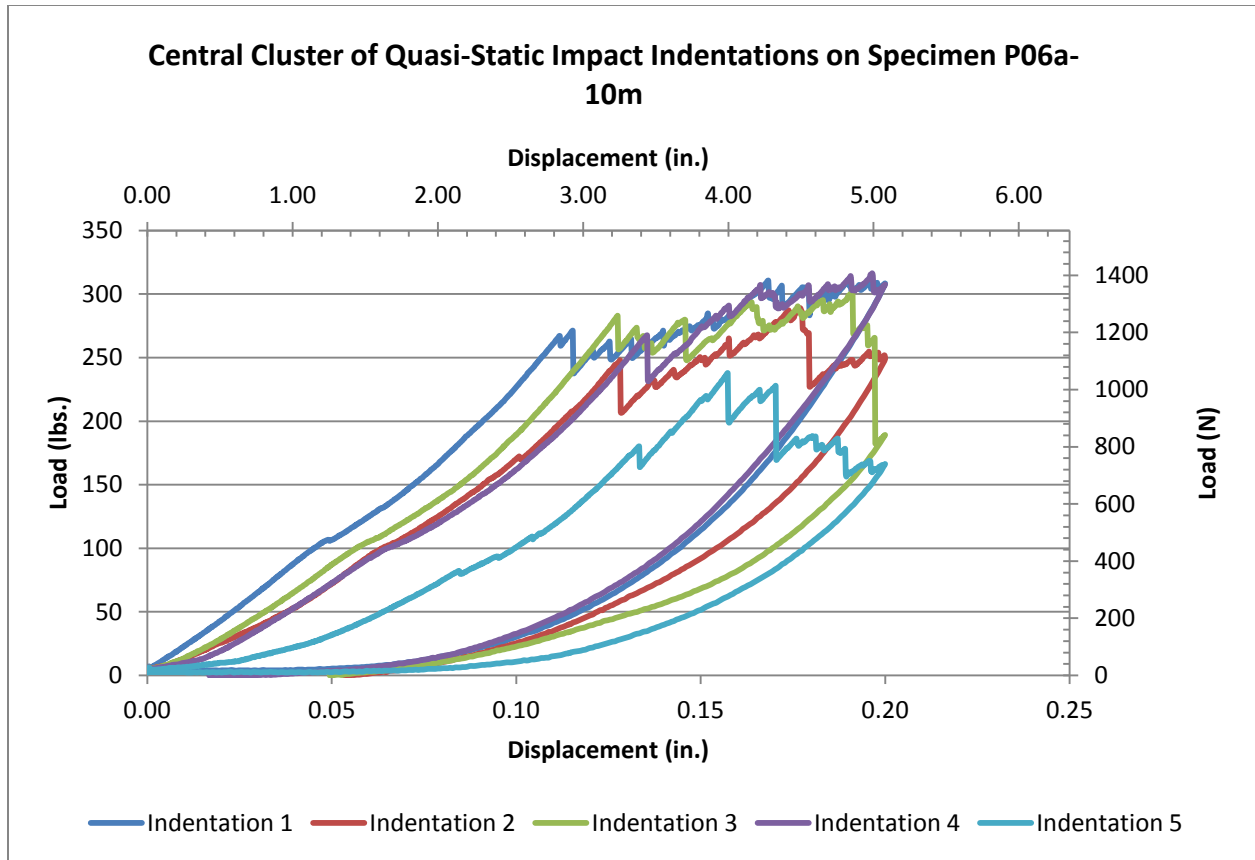


**Figure 10:** Load Displacement Curves for Multiple Indentations on a Single Panel Specimen.

*Group: 2 Drop-Weight Impact* specimens suffered damage in a specialized machine that tracks the energy of impact using a plate gauging force and impulse of the dropped weight.

*Group 3: Undamaged* specimens did not undergo any treatment between production and compression testing. The specimens were simply stored in a cool dry environment at room temperature until the time of testing.

Compression testing of all specimen panels was conducted in the ASTM D7137 fixture. Care to align the panels and fixture concentrically with the test loading machine was taken.<sup>[9]</sup> All bolts holding the fixture components in place were tightened to a standard torque in order provide adequate stabilization against plate buckling. Data (load, displacement, and time) were recorded by the standard test machine apparatus. Special potting and shimming of the ends of the laminate samples were not undertaken by this experiment, despite recommendations referenced in the test standard. The decision to forego these meticulous procedures at the ends of the specimens was based on the absence of end bearing failures and the presence of failure modes that the test standard deemed acceptable.

#### 4. Results and Discussion

Experimental results for the *Quasi-Static Indentation* and *Undamaged* test groups are included in this report. Specimens undergoing the drop-weight impacts await results. *Figure 11* illustrates commonly observed, acceptable, compressive strength failure modes for the ASTM D7137 fixture. The compressive residual strength failure mode commonly observed in all but three of seventeen compressed specimens is described by the ASTM D7137 test standard as **LGM**. The letter “L” describes a lateral failure type. The letter “G” describes the failure area as gage, away from damage. The letter “M” describes the failure location as the middle of the panel. A full array of character coding descriptions is given in the test standard of ASTM D7137 *Table 3*. The actual failure mode pictured in *Figure 12* represents the most common compressive failure mode observed, regardless of damage or no damage, in fourteen of the seventeen panels tested in this study. One of six panels indented with five-pattern quasi-static depressions, demonstrated the diagonal failure mode of *Figure 13*. Two of the seven undamaged, without impact, panels failed in compression at the bottom of the specimen as shown in *Figure 14*.

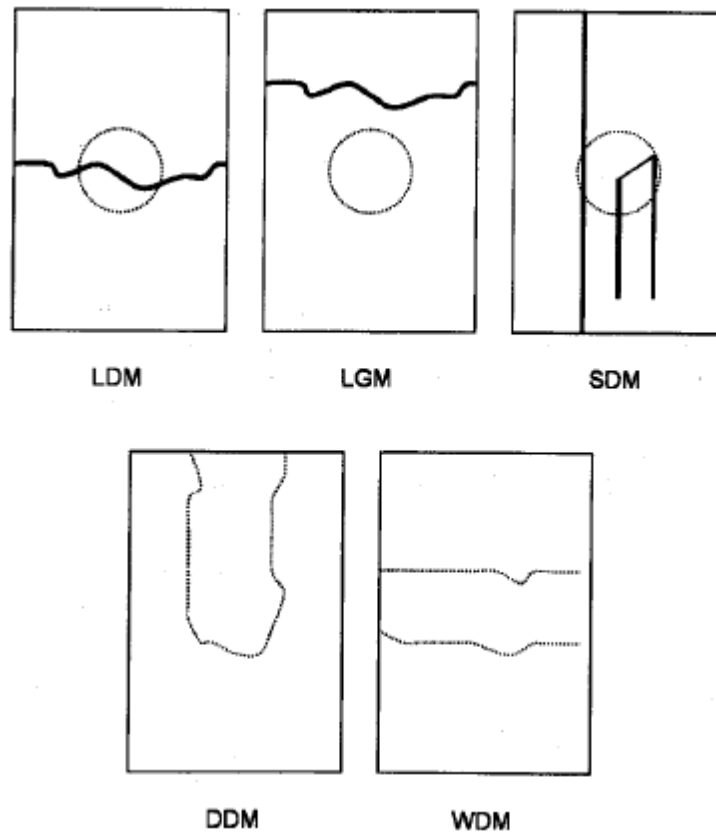


**Figure 11:** Commonly Observed Acceptable Compressive Residual Strength Failure Modes as Illustrated in ASTM D 7137.

First Character		Second Character		Third Character	
Failure Type	Code	Failure Area	Code	Failure Location	Code
Angled	A	At end/edge	A	Bottom	B
Brooming	B	at/through Damage	D	Left	L
end-Crushing	C	Gage, away from damage	G	Middle	M
Delamination growth to edge at final failure, lengthwise	D	Multiple areas	M	Right	R
through-thickness	H	Various	V	Top	T
panel Instability	I	Unknown	U	Various	V
Kink bands	K			Unknown	U
Lateral	L				
Multimode	M(xyz)				
delamination growth to edge prior to final failure, Restrained by edge	R				
long, Splitting	S				
delamination growth to edge at final failure, Widthwise	W				
explosive	X				
Other	O				

**Table 3:** Three-Place Failure Mode Codes, ASTM D 7137.

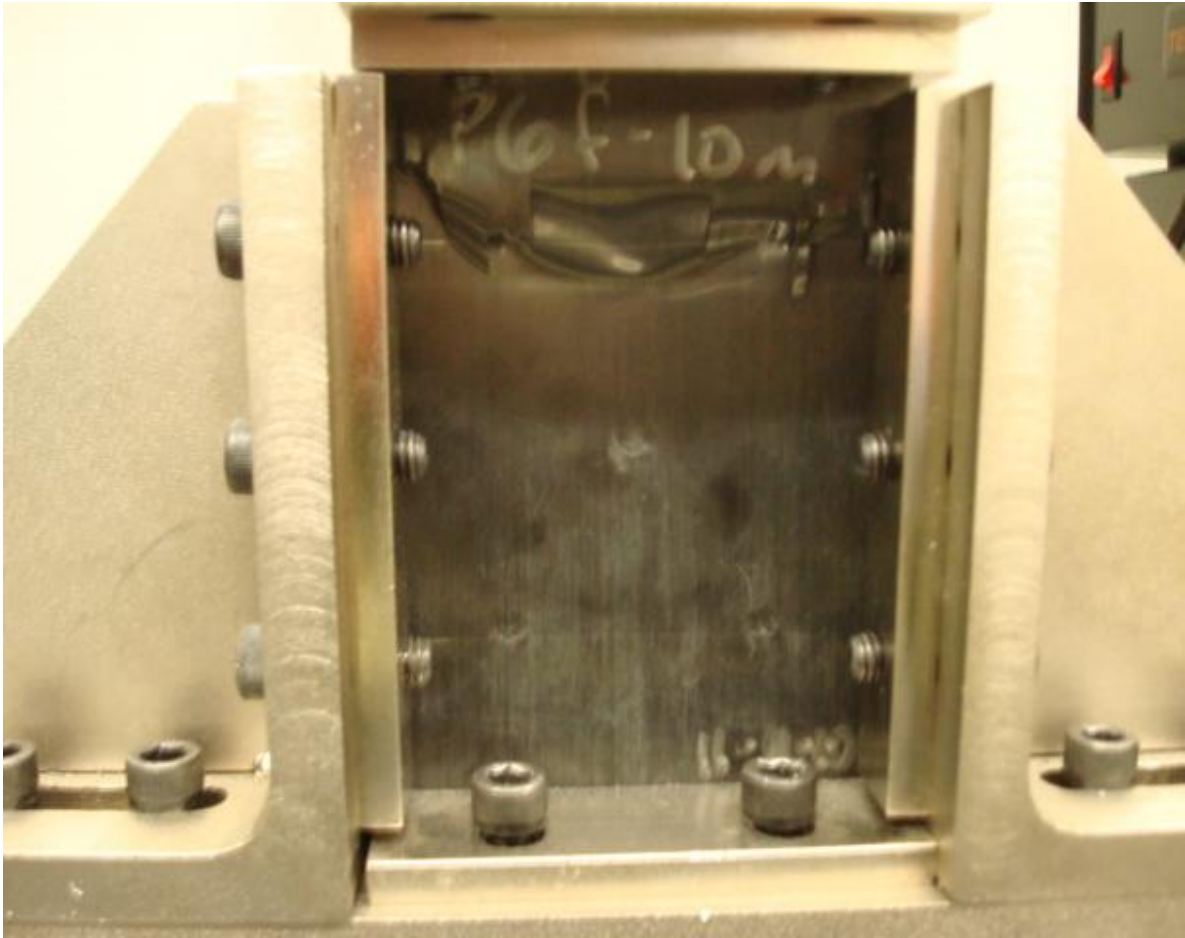


**Figure 12:** Commonly Observed Lateral Gage (Away from Damage) Middle (LGM) Failure Mode Observed in Every Specimen.



**Figure 13:** Angled Failure Mode through Center of Panel (ADM), Diagonal through Three Indentations.



**Figure 14:** Bottom Failure Mode (LAB).

The compressive strengths of seven undamaged 10-ply laminate specimens are represented by the load-displacement curves of *Figure 15*. *Table 4(a)* lists peak compressive strengths, median strength, and standard deviation, calculated from the load-displacement data of the seven previously undamaged specimens. The load-displacement curves charted in *Figure 16* yield the residual compressive strengths of four specimens with standard, central singular quasi-static indentation damage. Both specimen groups withstood compression up to (one-eighth inch) strain in the ASTM D7137 test fixture. Comparison by ratio of the mean results of peak residual compressive strength of the damaged panels, summarized in *Table 4(b)*, to the peak compressive strength of the undamaged panels yields a thirty percent drop in mean compression strength that might be attributable to the quasi-static impact. Statistical analysis of the results, however, reveals a lack of confidence in the mean comparison. All four of the damaged specimens achieved residual compressive strengths of at least 2000 pounds. Two of the four damaged specimens sustained loads near the mean load of the undamaged specimens.

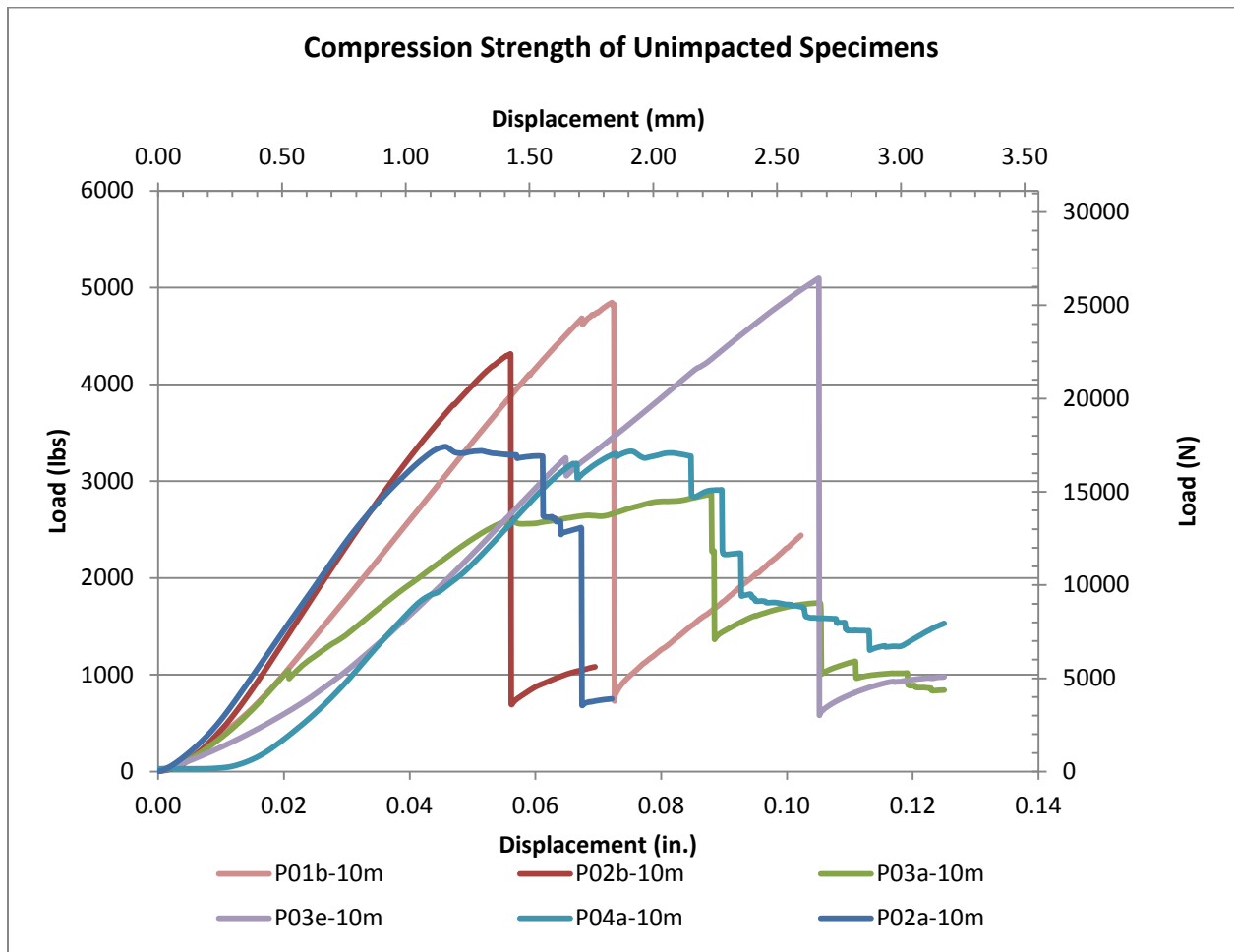


**Figure 15:** Load Displacement Curves for Un-impacted/Damage-free Specimens under Compression.

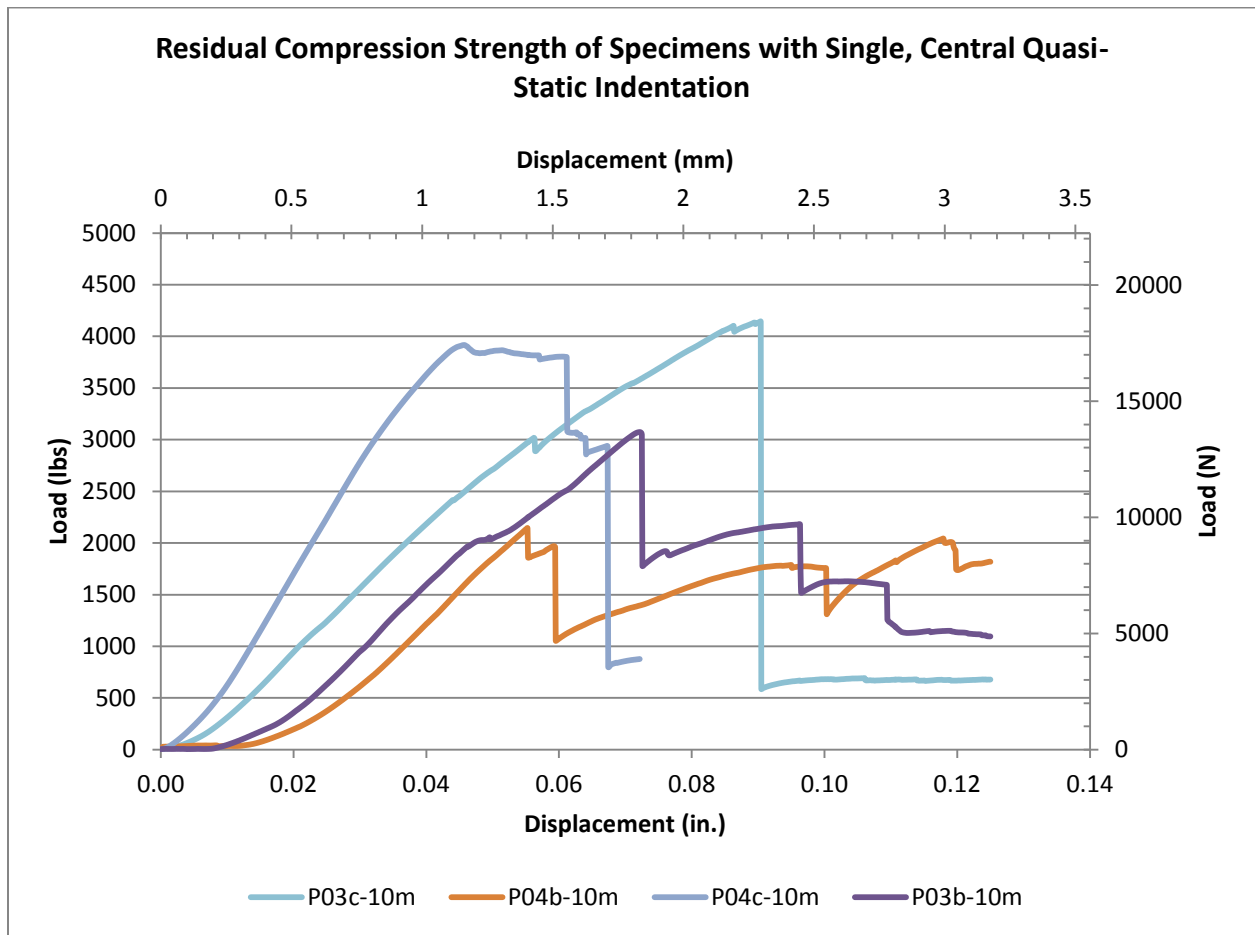


**Figure 16:** Load Displacement Curves for Residual Compression Strength of Specimens with Single, Quasi-Static Indentation.

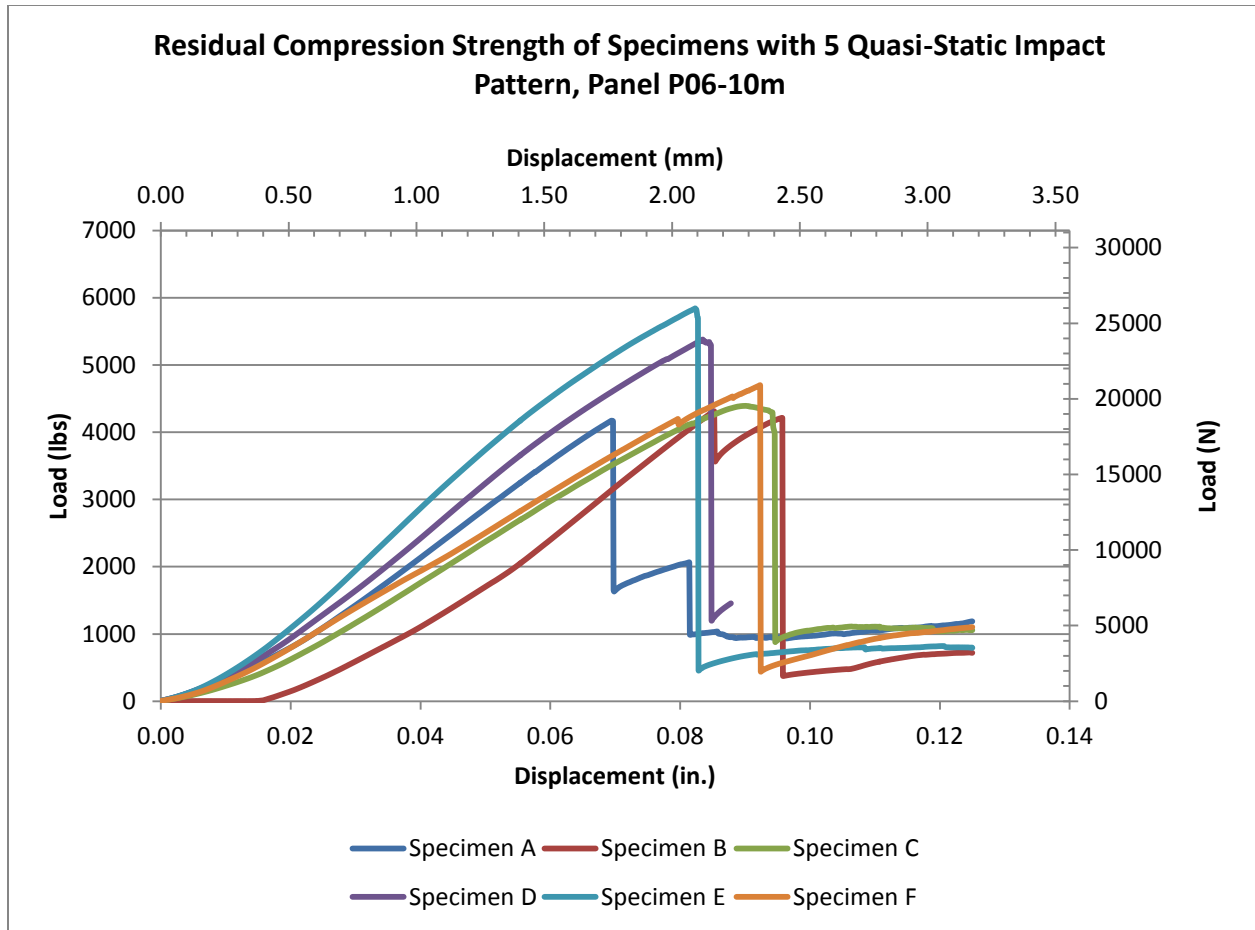


**Figure 17:** Load Displacement Curves for Residual Compression Strength of Specimens with Single, Quasi-Static Indentation.

Lack of statistical confidence in the mean comparison and lack of distinction in the commonly observed compression failure modes between the undamaged and impacted specimen groups prompted an effort to produce different results by increasing damage levels. Increasing damage was achieved by creating more indentations on a single specimen. Revisiting the load-displacement curves of *Figure 7* for the single-indentation specimens reveals a nearly linear and consistent resistance to fiber breakage on initial portions of the path to quasi-static damage. The initial fiber breakage loads varied among the specimens, but the matching slopes of lines characterize the elastic resistance to indentation and provide evidence that the carbon/epoxy laminate has consistent out-of-plane stiffness in each of the tests, until the fibers break. Peaks and valleys, occurring across the horizontal regions of the load-displacement curves, represent increases in load as the indenter engages different fibers and decreases with every breakage of another fiber layer. Near the end of the quasi-static damage test, larger increases in residual load occurred, but only because a larger diameter of the impact apparatus began engaging a larger diameter of the laminate plate. For subsequent damage paths on the five-dent specimens, the

impact ball was limited to 0.20 inches (5.1 mm) of downward displacement for a 0.50-inch (12.7 mm) diameter ball, to avoid this effect.

**(a) Unimpacted**

<b>Specimen Name</b>	<b>Peak Compression Load (lbs)</b>	<b>Peak Compression Load (N)</b>
P01b-10m	4828	21476
P02a-10m	3817	16979
P02b-10m	4315	19194
P03a-10m	2867	12753
P03d-10m	6551	29140
P03e-10m	5096	22668
P04a-10m	3292	14644

Mean Load = 4395 lbs (19.5 kN)
Standard Sample Deviation = 1230 lbs (5.47 kN)

**(b) Quasi-Static Indentation**

<b>Specimen Name</b>	<b>Peak Compression Load (lbs)</b>	<b>Peak Compression Load (N)</b>
P03b-10m	3073	13669
P03c-10m	4146	18442
P04b-10m	2146	9546
P04c-10m	3065	13634

Mean Load = 3108 lbs (13.8 kN)
Standard Sample Deviation = 818 lbs (3.64 kN)

**(c) Quasi-Static 5-Indentation Pattern**

<b>Specimen Name</b>	<b>Peak Compression Load (lbs)</b>	<b>Peak Compression Load (N)</b>
P06a-10m	4172	18558
P06b-10m	4312	19181
P06c-10m	4392	19537
P06d-10m	5378	23923
P06e-10m	5842	25987
P06f-10m	4700	20907

Mean Load = 4292 lbs (19.1 kN)
Standard Sample Deviation = 111 lbs (494 N)

Mean Load = 5307 lbs (23.6 kN)
Standard Sample Deviation = 574 lbs (2.55 kN)

**Table 4:** Summary of Compression Strengths of Specimen Groups.

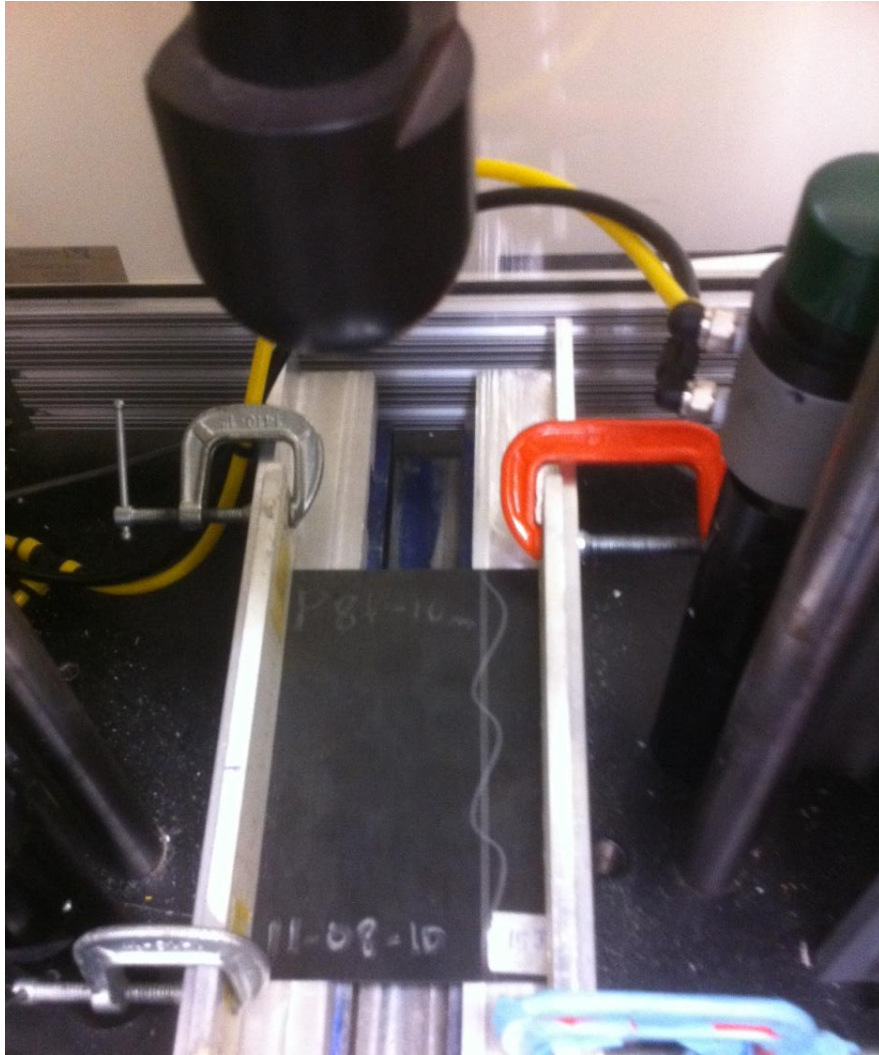


**Figure 18:** Drop-Weight Impact Test Apparatus per ASTM D7136. (Testing and Photo Courtesy of Professor Valeria La Saponara, Department of Mechanical and Aerospace Engineering, University of California—Davis).

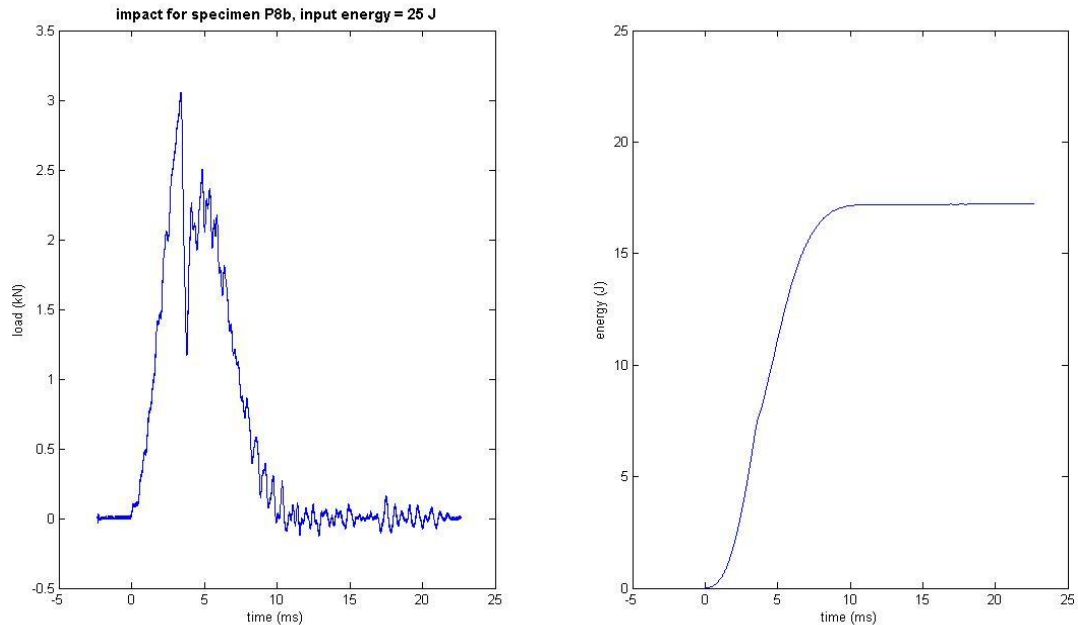


**Figure 19:** Drop-Weight Impact charts reporting load vs. time (right) and energy vs. time, per ASTM D7136. (Testing and Plots Courtesy of Professor Valeria La Saponara, Department of Mechanical and Aerospace Engineering, University of California—Davis).

Two damage modes that are described in *Figure 6* resulted on each panel subjected to the quasi-static indentation. The impact face suffered a *Dent/Depression* mode of damage. *Combined Large Cracks with Fiber Breakage, Indentation/Puncture* resulted on the face opposite the impact. Five indentations on a single specimen differ from a single indentation as evidenced by two important characteristics, area and stiffness. An increase in the damage area becomes obvious when comparing the damage opposite the impact faces of *Figure 5* and *Figure 9*. The single-indentation specimen shows fiber breakage locally concentrated and confined to the two-inch (50 mm) diameter hole in the backing plate. The five-indentation specimen shows plies of longitudinal fibers broken along the entire height of the panel. A change in stiffness, or a “softening” effect, occurring with subsequent indentations is illustrated by the changing slopes of *Figure 10*.

Compression tests were performed on six specimens with five indentations each. All six specimens were cut by wet saw from the same laminate panel. Three specimens (labeled “A”, “B”, and “C”) were impacted with dents spaced one inch (25 mm) apart, concentrating damage in the panel center. Three specimens (labeled “D”, “E”, and “F”) were impacted with dents

spaced one-and-a-half inches (38 mm) apart. Two interesting results occurred, exhibiting effects of the difference in damage concentration. Five of the six five-dent specimens failed in LGM mode of residual compression failure. The specimen with indentations spaced further apart, pictured in *Figure 13*, however, failed in an angle mode that did pass through some of the impact damage. ASTM D7137 states that:

Gage failures (away from the induced damage) are considered acceptable, but may not provide a true measurement of the residual strength of the specimen for the induced damage state. A gage failure may indicate that the panel is not sensitive to the induced damage, such that it fails at a compressive stress near the panel's undamaged strength. Alternatively, a gage failure may indicate that the undetected damage or a flaw was in the vicinity of the failure, such that the measured failure stress is lower than the panel's undamaged strength as well as its failure stress for the detected damage.

Therefore, the angled failure mode produced in compression of Specimen D of Panel 6 was the only example of a desirable failure mode, a mode that passed through the damage. All other compression failures were acceptable per the test standard, but not preferable.

The load-displacement curves of the six five-dent specimens tested to compression failure depict a trend in which Specimens "A", "B", and "C", with indentations concentrating damage at the center, failed at lower load levels than Specimens "D", "E", and "F", which spaced the damage further apart. Note, however, that Specimen "F" fails at a load that is indistinguishably higher than the test group with damage concentrated in the middle. Though a trend corresponding to differences in damage concentrations appears to exist among the specimens of Panel 6, the mean results listed in *Table 4* defy the hypothesis that increasing damage will further lower the compression strength results. For the three specimens with five indentations clustered in the middle, the mean strength nearly matched that of the undamaged panel group. The specimens with five dents spaced further apart exceeded the mean strength results of undamaged panels and changed the observed failure mode in only one case.

## 5. Conclusions

Seventeen specimens of 10-ply multi-directional carbon/fiber prepreg composite laminates were tested in compression, according to ASTM standard D7137. Seven undamaged specimens were tested for compression strength, and the results of residual compression strength tests on ten specimens with varying degrees and concentrations of quasi-static impact damage were compiled for comparison with the undamaged panels. Clearly quantifiable effects of the damage on the residual compression strength of panels, however, remain elusive. Load redistribution may be taking place in the material, hence masking the damage effects. Further study utilizing gages, digital image correlation, or other tools that may capture the strains acting within the field of the specimen panels is recommended to determine answers to the questions raised by the test results. Deeper understanding of compression behavior within the fixture and possibly an alternate fixture design will be required to achieve data that may assist in design and repair directives.

- Though gage failures, away from the induced damage, are acceptable per test standard ASTM D7137, it is likely that the panel is not sensitive to the induced damage.
- Five quasi-static indentations increase damage levels, but with only minor results evidence by changing the concentration of the damage. The panel still may not be sensitive enough to the damage.
- Edge restraint near the short, ¼-inch length of unsupported panel, between the fixture top plate and stabilizing side angles, may be producing higher stress effects such as combined bending and axial loads than the stress-concentration effects of the damaged zone.
- Testing of more samples might increase statistical confidence in the mean results and confirm the “emerging” trends cited in analysis of the experimental results.
- The 10-ply carbon epoxy material and layup, containing more zero-degree plies than ninety-degree and forty-five-degree orientations, may be capable of significant load redistribution that reduces the sensitivity to compression damage.
- As cautioned by standard ASTM D7137, results of these residual compression tests should not be used to establish allowable design stress values or plans of action regarding repair, without better understanding of the underlying behavior.

Whether ASTM D7137 test data may assist in directing a plan of action for addressing damage remains inconclusive in this study. Until the pattern of load redistribution may be measured in more detail at various stages of loading, pre-damage and post-damage, the underlying behavior producing the failure results cannot be quantified experimentally. Follow-up tests using strain gages and digital image correlation equipment to measure the strains in various regions of undamaged and damaged panels must be compared to determine whether redistribution of load is actually taking place. Various composite materials, furthermore, should be studied in order to determine whether similar modes and effects of failure occur regardless of material composition.

Current results defy the commonly expected conclusion that visible and extensive damage should result in a lesser value of overall specimen strength. The effects of damage on tensile strength, by contrast, are typically more evident and documented than the damage effects on compression failures. ASTM D7137 cautions users that compression tests may be subject to high variability resulting from numerous factors. Developing a deeper understanding of compression behavior in the fixture, therefore, shall become the focus of future study. Results of more study may lead to better determination of the fixture’s usefulness in establishing meaningful compression strength values, or an alternate design better suited to the objectives of design and repairs. *Figure 18* and *Figure 19* illustrate the drop-weight impact results on specimens that will be tested in compression as a continuation of this study.

## References

- [1] Soutis C, Duan D-M, Goutas P. *Compressive behaviour of CFRP laminates repaired with adhesively bonded external patches*. Composite Structures 1999; 45:289–301.
- [2] Gunnion AJ, Herszberg I. *Parametric study of scarf joints in composite structures*. Compos Struct 2006;75:364–76.
- [3] Cesim Atas , Yalin Akgun, Olgay Dagdelen, Bulent M. Icten, Mehmet Sarikanat, *An experimental investigation on the low velocity impact response of composite plates repaired by VARIM and hand lay-up processes*. Composite Structures 2011; 93:1178-1186.
- [4] Portanova, Poe, Whitcomb, *Open Hole and Post-Impact Compression Fatigue of Stitched and Unstitched Carbon/Epoxy Laminates*, June 1990, NASA, Langley Research Center, Hampton, VA
- [5] ASTM D 7137/D 7137M -05 *Standard Test Method for Compressive Residual Strength Properties of Damaged Polymer Matrix Composite Plates*.
- [6] ASTM D 6264/D 6264M -07 *Standard Test Method for Measuring the Damage Resistance of a Fiber-Reinforced Polymer-Matrix Composite to a Concentrated Quasi-Static Indentation Force*.
- [7] ASTM D 7136/D 7136M -07 *Standard Test Method for Measuring the Damage Resistance of a Fiber-Reinforced Polymer Matrix Composite to a Drop-Weight Impact Event*.
- [8] J. Tomblin, J. Sherraden, V. Senevirante, K.S. Raju, *A-Basis and B-Basis Design Allowables for Epoxy-Based Prepreg, TORAY T700GC-12K-31E/#2510 Unidirectional Tape [US Units]*, Advanced General Aviation Transport Experiments (AGATE-WP3.3-033051-132) National Institute for Aviation Research, Wichita State University, Wichita Kansas, 67260-0093, November 2002.
- [9] Eastland, C., Coxon, B., Avery, W., and Flynn, B., *Effects of Aspect Ratio on Test Results from Compression-Loaded Composite Coupons*, Proceedings of ICCM X, Whistler, BC, Vol IV, A. Poursatip and K. Street, eds., Woodhead Publishing, Ltd., 1995.

## Acknowledgements

Special thanks to Valeria La Saponara, Ph.D., Department of Mechanical and Aerospace Engineering, University of California—Davis for conducting the drop-weight impact testing on specimens included in this report.

# Experimental Determination of Flow and Heat Transfer Correlations for Passive Regenerators

Stefanie Knauf<sup>1</sup>

Department of Mechanical Engineering  
University of Wisconsin-Madison

## Abstract

The findings from this research are applied to a broader topic of Active Magnetic Regenerative Refrigeration (AMRR). Advancements in AMRR technology have the potential to add great value to the refrigeration and air conditioning field and as a result, the industries that utilize and depend on these services. In particular the space industry can benefit from refrigeration and air conditioning methods that do not depend on gravity or make use of a volatile refrigerant.

## Introduction

Active magnetic regenerative refrigeration (AMRR) systems have recently surfaced as an environmentally friendly alternative to vapor compression refrigeration cycles. AMRR systems make use of solid refrigerants rather than a fluorocarbon working fluid. With the use of an environmentally safe heat transfer fluid such as water or ethylene glycol, the ozone depletion potential and global warming potential for AMRR is essentially negligible. Further optimization of AMRR systems is required in order for them to be an economically attractive and viable substitute for current air conditioning and refrigeration units. Much of this optimization is focused on the regenerator matrix geometry and the thermal-fluid behavior of the packed bed of magnetocaloric material.

A passive single-blow test facility has been developed at the University of Wisconsin-Madison and will be used to measure the Nusselt number under conditions appropriate for AMRR systems (i.e., low Reynolds number and high Prandtl number where little data currently exists). Nusselt number correlations from the literature will be compared to the test data; if necessary, new correlations will be developed. The single-blow test facility consists of a passive regenerator, containing a packed bed of spheres. During the test, the regenerator is thermally stabilized at a uniform, low temperature (the cold soak process). This cold soak is immediately followed by a step change in fluid temperature that results in the introduction of hot fluid at the regenerator inlet. The temperature and flow rate versus time data is gathered from the beginning of the temperature step change to the new thermal equilibrium of the regenerator. The thermal behavior of the regenerator is correlated with its heat transfer, allowing the Nusselt number to be measured for a specific set of conditions.

This study is motivated by large discrepancies in the Nusselt number correlations in literature at the conditions of interest for AMRR systems. The data will be analyzed and compared to a range of existing correlations for Nusselt number through a packed bed of spheres.

---

<sup>1</sup> Funded in part by the Wisconsin Space Grant Consortium

## The Magnetocaloric Effect

Magnetic refrigeration is made possible by the magnetocaloric effect, which refers to the change in the entropy of a material due to magnetization. Understanding of the magnetocaloric effect is best achieved through an analogous comparison with the compression process for a common refrigerant used in vapor compression cycles. The fundamental property relation for a compressible substance is given by:

$$dU = T dS - P dV \quad (1)$$

A similar relation can be written for a magnetocaloric substance (provided that hysteresis is ignored):

$$dU = T dS + \mu_o H d(VM) \quad (2)$$

Examination of equations (1) and (2) reveals that pressure ( $P$ ) is comparable to the applied magnetic field ( $\mu_o H$ ) and the magnetic moment ( $VM$ ) is comparable to (the inverse of) volume ( $V$ ). When the compressible refrigerant is compressed adiabatically an increase in temperature will be induced; in an analogous process, an adiabatic magnetization of the magnetocaloric material causes an increase in its temperature. The next section discusses how the magnetocaloric effect may be used to produce refrigeration.

## The AMRR Cycle

Figure 1 shows a simplified version of the AMRR cycle. During an AMRR cycle, a porous regenerator bed constructed from a magnetocaloric material is exposed to a time-varying magnetic field and a time-varying flow of heat transfer fluid.

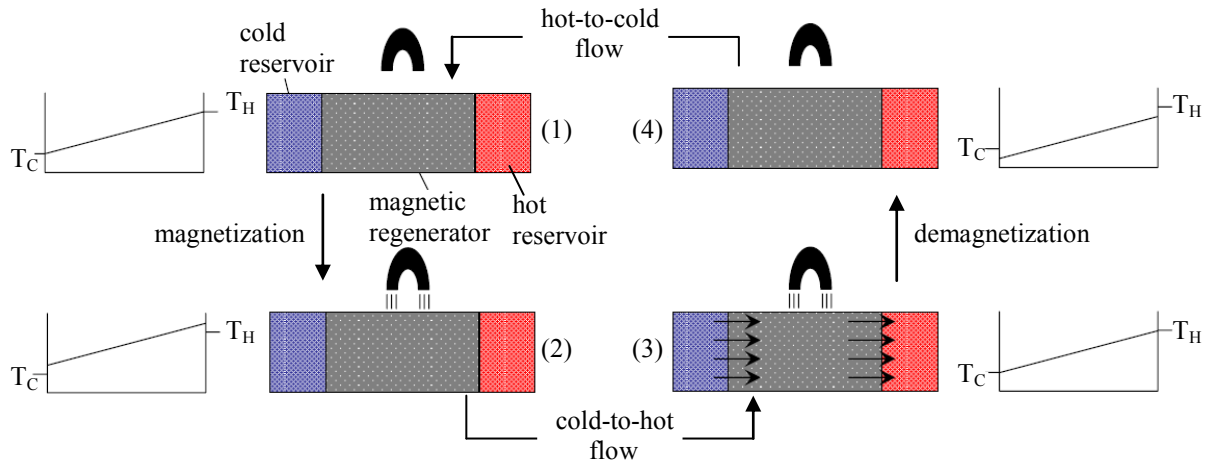


Figure 1: Active magnetic refrigeration cycle (Engelbrecht, 2005)

The process begins with the system at state (1) where the regenerator bed exhibits a temperature variation from the hot reservoir to the cold reservoir temperatures. The bed is magnetized causing it to transition from state (1) to state (2). There is no fluid flow during the magnetization process and therefore the temperature in the regenerator increases due to the magnetocaloric effect. The temperature distribution at state (2) (after magnetization) therefore results in temperatures that are higher than the hot temperature reservoir ( $T_H$ ) at the hot end. During the

cold-to-hot-flow process, the heat transfer fluid flows through the bed from the cold reservoir to the hot reservoir. This flow of fluid from the cold reservoir causes the bed temperature to decrease, as shown in state (3). As a result of this process, fluid at a higher temperature than the hot reservoir is forced from the hot end of the bed causing a heat rejection. The bed is demagnetized causing it to transition from state (3) to state (4); this process results in a reduction in the temperature in the regenerator leading to the distribution shown in state (4). To get from state (4) back to state (1), heat transfer fluid is pushed back through the bed from the hot reservoir to the cold reservoir. The hot fluid brings the bed back to its original temperature profile and causes fluid at a temperature lower than the cold reservoir ( $T_C$ ) to flow from the cold end of the bed, resulting in a cooling effect.

### Nusselt Number

The Nusselt number is defined according to:

$$Nu = \frac{h d_p}{k_f} \quad (3)$$

where  $h$  is the heat transfer coefficient,  $d_p$  is the particle diameter and  $k_f$  is the thermal conductivity of the fluid. The Nusselt number is a function of both the Reynolds ( $Re$ ) and Prandtl ( $Pr$ ) numbers as defined below.

$$Re = \frac{v_f d_p \rho_f}{\mu_f} \quad (4)$$

$$Pr = \frac{v_f}{\alpha_f} \quad (5)$$

where  $\rho_f$  is the density of the fluid,  $\mu_f$  is the viscosity of the fluid,  $v_f$  is the superficial velocity of the fluid as defined by the ratio of the volumetric flow rate of the fluid to the cross-sectional area of the test section,  $\nu_f$  is the kinematic viscosity of the fluid and  $\alpha_f$  is the thermal diffusivity of the fluid.

Several correlations exist for the Nusselt number inside a packed sphere regenerator:

Wakao and Kaguei (1982):

$$Nu_{Wakao} = 2 + 1.1 Re^{0.6} Pr^{1/3} \quad (6)$$

Kunii and Levenspiel (1969):

$$Nu_{Kunii} = 2 + 1.8 \left( \frac{Re}{\varepsilon} \right)^{1/2} Pr^{1/3} \quad (7)$$

and Macias – Mechin *et al.* (1991):

$$Nu_{Macias} = 1.27 + 2.66 \left( \frac{Re}{\varepsilon} \right)^{0.56} Pr^{-0.41} \left( \frac{1-\varepsilon}{\varepsilon} \right)^{0.29} \quad (8)$$

Figure 2 shows the Nusselt number predictions for these three correlations for a Prandtl number of 30 and a bed porosity ( $\varepsilon$ ) of 0.36. The three correlations differ by a factor of approximately 5

under these conditions. Discrepancies between these correlations have provided motivation for an experimental study of the Nusselt number for a packed bed at low Reynolds number and high Prandtl number.

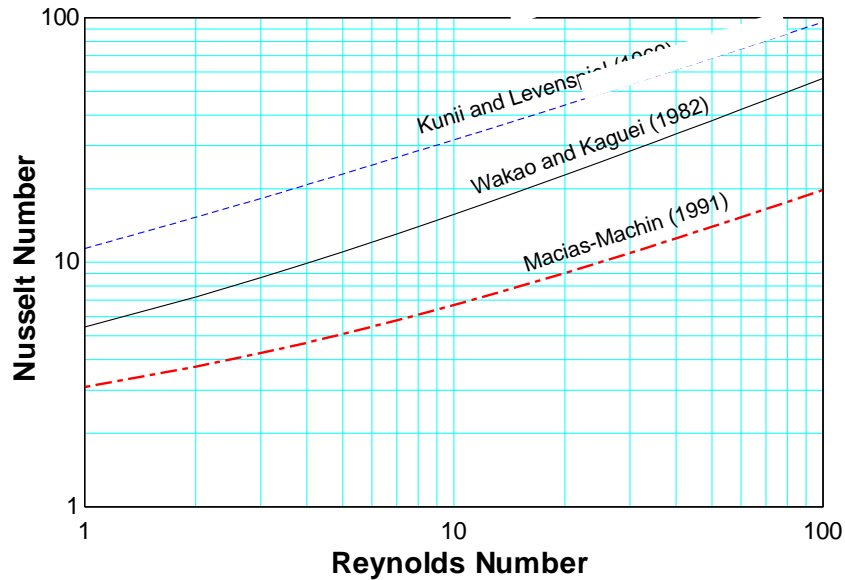


Figure 2: Nusselt number correlations from the literature as a function of Reynolds number with  $Pr = 30$  and  $\varepsilon = 0.36$

### Passive Regenerator Test Facility

A single-blow test facility has been developed and constructed at the University of Wisconsin-Madison in order to experimentally determine the Nusselt number associated with flow through a regenerator packing (Marconnet, 2007). The facility utilizes a passive regenerator, i.e. the material is not magnetocaloric. A schematic of the test facility is shown in Figure 3.

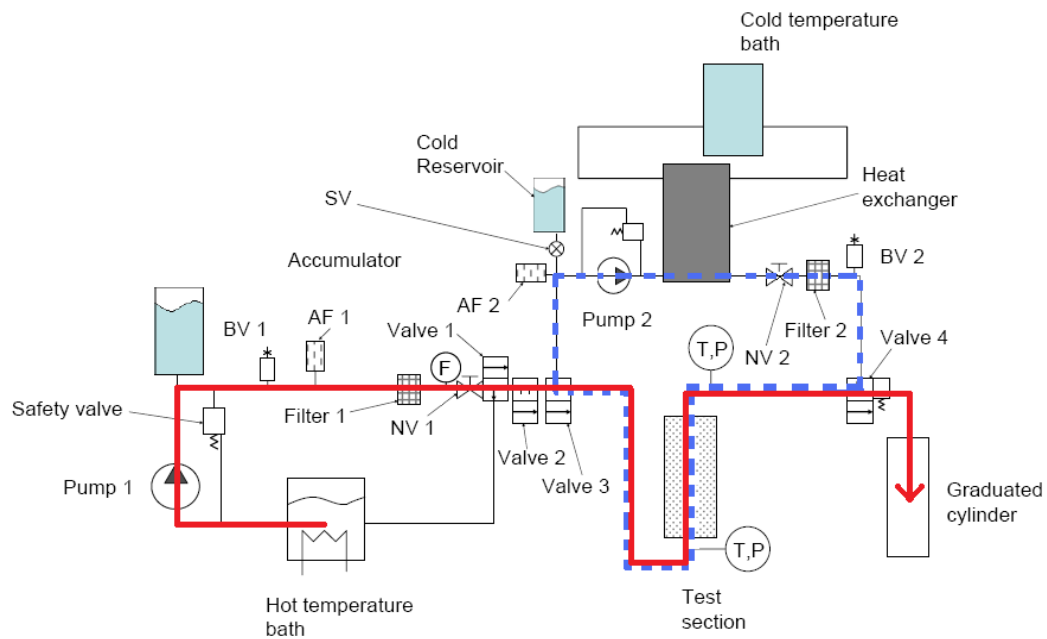


Figure 3: Passive regenerator test facility

Obtaining measurements of Nusselt number is a two step process. The first step is to run the cold soak loop, indicated in Figure 3 by the bold, dashed line. During the cold soak, a continual flow of fluid is pumped through a heat exchanger where the fluid is cooled by flow from the cold temperature bath. The cold fluid leaving the heat exchanger passes through the regenerator; the cold soak loop is run until the test section is thermally stabilized at a uniform, low temperature. Immediately following the cold soak, a series of valves are switched so that the hot blow loop (bold solid line) is run through the test section producing a step change in fluid temperature driven by hot fluid extracted from the hot temperature bath. Temperature versus time data are gathered from the beginning of the temperature step change until a new thermal equilibrium is reached by the regenerator. The thermal behavior exhibited by the regenerator can be directly related to the fluid-to-matrix heat transfer, which allows the Nusselt number to be measured for a specific set of conditions. A detailed set of test facility operation instructions are given by Engelbrecht (2008).

### **Design and Construction of Regenerator**

A new regenerator test section was designed and constructed in order to minimize temperature measurement error associated with the thermocouples mounted inside the previously installed regenerator in the test facility. The preceding regenerator (Frischmann, 2009) contained radially-mounted thermocouples at both the inlet and outlet of the test section. Each end consisted of seven thermocouples mounted on a plastic rod which was situated across the diameter of a retaining ring which is used to secure the packed bed of spheres at either end of the test section. The previous method for mounting the thermocouples required the removal of the two outer-radius thermocouples on both the inlet and the outlet from the temperature set used in the data analysis. These four thermocouples “lagged” the rest of the thermocouples in their respective groups, most likely due to their proximity to the outer-wall and retaining rings.

In order to minimize the amount of conduction heat transfer that can occur along the mounting device, the new design mounts the thermocouples onto a plastic mesh screen. By weaving the thermocouple wire through the screen, the thermocouples are stabilized in order to minimize noise that may otherwise occur if the thermocouples are allowed to move in response to the fluid flowing past them. A thermal analysis was performed in order to determine how close the outer-most thermocouples could be mounted to the regenerator wall without being affected by the temperature of the retaining ring and the regenerator housing. For modeling purposes, the mesh structure was simplified and represented as a cylindrical rod protruding from the retaining ring. The rod was modeled as an extended surface based on its small Biot number. A numerical model of the simplified structure was developed. Essentially, the goal of the thermal analysis was to determine the distance at which the temperature of the tip of the fin ( $T_t$ ) was unaffected by the base temperature of the fin ( $T_b$ ). To help determine this length, a dimensionless error was defined which is minimized at the optimal distance from the retaining ring as the temperature at the tip of the fin will asymptotically approach the temperature of the working fluid ( $T_f$ ) as the distance is increased.

$$Error = \frac{(T_t - T_f)}{(T_b - T_f)} \quad (9)$$

Using the definition in Eq. (9), it was found that a distance of 1.5 mm and larger from the wall of the regenerator would sufficiently prevent thermal communication between the thermocouple bead and the retaining ring/wall of the regenerator.

Based on the thermal analysis, the outer thermocouples were placed approximately 2.3 mm from the retaining ring and a distance of approximately 6 mm exists between adjacent thermocouples. Twelve additional thermocouples were packed into the test section in order to observe the temperature profile within the packed bed. Six of these thermocouples were positioned equidistant along the center axis of the cylinder. The remaining six thermocouples were placed at the same axial locations as the other spheres but are placed at the half radius in a helical shape extending the length of the packed bed.

### Single-Blow Data Collection

Single-blow data for a 30% propylene glycol and water solution by mass were collected per the method described in the test facility section. Table 1 shows the flow rates and corresponding Reynolds numbers chosen for data collection.

Table 1: Flow rates and corresponding Reynolds numbers chosen for single-blow data collection

Reynolds Number	30% PG Flow Rate (L/min)
3	0.28
4	0.38
5	0.47
7	0.67
9	0.86
12	1.15
15	1.43
20	1.91
25	2.39
30	2.87
35	3.34

Each test was run with a cold soak temperature of 290 K and a hot blow temperature of 305 K. At least three tests were run for each flow rate in order to obtain an average Nusselt number and Reynolds number for each run and ensure repeatability of the test facility.

### Numerical Model

Single-blow data were processed using a numerical model that is 1-D in the axial direction, although heat transfer in the radial direction is considered through thermal resistances defined between the regenerator packed bed and the foam lining and also between the foam lining and the stainless steel wall of the regenerator. Figure 4 shows a conceptual schematic of the 1-D model along with the key parameters. Hot blow fluid at a temperature of  $T_{in}(t)$  and a mass flow rate of  $\dot{m}_f(t)$  enters the inlet of the regenerator bed, which is initially at a uniform cold temperature,  $T_C$ .

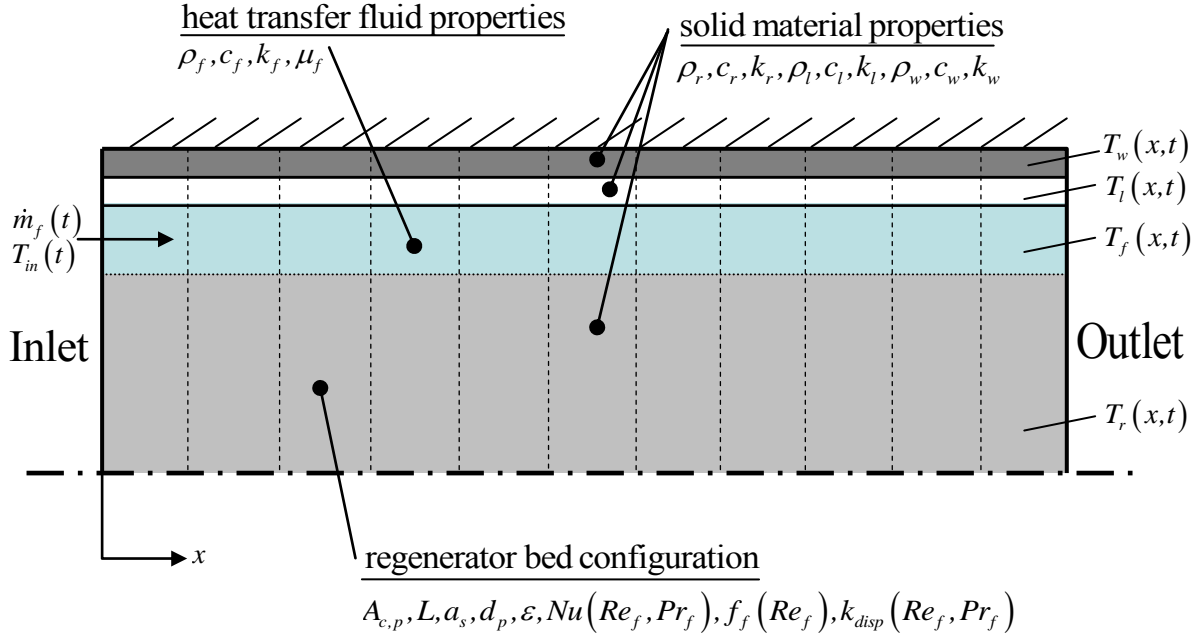


Figure 4: Conceptual schematic of 1-D model with key parameters listed.

Heat transfer fluid properties include density ( $\rho_f$ ), specific heat capacity ( $c_f$ ), viscosity ( $\mu_f$ ), and thermal conductivity ( $k_f$ ). The regenerator bed geometry is characterized by the cross-sectional area of the packed bed ( $A_{c,p}$ ), the bed length ( $L$ ), the specific surface area of the packing ( $a_s$ ), the particle diameter ( $d_p$ ), and the porosity ( $\epsilon$ ).

Regenerator thermal behavior is defined through the use of an appropriate correlation for friction factor ( $f(Re_f)$ ) which is assumed to be a function of the average Reynolds number of the fluid. The Nusselt number ( $Nu(Re_f, Pr_f)$ ) which is assumed to be a function of the average Reynolds number and Prandtl number of the fluid is a variable input to the model that will be later be used to determine an appropriate Nusselt number correlation which will be compared to Nusselt number correlations from literature.

An effective static thermal conductivity ( $k_{stat}$ ) is defined to characterize the actual rate of axial conduction through the regenerator/fluid matrix in the absence of fluid flow to the rate of conduction heat transfer that would occur in an analogous solid piece of packing material. Axial dispersion due to the eddy mixing of the fluid during flow is considered to be an extension of the thermal conductivity of the fluid ( $k_{disp}$ ).

The properties of the foam lining include density ( $\rho_l$ ), specific heat capacity ( $c_l$ ) and thermal conductivity ( $k_l$ ). The properties of the stainless steel wall of the housing include density ( $\rho_w$ ), specific heat capacity ( $c_w$ ) and thermal conductivity ( $k_w$ ). The geometry of the foam lining and stainless steel wall is defined by the cross-sectional area of each component, ( $A_{c,l}$ ) and ( $A_{c,w}$ ), respectively.

The temperature data collected during an experimental run is post-processed using MATLAB. The inlet thermocouple temperatures are averaged as well as the outlet thermocouple temperatures. These temperature profiles are interpolated using the numerical model time steps.

The inlet temperature profile is then supplied to the numerical model along with a best guess Nusselt number. The numerical model supplies the predicted outlet temperature profile as well as the outlet temperature profiles of the regenerator bed material at the locations of the bed thermocouples. The agreement between the experimentally measured temperature profile and the predicted temperature profile is quantified by the root mean square error between the two curves. The RMSE is defined in Eq. (10)

$$RMSE = \sqrt{\frac{\sum_{i=1}^{N_{exp}} (T_{exp,i} - T_{pre,i})^2}{N_{exp}}} \quad (10)$$

where  $N_{exp}$  is the number of experimental data points between 20% and 80% breakthrough of the experimental data,  $T_{exp,i}$  is the  $i$ th experimental temperature data point and  $T_{pre,i}$  is the  $i$ th model-predicted temperature. The temperatures defined in the RMSE equation can be those of the fluid outlet temperature of the regenerator or the regenerator bed temperature at any of the six axially distributed thermocouples within the regenerator bed. Nusselt number results are compared to four literature correlations presented below in equations (6)-(8).

## Results

Suspected flow maldistribution occurs near the outermost radial thermocouples located at the inlet and outlet of the regenerator bed. For this reason, the Nusselt number results presented below are calculated using only the 3 most central thermocouples at the fluid inlet and outlet. Figure 5 shows the average Nusselt number for the average Reynolds number for the 11 test flow rates. The data agree very well with the Wakao and Kaguei correlation with the exception of the data for Reynolds number 3 where it drops significantly below the correlation.

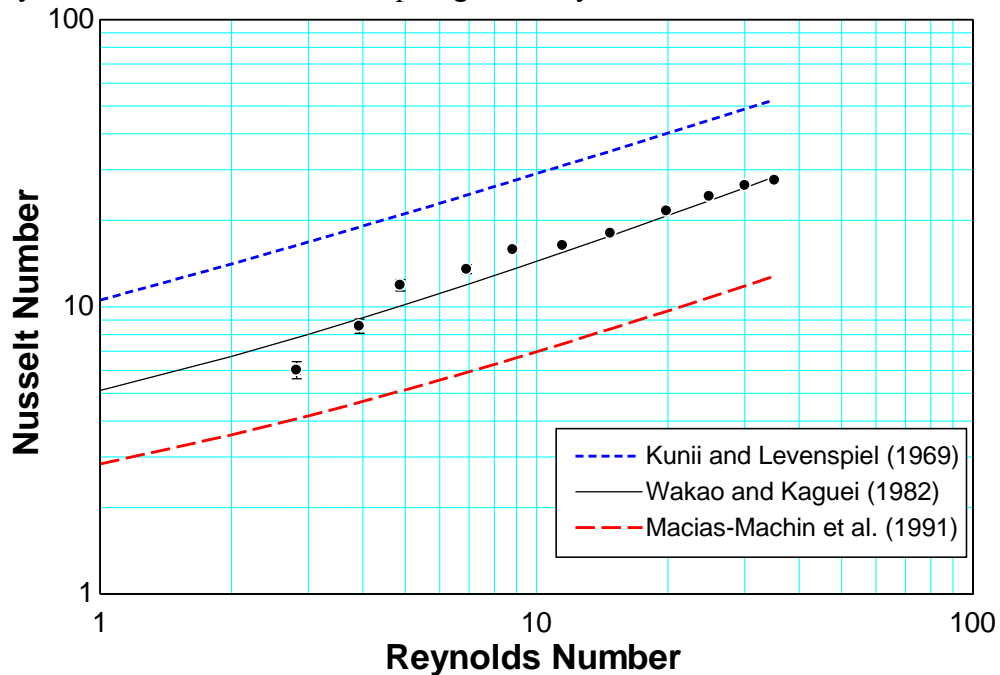


Figure 5: Average Nusselt number as a function of average Reynolds number utilizing the middle 3 fluid thermocouples at the inlet and outlet

Temperature profile data within the packed bed was also investigated. The temperature difference between the center axis thermocouple and mid-radius thermocouple at 3 different axial positions is shown below in Figure 6. The positions are numbered 3, 4, and 6 corresponding to the 3<sup>rd</sup> closest location to the inlet, 4<sup>th</sup> closest and 6<sup>th</sup> closest, respectively. The temperature difference between the center and mid-radius thermocouple increases as the Reynolds number decreases. However, there is no obvious correlation between the magnitude of the temperature difference and axial position as position 4 exhibits the smallest temperature difference and position 6 exhibits the largest temperature difference. The temperature span for these data is 15 K and therefore the temperature gradient is approximately 25% of the temperature span for lower Reynolds numbers.

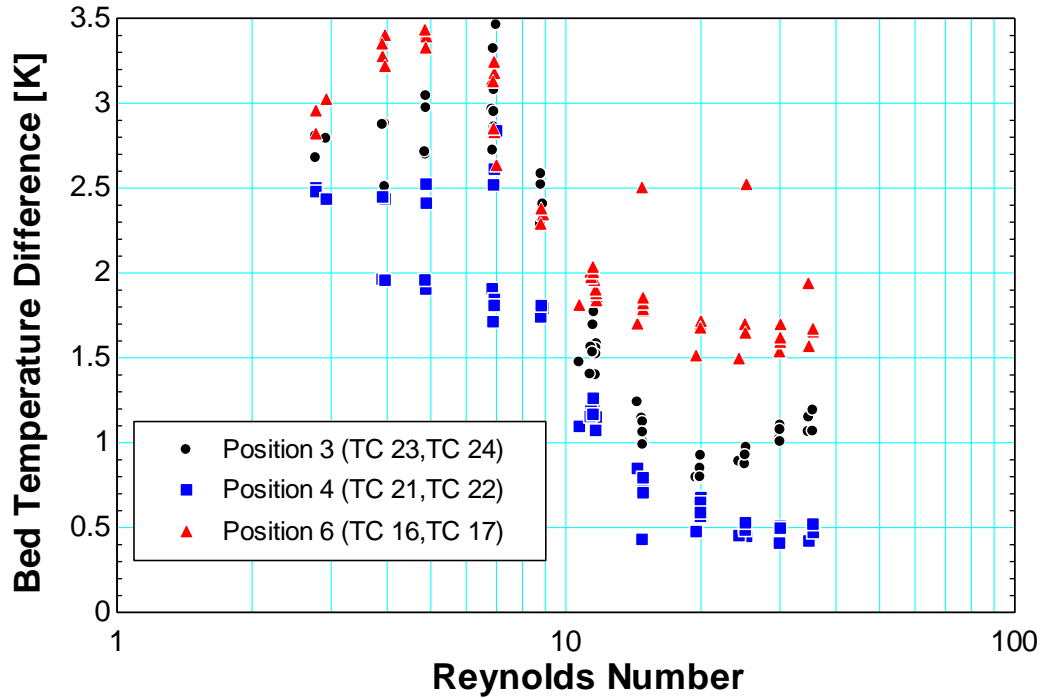


Figure 6: Temperature difference between the central bed thermocouple and mid-radius thermocouple at 3 separate bed positions as a function of Reynolds number

A dimensionless temperature ( $\theta_{diff}$ ) is defined in order to determine whether the mid-radius temperature is closer to the center thermocouple or the foam lining temperature of the regenerator

$$\theta_{Diff} = \frac{T_{center} - T_{radial}}{T_{center} - T_l} \quad (11)$$

Where  $T_{center}$  is the temperature of the center thermocouple,  $T_{radial}$  is the temperature of the mid-radius thermocouple and  $T_l$  is the temperature of the model-predicted foam lining. This dimensionless temperature difference is calculated for the same three axial positions and is shown in Figure 7.

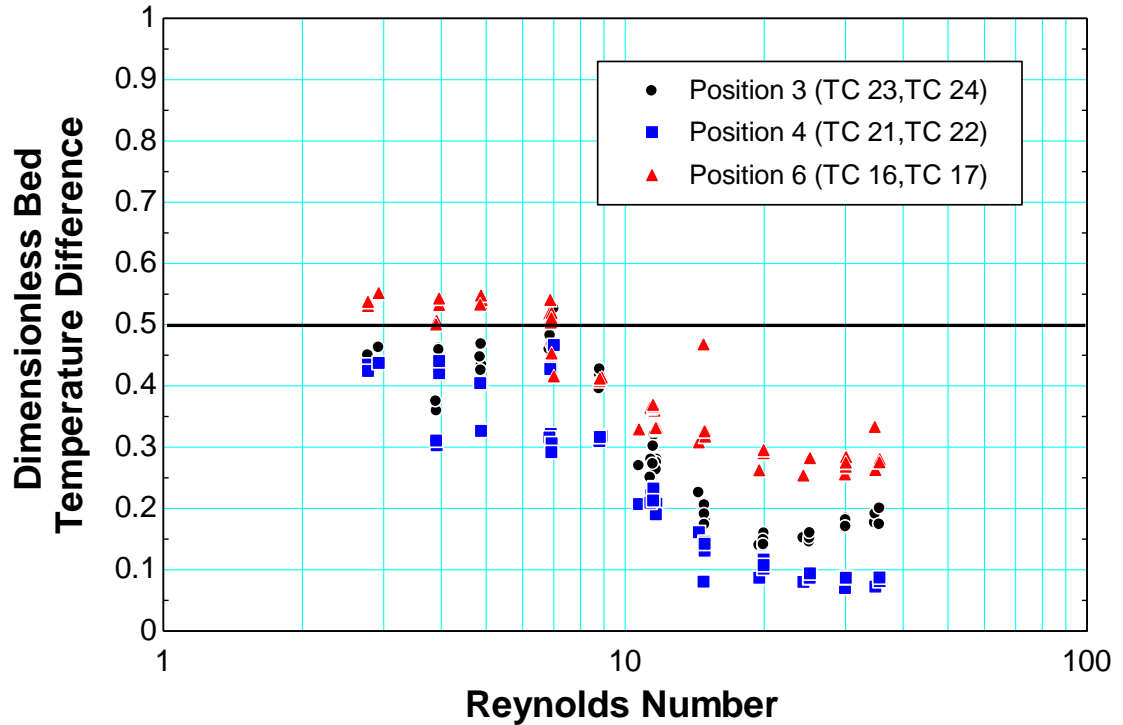


Figure 7: Dimensionless bed temperature difference at 3 separate bed positions as a function of Reynolds number

By the nature of the dimensionless temperature difference, values lower than 0.5 indicate the mid-radius temperature is closer to that of the center thermocouple and likewise a value higher than 0.5 indicates the mid-radius temperature is closer to the temperature of the foam lining. From Figure 7 it can be seen that the mid-radius temperature is almost always closer to the temperature of the center thermocouple which is consistent with heat loss due to the thermal capacitance of the foam lining and regenerator wall.

The bed thermocouples can also be used to calculate the Nusselt number for each test. There is an advantage to using the bed thermocouples because they are typically less noisy than the fluid inlet and outlet thermocouples. Since the bed itself acts as a flow straightener, the bed thermocouples are able to avoid any flow maldistribution effects that occur in the header of the regenerator. Figure 8 shows the results from using only the center bed thermocouple closest to the inlet as the inlet temperature to the model and the experimental outlet data from the center bed thermocouple closest to the inlet is used to minimize the RMSE between the model and experimental outlet data.

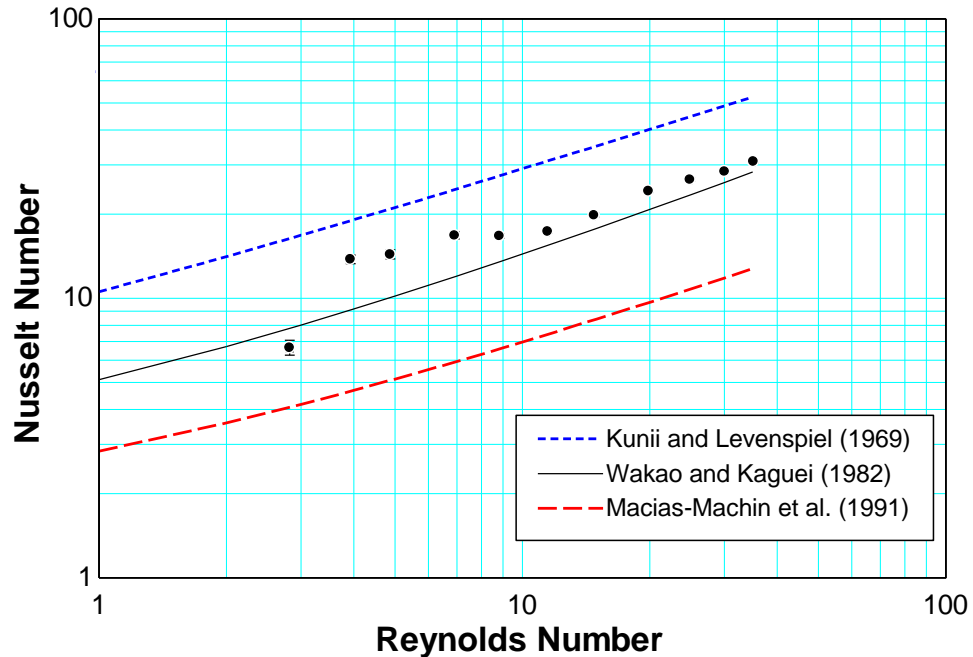


Figure 8: Average Nusselt number as a function of average Reynolds number utilizing the central bed thermocouple at the inlet and outlet

Figure 8 shows that there is again good agreement between the calculated Nusselt numbers and the Wakao and Kaguchi correlation, however, the moderate Reynolds number data tends to be quite a bit higher than the correlation, while data at Reynolds number 3 drops below the correlation similar to the data shown using the fluid inlet and outlet temperature data.

## Conclusions

Examination of the bed temperature profile data found that there is about a 25% temperature gradient present within the packed bed between the center axis of the bed and the temperature measured at the mid-radius of the regenerator. This radial temperature gradient was compared to the model-predicted foam lining temperature of the regenerator and it was found that the temperature gradient is consistent with heat loss due to the thermal heat capacitance of the foam lining and regenerator housing.

The regenerator bed acts as a flow straightener and therefore it can be advantageous to use the bed thermocouples to calculate the Nusselt number for each flow rate. The temperature data collected with these thermocouples tends to be much smoother than those collected with thermocouples mounted in the fluid streams at the inlet and outlet of the bed. It was found that using only the center axis bed thermocouples provided Nusselt numbers fairly consistent with those calculated using the fluid inlet and outlet thermocouples. The bed thermocouples offer versatility when determining the Nusselt number as different combinations of the thermocouples can be used to calculate the Nusselt number and can therefore provide repeatability tests without having to collect multiple experimental runs at each flow rate. However, due to the radial temperature gradient in the packed bed, in order to accurately calculate the Nusselt number, a 2-D numerical model is essential.

## References

- Engelbrecht, K., 2008, *A Numerical Model of an Active Magnetic Regenerator Refrigerator with Experimental Validation*, M.S. Thesis, University of Wisconsin Madison.
- Engelbrecht, K., 2005, *A Numerical Model of an Active Magnetic Regenerator Refrigeration System*, M.S. Thesis, University of Wisconsin Madison.
- Frischmann, M., 2009, *Heat Transfer Coefficient Using Liquid Heat Transfer Fluids for use in Active Magnetic Regenerative Refrigeration*, M.S. Thesis, University of Wisconsin Madison.
- Kunii, D., Levenspiel, O., 1969, *Fluidization Engineering*, Wiley, New York, NY, 534.
- Macias-Machin, A., Oufier, L., Wannemacher, N., 1991, Heat Transfer between an Immersed Wire and a Liquid Fluidized Bed, *Powder Technology*, vol. 66:281-284.
- Marconnet, A., 2007, *Predicting Regenerator Performance with a Single-Blow Experiment*, M.S. Thesis, University of Wisconsin Madison.
- Wakao, N., Kaguei, S., 1982, *Heat and Mass Transfer in Packed Beds*, Gordon and Breach Science Publishers, New York, NY, 364.

# Symbolic Computation Tools in Spacecraft Design Models

Capri Pearson

## Abstract

TeamX runs spacecraft design models for early mission formulation using Excel. The model equations contained within each cell are difficult to recognize and debug. I evaluated three symbolic computing programs: Maple, Mathematica, and Mathcad, and compared them to a representative TeamX Excel model. The method I used to accomplish this was Learn, Implement, Evaluate, and Repeat. I first became familiar with each program, implemented the Excel model, and evaluated the effectiveness for replacing Excel as the primary computer program for writing, documenting, and executing models. The programs were useful in documenting steps and displaying calculations and graphics but lacked a good user interface for large amounts of data. These programs would need either an additional user friendly interface on top of the program or be linked with Excel to display input and output tables.

## Introduction

I supported the Symbolic Computing Initiative at the Jet Propulsion Laboratory. The goals were to model engineering design calculations and evaluate the use of symbolic tools. I evaluated Maple, Mathematica, and Mathcad for use in TeamX. TeamX is a group of engineers working together to create rapid design models. They are able to combine all of a spacecraft's subsystems to find the total cost, weight, and feasibility of a given concept. They then evaluate the design for the designated mission. TeamX utilizes Excel Workbooks integrated together to quickly update spacecraft subsystem models. Together they can come up with a comprehensive model taking into account many factors simultaneously. They have 21 workbooks for the spacecraft subsystems, which contain 700,000 equations and over a million data points. Each subsystem adds components for the spacecraft and receives information from other subsystems, which require further adjustments to the model. The model also sums important values such as mass, average and maximum power consumption, and cost. I implemented parts of a representative Excel workbook into each of the symbolic computing programs above and evaluated them as an effective replacement.

Special thanks to Wisconsin Space Grant Consortium for their support of this research.

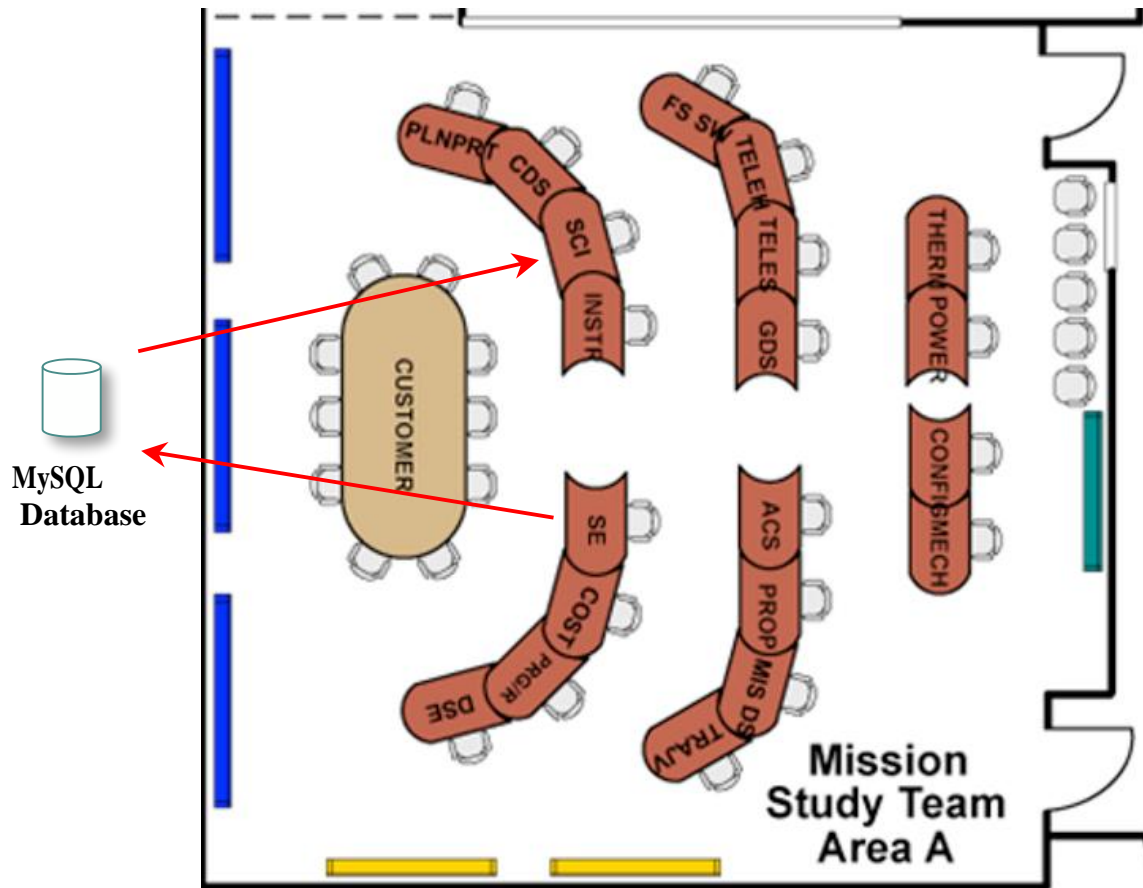


Figure 1: TeamX Layout

The TeamX area is laid out in Figure 1. Each subsystem has its own computer to input parameters and has a user interface specified for the parameters appropriate to that system. This also includes a risk and cost chair not normally in a “mission control” setting. The parameters are sent from each computer to a database for iterations between the data for a total weight, cost, power consumption, etc.

## Background

Excel has limited capabilities as an engineering tool. Its design does not show equations in an easy to read format. Also the equations are contained within cells so are difficult to debug and break easily. There is little space for comments on the model, which is hard to decipher. Symbolic tools are excellent at displaying equations and documenting the steps to solve a problem. My goal was to see if any one of the three programs could fully replace Excel. If not, I would search for any other options within the tools to possibly link with Excel.

## Objectives

TeamX has two main concerns they need addressed when improving the model capabilities. One is the engineer who will use the model. TeamX has resident experts in each field come in and work out a model of the spacecraft subsystems. These engineers have fulltime jobs outside of

TeamX so it is imperative that the models are easy to understand, and work quickly. On the other hand, the programmers who keep the models in working order do not want the code so complicated that it breaks and takes hours to fix or debug. I searched for a program that satisfied both concerns and improved documentation of the model.

## **Approach**

My approach was very systematic: Learn, Implement, Evaluate, and Repeat. Learn each program, implement the representative Excel model, evaluate as effective replacement and repeat for each program. My first step was to learn the current Excel model in TeamX. This system is iterative with input parameters at each subsystem relying on other chairs. The model needs to be quick and easy to use as a study can produce a preliminary spacecraft model in 9 hours. The next step was to learn the program I would be transferring the model to. I learned the basic functionality of each program through help topics, examples, and online forums. I then proceeded to start implementing the example model into the program. As I continued with this step, I looked further into more complex functions in the program such as graphical user interfaces, database transfer, compatibility with Excel, and lookup functions. Finally, I evaluated each program against a matrix of metrics for items such as ease of use, display of text and equations, and so on.

The first program I worked with was Maple. Maple was very good at displaying text and equations inline. The plotting functions were easy to use and manipulate. Maple has a package for use with Excel called ExcelTools, which has an import/export function. This can import the data directly from the Excel workbooks but displays the spreadsheet data poorly. It comes in as a mix of text and numbers so Maple displays it as an array. It does not have a grid format that is easy to read or customize. Maple's symbolic solvers are very robust. It is able to solve complicated systems of equations quickly. Maple has a custom user interface called a Maplet. This could be used to generate an easy to use interface although it would take the programmers quite some time to implement.

Next, I worked with Mathcad. Mathcad is very different from both Maple and Mathematica. It reads from left to right and top to bottom, allowing you to put an equation anywhere on the page as long as the variables are defined above or to the left. The units in Mathcad are the best I have come across allowing the user to easily type in any units. The program does the converting automatically. The default units can be specified to make outputs easy to read and logical. Mathcad has built-in lookup functions by column or row. Mathcad also has a compare tool which highlights the differences between two worksheets. Mathcad does all of its evaluation automatically, although that can be turned off. Since the calculations TeamX does are not math intensive this may be a better option than Maple or Mathematica which must be executed each time something is changed. One item Mathcad lacks is the option of a custom user interface. It has controls like the other programs but they are not as clean looking and lack useful options.

Finally, I worked with Mathematica. Mathematica has the best help documentation with many examples so the user can easily find what he/she is looking for. I found Mathematica, which I had the least experience in, the easiest to learn complex functions. Mathematica has a built-in search function to lookup values based on names instead of being hard coded by row and column. Mathematica has the most options for customizing data tables. It has very useful writing

palettes, which formats text and equation extremely well and easily.

A comparison of the three programs in symbolic representation of equations and data structure are below in Figures 2 and 3. All three are exceedingly good at what they were designed for. The lack of a good spreadsheet or table package is the limiting factor in implementing one of these programs directly.

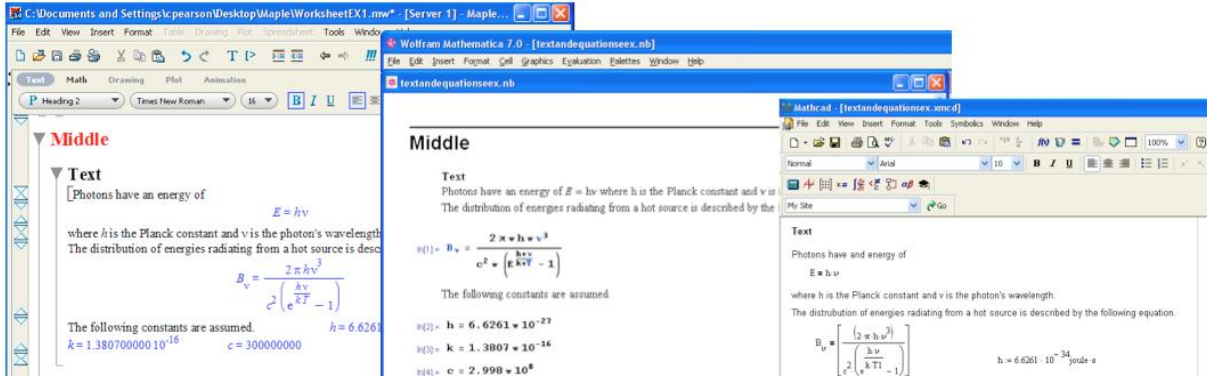


Figure 2: Symbolic Representation of Equations

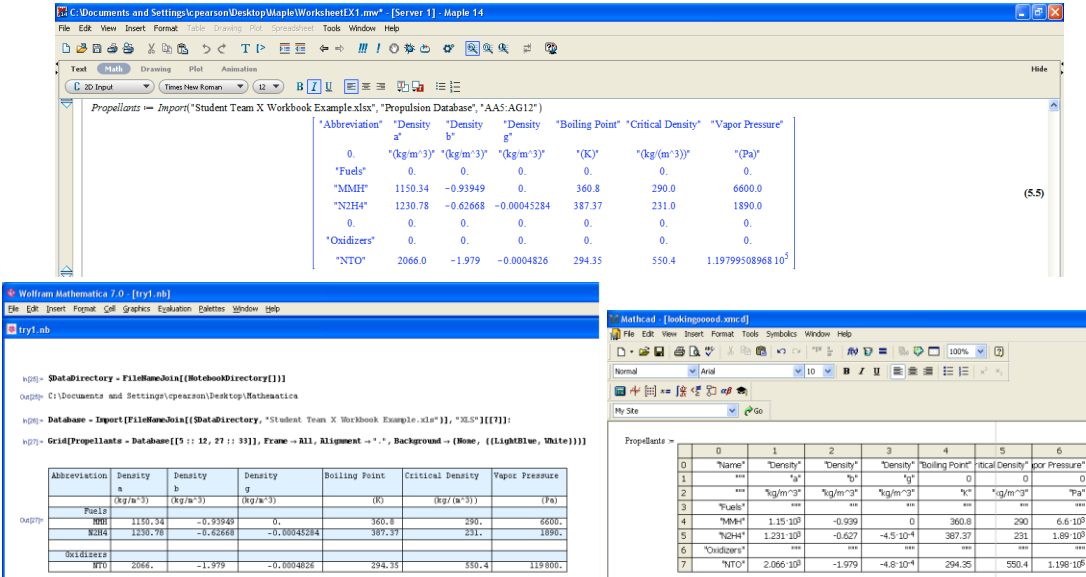


Figure 3: Table Display

## Results

All three programs are good at displaying text and equations in a readable, textbook-like format. This is ideal for documenting any work. All three have conditional statement capabilities for errors. Maple and Mathematica are very similar and hence have similar problems. Both would need an additional user interface built on top of the program for ease of use. The engineers who use the models have jobs outside of TeamX and may go for a while without working with TeamX. Therefore, the user interface has to be intuitive and easy to understand.

The greatest problem I have come across with these programs is the display of input and output tables. Excel handles large amounts of information exceedingly well. All three programs can link with Excel in various ways. Maple and Mathematica can import tables directly from Excel but they must be in the same directory as the current worksheet. Maple stores them as an array which can be hard to read and cannot be customized. Mathematica displays these tables as grids with options such as color, font, etc. Mathcad can insert an Excel component directly into the sheet so you can use Excel within the tool. Between Maple and Mathematica, I believe TeamX would benefit from Mathematica more. Its style and options are better suited for documenting and showing results. It even includes a slide show function, which outperforms Maple's equivalent.

One product of my search and evaluation was a Symbolic Tool Comparison Matrix. This table shows basic functions in all three programs. It was useful for me since I switched back and forth between the programs. Someone who is familiar with one program and needs to use another could use this matrix as a guide. This matrix also helped me compare attributes of each program and find problem areas where one program outperforms another. The comparison matrix is included in the appendix for reference.

## **Discussion**

I did not find a program that could completely replace Excel directly "out of the box". All three would need additional custom user interfaces in order to be easy for the engineers to use. A good user interface would take a lot of code which complicates the programming considerably. Unfortunately, this would mean the programmers would have a harder time implementing the program and it would be difficult to maintain. I expected the table functions and spreadsheets of the programs to be much better. I had not anticipated a way to link the program directly into Excel, which was a helpful find. This would allow them to maintain their user interface but allow the calculations to be viewed in a well documented and textbook like way. This would not provide a full replacement for Excel but two programs each exceedingly good at their specific task might be the best answer.

## **Conclusion**

None of these programs work directly "out of the box" as a full replacement for Excel. Using a different approach, each program could be linked inside of Excel adding the capabilities and functions of the program while keeping the user interface with which the engineers are most familiar. The attached Symbolic Tool Comparison Matrix shows basic functions in each program. Since Maple and Mathematica are so similar, a user familiar with one would have little difficulty switching to another. Also someone familiar with one of the three programs could find its equivalent in another program. I was not able to look in depth to the program link in Excel. This could be a place to start with further investigation of a system better than the current Excel models.

## Appendix

**Symbolic Tool Comparison Matrix (All)**

Action	Maple	Mathematica	Mathcad
<b>Documentation</b>			
Text to Equation	F5	Alt+7, arrow down to get back to equation	Once there is a space turns to text
New Section		Alt + 4	
Evaluate	Enter	Shift+Enter	Enter or down arrow
Next line w/o evaluation	Shift+Enter	Enter	None, auto executes after leaving edit box, but auto calculate can be turned off
Assign variable	:=	=	:=
Assign equation	=	:=	=
Evaluation order	Top to bottom	Top to bottom	Left to right, top to bottom
Greek	type word, greek bar	Esc [Letter or word].Esc, Palette-Typesetting	Ctrl+B, greek bar
Units	Mediocre	Confusing, Convert Function	Type right after numbers, auto converts
Subscript	_ auto places cursor, right arrow to get out of	Ctrl + -, right arrow to get out of, or Palette-Typesetting	[, right arrow to get out of
Superscript	^ auto places cursor, right arrow to get out of	Ctrl + 6, right arrow to get out of, or Palette-Typesetting	^, right arrow to get out of
Suppress Output	:	;	(Does not print output automatically)
Display variable value	Type variable and evaluate	Type variable and evaluate	Type variable and =
Code Comments	# Comments	(*Comments*)	
"Calculator"	Enter expression and evaluate	Enter expression and evaluate	Enter expression and =
<b>Reference</b>			
Equation	(1.1.3)	Must assign name, numbering changes	Must assign name
Database	Subscript Row and Column numbers	Position[Table,"Name"]	vlookup, hlookup, match
<b>GUI</b>			
Spreadsheets	Yes	No spreadsheet function, use Grid	Excel component directly in worksheet
Tables	String display or manual data input	String Display, use Grid	
Inputs/Outputs			
Components	Yes	Yes	

Action	Maple	Mathematica	Mathcad
Sharing			
Compare	?	Cell > Notebook History	Tools > Compare
Book	<a href="#">MaplePlayer</a> , Slide show (cuts off if too long, does not scroll)	Slide Show	e-book
Web Service	<a href="#">MapleNet</a>	<a href="#">webMathematica</a>	Mathcad Calculation Server
Import Formats	Excel, Matlab, Image, Audio, Matrix Market, and Delimited	PDF, <a href="#">LaTeX</a> , RTF, TXT, ZIP, XML, XLS (not XLSX), etc	Delimited Text, Fixed-Width text, Microsoft Excel, MATLAB, Binary
Export Formats	PDF, <a href="#">LaTeX</a> , RTF, TXT, ZIP	PDF, <a href="#">LaTeX</a> , RTF, TXT, ZIP, XML, lots more	XML, HTML, PDF, RTF
Excel Link	Import/Export	Import/Export	
Conditionals			
If	if condition then statement end if	<a href="#">If</a> [condition, true, false]	<a href="#">if</a> (condition, true, false), or use programming toolbar statement <a href="#">if</a> condition
Else	if condition then statement else statement end if	The false part of above statement.	The false part of above statement. Or statement <a href="#">otherwise</a>
Else if	if condition then statement elif condition then statement else statement end if	<a href="#">Which</a> [condition1, statement1, condition2, statement2, ...]	Use multiple if statements
For	for variable from min by increment to max do statement end do	<a href="#">For</a> [start, condition, increment, statement]	Ctrl + Shift + ' (don't type for) for variable € min..max statement
While	for variable from min by increment do statement end do (or) for variable in expression while condition do statement end do	<a href="#">While</a> [condition, statement]	Ctrl + ] (don't type while) while condition statement

# **Modeling Complex Dynamics with Symbolic Computation Software**

## A Comparison between Maple and Mathematica

Collin Bezrouk  
NASA Jet Propulsion Laboratory

Mentor:  
John Gallon

### **Abstract**

This paper describes research into the effectiveness of using symbolic computation software for solving systems of complicated, coupled differential equations. Maple and Mathematica were the two software packages under review. They were compared using a dynamics model of the Mars Science Lab's Skycrane landing architecture which contained four coupled differential equations. Their effectiveness was judged with six criteria: unique features, learning material, symbolic formatting, computational power/speed, quality of help support, and presentation methods. Maple was the only symbolic program able to solve the system of equations and proved to be superior in more categories than Mathematica, such as computational power and symbolic formatting.

### **Motivation for Using Symbolic Solvers**

The engineers working at NASA's Jet Propulsion Laboratory (JPL), and other NASA center, rely heavily on numerical methods and programs for solving a variety of engineering problems. Unfortunately, the formats and programming languages used in these tools often makes them difficult for other engineers to validate the physics behind the equations being used. This process of verification and validation (V and V) is tedious, time consuming, and prone to error, since it is easy to miss a small mistake.

Two examples of these numerical programs are Microsoft Excel and MATLAB. A common issue between these two is that each allows input only on a single line. Equations written this way need to use parentheses heavily to define the order of operations. When written this way, it is difficult to spot where parentheses pairs begin and end, making the correct order of operations in the equations difficult to check for accuracy. Furthermore, when attempting to review a series of calculations made in Excel, one has to select an output cell to see the calculations that produced the solution. Because of this, only one equation can be seen at a time. Also, the parameters in the equations are usually cell coordinates. This means that a reviewer would need to check each parameter's position in the spreadsheet before knowing what it actually represents.

A second example of a difficult to validate software is MATLAB. This tool requires knowledge of the programming language in order to understand the calculations being made. This can be difficult if the reviewer is unfamiliar with certain syntax, or obscure or user-defined functions. Just as with Microsoft Excel, all the equations are written in a single line, so ensuring the correct form of the equation is difficult. Finally, if the programmer decides to write and use his own functions in the script, they are often saved in separate files or in a different location in the script. Someone performing “V and V” on this script will have to search the script for the function definition to find out what it does, which ultimately creates a disorganized document. Sample equations from both of these numerical programs are shown in Figure 1.

```
>> Lpayout = payout - (a/2*((theta2-x(5)).*sqrt(c2+(theta2-x(5)).^2) + c2*asinh(...
(theta2-x(5))/c)) - a/2*(theta1*sqrt(c2+theta1^2)+c2*asinh(theta1/c)));

>> twr_cp_dist = sqrt((Zo - (cp_exit(3) - cp_top(3)) - bell_h + (y(3)-y(1)))^2 ...
+ (Do - bell_r)^2) + sqrt(bell_r^2 + bell_h^2);
```

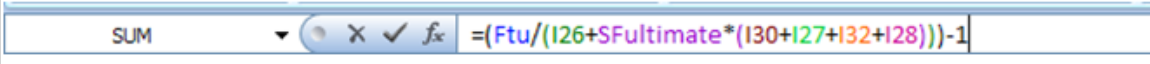


Figure 1: Sample equations in MATLAB and Microsoft Excel

A more effective way to display equations is to use a type of program known as a symbolic (or analytical) solver. These programs write and solve equations symbolically and display them with a type-set formatting that appears similar to how one would see it in a text book. The correct order of operations is easily seen through the structure of the equation instead of heavy use of parentheses. An example of a symbolic solver’s formatted equations can be seen in Figure 2 below. These programs also have a broad range of capabilities that both match and exceed those found in other tools. This includes solving systems of ordinary or partial differential equations, linear algebra and matrices, units, tolerances, etc. Unfortunately, they are generally slower computationally, so they are not ideal for solving huge sets of calculations or solving repetitively. Therefore, rather than replace numerical solvers in analysis, it would be more effective to translate the key parts of the model into a symbolic format and run several sample calculations to compare with the numerical model. Doing so will verify that the numerical model is correct, which can then be used to perform multiple or more computationally intensive calculations.

Axial stress to Ultimate stress ratio:

$$R_{h, UAx} := \frac{\sigma_{h, ax, preload} + SF_{ult} (\sigma_{h, bend, slip} + \sigma_{h, ax, app} + \sigma_{h, bend, assem} + \sigma_{h, ax, climb})}{\sigma_{TU}} = R_{h, UAx} := 0.614438$$

Figure 2: Example of symbolic type-set formatted equations.

The purpose of the Symbolic Computing Initiative (SCI) is to evaluate and compare two symbolic computation programs: Maple, developed by Maplesoft, and Mathematica, developed by Wolfram. The purpose of the comparison is to determine which one would be best suited for the task of improving the accuracy and timeliness of the “V and V” procedure. It is the hope of the initiative supervisor, Howard Eisen, that at the end of the fiscal year, the funds remaining at

JPL can be used to purchase licenses for one of these programs to be made available as a lab-wide tool.

## **Judging Criterion**

These programs have been compared in five main categories. First is how easy the program was to use and how quickly someone can pick it up with its “Getting Started” materials (videos, examples, documentation, etc.). It is important that if all JPL employees are provided with this program, they can learn it without getting frustrated and resorting back to programs that they are familiar with, but are still difficult for “V and V”. Second, the purpose of using a symbolic computation program is that the calculations are written and displayed in a type-set format that makes equations easy to read and verify. Both programs use different formats and have been judged accordingly. Third, I looked at computational power and speed compared to each other and to the numeric tools currently in place. Fourth, the types and quality help support that was available for each program was reviewed to see how quickly and easily a user can get solutions to trouble they experience. The final criterion was to judge how these tools could be used to present the calculations they performed. Each comes with a presentation tool which would be much more efficient and timely than making a PowerPoint.

## **The Bridle and Umbilical Device Dynamic Response Solver**

My comparison between Maple and Mathematica was made by creating a document in each that model's the dynamic's of the Mars Science Laboratory's “Skycrane” architecture. This architecture enables the final stage in landing the rover onto Mars's surface. When entering Mars's atmosphere, the rover will be stowed onboard a rocket powered “Descent stage” (DS). Both craft are housed within a protective aeroshell and heat shield. After decelerating with aerobraking and a parachute, the heat shield will separate and the aeroshell will release the DS and rover. As the rover and DS approach the surface, the DS control descent speed and orientation. About 10-20 seconds before landing, the Bridle and Umbilical Device (BUD) system will activate. The DS will slow to a constant -1 m/s descent rate, and fire the three pyrotechnic release nuts that hold the rover to the DS. The rover will be lowered by the descent stage on three nylon bridles, which are unwound from a conical helical spool attached to an electromagnetic descent brake. After the rover touches down on the surface of Mars, tension will be relieved in the bridle, which triggers the rover to cut the cables and the DS to fly down range for a hard landing away from the rover (Mitcheltree, et al. n.d.). The diagram below shows all of the components of the BUD system.

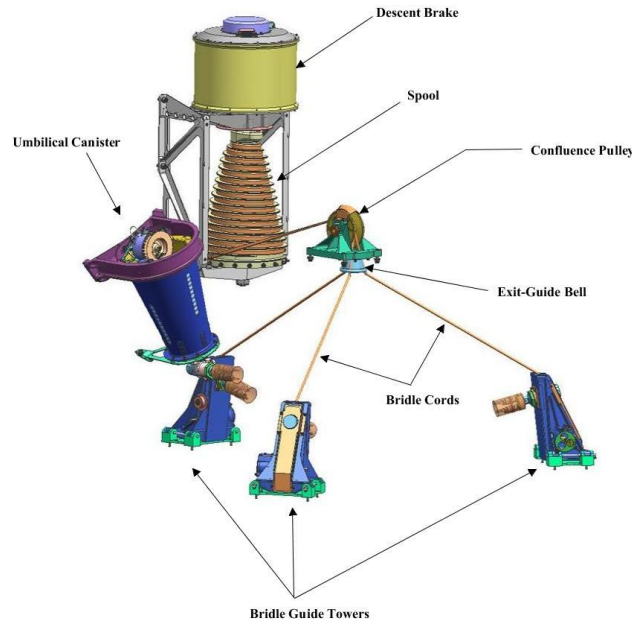


Figure 3: A CAD model of the BUD system and all of its components.

This dynamics model was originally written in MATLAB and solved numerically with a fourth-order accurate Runge Kutta method. The work was documented in an 85 page memorandum (Gallon and Gradziel 2009). The model contains four degrees of freedom (dof): the position of the DS, the position of the rover, the rotations of the spool, and the rotations of the brake. The worksheets were expected to handle the input and symbolic simplification of many nested piecewise expressions that all compiled into four coupled ordinary differential equations (ODE). These equations contained discontinuities many repetitive calculations that could be simplified. The system of ODE's was solved numerically using the programs' built in differential equation solvers. The results were then displayed in 15 plots with the available plotting tools. The performance between Maple and Mathematica in the specified areas were then compared.

### Maple's Advantages and Disadvantages

Maple employs two strong features that distinguish it among other symbolic solvers. The first is its organization of features into 21 collapsible "palettes" which are displayed along the edge of the worksheet. These contain nearly all of Maple's mathematical capabilities that can be represented symbolically, and the user simply needs to find and click the symbol or operator they are looking for. Furthermore, if a user cannot find the symbol they are looking for, there is a palette that lets you draw the symbol and it will match it to ones it recognizes.

The second main feature is the context-sensitive menus. At any point in your worksheet, a user can right click on any input or output and a menu will appear with every possible option available to work with that selection. These options range from solving equations, making substitutions, assigning units, making plots, rearranging equations, differentiating, integrating,

etc. This tool makes it easy to see everything that Maple is capable of, but also limiting it to things you can do with your particular application so it doesn't become overwhelming. Using this, even beginners can use advanced features of the software.

The only strong negative aspect of the program is the time that it takes to save large Maple documents gets to be excessive when a document becomes larger than 4 MB. It is easy for this to happen, especially if the author is adding a lot of documentation in the form of images. My worksheet, at the time of this paper, is approaching 8.5 MB and it takes an average of 14 seconds to save it. This becomes quite disruptive while editing.

## **Mathematica's Advantages and Disadvantages**

Mathematica is a powerful program as well, and also contains several unique features. The first is a color-coding system for input that makes a very useful debugging tool. When the user begins typing input, the text is blue. However, as soon as the name matches either a variable with an assignment or a function name, the text turns black. Similarly, unclosed parentheses or brackets are displayed in pink until they are closed. This makes it easy to identify misspellings or syntax errors in your code. The nature of symbolic solvers makes them difficult to debug, and so this feature is very useful for completing a document quickly.

The second feature is referred to as "Computable Data" in Mathematica. Wolfram has compiled huge data sets across a variety of fields including geography, chemistry, linguistics, finances and economy, weather, astronomy, etc. Within each of these fields, there are hundreds of properties that can be accessed for thousands of different objects. For example, Wolfram's chemical data set contains 101 chemical properties for 42,796 different chemicals. These data sets are well curated, constantly updated, and accessible to anyone with a Mathematica license. Maple can access datasets like these from online sources, but it is a much more complicated process, whereas in Mathematica, it is as simple as calling a function.

Finally, this program also has a broader use of hot-keys to improve speed and efficiency of programming. In Maple, the user types the name of the command he or she wants and then has to choose its symbolic representation from a pop-up list. Mathematica does the same, but also has many commonly used symbolic operators hot-keyed. For example, the square root symbol is created with Ctrl+2. In Maple, one would have to type out "sqrt"+Ctrl+Spacebar+Enter. Overall, typing in Mathematica was much faster and didn't require me to move my hands from home row nearly as much as Maple did.

## **Comparison by Judging Criterion**

### **1) Introductory Material**

When initially installed, Maple comes with the Maple Portal, or its “Getting Started” materials, which contains several worksheets with instructions and examples as well as links to online video tutorials. The majority of the tutorials are spent teaching the user where to find the options and capabilities they are looking for through the palettes and context-sensitive menus rather than to how to do specific tasks. Overall, this makes them very quick to learn from and effectively fosters more advanced use of the program.

Mathematica’s “Getting Started” documentation opens every time you launch the program in a Welcome screen, and is comprised of a promotional video, a promotional slide show, and a 22 slide presentation of guided examples. The promotional material is meant to show the user what advanced capabilities the program has, while the guided examples introduce syntax. Three and a half weeks after activating my Mathematica license, I received an email with additional “getting started” material including two video tutorials, which I found to be very helpful. Had I received these videos in a timely fashion or if links to the videos were provided in the Welcome screen, Mathematica’s introductory material would have matched Maple’s in usefulness.

## 2) Symbolic Formatting

Symbolic formatting is the default math input for Maple, and controlling the appearance equations comes naturally from the keystrokes one would use to type an equation in any other program. It is also easy to use subscripts to add descriptors to your variable names. I preferred to use the variable’s measurement type to define its main line representation, such as “r” for radius or “θ” for angles, and then would use a subscript to make the variable unique to what it was representing. The advantage with this approach in terms of “V and V” is that a reviewer could focus on the main-line variable names and ensure that the equation being used was being supplied the correct variable types and in the correct order. Then, he or she could observe the subscripts to verify that the proper specific values are being used. An example of Maple’s input is shown in Figure 4 below.

$$\phi := \begin{cases} \cos^{-1}\left(\frac{r_2 - a\theta_{spool}(t)}{d_{spool, ctr2CPtop}}\right) & \theta_{spool}(t) \leq \theta_3 \\ \cos^{-1}\left(\frac{r_1}{d_{spool, ctr2CPtop}}\right) & \theta_3 < \theta_{spool}(t) < \theta_5 : \\ \cos^{-1}\left(\frac{-r_1}{d_{spool, ctr2CPtop}}\right) & \theta_5 \leq \theta_{spool}(t) \end{cases}$$

Figure 4: An example of Maple input in the form of a piecewise expression with trigonometric functions.

Mathematica, does not distinguish between different types of math input. The single available type can be used for single line or symbolic notation. Unfortunately, unless a user knows the hot-

keys for symbolic notation or knows how to find the symbolic expression palette (neither of which is discussed in the “Getting Started” documentation), then natural keystrokes for writing equations will yield single-line formatted equations. Additionally, Mathematica was not intended to use subscripted variables in its calculations. Subscripted variables do not work with the color coding feature that Mathematica uses to identify errors. They will always appear blue (unassigned) regardless of whether or not they are storing a value or expression.

Furthermore, Mathematica handles symbolic input by shrinking the size of the font used in multi-line expressions. This is the case with subscripts, which by default are made very small. Combining subscripted variables in a piecewise expression with a denominator will make it impossible to read, even at close range. I resorted to using descriptive names such as “spoolRot[t]” as opposed to “ $\theta_{\text{spool}}(t)$ ”. Because of this, and how all of the help documentation is formatted, I have concluded that input for Mathematica was intended to use single-line input, while the output would be formatted in a clean and verifiable way. This was ineffective for my uses however, since I was using dozens of nested piecewise expressions that were constantly substituted into later variables. Within a few calculations, my output was becoming excessively large and difficult to read. I had to suppress the output, and someone reviewing the document would only have the input to verify. An example of Mathematica input using symbolic input is shown in Figure 5 below.

$$\phi = \begin{cases} \text{ArcCos}\left[\frac{\text{radiusSpoolBottom}-\text{radialLeadSpool}+\text{spoolRot}[t]}{\text{distspoolCtr2PulleyTop}}\right] & \text{spoolRot}[t] \leq \theta 3 \\ \text{ArcCos}\left[\frac{\text{radiusCylinder}}{\text{distspoolCtr2PulleyTop}}\right] & \theta 3 < \text{spoolRot}[t] < \theta 5 \\ \text{ArcCos}\left[\frac{-\text{radiusCylinder}}{\text{distspoolCtr2PulleyTop}}\right] & (* \theta 5 \leq \text{spoolRot}[t] *) \text{True} \end{cases} ;$$

Figure 5: An example of Mathematica input. This expression is the same as the example shown in Figure 4.

### 3) Computational Ability and Speed

To compare the speed and power of the differential equation solvers, I ran timed trials on both symbolic programs under a variety of conditions and restrictions. Refer to Table 1 below to view the compiled results of the tests. During the timed runs, three events were timed and compared. The first is *Assignment Time*, which is the time that it took the symbolic solver to accept all of the user’s input and assemble the four ODE’s prior to running the ODE solver. This is usually pretty consistent across the tests since the input is never changed. The second timed event, known as *Solve Time*, records how long the solver took to process the input, solve the system, and process the output into a usable solution, usually in the form of an interpolating function or procedure. The final timer, *Plot Time*, measures how long each program takes to create the 15 plots that display the solution for various intermittent variables.

Table 1: A compilation of the results from timed tests on the symbolic program's differential equation solvers.

	Success	Assignment Time	Solve Time	Plot Time	Total Time
<b>MATLAB Baseline</b>	✓	0:00.002	0:02.27	0:04.18	0:07
<b>Default Solver Settings</b>					
Maple	✓	1:42	0:53	0:10	2:45
Mathematica	✗	0:02	>1:30:00	-:--	-:--
<b>Reduced Error Tolerance</b>					
Maple	✓	1:36	0:21	0:10	2:07
Mathematica	✗	0:02	>1:30:00	-:--	-:--
<b>Fixed Step (<math>10^{-4}</math>)</b>					
Maple	✓	1:38	0:06	0:33	2:17
Mathematica	✗	0:02	0:35	1:01	1:38
<b>Simplified Expressions</b>					
Maple	-	-:--	-:--	-:--	-:--
Mathematica	✓	0:03	0:08	0:14	0:25

In Table 1, there are five scenarios under which the time comparison occurred. The first simply shows how long the original MATLAB simulation took to complete each step. This is used as a baseline from which Maple and Mathematica will be judged. The MATLAB simulation used a fourth order accurate Runge Kutta method, called with its *ode45*( ) function. By observing the *Total Time* column, it is easy to see that neither symbolic solver comes close to the MATLAB simulation time.

Second, *Default Solver Settings* was a timed trial that used each program's default settings within the ODE solver. In both programs, this used an adaptive step solver, or a solver that changes the time step it uses based on how much error is generated, and a Runge Kutta (4<sup>th</sup> order) method. Maple took just under 3 minutes to complete the worksheet, while Mathematica was unable to reach a solution after one hour and thirty minutes, at which point, I aborted the calculation. Every plot that Maple produced matched the MATLAB plots perfectly.

Third, *Reduced Error Tolerance* was a condition that I ran when my research revealed that Maple and Mathematica use much stricter error tolerances than MATLAB by default. For this trial, I reduced the tolerances manually to 1e-3 for relative error and 1e-6 for absolute error, which is what MATLAB's *ode45*( ) function uses. Doing so reduced Maple's solve time by 60%. Unfortunately, Mathematica was still unable to come to a solution within an hour and thirty minutes.

Fourth, *Fixed Step ( $10^{-4}$ )* was a trial where I made the ODE solver use a fixed time step instead of changing it after every iteration. In cases where differential equations are stiff or have discontinuities, the solver might not know how to adjust the time step appropriately, and so it generally defaults to the smallest allowable time step. I concluded that this was why the Mathematica model was not solving. I chose a time step of  $10^{-4}$  seconds because that was the largest that I could use that would produce accurate results in the Mathematica model. The solutions produced by Mathematica were all correct except for the second derivatives of the dof's. Decreasing the step-size further did not resolve this issue, and so the solution was considered partially incomplete. In this test, Maple solved the system over five times faster than Mathematica, but was very slow at producing plots, often taking longer than 10 minutes per plot. In response to this issue, Maplesoft produced a customized plotting module for me that can better handle the solutions generated by large, nested piecewise ODE's. The plotting was significantly reduced and finished in approximately 60 seconds. This made the total time very comparable to Mathematica's solution. It is important to note that Maple's fixed time step solution contains correct representations for the dof's second derivatives in the plots.

Finally, the *Simplified Expressions* trial was only run for Mathematica. After failing two attempts to get in touch with Wolfram regarding the inability of Mathematica to solve my ODE system using an adaptive step solver, I sent my document to Mark Adler, a senior engineer and long-time Mathematica user at JPL. He simplified the document by changing all of the expressions I use to define the ODE's into functions that use the dof's as input. Furthermore, in piecewise expressions that had conditions that were not specified explicitly in terms of the degrees of freedom (rather, they were dependent on other piecewise expressions), Mr. Adler used the symbolic tools to find an equivalent conditions in terms of the dof's. This removed a large amount of repetitive calculations and allowed the default solver settings to produce the first completely correct solution. The equivalent changes have not been made to the Maple worksheet, so a comparison cannot be made.

The amount of work that went into editing the Mathematica notebook was extensive and used a lot of syntax that beginner and moderate users would not understand. The purpose of the evaluation is to see which program would be best for a new user to pick up and begin solving problems without needing heavy editing from an experienced user. Overall, it appeared that Maple has the stronger math engine. It was able to handle the discontinuities, the large sets of nested piecewise expressions, and the simplification more effectively than Mathematica could and consistently provided an accurate solution. Mathematica was only able to solve after the complex simplification was done for it.

#### **4) Types and Quality of Help Support**

While we are working to select the easiest symbolic program to use, inevitably everyone will need help beyond what the introductory material will teach. Therefore, the types, availability, and quality of support that Maplesoft and Wolfram provide for their product is important to review. This evaluation will be divided into two categories: online support and personal support via phone or email.

Both Mathematica and Maple have extensive help documentation for their contents. This is all available within the program or online. In general, Mathematica's documentation seems far better organized. Maple sometimes has multiple help pages that cover similar topics. For example, there is a help page for *dsolve*, *dsolve/numeric*, and *dsolve/numeric/details*. Each page is long and contains a lot of detail, but I often had to search all three to find the information I was looking for. Mathematica's documentation seems to use fewer examples than Maple's equivalent, but I have found that the ones they use are sufficient to show a user most uses of that function.

Furthermore, it seemed that both programs had very unhelpful error messages. In many cases, the error message given would not be related to the problem that needed to be fixed. For example, my Maple model threw an error that said that my input into the ODE solver was not a system of ODE's. Of course, it was a system of ODE's, one of the variables merely didn't have a value assigned due to a misspelling. This same type of problem in Mathematica threw an error that said that not all of my symbolic variables had been provided a value prior to solving. It was completely possible for Mathematica to report which variables did not have an assigned value. In this sense, the error messages were unhelpful at best and misleading at worst. Both programs also provide HTML links in their error messages to open web pages on the results. However, neither program has significant documentation on most of its error messages. I was usually directed to empty web pages or to the function that I used and produced the error with.

In some cases, it is faster to have personal support that can be tailored to a specific problem a user is experiencing. Maple excels in this type of customer support. After completing my Maple document, I had a list of 13 items that I considered important for Maplesoft to address and potentially fix. These items pertained to improving performance and ease-of-use. Maplesoft engineers created two customized modules for me to improve the performance of my worksheet.

The first was an ODE solver package that was more adequately suited for ODE's produced by large, nested piecewise expressions, which reduced solving time by an average of 45%. The second was a plotting module, which was described in the *Computational Ability and Speed* section. This module reduced the plotting time down to a consistent 10 seconds, or an 85% improvement from the standard plotting function. Maplesoft has assured me that both of these custom packages will be integrated into their standard functions for future releases of the software.

Contrarily, Mathematica's personal customer support was not impressive. On two occasions, I attempted to contact Wolfram regarding the program's inability to solve my ODE system with an adaptive step solver. The first time, I contacted the general help support team, clearly outlining my issue, and I received no response. Two weeks later, after viewing the video tutorials for Mathematica, the presenter, Cliff Hastings, offered his contact information and so I emailed him. He was enthusiastic about helping out, and forwarded my email to the appropriate people. Twice afterwards, I heard that my email had been forwarded to other teams. I never heard back after that and so my issues remain unresolved.

## **5) Presentation Methods**

After completing a Maple worksheet or a Mathematica notebook, engineers must be able to share the results of their work with their colleagues, especially if they are not equipped with the program's used. Both programs offer a number of ways to do so. An initial option that is available is to publish the documents to universally compatible formats such as PDF or HTML. Any other engineer should be able to read through the document and calculations in this format with just about any computer.

Secondly, Maple provides a service called MapleNet. Using MapleNet, anyone with access can upload their document to a server. Then anyone connected to that server can access the document with a web browser. These documents are interactive through the use of components, such as slider bars, text boxes, expression windows, buttons, etc. The viewer can alter these components and view the changes that result. They will be unable to edit the equations in the document, but these equations will be visible, so they can decide whether the document is useful for their purposes or not. Mathematica provides a similar feature known as a Demonstration Project. This creates a small graphical user interface (GUI) through which the user can interact with a model and view the changes dynamically. Unfortunately, this feature does not show the calculations used, and so there is a "black box" aspect where the user must trust the source has verified and validated the document. Since avoiding "black box" computations is one of the main reasons to implement symbolic software, this presentation feature is less useful than MapleNet.

Finally, both programs can be used to create a slide show (similar to Microsoft PowerPoint) that is useful for presentations. Maple's Slideshow mode distinguishes between slides by the user's defined collapsible sections. If a section is too long to fit on the screen, it simply trails off the

screen and that data is unreadable. There is no way to choose a different slide start/end point, and so this mode is highly inflexible and not very useful. In Mathematica, a user can create a presentation from a notebook by creating slides and choosing what sections of the notebook are shown in each slide. This is a much stronger and useful tool since there is a high level of control over what is displayed.

## Final Recommendation

In summation, Maple and Mathematica are very similar programs but they have several key differences which I have been isolated and explored through a judging criterion. The preferred program for each category is shown in Table 2 below. Overall, it was apparent that Maple had the stronger math engine powering it, as it was able to obtain a solution in every test it was run though. It also had far superior help support on a personal level, as demonstrated by the customized modules that enabled a faster solution for all problems of this nature. The symbolic input that Maple uses makes  $V$  and  $V$  a much easier process. Finally, it is an easier program for a new user to learn and use, increasing the likelihood that it will continue to be used. Maple is the stronger program in most of the categories, and in the ones deemed most critical.

Table 2: The superior program in the five judged criterions.

Category	Maple	Mathematica
Unique Features		✓
Intro. Materials	✓	
Symbolic Formatting	✓	
Computational Power/Speed	✓	
Quality of Help Support	✓	
Presentation Methods		✓

## **Works Cited**

Gallon, John, and Michael Gradziel. *Bridle and Umbilical Device Characteristic Equations: Revision 6a*. Pasadena, CA: Jet Propulsion Laboratory, 2009.

Mitcheltree, Robert, Adam Steltzner, Allen Chen, Miguel SanMartin, and Tomasso Rivellini. *Mars Science Laboratory Entry Descent and Landing System Verification and Validation Program*. Pasadena, CA: NASA Jet Propulsion Laboratory.

# A Tool to Create *Stories* About Software Evolution

Mark Mahoney<sup>1</sup>, Cassandra Kawell<sup>1</sup>, Isaac  
Rothenbaum<sup>1</sup>

<sup>1</sup> Carthage  
College  
Kenosha,  
WI

{mmahoney, ckawell,  
irothenbaum}@carthage.edu

**Abstract.** Software systems are constantly evolving. However, we do not do a good job of recording data about the code development process and manipulating it into useful information. This paper describes a tool that was created to capture and manipulate data about the code development process. Further, it allows a developer to manipulate this data into stories about how the code in a complex software system has evolved.

**Keywords:** Software Evolution, Documentation.

## 1 Introduction

As time goes by, a developer's understanding of the system they're working on gets better and better. As a result, implementations change to reflect that hard-earned knowledge. One can learn a great deal about a piece of software by understanding how it has evolved. Unfortunately, important evolutionary information is typically lost during the development process due to our current documentation techniques.

Software created for a NASA space mission, for example, is particularly sensitive to the loss of this kind of information. When something goes wrong in the software for a space mission after it's underway, one or more software engineers must analyze the software to piece together the cause of the problem and find a solution. If a long period of time has passed from the creation of that software to its use in a mission (perhaps years later), simply understanding the system is incredibly difficult.

It is true that mission critical software is often very well documented. However, the documentation typically describes the software's state when it was released. Understanding how the software has evolved over time allows engineers to quickly evaluate and diagnose problems, and more importantly, to see what decisions were made along the way. The main problem is that, currently, we do not do a good job of documenting the evolution of a piece of software.

Understanding software evolution is not a new area of research. Research has been going on since the 1980's [2] and continues to this day [1, 4, 5]. It has been observed that long-lived software systems continuously change, get more complex over time, and generally decrease in quality. Most software engineers are familiar with the term

'software rot'. This describes what happens to software over time. Great effort is required to circumvent this phenomenon.

The primary tool to record the evolution of software is Source Control Management (SCM). SCM systems track the state of source code files at fixed points in time. These tools have proven to be invaluable in for managing complex development efforts and do store some history. However, the history that these tools record is very coarse grained.

Electronic files and version control systems only store the state of a set of documents at fixed points in time- if and when a developer chooses to commit. Important evolutionary information is lost since not all pertinent changes make it into the version control system.

Software developers are constantly making decisions about their code without recording the reasons why they make them. Developers add new functionality, find and fix defects, and restructure their code to make it more readable and maintainable. The time in between traditional SCM snapshots can be too long to capture these fine grained evolutionary changes. Furthermore, the meta-information that developers add about the snapshots they check in to the SCM system tend to be short and of relatively little value. This is because describing even a few hours worth of work on source code cannot be summed up easily. The changes made are typically non-linear and touch many different components.

Evolutionary information stored in version control systems is hard to visualize because of the lack of an animated narrative in the successive snapshots. Source control management systems are more like collections of still photographs than moving pictures. Still photography is not ideal when trying to capture evolutionary changes. Moving pictures do a much better job [3]. One cannot easily use a 'diff' tool to get a complete picture of how a system has evolved. Similarly, one cannot simply examine a series of commit logs to get an accurate picture of the historical evolution of a set of files. Version control systems store some historical information but not nearly enough to breathe life into static, lifeless code repositories.

Evolutional information is valuable to the author of the code because the reasons for the decisions we make do not stay in our heads very long. It is valuable to any other developer who has to maintain or understand the source code. It is valuable to new team members so they can see how the code has evolved from inception to the present state. It is also valuable as a learning tool to experience how other people go about developing code.

A storyteller armed with this information can explicitly show what is important, to whom it is important, and how one piece relates to another. Occasionally, the same information can be found in traditional written documentation but most authors don't put in the effort to guide the reader to those conclusions. It takes a good deal of effort to understand most technical documents. Stories, on the other hand, are inherently digestible.

If moving pictures are better for telling stories about evolution, then one might ask why we use the equivalent of a still medium (version control systems) to record

programming history? It would seem the equivalent of a moving medium would allow us to understand our systems better. If we have this information we can tell interesting stories about how our systems have evolved. We can tell Architecture stories, Feature stories, Algorithm stories, Refactoring stories, Security stories, Bug Fix stories, Debugging stories, etc. A story is not required for every single aspect of a system, only the really interesting and useful aspects warrant a story. The uninteresting parts of the system are still very important and are present in the code and can be referenced when necessary.

## 2 Our Tool

With this idea in mind, we created a brand new tool to capture evolutionary information and provide tools to manipulate it into stories about how a system has evolved. The framework we created is embedded into a typical source code editor and records every single keystroke, typical file operations (creating a new file, etc.), and cut/copy and pastes. If the time in between commits is too long, then why not use the smallest possible time in between commits?

The programming events are stored in a database rather than in files. Each event is retrievable and no historical information about the development of source code is lost (as is the case with leaky electronic files and version control systems). Each event is related to an abstract file and associated with the developer who created it. An abstract file is a collection of events that represent a file. True electronic files can be generated at any point in time in the history of the system to be consumed by tools that require them- like compilers, interpreters, and even version control systems. In addition, one can playback the events in different orders and with different filters to emphasize interesting bits of code while skipping past uninteresting bits.

### 2.1 Playback

One of the inspirations for this work came when one of the authors experienced a series of coding decisions being played back on the screen during a very long 'undo/redo' operation that is common when programming. Most programmers have written some code, decided it was not the right solution, wiped out the work and started over. Then, while working on the new solution they recall that there is a piece of code from the old solution that might be useful. So, they continuously 'undo' in their editor until they're brought back to the original solution, copy the code in question to the clipboard, and then 'redo' until they are back to their new solution where they paste the copied code from the clipboard. Watching that code be played back during the 'redo' can be fascinating. One can reflect on all the tough decisions made over the course of a long programming session. Watching the decisions play out can cause a developer to form a narrative about the code being developed. This information is hard to embed in code comments and is unlikely to be documented anywhere else.

The idea behind playback is to be able to capture these scenarios and use them to tell stories about how the system was constructed and how it has evolved. A story can be created each time the developer has reached a commit point. A *story* about the changes since the last commit is typically far more valuable than a traditional commit

message. These playbacks are recorded and audio is added from the developer to make a moving picture. An animated story with audio from the developer shows the changes while they are still fresh in the mind of the developer. Further, stories can be created that cut across commit points about larger issues- such as stories about features, architecture, and so on.

Our tool extends simple playbacks such as the ‘undo/redo’ scenario above so that the entire history of events is available for playback. Events from multiple files can be a part of a single playback and there are several sort orders, groupings of events, and filters that can be combined to create interesting scenarios. The time in between events being displayed is an adjustable parameter so playback can be sped up or slowed down while the playback is under way.

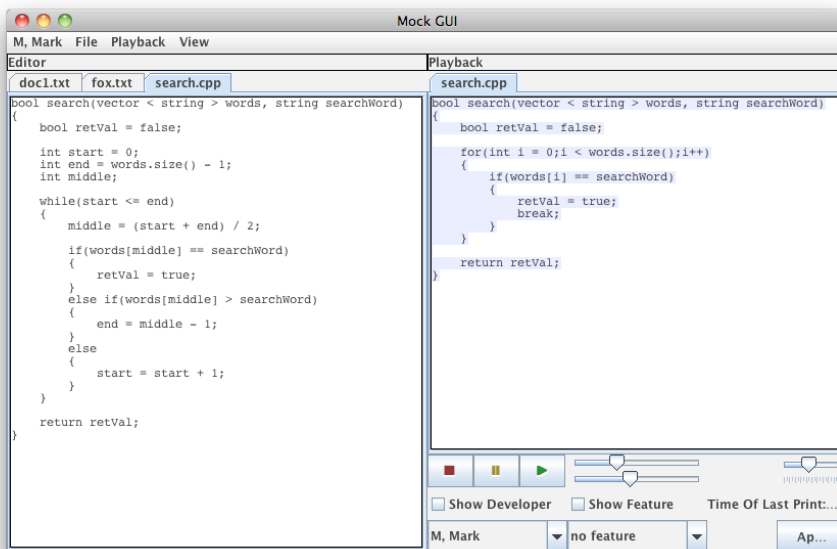


**Fig. 1.** This shows the tool with an editor window opened (left) and a playback window opened (right). The playback window is in the middle of playing back the development of a search function that started as a linear search but then evolved into a binary search.

## 2.2 Clips and Storyboards

The metaphor we used when creating the tool was to emulate video editing software. Most video editing software allows one to import clips or snippets of video and place the snippets on a timeline. A ‘movie’ is created by running through all the snippets in the order specified by the moviemaker. The snippets and the timeline are editable.

Playbacks can be stored as clips. A clip holds the parameters for the playback so that it can be recreated at anytime. One can group clips into storyboards. A storyboard is a container of clips that allow them to be played back as a single unit. Clips and storyboards can be used as a new form of documentation. Once an interesting storyboard has been produced one can make a moving picture showing how some aspect of the code has evolved. Screen capture tools allow one to record what is happening on one’s computer screen and provide audio input. A movie can be created

by recording the screen during a playback. While the playback is being recorded, a developer explains the context that is not apparent from the code itself into a microphone. The audio from the developer and the playback combine to make a new and very powerful form of documentation.

### 2.3 Types of Playback

In order to tell compelling stories a developer needs to be able to quickly and efficiently manipulate the enormous amount of data that is recorded. Playback was designed so that interesting bits of code can be isolated and uninteresting bits can be skipped.

The most straightforward type of playback is called *Playback By Time*. In this type of playback all relevant events are ordered by the time they were created. The events are then played back with a certain amount of time (this time is adjustable during a playback) in between successive events. This is useful for when one is interested in showing how some code has changed over time. For example, a line of code, a block of code, a method, a file, or all files can be shown in the order they were created. This shows how the software has evolved through every painful dead end, refactor, optimization, and plain old wrong solution. This is very important information that tends to escape into the ether over time or walks out the door when there is turnover. One can use this information when adding new features, fixing bugs, or trying to understand why someone did something one way instead of another.

However, there are times when one doesn't need to see a complete history in order to tell a compelling story. Sometimes mistakes we make aren't worth rehashing. Some of the dead paths that we go down are better left forgotten. For these situations *Playback By Position* is preferred. In this case, selected events are shown in their final positions. In other words, events that were inserted and then later deleted are ignored. After seeing this type of playback it can best be described as a *Perfect Programmer* experience. A selection of code is shown how a perfect programmer would have written it (even if that was not how the developer actually wrote it). There are no mistakes or alterations and relevant code is played back left to right, top to bottom. This is useful for emphasizing the good solutions while skipping the bad ones.

Combining clips of the two types of playback into a single storyboard affords the most flexibility in creating a story. Sometimes we care about the history of a chunk of code, other times the history would just get in the way of describing the latest and greatest solution. Being able to mix and match the two styles in different sections of code yields a powerful storytelling tool.

### 2.4 Filters

Each event is associated with a developer who created it and, optionally, a feature. One can then filter events by either of these parameters. A filter marks certain events as relevant and highlights them during playback. Events that don't meet the conditions of the filter are marked as irrelevant and are dumped to the document in large groups to show the context. Highlighting keystroke events created by a developer can quickly show which developers have contributed to a selected section of

code. This information can be used to indicate how much a developer knows about the selected code, what influence they have had on it over time, and to help choose the best person to fix a bug or to extend the code. This information is typically not available in traditional version control systems and can help bring order to the tangled mess of interactions multiple developers have with a file. In the tool, one can choose a developer during playback and have their events highlighted.

## 2.5 Time Frames

Playbacks can be specified by different time frames. One can choose to see the entire history of a group of abstract files or one can narrow the selection down to a specified time frame measured to the second. The prototype allows a user to enter in a start and end time for each playback. Only events in that time frame will be played back.

Whenever a start time is chosen that comes after the first recorded event, the events to be played back might be interspersed with events that were created before that time. The tool accounts for this by recreating the files up to the start time. Events in the specified time frame then have an accurate context to work from. As a result, at the beginning of a playback one sees the state of the files at the start time and then relevant events are injected into the file abstractions one by one.

**Acknowledgments.** The NASA Wisconsin Space Grant Consortium generously provided support for this research. Carthage College also provided support for two Summer Undergraduate Research Experience students.

## References

1. International Workshop on Principles on Software Evolution, <http://www.pleiad.cl/iwpse-evol/>
2. Lehman, Meir M., "Programs, Life Cycles, and Laws of Software Evolution". Proc. IEEE 68 (9): 1060-1076. 1980.
3. Mahoney, M., Software Evolution and the Moving Picture Metaphor. Onward! Essay held in conjunction with OOPSLA 2009 Orlando, Fla. 2009
4. Mens, T., Demeyer, S., (Eds.) Software Evolution. Springer; 1 edition March 11, 2008
5. Mining Software Repositories Conferences, <http://2011.msrconf.org/>

# Experimentation for Diagnostic Algorithm Benchmarking

Callie Kwiatkowski<sup>1</sup>

Department of Mathematics, University of Wisconsin–Milwaukee,  
Intelligent Systems Division, NASA Ames Research Center

## Abstract

NASA Ames Research Center and Palo Alto Research Center have jointly developed a software framework to quantitatively assess the effectiveness of diagnostic algorithms in detecting and isolating known faults injected into complex systems. This framework has been used in a diagnostic competition series held annually at the International Workshop on Principles of Diagnosis (DX). This competition is specifically designed to provide algorithm developers with software tools and data that allow for advancement and maturation of diagnostic techniques. To provide data for a third diagnostic competition, an Electrical Power System (EPS) has been used to inject faults in a controlled manner. Experiments consist of nominal, as well as single, double, and triple fault runs. Faults may be manually induced (unplugging a load), induced through software (opening relays), or added later using Perl scripts (temperature sensors). Once acquired, the data must be processed to ensure that time stamps are accurate, there are no glitches or anomalies, and we have consistency with previous competitions.

## Nomenclature

DP1 = Diagnostic Problem One  
DP2 = Diagnostic Problem Two

## Introduction

In 2009, NASA Ames Research Center and Palo Alto Research Center began a diagnostic competition series held annually at the International Workshop on Principles of Diagnosis (DX). As a contribution to the study of Systems Health Management, this competition series utilizes a software framework to assess and develop computational techniques for the monitoring and diagnosis of complex systems. As well, this competition series provides a forum that can be used by algorithm developers to test and validate their technologies on real-world physical systems. During the competition, algorithms are assessed on their effectiveness in detecting and isolating known faults, and in deciding the correct recovery action in response to any scenario. To provide data for a third diagnostic competition, an Electrical Power System (EPS) has been used to inject faults in a controlled manner. Experiments include a distribution of nominal runs, as well as single, double, and triple fault runs. Faults are induced manually (unplugging a load), induced through software (opening relays), or added later using Perl scripts (temperature sensors). Before experimentation, a run schedule must be written to ensure new data can be analyzed in collaboration with the results of past competitions. Once acquired, the data are processed to ensure that time stamps are accurate, there are no glitches or anomalies, and the behavior of the system is consistent with previous competitions.

## DP2 Configuration

---

<sup>1</sup> Wisconsin Space Grant Consortium

**Preparation.** The DXC11 competition is considered a rematch for the DXC10 competition. Consequently, all of the data used in DXC10 is again used in the 2011 competition. To prevent an unfair advantage of already being exposed to the data, or an advantage that is not accounted for in the project, new data must also be added. The collection and processing of this new data is the goal of the summer 2011 internship. To keep the number of experiments at a manageable level only half as many supplemental runs were taken. The competition is organized into two set ups called Diagnostic Problem One (DP1) and Diagnostic Problem Two (DP2). In the end, sixty new experiments were collected for DP2 and seventy-seven were collected for DP1. As mentioned earlier, this new data must include a distribution of runs consistent with the previous data. To accomplish this, the first step was to make a tally of the different combinations of faults used in DXC10. Not only did this tally take into account the number of nominal, single fault, double fault, and triple fault runs, but it also noted the number of recovery actions, or commands required for each type of fault. The distribution decided upon for the new DP2 data can be seen in Figure 1. The second step, which will be discussed further in the next section, was to create a run schedule laying out exactly which faults will be injected at what time and what the correct response would be.

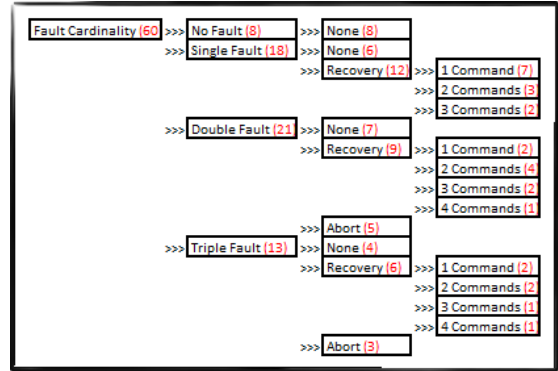


Figure 1. DP2 Fault Distribution

**Experimentation.** The Electrical Power System test bed used for DP2 experimentation was set up in the arrangement pictured in Figure 2. There are twenty-four possible nominal configurations that can be implemented. For all nominal configurations, the two load banks are each connected to one of the three batteries. Each load bank consists of six AC loads (fans, light bulbs, small water pump) and one DC load. Also found throughout the system are relays, circuit breakers, two inverter boxes and a variety of sensors which keep track of data such as temperature, current, and voltage levels. Each nominal configuration includes a group of AC loads and one DC load. The choices for AC loads are either the loads connected to relays EY170, EY171, EY270, and EY271, or the loads connected to relays EY174, EY175, EY274, and EY275. In either case, a group of three light bulbs, a fan, a water pump, and a lamp will be on. The DC load can be either DC482 or DC485. Some of the loads and sensors are considered critical and some are not. All of the above mentioned AC and DC loads, along with certain sensors, are considered critical. If a critical load experiences a problem, or “fault,” a recovery action must be taken. For example, if the water pump on load bank 1 loses function, the correct recovery action would be to turn on the water pump on load bank 2. If a sufficient recovery action is not available then the correct response is to “Abort.” If a fault occurs that only affects a non-critical load, such as if relay EY172 opens causing FAN480 to lose power, then a recovery action is not required. It is the algorithm developer’s job to determine the proper response for each experiment.

Actually running the experiments was a bit complicated at first. There were many steps to get used to. First a variety of programs must be started each on separate computers. Generally, if one step of the process is not done in precise order exceptions may be thrown and the whole system

could crash. If that happened, one or more experiments would be lost and they would have to be performed over again. As well, all of the programs would have to be shut down and restarted in the correct order. The first couple days of experimentation system crashes were a frequent occurrence. Some of the time a mistake would be made in setting up the system, but often times the system would still crash on its own even when every step was done right. One possible explanation was that the computer network for NASA Ames Research Center was noticeably busy at the time.

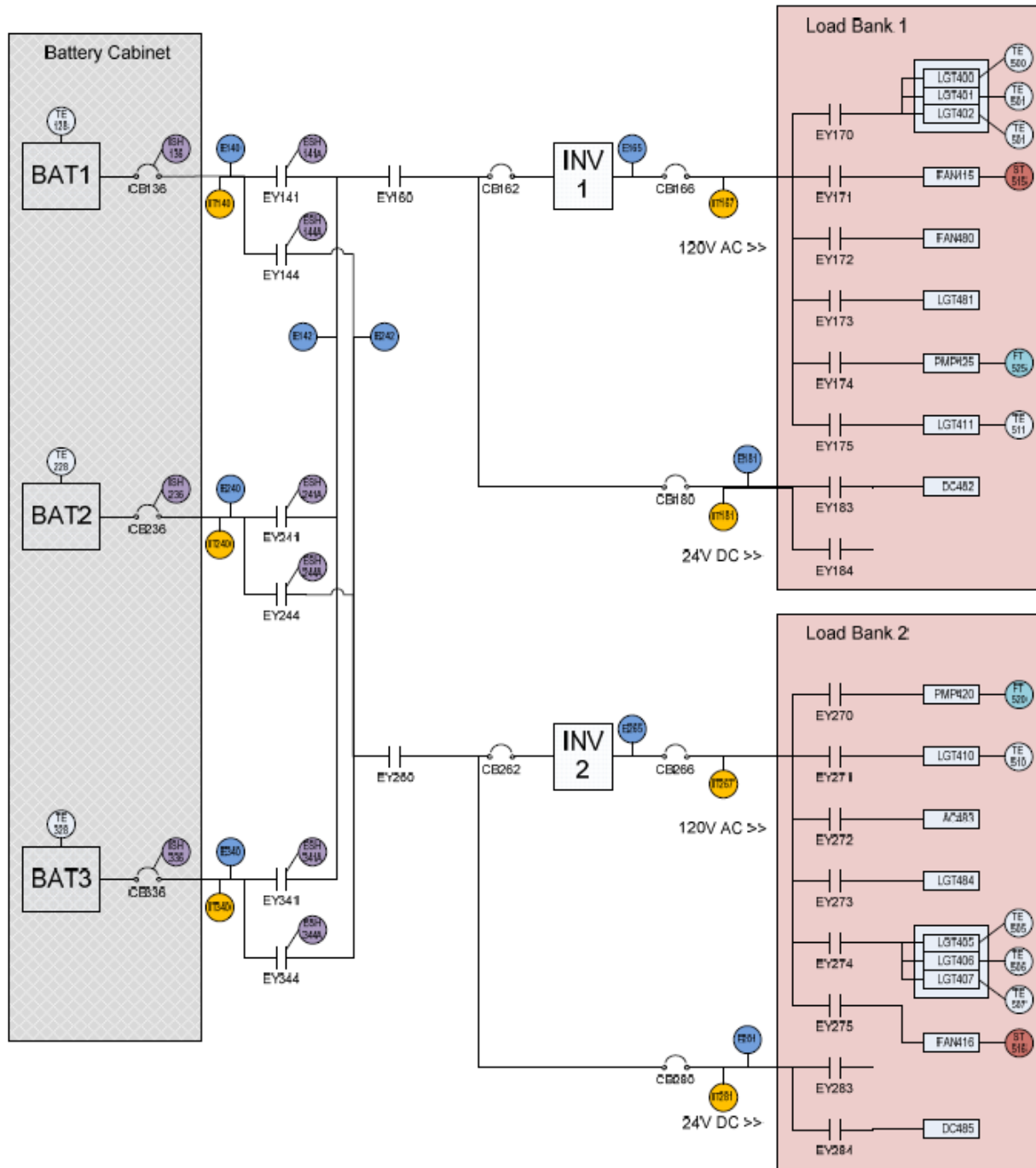


Figure 2. DP2 Configuration

The setup process for experimentation was as follows. First the computer called the Observer and its corresponding programs were started. The Observer provided a visual representation of the test bed on screen. It also has the controls to start an experiment. Second, the ADAPTDQA, which stands for ADAPT Data Acquisition, and its programs were started. This is used to establish communication between the computers and the test bed. Then the data it receives is sent to the Observer and displayed on screen. The Antagonist is next started. Its programs are used to inject the fault messages into the system. In the case of software faults, the Antagonist injects the actual fault into the system. Fourth, the User is started. The User provides the ability to turn the loads on and off and to connect the batteries to the load banks. Finally, a remote desktop connection is established for the ADAPT Database (ADAPTDDB). The program started on ADAPTDDB is used to store the data collected into a permanent file.

Once the entire computer system is set up experimentation can begin. First the details of a particular run must be established on the Observer such as what nominal configuration is going to be used and what faults will be injected. Once an experiment has started, the loads that make up the decided upon nominal configuration need to be turned on using the control panel on the User before thirty seconds have passed. Then the non-critical loads FAN480, LGT481, AC483, and LGT484 may be turned on and off periodically. Doing so not only tests the algorithm developer's ability to recognize the change in data is due to a non-critical load instead of a fault, but it also brings character to the data. When a fault run is occurring, the fault inject message is sent using the Antagonist and it is timed so that the actual fault is injected as close to the same second as possible. This may mean setting the fault inject message to be sent ten seconds after it is initiated on the Antagonist, leaving ten seconds to walk over to a load and shut it off as soon as a beep is heard, indicating the fault inject message has been sent. To finish the experiment, the system is stopped at precisely four minutes and then the data file is collected from the ADAPTDDB. Before starting another run, all loads, relays, circuit breakers and inverters boxes need to be returned to their nominal state. Also, time must be given for the light bulbs to cool back down to room temperature.

*Experiment 1678.* Experiment 1678 is a prime example for the type of data collected during a run. It is a triple fault run and it includes a sensor fault, software fault, and a manual fault. In Figure 3 the outcome of the sensor fault can be seen. Sensor ST516 measures the speed in rotations per minute (RPM) of FAN416 on the second load bank. After 53 seconds ST516 experiences a fault where the data the sensor takes from the fan is offset by -600 RPM. This does not mean that the fan itself suddenly dropped speed, but simply the reading by the sensor is being altered. The software fault can be observed in Figure 4. Relay EY274 is opened at 125 seconds causing three light bulbs to lose power. Since in this configuration load bank 2 is connected to battery 2, the level of current drops about 3.25 Amps near battery 2. At 190 seconds a manual fault was injected. Circuit breaker CB166 is opened causing the AC loads on load bank 1 to lose power and voltage to increase around 0.25 Volts near battery 1. This can be seen in Figure 5. ST516 is considered a critical sensor and is connected to a critical load. EY274 is also connected to a critical load. Initially, the correct response would be to turn on the corresponding loads in load bank 1. However, the fault of CB166 eliminates that solution. Thus, the combination of these three faults would require an "Abort."

## **Post Processing**

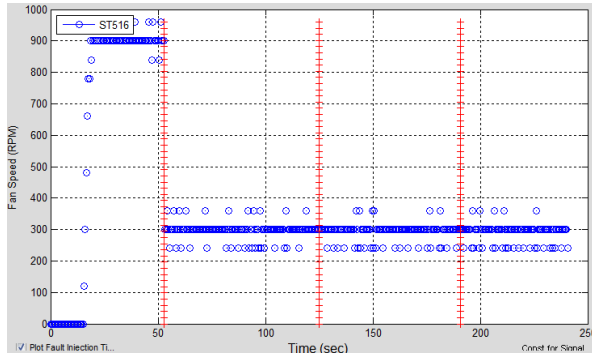


Figure 3. Sensor Fault ST516 Offset

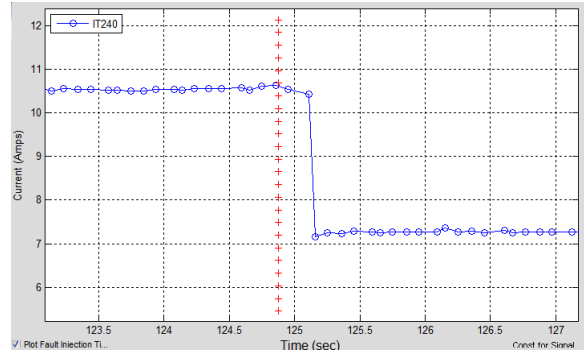


Figure 4. Software Fault EY274 StuckOpen

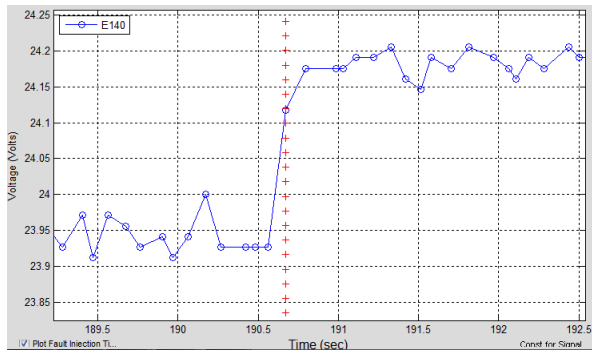


Figure 5. Manual Fault CB166 FailedOpen

*Compare to 2010 Data.* Running the experiments is only half the battle. Once the data has been collected, it is then looked over to check that time stamps are accurate, there are no unexpected glitches, and the data is consistent with past competitions. When comparing the new data to the data of DXC10, there are a few things to look for. First, the data of a particular experiment must reflect the nominal configuration that it was claimed to have. For example, sensor ESH141A should not read ‘zero’ if battery 1 was said to be connected to load bank 1. If

relay EY141 is closed then ESH141A should read ‘one’. These types of mistakes can easily be identified by viewing the graphs of the data side by side with the graphs of the data for a past experiment which has the same nominal configuration. Of course if an inconsistency is found, it is also necessary to double check that it is not the past experiment with the issue. It is also important to note whether the readings coming from each sensor are at relatively the same level as past data. Not all data, especially from the temperature sensors, will be exactly the same as last year but they should be close. Any data which is at a noticeably different level should at least have a reasonable explanation for why the behavior is different. As well, the change in level may not significantly affect other aspects of the project in order for the experiment to be used in the competition. Finally, if there is any weird behavior in the data, it must be compared to last year’s data to see if similar behavior occurred. If no similar data is found then the run must either be fixed or discarded.

*Insert Sensor Faults.* As mentioned before, sensor faults are added using Perl scripts after an experiment has been taken. This may mean adding sensor faults to a nominal run to create an experiment with purely sensor faults, or adding a sensor fault to a run which currently has manual or software faults. Either way, the process is the same. The first step is to view the graph for that particular sensor. Then consider what kind of fault will be injected. Commonly sensors experience an offset, as was the case in Experiment 1678, or they get stuck at a particular value and don’t change for the rest of the run. When choosing the degree of offset or the value at which the data gets stuck, the decision must create a visible change in the data. What type of sensor is being modified also plays a role. Sensors associated with relays and circuit breakers, such as

ESH244A and ISH136, can only take on the values one and zero. Therefore, any stuck or offset fault is limited by those values. Once a value has been chosen, the parameters for the fault are specified in a faults.txt file and then this file is used with a series of Perl scripts to inject the change. The final step is to view the updated graph and make sure the change is sufficient.

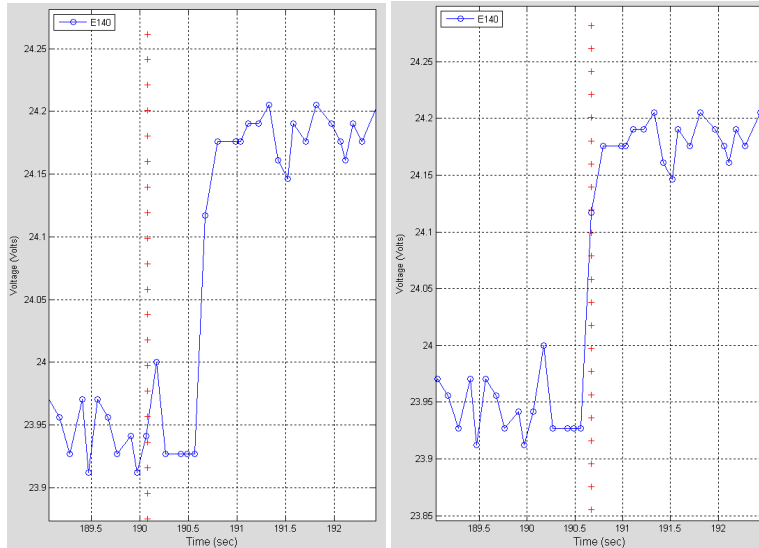


Figure 6. E140 Time Stamp Before (left) and After (right)

*Adjust Time Stamps.* Pictured in Figure 6 is the battery voltage read by sensor E140 for Experiment 1678. As mentioned in the previous section, circuit breaker CB166 is opened, causing AC loads from load bank 1 to lose current and the voltage near the battery to increase. Unfortunately, as seen from the red line in the graph on the left, the time stamp of the fault does not perfectly match the change in data. Manual and software faults have a delay caused by either the reaction time it takes a human being to flip a switch, or

the time it takes for multiple programs to communicate while organizing the data. Time stamps for manual faults, such as this one, were adjusted to match the earliest sign of the fault in the data (right graph). Software fault time stamps are adjusted to match the fault inject command of the Antagonist. The time stamps of sensor faults do not need to be adjusted because the exact intended time of the fault is specified in the faults.txt file. Adjusting time stamps can be tricky and since choosing the time of the fault is partly dependent on the visual perception of the person editing, the outcome may fluctuate slightly. Both manual and software time stamps are shifted simply editing the text file for that particular experiment.

*IT281 and IT240 Glitches.* Despite careful planning, reliable and tested equipment, and a soundly developed framework, glitches and anomalies do occur in the data. Two particularly persistent culprits are the sensors IT281 and IT240. Both of these sensors measure the current flowing through different parts of the Electrical Power System test bed. In Figure 7 can be seen an example of an IT281 glitch. Sensor IT281 is located on the second load bank and measures the current flow near the DC load. As seen in the left picture, chunks of the data are found out of place. These “glitchy” chunks may be manually shifted to their proper position using Excel. First, the graph for the sensor is viewed to determine an approximate value for which the glitch needs to be shifted up or down. Then that value is added or subtracted from each of the necessary data points in the text file. A separate graph is viewed in Excel and the exact value of the shift is adjusted until the glitch is no longer noticeable in the graph. The cause is currently unknown but these glitches must be fixed so that algorithm developers do not mistake them for faults.

### Collect Finalized Data.

Once post processing is perceived to be complete, all sensor glitches are fixed to satisfaction, time stamps are properly placed, all types of faults have been included, and the experiments have been compared for consistency with past competitions, there are a few steps left before the data is ready for the next competition. The graphs of the data are created in a Matlab file which is produced from each experiment's text file.

These Matlab files must be updated each time a change

has been made to its corresponding text file. Once everything has been updated and perfected, a .scn file is also created for each experiment. A .scn file is just a text file of a different format used by some of the algorithm developers who enter the competition. Then another Excel file is created using a Perl script which collects and summarized all of the basic information about each experiment into one table. It includes information such as file name, what faults were injected, the times the faults were injected, and what the proper recovery action should be. Finally this summary file along with the .txt file, .mat file, and .scn file for each experiment is collected into a .zip file for review. All of the data is then looked over by another party and assessed for any issues. Sometimes changes have to be made and these last few steps are repeated multiple times until the collection of data is perfected.

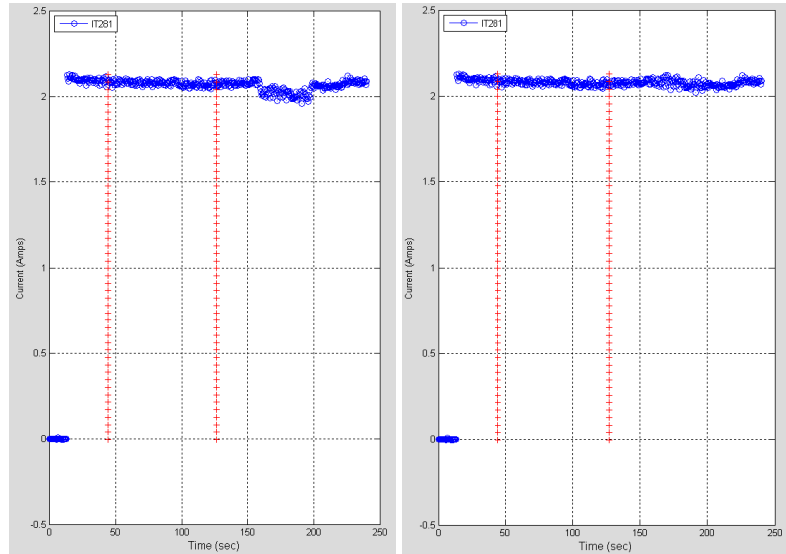


Figure 7. IT281 Glitch Fix Before (left) and After (right)

### DP1 Configuration

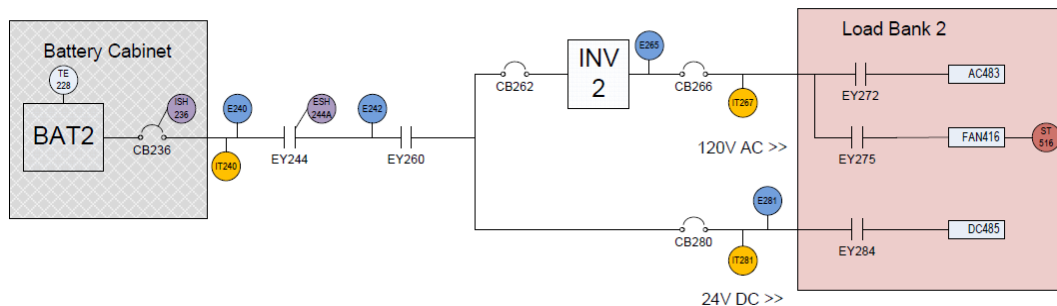


Figure 8. DP1 Configuration

**Set Up and Distribution.** Although much time was spent on perfecting the data from Diagnostic Problem Two, Diagnostic Problem One also had some cleaning up to do. The majority of the experiments had already been taken before this internship began. However, the data needed to be organized and a large amount of post processing was waiting to be completed.

As seen in Figure 8, the configuration for DP1 is made up of some of the same components as found in DP2, only rearranged differently. For DP1, the nominal configuration is always the same with battery 2 connected to load bank 2 on which AC483, FAN416, and DC485 are connected. Another difference with DP1 is that all of the loads are turned on before the start of an experiment. This makes taking nominal runs extremely easy as all that needs to be done is to start the experiment and then stop it after four minutes. Finally, since there is only one load bank, it is impossible to find a recovery action for each of the faults. Therefore, every experiment can either result in an “Abort” or “NOP,” meaning no action is taken.

## Post Processing

*Time Stamps and Glitches.* Just as with Diagnostic Problem Two, Diagnostic Problem One required both shifting time stamps and fixing glitches. The issues with, as well as procedure for fixing time stamps is much the same as with DP2. The time stamp for a manual fault should be shifted to match the first visual sign of the fault in the graph. Similar to DP2, this will often mean looking at the graphs of E240 and IT240, which measure the voltage and current near the battery, and then editing the text file accordingly. The software faults, which are again the relay faults, need to share the time stamp of the Antagonist fault inject message. The time stamps for sensor faults do not need to be shifted as their exact time of injection is specified in the faults.txt file. Once the time stamp for the fault has been moved, the Matlab file for that experiment must also be updated. Then the graphs of E240 and IT240 are viewed again to see that the fault inject indicator line has been sufficiently shifted.

Unfortunately, sensor glitches were abundant in Diagnostic Problem One. The only noticeable difference with DP1 from DP2 is that IT240 also needed fixing, while the single culprit for DP2 was IT281. The same procedure was used for identifying and fixing these glitches. The new data was viewed and compared side by side with data from last year. Glitches are easily recognized as chunks of data which are randomly shifted up or down in respect to the rest of the run. Often these “glitchy” chunks are noisier than the rest of the data and they are usually shorter segments of time. Once a glitch is identified, the value that it needs to be shifted up or down is approximated. Then the change is made and perfected by viewing the data and editing the text file in Excel. Finally, the Matlab file is updated and the graph is viewed to check that the change has been made correctly.

*ResistanceOffset Faults.* Another difference with Diagnostic Problem One is that new types of faults occur. One type of fault not found in DP2 is called ResistanceOffset. This is where the resistance level at either AC483 or DC485 is offset from its nominal value. The nominal resistance value for the AC load is 80 Ohms. The nominal resistance value for the DC load is 9.5 Ohms. These are ideal levels. The nominal levels during an actual experiment fluctuate somewhat. Figure 9 is the graph of the current read by the sensor IT240 for Experiment 1526. In this experiment the

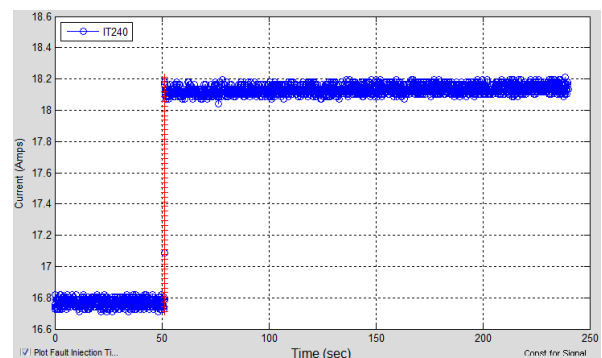


Figure 9. ResistanceOffset AC483

resistance for AC483 is offset -11 Ohms from its nominal level. With this decrease in resistance, the current near the battery increases about 1.35 Amps. There is an imperfection in the programs used where the text file for an experiment records the resistance once the fault has been injected, while the offset is what is really needed. This offset can be calculated for the text file simply by subtracting the ideal resistance from the resistance recorded after the fault. The way to determine whether a ResistanceOffset fault is an “Abort” or “NOP” depends on an abort threshold. The abort threshold for an AC483 ResistanceOffset fault is -16.8 to 29.1 Ohms. If the offset is outside of this threshold then it is considered an “Abort.” Otherwise it is considered a “NOP,” and no action is necessary. The offset for this experiment is within the abort threshold; therefore, no action is taken.

*ResistanceDrift Faults.* Another new fault found in DP1 is the ResistanceDrift fault. This is where the resistance at AC483 or DC485 gradually increases or decreases according to a specified slope. There is again an issue with the text file. Instead of recording the slope for the fault, the resistance after the fault occurs is recorded. This calculation can be approximated by subtracting the nominal resistance from the recorded resistance and then dividing that by the time the experiment ends subtracted by the time the fault is injected. This way the text file will have the change in resistance divided by the change in time. A ResistanceDrift fault is determined to be an “Abort” or “NOP” according to its own abort threshold. The abort threshold for a DC485 ResistanceDrift fault is -1.5 to 2.5 Ohms. In order to tell how much the resistance has been shifted the graphs of current sensors must be viewed and the relationship between the rate at which the current increases or decreases and the rate at which resistance changes must be assessed. Experiment 1553, as seen in Figure 10, would be considered an “Abort.”

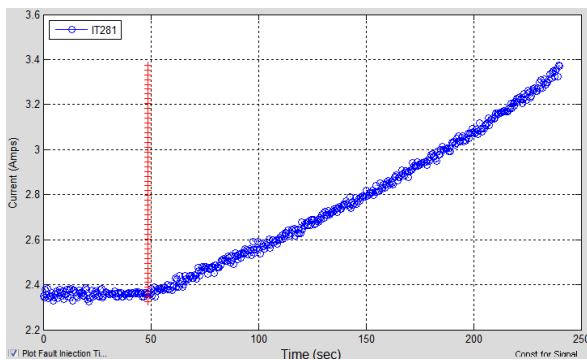


Figure 10. ResistanceDrift DC485

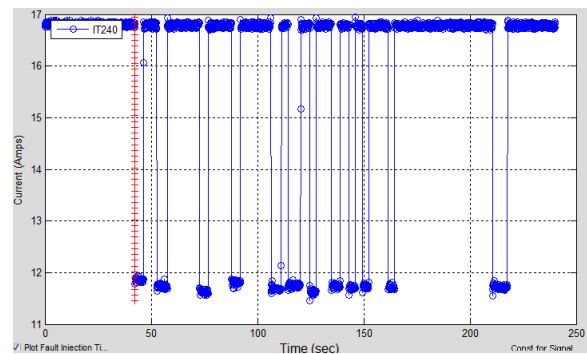


Figure 11. Intermittent ResistanceOffset AC483

*Intermittent ResistanceOffset Faults.* The final fault unique to Diagnostic Problem One is the Intermittent ResistanceOffset fault. As the name suggests, this is similar to the ResistanceOffset fault, except the data periodically shifts back and forth between its nominal resistance level and its offset resistance level. Inconveniently, there are certain parameters from the data that must be written down while the experimentation is taking place. These parameters are the MeanOffset, MeanFaultDuration, and MeanNominalDuration. Although the ideal values for these parameters are chosen ahead of time, the actual values recorded from the experiment are slightly different. These actual values need to be added later to the text file for a particular experiment. Unfortunately, these values were not written down when some of the experiments were taken. Thankfully, however, these types of experiments are much easier to implement than the

experiments for DP2. First all three loads are turned on before the experiment is started. Then the ideal parameters are specified using a feature found in the program loaded onto the ADAPTDAQ computer. Then the nominal configuration and fault information are specified on the Observer. After the experiment has been started, the fault inject message and the actual fault are injected on the Antagonist. Intermittent ResistanceOffset faults must be injected between thirty and forty-five seconds into the run so that the intermittent behavior can be adequately viewed. It is not necessary to turn on or off any additional loads, as the only three loads included in the system are considered critical. It is only important to remember to write down the actual parameters discussed earlier. The experiment is again stopped after four minutes and the text file for the run is collected and later post processed.

*Final Steps.* Once the Intermittent ResistanceOffset experiments have been collected and post processed, there are only a few loose ends to tie up. First, there were not enough nominal runs taken and sensor faults still needed to be added. The process for adding sensor faults for DP1 is the same as it was for DP2. Once all of the data has been taken, sensor faults are added and every experiment is edited to satisfaction, the .scn files are again created. As well the summary file is created similar to DP2. Then the .txt file, .mat file, .scn file and summary file are collected into another .zip file for review. This collection of files is finally looked over by a second party and tweaked to perfection. Then the data for DP1 and DP2 is complete.

## **Conclusion**

This project has developed extensively over time, but there are still questions to be answered and things to be perfected. For instance, why do temperature sensors show minor differences when they should all read the same value when the instruments are at room temperature? What causes the IT281 glitches and how can they be prevented? Can code be written to make the fault time stamps accurate automatically? This project took a lot of time and patience. It was necessary to insure that the data collected reflected that of past competitions, all of the time stamps were accurate, and all of the glitches were fixed. Although Diagnostic Problem One offered many differences from Diagnostic Problem Two the dedication toward preparing quality data was the same. Once the competition data is final, the algorithm developer's adventure has only just begun.

## **Acknowledgments**

I would like to thank my mentors Scott Poll and David Nishikawa for all of their help and support in this project. As well I would like to thank Wisconsin Space Grant and NASA Ames Research Center for making this unique opportunity possible. Finally, I give gratitude to my family, friends, and fellow interns for their encouragement and shared experiences along the way.

## **References**

Poll, S., de Kleer, J., Feldman, A., Garcia, D., Kurtoglu, T., and Narasimhan, S., "Second International Diagnostic Competition (DXC'10)," 2010.

# **21st Annual Conference Part Seven**

Physics and Astronomy

# Structure and Behavior of AWM and MKW Clusters

Michael Ramuta<sup>1</sup>

Astronomy Department, University of Wisconsin-Madison

## Abstract

A grasp of the life-cycles of large-scale structures is critical to understanding the Universe. This can be accomplished through the study of poor clusters-- that is, younger clusters that are likely evolving to another state. The selected clusters are significant in that they are poor but also possess a type-cD galaxy. This brighter central galaxy suggests that these clusters may be dynamically evolved and are potential candidates for fossil groups. In order to more fully understand the structure and behavior of poor galaxy clusters, 13 clusters were selected and analyzed. Using data from the Sloan Digital Sky Survey, we present structural descriptions and mass estimates of these 13 galaxy clusters.

## Procedure

The 13 clusters had originally been selected by Morgan, Kayser, & White (1975) and Albert, White, & Morgan (1977) in searches for poor clusters with type-cD galaxies. With the SDSS, spectroscopic data was found for 983 galaxies within the 13 clusters, increasing Koranyi & Geller's count by 572. With right ascension, declination, redshift, and brightness data of galaxies within the clusters, a series of graphs were made to observe substructure. Histograms were made measuring redshift distribution of clusters with fitted Gaussian curves [figure 1]. Clusters were plotted with galaxies colored on a gradient such that the galaxy with the highest velocity was red and the galaxy with the lowest velocity was blue. The large circle represents the half-light radius and the small circle surrounds the type-cD galaxy. To more easily analyze structure, galaxies over select velocities were changed to symbols while the rest remained black dots for contrast [figure 2]. Clusters were then plotted measuring the distance from the type-cD galaxy against the difference from the average velocity of the system [figure 3].

## Mass Determination

Mass Determination: To estimate the mass of the clusters, the half-light radius around the type-cD galaxy was used as the effective radius and the velocity dispersion was measured as the standard deviation of the velocities. A mass approximation similar to one used by Heisler & Tremaine (1985) was used:

$$M \approx \frac{5 \cdot R_e \cdot \sigma_v^2}{G}$$

The results [table 1] should be accurate for the apparently virialized clusters but are less accurate for the clusters not distributed on a gaussian.

---

<sup>1</sup> This author would like to acknowledge the support of the National Space Grant College Fellowship Program and the Wisconsin Space Grant Consortium.

# MKW12

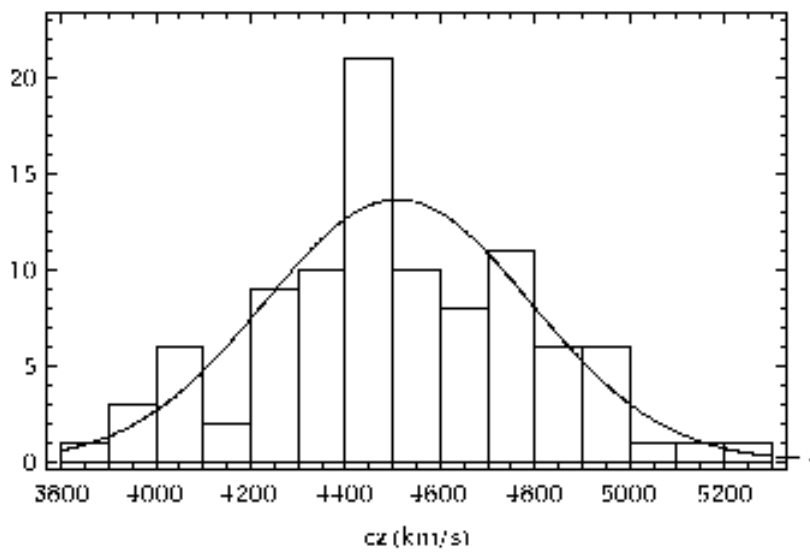
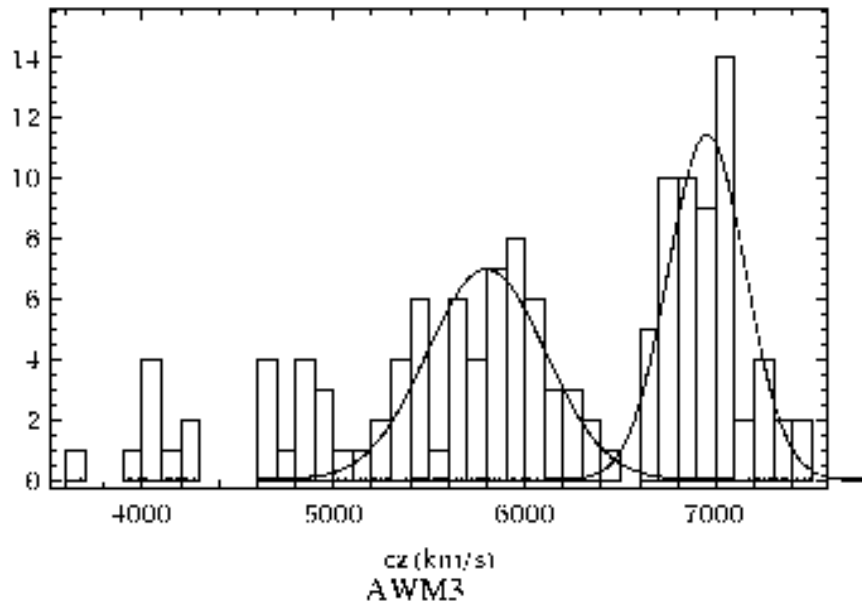


FIGURE 1: Redshift distributions of clusters MKW12 and AWM3

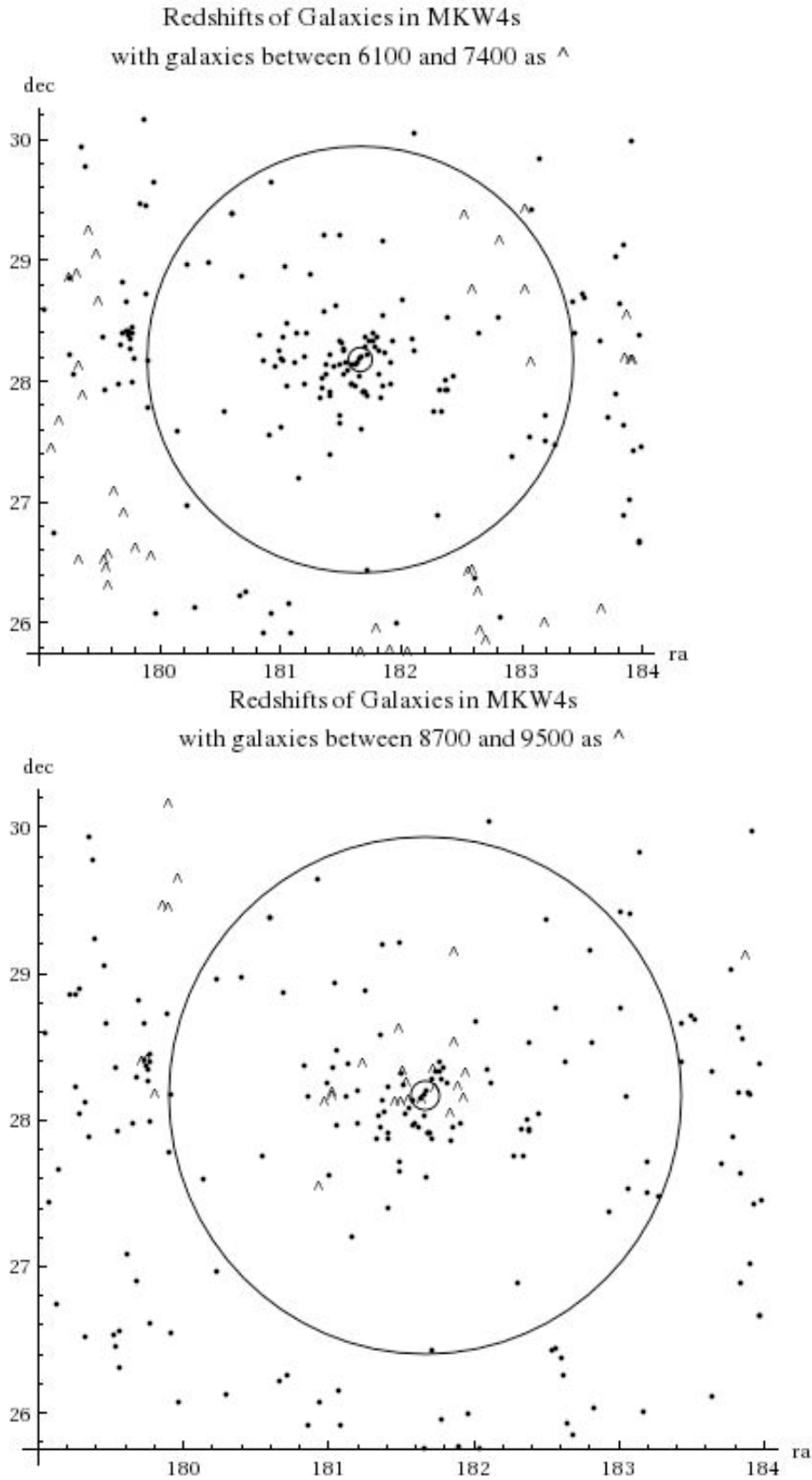


FIGURE 2: Selected Skyplots of MKW4s

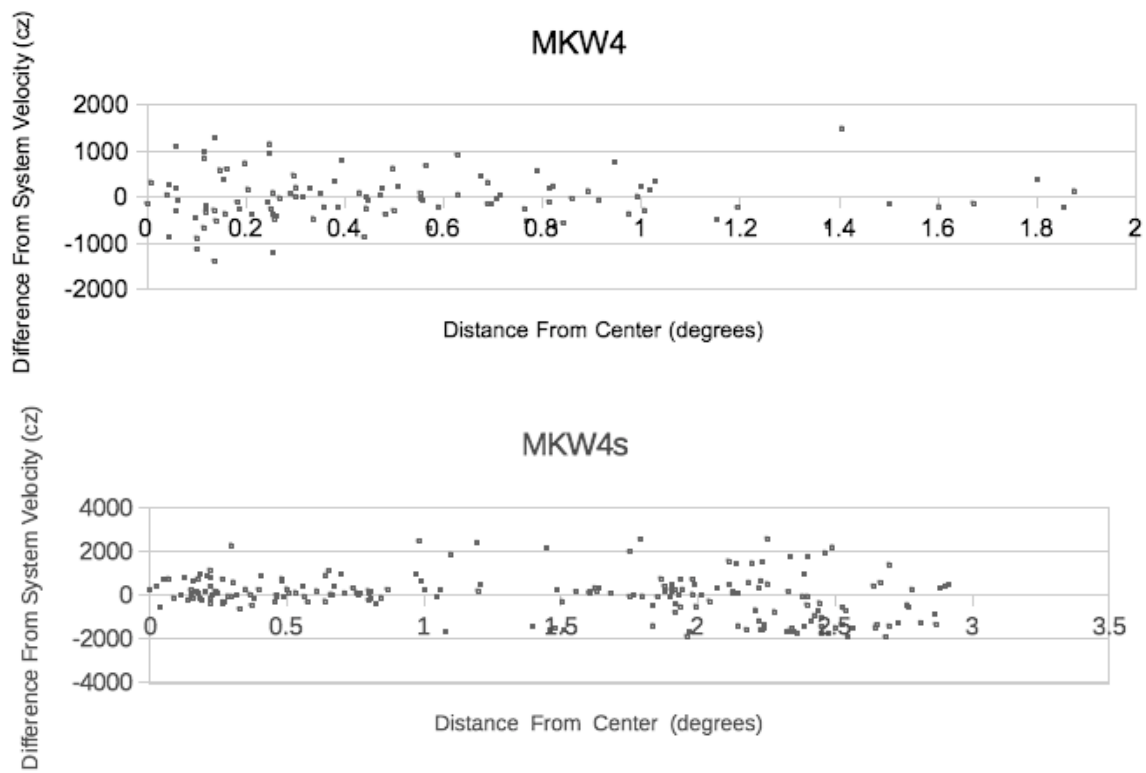


FIGURE 3: Distance from cluster center vs. velocity dispersion of MKW4 and MKW4s

Cluster	Calculated Mass ( $10^{14}$ Solar Masses)	Two Estimates by Jones & Forman (1999) ( $10^{14}$ Solar Masses)
AWM1	3.5	-
AWM2	.48	-
AWM3	.69	-
AWM4	1.5	.23/.93
AWM5	1.2	.78/1.14
MKW1s	.090	-
MKW4	1.4	.28/.55
MKW4s	14.4	.41/.88
MKW5	.31	-
MKW7	1.7	.48/.60
MKW8	1.4	-
MKW10	.091	-
MKW12	7.4	-

TABLE 1: Estimated Cluster Masses

## Results

*AWM2*, *AWM3*, *MKW1s*, *MKW4*, *MKW5*, and *MKW10* all align closely with gaussians and their galaxies are evenly distributed throughout their areas. This implies that these clusters are all in dynamically equilibrium.

*AWM1* contains a high velocity tail that implies that it is not yet virialized. This high velocity tail is spread out on the edges of the half-light radius and is likely a sign of ongoing galactic accretion (Dariush et al., 2007).

*AWM4* has a noticeable gap in the center of its redshift distribution as well as a high velocity tail. This high velocity tail all lies centrally in its half-light radius, which indicates continuing accretion.

*AWM5* has an unusually uniform distribution of redshift and apparent substructure at the lower right at lower redshifts.

*MKW4s* has a high velocity tail which lies in the center and the upper left which indicates ongoing accretion in these areas. *MKW4s* also has a low velocity bump which can be seen in a halo which lies right around the half-light radius. This substructure may indicate that *MKW4s* is a result of two clusters colliding.

*MKW7* has both high and low velocity tails that appear to be evenly distributed throughout the cluster.

*MKW8* has a high velocity tail which lies in the bottom half of the cluster.

*MKW12* fits best with two separate gaussians, meaning *MKW12* is probably two colliding clusters. The lower velocity Gaussian is circular shaped in the middle of the plot with a satellite near the top. The higher velocity bump is disk shaped and lies in the upper section of the plot. The galaxies between the gaussians seem to form a bridge between the structures.

## Further Research

Moving forward, the mass estimates must be revised, as there is a systematic error resulting in overestimation. As most of these clusters should be within the search area for the NRAO VLA Sky Survey, the radio data from the survey could help find their radio luminosity functions, yielding a more accurate mass. Further, more analysis of the irregular clusters (*AWM5*, *MKW4s*, and *MKW12*) would provide further information on their structures.

## References

- Albert, C., White, R. & Morgan, W. 1977, ApJ, 211, 309
- Dariush, A., Khosroshahi, H., Ponman, T., et al. 2007, MNRAS, 382, 433
- Heisler, J., Tremaine, S., & Bahcall, J. N. 1985, ApJ, 298,8
- Jones, C., & Forman, W. 1999, ApJ, 511, 65 (JF)
- Koranyi, D., & Geller, M. 2002, AJ, 123, 100
- Ledlow, M. J., Loken, C., Burns, J. O., Hill, J.M., & White, R. A. 1996, AJ, 112,388
- Morgan, W.W., Kayser, S. & White, R.A. 1975, ApJ, 199,545

# Big Bang Blackbody Simulator

Sara Stanchfield

University of Wisconsin – Madison

## ABSTRACT

The Cosmic Microwave Background (CMB) is a remnant glow from the Big Bang, and as such it provides us with a direct view into the early universe. By mapping out the CMB we are able to view the universe as it appeared when it was only 400,000 years old. The CMB radiates as an almost perfect blackbody at a temperature of 2.7 Kelvin. It is necessary to be able to simulate the CMB as a blackbody source in order to allow us to test instrumentation intended for CMB observation. The purpose of the Big Bang Blackbody Simulator is to construct a blackbody ‘cold load’ to measure the microwave response of superconducting Transition-Edge Hot-Electron Microbolometers. These detectors will allow us to measure the faint polarization signals in the CMB that are expected to be the result of gravitational waves generated in the very first moments of the universe.

## Introduction

Around 400,000 years after the Big Bang, during an era termed ‘recombination’ the universe had cooled to a point where the photons could no longer scatter with the surrounding baryons. These photons were then allowed to travel freely through space and are what we observe as the Cosmic Microwave Background (CMB) today. The CMB radiates as a nearly perfect blackbody at 2.7 Kelvin. The CMB also contains very faint temperature and polarization inhomogeneities. Around  $10^{-34}$  seconds after the Big Bang a period of rapid expansion occurred. This rapid expansion period, called inflation, produced gravitational waves which would have left an imprint on the polarization of the CMB.

The focus of the Big Bang Blackbody Simulator (BBS) is to create a calibrated source of microwave photons that simulate the CMB as observed from space or the ground in order to measure the response of superconducting the Transition-Edge Hot-Electron Microbolometer (THM). These THM detectors are specifically optimized to take measurements of the CMB. Arrays of 1000’s of THM detectors would be sensitive enough to measure the very faint B-mode polarizations in the CMB, the imprint left by gravitational waves.

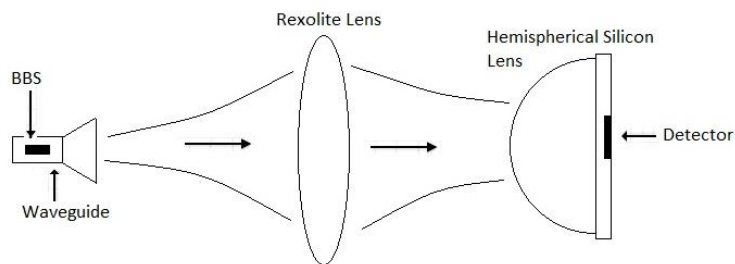


Figure 1: The BBS radiation will be coupled to the THM detector through multiple lenses.

## Acknowledgements:

Special thanks to Peter Timbie, Emily Barrentine, and Eric Katzelnick, also to Wisconsin Space Grant Consortium for financial support.

Figure 1 shows how the BBS will be used to test the THM detector. The radiation produced by the BBS will be coupled to the detector through a series of lenses. This entire set up will be then be placed in a cryostat with the left side being cooled to 4 Kelvin and the right to approximately 100 mKelvin to reduce noise.

## Construction

The BBS consists primarily of a 100 Ohm chip resistor and a copper finline structure, shown in figure 2. When heated, the chip resistor emits thermal radiation which is then coupled into a copper waveguide by the microwave circuit created by the copper finline structure. The copper finline structure is placed between two pieces of Kapton to electrically and thermally isolate the structure as well as provide mechanical stability.

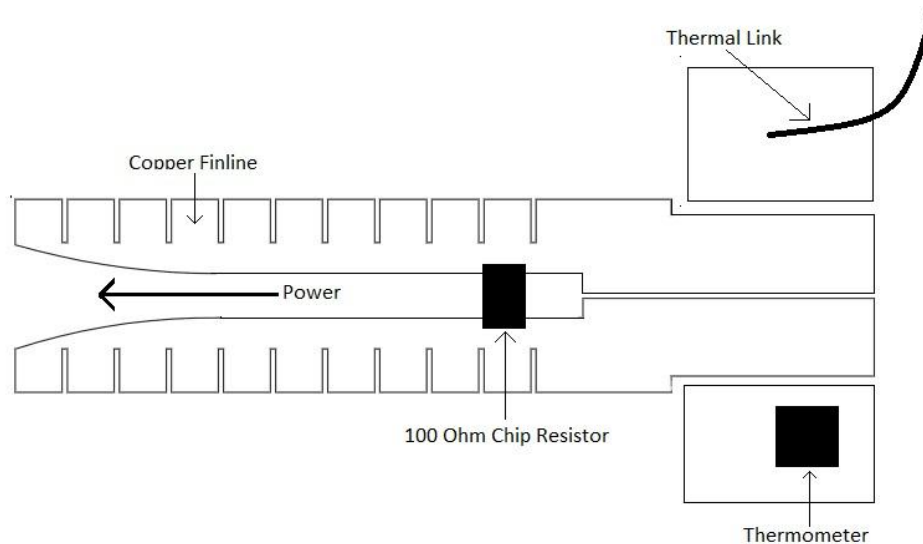


Figure 2: The structure of the BBS.

A Ruthenium Oxide thermistor is used to monitor the temperature of the BBS. A thick copper wire also acts as a thermal link between the BBS and the cold stage, which is used to control how quickly the BBS can be heated and cooled.

## Requirements of the Big Bang Blackbody Simulator

In order for the BBS to be effective it must meet a few basic requirements. The first is that it simulates an almost perfect blackbody with an emissivity of 90% or greater. It also needs to emit at the peak of the CMB spectrum, 75 to 110 GHz or approximately 3 mm. Next we must be able to heat the BBS to the desired temperature using low power, 10 mWatts or less. The desired temperature for CMB simulation is 4 to 20 Kelvin. This process of heating and cooling must also happen very quickly in order to be viable for laboratory experiments, on the order of one second. To achieve this, the BBS must have low heat capacity and an optimal thermal conductance.

## Results

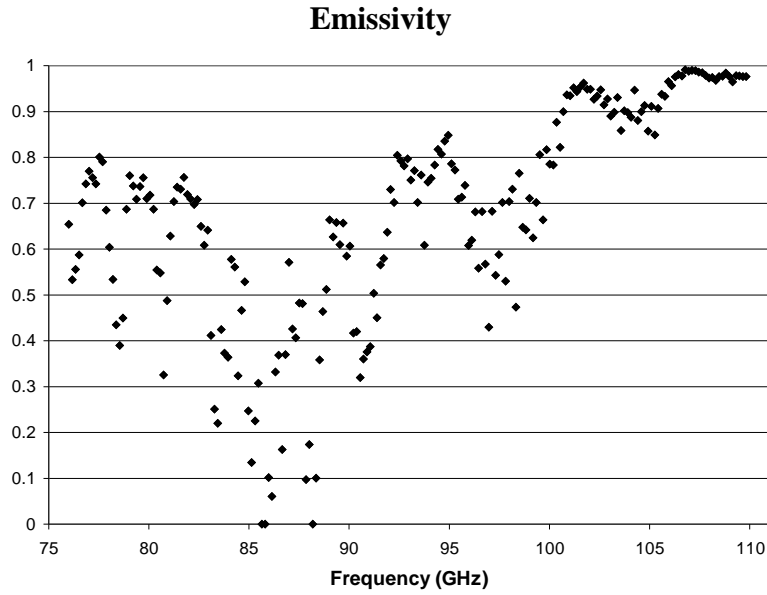


Figure 3: Plot of the emissivity of the BBS versus frequency

Figure 2 shows the emissivity of the BBS as a function of frequency. The emissivity of the BBS peaks around 98% with average emissivity of 69%, which is near the desired level.

To measure the time constant of the BBS, the BBS was placed in a copper waveguide block and then attached to the cold stage in a cryostat cooled with liquid helium to 4 Kelvin. The BBS was then heated to a maximum of 20 Kelvin using Joule power. Figure 4 shows the rise and fall of the temperature of the BBS. Joule power was applied until the temperature stabilized, then the power was shut off and the BBS was allowed to cool.

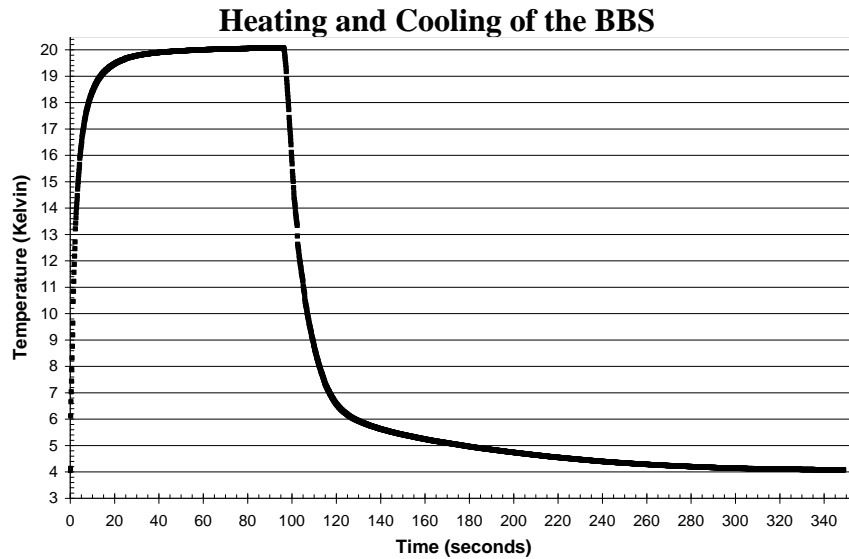


Figure 3: The BBS reaches a maximum temperature of 20 Kelvin when 34 mWatts power applied.

Fitting the temperature versus time curve to an exponential gives a time constant of 3.3 seconds. Varying amounts of power were applied to the BBS to reach maximum temperatures between 12 and 20 Kelvin. Using the power versus temperature graph, figure 4, the thermal conductance, G, was determined by fitting the line to the equation

$$P=C*(T^n-4^n)$$

Then,

$$G= \frac{dP}{dT} = n*C*T^{(n-1)}$$

Using these equations, the thermal conductance of the BBS was found to be  $2.9 \times 10^{-3} \text{ W/K}$ . The heat capacity, the product of the time constant and thermal conductance, was determined to be  $9.7 \times 10^{-3} \text{ J/K}$ .

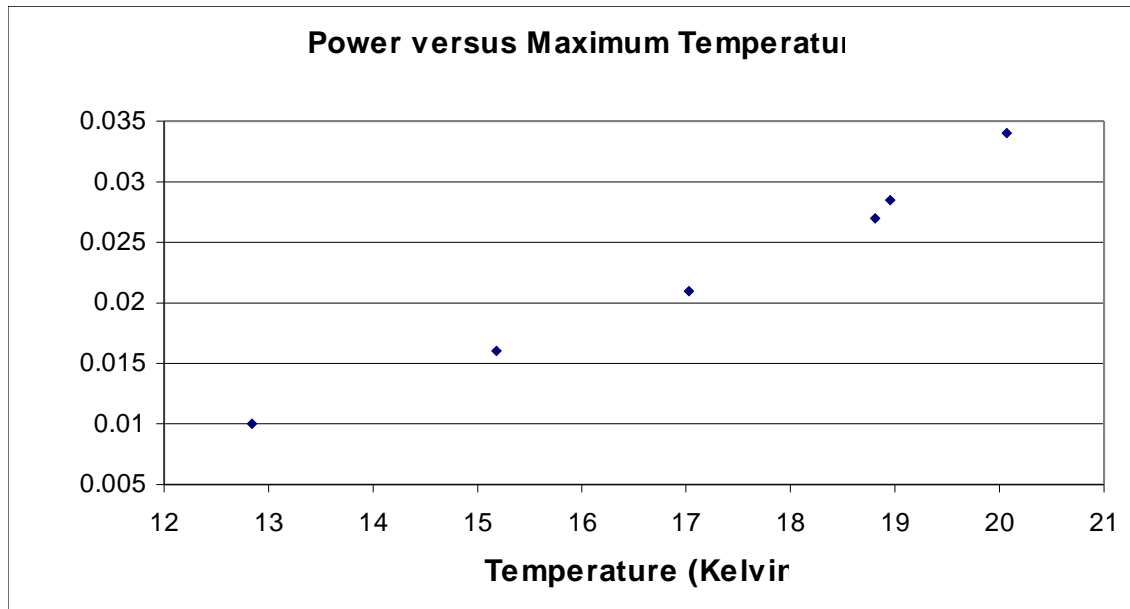


Figure 4: Plotting the power needed to heat the BBS to each maximum temperature gives a thermal conductance of  $2.9 \times 10^{-3} \text{ W/K}$ .

## Conclusions

The initial thermal requirements placed on the BBS, a short time constant and low power usage have been satisfied. The time constant to heat or cool the BBS is approximately 3 seconds, and a maximum of 35 mWatts of power was used, both of which are in the desired range. While the emissivity of the BBS is reasonable, there is some room for improvement. Future work will use two chip resistors in the place of the current one, as preliminary simulations have shown higher emissivity when this resistive area is better distributed in the finline structure.

Next, the Big Bang Blackbody Simulator will be used to test the microwave sensitivity of Transition-Edge Hot-Electron Microbolometer detectors. If successful, these detectors may be used in NASA's CMBPol mission at the end of the decade.

# Cancellation of Space-Based Interference in Radio Telescopes<sup>1</sup>

Lou Nigra<sup>2</sup>

Department of Astronomy  
University of Wisconsin  
Madison, Wisconsin

## Abstract

A concept is presented that was developed at the National Astronomy and Ionosphere Center (NAIC) at Arecibo, Puerto Rico, for suppression of Global Positioning System (GPS) signals in the 305 m dish radio receiver path prior to back-end processing. The subsystem requires no auxiliary antenna and is intended for easy integration with virtually any radio telescope system. The design focuses on the GPS L3 signal at 1381.05 MHz which, during periodic tests, interferes with observations of objects in an important range of redshifts. The signal dynamically change modulation modes and our scheme has demonstrated, through simulations using actual telescope data, the ability to acquire and track the signal as well as detect mode changes in order to to apply cancellation or blanking, as appropriate. A follow-up is planned to develop a prototype to deploy and evaluate at NAIC.

## Introduction

Navigation satellite systems, such as Global Positioning System (GPS) and the Russian *Globalnaya Navigatsionnaya Sputnikovaya Sistema* (GLONASS), are inherently troublesome to radio astronomy. Ground-based Radio Frequency Interference (RFI) typically enters the system from near the horizon through antenna side lobes far from the antenna pointing direction where the system response is highly suppressed. Satellite signals can arrive at any angle through close-in side lobes with much higher gain. In this work, we describe a concept for mitigating the troublesome GPS signal at L3, which frequently interferes with the operation of neutral Hydrogen (HI) surveys at the National Astronomy and Ionosphere Center's Arecibo observatory (AO), in Puerto Rico.

## The Problem

The problem presented by the GPS L3 signal to radio telescope systems is illustrated in Figure 1, where several GPS satellites are generally close enough to the antenna pointing direction at a given time to produce a strong interfering system response. Sometimes, in addition to the standard L1 signal, the L3 signal is active and while tuned to the range of frequencies interesting

- 
- 1 NAIC provided support through a pre-doctoral appointment. Partial support was provided through the National Space Grant College and Fellowship Program and the Wisconsin Space Grant Consortium. Partial support was also provided through NSF grant AST 0908134.
  - 2 The following collaborators are acknowledged: B. Murray, Lewis (NAIC), Clyde Edgar (The Aerospace Corporation) Phil Perillat (NAIC), Luis Quintero (NAIC), Snežana Stanimirović (University of Wisconsin – Madison) and J. S. Gallagher, III (University of Wisconsin – Madison).

to HI surveys such as the Arecibo Legacy Fast L-band Feed Array survey (ALFALFA), its interfering signal spectrum overlaps red-shifted 21 cm HI emission (1420.4 MHz at rest) from the Coma galaxy supercluster at  $z=0.03$ . Making matters worse, its 220 km sec<sup>2</sup> wide spectrum is similar to that of spiral galaxy signatures.

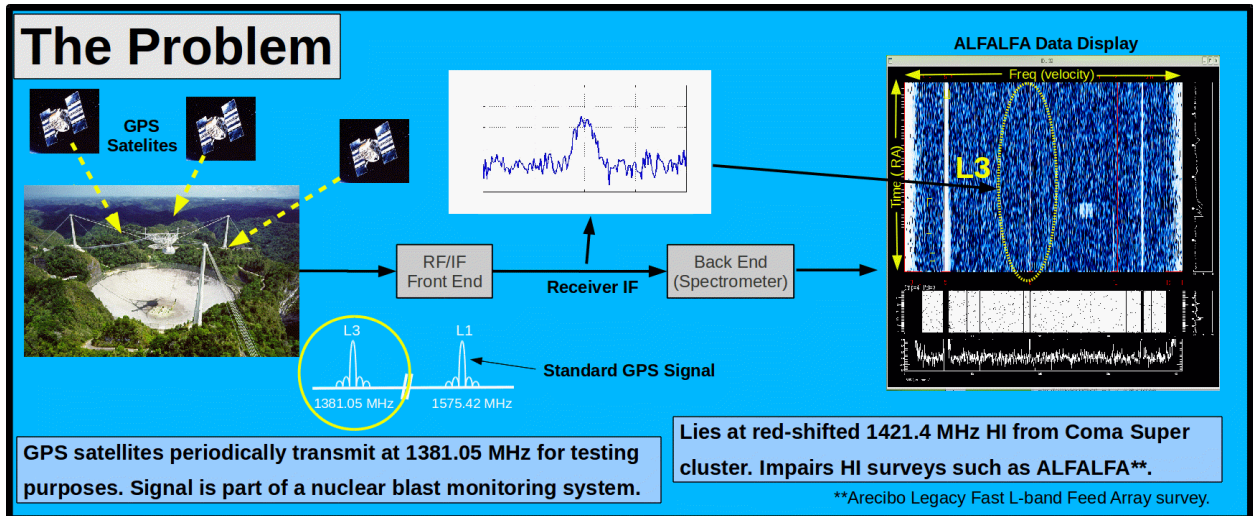


Figure 1 - The GPS L3 Problem.

Although L1 is present continuously, L3 is sporadic. Several times daily, satellites undergo tests and transmit for seconds at a time. System-wide tests are performed quarterly in windows

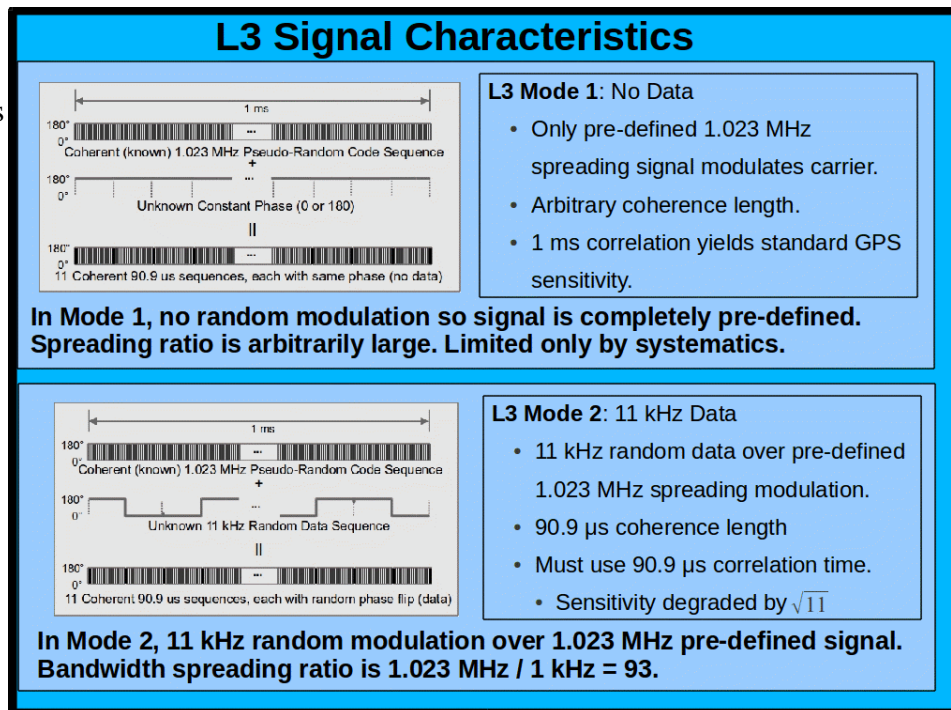


Figure 2 - GPS L3 Signal Characteristics.

lasting for days where satellites can transmit for minutes at a time. The occurrence and length of transmissions are unpredictable. The authorities coordinate with the radio astronomy community, giving advance notice of these test windows. While transmitting, the signal can operate in two modulation modes, described in Figure 2. The signal is generally in Mode 1, un-modulated by data with only PRN modulation present, but will periodically switch to Mode 2 and overlay its unique 11 kbps data for a number of 1.5 sec slots. Currently, the strategy at AO is to manually flag data when daily tests corrupt observations and the band is avoided entirely during announced system test windows resulting in shutting down surveys for days at a time.

### Prior Work

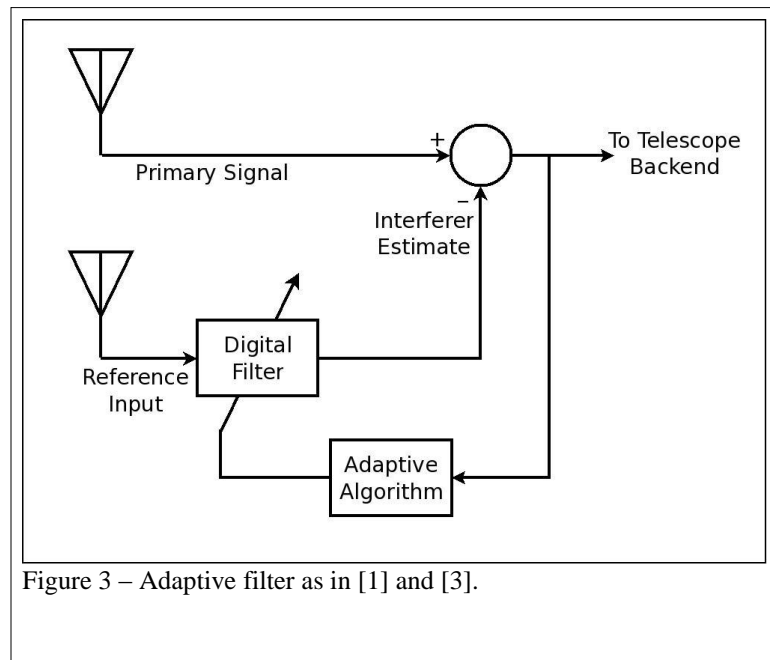
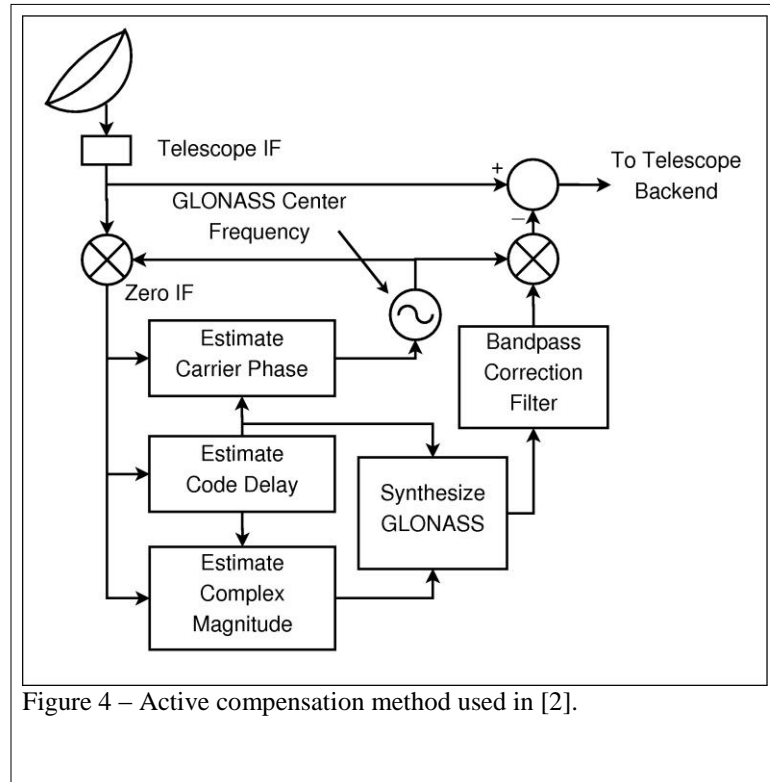


Figure 3 – Adaptive filter as in [1] and [3].

The adaptive filter [4] has a long history in electronic systems and is well-suited for canceling a time-varying, unwanted signal. Figure 3 shows a time domain adaptive filter in a RFI canceling configuration. A high quality replica of the transmitted interferer is required as input and its output is subtracted from the system channel. An algorithm adapts the filter's characteristics to optimally match the channel response by minimizing the interferer after subtraction. In [1], suppression of commercial FM signals with such an adaptive filter was successfully demonstrated. Relevant to the problem at hand, in [3] a similar technique was applied to navigation satellite RFI, successfully suppressing a GLONASS signal. In both of these implementations, a separate antenna is required to obtain a reference signal with much higher signal-to-noise ratio (SNR) than the interference. In [3], a tracking dish is required to track the satellite. Given that 4-11 GPS satellites are in the sky at a given time, it is likely that several satellites produce strong interference at any given time from different directions. In fact, we have detected three GPS satellites in a single 30-second sample signal from the AO telescope. Using the method of [3] would require as many tracking dishes as the number of satellites, making it impractical and is clearly inconsistent with our "turn-key" concept.



The need for reference antennas is eliminated for a class of high bandwidth ratio, spread spectrum interferers by a clever approach described in [2], and shown in Figure 4. It exploits the fact that most of the bandwidth of spread-spectrum systems such as GPS and GLONASS is redundant, produced by the pre-defined PRN waveform. In this scheme, the reference signal is obtained from the telescope signal channel itself, the PRN modulation is removed, and the signal is filtered to a lower bandwidth, thus increasing its SNR. This is then noiselessly re-expanded with the PRN, producing the necessary high SNR reference signal. In this case, a frequency domain adaptive filter implementation is used rather than time domain, but the principles are similar. A limitation of this approach is that with narrower reference bandwidth, group delay in the reference signal filter increasingly de-correlates the replica signal with the interferer, limiting the SNR improvement to about 1/10 of the PRN-to-data bandwidth ratio. In the case of standard GPS (L1), SNR improvement by a factor of 2000 can be obtained, but only by a factor of 9 for L3 with its high data rate. Still, this approach eliminates the multiple antenna requirement and with improvements, serves as the basis for our turn-key subsystem.

## The Solution

The concept is illustrated in Figure 5, which shows RFI Suppression Subsystem (RSS) operation when directly inserted into the existing receiver system at the Intermediate Frequency (IF) stage with no modifications required to the rest of the system. The IF signal is simply diverted to the RSS, which processes the signal, selectively suppressing the undesired GPS signals from multiple satellites while minimally affecting the rest of the signal, and returns the cleaned IF signal to its original destination, the telescope's Back End Processor. Virtually all radio telescopes have a similar IF stage in their architecture, and the RSS requires minimal automated coordination communication with the telescope control system through standard interfaces, so

the RSS can be considered a “turnkey” operation, easily integrated with virtually any radio telescope system.

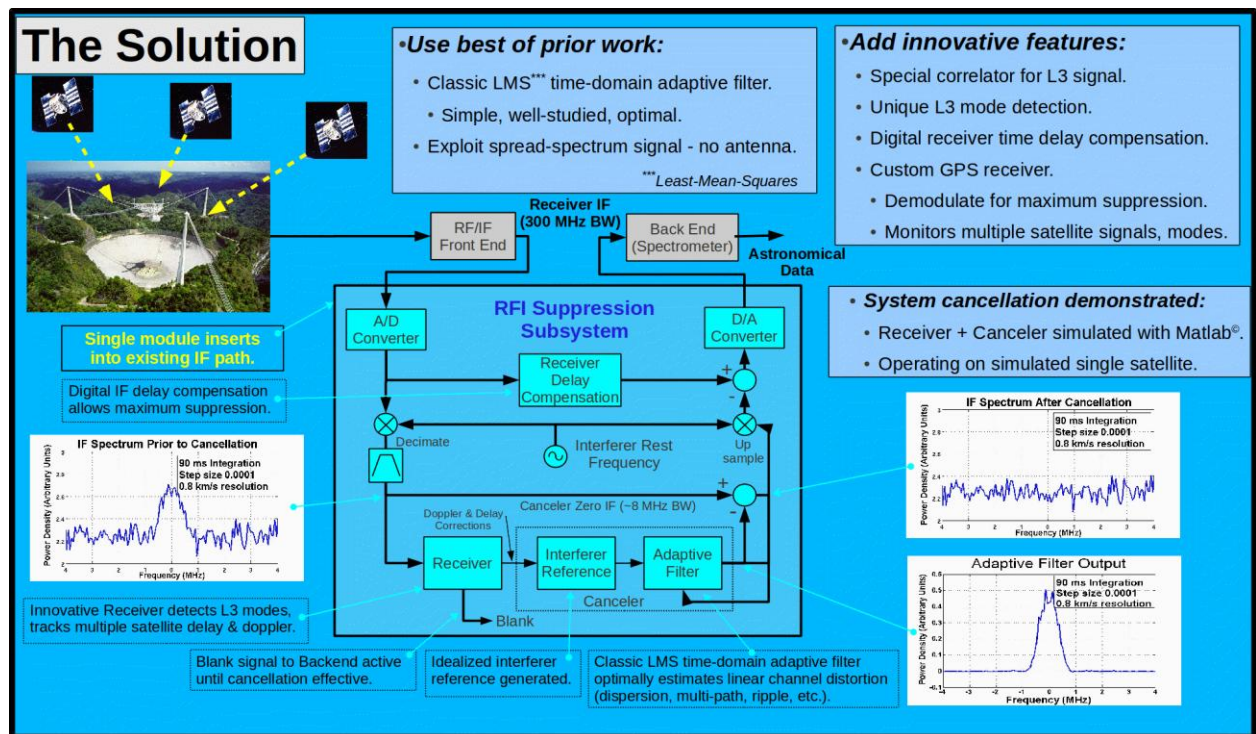


Figure 5 - The GPS Signal Suppression System inserted in the Arecibo radio telescope.

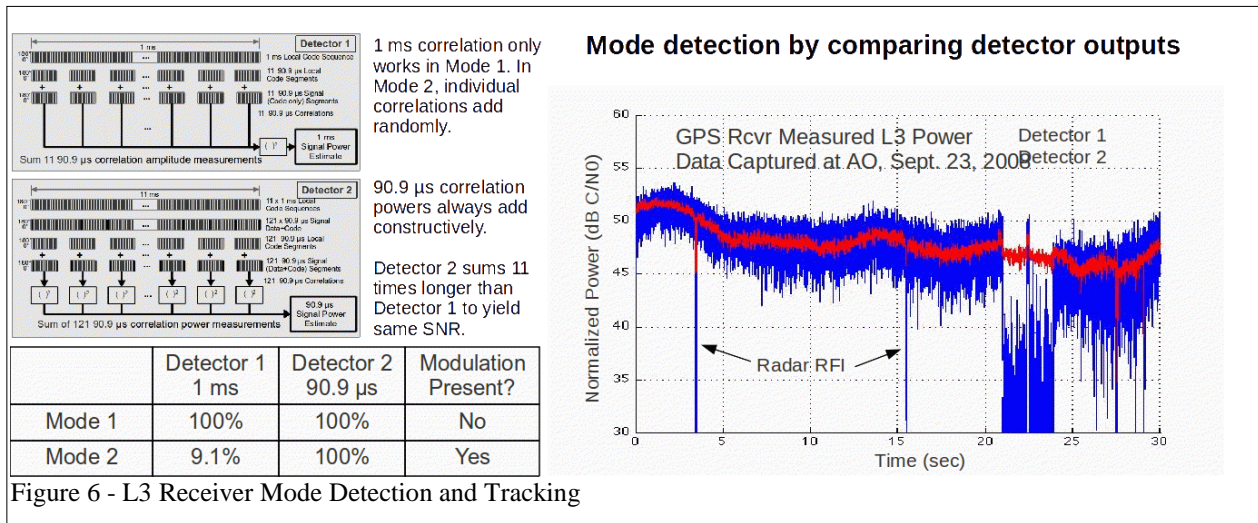
This turnkey capability is in sharp contrast to conventional GPS-type RFI suppression concepts, which require a separate high-gain tracking dish antenna for each satellite to be suppressed. Such a system for one GPS L3 signal is certainly feasible (albeit very expensive), but cannot be considered “turnkey”. In fact multiple satellites in different sky positions will produce signals strong enough to interfere with telescope operation, leading to a requirement for several tracking dish antennas, making these approaches completely impractical.

What allows this RSS to avoid the external antenna pitfall is the clever approach devised by [2], mentioned previously, which exploits the spread-spectrum modulation technique used in GPS and other similar satellite systems. Actually, this exploitation is also possible with many other potential ground and space-based interfering signals since direct sequence spread spectrum modulation of some form is commonly used in many radio communications systems, including mobile consumer systems like smart phone networks.

### RFI Suppression Subsystem (RSS) Operation

The subsystem has been successfully simulated with MATLAB®. Figure 5 illustrates the detailed operation of the RSS and shows simulator signal spectra produced in the process using realistic simulated inputs. The diverted IF signal from the telescope is digitized with high-speed Analog-to-Digital Converters (ADCs). The digitized signal then follows two paths. In one, the signal is

analyzed and processed to produce a replica of the interfering L3 signal (discussed further below), but to obtain a replica of maximum quality and achieve maximum suppression, the process takes considerable time (10's of milliseconds), so the replica is delayed in time with respect to the incoming interferer. Because of this, in the second path, the digitized IF signal must be delayed by the exact same amount with a simple digital memory-based variable time delay prior to subtracting the replica interferer from it. Compared to previous work [1, 3, 2] this variable in-line delay feature is unique and allows maximum suppression of the signal by avoiding time delay distortion when subtracting the replica from the signal.



The system produces the interferer replica (graph at lower right) by detection and analysis of the interfering signal (lower left) using an innovative GPS receiver capable of handling the unique L3 modulation characteristics. It produces an idealized interferer reference or replica, which is input to a classical Least Mean Squares (LMS) adaptive filter [4]. The receiver, reference generator and adaptive filter are embedded in a unique frequency down/up conversion (decimation/up-sampling) and signal combining network that allows processing the signal at the desired zero-frequency IF, but translates the interferer-suppressed signal (middle right) back to the exact IF frequency at which it was sampled. The translations account for both the rest frequency and the Doppler shift of the interfering satellite signals. Figure 6 describes the method used to detect both unique L3 modulation modes. This is subsequently used to time-align the receiver with the modulation and also to control suppression strategy. There are two detection algorithms, one of which detects both modes when time-aligned with the signal while the other can only detect Mode 1. This indicates the active mode as well as time alignment, which is used in feedback to track the time delay and Doppler shift of GPS signal. Figure 4 includes a plot of the output of these two signals while the simulated receiver detected and tracked an actual GPS L3 signal throughout a 30-second sample of an actual signal from the Arecibo telescope.

### Summary

The system has demonstrated, through simulations, the ability to detect, identify and track actual GPS L3 signals in both of its modulation modes. It has also demonstrated that it can suppress a single simulated interferer, but the simulator has not been upgraded to include multiple adaptive filter channels, necessary to simultaneously suppress multiple signals. This work is still in

progress, but is conceptually simple, with high likelihood of success. The programming involved is the main challenge. A second challenge is that for very long (40-second) signal integrations used for sensitive astronomical measurements, there is a small residual structure in the spectrum. This structure, although it would only interfere with the weakest of detectable astronomical signals, is still of concern and must be understood and characterized. It is expected that this effect is precisely predictable and can therefore be eliminated. Work will continue along these lines for the remainder of the year under complementary funding and will culminate in a final peer-reviewed paper and transfer to Arecibo Engineering for further development.

## **References**

- [1] Barnbaum, C., & Bradley, R. F. 1998, A New Approach to Interference Excision in Radio Astronomy: Real-Time Adaptive Cancellation, 1998 AJ 116, 2598
- [2] Ellingson, S., Bunton, J. Bell, J., Removal of the GLONASS C/A Signal from OH Spectral Line Observations Using a Parametric Modeling Technique, 2001 ApJS 135, 87E
- [3] Poulsen, A. J., Jeffs, B. D., Warnick, K. F., Fisher, J. R., Programmable Real-Time Cancellation of GLONASS Interference with the Green Bank Telescope, 2005 AJ 130, 2916P
- [4] Widrow, B., et al., Adaptive noise canceling: Principles and applications, 1976 Proc. IEEE, 63, 1692

# Detection of non-Einsteinian Gravitational Waves using a Pulsar Timing Array

Sydney J. Chamberlin

Center for Gravitation and Cosmology  
Department of Physics  
University of Wisconsin-Milwaukee  
Milwaukee, Wisconsin

## Abstract

In the next decade gravitational waves may be detected using a pulsar timing array. In an effort to develop optimal detection strategies for stochastic backgrounds of gravitational waves in general metric theories of gravity, we investigate the overlap reduction functions for these theories and discuss their characteristics. We show that sensitivity increases for non-transverse gravitational waves and discuss the physical origin of this effect. We calculate the overlap reduction functions for the current NANOGrav Pulsar Timing Array (PTA) and show that the sensitivity to the vector and longitudinal modes can increase dramatically for pulsar pairs with small angular separations.

## Introduction

Advancements in gravitational wave astronomy are making it possible to test Einstein's theory of gravity. The detection of gravitational waves (GWs) could support or rule out modified gravity (non-Einsteinian) theories. Furthermore, the detection of GWs will open a new era of astronomy, making it possible to learn more about astrophysical objects in the universe and the beginnings of the universe itself.

Current GW detection efforts focus primarily on ground-based laser interferometric detectors and the use of pulsar timing arrays. Pulsar timing arrays search for GWs by exploiting the microsecond regularity of pulsar signals. The presence of a GW in the space between the Earth and the pulsar would be manifested by a redshift,  $z(t)$ , in the pulsar's signal. Radio telescopes are used to determine a quantity known as the *timing residual*, which is defined as the difference between the actual and expected time of arrival of a pulse:

$$R(t) = TOA_{\text{actual}} - TOA_{\text{expected}}. \quad (1)$$

The timing residual is directly related to the redshift of the pulse,

$$R(t) = \int_0^t dt' z(t') \quad (2)$$

---

<sup>0</sup>We would like to extend our thanks to the members of the NANOGrav data analysis working group for their comments and support, especially Jim Cordes, Paul Demorest, Justin Ellis, Rick Jenet, Andrea Lommen, Delphine Perrodin, and Joe Romano. We would also like to thank Jolien D. E. Creighton for numerous useful comments and suggestions. This work was funded in part by the Wisconsin Space Grant Consortium and the NSF through CAREER award number 09955929 and PIRE award number 0968126.

which can also be defined geometrically using the techniques discussed by (Detweiler 1979). The metric perturbation due to a GW has the plane-wave expansion

$$h_{ij}(t, \vec{x}) = \sum_A \int_{-\infty}^{\infty} df \int_{S^2} d\Omega e^{2\pi i f t(t - \hat{\Omega} \cdot \vec{x})} h_A(f, \hat{\Omega}) \epsilon_{ij}^A(\hat{\Omega})$$

where the sum is over all possible GW polarization modes (plus, cross, breathing, longitudinal, vector x, vector y) and  $\epsilon_{ij}$  are the polarization tensors given in Table 1, and for pulsar signals originating in the direction  $\hat{p}$  (see Fig. 1), induces the redshift

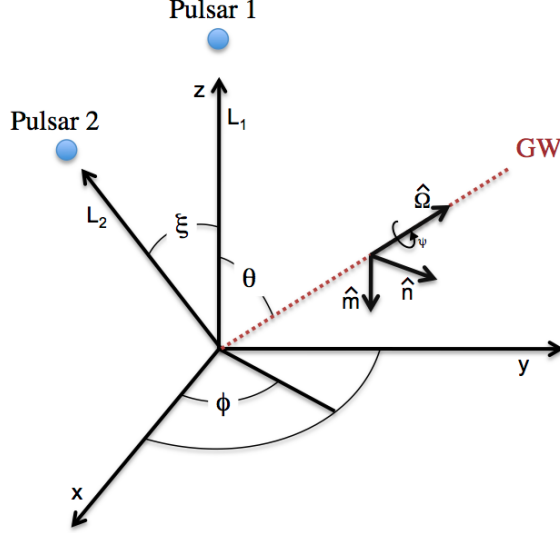


Figure 1: Geometry of the two pulsar-Earth system;  $\xi$  is the pulsar separation angle and  $L_1, L_2$  are the distances of the two pulsars from the Earth (origin). Pulsar 1 has been placed on the z-axis for convenience, though the initial choice of basis is arbitrary.

$$z(t, \hat{\Omega}) = \frac{\hat{p}^i \hat{p}^j}{2(1 + \hat{\Omega} \cdot \hat{p})} [h_{ij}(t_p, \hat{\Omega}) - h_{ij}(t_e, \hat{\Omega})] \quad (3)$$

where  $t_p, t_e$  represent the time of pulse emission and the time the pulse is received at the Earth. Writing (3) in the frequency domain, the redshift can be expressed in terms of the antenna patterns  $F^A(\hat{\Omega})$

$$\tilde{z}(f, \hat{\Omega}) = (e^{-2\pi i f L(1 + \hat{\Omega} \cdot \hat{p})} - 1) \sum_A h_A(f, \hat{\Omega}) F^A(\hat{\Omega}). \quad (4)$$

For a stochastic background of GWs, the signal appears in data as correlated noise between measurements from different detectors. The output of the  $i^{th}$  detector is of the form

$$s_i(t) = z_i(t) + n_i(t) \quad (5)$$

$$\begin{array}{cc}
\epsilon_{ab}^+ = \hat{m} \otimes \hat{m} - \hat{n} \otimes \hat{n} & \epsilon_{ab}^\times = \hat{m} \otimes \hat{n} + \hat{n} \otimes \hat{m} \\
\epsilon_{ab}^b = \hat{m} \otimes \hat{m} + \hat{n} \otimes \hat{n} & \epsilon_{ab}^l = \hat{\Omega} \otimes \hat{\Omega} \\
\epsilon_{ab}^x = \hat{m} \otimes \hat{\Omega} + \hat{\Omega} \otimes \hat{m} & \epsilon_{ab}^y = \hat{n} \otimes \hat{\Omega} + \hat{\Omega} \otimes \hat{n}
\end{array}$$

Table 1: Polarization tensors

where  $z_i(t)$  corresponds to the unknown GW signal and  $n_i(t)$  to noise (assumed in this case to be stationary and Gaussian). For coincident, co-aligned detectors, the cross-correlation statistic is defined as

$$S = \int_{-T/2}^{T/2} dt \int_{-T/2}^{T/2} dt' s_1(t) s_2(t') \delta(t - t'). \quad (6)$$

In general, detectors are neither coincident nor co-aligned and it is necessary to generalize the delta function in (6). This generalization appears in the statistic as

$$S = \int_{-T/2}^{T/2} dt \int_{-T/2}^{T/2} dt' s_1(t) s_2(t') Q(t - t') \quad (7)$$

where  $Q(t - t')$  is the *filter function*. The optimal detection statistic is found by optimizing the filter function; this method is known as *matched filtering* and is the primary strategy for GW signal detection. To do the matched filtering, the expected signal-to-noise ratio

$$SNR = \frac{\langle S \rangle^2}{\sqrt{\langle S^2 \rangle - \langle S \rangle^2}} \quad (8)$$

is maximized to find the optimal filter function. In the frequency domain, this appears as

$$\tilde{Q}(f) = \chi \frac{\Omega_{GW}(|f|) \Gamma(|f|)}{|f|^3 P_1(f) P_2(f)} \quad (9)$$

where  $\Omega_{GW}(|f|)$  is the stochastic GW spectrum,  $P_1(f)$  and  $P_2(f)$  are power spectra,  $\chi$  is a normalization constant and  $\Gamma(|f|)$  is the *overlap reduction function*, which characterizes the loss of sensitivity due to detectors being non-coincident and non-aligned.

The overlap reduction function is defined as

$$\Gamma(|f|) = \beta \sum_A \int_{S^2} d\Omega (e^{\{2\pi i f L_1(1 + \hat{\Omega} \cdot \hat{p}_1)\}} - 1) (e^{\{-2\pi i f L_2(1 + \hat{\Omega} \cdot \hat{p}_2)\}} - 1) F_1^A(\hat{\Omega}) F_2^A(\hat{\Omega})$$

where the sum is over all possible GW polarizations (Lee et al. 2008) and the exponential terms (or so-called pulsar terms) describe the metric perturbation at each pulsar. In the regime of alternative gravity theories, each term in the sum may be explicitly computed, i.e.

$$\Gamma(|f|) = \Gamma_+(|f|) + \Gamma_\times(|f|) + \Gamma_b(|f|) + \Gamma_l(|f|) + \Gamma_x(|f|) + \Gamma_y(|f|),$$

and it is advantageous to consider each term in (10) separately since various gravity theories require different polarizations (Will 1993; Nishizawa et al. 2009; Lobo 2008; Alves et al. 2009; Capozziello and Francaviglia 2008; De Felice and Tsujikawa 2010; Brunetti et al. 1999; Clifton et al. 2011; Sagi 2010; Clifton et al. 2010; Skordis 2009; Milgrom 2009). It is convenient to note at this point that the first three terms listed in (10) correspond to transverse wave propagation (the first two being the modes of General Relativity), while the latter three correspond to non-transverse wave propagation.

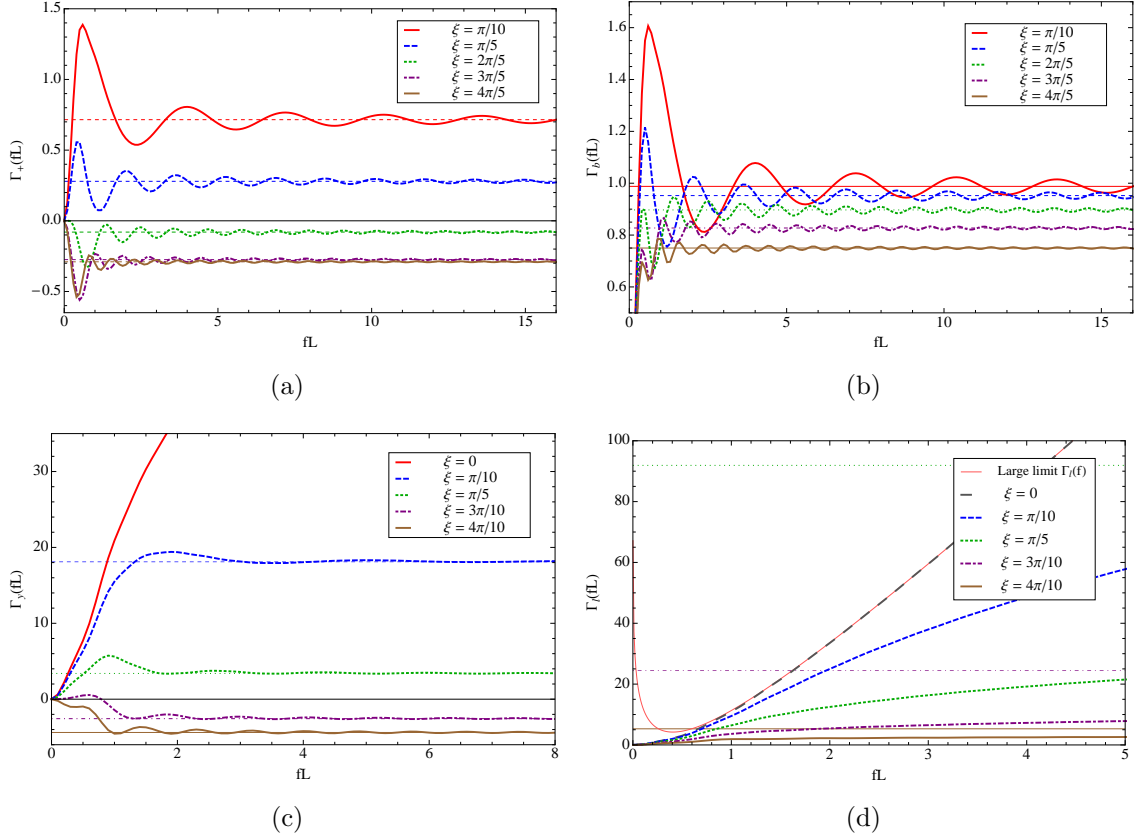


Figure 2:  $\Gamma(fL)$  for the various polarization modes: plus (a), breathing (b), shear (c) and longitudinal (d). In the latter two modes, smaller pulsar separation angles correspond to retained frequency dependence in  $\Gamma(fL)$ . Nearly all the non-transverse curves eventually converge, but at rather high values of  $\Gamma(fL)$  relative to the transverse modes, indicating increased sensitivity to GWs with these polarizations.

## Overlap reduction functions

The overlap reduction function has a closed analytic form for transverse GWs. The overlap reduction function for the plus mode has been calculated by (Anholm et al. 2009) and is given by

$$\Gamma_+(\xi) = 3 \left[ \frac{1}{3} + \frac{1 - \cos \xi}{2} \left[ \log \left( \frac{1 - \cos \xi}{2} \right) - \frac{1}{6} \right] \right], \quad (10)$$

where  $\xi$  is the angular separation of the pulsars. For the breathing mode, a closed form is given by (Lee et al. 2008):

$$\Gamma_b(\xi) = \frac{3}{4\pi} \frac{\pi}{3} (3 + \cos \xi). \quad (11)$$

For the case of non-transverse GWs, the overlap reduction function cannot be integrated analytically and must be treated numerically.

In general relativity the pulsar term is typically excluded from the integral (10) without any loss of optimality (Anholm et al. 2009); see Fig. 2a. The same is not true for scalar and vector GW modes. For non-transverse GW polarization modes, frequency must be retained in the overlap reduction function for pulsars that are nearly co-aligned in order to maintain optimality (Fig. 2). Furthermore, larger values of the non-transverse overlap reduction functions (Figs. 2) indicate increased sensitivity to these modes, in agreement with the results of (Lee et al. 2008; Alves and Tinto 2011). This behavior is absent for transverse GW polarization modes.

The effect on non-transverse GW polarization modes can be understood by studying the induced frequency changes for GWs of different polarizations. Consider the spacetime metric due to a longitudinal mode GW perturbation:

$$g_{ab} = \eta_{ab} + h_{ab}(t - z). \quad (12)$$

It can be shown using (12) that the redshift for this perturbation is

$$\tilde{z}_l(f, \hat{z}) = \frac{\cos^2 \theta}{2(1 + \cos \theta)} (e^{-2\pi i f L(1 + \cos \theta)} - 1) h_l. \quad (13)$$

The analogous redshift for a plus mode GW perturbation is

$$\tilde{z}_+(f, \hat{z}) = \frac{-\sin^2 \theta}{2(1 + \cos \theta)} (e^{-2\pi i f L(1 + \cos \theta)} - 1) h_+. \quad (14)$$

In the region where  $\theta \rightarrow \pi$ , (13) and (14) appear to become singular, though a simple series expansion shows that only the longitudinal mode retains any unusual behavior in this sky region: Let  $\theta = \pi - \delta$ , where  $\delta$  is a real parameter satisfying  $\delta \ll 1$ . One may easily conclude that

$$\tilde{z}_l(f, \hat{z}) \sim \pi i f L (1 - \delta^2) h_l \quad (15)$$

for the longitudinal case, while

$$\tilde{z}_+(f, \hat{z}) \sim \pi i f L \delta^2 h_+ \quad (16)$$

for the plus mode. In the limit as  $\delta \rightarrow 0$ ,  $\tilde{z}_+$  vanishes while  $\tilde{z}_l$  approaches a constant proportional to  $fL$ . In the time domain, the longitudinal mode redshift for  $\theta \approx \pi$  goes as

$$z_l(t, \hat{z}) \propto L \dot{h}. \quad (17)$$

The right hand side of (17) may be identified as a velocity.

For co-aligned pulsars in the problematic sky region ( $\theta \approx \pi$ ),  $\Gamma_l(f)$  is proportional to the square of the redshift,

$$\Gamma_l(f) \propto -2\pi \int_{-1}^1 d(\cos \theta) |(e^{-2\pi i f L(1 + \cos \theta)} - 1)|^2 \frac{\cos^4 \theta}{4(1 + \cos \theta)^2} \quad (18)$$

which may be evaluated analytically. In the limit of large  $fL$ ,

$$\begin{aligned} \Gamma_l(f) &= \pi \left\{ 37/6 - 4\gamma - 1/(\pi(fL)^2) + 4 \text{Ci}(4\pi fL) \right. \\ &\quad \left. - 4 \log(4\pi fL) + 2\pi fL \text{Si}(4\pi fL) \right\} (fL \gg 1) \\ &\sim (37/6 - 4\gamma) \pi - \frac{4}{5} 4\pi \log(4\pi fL) + \pi^3 fL \end{aligned} \quad (19)$$

so that  $\Gamma_l(f)$  goes like  $fL$  up to some large frequency<sup>1</sup>. This large limit  $\Gamma_l(f)$  is plotted with the overlap reduction functions in Fig. 2d and, with the exception of the singular behavior near the origin, fits the  $\Gamma_l(f)$  curve for co-aligned pulsars ( $\xi = 0$ ). As  $\xi$  increases, correction terms in (19) restrict  $f$  dependence of  $\Gamma(f)$  until it is approximately constant as a function of frequency.

An identical analysis for the shear GW modes produces similar results. Given a metric perturbation of the same form as (12), the redshift for the vector-y mode goes as

$$\tilde{z}_y(f, \hat{z}) = \frac{-\cos\theta \sin\theta}{(1 + \cos\theta)} (e^{-2\pi i f L(1+\cos\theta)} - 1) h_y. \quad (20)$$

Doing the expansion about  $\delta$ ,

$$\tilde{z}_y(f, \hat{z}) \sim -2\pi i f L \delta \left(1 - \frac{\delta^2}{2}\right) h_y. \quad (21)$$

As in (19),  $\tilde{z}(f, \hat{z})$  retains dependence on  $fL$  near  $\theta = \pi$ , but the growth in  $fL$  is constrained by a factor of  $\delta$  (see Fig. 2c).

The same behavior is not present in other sky locations. If the GW propagates perpendicular to the earth-pulsar line ( $\theta = \pi/2 + \delta$ ), then up to second order in  $\delta$  the redshifts

$$\tilde{z}_l = (e^{-2\pi i f L(1-\delta)} - 1) \frac{-\delta^2}{2(1-\delta)} \text{ (longitudinal)} \quad (22)$$

$$\tilde{z}_y = (e^{-2\pi i f L(1-\delta)} - 1) \frac{\delta}{(1-\delta)} \text{ (shear)} \quad (23)$$

$$\tilde{z}_+ = (e^{-2\pi i f L(1-\delta)} - 1) \frac{-1}{2(1-\delta)} \text{ (plus)} \quad (24)$$

are obtained. Even while  $\delta$  is small, the exponential cannot be fully expanded. Oscillatory behavior dominates the redshift in this sky location. Physically, this is due to the fact that the pulse “sees” different phases of the GW and the contribution to the redshift varies based on this phase.

In the regime where  $\theta \approx \pi$ , the pulse is effectively in the long wavelength limit in which the redshift can increase monotonically up to some limiting  $f$  at which point the Taylor series expansion of the pulsar term (15) is no longer valid. Given a large initial “kick”, the velocity term  $L\dot{h}$  becomes quite large. This is what is responsible for the much larger values of the longitudinal and shear mode overlap reduction functions compared to those of the transverse modes.

## Overlap reduction functions for the NANOGrav pulsars

The NANOGrav PTA consists of 24 pulsars. Australia Telescope National Facility data

---

<sup>1</sup>Here  $\gamma$  is Euler’s constant.

PSRJ	Distance (kpc)	PSRJ	Distance (kpc)
J0030+0451	0.23	J1853+1303	1.60
J0218+4232	5.85	J1857+0943	0.70
J0613-0200	2.19	J1903+0327	6.45
J1012+5307	0.52	J1909-3744	0.55
J1024-0719	0.35	J1910+1256	1.95
J1455-3330	0.74	J1918-0642	1.40
J1600-3053	2.67	J1939+2134	3.58
J1640+2224	1.19	J1944+0907	1.28
J1643-1224	4.86	J1955+2908	5.39
J1713+0747	0.89	J2010-1323	1.29
J1738+0333	1.97	J2145-0750	0.50
J1744-1134	0.17	J2317+1439	1.89

Table 2: NANOGrav Pulsar Data

for these pulsars is given in Table 2 (Manchester et al. 2005). Using numerical techniques, the overlap reduction function for each pulsar pair was computed. Results are given in Fig. 3 a–d and show that the calculated values of the  $\Gamma(f)$  are consistent with analytical results discussed in previous sections of this document. for the non-transverse modes for frequencies up to  $\sim 10^{-9}$  Hz.

Pulsar pairs with the smallest ( $\xi < 12^\circ$ ) separation angles (starred curves in Fig. 3 b, d) are characterized by large values of the overlap reduction function and monotonic growth up to some limiting frequency. Pulsar pairs with larger ( $\xi > 12^\circ$ ) separation angles (un-starred curves in Fig. 3 b, d and all curves in Fig. 3) do not display monotonic growth up to a limiting frequency, but still obtain much larger values than those of the plus and cross modes. Fig. 3 shows that sensitivity is greater for scalar and vector modes than tensor modes, and increases rapidly for pulsars that are nearly co-aligned in the sky. Theoretical sensitivity estimates using (19) support this result. In these plots, increased variation in curve amplitudes appears due to the fact that the pulsars are not equidistant from the Earth.

Over the entire range of frequencies relevant to pulsar timing experiments (up to  $\sim 10^{-7}$ ), the overlap reduction functions are roughly constant. In practice, some optimality is lost due to the fact that pulsar distances are known at best to only  $\sim 10\%$  (Cordes and Lazio 2002).

## Discussion

Direct detection of GWs is possible in the next decade using a pulsar timing array. This detection will provide a mechanism for testing various metric theories of gravity. To develop robust detection strategies, we have analyzed overlap reduction functions for all possible GW polarization modes. For non-transverse GWs, there exists a region of the sky for which the pulse is in the long wavelength limit, leading to a frequency dependent

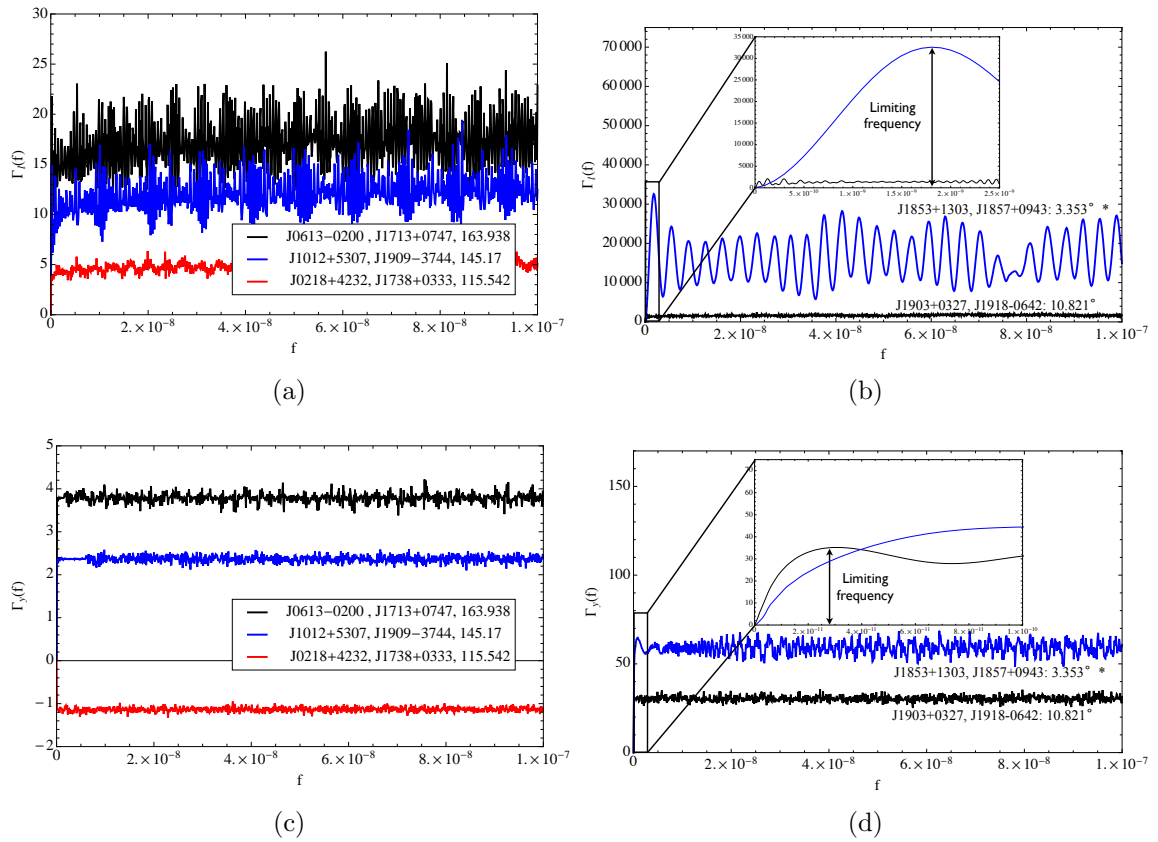


Figure 3:  $\Gamma(f)$  for some of the NANOGGrav pulsar pairs. Pulsar pairs, along with their angular separation in degrees, are given in the legend. As  $f$  increases,  $\Gamma(f)$  approaches a constant value. The asterisk indicates the NANOGGrav pulsar pair with the smallest angular separation ( 3.35 degrees). Note the larger values of the  $\Gamma(f)$ s for this pair.

overlap reduction function. Large values of  $\Gamma(f)$  for these non-transverse modes indicates increased sensitivity to scalar-longitudinal and vector GWs. A study of current data from the NANOGrav collaboration indicates that pulsar timing measurements are in the optimal regime for most pulsars.

## References

- S. Detweiler, *Astrophys. J.* **234**, 1100 (1979).
- K. J. Lee, F. A. Jenet, and R. H. Price, *Astrophys. J.* **685**, 1304 (2008), URL <http://stacks.iop.org/0004-637X/685/i=2/a=1304>.
- C. M. Will, *Theory and Experiment in Gravitational Physics* (Cambridge University Press, 1993).
- A. Nishizawa, A. Taruya, K. Hayama, S. Kawamura, and M.-a. Sakagami, *Phys. Rev. D* **79**, 082002 (2009), URL <http://link.aps.org/doi/10.1103/PhysRevD.79.082002>.
- F. S. N. Lobo, *ArXiv e-prints* (2008), 0807.1640.
- M. E. S. Alves, O. D. Miranda, and J. C. N. de Araujo, *Phys. Lett. B* **679**, 401 (2009), 0908.0861.
- S. Capozziello and M. Francaviglia, *Gen. Rel. Grav.* **40**, 357 (2008), 0706.1146.
- A. De Felice and S. Tsujikawa, *Living Rev. Rel.* **13**, 3 (2010), 1002.4928.
- M. Brunetti, E. Coccia, V. Fafone, and F. Fucito, *Phys. Rev. D* **59**, 044027 (1999), URL <http://www.citebase.org/abstract?id=oai:arXiv.org:gr-qc/9805056>.
- T. Clifton, P. G. Ferreira, A. Padilla, and C. Skordis, *ArXiv e-prints* (2011), 1106.2476.
- E. Sagi, *Phys. Rev. D* **81**, 064031 (2010), 1001.1555.
- T. Clifton, M. Banados, and C. Skordis, *Class. Quant. Grav.* **27**, 235020 (2010), 1006.5619.
- C. Skordis, *Class. Quant. Grav.* **26**, 143001 (2009), 0903.3602.
- M. Milgrom, *Phys. Rev. D* **80**, 123536 (2009), 0912.0790.
- M. Anholm, S. Ballmer, J. D. E. Creighton, L. R. Price, and X. Siemens, *Phys. Rev. D* **79**, 084030 (2009), URL <http://link.aps.org/doi/10.1103/PhysRevD.79.084030>.
- M. E. d. S. Alves and M. Tinto, *Phys. Rev. D* **83**, 123529 (2011), URL <http://link.aps.org/doi/10.1103/PhysRevD.83.123529>.
- R. N. Manchester, G. B. Hobbs, A. Teoh, and M. Hobbs, *Astrophys. J.* **129**, 1993 (2005), URL <http://stacks.iop.org/1538-3881/129/i=4/a=1993>.
- J. M. Cordes and T. J. W. Lazio, *ArXiv Astrophysics e-prints* (2002), [arXiv:astro-ph/0207156](http://arxiv.org/abs/astro-ph/0207156).

# Extracting Equation of State Parameters from Black Hole-Neutron Star Mergers

Benjamin D. Lackey<sup>1</sup>, Koutarou Kyutoku<sup>2</sup>, Masaru Shibata<sup>2</sup>, Patrick R. Brady<sup>1</sup>, John L. Friedman<sup>1</sup>

<sup>1</sup>Department of Physics, University of Wisconsin–Milwaukee, Milwaukee, WI, USA

<sup>2</sup>Yukawa Institute for Theoretical Physics, Kyoto University, Kyoto, Japan

The late inspiral, merger, and ringdown of a black hole-neutron star (BHNS) system can provide information about the neutron-star equation of state (EOS). Candidate EOSs can be approximated by a parametrized piecewise-polytropic EOS, and we report results from a large set of BHNS inspiral simulations that systematically vary two parameters. To within the accuracy of the simulations, we find that a single physical parameter  $\Lambda$ , describing its deformability, can be extracted from the late inspiral, merger, and ringdown waveform. This parameter is related to the radius, mass, and  $\ell = 2$  Love number,  $k_2$ , of the neutron star by  $\Lambda = 2k_2 R^5 / 3M_{\text{NS}}^5$ , and it is the same parameter that determines the departure from point-particle dynamics during the early inspiral. Using various configurations of a single Advanced LIGO detector, we find that  $\Lambda^{1/5}$  or equivalently  $R$  can be extracted to 10–40% accuracy from single events for mass ratios of  $Q = 2$  and 3 at a distance of 100 Mpc, while with the proposed Einstein Telescope, EOS parameters can be extracted to accuracy an order of magnitude better.

## Introduction

Construction of the second-generation Advanced LIGO (aLIGO) detectors is underway, and will soon begin for Advanced VIRGO and LCGT, making it likely that gravitational waveforms from compact binaries will be observed in this decade. Plans are also in development for the third generation Einstein Telescope (ET) detector with an order-of-magnitude increase in sensitivity over aLIGO. Population synthesis models predict that with a single aLIGO detector black hole–neutron star (BHNS) systems be observed with a signal-to-noise ratio (SNR) of 8, at an event rate between 0.2 and 300 events per year at the same SNR and with a most likely value of 10 events per year for a canonical  $1.4 M_{\odot}$ – $10 M_{\odot}$  system [1]. The expected mass ratios  $Q = M_{\text{BH}}/M_{\text{NS}}$  of BHNS systems are also highly uncertain and may range from just under 3 to more than 20 [2, 3].

A major goal of the gravitational-wave (GW) program is to extract from observed waveforms the physical characteristics of their sources and, in particular, to use the waveforms of inspiraling and merging binary neutron star (BNS) and BHNS systems to constrain the uncertain EOS of neutron-star matter. During inspiral the tidal interaction between the two stars leads to a small drift in the phase of the gravitational waveform relative to a point particle system. Specifically the tidal field  $\mathcal{E}_{ij}$  of one star will induce a quadrupole moment  $Q_{ij}$  in the other star given by  $Q_{ij} = -\lambda \mathcal{E}_{ij}$  where  $\lambda$  [24] is an EOS dependent quantity that describes how easily the star is distorted. A method for determining  $\lambda$  for relativistic stars was found by Hinderer [4]; its effect on the waveform was calculated to Newtonian order (with the relativistic value of  $\lambda$ ) by Flanagan and Hinderer [5] and to first post-Newtonian (PN) order by Vines, Flanagan, and Hinderer [6, 7]. This tidal description has also been extended to higher order multipoles [8, 9].

Numerical BHNS simulations have been done to examine the dependence of the waveform on mass ratio, BH spin, NS mass, and the neutron-star EOS. However, an analysis of the detectability of EOS information with GW detectors using these simulations has not yet been done, and the present paper presents the first results of this kind. EOS information from tidal interactions is present in the inspiral waveform. For BHNS systems, however, the stronger signal is likely to arise from a sharp drop in the GW amplitude arising from tidal disruption prior to merger or, when there is negligible disruption, from the cutoff frequency at merger [10].

We find from simulations of the last few orbits, merger, and ringdown of BHNS systems with varying

---

[1] We thank Alessandro Nagar for significant help with understanding the EOB formalism, Yi Pan and Alessandra Buonanno for providing EOB waveforms with spinning black holes, Jocelyn Read for providing routines used in the data analysis, and Jolien Creighton for generating narrowband noise curves. This work was supported by NSF Grants PHY-1001515 and PHY-0923409, by Grant-in-Aid for Scientific Research (21340051), by Grant-in-Aid for Scientific Research on Innovative Area (20105004) of Japanese MEXT, and by a Grant-in-Aid of JSPS. BL would also like to acknowledge support from a UWM Graduate School Fellowship and the Wisconsin Space Grant Consortium. KK is also supported by the Grant-in-Aid for the Global COE Program “The Next Generation of Physics, Spun from Universality and Emergence” of Japanese MEXT.

EOS that, to within numerical accuracy, the EOS parameter extracted from the waveform is the same tidal parameter  $\Lambda$  that determines the departure from point particle behavior during inspiral; here  $\Lambda$  is a dimensionless version of the tidal parameter:

$$\Lambda := G\lambda \left( \frac{c^2}{GM_{\text{NS}}} \right)^5 = \frac{2}{3}k_2 \left( \frac{c^2 R}{GM_{\text{NS}}} \right)^5, \quad (1)$$

where  $k_2$  is the quadrupole Love number.

*Conventions:* Unless otherwise stated we set  $G = c = 1$ .

### Parametrized EOS

To understand the dependence of the BHNS waveform on the EOS we systematically vary the free parameters of a parametrized EOS and then simulate a BHNS inspiral for each set of parameters. We choose the piecewise polytropic EOS introduced in Ref [11]. Within each density interval  $\rho_{i-1} < \rho < \rho_i$ , the pressure  $p$  is given in terms of the rest mass density  $\rho$  by

$$p(\rho) = K_i \rho^{\Gamma_i}, \quad (2)$$

where the adiabatic index  $\Gamma_i$  is constant in each interval, and the pressure constant  $K_i$  is chosen so that the EOS is continuous at the boundaries  $\rho_i$  between adjacent segments of the EOS. The energy density  $\epsilon$  is found using the first law of thermodynamics,

$$d\frac{\epsilon}{\rho} = -pd\frac{1}{\rho}. \quad (3)$$

Ref. [11] uses a fixed low density EOS for the NS crust. The parametrized high density EOS is then joined onto the low density EOS at a density  $\rho_0$  that depends on the values of the high-density EOS parameters. The high-density EOS consists of a three-piece polytrope with fixed dividing densities  $\rho_1 = 10^{14.7} \text{ g/cm}^3$  and  $\rho_2 = 10^{15} \text{ g/cm}^3$  between the three polytropes. The resulting EOS has four free parameters. The first parameter, the pressure  $p_1$  at the first dividing density  $\rho_1$ , is closely related to the radius of a  $1.4 M_\odot$  NS [12]. The other three parameters are the adiabatic indices  $\{\Gamma_1, \Gamma_2, \Gamma_3\}$  for the three density intervals. This parametrization accurately fits a wide range of theoretical EOS and reproduces the corresponding NS properties such as radius, moment of inertia, and maximum mass to a few percent [11].

Following previous work on BNS [13] and BHNS simulations [14, 15] we use a simplified two-parameter version of the piecewise-polytrope parametrization and uniformly vary each of these parameters. For our two parameters we use the pressure  $p_1$  as well as a single fixed adiabatic index  $\Gamma = \Gamma_1 = \Gamma_2 = \Gamma_3$  for the core. The crust EOS is given by a single polytrope with the constants  $K_0 = 3.5966 \times 10^{13}$  in cgs units and  $\Gamma_0 = 1.3569$  so that the pressure at  $10^{13} \text{ g/cm}^3$  is  $1.5689 \times 10^{31} \text{ dyne/cm}^2$ . (For most values of  $p_1$ ,  $\Gamma_1$ , and  $\Gamma_2$ , the central density of a  $1.4 M_\odot$  star is below or just above  $\rho_2$ , so the parameter  $\Gamma_3$  is irrelevant anyway for BNS before merger and BHNS for all times.)

We list in Table I the 21 EOS used in the simulations along with some of the NS properties. In addition, we plot the EOS as points in parameter space in Fig. 1 along with contours of constant radius, tidal deformability  $\Lambda$ , and maximum NS mass. The  $1.93 M_\odot$  maximum mass contour corresponds to the recently observed pulsar with a mass of  $1.97 \pm 0.04 M_\odot$  measured using the Shapiro delay [16]. In this two-parameter cross section of the full four-parameter EOS space, parameters below this curve are ruled out.

### Description of waveforms

Using the 21 EOS described in Table I, we have performed 30 BHNS inspiral and merger simulations with different mass ratios  $Q = M_{\text{BH}}/M_{\text{NS}}$  and neutron star masses  $M_{\text{NS}}$ . A complete list of these simulations is given in Table II. For the mass ratio  $Q = 2$  and NS mass  $M_{\text{NS}} = 1.35 M_\odot$ , we performed a simulation for each of the 21 EOS. In addition, we performed simulations of a smaller NS mass ( $Q = 2$ ,  $M_{\text{NS}} = 1.20 M_\odot$ )

TABLE I: Neutron star properties for the 21 EOS used in the simulations. The original EOS names [13–15] are also listed.  $p_1$  is given in units of  $\text{dyne/cm}^2$ , maximum mass is in  $M_\odot$ , and neutron star radius  $R$  is in km.  $R$ ,  $k_2$ , and  $\Lambda$  are given for the two masses used:  $\{1.20, 1.35\} M_\odot$ .

EOS	$\log p_1$	$\Gamma$	$M_{\max}$	$R_{1.20}$	$k_{2,1.20}$	$\Lambda_{1.20}$	$R_{1.35}$	$k_{2,1.35}$	$\Lambda_{1.35}$
p.3 $\Gamma$ 2.4 Bss	34.3	2.4	1.566	10.66	0.0765	401	10.27	0.0585	142
p.3 $\Gamma$ 2.7 Bs	34.3	2.7	1.799	10.88	0.0910	528	10.74	0.0751	228
p.3 $\Gamma$ 3.0 B	34.3	3.0	2.002	10.98	0.1010	614	10.96	0.0861	288
p.3 $\Gamma$ 3.3	34.3	3.3	2.181	11.04	0.1083	677	11.09	0.0941	334
p.4 $\Gamma$ 2.4 HBss	34.4	2.4	1.701	11.74	0.0886	755	11.45	0.0723	301
p.4 $\Gamma$ 2.7 HBs	34.4	2.7	1.925	11.67	0.1004	828	11.57	0.0855	375
p.4 $\Gamma$ 3.0 HB	34.4	3.0	2.122	11.60	0.1088	872	11.61	0.0946	422
p.4 $\Gamma$ 3.3	34.4	3.3	2.294	11.55	0.1151	903	11.62	0.1013	454
p.5 $\Gamma$ 2.4	34.5	2.4	1.848	12.88	0.1000	1353	12.64	0.0850	582
p.5 $\Gamma$ 2.7	34.5	2.7	2.061	12.49	0.1096	1271	12.42	0.0954	598
p.5 $\Gamma$ 3.0 H	34.5	3.0	2.249	12.25	0.1165	1225	12.27	0.1029	607
p.5 $\Gamma$ 3.3	34.5	3.3	2.413	12.08	0.1217	1196	12.17	0.1085	613
p.6 $\Gamma$ 2.4	34.6	2.4	2.007	14.08	0.1108	2340	13.89	0.0970	1061
p.6 $\Gamma$ 2.7	34.6	2.7	2.207	13.35	0.1184	1920	13.32	0.1051	932
p.6 $\Gamma$ 3.0	34.6	3.0	2.383	12.92	0.1240	1704	12.97	0.1110	862
p.6 $\Gamma$ 3.3	34.6	3.3	2.537	12.63	0.1282	1575	12.74	0.1155	819
p.7 $\Gamma$ 2.4	34.7	2.4	2.180	15.35	0.1210	3941	15.20	0.1083	1860
p.7 $\Gamma$ 2.7	34.7	2.7	2.362	14.26	0.1269	2859	14.25	0.1144	1423
p.7 $\Gamma$ 3.0 1.5H	34.7	3.0	2.525	13.62	0.1313	2351	13.69	0.1189	1211
p.7 $\Gamma$ 3.3	34.7	3.3	2.669	13.20	0.1346	2062	13.32	0.1223	1087
p.9 $\Gamma$ 3.0 2H	34.9	3.0	2.834	15.12	0.1453	4382	15.22	0.1342	2324

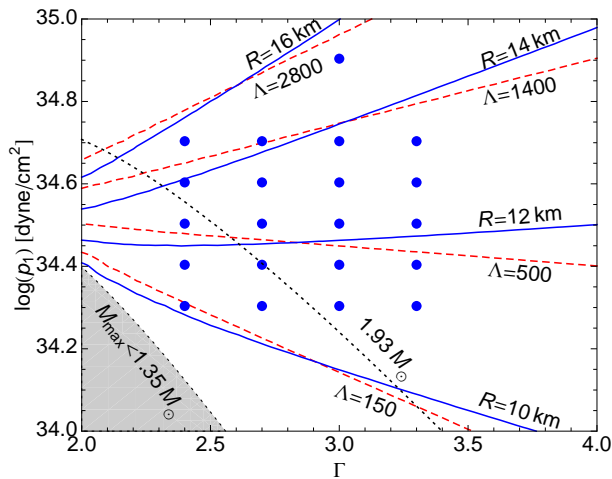


FIG. 1: The 21 EOS used in the simulations are represented by blue points in the parameter space. For a NS of mass  $1.35 M_\odot$ , contours of constant radius are solid blue and contours of constant tidal deformability  $\Lambda$  are dashed red. Also shown are dotted contours of maximum NS mass. The shaded region does not allow a  $1.35 M_\odot$  NS.

and a larger mass ratio ( $Q = 3$ ,  $M_{\text{NS}} = 1.35 M_\odot$ ), in which we only varied the pressure  $p_1$  over the range  $34.3 \leq \log(p_1/(\text{dyne cm}^{-2})) \leq 34.9$  while holding the core adiabatic index fixed at  $\Gamma = 3.0$ .

TABLE II: Data for the 30 BHNS simulations. NS mass is in units of  $M_\odot$ , and  $\Omega_0 M$  is the angular velocity used in the initial data where  $M = M_{\text{BH}} + M_{\text{NS}}$ .

$Q$	$M_{\text{NS}}$	EOS	$\Omega_0 M$	$Q$	$M_{\text{NS}}$	EOS	$\Omega_0 M$
2	1.35	p.3 $\Gamma$ 2.4	0.028	2	1.35	p.6 $\Gamma$ 3.3	0.025
2	1.35	p.3 $\Gamma$ 2.7	0.028	2	1.35	p.7 $\Gamma$ 2.4	0.025
2	1.35	p.3 $\Gamma$ 3.0	0.028	2	1.35	p.7 $\Gamma$ 2.7	0.025
2	1.35	p.3 $\Gamma$ 3.3	0.025	2	1.35	p.7 $\Gamma$ 3.0	0.028
2	1.35	p.4 $\Gamma$ 2.4	0.028	2	1.35	p.7 $\Gamma$ 3.3	0.025
2	1.35	p.4 $\Gamma$ 2.7	0.028	2	1.35	p.9 $\Gamma$ 3.0	0.025
2	1.35	p.4 $\Gamma$ 3.0	0.028	2	1.20	p.3 $\Gamma$ 3.0	0.028
2	1.35	p.4 $\Gamma$ 3.3	0.025	2	1.20	p.4 $\Gamma$ 3.0	0.028
2	1.35	p.5 $\Gamma$ 2.4	0.025	2	1.20	p.5 $\Gamma$ 3.0	0.028
2	1.35	p.5 $\Gamma$ 2.7	0.025	2	1.20	p.9 $\Gamma$ 3.0	0.022
2	1.35	p.5 $\Gamma$ 3.0	0.028	3	1.35	p.3 $\Gamma$ 3.0	0.030
2	1.35	p.5 $\Gamma$ 3.3	0.025	3	1.35	p.4 $\Gamma$ 3.0	0.030
2	1.35	p.6 $\Gamma$ 2.4	0.025	3	1.35	p.5 $\Gamma$ 3.0	0.030
2	1.35	p.6 $\Gamma$ 2.7	0.025	3	1.35	p.7 $\Gamma$ 3.0	0.030
2	1.35	p.6 $\Gamma$ 3.0	0.025	3	1.35	p.9 $\Gamma$ 3.0	0.028

Two of the gravitational waveforms are shown in Fig. 2 below. The waveforms are compared with effective one body (EOB) binary black hole (BBH) waveforms of the same mass ratio and NS mass which are also shown. The most significant differences begin just before the merger of the black hole and neutron star. For neutron stars with a small radius, the black hole does not significantly distort the neutron star which crosses the event horizon intact. As a result, the merger and ringdown of these waveforms are very similar to the BBH waveform. However, a larger NS may be completely tidally disrupted just before merger resulting in a suppressed merger and ringdown waveform. Disruption suppresses the ringdown for two reasons related to the spreading of the matter: The ringdown is primarily a superposition of nonaxisymmetric quasinormal modes, dominated by the  $l = m = 2$  mode, while the disrupted matter is roughly axisymmetric as it accretes onto the black hole; and the accretion timescale of the spread-out matter is long compared to the periods of the dominant modes.

The monotonic dependence of the waveform on  $\Lambda$  can be seen in its Fourier transform  $\tilde{h}$ , shown in Fig. 3. The predicted EOS dependent frequency cutoff in the waveform [10] is clearly shown in the amplitude. Neutron stars that are more easily disrupted (larger  $\Lambda$ ) result in an earlier and lower frequency drop in their waveform amplitude than NS with smaller  $\Lambda$ .

### Hybrid Waveform Construction

Since our numerical simulations typically begin  $\sim 5$  orbits before merger, it is necessary to join the numerical waveforms to analytic waveforms representing the earlier inspiral. There is a substantial literature comparing analytic and phenomenological waveforms with numerical waveforms extracted from simulations of BBH coalescence. For unequal mass systems, the EOB formalism (see Ref. [17] for a review) has proven to be a powerful tool to generate analytic waveforms that agree with numerical simulations.

We use a method similar to that described by Read et al. [13] to join each of the numerical BHNS waveforms to a reference EOB waveform, generating a hybrid EOB–numerical waveform. Denote a complex numerical waveform by  $h_{\text{NR}}(t) = h_+^{\text{NR}}(t) - ih_\times^{\text{NR}}(t)$  and an EOB waveform with the same  $Q$  and  $M_{\text{NS}}$  by  $h_{\text{EOB}}(t) = h_+^{\text{EOB}}(t) - ih_\times^{\text{EOB}}(t)$ . A constant time-shift  $\tau$  and phase-shift  $\Phi$  can be applied to the EOB waveform to match it to a section of the numerical waveform by rewriting it as  $h_{\text{EOB}}(t - \tau)e^{-i\Phi}$ . We hold the numerical

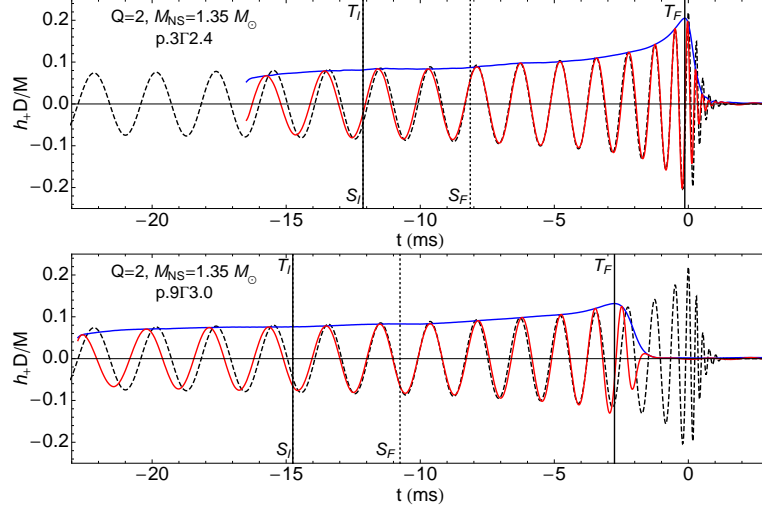


FIG. 2:  $h_+$  and  $|h| = |h_+ - ih_-|$  for BHNS waveforms for  $(Q = 2, M_{\text{NS}} = 1.35 M_\odot)$  with two different EOS are represented by solid red and blue curves respectively. The softest EOS p.3 $\Gamma$ 2.4 is on top and the stiffest EOS p.9 $\Gamma$ 3.0 is on bottom. An EOB BBH waveform (dashed) with the same values of  $Q$  and  $M_{\text{NS}}$  is matched to each numerical waveform within the matching window  $T_I < t < T_F$  bounded by solid vertical lines. A hybrid EOB BBH–Numerical BHNS waveform is generated by splicing the waveforms together within a splicing window  $S_I < t < S_F$  bounded by dotted vertical lines. The matching window is 12 ms long and ends at the numerical merger time  $t_M^{\text{NR}}$  (time when the numerical waveform reaches its maximum amplitude), while the splicing window is 4 ms long and begins at the start of the matching window ( $S_I = T_I$ ).

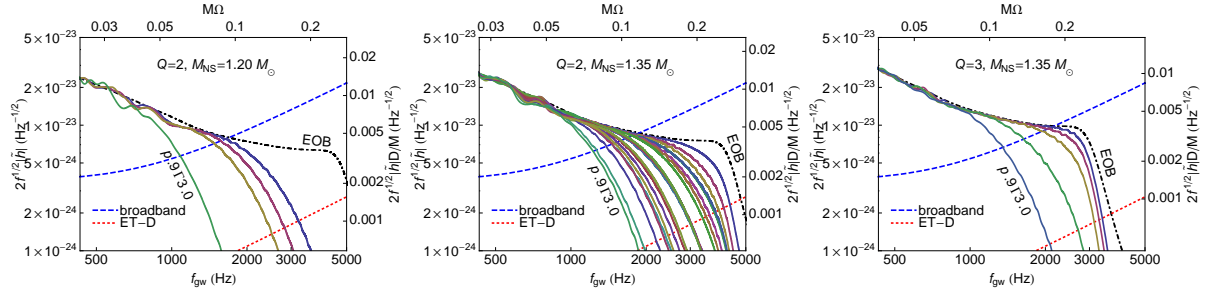


FIG. 3: Weighted Fourier transform  $2f^{1/2}|\tilde{h}(f)|$  of numerical waveforms where  $\tilde{h} = \frac{1}{2}(\tilde{h}_+ + \tilde{h}_-)$ . Dot-dashed curves are EOB waveforms with the same  $Q$  and  $M_{\text{NS}}$ . The left axis is scaled to a distance of 100 Mpc, and the noise  $S_n^{1/2}(f)$  for broadband aLIGO and ET-D are shown for comparison. In each plot the numerical waveform monotonically approaches the EOB waveform as the tidal parameter  $\Lambda$  decreases. Matching and splicing conventions are those of Fig. 2.

waveform fixed because we must specify a matching window  $T_I < t < T_F$ , and as discussed below, there is only a small region of the numerical waveforms over which a valid match can be performed. Once the values of  $\tau$  and  $\Phi$  are determined, we will then choose to instead hold the EOB waveform fixed and shift the numerical waveform in the opposite direction by rewriting it as  $h_{\text{NR}}^{\text{shift}}(t) = h_{\text{NR}}(t + \tau)e^{+i\Phi}$ . This is done so that all of the numerical waveforms with the same  $Q$  and  $M_{\text{NS}}$  are aligned relative to a single fixed reference EOB waveform.

Over a matching window  $T_I < t < T_F$  (bounded by solid vertical lines in Fig. 2), the normalized match between the waveforms is defined as

$$m(\tau, \Phi) = \frac{\text{Re} [z(\tau)e^{i\Phi}]}{\sigma_{\text{NR}}\sigma_{\text{EOB}}(\tau)}, \quad (4)$$

where

$$z(\tau) = \int_{T_I}^{T_F} h_{\text{NR}}(t) h_{\text{EOB}}^*(t - \tau) dt \quad (5)$$

and the normalizations for each waveform in the denominator are defined as

$$\sigma_{\text{NR}}^2 = \int_{T_I}^{T_F} |h_{\text{NR}}(t)|^2 dt \quad (6)$$

and

$$\sigma_{\text{EOB}}^2(\tau) = \int_{T_I}^{T_F} |h_{\text{EOB}}(t - \tau)|^2 dt. \quad (7)$$

The time-shift  $\tau$  and phase  $\Phi$  are chosen to maximize the match  $m(\tau, \Phi)$  for a fixed matching window. Explicitly, the phase is determined analytically to be  $\Phi = -\arg[z(\tau)]$ ; plugging this result back into Eq. (4), the time-shift is given by maximizing  $|z(\tau)|/[\sigma_{\text{NR}}\sigma_{\text{EOB}}(\tau)]$  over  $\tau$ . As stated above, once  $\tau$  and  $\Phi$  are found we shift the numerical waveform in the opposite direction to generate  $h_{\text{NR}}^{\text{shift}}(t) = h_{\text{NR}}(t + \tau)e^{+i\Phi}$ .

A hybrid waveform is generated by smoothly turning off the EOB waveform and smoothly turning on the shifted numerical waveform over a splicing window  $S_I < t < S_F$  (bounded by dotted vertical lines in Fig. 2) which can be chosen independently of the matching window. As in Ref. [13], we employ Hann windows

$$w_{\text{off}}(t) = \frac{1}{2} \left[ 1 + \cos \left( \frac{\pi[t - S_I]}{S_F - S_I} \right) \right] \quad (8)$$

$$w_{\text{on}}(t) = \frac{1}{2} \left[ 1 - \cos \left( \frac{\pi[t - S_I]}{S_F - S_I} \right) \right]. \quad (9)$$

The hybrid waveform is then written

$$h_{\text{hybrid}}(t) = \begin{cases} h_{\text{EOB}}(t) & t < S_I \\ w_{\text{off}}(t)h_{\text{EOB}}(t) + w_{\text{on}}(t)h_{\text{NR}}^{\text{shift}}(t) & S_I < t < S_F \\ h_{\text{NR}}^{\text{shift}}(t) & t > S_F \end{cases}. \quad (10)$$

As shown in Fig. 2, we choose the start of the splicing interval to be the same as the start of the matching window  $S_I = T_I$  and choose the end of the splicing window to be  $S_F = T_I + 4$  ms. It is also necessary to use these windows to smoothly turn on the hybrid waveform at low frequency when performing a discrete Fourier transform to avoid the Gibbs phenomenon. Unlike the case for BNS waveforms, it is not necessary to window the end of the hybrid waveform as the amplitude rapidly decays to zero anyway during the ringdown.

### Parameter estimation

The output of a gravitational-wave detector  $s(t) = n(t) + h(t)$  is the sum of detector noise  $n(t)$  and a possible gravitational-wave signal  $h(t)$ . Stationary, Gaussian noise is characterized by its power spectral density (PSD)  $S_n(|f|)$  defined by

$$\langle \tilde{n}(f) \tilde{n}^*(f') \rangle = \frac{1}{2} \delta(f - f') S_n(|f|). \quad (11)$$

The gravitational wave signal is given in terms of the two polarizations of the gravitational wave by

$$h(t) = F_+ h_+(t) + F_\times h_\times(t), \quad (12)$$

where  $F_{+, \times}$  are the detector response functions and depend on the location of the binary and the polarization angle of the waves. We assume the binary is optimally located at the zenith of the detector and optimally oriented with its orbital plane parallel to that of the detector. This condition is equivalent to averaging  $h_+$  and  $h_\times$  ( $F_+ = F_\times = 1/2$ ).

It is well known [18] that the optimal statistic for detection of a known signal  $h(t)$  in additive Gaussian noise is

$$\rho = \frac{(h|s)}{\sqrt{(h|h)}} \quad (13)$$

where the inner product between two signals  $h_1$  and  $h_2$  is given by

$$(h_1|h_2) = 4\text{Re} \int_0^\infty \frac{\tilde{h}_1(f)\tilde{h}_2^*(f)}{S_n(f)} df. \quad (14)$$

In searches for gravitational-wave signals from compact binary mergers, a parametrized signal  $h(t; \theta^A)$  is known in advance of detection, and the parameters  $\theta^A$  must be estimated from the measured detector output  $s(t)$ . The parameters  $\theta^A$  of an inspiral are estimated by maximizing the inner product of the signal  $s(t)$  over the template waveforms  $h(t; \theta^A)$ . In the high signal-to-noise limit, the statistical uncertainty in the estimated parameters  $\hat{\theta}^A$  arising from the instrumental noise can be estimated using the Fisher matrix

$$\Gamma_{AB} = \left( \frac{\partial h}{\partial \theta^A} \left| \frac{\partial h}{\partial \theta^B} \right. \right) \Bigg|_{\hat{\theta}^A}. \quad (15)$$

Note that  $\hat{\theta}^A$  are the parameter values that maximize the signal-to-noise. The variance  $\sigma_A^2 = \sigma_{AA} = \langle (\Delta\theta^A)^2 \rangle$  and covariance  $\sigma_{AB} = \langle \Delta\theta^A \Delta\theta^B \rangle$  of the parameters are then given in terms of the Fisher matrix by

$$\langle \Delta\theta^A \Delta\theta^B \rangle = (\Gamma^{-1})^{AB}. \quad (16)$$

For hybrid waveforms, the partial derivatives in the Fisher matrix must be approximated with finite differences. It is most robust to compute the derivatives of the Fourier transforms used in the inner product. We rewrite the Fourier transform of each waveform in terms of the amplitude  $A$  and phase  $\Phi$  as  $\exp[\ln A - i\Phi]$ . The derivatives  $\partial \ln A / \partial \theta^A$  and  $\partial \Phi / \partial \theta^A$  are then evaluated with finite differencing.

In general, errors in the parameters  $\theta^A$  are correlated with each other forming an error ellipsoid in parameter space determined by the Fisher matrix  $\Gamma_{AB}$ . The uncorrelated parameters that are best extracted from the signal are found by diagonalizing  $\Gamma_{AB}$ . These new parameters are linear combinations of the original parameters  $\theta^A$ . We focus attention below on the two parameters  $\log(p_1)$  and  $\Gamma$ , and fix all other parameters. We therefore construct the error ellipses in  $\{\log(p_1), \Gamma\}$  parameter space and identify the parameter with the smallest statistical errors.

For the BHNS systems discussed here, the greatest departure from BBH behavior occurs for gravitational-wave frequencies in the range 500–5000 Hz. As a result, detector configurations optimized for detection of BHNS systems with low noise in the region below 500 Hz are not ideal for estimating EOS parameters. We therefore present results for the broadband aLIGO noise curve [19] and the ET-D noise curve [20] shown in Fig. 4.

In Fig. 5, we show the resulting  $1\text{-}\sigma$  error ellipses in the 2-dimensional parameter space  $\{\log(p_1), \Gamma\}$  for an optimally oriented BHNS with  $Q = 2$  and  $M_{\text{NS}} = 1.35M_\odot$  at a distance of 100 Mpc. Surfaces of constant  $\Lambda^{1/5}$  and NS radius, which are almost parallel to each other, are also shown. One can see that the error ellipses are aligned with these surfaces. This indicates that, as expected,  $\Lambda^{1/5}$  is the parameter that is best extracted from BHNS gravitational-wave observations. Because  $\Lambda^{1/5}$  and  $R$  are so closely aligned we will use these two parameters interchangeably.

As mentioned above, there is some freedom in construction of the hybrid waveforms. The size and orientation of the error ellipses also depend on the details of this construction. We find that as long as the matching window is longer than approximately four gravitational-wave cycles to average out the effects of eccentricity and does not include the first two gravitational-wave cycles, the orientation of the error ellipses does not change significantly. As expected, the size of the ellipses decreases as more of the numerical waveform is incorporated into the hybrid

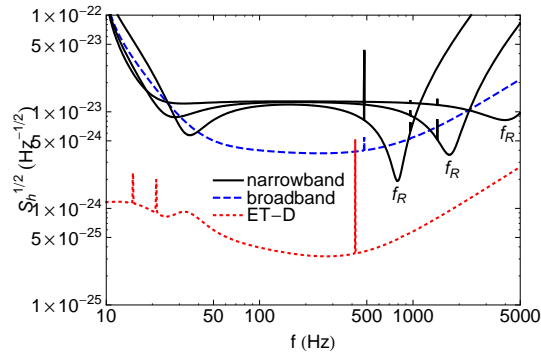


FIG. 4: Noise PSD for broadband aLIGO (dashed blue), ET-D (dotted red) and various configurations of narrowband aLIGO (solid black). The minima of the narrowband configuration are labeled  $f_R$

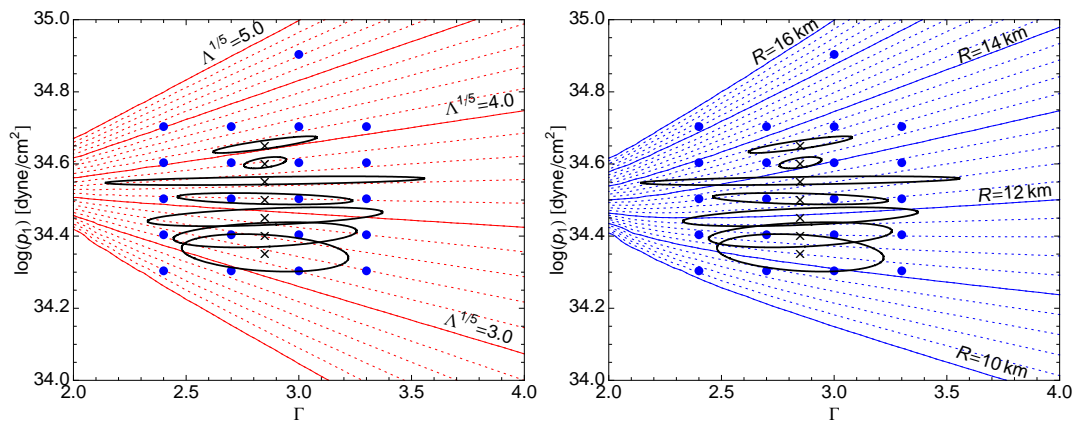


FIG. 5:  $1\text{-}\sigma$  error ellipses for ET-D. Evenly spaced contours of constant  $\Lambda^{1/5}$  ( $R$ ) are also shown on the left (right). Matching and splicing conventions are those of Fig. 2.

waveform. We therefore adopt the last 12 ms before merger of each numerical waveform as the matching window and the first 4 ms of the matching window for splicing as shown in Fig. 2.

We have emphasized that, to within present numerical accuracy, the late-inspiral waveform is determined by the single parameter  $\Lambda^{1/5}$ . This implies that, by using contours of constant  $\Lambda$  in the EOS space, one could have obtained the constraint on the EOS, summarized in Fig. 5 by varying only a single EOS parameter. For the simulations with other mass ratios and neutron star masses, we have used as our single parameter  $\log(p_1)$  and not  $\Gamma$  because contours of constant  $p_1$  more closely coincide with contours of constant  $\Lambda$  and because  $\Lambda$  is a one to one function of  $\log(p_1)$  throughout the parameter space. The one-parameter Fisher matrix can then be evaluated with finite differencing using the waveforms and values of  $\Lambda$  at two points in EOS parameter space with different  $\log(p_1)$ .

The uncertainties in  $\Lambda^{1/5}$  and  $R$  are shown in Fig. 6 for broadband aLIGO. The uncertainty in these quantities is  $\sim 10\text{--}40\%$  for broadband aLIGO and are shifted down by an order of magnitude to  $\sim 1\text{--}4\%$  for ET-D. The uncertainties for the higher mass ratio  $Q = 3$  are somewhat larger than for  $Q = 2$ , but not significantly so. It is not clear how rapidly the uncertainty in  $\Lambda^{1/5}$  and  $R$  will increase as the mass ratio is increased toward more realistic values. On the one hand the tidal distortion is likely to be much smaller for larger  $Q$ . On the other hand the overall signal will be louder, and the merger and ringdown will occur at lower frequencies where the noise is lower. Additional simulations for higher  $Q$  are needed to address this question.

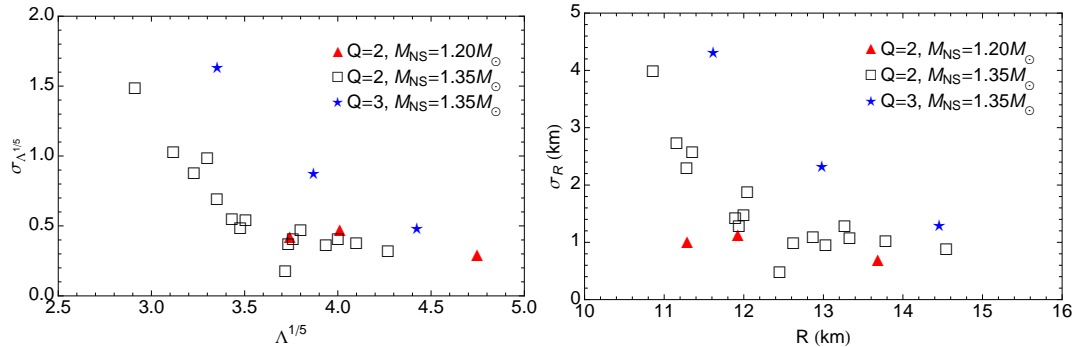


FIG. 6:  $1\text{-}\sigma$  uncertainty  $\sigma_{\Lambda^{1/5}}$  and  $\sigma_R$  as a function of the parameters  $\Lambda^{1/5}$  or  $R$  for the broadband aLIGO noise PSD. Matching and splicing conventions are those of Fig. 2.

The presence of a signal-recycling cavity in the aLIGO instruments will allow them to be tuned to have improved narrowband sensitivity at the expense of bandwidth. We have examined several narrowband tunings with central frequencies that vary between approximately  $f_R = 500$  Hz and 4000 Hz. Three of these noise curves are shown in Fig. 4. In Fig. 7 we plot the  $1\text{-}\sigma$  uncertainty in NS radius  $\sigma_R$  as a function of the narrowband central frequency  $f_R$ . For the waveforms considered in this paper the optimal narrowband frequency is in the range  $1000 \text{ Hz} \lesssim f_R \lesssim 2500 \text{ Hz}$  and depends on the mass ratio, NS mass, and EOS. Narrowband configurations usually give smaller errors than the broadband configuration if  $f_R$  happens to be tuned to within a few hundred Hz of the minimum for that BHNS event.

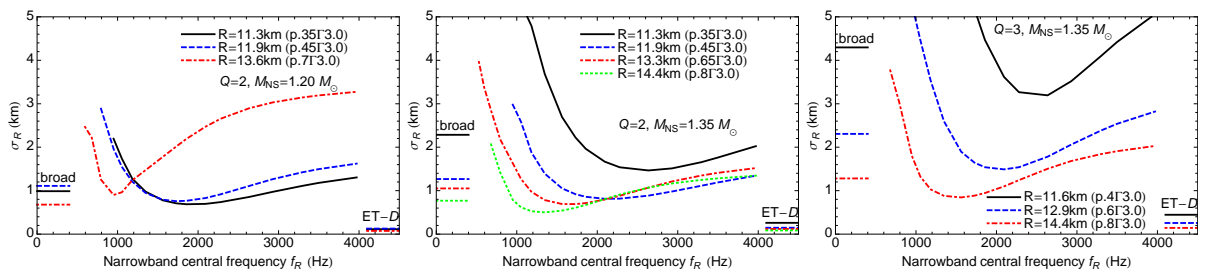


FIG. 7:  $1\text{-}\sigma$  uncertainty in  $R$  for different configurations of narrowband aLIGO and for different EOS.  $f_R$  defines the frequency where  $S_n$  is a minimum as shown in Fig. 4. Horizontal lines on the left and right indicate the corresponding  $1\text{-}\sigma$  errors for broadband aLIGO and ET-D respectively. Matching and splicing conventions are those of Fig. 2.

## Discussion

Using a large set of simulations incorporating a two-parameter EOS, we have found that the tidal deformability  $\Lambda^{1/5}$ , or equivalently the NS radius  $R$ , is the parameter that will be best extracted from BHNS waveforms. These parameters can be estimated to 10–40% with broadband aLIGO for an optimally oriented BHNS binary at 100 Mpc. The narrowband aLIGO configuration can do slightly better if it is tuned to within a few hundred Hz of the ideal frequency for a given BHNS event. The proposed Einstein Telescope will have an order-of-magnitude better sensitivity to the EOS parameters.

The results presented here can be compared with recent work to determine the mass and radius of individual NS in Type-1 X-ray bursts. Özel et al. [21] have obtained mass and radius measurements from several systems by simultaneously measuring the flux  $F$ , which is likely close to the Eddington value, and the blackbody temperature  $T$  during X-ray bursts of systems with accurately determined distances. They obtain estimates of NS mass and

radii with  $\mathcal{O}(10\%)$   $1-\sigma$  uncertainty. These radius error estimates are slightly smaller than those for the BHNS systems we have considered at 100 Mpc. However, we note that binary inspiral observations are subject to less systematic uncertainty due to questions of composition of the photosphere and associating it with the NS surface.

The uncertainty in NS radius for the merger and ringdown of BHNS systems examined here is of roughly the same size as that found for the last few orbits up to merger of BNS systems at the same 100 Mpc distance [13, 22]. BNS inspirals, however, will likely occur more frequently, and, including a tidally corrected inspiral–numerical hybrid, BNS systems are likely to have uncertainties that are smaller than BHNS systems by a factor of a few. Considering the post-merger phase for BNS waveforms may also provide additional information. Expected NS masses in both BNS and BHNS systems are slightly smaller than those measured for X-ray bursters which have accreted matter from their companion, so BNS and BHNS GW observations may complement X-ray burst observations by better constraining the lower density range of the EOS which is not well constrained from X-ray burst observations [21, 23].

- 
- [1] J. Abadie, B. P. Abbott, R. Abbott, M. Abernathy, T. Accadia, F. Acernese, C. Adams, R. Adhikari, P. Ajith, B. Allen, et al., *Classical and Quantum Gravity* **27**, 173001 (2010), 1003.2480.
  - [2] K. Belczynski, M. Dominik, T. Bulik, R. O’Shaughnessy, C. Fryer, and D. E. Holz, **715**, L138 (2010), 1004.0386.
  - [3] K. Belczynski, V. Kalogera, and T. Bulik, *Astrophys. J.* **572**, 407 (2002), arXiv:astro-ph/0111452.
  - [4] T. Hinderer, *Astrophys. J.* **677**, 1216 (2008), 0711.2420.
  - [5] É. É. Flanagan and T. Hinderer, *Phys. Rev. D* **77**, 021502 (2008), 0709.1915.
  - [6] J. Vines and É. É. Flanagan, *ArXiv e-prints* (2010), 1009.4919.
  - [7] J. Vines, T. Hinderer, and É. É. Flanagan, *ArXiv e-prints* (2011), 1101.1673.
  - [8] T. Damour and A. Nagar, *Phys. Rev. D* **80**, 084035 (2009), 0906.0096.
  - [9] T. Binnington and E. Poisson, *Phys. Rev. D* **80**, 084018 (2009), 0906.1366.
  - [10] M. Vallisneri, *Physical Review Letters* **84**, 3519 (2000), arXiv:gr-qc/9912026.
  - [11] J. S. Read, B. D. Lackey, B. J. Owen, and J. L. Friedman, *Phys. Rev. D* **79**, 124032 (2009), 0812.2163.
  - [12] J. M. Lattimer and M. Prakash, *Astrophys. J.* **550**, 426 (2001), arXiv:astro-ph/0002232.
  - [13] J. S. Read, C. Markakis, M. Shibata, K. Uryū, J. D. E. Creighton, and J. L. Friedman, *Phys. Rev. D* **79**, 124033 (2009), 0901.3258.
  - [14] K. Kyutoku, M. Shibata, and K. Taniguchi, *Phys. Rev. D* **82**, 044049 (2010), 1008.1460.
  - [15] K. Kyutoku, H. Okawa, M. Shibata, and K. Taniguchi, *ArXiv e-prints* (2011), 1108.1189.
  - [16] P. B. Demorest, T. Pennucci, S. M. Ransom, M. S. E. Roberts, and J. W. T. Hessels, *Nature (London)* **467**, 1081 (2010), 1010.5788.
  - [17] T. Damour and A. Nagar, *ArXiv e-prints* (2009), 0906.1769.
  - [18] L. A. Wainstein and V. D. Zubakov, *Extraction of signals from noise* (Prentice-Hall, Englewood Cliffs, NJ, 1962).
  - [19] D. Shoemaker (LSC, 2009), URL <https://dcc.ligo.org/cgi-bin/DocDB/ShowDocument?docid=2974>.
  - [20] S. Hild, M. Abernathy, F. Acernese, P. Amaro-Seoane, N. Andersson, K. Arun, F. Barone, B. Barr, M. Barsuglia, M. Beker, et al., *Classical and Quantum Gravity* **28**, 094013 (2011), 1012.0908.
  - [21] F. Özel, G. Baym, and T. Güver, *Phys. Rev. D* **82**, 101301 (2010), 1002.3153.
  - [22] L. Baiotti, J. Creighton, B. Giacomazzo, K. Kyutoku, C. Markakis, J. Read, L. Rezzolla, M. Shibata, K. Taniguchi, and J. Friedman, in progress (2011).
  - [23] F. Özel and D. Psaltis, *Phys. Rev. D* **80**, 103003 (2009).
  - [24] The tidal deformability for the  $\ell$ th multipole is often defined in terms of the NS radius  $R$  and its dimensionless  $\ell$ th Love number  $k_\ell$  by  $\lambda_\ell = \frac{2}{(2\ell-1)!!G} k_\ell R^{2\ell+1}$ . Here we will discuss only the  $\ell = 2$  term so we write  $\lambda := \lambda_2$ .

# Towards a Better Understanding of Dark Matter Halo Structures around Galaxies

Melissa Wheeler

Physics Department  
University of Wisconsin- La Crosse, La Crosse, WI

## Abstract

There is substantial evidence that the stars, dust, and gas visible in galaxies are enveloped in “halos” of unseen dark matter. The goal of this research is to explore the effects varying initial conditions have on final equilibrium distributions of simulated dark matter halo density and velocity, and to assess how well analytical models fit these data. In particular, we pay special attention to the velocity distributions of our models, something often overlooked in other studies. Eighty separate computer simulations representing dark matter halos were made under various initial conditions, involving two halo types and three variables. Analytical density and velocity models were fitted to the 80 halos, including de Vaucouleurs, Plummer, generalized Navarro-Frenk-White, and non-extensive thermodynamics models. Statistical chi-squared ( $\chi^2$ ) tests, quantifying how well a model fits data, were applied. Relative  $\chi^2$  values for each model were plotted, reflecting which analytical models performed best for various simulations.

## Background

While it may sometimes seem as if science has the universe pretty much figured out, that is far from the truth. One of the most mysterious aspects of the universe discovered over the last century is the apparent necessity of dark matter. By the term “dark matter”, we mean an unidentified type of matter that appears to give off little or no light (hence the “dark”), yet whose gravity influences the “light” matter that we can see, like stars and galaxies. The need for dark matter was first highlighted in the 1930s by astronomer Fritz Zwicky. According to the laws of physics, the observed motion of galaxies in clusters is incompatible with the mass inferred from the light present (Zwicky 1933, 1937). Galaxy clusters contain hundreds to thousands of individual galaxies that move under the influence of their combined gravity, and more details on how they can be used to investigate dark matter are given below. In the intervening decades, a large body of evidence for the existence of this unseen matter has been gathered. Current measurements and calculations suggest that the mass of dark matter in galaxies is at least 10 times greater than the mass in the form of stars and gas.

When we look at our own Milky Way galaxy (called the Galaxy for short), it is logical to infer that the majority of the Galaxy’s mass must lie in the center, where the high brightness shows that the mass of the stars is concentrated. Given this, we would expect the speed of stars orbiting the Galactic center to decrease with distance as the force of gravity from the center decreases. This relationship between orbital speed, distance, and gravitational force follows from the understanding that gravity acts as a centripetal force in the Galaxy.

$$G \frac{Mm}{r^2} = m \frac{v^2}{r},$$

where  $G$  is Newton’s gravitational constant,  $M$  is the mass of the Galaxy interior to distance  $r$ ,  $m$  is the mass of a star, and  $v$  is the orbital speed of the star. Gravity continually changes the direction of stars’ velocities so that they follow a circular path in the Milky Way.

We gratefully acknowledge the National Space Grant College and Fellowship Program and the Wisconsin Space Grant Consortium for supporting this research.

This relationship holds for the planets in our solar system. Since the sun contains far more mass than all the planets combined,  $M$  in this case is just the mass of the sun. Planets that are further from the sun take longer to complete one orbit of it (e.g. Earth takes one year to complete an orbit, whereas Jupiter takes almost 12 years). However, this is not what we see with stars orbiting in galaxies. Plots of orbital speed versus orbital distance are called rotation curves. The rotation curve of our solar system drops off as distance from the sun increases (Figure 1), illustrating the prediction from the above equation.

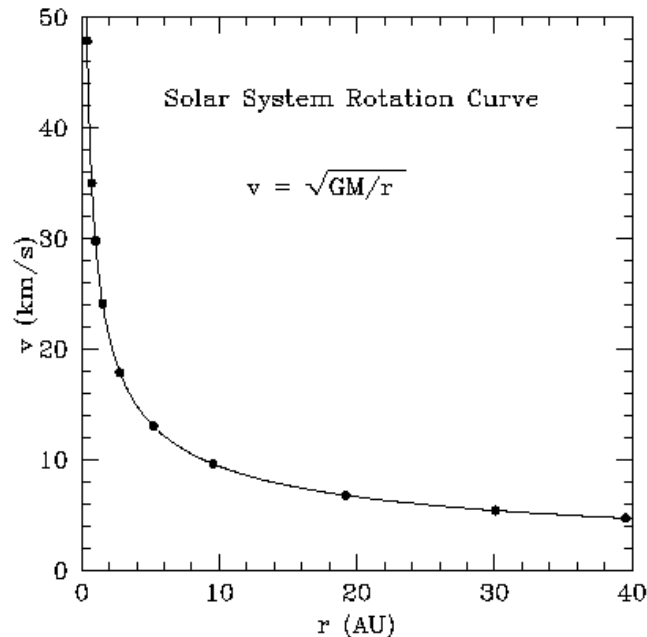


**Figure 1.** Velocity vs. distance graph showing predicted orbital speeds for planets in the solar system. As distance from the sun increases, velocity of the orbiting body decreases. Taken from [bustard.phys.nd.edu/Phys171/lectures/dm.html](http://bustard.phys.nd.edu/Phys171/lectures/dm.html).

When the orbital speed of stars (or gas) is graphed against their average distance from the center of the Galaxy, the resulting rotation curve is relatively flat (Figure 2), showing that the orbital speed remains large far from the galactic center. This implies that most of the Galaxy's mass lies not at the center, but surrounds the visible Galaxy in what is referred to as a halo, which is usually assumed to be spherical. Since very little radiation can be detected from this halo, it is assumed to be composed of dark matter. Detailed analysis of this rotation curves suggests that the Galactic dark matter mass is roughly 10 times the amount of mass in all the stars in the Milky Way.

Evidence for dark matter is also seen elsewhere in the universe. In other spiral galaxies, we can also use rotation curves to estimate their total masses. The figure below shows the orbital speeds of stars and gas in another galaxy as a function of distance from that galaxy's center. As with the Milky Way, the rotational speed does not decrease as expected far from the central mass concentration.

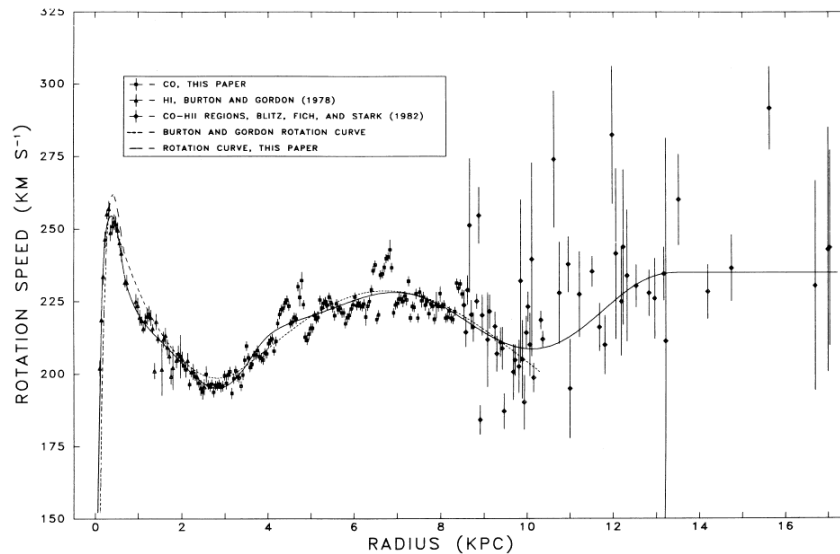


**Figure 2.** The rotation curve for the Milky Way Galaxy, showing a relatively flat result, which signifies fairly constant, large orbital speeds as distance from the Galactic center increases. Taken from [web.njit.edu/~gary/202/Lecture25.html](http://web.njit.edu/~gary/202/Lecture25.html). Data taken from Clemens (1985).

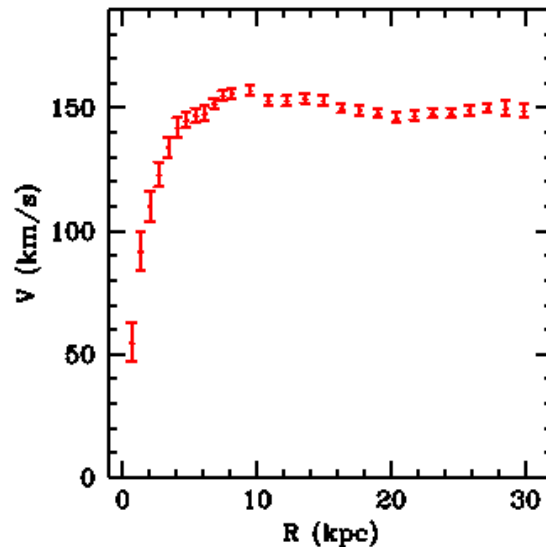


**Figure 3.** Graph of orbital velocity against distance from galactic center of a spiral galaxy, showing a relatively flat rotation curve. Image taken from [astro.berkeley.edu/~mwhite/darkmatter/rotcurve.html](http://astro.berkeley.edu/~mwhite/darkmatter/rotcurve.html); graph data from Begeman (1989).

The galaxy's total mass is found by using the law of gravity and the orbital velocities of stars and gas clouds. The luminosity, i.e. how much light the stars produce, can be used to infer the amount of mass that is in the form of stars. For example, we know how much light is emitted by our sun and we know its mass. Decades of astronomy have fine-tuned relationships between the light and mass of a wide variety of stars that exist in galaxies. If the total mass is greater than the mass attributed to the stars (and gas), the rest is inferred to be dark matter. Just like with the Milky Way, further analysis also suggests that other spiral galaxies contain at least 10 times as

much dark matter as they do stars; this means that the composition of a typical spiral galaxy is about 10% normal matter like stars and 90% dark matter.

In elliptical galaxies, we cannot use rotation curves because the stars' motions are more disorganized, so we measure the combined Doppler shifts of the stars (which tell us if they are moving towards or away from us and how fast) in the light the galaxy emits. These shifts change the light from a narrow spectral line of a certain wavelength to a broadened line that covers a range of wavelengths; the wider the spectral line, the faster the stars are moving. When spectral lines from different areas of the galaxy are compared, it is seen that the speeds of the stars remain fairly constant as we get farther from the galaxy's center, just as with spiral galaxies. While the analysis of the motions of stars in elliptical galaxies is not as simple as in spiral galaxies, it is commonly accepted that elliptical galaxies also contain large amounts of dark matter.

Concerning clusters of galaxies, there are three different ways of measuring the mass of the cluster, each of which gives more evidence for dark matter. First, the speeds of galaxies that orbit the cluster center are measured; this is the method that led to Zwicky's initial proposition of the existence of dark matter. After finding the average orbital velocity of the galaxies within the cluster and using the laws of physics to estimate the mass of the cluster, the cluster's mass is compared to its luminosity. Again, the stellar and gas mass necessary to generate that luminosity is found to be far less than the mass measured from galaxy speeds. The second method utilizes observations of X-rays from hot gas that resides between galaxies in a cluster. This gas can contain a great deal of mass, at times outweighing even the total mass in stars in the galaxies in the cluster. The temperature of this gas depends on the overall mass of the cluster, as the gas pressure outward is balanced by the inward pull of the cluster's gravity. As temperature reflects the kinetic energy of the particles and therefore the average speed of the particles, we can use these speeds to find the total mass of the cluster. These results agree with those of the first method, in that even with the added mass of the hot gas, the amount of dark matter is up to 50 times as great as the mass of the stars in the cluster's galaxies (Binney & Tremaine 1987). A third way to measure the mass of a galaxy cluster is by using gravitational lensing, which is especially useful because it does not use Newton's laws of gravity and so allows another method of checking results. Predicted by Einstein's general theory of relativity, gravitational lensing occurs because masses distort space-time; massive objects can bend light beams as they pass, instead of allowing the photons to travel in a straight line from their source. The angle of the bending depends on the mass of the object acting as a gravitational lens, so we can measure the mass by looking at how strongly the light paths are distorted. These results generally agree with those obtained by the first two methods, all suggesting that galaxy clusters contain a large amount of dark matter.

Researchers are yet unsure exactly what dark matter may be made of. It is believed that it falls into two categories: baryonic dark matter (i.e. "normal" matter made of protons, neutrons, etc. that simply does not emit very much light) and non-baryonic matter made of more extraordinary particles. Baryonic dark matter includes brown dwarfs, which are celestial objects too small to generate nuclear fusion to shine like a normal star, and a faint red star type; it is possible that many such small, dim objects (sometimes called massive compact halo objects or MACHOs) continue to roam in galaxy halos, but studies have shown that they do not exist in large enough

numbers to compose all of the dark matter. Non-baryonic dark matter is thought to consist of subatomic particles similar to neutrinos but heavier; these hypothetical particles are called weakly interacting massive particles, or WIMPs. WIMPs would have no electrical charge (and therefore not be able to emit any electromagnetic radiation), and could only interact with other matter through gravity and the weak force, making them difficult to detect directly. As a galaxy formed and normal matter collapsed into a flattened disk due to gravity and the loss of orbital energy through collisions, these particles would rarely interact with other particles, and so maintain their farther out orbits, forming the halo. Many researchers think that WIMPs may compose the majority of dark matter.

If dark matter does not exist, then there must be something wrong with our current understanding of the laws of physics and gravity. Many scientists have attempted to come up with alternative theories of gravity that would rule out the need for the existence of unseen dark matter, though none have successfully been able to do so while still explaining many other observations that the dark matter-based theories can explain. There is much evidence for the existence of dark matter, and some observations that are difficult to explain without it. For example, the “bullet” cluster (Clowe et al. 2006) is often referred to as the most compelling evidence for dark matter. In this case, two galaxy clusters collided at some point; the stars and galaxies of the clusters simply passed each other by, but the gas violently collided. Gravitational lensing measurements suggest that the majority of the mass in the clusters is centered around the galaxies, as predicted by a dark matter picture.

Much remains unknown concerning the nature and behavior of dark matter. Our work involved computer simulations that aimed to investigate the behavior of self-gravitating systems, a category into which dark matter halo structures fall, under a variety of initial conditions. The simulations were given initial positions and velocities for particles representing masses of dark matter. The computer then evolved the subsequent motions of the particles as acted on by gravity, resulting in data on the final equilibrium distribution of the system. We created a total of 80 simulations of 100,000 particles that span a range of initial conditions, which will be described in greater detail in the next section. Analysis has been done on the density and velocity profiles for the halos, and several analytical models that have been used to describe dark matter distributions have been fitted to the data. We were specifically interested in the performance of non-extensive thermodynamic models, a class of analytical models that has been discussed for dark matter halos (e.g., Kronberger et al. 2006, Barnes et al. 2007). Analysis, such as the statistical chi-squared test, has been done to determine how well each model fits the data for specific initial conditions. Also, several types of plots have been created to illustrate different aspects of the comparison of models to the data and to each other. These will be explained and findings described in Results section.

## **Methods**

This research used a computer to create simulations of particles representing masses of dark matter. These simulations that involve large numbers of massive particles being influenced by gravity are known as  $N$ -body models and are approximately collisionless. The particles' individual motions are affected by the gravity of the system as a whole, not by interactions with their close neighbors. We utilized  $N$ -body systems of 100,000 particles to simulate the behavior of dark matter particles as they interact gravitationally within the halo. We were interested in the

final equilibrium state of the halo and how the density and velocity distributions of particles have settled, i.e. where they end up and how they are moving. Each simulation was evolved from a certain set of initial conditions involving three variables and two particle distribution types.

We have used a variety of initial conditions in the creation of our simulations to compare the effect such differences may have on the analytical model fits. First, two types of model halos were simulated --- "single" and "clumpy". In single simulations, the particles were evenly and smoothly distributed throughout the system, and individual particles were given random initial velocities. Particles in clumpy halos were bound by gravity in groups, or clumps. This affects how the particles interacted within their own clump and with other clumps in the system, and influenced the final shape of the halo. We will discuss in more detail the clumpy models first.

Within our initial conditions for the clumpy halo models there were three variables, resulting in a total of 60 clumpy simulations. The first variable deals with the initial density  $\rho$  profile, which determines whether the particles are likely to be found near the center of the system or more uniformly spread throughout. The initial density profile followed  $\rho \propto 1/r$  (cuspy) or  $\rho \propto e^{-r^2}$  (Gaussian). The second variable is the virial ratio, represented by  $Q$  and ranging from 0.10, 0.20, ..., 1.00. The virial ratio is defined as twice the kinetic energy divided by the potential energy. A low value of  $Q$  means the system has little kinetic energy, which leads to low particle speeds and initial collapse of the system. Systems with high values of  $Q$  do not collapse as notably as those with low  $Q$  values, as the particles have more kinetic energy and higher speeds initially. The clumpy models also had three different temperature fractions, or  $T$  values: 0.0, 0.5, or 1.0. A system with  $T = 1.0$  is said to have "cold" conditions, where all particles in the clump move together with the clump center-of-mass.  $T = 0.0$  is a "hot" system, and clump particles have random initial velocities and center-of-mass velocities are zero. A system with  $T = 0.5$  is a "warm", intermediate system. Each clumpy simulation was given a specific density profile,  $Q$  value, and  $T$  value, requiring 60 separate models to span the clumpy initial condition parameter space.

Single halo models, where particles were distributed evenly throughout the system, resembled clumpy  $T = 0.0$  systems in that all particles had random initial velocities. Since they were not bound gravitationally in clumps, single simulations did not include a temperature fraction  $T$  variable. The cuspy and Gaussian density profile types and range of  $Q$  values remained the same, leading to 20 different single halo simulations. This gave us a grand total of 80 dark matter halo evolutions spanning a variety of initial conditions.

Once the simulated dark matter halos had been evolved, output data were given on the final state of the halo after it had reached dynamic equilibrium. We were concerned with the end-state of the density and velocity profiles, i.e. where the particles end up and how they are moving. Plots of these data were created, and then analytical models were fitted to the data. Computer code found the best-fit parameters for each of the de Vaucouleurs, Plummer, Navarro-Frenk-White (NFW), and non-extensive models to each of the 80 halo simulations. From these density profile fits, velocity profiles were estimated and also compared to the data. Statistical chi-squared ( $\chi^2$ ) tests, quantifying how well a model fits data, were applied to the analytical fits. From these values plots of the relative  $\chi^2$  values for each model were plotted, reflecting which analytical models performed best for various simulations. Our particular focus was on the performance of

the non-extensive thermodynamics model in fitting the data and how it compares to the other models. We also paid special attention to the velocity distributions of our models, something often overlooked in other studies.

### Results

From these relative  $\chi^2$  values, it can be seen which analytical models fit the simulations best for various initial conditions. Plots were created for each set of clumpy and single halos, differing in initial density  $\rho$  profile and/or temperature fraction  $T$ . These graphs show how the analytical models performed for each set as  $Q$  varies; each includes data for 10 simulations. Density, velocity and combined  $\chi^2$  values were studied. Every analytical model's  $\chi^2$  is divided by the lowest  $\chi^2$  value for each  $Q$ . Therefore the best-fitting model at every  $Q$  is given a relative  $\chi^2$  of 1; the true  $\chi^2$  value for the model is likely higher. Several plots of relative  $\chi^2$  values are included as examples. These plots reflect the results for the group of 10 simulations of clumpy halos with cuspy initial density and  $T=1.0$ , showing relative model performance as  $Q$  changes.

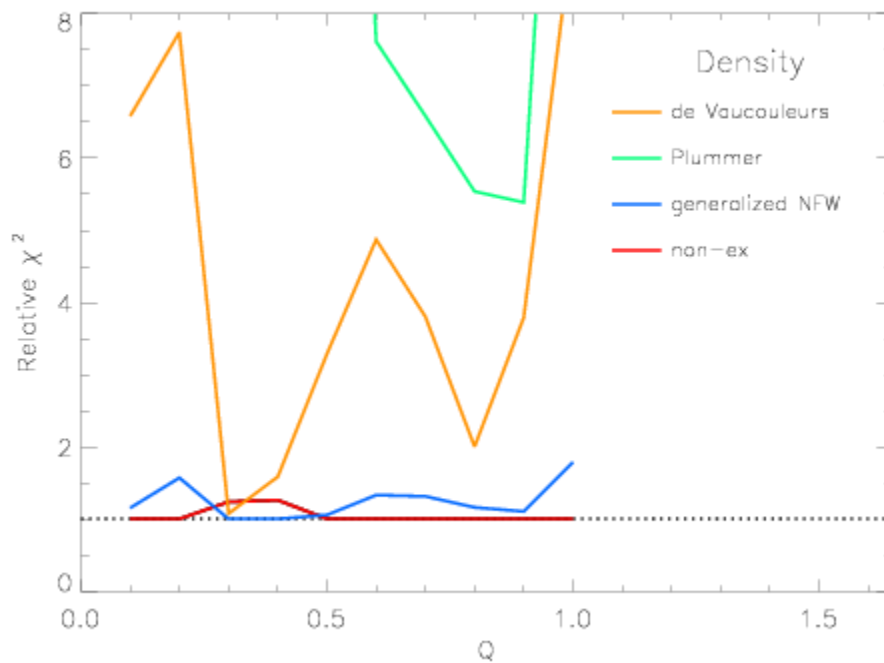


Figure 4.- The relative  $\chi^2$  density results for the set of clumpy  $T=1.0$  simulations with cuspy initial density. The density data obtained from the clumpy, cuspy  $T=1.0$  simulations are best fit by the non-extensive analytical model for most values of  $Q$ , particularly the higher ones.

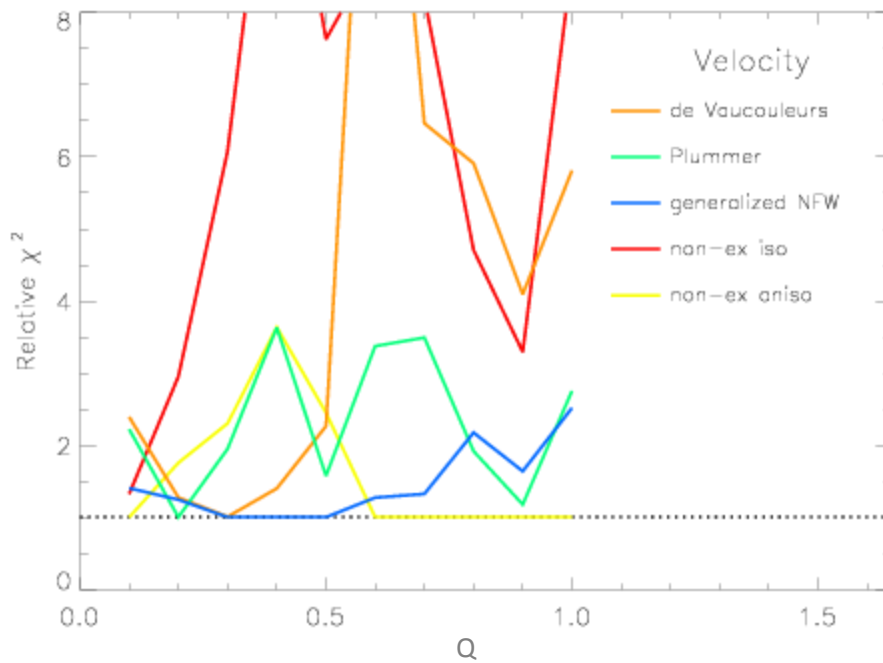


Figure 5.- The relative  $\chi^2$  velocity results for the set of clumpy, cuspy  $T=1.0$  simulations. Two possible non-extensive velocity profiles – isotropic (red) and anisotropic (yellow) – are given. The velocity  $\chi^2$  results for this set of simulations show that the non-extensive anisotropic velocity profile described the data best at high values of  $Q$ , while the NFW model did better for mid- to low-range  $Q$  values.

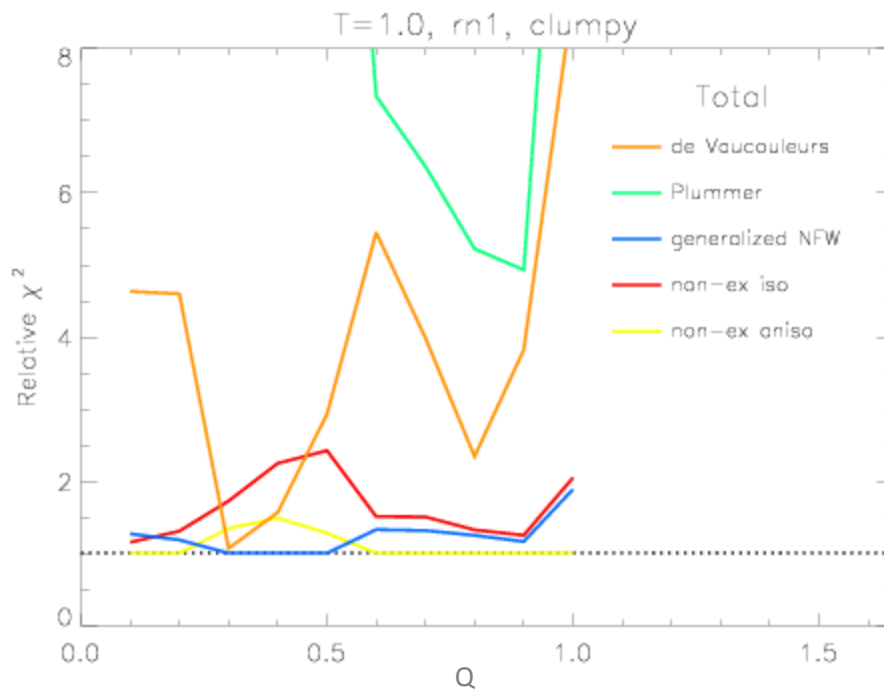


Figure 6.- The total relative  $\chi^2$  comparison, combining both the density and velocity  $\chi^2$  results for the clumpy, cuspy (rn1)  $T=1.0$  simulations. The non-extensive model values are found combining the single density fit  $\chi^2$  values with each of the isotropic and anisotropic velocity fits.

As demonstrated by these plots, for this particular set of simulations (clumpy, cuspy  $T=1.0$ ), the non-extensive thermodynamics model (allowing for anisotropic velocities) was found to have the relative best fits for very low and mid- to high-range values of  $Q$ , while the gNFW model performed best for  $Q=0.30 - 0.50$ .

For the other clumpy halos with cuspy initial densities, the family of clumpy, cuspy  $T=0.5$  simulations were found to be fit best overall by the non-extensive model for  $Q \geq 0.40$ , though the Plummer model was a slightly better density fit at  $Q=0.70$ . Both the non-extensive isotropic and anisotropic velocity profiles were better fits at high  $Q$  values, with isotropic doing slightly better at the higher values. The  $T=0.0$  clumpy, cuspy halos also showed good fits by the non-extensive model above  $Q=0.30$ , with the exception of  $Q=0.5$  where Plummer had a better density fit.

Clumpy halos with Gaussian initial density and  $T=1.0$  were actually fit better by the gNFW model for 6 of the simulations, in some cases due to a better velocity fit than the non-extensive. The non-extensive model, particularly when allowing for anisotropic velocities, performed best toward the high  $Q$  values. The set of clumpy, Gaussian  $T=0.5$  simulations had density profiles fit best almost completely by the non-extensive model, and best non-extensive velocity fits at higher  $Q$  values. The combined results show this same model fitting best for mid- to high-range  $Q$  values, favoring the anisotropic velocity profile. Finally, the clumpy, Gaussian  $T=0.0$  family of halos was best fit by the non-extensive (anisotropic) model for  $Q \geq 0.30$  except for the  $Q=0.60$  and  $Q=0.70$  simulations, where the Plummer model had a better relative total  $\chi^2$ .

Similar results were seen with the single halo simulations. The single halos only involved two variables, initial density  $\rho$  profile and virial ratio  $Q$ . The set of single, cuspy halos were described best overall by the non-extensive model (allowing for anisotropic velocities) with only one exception ( $Q=0.50$ , Plummer model). Density was best fit at every  $Q$  by the non-extensive model, and the anisotropic non-extensive velocity model performed best at higher  $Q$  values. Single halos with Gaussian initial density showed best total fits from the anisotropic non-extensive model for middle and high  $Q$  values, with the Plummer model fitting better at  $Q=0.60$  and  $Q=0.70$ . The de Vaucouleurs model provided the best velocity fit for the lower half of the  $Q$  range.

## Conclusions

Overall, while the best-fit model varied for differing initial conditions, there are trends in the data. We find that the non-extensive models generally provided the relative best fits to our data for density, especially as  $Q$  increases. The de Vaucouleurs model performed better with low values of  $Q$  for velocity distributions; however, it did not fit simulation density distributions well. The Plummer model was generally a very poor fit for low  $Q$  halo densities, but tended to improve in the mid-high  $Q$  range. In many cases this model performed second-best to the non-extensive. The generalized NFW model fit the data better at some lower  $Q$  values, and its overall best performance- though not necessarily with the lowest  $\chi^2$  values- was with the clumpy  $T=1.0$  halos. The anisotropic non-extensive model tended to fit the velocity profiles better than the isotropic and other models for high  $Q$  values. Given this, our research shows that the non-extensive model in general provides the relative best fit to these data, particularly for higher values of  $Q$ .

In both single and clumpy simulations, there was more variation in model performance at lower  $Q$ . This is likely due to the fact that systems with a low virial ratio have little kinetic energy, and so initially collapse violently. The resulting halo distributions are less “well-behaved” than their higher- $Q$  counterparts, making it more difficult for analytical models to find a good fit. The non-extensive model did not always provide a relative best fit for lower  $Q$  values, especially for the velocity distributions, and is overall more suitable for higher  $Q$  values. It is also worth noting that a model with the lowest  $\chi^2$  value is not necessarily an excellent fit to the data; it simply resulted in a better fit than the other models.

This research has helped lay a ground work for further investigation into the appropriateness of these analytical models to describe dark matter halo distributions, particularly the non-extensive thermodynamics model. We may in the future investigate cosmological models that include Hubble expansion. As the simulations we have run are collisionless, another possible path is to allow collisions and see if the non-extensive model continues to do well in describing that data.

### References

- Barnes, E., Williams, L., Babul, A., Dalcanton, J. 2007, ApJ, 655, 847  
Begeman, K. 1989, A&A, 223, 47  
Binney, J., Tremaine, S. 1987, Galactic Dynamics, Princeton Univ. Press, Princeton, NJ  
Clemens, D. 1985, ApJ, 295, 422  
Clowe, D., Bradač, M., Gonzalez, A., Markevitch, M., Randall, S., Jones, C., Zaritsky, D. 2006, ApJ, 648, 109L  
Kronberger, T., Leubner, M., van Kampen, E. 2006, A&A, 453, 21  
Zwicky, F. 1933, H. Phys. A., 6, 110  
Zwicky, F. 1937, ApJ, 86, 217

# Identification of Crystallized Ice on Kuiper Belt Objects

Victoria Hartwick

Department of Astronomy-Physics, University of Wisconsin-Madison

## Abstract

The processes responsible for the presence and preservation of crystallized ice on Kuiper Belt Objects are presently unknown. However, a correlation between KBO radial size and its presence is potentially illuminative of dynamical and inter-object interactions throughout the history of the solar system. By analysis of three filter NIR observations of four Kuiper Belt Objects in combination with later observations, we hope to construct rough NIR spectra that indicate the presence or non-presence of crystallized ice on an object and together with other spectra confirm any existing correlations. My objective for the summer is to proceed with data reduction and analysis of my October observations of four Kuiper Belt Objects. Together with new observations in July, I can then construct up to 12 rough spectra and identify the presence of crystallized ice on objects of varying radii. A correlation between radial size and presence of crystallized ice will provide important information about the feasibility of current theorized processes for its creation and preservation.

## Background Research

The Kuiper Belt consists of an estimated >100,000 of primarily icy objects ranging in size from less than one kilometer to several hundred kilometers (the largest being the newly classified dwarf planets: Eris, Pluto, etc). The Kuiper Belt extends over an average distance of 100 AU ranging from approximately 40 AU up to 150 AU or more. This extremely large volume of space limits the amount of interaction between Kuiper Belt objects and contributes to the pristine nature of KBOs. The study of KBOs is then an exploration of the initial conditions of our forming solar systems that probes the ingredients of the protoplanetary disk from which the eight planets formed. However, some dynamical processes have occurred over time. An explanation for the presence of crystallized ice on the surface of some observed KBOs may shed light on some of these past and current processes.

The presence of crystallized ice as a common surface component of Kuiper Belt Objects represents an unsolved mystery in our understanding of the evolution of the solar system. Both its initial formation and continued presence despite bombardment by cosmic rays and solar photons are unexplained. Current models suggest a variety of methods to explain both the formation and preservation of crystallized ice on objects that reside at an average distance of 40 AU. The initial creation requires heating of KBOs to a temperature double their current one of 40 to 50 K[1]. Ice formed at 40K does not have enough energy to crystallize and is instead amorphous. Dismissing the possibility of an outward migration of KBOs after formation to their present position, a number of proposed processes could provide the heat needed to allow for the formation of crystallized ice in situ: (1) the conversion of gravitational potential energy to heat during the object's formation; (2) the decay of radionuclides trapped in recesses in amorphous ice; or, (3) bombardment by micrometeorite impacts. The successful determination of each hypothesis' validity would give valuable information about the conditions of the protoplanetary disk from which the KBOs formed. For example, a materially diverse disk would provide ample opportunity for trapped radionuclides in amorphous ice. Their decay and the subsequent heating of amorphous ice could lead to its crystallization. Similarly, formation of objects by core

accretion could lead to the presence of a potentially large number of micrometeorites in a more mature disk. Evidence supporting the third process for crystallization of ice would validate hypotheses for an abundantly populated early protoplanetary disk. However, once the ice is crystallized, there is the additional problem of its preservation in the face of constant irradiation by high-energy solar photons and cosmic rays, which return the ice to its amorphous form. Since these two processes can independently amorphosize all ice well within the lifetime of the solar system (within  $< 1$  Myr) [3], the persistence of crystallized ice requires either the continual annealing or resurfacing of new crystallized ice on the KBO. An additional set of models predict (1) cryovolcanism, (2) impact gardening, or (3) thermal jostling as possible methods of recreating or resurfacing crystallized ice.

Models for both the original creation and preservation of crystallized ice predict an observable correlation between the size of KBOs and the presence of crystallized ice. We can confirm the presence of crystallized ice on a KBO from construction of NIR spectrum of KBOs. The spectrum of crystallized water ice contains a unique spectral line at 1.65  $\mu\text{m}$ . KBOs that show this spectral line have surface crystallized ice. Those that do not have only amorphous ice. A survey of KBOs looking specifically for the 1.65  $\mu\text{m}$  spectral line diagnostic of crystallized ice is necessary to gain a better understanding of ongoing processes, of which the viability of several is strongly dependent on radial size. Of the total six proposed methods for the formation and preservation of crystallized ice formation, half are only possible on KBOs with a radius greater than 500 km [1]. Cryovolcanism, conversion of gravitational potential energy to heat, and decay of radioactive nuclei, processes that require internal differentiation, large mass, and sufficient capturing ability respectively, are impossible on objects with small radii. Even impact gardening, though theoretically possible on all KBOs, is significantly more probable on large objects with greater surface areas. Observations supporting these processes would reveal a distinct split between large bodies with crystallized ice and small bodies with amorphous ice. Conversely, micrometeorite impact and thermal jostling are possible on all KBOs and therefore the distribution of crystallized ice among KBOs would be independent of size.

## **Methods**

In October 2009, we conducted a preliminary survey at WIYN telescope of ten Kuiper Belt objects of varying size (nine with radii less than 500km and one with a radius greater than 500km) observing with the J, H and [FeII]-45 filters at 1.250, 1.651 and 1.668  $\mu\text{m}$  to search for the 1.65  $\mu\text{m}$  crystallized ice line. Object size was estimated from its absolute magnitude and a predicted albedo of 0.25 to 0.05 using the Minor Planet Electronic Circulars conversion table [5].

Each object was observed for a total of three hours in three filters. Integration time per individual image varied with filter. Observations in J had 100 second integration times and were performed using Fowler I. Observations in K had 75 second integration times using Fowler I, and observations in [FeII]-45 had 240 second integration times using Fowler 4.

Data was reduced in the standard way using IRAF. In images where no object was identified, we used background objects with known visual magnitudes to find the minimum observed magnitude in the image.

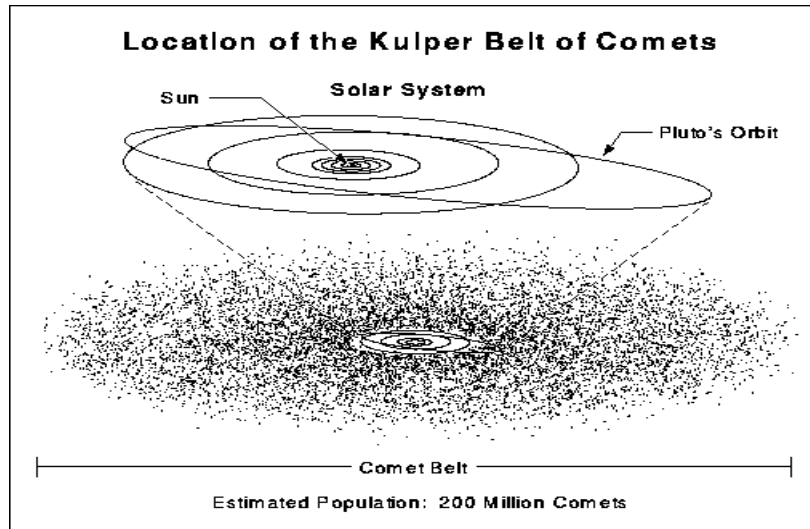
## **Results**

A total of 10 objects were observed, however, due to inclement weather, of these 10 only 2 received the total planned integration time (OR10 and TG422). Individual images were stacked to create 3 final images of each object (one for each filter – J, K and FeII-45). Comparison of the final images with 2MASS and SDSS has allowed for tentative identification of Kuiper Belt objects in filters J and K for two sets (2007 VK305 and AS13, both from the first night of observation). Of the images in which background sources have been identified, we are fairly confident that observations were deep enough in each filter. On average our observations reached magnitudes of 21<sup>st</sup> to 23<sup>rd</sup> magnitude in V.

### Conclusion

Unfortunately, while Kuiper Belt Objects were identified in individual images, we were not able to identify a KBO in each image in the set of three (J, K and FeII-45). Because of this we are unable to construct a rough NIR spectrum which would in turn enable us to identify the presence or nonpresence of the crystalline ice absorption line at 1.65  $\mu\text{m}$ . Because our objects are near the magnitude limit of the WIYN telescope, the best solution to our problems would be longer integration times. However, weather conditions at Kitt Peak have made this very difficult. We do not currently have plans for another observing run.

### Figures



PR95-26 • ST Sci OPO • June 14, 1995 • A. Cochran (U. TX), NASA

Figure 1: Basic Diagram of the Kuiper Belt. Orbit of Pluto indicated  
[[http://wps.prenhall.com/esm\\_chaisson\\_astronomytoday\\_5/21/5409/1384765.cw/content/index.html](http://wps.prenhall.com/esm_chaisson_astronomytoday_5/21/5409/1384765.cw/content/index.html)]

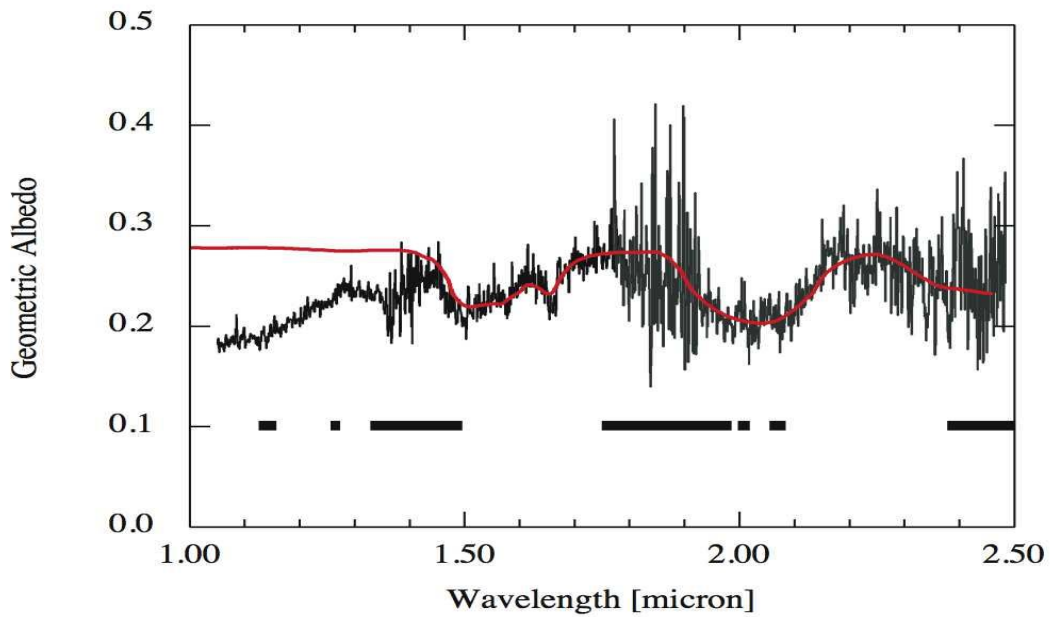


Figure 2: Example NIR reflectance Spectra of Quaoar (black) compared with reflectance spectrum of water-ice (red). Sharp dip at 1.65um is indicative of crystallized rather than amorphous ice. [2]

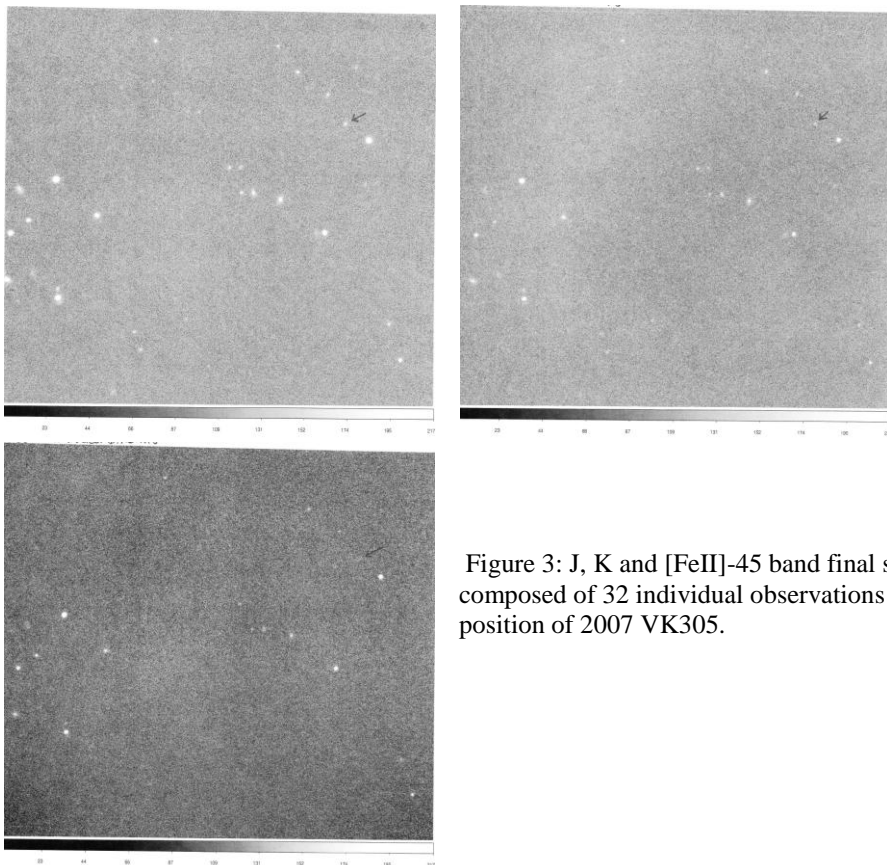


Figure 3: J, K and [FeII]-45 band final stacked image of 2007 VK305 – composed of 32 individual observations per filter. Arrow indicates position of 2007 VK305.

### **Works Cited**

- [1] Desch, S.J., Cook, J.C., Hawley, W., Doggett, T.C. Cryovolcanism on Charon and other Kuiper Belt Objects. 38th Lunar and Planetary Science Conference, (Lunar and Planetary Science XXXVIII), held March 12-16, 2007 in League City, Texas. LPI Contribution No. 1338, p.1901
- [2] Jewitt, D.C, Luu, J. Crystalline Water Ice on Kuiper belt object (5000) Quaoar. 2004. Nature 432: 731-733
- [3] Cook, J.C., Desch, S.J., Roush, T.L. Near-Infrared Spectroscopy of Charon: Possible Evidence for Cryovolcanism on Kuiper Belt Objects 2007. The Astrophysical Journal 663 issue 2:1406-1419.
- [4] Barkume, K. M., Brown, M.E., Schaller, E.L. Near Infrared Observations of Centaurs and Kuiper Belt Objects. 2008. The Astrophysical Journal 135:55-67
- [5] Minor Planet Electronic Circulars. <http://www.cfa.harvard.edu/iau/services/MPEC.html>

# Using Networking Algorithms to Assess the Environment of Galaxy Groups

Ali M. Bramson, Eric M. Wilcots

Department of Astronomy, University of Wisconsin-Madison, Madison, WI

## Abstract

Understanding the environment in which a galaxy resides is crucial to our understanding of galaxy evolution. Most galaxies (~70%) live in groups and it is important to develop a quantitative understanding of how galaxies are distributed within groups and how groups are distributed in the larger scale structure. In addition to the traditional friends-of-friends algorithm, I have applied various concepts from networking algorithms to understand the network of galaxy groups in clusters, and to understand the substructure within groups. Doing so provides a new method of gauging the large scale environments of galaxies and groups, and will result in a more concrete way to define a group and to quantify the strength of the community structure that exists.

## Background

**Galaxy structures** Galaxies are the fundamental unit of the universe, and most reside in groups, seen in Figure 1, or the even bigger clusters. Our own Milky Way Galaxy resides in a small group of galaxies creatively called the "Local Group". Approximately 70% of galaxies reside in groups, qualitatively defined as a gravitationally bound system with a mass of  $10^{13} - 10^{14}$  solar masses, in between that of an individual galaxy and a cluster.



Figure 1: Optical image from Sloan Digital Sky Survey (SDSS) of a galaxy group.

The evolution of galaxies occurs in groups. The first step for learning about galaxy evolution is to establish what these groups are. The environment of a galaxy greatly affects its development, and the properties of galaxies, including luminosity, color/morphology and star formation rate, depend on their surroundings.

**Current group finding techniques** Currently there are several ways of quantitatively identifying groups, but these methods do not yield consistent results. In addition, the distribution of galaxies within a group is not homogenous; groups themselves can be clumpy. Different techniques might identify the clumps as separate groups while another technique would simply find the larger group (Fig. 2). Other techniques depend on just looking at the number of bright galaxies within a specific radius [10].

A common technique uses the friends-of-friends (FoF) algorithm [4]. FoF starts with one galaxy and then looks for nearby galaxies that satisfy the linking criterion. It then looks at these galaxies, iterating until the nearest galaxy exceeds some specified threshold of distance or velocity [4]. The galaxy group is then classified as all of the linked galaxies. FoF succeeds at finding concentrations of galaxies but falls short in determining where one group of "friends" ends and another begins.

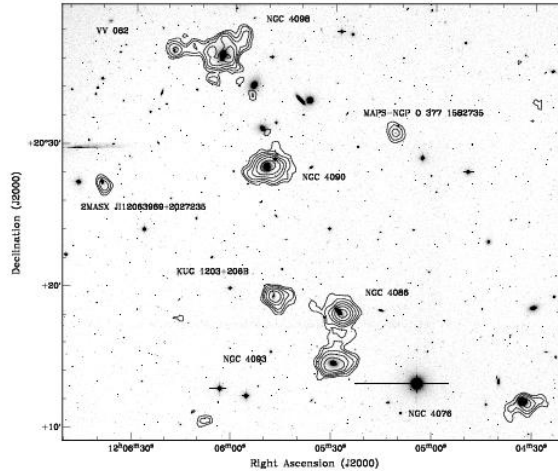


Figure 2: Image showing contours of neutral hydrogen gas with grayscale being optical observations from the Digitized Sky Survey. This is one group as determined by the FoF method but could be broken into two groups [3].

**Problems with the current methods** While useful, this FoF algorithm cannot adequately distinguish between two close groups. Another downfall to the current methods of identifying galaxy groups is that the various different techniques yield different sets of groups, and many automated group finders identify far too few galaxies as members. For example, most of the groups in the recent catalogs consist of only three or four galaxies [1] while nearby groups are known to contain tens of galaxies.

**Objectives for the current work** Determining which galaxies belong in which group is not the only important thing to learn. Knowing how tightly linked galaxies are within and between groups will be important for figuring out the scales on which galaxy interactions occur. Finding the most important spatial scale on which the environment influences galaxy evolution is crucial to understanding how galaxies evolve. Subgroups indicate that a group is dynamically young and, possibly, more susceptible to galaxy-galaxy mergers. Determining substructure is important for learning if groups are built up of subgroups like clusters are built up by groups.

**Science of networks as a solution** Simulations of the formation of structure in the universe, as shown in Figure 3, show that links between galaxies are numerous and complicated. Determining the strength of these links and the breakage points in which we can definitively say where galaxy groups separate is important in learning about the environment galaxies live in. What is really needed are observational methods to understand how linked galaxies and groups are, and

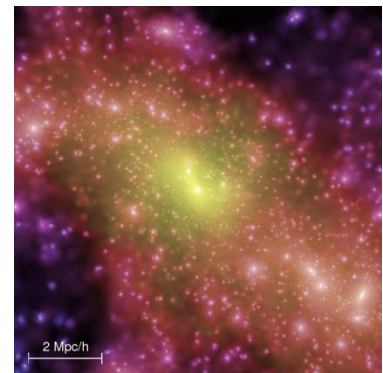


Figure 3: This simulation from the Millenium Simulation Project [8] shows the complicated network of galaxies that exists. Bright spots indicate areas of high mass, with the brightest spots representing galaxy groups. The boundaries between the galaxies are not well defined and there are many connections between.

that is where this project comes in. The science of networks has been developing algorithmic detection methods for determining community structure in various settings for over a decade. Seeing what networking algorithms can tell us about the physical world is a very new idea with many potential applications. I have applied these techniques to the distribution of galaxies, but the applicability could be much broader.

**Networking algorithms** Community structure in networks can be seen across all disciplines: natural, social and information sciences [5]. An example is in the case of the popular Zachary’s Karate Club network, a benchmark network [5]. In this real-world example, social interactions were observed between an American university’s club members, including when the club split into two during a dispute between two of the club’s leaders [6]. Algorithms developed were able to correctly model these interactions and properly showed a strong natural division when the club split. This has been applied to many other data [2], including communities on social networking websites such as Facebook ([www.facebook.com](http://www.facebook.com)) as well as analyzing individual and group voting dynamics in Congress [5]. Community structure and networks have been worked on for a long time in these other disciplines; now we have applied them to astronomy!

## Methods

**Modifying friends-of-friends to identify centers of groups** I wrote an algorithm that works like the traditional friends-of-friends algorithm [4], searching out galaxies that are connected to a given “seed” galaxy through some path of other galaxies that are all linked by a given distance. This distance criterion is chosen based on the average separation between the galaxies occupying a given area in the data set. My algorithm keeps track of the galaxies found at each step away from the seed galaxy. It sums the total number of friends every galaxy has at each step, as a measure of how closely connected the group is to the seed galaxy. Outputting the results in this way (Figure 4) has provided us with a new way to look at FoF, and be able to use it to look for the best central galaxy as a start to finding structure.

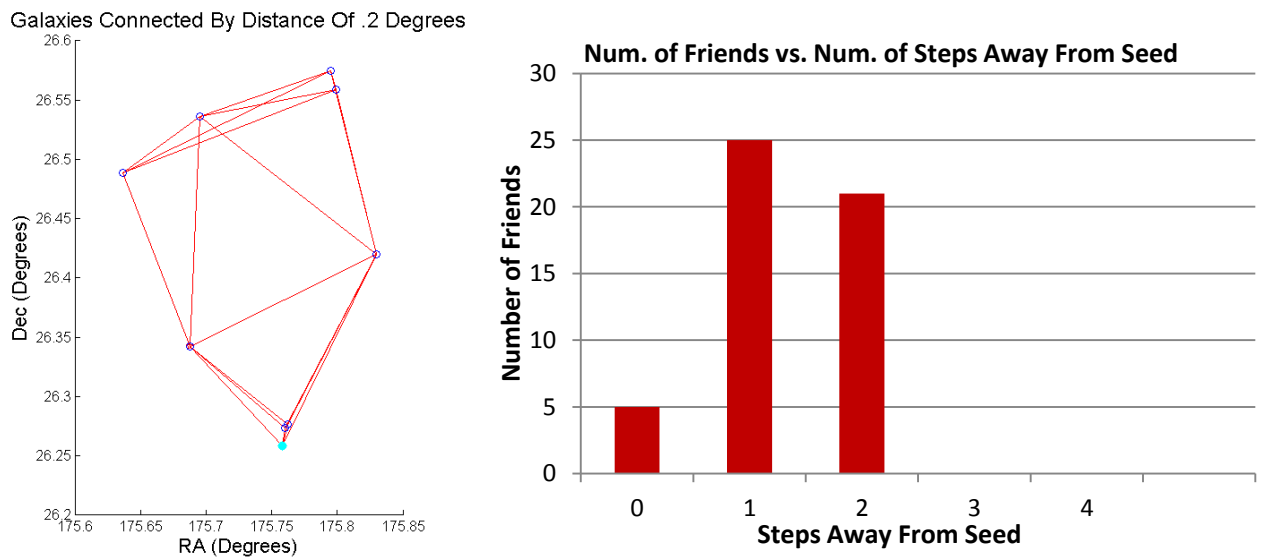


Figure 4: Diagrams showing connections (left) starting with the seed galaxy (bottommost galaxy) and the corresponding histogram (right) showing the numbers of “friends” at each step away from the seed galaxy.

**Interpretation** One example of a galaxy group structure that we have looked at with the current algorithm is NGC 2563. Zabludoff & Mulchaey [9] identified well over 20 individual galaxies that belong to the group. The results of our algorithm suggests that NGC 2563 is likely two separate groups, with a few galaxies connecting the two, and a few others not being included at all. The shape of histograms showing the number of connections at steps away from the “seed” galaxy can help identify the best central galaxy. Histograms that peak at one step away and fall rapidly indicate good “seeds”, while distributions that are shifted indicate that the galaxy is on the outskirts. These histograms for NGC 2563 are shown in Figure 5.

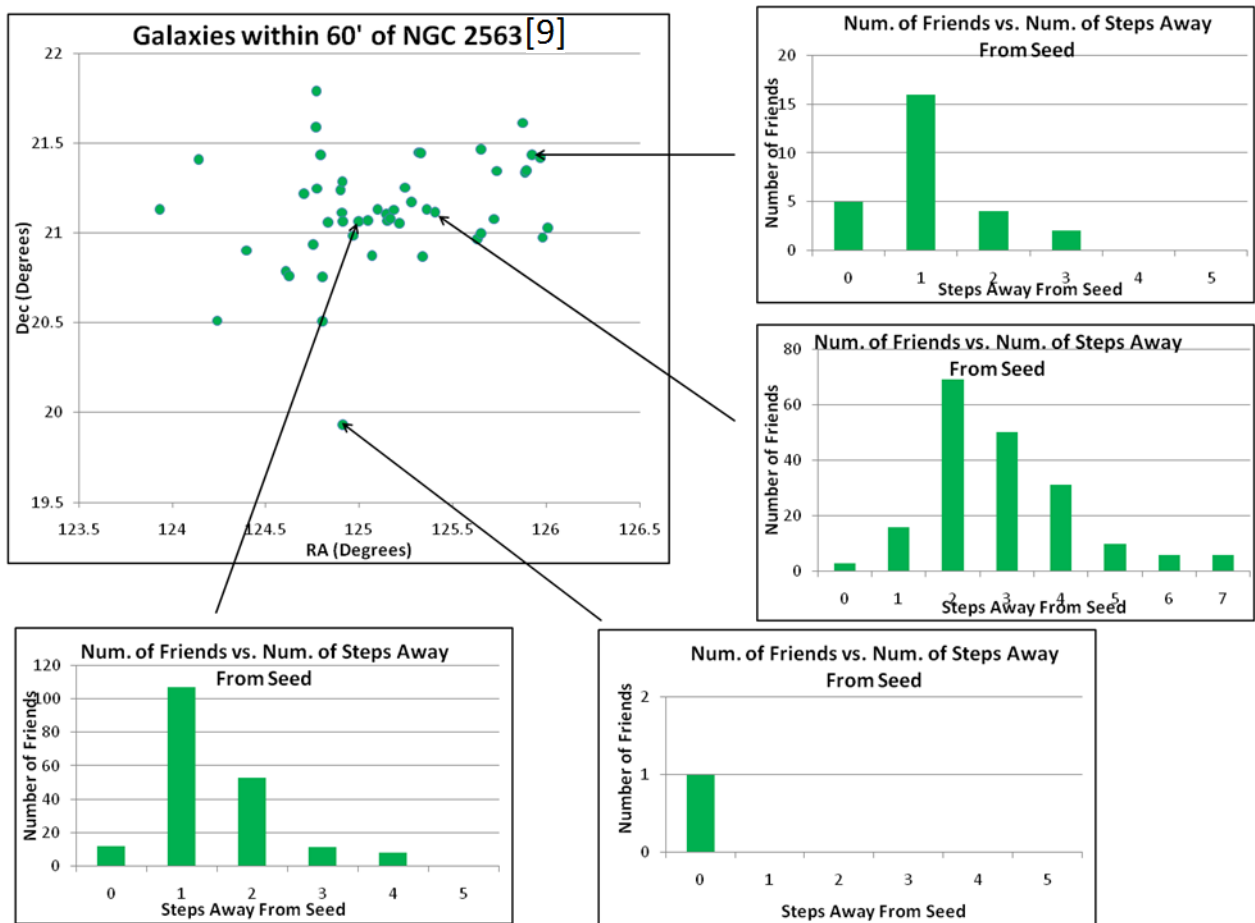


Figure 5: This shows the outputted histograms from our friends-of-friends algorithm for galaxies located in different parts of the group. These histograms show the number of friends that the galaxies at a given step number away from the “seed” have, in sum. Good “seed” galaxies at the center of a group peak at one step away and fall off rapidly, while galaxies on the edge of the group peak further away. The histogram on the top right shows that a good seed galaxy may exist far away from what appears to be the center of the group. This could indicate a separate community structure from the main group. We are also able to find outliers, galaxies that do not belong in any group.

**Distance matrices** Many social networking methods use the concept of distance matrices to assess community structure. These are matrices of “similarity”, with each element being the distance between two sets of nodes (galaxies). Calculating the similarity between galaxies is simply how far away they are from each other. The separation in the projection of the sky is easy to calculate, but the third dimension is trickier. Velocities and redshifts are used as a measure of

how far away galaxies are from us. To combine velocity with separation in right ascension (RA) and declination (Dec) requires a special calculation due to the difference in units. The 3D measure of distance that is used is zeta [7], defined in equation 1.

$$\zeta = \sqrt{\left(\frac{\Delta R}{\Delta R_{max}}\right)^2 + \left(\frac{\Delta vr}{\Delta v_{max}}\right)^2}$$

Equation 1: The calculation of zeta, a 3D measure of distance between two galaxies.

Each element of the distance matrix (Figure 6) is the value of zeta calculated between the galaxies associated with that element's row and column. These values are then quantized on a scale related to the average size of a group to correspond to numbers between 0 and 1, with 1 meaning the two galaxies are extremely close and likely interacting and 0 meaning the galaxies are far apart and not interacting. The element corresponding to a galaxies distance from itself is assigned to be 0 so as to have a galaxy not appear to be interacting with itself.

	Gal 1	Gal 2	Gal 3	Gal 4	Gal 5	Gal 6	Gal 7	Gal 8
Gal 1	0	0.5	0.5	0.8	0.5	0.5	0.5	0.8
Gal 2	0.5	0	1	0.8	0.8	0.5	0.8	0.5
Gal 3	0.5	1	0	0.8	0.5	0.5	0.8	0.5
Gal 4	0.8	0.8	0.8	0	0.5	0.5	0.5	0.8
Gal 5	0.5	0.8	0.5	0.5	0	0.5	0.5	0.5
Gal 6	0.5	0.5	0.5	0.5	0.5	0	0.5	1
Gal 7	0.5	0.8	0.8	0.5	0.5	0.5	0	0.5
Gal 8	0.8	0.5	0.5	0.8	0.5	1	0.5	0

Figure 6: Example of a distance matrix, a matrix of values corresponding to how close or far away two galaxies are from each other. A 1 implies that galaxies are very close to each other and likely interacting while a 0 implies the galaxies are not interacting, with varying values between according to the separation.

**Viewing distance matrices** This matrix can be converted into a grayscale image so that it can be easily viewed. The columns are organized by increasing RA and the rows are organized by increasing Dec so that the matrix is roughly related to the positions on the sky. Using these distance matrix images, we can look for bright areas which indicate groups and look for connections between groups. In Figure 7, I made a fake data set with two groups and a “bridge” of galaxies connecting them. These two groups show up very clearly in the distance matrix image, with elements between galaxies in the same group being bright, and elements between galaxies of different groups being dark. The groups are easy to pick out.

**Distance matrices for large sections of the sky** Real data sets, such as for a subsection of the Abell 1367 Coma Supercluster (Figure 8), are much more complicated. However, it is still possible to see structure within the distance matrix. Bright areas indicate groups and gray areas suggest structures exist linking the groups.

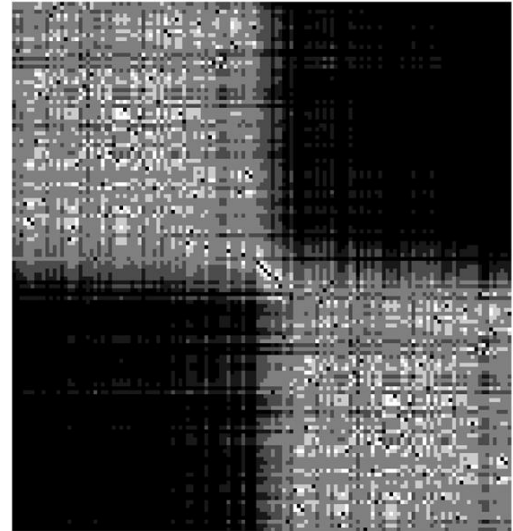
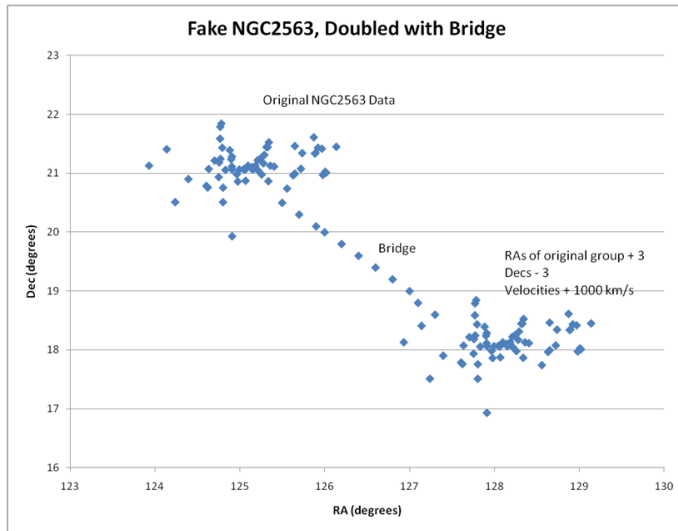


Figure 7: The distance matrix converted into a grayscale image (right) that corresponds to a fake data set (left). Here, the group NGC2563 has been duplicated and shifted, with a fake “bridge” of galaxies connecting the two. The distance matrix is sorted by RA and Dec and the two separate groups are very apparent as bright regions, with a small bridge of points between them. The dark areas consist of elements between two galaxies from different groups, which are not interacting.

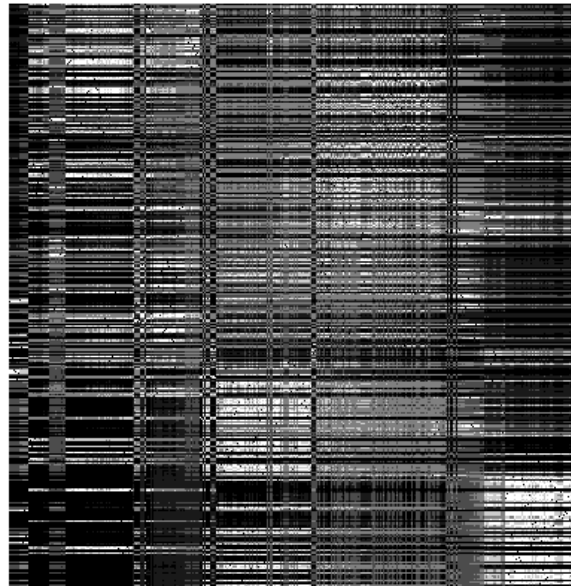


Figure 8: Distance matrix image for a subsection of the Abell 1367 Coma Supercluster. This large area of the sky contains 383 galaxies and connections are much more complicated than for the fake data set in Figure 7. However, bright areas containing groups can still be seen and grey areas suggest linkages between groups. Dark areas indicate no galaxy interactions there.

**Agglomerative Hierarchical Clustering** One networking technique that uses distance matrices is hierarchical clustering. This technique iteratively builds a hierarchy of clusters by either starting with all nodes (galaxies, in our case) connected in one big group and splitting them into separate groups (divisive clustering) or starting with all nodes as separate groups and connecting them until they are all in the same group (agglomerative). The agglomerative method runs as follows:

1. Assign each galaxy to a separate cluster
2. Create a distance matrix of the distances between all pairs of galaxies
3. Merge the two galaxies that are the closest into one cluster
4. Remove the galaxies from the distance matrix and add in our new cluster
5. Iterate until all have been merged into one cluster

**Dendrograms** Using the agglomerative hierarchical clustering above, I then create a dendrogram. Dendrograms show the order in which galaxies have been merged together in this technique (Figure 9).

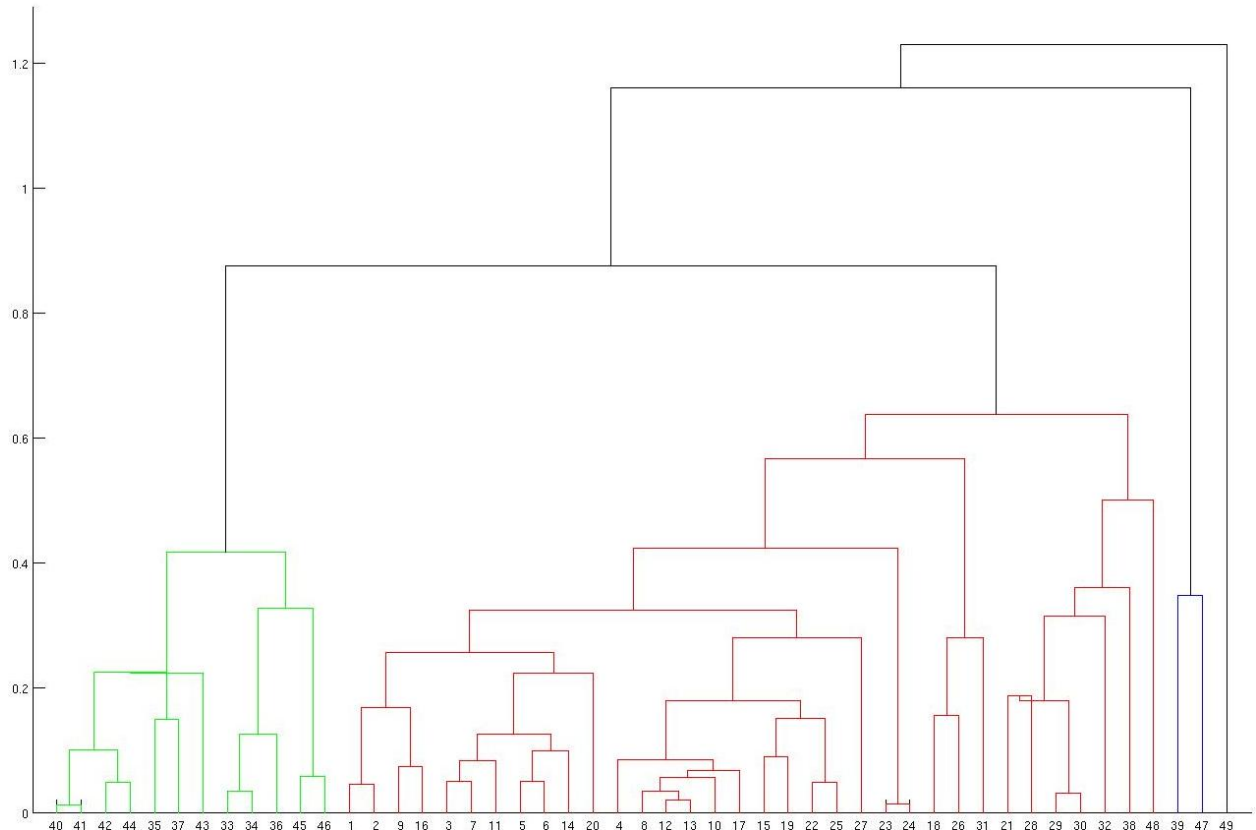


Figure 9: Dendrogram showing connections between galaxies in NGC2563. This shows that NGC2563 should perhaps be split into two groups, with three outliers not in either group. Outliers are identified by galaxies that are connected much higher than the rest. The dendrogram also shows substructure within identified groups.

The value on the left side of the dendrogram, referred to as the modularity, is a way to quantify the value at which structures are merged. This value is simply the value in the distance matrix between the two groupings or galaxies.

### Conclusions

Many techniques exist for determining galaxy groups. However, the techniques are not consistent and yield different results. These techniques are poor at addressing the following questions:

1. Which galaxies belong in which group?
2. How tightly linked are galaxies within and between groups?

3. What is the most important spatial scale on which the environment influences galaxy evolution?

I have combined various concepts from the science of networks to address these questions.

Using the traditional group-finding friends-of-friends technique, I can identify good “seed” galaxies, galaxies that are central to the group. I can also identify galaxies that are on the outskirts. Identifying these is important because they will have different properties due to their differences in environment.

I can also identify which galaxies belong in which group by looking at the dendrograms in the agglomerative hierarchical clustering technique. Using the modularity that the technique uses to create the dendrograms, we can quantify levels at which galaxies become connected with each other, as well as when groups become connected to each other. We can further identify outliers that should not be included in any group. These isolated galaxies will have completely different properties than the galaxies that exist in groups.

**Next Step** The next step is to combine all of the techniques used to address the third question above. By analyzing the results of the various techniques as applied to several different groups and clusters, I will look at the spatial scales that affect the properties of galaxies. This will lead me to identify the scales on which galaxy evolution occurs.

## References

1. Berlind, A.A., et al. 2006 ApJ, **167**, 1.
2. Fortunato, S. 2009, arXiv:0906.0612v1.
3. Freeland, E.E., Stilp A., & Wilcots, E.M. 2009 AJ, **138**, 295.
4. Li, I. H., Yee H. K. C. 2008 AJ, **135**, 809.
5. Mucha, P.J., Richardson, T., Macon, K., Porter, M..A., & Onnela, J-P. 2009, arXiv:0911.1824.
6. Newman, M.E.J. & Girvan, M. 2004 Phys. Rev. E, **69**, 026113.
7. Rasmussen, J., et al. Astrophysical Journal submitted 2011
8. Springel, V., et al. 2005 Nature, **435**, 7042, 629.
9. Zabludoff, A. & Mulchaey, J. S.1998 ApJ, **496**, 39.
10. Zirbel, E.L. 1997 ApJ, **476**, 489.

# Magnetohydrodynamic Turbulence at High-Latitude Regions of the Milky Way

Nickolas Pingel, Snežana Stanimirović, Min-Young Lee

University of Wisconsin-Madison<sup>1</sup>

## Abstract

We performed statistical analysis on the high-latitude molecular cloud MBM16 with data collected from the Galactic Arecibo L-Band Feed Array HI (GALFA-HI) Survey. We developed a code to convolve a circular kernel across a spatial column density image to create maps of the 3<sup>rd</sup> and 4<sup>th</sup> statistical moments. With these higher-order moment maps, we utilized a relationship derived purely from the theoretical MHD simulations of Burkhart et al. (2010) to directly estimate the sonic Mach number ( $M_S$ ). We then looked at an estimate for the slope of the spatial power of our region to check our range of calculated Mach numbers and verify the reliability of our results. We found that the translucent, non-star forming molecular cloud, MBM16, can be considered largely subsonic to transonic, which is consistent with the conception of stars being dominant drivers of interstellar turbulence.

## Introduction

Throughout the last decade, there has been much progress in both observations and theoretical models characterizing the evolution and overall workings of the interstellar medium (ISM). It is evident that interstellar turbulence plays an important role in ISM structure formation and evolution. While there have been many advances in understanding the functionality of turbulence within the ISM, many questions remain open about exactly how turbulence influences processes within the ISM. For instance, what are the prominent energy sources and physical processes that induce turbulence? At what scales and through which modes does turbulence energy dissipate in the ISM? How do different characteristics about the interstellar gas (e.g., presence/absence of star formation, strength of magnetic field, presence/absence of tidal effects) affect the amount and type of turbulence exhibited? These are difficult questions to answer in the absence of a complete astrophysical theory describing turbulence, which is why an approach combining numerical techniques and observations is required.

To address some of these questions, specifically about the presence or absence of star formation drives turbulence, we first looked at the numerical isothermal simulations of HI gas developed by Burkhart et al. 2010 (hereby referred to as BHK) to aid in a numerical approach. Our study is the first attempt for the Milky Way to study the spatial distribution of turbulence and will be extended to other clouds. We used a simple relationship between higher-order moments of column density distributions and the sonic Mach number to

---

<sup>1</sup>We acknowledge the Wisconsin Space Grant Consortium for providing funding for this research.

determine how turbulence is disseminated across the cloud. We compared our results of our non-star forming cloud to BHK's estimate for turbulence for the Small Magellanic Cloud (SMC). This is important because star formation is present in the SMC, which enabled us to test the idea of stars being dominant drivers of turbulence. Finally, we tested the reliability of results by comparing our estimates of turbulence with an independent measure of turbulence for our region by Chepurnov et al. 2010.

In particular, this paper is organized as follows. We begin section 2 by giving a brief background on the data used to create the column density distribution maps used by our code to ultimately estimate the spatial distribution of turbulence in MBM16, and also highlight the important properties of this cloud. In section 3 we introduce the higher-order statistical moments used in this study, and explain their relationship to the sonic Mach number. We then explain how our code uses this relationship to create a sonic Mach number map, which describes the spatial distribution of turbulence in a region or cloud. In section 4 we present our results and compare them to BHK's work on the SMC, and test the reliability of our results by examining the slope of the power law of our region's spatial power spectrum. Lastly, in section 5, we discuss our results and discuss future works.

## **The GALFA-HI Survey and MBM16**

**Background on GALFA-HI.** The GALFA-HI survey is a high-resolution, ( $4'$ ) large-area ( $13,000 \text{ deg}^2$ ), survey conducted at the Arecibo radio telescope in Puerto Rico using Arecibo's ALFA receiver and the GALSPECT spectrometer. ALFA is a seven-element array primarily designed for 21 cm observations. GALSPECT is a special-purpose spectrometer with a spectral resolution of  $0.18 \text{ km s}^{-1}$  used for Galactic science in conjunction with ALFA. Data were reduced with the standard GALFA-HI reduction strategy detailed in Peek et al. (2007) and observed in a "basket-weave" mode, interlacing scans from day to day. All of the data cubes used in this study are part of a general data release available for public use at <http://purcell.ssl.berkeley.edu/> with specific details outlined in Peek et al. (2011).

Approximately 82 % of the survey data collected has been obtained while operating communally with other large survey projects such as ALFALFA. This is a unique strength, with which multiple backends can be used in parallel, enabling different science projects to use the same telescope pointing simultaneously. Communal observing is especially powerful for a sky survey, and will be an imperative observation strategy with future generations of radio telescopes, most notably the SKA (Square Kilometer Array).

**Properties of MBM16.** The translucent, non-star forming molecular cloud, MBM16 (Figure 1), was first cataloged by Magnani, Blitz & Mundy (1985) and has an estimated distance of about 80 pc (Hobbs et al 1988). We chose to look specifically in high-latitude regions because the HI gas is considered less "contaminated" than HI in the plane—meaning there is a more pristine turbulent environment due to the lack of star formation. The relatively short distance to this cloud gives us a good spatial resolution of about 0.1 pc. The absence of stellar activity in MBM16 presented us with the opportunity to directly compare our results with BHK's work on the SMC, a star forming dwarf galaxy.

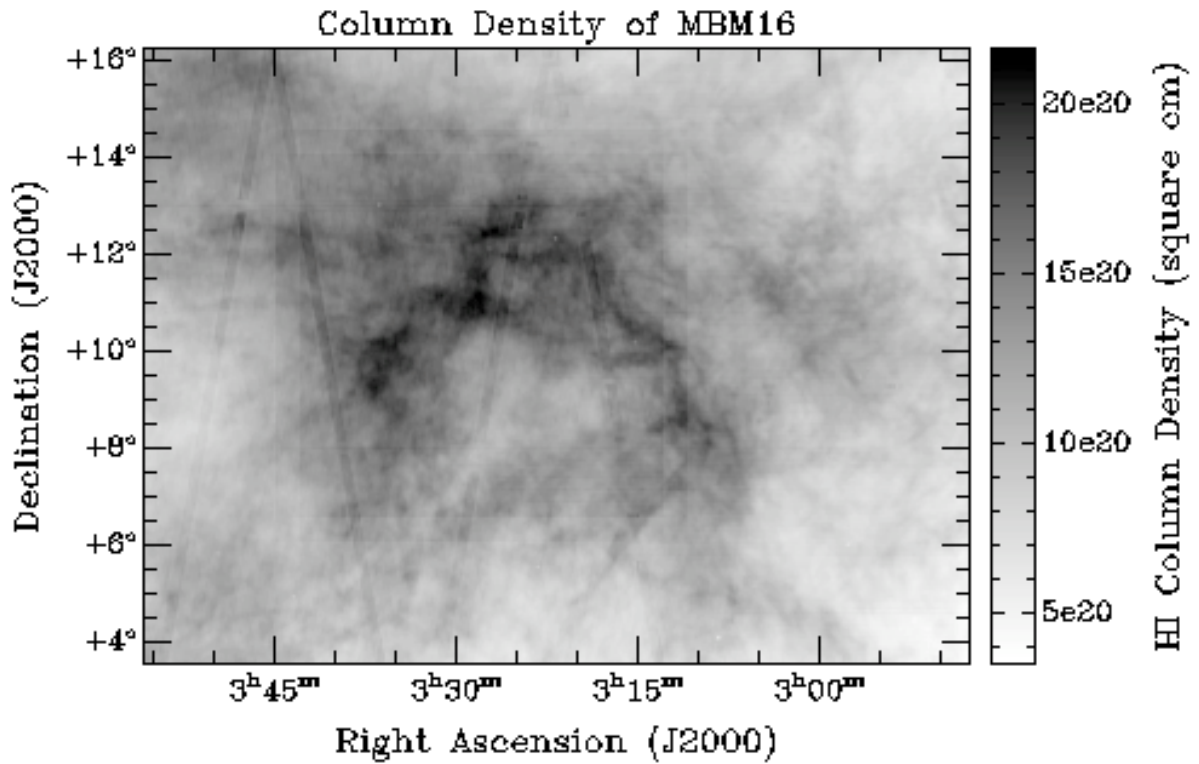


Figure 1-A column density map of MBM16. The lines through the image are remnants of the telescope observing pattern; data reduction techniques are still being modified.

### The Statistical Moments Used in this Study, Their Relationship with Turbulence and the Sonic Mach Number Map.

**Skewness and kurtosis.** The two simplest properties of a distribution are the mean value and variance. While these are not directly used in this study, they are still required to calculate skewness and kurtosis—the more applicable statistical properties of our study. Skewness is defined as:

$$\gamma_{\xi} = \frac{1}{N} \sum_{i=1}^N \left( \frac{\xi_i - \bar{\xi}}{\sigma_{\xi}} \right)^3$$

Where  $\sigma$  is the variance of the distribution  $\xi$  of column density values and  $N$  is the number of samples. Skewness measures how skewed towards high or low data values a distribution is. Kurtosis is defined as:

$$\beta_{\xi} = \frac{1}{N} \sum_{i=1}^N \left( \frac{\xi_i - \bar{\xi}}{\sigma_{\xi}} \right)^4 - 3$$

Kurtosis measures how “peaked”, or bunched a data set is. If a distribution has positive kurtosis, the probability density function (PDF) will have a distinct peak near the mean and elongated tails. Conversely, a negative kurtosis value will be flat at the mean.

**Relationship to  $M_s$ .** BHK found that variance, skewness and kurtosis of their simulated column density distribution depended on turbulent properties, specifically the sonic Mach number. Figure 2 describes the correlation revealed by their simulations.

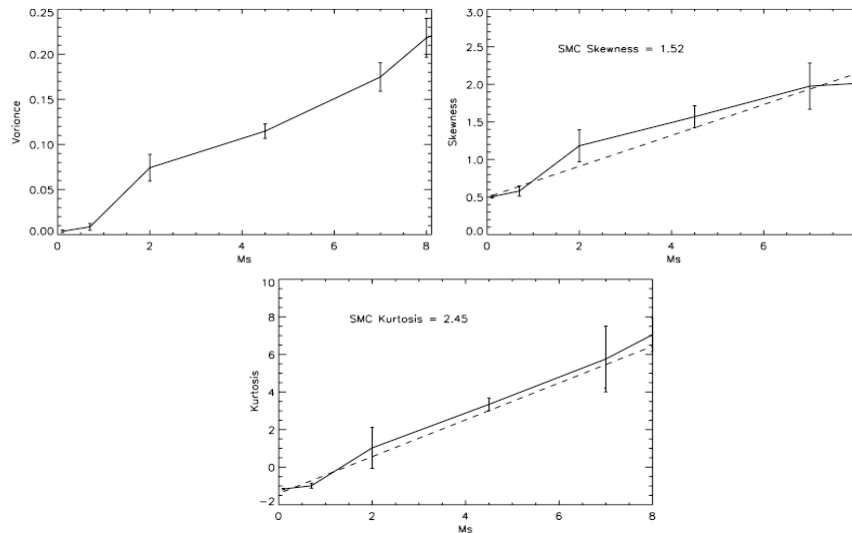


Figure 2-Taken from BHK. Skewness (top right) and kurtosis(bottom) show the best correlations between the higher-ordered moments, though kurtosis exhibits the simplest linear fit.

In order to develop these relationships, BHK essentially fixed the sonic Mach number for each numerical isothermal simulation and looked for a relationship between the higher-order moments and  $M_s$ . They were able to determine that the simple equation:  $M_s = (\text{Kurtosis} + 1.44) / 1.05$  effectively estimates the Mach number of a distribution. In essence, the increase of higher order moments with  $M_s$  can be explained in that as Mach number increases, the amount of small-scale structure increases, resulting in a broader PDF.

**Determining the spatial distribution of skewness and kurtosis.** In order to characterize small-scale departures from Gaussianity of the column density distributions across MBM16, we first had to spatially calculate skewness and kurtosis. To accomplish this, we developed a code that convolves the column density image with a circular kernel with a given radius  $r$  that calculates skewness and kurtosis at all points. BHK decided on a kernel with a radius of  $r=35$  pixels to maximize signal-to-noise. We should note that the column density image of MBM16 was scaled using the standard score method to be consistent with the procedure from BHK.

Our code begins this process by creating a box kernel in the lower left corner of the column density image in Figure 1. It then focuses on the central pixel of the box, and traces a circle with a radius of 35 pixels. Any pixel of the column density image within that circle is considered part of the distribution, which is multiplied by a Gaussian function to give more weight to the central pixels to minimize edge effects. Statistics are then run on the distribution within the circular kernel, calculating skewness and kurtosis at all points. The single value calculated for skewness and kurtosis then replaces all column density values within the circular kernel to start building the respective moment maps. The box kernel then moves to the right one pixel, and this

process is repeated until it reaches the right edge; it will then elevate itself one pixel and begin again on the left edge. It should be noted that this is similar to convolving the image with a Gaussian function with a FWHM of 30' giving the resultant maps a lower spatial resolution of  $\sim 0.7$  pc. We find that MBM16 and surrounding mapped region has a kurtosis value of 2.45 and a skewness value of 1.57. The resulting moment map for kurtosis is displayed in Figure 3.

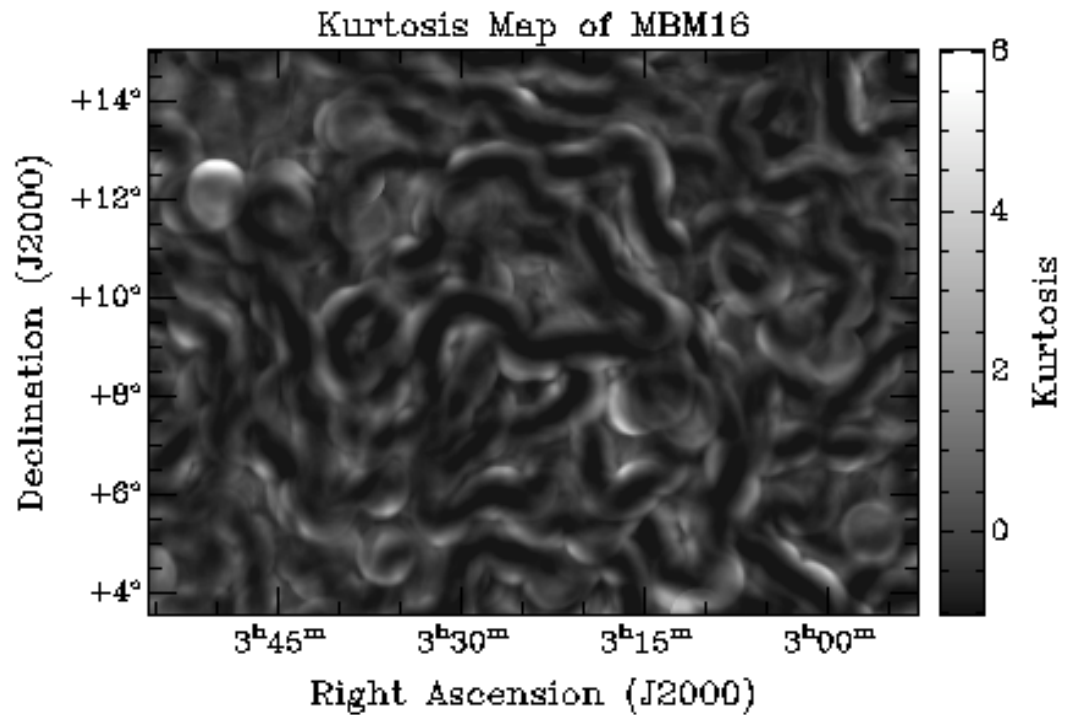


Figure 3-Kurtosis map. The moment maps are only intermediate steps to the final goal of a Sonic Mach number map. It is difficult to discern any spatial information from these maps, but we show them to highlight the raw output of our code.

Kurtosis has the best correlation to  $M_s$  so we focused exclusively on the kurtosis map to create the end product of a Mach number map. To do this we took each pixel's value on the kurtosis map and put it into the simple equation:  $M_s = (\text{kurtosis} + 1.44) / 1.05$ . The end product of a sonic Mach number map is presented in Figure 4.

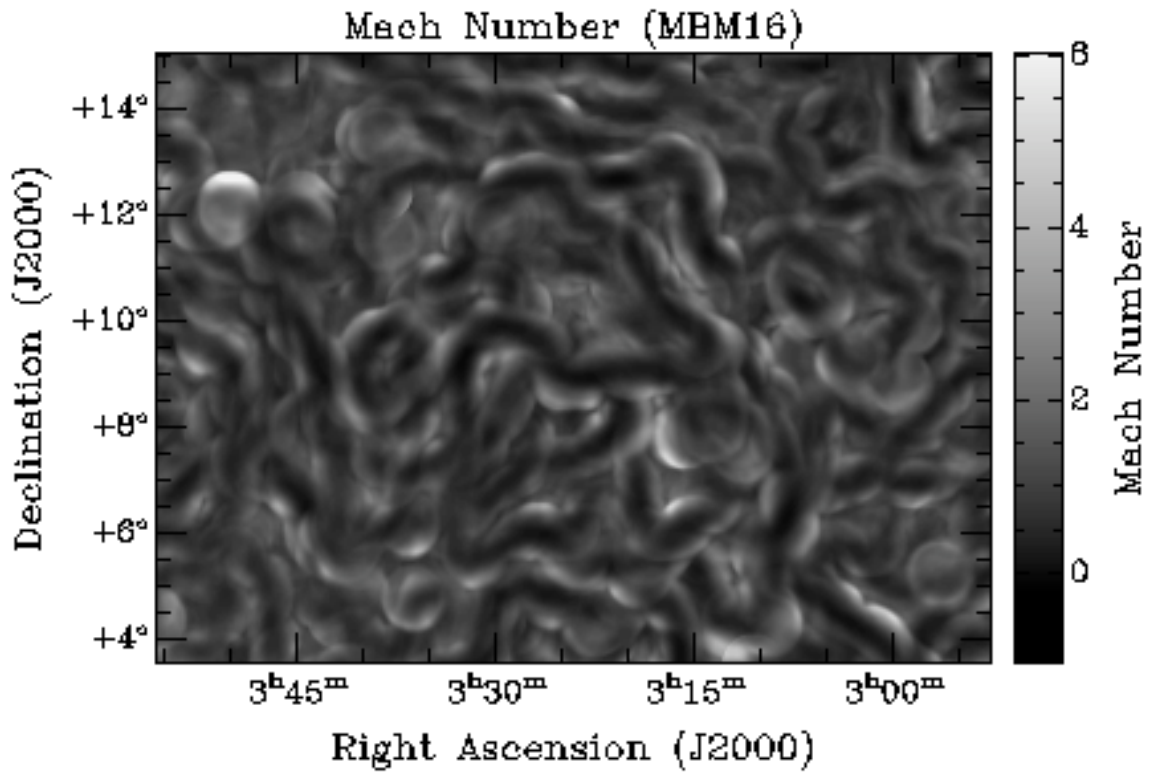


Figure 4-The Sonic Mach Number map of MBM16. This is the final product of our statistics code and highlights the spatial distribution of turbulence in MBM16.

### Results and Interpretation of Statistics

**Spatial distribution of turbulence.** Though the sonic Mach number map is the targeted end product, it is not entirely effectual in highlighting the spatial relationship between column density distributions and sonic Mach numbers across the cloud. To accentuate any associations, we overlaid higher levels of mach numbers in Figure 5, along with smoothed HI contours.

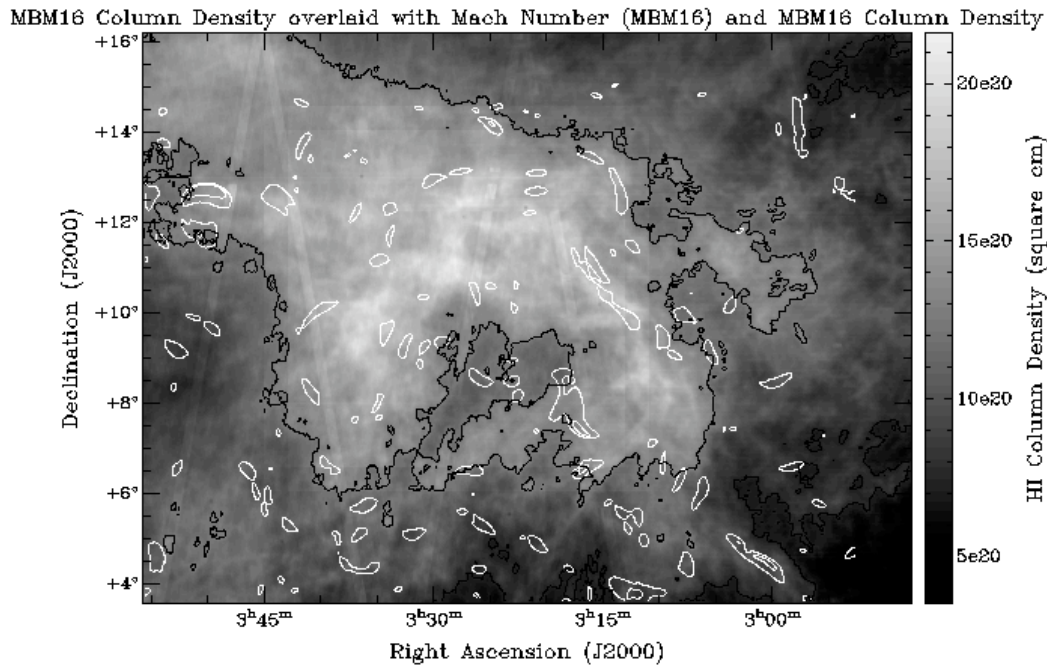


Figure 5-The original column density map of MBM16 with higher-level mach numbers overlaid with white contours, and smoothed HI contours in black. We see the most turbulent regions are small and localized compared to the entire cloud.

These contours show a few localized regions of high turbulence, and most of these regions are associated with an HI contour line. An interesting feature is a semi-circular shaped turbulent region located in the top left corner of the image at coordinates of RA=3h50m, DEC=12.30°. It is easily the most conspicuous turbulent region across the cloud, which enticed us for further examination. We examined the velocity space of the original data cube used to generate the column density map, but could not identify a physical process that we could associate with this feature. Nonetheless, it is very intriguing. We concluded that, as a whole, MBM16 is not turbulent expect for a few small localized regions.

**Star forming vs. non-star forming environments.** BHK developed the method used in this study, and first tested it on observations of the SMC, a dwarf satellite galaxy of the Milky Way. To test the notion of stars being major drivers of turbulence, we compared our results of our non-star forming cloud to BHK's results for the star forming SMC in Table 1, and in Figure 6 with histograms and plots of skewness vs. kurtosis.

$M_s$	SMC	MBM16
0-1	45%	55%
1-2	45%	39%
>2	10%	6%

Table 1-Comparison of the turbulence across the mapped areas of MBM16 and the SMC.

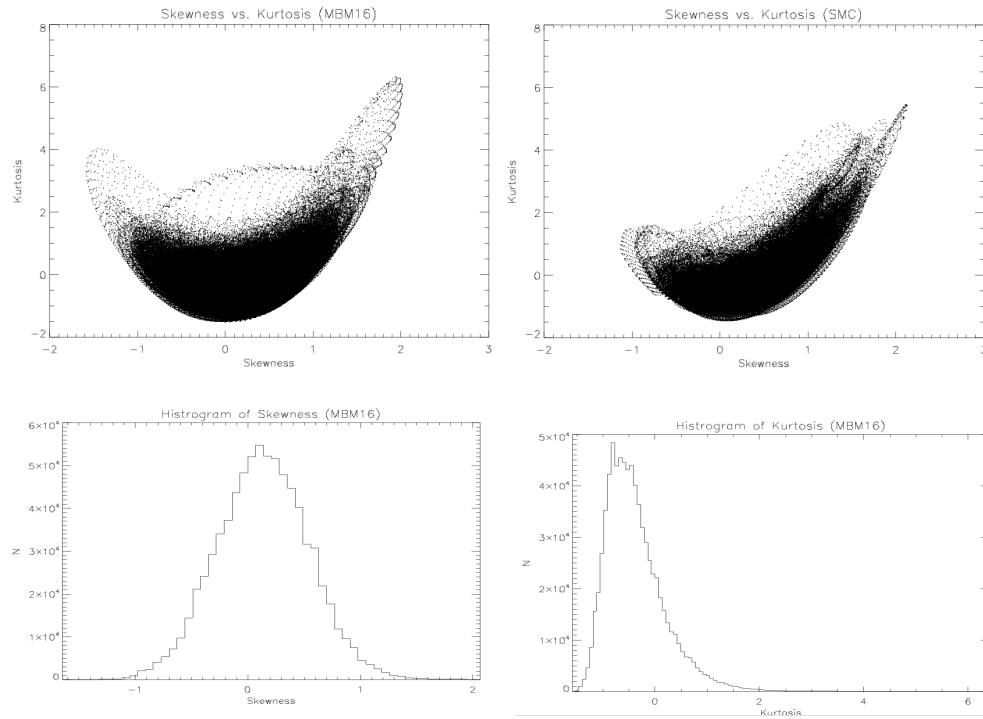


Figure 6- Skewness vs. Kurtosis plots of MBM16(left) and of the SMC(right). Below are histograms of skewness(left) and kurtosis(right) of MBM16.

Table 1 shows how supersonic ( $M_s \geq 2$ ) the SMC and MBM16 are by the percentage of their mapped area. MBM16 is less turbulent in every  $M_s$  bin with just over half of the mapped area being subsonic ( $M_s \leq 1$ ) and only 39% being transonic ( $1 \leq M_s \leq 2$ ), while 10% of the SMC is supersonic to just 6% of MBM16. BHK found if there is a good correlation (i.e. linear relationship) between high levels of skewness and kurtosis, this region has non-gaussianities in the column density distributions, which means the region is more turbulent. The skewness vs. kurtosis plots at the top of Figure 6 shows this linear relationship between the higher values of the two moments for the SMC, but is not as pronounced in MBM16. We see why there should not be a good correlation by examining MBM16's histograms of skewness and kurtosis at the bottom of Figure 6. Skewness has values falling between -1 and 1, while most of the kurtosis values fall between 0 and 2. With no obvious linear relationship, we

concluded that the MBM16 is less turbulent than the SMC, which we expected due to the vast differences in stellar environments.

**Testing the reliability of our results.** BHK tested the dependability of their results by examining the slope of the spatial power spectrum for the SMC. We used the same strategy by examining Figure 7.

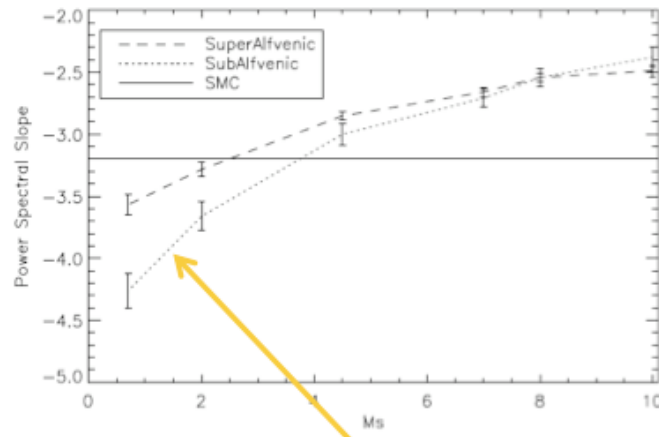


Figure 7- Taken from BHK. This plot is the power spectral slope as a function of Mach number for BHK's simulations. The solid horizontal line shows the SMC, while the arrow points to the measure slope for our region of -3.9.

Chepurnov et al. (2010) measured the power spectral slope of our region to be -3.9. The basic concept of a spatial power spectrum is to quantify how much small scale structure exists; the steeper the slope, the less turbulent energy has cascaded down from large scales and mixed up the gas on small scales. A slope as steep as 3.9 indicates Mach numbers of around 2 and lower, meaning we should not expect to see much small scale structure across MBM16. This is because such low Mach numbers will not allocate enough turbulent energy to cascade down to the smaller scales. Our estimated range of Mach numbers is consistent with the power spectral slope measured by Chepurnov et al. (2010), and enforces our results.

### Discussion and Future Works.

In this study we applied a statistical method on Galactic observations for the first time developed by BHK to estimate turbulence. We found that MBM16 can be characterized as a mostly subsonic to transonic with a few localized regions of high turbulence. We then compared our results with BHK's SMC work, and found MBM16 to be less turbulent than the SMC. Considering the absence of star formation in MBM16, we concluded that MBM16 is less turbulent than many Galactic regions, which is consistent with the notion of stars being dominant drivers of interstellar turbulence. We also found that our estimate for the range of mach numbers for MBM16 agree with the range indicated by the independently measured power spectrum slope by Chepurnov et al. 2010.

In a paper that is in preparation we will obtain our own estimate of the spatial power spectrum slope of MBM16 and compare it with the estimate of Chepurnov et al. 2010. We will also examine the spectral information of MBM16 in an attempt to better understand its

velocity components. We plan to obtain an observational estimate of the sonic Mach number by examining background sources to see if any comparisons can be made to the results of the method used in this study. We can apply this method to the many cataloged MBM clouds within the GALFA-HI data, which will allow us to investigate how turbulence affects different environments and properties of interstellar gas. There is a plethora of CO data for MBM16, enabling us to use this statistical method on CO column density maps. It is intriguing to see what kinds of correlations and relationships may arise between the HI and CO data. These are preliminary results, which will quickly lead to a comprehensive paper.

We are very thankful for the NASA Wisconsin Space Grant Consortium for the generous funding of this research.

### **References.**

Burkhart, B., Stanimirovic, S., Lazarian, A., & Kowal, G. 2010, ApJ, 708, 1204

Chepurnov, A., Lazarian, A., Stanimirovic, S., Heiles, C., & Peek, J.E.G., 2010. ApJ, 714, 1398

Hobbs, L.M., Blitz, L., Penprase, B.E., Magnani, L., Welty, D.E., 1988, ApJ, 327, 356

Magnani, L., Blitz, L., & Mundy, L. 1985, ApJ, 402, 295 (MBM)

Peek J.E.G., Heiles, C., Douglas, K.A., Lee, M.Y., Grecevich,

J., Stanimirovic, S., Putman, M.E., Korpela, E. J,

Gibson, S. J., Begum, A., Destry, S., Robishaw, T.,

Krco, M., 2011 ApJS, 194, 20

Peek J.E.G., Putman, M.E., McKee, C.F., Heiles, C., & Stanimirović, S. 2007, ApJ, 656, 907

# Studying Interstellar Shells in our Milky Way Galaxy<sup>1</sup>

Dr. Shauna Sallmen

University of Wisconsin – La Crosse

## Abstract

The effects of generations of stars within the interstellar medium (ISM) have produced a turbulent, multiphase medium whose evolution has shaped how solar systems like our own form within a galaxy. It is clear that the distribution of energy and material in the ISM of our Milky Way Galaxy is largely driven by the stellar winds and supernova explosions of dying stars, forming hot, expanding bubbles that sweep up shells of neutral material. These Interstellar shells gradually cool, slow down, and mix with the ambient ISM, however we still lack a complete picture of the relevant interstellar processes. Studies of numerous shells are required to improve our understanding of their role in the evolution of our Galaxy. The author and undergraduate students have searched the SETHI radio survey database for new shells. In this project, the properties of 76 such shells were explored to evaluate their suitability for (1) follow-up multi-wavelength imaging and (2) follow-up absorption-line spectroscopic studies. These investigations of interstellar shells will improve our understanding of their properties, characteristics, and interactions with the surrounding ISM.

## Introduction

The space between the stars of our galaxy is filled with the low-density gas and dust of the interstellar medium (ISM). The ISM in the disk of our galaxy consists of several physical phases that range from dense and cold molecular gas to hot and fully ionized regions. This non-uniform gas exhibits a complex set of interacting structures. Shells, bubble-like features, “chimneys”, and worms are driven by stellar winds and supernova (SN) explosions. The hot, ionized material ejected into the ambient ISM through these processes has been enriched in heavy elements through nuclear fusion inside of stars and during the supernova explosions. As the gas expands outward, it sweeps up cold neutral material into a shell surrounding a bubble of hot gas. Over time, the shells gradually expand and cool. The enriched gas mixes with the turbulent ambient ISM, portions of which eventually cool into dense molecular clouds that are the birthplace of new solar systems. Understanding these processes has a direct impact on our studies of (1) galaxy evolution during the history of the universe, and (2) the history of our own solar system. This topic therefore links explicitly to the objectives of the NASA Science Mission Directorate (SMD), which seeks to scientifically understand the solar system<sup>2</sup>, “[...] the universe and to understand the nature of the strange phenomena that shape it.”

---

<sup>1</sup> Financial support for this research was provided by the Wisconsin Space Grant Consortium, the Research Corporation, and the National Science Foundation.

<sup>2</sup> <http://nasascience.nasa.gov/about-us>

Thus, the physical state and dynamics of the ISM in galaxies determine how energy and matter released by stars are redistributed throughout the Universe, and incorporated into new solar systems. It is therefore critical to first understand the interstellar gas in the Milky Way, which can be observed with greater sensitivity and resolution than other galaxies. Although the physical state and evolution of gas phases in our galaxy have been broadly explained, a detailed understanding has not been achieved. In the three-phase model of McKee & Ostriker (1977), random supernovae result in a turbulent ISM in which hot, low-density gas fills ~70% of the volume, surrounding warm and cold clouds. In the galactic fountain model of Shapiro and Field (1976), hot gas rises out of the galactic plane, cools, then falls back into the galactic plane. Superbubbles (caused by clusters of supernovae) can break out of the galactic plane, enhancing the possibility of a galactic fountain. Cox & Slavin (1992) incorporated the effects of magnetic fields in their models of supernovae evolution. The results indicate that the filling factor of hot gas is substantially less than original estimates. However, the Slavin & Cox (1993) picture assumes that the disrupting influence of supernova is small, a view which is controversial (see Cox 2005). There are still many outstanding problems with these (and all other current) models of the ISM (See Cox (2005) and Ferrière (2001) for detailed reviews of these issues).

Intensive study of the interactions of particular supernova remnants (SNRs) with their environment will improve our understanding of the overall processes in the ISM. According to various models, shells of material from old supernova remnants should be ubiquitous (Slavin & Cox 1993, Shelton 1996). A detailed knowledge of their physical properties is therefore essential to understanding the important processes of the ISM. Nevertheless, the energy inputs of shells are imperfectly understood, since “there is no one-to-one relationship of shells with young star clusters and associations” (Heiles 1984). Most well-studied shells are either quite close to the Sun, or are extremely large and distant. The number and size of large shells in the outer galaxy cannot yet be explained by the expected level of star formation in those regions, despite consideration of numerous alternatives (see McClure-Griffiths et al 2002). To make progress, we must increase the number of well-studied galactic shells.

Clearly, a first step is to identify for follow-up study neutral hydrogen (HI) shells which have previously been neglected. Recent radio surveys of neutral hydrogen with unprecedented sensitivity and angular resolution such as the Search for Extraterrestrial HI (SETHI; Korpela et al 2002), and the Southern Galactic Plane Survey (SGPS; McClure-Griffiths et al 2005) have resulted in the discovery of new shells of neutral gas (McClure-Griffiths et al 2001, Korpela et al 2004). Newer surveys such as the Parkes Galactic All-Sky Survey (GASS; McClure-Griffiths et al 2009) and the Galactic Arecibo L-Band Feed Array survey (GALFA-HI; Stanimirovic et al. 2006, Peek & Heiles 2008) provide data at even greater sensitivity and angular resolution. These rich new resources are resulting in the identification of previously neglected interstellar shells ripe for further study (e.g. Sallmen et al. in preparation)

For best results, each shell must be investigated using a variety of methods. Because “the multi-wavelength whole is far more than the sum of its parts” (Heiles, Haffner & Reynolds 1999), the interaction of SNRs with the surrounding ambient ISM must be studied at multiple wavelengths. When combined with 21-cm radio images of the cold, neutral gas in a shell, H- $\alpha$  images showing the warm, ionized hydrogen gas and X-ray images displaying the structure of hot gas will give us a more complete picture of how that shell is evolving and mixing with the ambient medium.

In addition, absorption lines in the spectra of stars lying beyond the shell can tell us about the location, physical conditions and expansion (because of the Doppler effect) of the shell. Such absorption-line studies provide more accurate distance determinations for the shells, as well as a crucial diagnostic of the physical conditions of the gas within the shell. HI distance estimates derived by interpreting HI emission with a standard galactic rotation model are necessarily uncertain. By comparing absorption spectroscopy of stellar continuum sources with increasing sightline distances, the physical location and distance of absorbing gas at various velocities can be confidently identified. This allows their association with actual interstellar structures. For example, this technique was used to confirm the distance and origin of the IC 443 SNR (Welsh & Sallmen 2003). More accurate distance estimates to HI shells also directly affect their derived sizes, and thus improve determinations of the energy required to produce such large interstellar features. In addition, the velocities of approaching and receding absorbing material can be used to determine the kinematic properties of the expanding shell.

Finally, by comparing absorption caused by both neutral species (reflecting cold gas) and ionized species (reflecting warmer gas), we can probe the physical conditions of gas within the shell. For example, the ionization state and column density of gas in the Shajn 147 SNR were determined using absorption-line studies (Sallmen & Welsh 2004). The NaI doublet absorption lines (5890 & 5896Å) are ideal for this work because they probe neutral gas associated with cold HI. The CaII lines (3933 & 3968Å) trace slightly warmer, ionized gas. These absorption lines reveal both the velocity structure and column density of the low-ionization interstellar gas lying foreground to an emitting continuum object. The  $N(\text{NaI})/N(\text{CaII})$  ratio is also an important physical diagnostic of the gas. When it is small (e.g.  $< 0.5$ ), this is interpreted as being indicative of the presence of warm (7000K) interstellar gas in which Ca dust grains have been destroyed by shocks or strong ionization effects (e.g. Bertin et al 1993). It is true that absorption measurements from stars will only probe a few pencil beams within each shell, so variable conditions within the shells will cause spatial variations in our results. Comparison of these absorption measurements with existing emission measurements at a variety of wavelengths will alleviate this issue by allowing us to assess the conditions for each sightline.

One example of a well-studied nearby SNR is the Cygnus Loop, at a distance of  $\sim 440$  pc. Detailed investigation of the velocity structure of the neutral hydrogen (Leahy 2003), optical absorption-line studies of the cool, neutral gas (Welsh, Sallmen, Sfeir & Lallement 2002), investigations of the shock using X-ray spectroscopy (Levenson, Graham & Walters 2002), OVI emission (Raymond et al 2003), HST imaging (Levenson & Graham 2001) and H- $\alpha$  imaging (Fesen, Kwitter & Downes 1992) have all contributed to our understanding of this object. Similar exhaustive multi-wavelength studies of a wide variety of SNRs at varying galactic distances are necessary for a complete understanding of the processes in the galactic interstellar medium.

## Methods

Over the past several years, the author has involved undergraduate students in searching for interstellar shells, and studying their properties through images at a variety of wavelengths. With the help of undergraduate students, the SETHI neutral hydrogen dataset has been searched, producing a list of shell-like features which are missing from previous catalogs (Sallmen et al., in preparation).

The goal of this project is to select newly identified shells which are suitable for further study:

- Explore existing archival images at multiple wavelengths for shells of potential interest for follow-up multi-wavelength observations
- Use kinematic distance information to identify shells suitable for absorption-line work
- Select appropriate stellar targets for each shell, and explore availability of absorption-line data for these stars

With the help of undergraduate students, archival images at multiple wavelengths were explored for 76 shells that were already identified using the SETHI radio data. Each shell's coordinates, velocity and angular size were measured and checked against existing catalogs. For each shell not previously known, archival data was downloaded from the *SkyView* Virtual Observatory<sup>3</sup>. Images of the shell at were compared for ¼ keV X-rays (RASSband1 & RASSband2), H- $\alpha$  (H-Alpha Composite Survey), 100  $\mu\text{m}$  infrared light (IRIS), as well as the 21-cm neutral hydrogen from the SETHI data. These reveal the presence of hot ( $\sim 10^6\text{K}$ ) gas, warm ionized ( $\sim 10^4\text{K}$ ) hydrogen gas, warm interstellar dust, and cold ( $\sim 100\text{K}$ ) neutral hydrogen gas, respectively. Shells showing clear shell-like features and multiple wavelengths, and/or correlations or anti-correlations between images are more suitable for further multi-wavelength analysis, as they give a more complete picture of the shell's evolution and mixing into the ISM. Each shell was assigned a ranking 1-3 describing its potential for multi-wavelength follow-up. For details of the procedure, see the proceedings paper by E. Tennyson (this volume).

To get the most out of such multi-wavelength studies, the distance to the shell must be known. At some galactic longitudes, the HI emission velocity can be interpreted in light of a galactic rotation model to estimate the distance. For each shell in our list, the radial velocity & range of velocities were compared with the rotation curve of Brand & Blitz (1993) to estimate its distance. This kinematic distance was then used to estimate the shell's physical size. Based on existing catalogs, HI shells are typically 100 to 300 pc in size (Ehlerová & Palouš 2005). We therefore wish to focus our attention on those shells with relatively well-defined kinematic distances which yield shell size estimates less than 300pc in size. These preliminary distance estimates also allow us to identify more appropriate potential stellar targets for absorption-line studies of these shells.

Several considerations apply when determining shells of interest for absorption-line spectroscopic studies. Such studies are particularly applicable to nearby shells with large expansion velocities. Nearby shells are more likely to have sufficient foreground and background target stars. Shells which have large expansion velocities (based on HI emission from the approaching / receding walls) must be selected to ensure that the absorption components due to the shell are well-separated in the spectrum from those due to the ambient ISM.

The existence of appropriate stellar targets is also an important consideration. Hot, luminous (early-type O and B) stars are the best background continuum sources for NaI and CaII spectroscopic studies, and must be present at several distances along the line of sight towards the shell. The preliminary kinematic distance estimate allows us to identify the most appropriate potential stellar targets for each shell. For a shell expansion velocity  $\geq 20$  km/s ( $\Delta v \geq 40$  km/s), we require spectral resolution  $R \sim 5$  km/s in order to separate absorption components from the

---

<sup>3</sup> <http://skyview.gsfc.nasa.gov>

main (and saturated) central line-of-sight absorption. Suitable spectra are typically taken with instruments such as the Hamilton echelle on the University of California Lick CAT, or the Giraffe echelle spectrograph mounted on the 1.9m Radcliffe telescope of the South African Astronomical Observatory. High-velocity components are easily detectable in 7<sup>th</sup> magnitude stars out to  $\sim 0.5$  kpc using the Lick CAT. For more distant stars, background early-type target stars ( $M_v = 6.0 - 9.5$ ) with distances 0.5 – 3 kpc are observable on a 2-m class telescope. On such a telescope it is possible to record the spectrum of an OB star of  $M_v \sim 9.0$  at a resolving power of 60,000 in one hour with a S/N ratio  $> 40:1$ . Suitable early-type stellar targets can be extracted from online stellar catalogs<sup>4</sup> for each selected shells. Shells with few available stellar targets are eliminated from further consideration for follow-up absorption-line work.

## Results

Of the 76 shells examined, 21 were determined to be found in the existing catalog of Ehlerová & Palouš (2005). Based on the existing multi-wavelength data, 23 of the remaining 55 shells are unsuited to follow-up multi-wavelength studies, 23 may be suited to follow-up multi-wavelength studies, and 9 are likely targets for such follow-up studies.

Table 1 shows the properties of these 9 shells, based on the SETHI data. Column 1 gives the name of the shell, based on its Galactic coordinates and velocity at which it is most “shell-like”. Columns 2 and 3 give the equatorial coordinates of the shell, while Column 4 gives the velocity range over which the shell is visible, and Column 5 gives the mean angular diameter of the shell. The final column gives the size estimate based on the mean angular diameter and kinematic distance estimates. Kinematic distance information may be found in Table 3 of Tennyson (proceedings this volume).

**Table 1: Shells most suited to multi-wavelength follow-up observations**

Shell ID GSH lll+bb+vvv	RA hh mm	Dec °	$\Delta V$ km/s	Mean Ang. Diam. (°)	Size pc
<b>GSH029+38+005</b>	16 28	13.75	4.64	3.1	$29_{-24}^{+23}$ or $990_{-30}^{+20}$
<b>GSH034+20+011</b>	17 42	9.5	10.83	2.8	$41_{-27}^{+25}$ or $690_{-20}^{+30}$
<b>GSH044+38+022</b>	16 45	24.75	6.21	1.9	$<16$ or $51_{-2}^{+2}$
GSH114-54-005	00 30	8.5	9.28	N/A	N/A (incomplete)
GSH208+32+006	08 43	18	15.46	5.8	$110_{-110}^{+150}$
<b>GSH213+28+012</b>	08 34	12	12.38	3.7	$110_{-60}^{+70}$
GSH274+74-006	12 19	12.5	10.82	6.4	$< 890$
GSH294+76+000	12 43	13.25	9.28	4.1	$<950$ or $>1130$
GSH325+78-001	13 10	15.75	7.74	8.4	$290_{-290}^{+1130}$

Based on the kinematic distance and resulting size estimates for these 9 shells, there are 4 shells with relatively well-defined distance / size estimates consistent with the expected 100-300pc maximum shell size. These entries are bold-faced in Table 1, and represent the 4 shells most suited to follow-up multi-wavelength observations.

<sup>4</sup> Accessed via the SIMBAD astronomical database (<http://simbad.u-strasbg.fr/simbad/>)

For each shell in Table 1, online stellar catalogs were used to search for O & B stars in a rectangular region containing the shell. The results are shown in Table 2. The left-hand table shows the results for the shells deemed most interesting based on both archival multi-wavelength image exploration & kinematic distance estimates. None of these have enough potential stellar candidates to merit further consideration for absorption-line studies. The right-hand table shows the results for the remaining shells highlighted through the exploration of archival multi-wavelength images. Although these have less well-defined kinematic distance estimates, two of these do have sufficient stellar target candidates to merit further consideration for absorption-line studies.

**Table 2: Candidate Stellar Targets**

Shell ID	# O & B stars	Shell ID	# O & B stars
<b>GSH029+38+005</b>	3	GSH114-54-005	8
<b>GSH034+20+011</b>	2	GSH208+32+006	8
<b>GSH044+38+022</b>	1	GSH274+74-006	4
<b>GSH213+28+012</b>	3	GSH294+76+000	0
		GSH325+78-001	2

## Future Work

Multi-wavelength image exploration based on archival data must still be completed for at least 7 more newly identified shells, to complete the selection of shells suitable for multi-wavelength follow-up studies.

Stellar target candidate identification must be completed for all of the newly identified shells, focusing on the 23 which are potentially interesting based on the comparison of archival images at multiple wavelengths. In an ideal world, we would perform absorption-line studies on shells which are also suited to multi-wavelength imaging studies. However, lack of availability of stellar targets may force us to do absorption-line studies of some shells which are less suited to multi-wavelength imaging studies.

Once suitable targets are selected, existing and newly obtained absorption-line spectra will be used to analyze the physical properties of the interstellar shells, and to refine their distances. Absorption-line spectra have likely already been acquired for some of these stellar targets. For example Welsh et al. (2010) contains NaI and CaII measurements to hundreds of bright, relatively nearby stars, and colleagues active in this area will be contacted to gain access to the relevant spectra. Absorption-line spectra of stellar continuum targets are used to analyze the properties of gas in an intervening interstellar shell. For some targets, the gas cloud velocity, cloud dispersion parameter, and column density may already be available in the literature. Other existing absorption-line spectra will be searched for interstellar absorption features formed in the expanding nebular shell gas. The observations will be of sufficient spectral resolving power to separate absorption components due to shell expansion from the central line-profiles (formed from line-of-sight gas in the ISM between the Sun and a shell, and usually saturated). Overall, improved shell distance estimates will help constrain the energy requirements and spatial distributions of these objects. This will lead to an improved understanding of their formation mechanism and interaction with each other and the ambient ISM in our galaxy.

## Acknowledgements

I acknowledge the support of the Wisconsin Space Grant Consortium in carrying out this research, and the Research Corporation and National Science Foundation for supporting my research program.

I acknowledge the use of NASA's *SkyView* facility (<http://skyview.gsfc.nasa.gov>) located at NASA Goddard Space Flight Center, and the SETHI database (<http://setiathome.berkeley.edu/~korpela/sethi>), which uses data acquired at Arecibo Observatory. The Arecibo Observatory is part of the National Astronomy and Ionosphere Center which is operated by Cornell University under a Cooperative Agreement with the National Science Foundation.

I would like to acknowledge the participation in this project of undergraduate students Elizabeth Tennyson and Cheuk Man Lo, as well as the past contributions of Brooke Baldwin and Kurt Grunwald, who searched for shells in the SETHI data.

## References

- Bertin, P., Lallement, R., Ferlet, R., & Vidal-Madjar, A. 1993, *A&A*, 278, 549
- Brand, J. & Blitz, L. 1993, *A&A*, 275, 67
- Cox, D.P. & Slavin, J. 1992, *ApJ*, 392, 131
- Cox, D.P. 2005, *Ann. Rev. Astron. Astrophys.*, 43, 337
- Ehlerová, S. & Palouš, 2005, *A&A*, 437, 101
- Ferrière, K. 2001, *Rev. Mod. Phys.*, 73, 1031
- Fesen, R., Kwitter, K. & Downes, R. 1992, *AJ*, 104, 719
- Heiles, C. 1984, *ApJS*, 55, 585
- Heiles, C., Haffner, L.M. & Reynolds, R.J. 1999, in *ASP Conf. Series* 168, p211, Ed. A.R. Taylor, T.L. Landecker & G. Joncas (San Francisco: ASP)
- Korpela, E. J., Demorest, P., Heien, E., Heiles, C. & Werthimer, D. 2002, “SETHI@Berkeley - A Piggyback 21-cm Sky Survey at Arecibo” in *ASP Conf. Series* 276, p100, Ed. A.R. Taylor, T.L. Landecker & A. Willis (San Francisco: ASP)
- Korpela, E. J., Demorest, P., Heien, E., Heiles, C., & Werthimer, D. 2004, in Proceedings from the 2003 June Galactic Tertulia *How Does the Galaxy Work*, p 97, Ed. E.J. Alfaro, E. Perez & J. Franco (Dordrecht: Kluwer Academic Publishers)
- Leahy, D.A. 2003, “Structure of the HI near the NE Limb of the Cygnus Loop”, *ApJL*, 586, 224
- Levenson, N. & Graham, J. 2001, *ApJL*, 559, 948
- Levenson, N., Graham, J. & Walters, J. 2002, *ApJ*, 576, L798
- McClure-Griffiths, N. M., Green, A.J., Dickey, J.M., et al. 2001, *ApJ*, 551, 394
- McClure-Griffiths, N. M., Dickey, J. M., Gaensler, B. M., & Green, A. J. 2002, *ApJ*, 578, 176
- McClure-Griffiths, N. M., Dickey, J. M., Gaensler, B. M., et al. 2005, *ApJS*, 158, 178.
- McClure-Griffiths, N. M., Pisano, D. J., Calabretta, M. R., et al. 2009, *ApJS*, 181, 398
- McKee, C. & Ostriker, J. 1977, *ApJ*, 218, 148
- Peek, J.E.G., & Heiles, C. 2008 [arXiv:0810.1283](https://arxiv.org/abs/0810.1283)
- Raymond, J.C., Ghavamian, P., Sankrit, R., Blair, W. P. & Curiel, S. 2003, *ApJ*, 584, 770
- Sallmen, S. and Welsh, B.Y. 2004, *A&A*, 426, 555
- Shapiro, P. & Field, G., 1976, *ApJ*, 205, 762
- Slavin, J. & Cox, D.P. 1993, *ApJ*, 417, 187
- Shelton, R.L. 1996, “The ISM in Our Galaxy”, PhD Thesis, Univ. of Wisconsin-Madison
- Stanimirovic, S., Putman, M., Heiles, C., et al. 2006, *ApJ*, 653, 1210
- Welsh, B.Y., Sallmen, S., Sfeir, D. & Lallement, R. 2002, *A&A*, 391, 705
- Welsh, B.Y. & Sallmen, S., 2003, *A&A*, 408, 545
- Welsh, B.Y., Lallement, R., Vergely, J.-L., & Raimond, S. 2010, *A&A*, 510, A54

# Studying Neutral Hydrogen Shells in the Interstellar Medium

Elizabeth M. Tennyson, Dr. Shauna Sallmen

*Department of Physics, University of Wisconsin - La Crosse, La Crosse, WI 54601*

Dr. Eric J. Korpela

*Space Sciences Laboratory, University of California at Berkeley, Berkeley, CA, 94720*

## ABSTRACT

One of the many processes that occur in our Milky Way Galaxy is the interaction of Neutral Hydrogen (H I) shells with the Interstellar Medium (ISM). H I shells are formed when material from stellar winds and supernova explosions expands outward and mixes with the ISM. Without this phenomenon the heavy elements made in stars would not be recycled and reused for future star and planet systems. The goal of this project is to better understand how interstellar shells evolve. To acquire a better grasp of a shell's characteristics and development, we compared images for 55 shells that were discovered in the Search for Extraterrestrial Neutral Hydrogen (SETHI) radio database. The SETHI images show cold, neutral gas, the H-Alpha Composite Survey images show warm, ionized gas, the IRIS (infrared) images show warm dust, and the RASS (X-ray) images reveal hot gas. The initial comparison identified nine potentially interesting shells. Of these, four are most suitable for detailed follow-up study, based on information available from their kinematic distances. We present a catalog of the shells we classified, including details of those that are likely targets. Follow-up detailed multi-wavelength comparisons can give us estimates on a shells's age and evolutionary status.

*Subject headings:* ISM: general — ISM: bubbles, ISM: supernova remnants

## 1. Introduction

Neutral Hydrogen (H I) shells are found throughout the Interstellar Medium (ISM) of our Milky Way Galaxy. These interstellar shells are formed by supernova explosions and stellar winds, which eject hot, ionized material. Over time, the ionized gases cool and become neutral gases. The materials that are dispersed from these events mix with the

surrounding ISM and enrich it with heavy elements like gold, silicon, and iron. This process is an important part of the stellar evolution cycle that leads to the formation of new stars and planetary systems. Examining these shells in detail will give a better understanding of both H I shells and interstellar processes in our Galaxy.

One way to analyze interstellar shells in more detail is to observe the distributions of material at different temperatures. Comparing images taken of a specific object at different wavelengths can reveal important characteristics of the expanding shell (e.g. Heiles, Haffner, & Reynolds 1999). At higher temperatures, higher energy radiation such as X-rays will be emitted. Lower energy radiation is an indication of cooler gas. It is expected that a young supernova remnant (SNR) will emit high energy radiation at its core because it would be very hot inside. The lower energy radiation will be emitted by cooler gas surrounding the object in question. As the SNR expands and cools, the distribution of hot and cold material changes. Therefore, using the information that different wavelengths can give, it is possible to determine the evolution of an object like an H I shell.

Recent radio surveys have allowed us to identify new H I shells. For example, the Search for Extraterrestrial H I (SETHI) database is based on 21-cm data taken at the Arecibo Radio Telescope in Puerto Rico. This survey maps the neutral hydrogen in our Galaxy at a higher resolution and sensitivity than previous efforts. These high-quality data have resulted in the discovery of new shells (e.g. Korpela et al. 2004).

In this project, images at multiple wavelengths are compared to better comprehend the morphology of shells recently discovered in a search of the SETHI data (Sallmen et al., in preparation). The wavelengths that were chosen (X-ray, H $\alpha$ , infrared, and 21-cm) are emitted by gas at different temperatures in and around the H I shells. These four images compared to one another help identify shells suitable for more detailed study, and give information about the inter-workings of gas at various temperatures within such shells.

## 2. Methods

Searching the high-resolution SETHI data by eye resulted in a list of 55 potential new H I shells, including their location and size (Sallmen et al., in preparation). In order to view these shells at the wavelengths of interest, the public Astronomical Database *SkyView* was used (McGlynn et al. 1996). This database contains surveys in a variety of wavelengths. For each shell, appropriate regions of these data were extracted from *SkyView* for three surveys. (1) The ROSAT X-ray All Sky Survey corresponding to X-rays of approximately 1/4 keV (RASSband1 & RASSband2) was used to analyze the hot ( $\sim 10^6$  K) X-ray emitting gas.

(2) The H-Alpha Composite Survey ( $H\alpha$ ) was used to map the warm ( $\sim 10,000$  K), ionized hydrogen gas. (3) The Infrared Imaging Survey (IRIS) showed the warm infrared emitting dust that resides in and/or around the shell. The cold ( $\sim 100$  K) neutral hydrogen gas was shown in the SETHI data.

The program SAOImage ds9 was used to compare H I data versus data at other wavelengths. This software assisted with the comparison process because it enabled a viewer to blink through images as well as draw the same regions on multiple images. The correlations between images for each shell were examined and quantified. For example, if there were low H-Alpha emission levels in the same region as the low H I emissions, the images were correlated. Similarly, bright X-ray emissions within the region of low H I emissions represented a correlation between the two surveys. Such correlations make the shell more appropriate for further multi-wavelength analysis.

### 3. Results

We quantified such correlations for 55 shells in our list. The number 1 was assigned to shells where multiple correlations between multiwavelength images were easy to identify. The quantification number 3 denotes no identifiable correlation at all between survey images.

After quantifying the multi-wavelength correlations, 9 shells had a quality of 1, 23 had a quality of 2, and 23 had a quality of 3. The image set in Figure 1 shows shell GSH 034+20+011, which was assigned a quality of 1.

Each survey image of this shell GSH 034+20+011 is correlated to at least one of the other survey images it was compared with. The ionized hydrogen gas emissions in Figure 1b generally match the cold, neutral hydrogen emissions in Figure 1a. The detailed correlation will reveal where warm, ionized gas is cooling into neutral hydrogen near the edges of the shell. The warm, infrared dust (Figure 1c) is anti-correlated to the hot gas (Figure 1d) because the dust blocks some of the X-ray emissions from getting through. The presence of the warm dust causes the lack of X-ray emissions. The regions of slightly brighter X-ray emission (seen in Figure 1d) in the center of the interstellar shell suggest it may contain hot, X-ray emitting gas. Typically, young expanding shells contain X-ray emission. Faint or no X-ray emission indicates an older shell expanding more slowly.

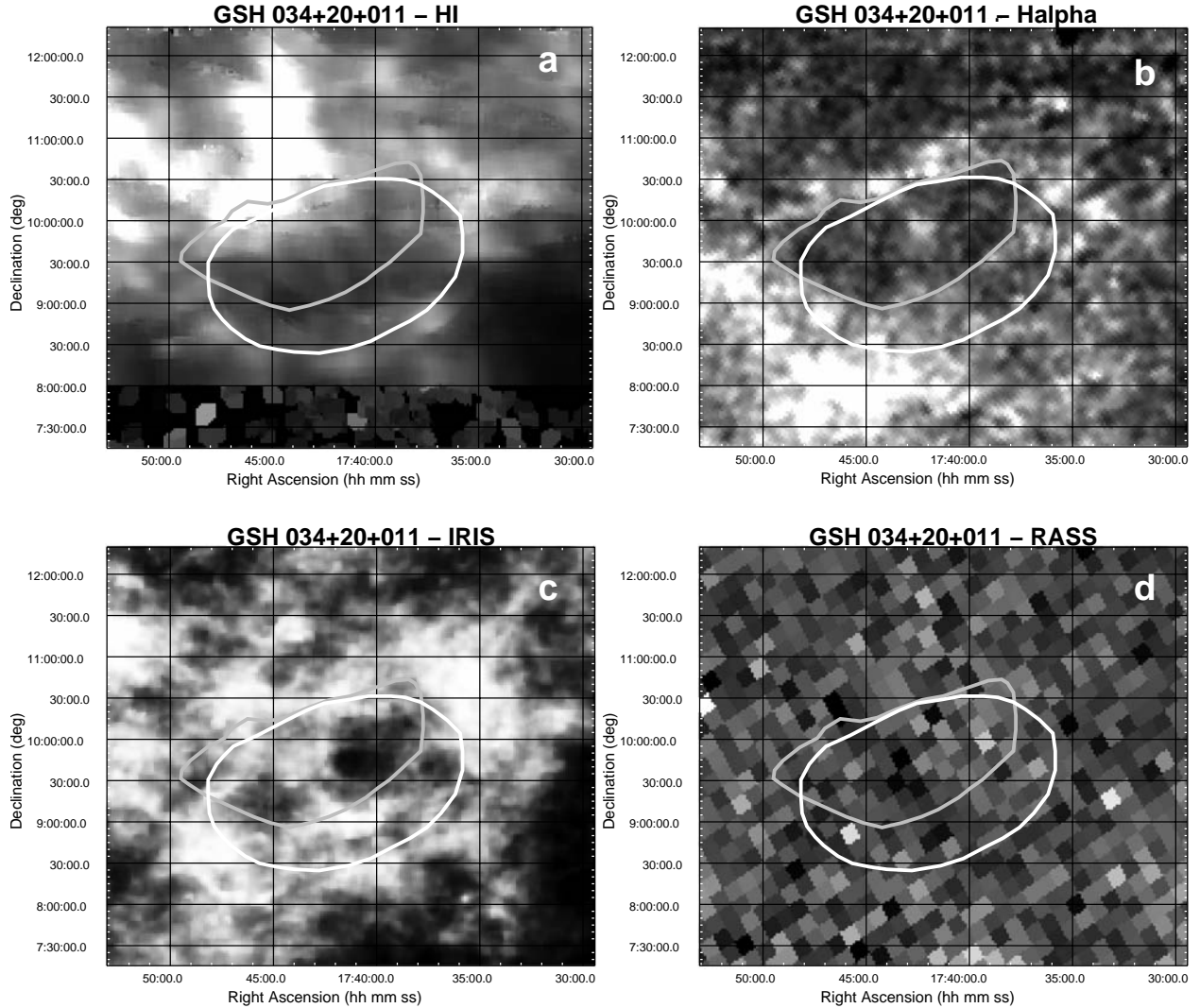


Fig. 1.— Four images of shell GSH 034+20+011. (a) Neutral Hydrogen shell at 21-cm. The inner edges of the H I emission are outlined in white. This region is marked on all four images for comparison purposes. (b) H-Alpha Composite image. The inner edges of the H-Alpha emission are outlined in grey. This region is also marked in all four images for comparison purposes. The overlapping low-emission regions of the H-Alpha and H I images suggests a correlation between the warm ionized gas and the cold neutral gas in the shell. (c) IRIS 100 micro-meter Survey image of the same shell. The warm infrared emitting gas is less predominant in the H I hole region, and plentiful where the neutral and ionized hydrogen gases are plentiful. (d) RASSband1 and RASSband2 Survey images added together. Within the H I hole hot gas X-Ray emissions are weakest where the IR image suggests the presence of warm infrared dust.

Table 1: SETHi Quality 1 Shell Information

Shell ID	$\alpha$	$\delta$	$\theta$	$\Delta V$
GSH lll+bb+vvv	hh mm	°	°	km s <sup>-1</sup>
<b>GSH029+38+005</b>	16 28	13.75	3.1	4.64
<b>GSH034+20+011</b>	17 42	9.5	2.8	10.83
<b>GSH044+38+002</b>	16 45	24.75	1.9	6.21
GSH114-54-005	00 30	8.5	N/A	9.28
GSH208+32+006	08 43	18	5.8	15.46
<b>GSH213+28+012</b>	08 34	12	3.7	12.38
GSH274+74-006	12 19	12.5	6.4	10.82
GSH294+76+000	12 43	13.25	4.1	9.28
GSH325+78-001	13 10	15.75	8.4	7.74

Table 1 lists the 9 H I shells that were identified based on the quality parameter as potentially interesting targets for follow-up studies. Table 2 lists the 23 H I shells that were classified as quality 2. These are shells that had some correlations between multiple wavelength images, but not as many as those in Table 1.

Tables 1 and 2 both give the same information for each shell. The Shell IDs in column 1 describe the location of the shell. The three characters immediately following the GSH letters represent the galactic longitude of the shell center. The next three characters represent the galactic latitude of the shell. The following four characters give the radial velocity ( $V_{\text{ref}}$ ) at which the feature is most “shell-like”. Columns 2 and 3 give the shell’s location in celestial coordinates ( $\alpha, \delta$ ). The mean angular diameter ( $\theta$ , column 4) for our shells was found by averaging the angular size of the longest and shortest diameters of each shell, correcting for the fact that a given  $\Delta\alpha$  is closer together at higher declination. If the H I shell were oval, the long diameter would correspond with the major axis while the short diameter would correspond with the minor axis.  $\Delta V$ , listed in column 5, is the difference between the maximum and minimum velocities at which the H I shell is visible and “shell-like”. The center coordinates, velocity range  $\Delta V$ , and mean angular diameter  $\theta$  all come from the search in which the shells were first identified (Sallmen et al., in preparation).

Table 2. Quality 2 Shell Information

Shell ID	$\alpha$ hh mm	$\delta$ °	$\theta$ °	$\Delta V$ km s <sup>-1</sup>
GSH029+34+005	16 42	12.25	1.5	12.37
GSH030+67-006	14 33	23.5	3.3	7.55
GSH040+04+048	18 49	8.25	1.8	15.47
GSH042+21+019	17 50	17	12.0	10.83
GSH045+14+031	18 23	17	2.3	10.85
GSH054-00+003	19 31	18.25	N/A	7.76
GSH055+18-005	18 20	27.25	4.7	6.18
GSH062+04-102	19 35	27	N/A	7.74
GSH065-01-079	19 58	27.5	N/A	24.75
GSH110-35-034	00 05	26.5	4.1	15.46
GSH112-46-008	00 19	16.25	4.0	9.28
GSH116-49-006	00 34	13.5	2.7	4.64
GSH156-37-003	02 43	19	4.4	6.16
GSH180-31+020	04 00	10	3.3	9.28
GSH182-18+005	04 46	17.5	3.9	6.19
GSH187-12+012	05 18	16.5	9.0	9.28
GSH192+06-017	06 33	21	3.4	21.66
GSH196+10+008	06 57	19	5.2	6.18
GSH210+54-003	10 12	23.25	2.8	10.83
GSH221+60+000	10 45	19.25	2.9	6.19
GSH231+55-009	10 36	12.5	3.4	6.19
GSH236+75-008	11 51	20.25	1.2	9.28
GSH262+73+003	12 05	13.5	8.7	6.18

#### 4. Discussion

For the Quality 1 shells presented in Table 1, we used the Galactic rotation curve of Brand & Blitz (1993) to estimate the shell distances and sizes. Such kinematic distances are calculated by using the Galactic rotation curve, which describes the assumed circular orbital velocity at different distances from the Galactic center. Depending on the direction and distance of the target, Galactic rotation produces a particular radial velocity for the object. Since the direction of the H I shells are known, we can use the equations for the kinematic distances to calculate how far away the Earth is from a shell. In the inner Galaxy, there are generally two possible solutions for the distance, resulting in a distance ambiguity. In addition, this method has limitations because the motions of objects in the Galaxy are more turbulent and complex than for simple circular motion (Brand & Blitz 1993).

Table 3: SETHI Kinematic Distances and Sizes

Shell ID	$D_{\text{ref}}$	$D_{\text{min}}$	$D_{\text{max}}$	Size
GSH lll+bb+vvv	kpc	kpc	kpc	pc
<b>GSH029+38+005</b>	0.50 or 18.3	0.06 or 17.9	0.92 or 18.7	$27_{-24}^{+23}$ or $990_{-30}^{+20}$
<b>GSH034+20+011</b>	0.84 or 14.2	0.29 or 13.7	1.36 or 14.7	$41_{-27}^{+25}$ or $690_{-20}^{+30}$
<b>GSH044+38+002</b>	15.5	15	0.47 or 15.9	$< 16$ or $51_{-2}^{+2}$
GSH114–54–005	1.83	0.27	3.32	N/A
GSH208+32+006	1.10	N/A	2.58	$110_{-110}^{+150}$
<b>GSH213+28+012</b>	1.74	0.83	2.78	$110_{-60}^{+70}$
GSH274+74–006	N/A	N/A	7.9	$< 890$
GSH294+76+000	N/A	N/A or 15.7	13.3 or N/A	$< 950$ or $> 1130$
GSH325+78–001	1.95	N/A	9.43	$290_{-290}^{+1130}$

Table 3 lists the results. Column 1 is the Shell ID, and column 2 describes the distance  $D_{\text{ref}}$  corresponding to the reference velocity  $V_{\text{ref}}$ . Columns 3 and 4 give the minimum and maximum distance ( $D_{\text{min}}$  and  $D_{\text{max}}$ ) to the shell based on the velocity range ( $\Delta V$ ) from Tables 1 and 2. The final column of Table 3 shows the size estimates for each shell that result from these distance estimates and the mean angular diameter  $\theta$  from Tables 1 and 2. The quoted errors incorporated into this method are based on  $D_{\text{min}}$  and  $D_{\text{max}}$  resulting from the observed velocity range of the shell.

The maximum expected size for H I shells is 100 to 300 pc (Ehlerová & Palouš 2005). Shells with well-determined distances and sizes are more suitable for further study because

this allows more accurate modeling of the energy requirements for shell evolution. The four shells listed in bold in Tables 1 and 3 are those that were selected as most interesting, because their kinematic distances are relatively well-constrained and yield reasonable sizes. This is assuming that the nearby distances and inferred sizes in Table 3 are correct.

## 5. Conclusions & Future Work

Based on examining 55 shells, four of our shells were identified as excellent candidates for follow-up studies. These would include more detailed multiple wavelength comparisons and modeling the H I shells' properties and evolution. In addition, seven shells were identified in the SETHI data that have not yet been examined for multi-wavelength correlations.

## Acknowledgements

I would like to acknowledge the Wisconsin Space Grant Consortium (WSGC) for granting me this award, giving me the opportunity to further my education and interest in Astronomy research.

We also acknowledge the use of NASA's *SkyView* facility (<http://skyview.gsfc.nasa.gov>) located at NASA Goddard Space Flight Center. This research has also made use of SAOImage DS9, developed by Smithsonian Astrophysical Observatory.

Also, a big thank you to the SETHI database (<http://setiathome.berkeley.edu/~korpela/sethi/>), which uses data acquired at Arecibo Observatory. The Arecibo Observatory is part of the National Astronomy and Ionosphere Center which is operated by Cornell University under a Cooperative Agreement with the National Science Foundation.

## REFERENCES

- Brand, J. & Blitz, L. 1993, *A&A*, 275, 67
- Ehlerová, S., & Palouš, J. 2005, *A&A*, 437, 101
- Heiles, C., Haffner, L.M., & Reynolds, R.J. 1999, *The Eridanus Superbubble in its Multi-wavelength Glory* in *ASP Conf. series* 168, 211, Ed. A.R. Taylor, T.L. Landecker & G.Joncas (San Francisco: ASP, 1999)
- Korpela, E. et al. 2004, *ASSL Volume. 315 How Does the Galaxy Work*, 97
- McGlynn, T., Scollick, K. & White, N. 1996, *SkyView: The Multi-Wavelength Sky on the Internet* in *IAU Symposium No. 179, New Horizons from Multi-Wavelength Sky Surveys*, 465, Ed. B.J. McLean et al. (Kluwer, 1996).

# **21st Annual Conference Part Eight**

Education and Public Outreach

## Round 2: Flight, Floating, and Mars Courses

Sarah J. Desotell

Department of Physics, Ripon College  
Ripon, Wisconsin

**Abstract.** “Exploring Mars” and “Flight and Floating” are new courses that have been integrated into the Ripon College curriculum. “Exploring Mars” was developed for non-science major students to increase their general scientific interest through topics of space exploration and space science. “Flight and Floating” was designed for students with physics, math, and engineering interests, combining experimental design and mathematical modeling to study drag, lift, thrust, and buoyancy.

### Overview

The goal of this two-year project was to develop new undergraduate courses for a diverse audience of students, in topics of space exploration and aerospace studies. The first course, “Exploring Mars,” introduced first-year students to the science of space exploration through topics such as space travel and energy technology, terraforming and colonizing Mars, and current events in space discoveries. One objective of this course was to increase general scientific interest in students who were not planning to major in the natural sciences. The second, two-part course sequence, “Introduction to Flight” and “Flight and Floating,” combined mathematical modeling with experiments to observe and analyze floating and flying objects. The flight course sequence was intended for students with experience in physics and mathematics, and was especially suited for students planning to pursue further studies and/or careers in engineering and aerospace science. Each new course has been offered twice at Ripon College. With some revisions in course activities and content, “Exploring Mars” will be offered for a third time in the fall of 2011, and “Flight and Floating” will likely be offered on a two or three-year rotation in the future. This paper describes several course activities and provides examples of the course development that has occurred over the past two years.

### Exploring Mars: Course Design and Development

Through labs, field trips, lecture, and other activities, first-year students in “Exploring Mars” covered a wide variety of topics in space science. The course largely focused on Mars (climate, weather, geography, rover and orbiter missions, life and water, terraforming and colonization), but also engaged students in broader topics such as energy technology (solar cells, fuel cells), space travel (rockets, magnetic sails), space ethics (space garbage, animals in space, terraforming), and current events in space exploration. The course was first taught in the fall of 2009 with an enrollment of twenty students, clustered with another first-year course entitled “Plants in Space.” A detailed description of the original course curriculum, goals, and activities is provided in the 2010 WSGC Conference Proceedings (Desotell, 2010).

---

This project has been supported by the Wisconsin Space Grant Consortium Higher Education Incentives Program and by Ripon College. Special thanks to Skip Wittler, Ripon College Professor of Biology, for the development of the “Plants in Space” course.

During the fall of 2010, “Exploring Mars” was offered a second time to twenty first-year students, maintaining the same general course structure and content, with minor revisions in assignments and activities. For example, a solar cell lab was added to the 2010 curriculum. In this lab activity, accompanied by a lecture on solar cell operation and applications, each group of three or four students was given a solar-powered vehicle, and calculated the minimum intensity and power required for the vehicle to operate, based on the distance and power of a given light source. Students could then confirm whether or not their solar vehicle could operate on Mars. This lab followed a few weeks behind the “Power of the Sun” lab, where students were first introduced to concepts and mathematical relationships involving intensity and power and calculated the intensity of the sun on Mars. Typically, in this non-major course of first-year students, there is a broad range of mathematical background and skill among the students. Using the same mathematical relationships to study different systems can be a helpful way to increase students’ comfort level with mathematical analysis. On the other hand, a time-consuming 2009 lab, “Heating the Surfaces of Earth and Mars” was eliminated from the course in 2010. The lab was focused on temperature differences of materials with unequal specific heats, and produced large amounts of data for students to analyze. Without including differences in atmosphere and distance to the sun, the lab is not a good representation of Earth/Mars temperature differences.

Additional course revisions in 2010 devoted more attention to current events in space science by assigning students to find, review, and share articles related to space exploration. Also, a more clearly defined final course project was assigned, requiring students to develop a habitat for humans on Mars including plans for power, water, shelter, and agriculture. Student presented the group project in a formal paper as well as in poster session with the students from “Plants in Space,” who presented habitat designs as well. This assignment was a suitable final project, challenging students to combine ideas from the entire semester to produce a complete proposal, with infinite possibilities inviting creative solutions. Student evaluations for the 2009 and 2010 Mars courses were largely positive and reflected that many students were interested and engaged in the material and enjoyed a wide range of course activities, although some students commented that the course was repetitive and slow-paced.

### **Round 3: Mars in 2011**

“Exploring Mars” will be offered for a third time in the fall of 2011, with the course goals as listed in Table 1. Although the course will retain similar structure and activities to previous years, revisions will continue to be made to create effective teaching strategies and assignments, and to keep up with current events and resources. For example, the second lab of the semester, “How High Can You Jump on Mars?” students take measurements of Earth-bound jump heights, calculations of take-off velocity (knowing the rate of gravitational acceleration on Earth), and the equivalent jump height on Mars. This year, the lab will be extended to include calculation of the gravitational acceleration on Mars, for use in jump calculations. Determination of gravitational acceleration will require students to find the sun’s mass and the radius of Mars using external sources, and will be an exercise in unit analysis and conversions and increase students’ familiarity with scientific notation. The 2011 presentation assignment has also been modified from previous years. In the past, students presented movie reviews with scientific analyses using fictional movies set in outer space. During the fall of 2011, the presentation assignment will instead focus on real missions to Mars; Students will focus on mission goals, scientific

instrumentation, challenges, failures, and successes. The assignment will be introduced near the beginning of the course when many students are just becoming acquainted with Mars.

**Table 1: Course goals for “Exploring mars” in 2011**

<ul style="list-style-type: none"> <li>• Develop skills in written and oral communication and quantitative analysis</li> <li>• Gain experience in experimental design and measurement techniques</li> <li>• Study the climate of Mars with comparisons to Earth’s climate</li> <li>• Understand the physics and applications of various energy technologies</li> <li>• Understand past and recent evidence of life and water on Mars</li> </ul>
---

### **Flight and Floating: Course Design and Development**

“Introduction to Flight” was a semester-long course immediately followed by a three-week “Flight and Floating” Maymester. The course sequence focused on flying and floating objects (rockets, parachutes, kites, balloons, airplanes, birds, and many more) through experimental and mathematical analysis, field trips, and guest speakers. The sequence was designed for students with experience in physics and math, and was especially suited for students interested in pursuing careers in the aerospace and aeronautics industries or in engineering. The introductory course met on a weekly basis and often consisted of a conceptual and mathematical introduction to a force (drag, lift, thrust, buoyancy), followed by a lab activity that required measurements and analysis. During the second course of the sequence, “Flight and Floating” students applied these concept and models to design and analyze more complex systems demonstrating lift, drag, gravity, buoyancy, and thrust.

Rockets, for example, were studied extensively during the course sequence through a variety of experiments, using several different modeling and analysis techniques. During “Introduction to Flight,” the rocket unit began with a basic explanation of rocket thrust resulting in forward motion. Students launched Alka-Seltzer® rockets and balloon rockets to demonstrate the concept. This was followed by a derivation describing the time-varying acceleration and velocity of a rocket in flight. The derivation begins with the change in momentum,  $\Delta p$ , of the system as a mass of burned fuel,  $\Delta m$ , leaves the rocket with an exhaust velocity  $v_e$  (relative to the rocket). Figure 1 shows a rocket with mass  $M$  and velocity  $V$  at some initial time  $t$ . A short time later ( $t + \Delta t$ ), the rocket velocity and mass have changed to  $V + \Delta V$  and  $M - \Delta m$ , respectively. The total change in momentum, observed from a stationary reference frame (the ground) is given by equation 1. The exhaust velocity relative to the ground,  $v_{e,g}$ , is given by equation 2 (where  $v_e$  is a positive quantity), and the total change in momentum is simplified to equation 3, assuming that the product  $\Delta m \cdot \Delta V$  is negligible compared to other terms for small time steps.

$$\Delta p = [(M - \Delta m)(V + \Delta V) + \Delta m \cdot v_{e,g}] - M \cdot V \quad (1)$$

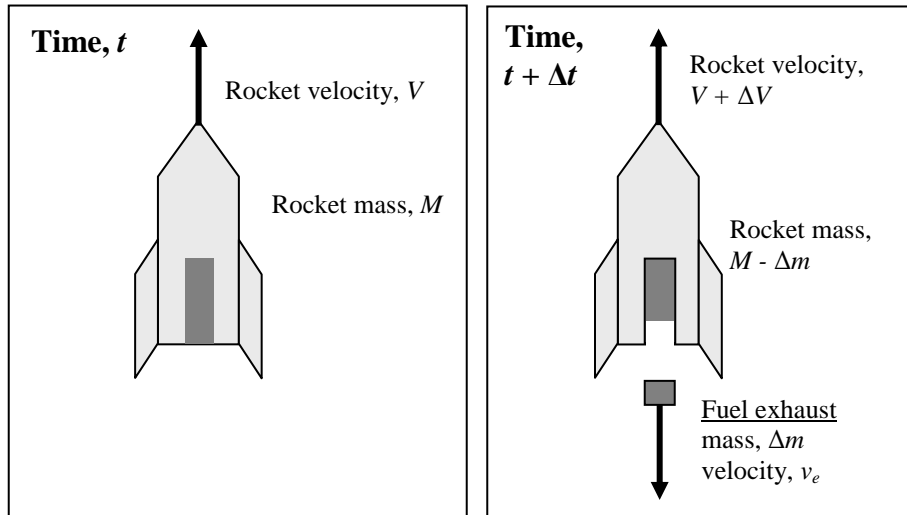
$$v_{e,g} = V - v_e \quad (2)$$

$$\Delta p = M \cdot \Delta V - \Delta m \cdot v_e \quad (3)$$

When equation 3 is applied in Newton's Second Law ( $F_{net} = \Delta p / \Delta t$ , where  $F_{net}$  is the net external force), equation 4 is derived, including rocket acceleration,  $a = \Delta V / \Delta t$ , and fuel burn rate,  $\dot{m} = \Delta m / \Delta t$ . The governing equations simplify to  $F_{net} = M \cdot a$  when the fuel is exhausted and rocket mass becomes constant.

$$\sum F = M \cdot a - \dot{m} \cdot v_e \quad (4)$$

**Figure 1: The mass and velocity of a rocket change as fuel is exhausted.**



The rocket equation was applied to analyze several different systems during the two-course sequence. During the introductory course, students programmed the rocket equation in a Microsoft® Excel spreadsheet with a simple numerical scheme including forces of drag and gravity, to model the motion of pre-constructed solid-fuel Estes® rockets. Although many variations of this experiment could be executed, in this case, students combined experimental data with modeling assumptions to determine the average exhaust velocity,  $v_e$ , of a rocket motor. To do so, the initial and final rocket masses were measured before and after the launch, respectively, and the average fuel burn rate was calculated using the total mass difference (the amount of fuel burned) and the total burn time, taken from Estes® reported data or using experimental measurements of burn time. Drag force parameters such as projected rocket area and air temperature were measured before the launch, and a drag coefficient was estimated in the 0.3 – 0.5 range (nosecone.com). Finally, the apogee of the rocket was measured during flight using an altimeter carried within the rocket, and by students measuring the angle above the horizon at apogee from a known horizontal distance. With these parameters and measurements, each student developed a numerical model calculating time-varying mass, acceleration, velocity, and altitude of the rocket. Students determined the unknown exhaust speed by matching the numerically predicted apogee to the launch results.

During the Maymester course, “Flight and Floating,” rockets were analyzed even further: Student built their own solid fuel rocket from an Estes® kit (skill level 2 or higher), and modified their rocket to include an electronics bay housing an altimeter. Each student chose one

parameter to vary among launches, such as engine strength, total weight, or fin design. Each rocket was launched several times for each set of experimental conditions, and altimeters returned apogee measurements upon recovery. Students were introduced to RockSim rocket modeling software during this project, and developed RockSim models of the rockets they had constructed. Apogee data from the altimeters was compared to RockSim predictions, with good agreement in most cases. One altimeter also returned measurements of top speed and apogee time, which were compared to RockSim modeling predictions. The last rocket system studied during the Maymester was compressed air-water rockets. Students constructed simple rockets by attaching homemade fins and nose cones to one-liter or two-liter plastic bottles, and by adjusting the weight and pressure distributions to ensure stable flight. The rockets were launched using a custom-built launching mechanism and each flight was video recorded for analysis purposes. Students used an additional analysis tool, *Logger Pro* video analysis software, to determine variations in position, velocity, and acceleration of the water rocket. Although a numerical model was not applied to the water rockets, the time-dependent altitude profiles were compared to the experimental and modeling results of Gomme (Gomme, 2010), who presented a numerical model including thermodynamic analysis and other complex factors, attempting to predict the performance of pressurized water rockets.

Additional activities from the original course series are described in the 2010 Wisconsin Space Conference Proceedings (Desotell, 2010). In 2010, when “Introduction to Flight” was first offered, eight physics students enrolled in the introductory course and six of these students completed the 2010 Maymester. In 2011, eight students enrolled in the introductory course (including three physics majors, one math major, and four students with little experience in math or physics). Three physics majors completed the 2011 Maymester course. Because of the broad range of skill level in the 2011 class, two complex mathematical modeling assignments from 2010 were eliminated (modeling horizontal balloon rockets and pressure- and temperature-dependent high-altitude balloon calculations). Instead, in 2011, an oral presentation assignment was created. Examples of presentation topics chosen by the students included albatross flight, breaking the sound barrier, and hot air balloons, to name a few.

Finally, the course sequence concluded with unique, student-designed experiments that relied on helium balloons (~3-foot-diameter) to carry experimental payloads to “high” altitudes. In 2011, the projects focused on 1) relating drag coefficients to parachute shape, 2) comparing the energy dissipation of a superball on different impact surfaces, and 3) temperature and heat transfer variations with altitude. However, wind speeds of 15-20 mph and 50 mph gusts persisted for four days during the course, and the three balloon experiments were moved indoors to a gymnasium where the balloon height was limited to about 30 feet. The temperature experiment was modified for the gymnasium to detect a temperature gradient between floor and ceiling in the indoor facility. Although altitude was severely limited within the gymnasium, the balloon experiments were well designed and executed, and students learned about the need for flexibility in planning. In fact, the controlled conditions and absence of wind made the experimental procedures run more smoothly than would have been possible outdoors. Even when problems occurred, troubleshooting was relatively easy under the calm, indoor conditions of the gym. In the future, indoor facilities might be used to work through and refine experimental procedures before conducting outdoor experiments.

### **Round 3: Future Flight and Floating**

“Introduction to Flight” and “Flight and Floating” provided unique opportunities for students to engage in aerospace science. The course will likely be offered on a two or three-year rotation based on student interest and faculty course loads. The ideal enrollment for “Flight and Floating” is 6-10 students, and the course will continue to be designed for students with some experience in math and physics. In the future, the course sequence will likely be combined into one 3- or 4-credit Maymester course (17-19 days long instead of 14) without the required pre-requisite semester-based portion of the course. This combined structure will improve continuity in the subject matter and there will be less need for repetition, compared to the two-course sequence. With the combination of the two courses into one longer Maymester course, more theoretical background will be incorporated into the typical Maymester day and more time will be needed for students to develop their modeling tools during the Maymester sessions. One or more lab activities will be eliminated to meet time constraints. Several experiments will be repeated next time the course is offered, such as determining wind speed by flying a kite, rocket launch and analysis, determining drag coefficients of parachutes, and an open-ended helium balloon project.

### **Summary**

New courses on space exploration and aerospace science have been successfully integrated into the curriculum at Ripon College. “Exploring Mars” has been completed by 39 first-year students over the past two years, bringing the excitement of space exploration to the classroom through a variety of activities. Many of the students enrolled in the course did not intend to major in the sciences, but now have an increased general interest in space science as a result of this course. Student feedback has been largely positive and with on-going course revisions, “Exploring Mars” will be offered with “Plants in Space” for a third time during the fall of 2011. “Introduction to Flight” has been completed by 16 students over the past two years and 9 of these students completed the complimentary course, “Flight and Floating.” This course sequence has been extremely successful in introducing students to aerospace science and in the development of experimental design and measurement skills through experiments, modeling, field trips, and other activities. Although geared towards students with interests in math, physics, and engineering, the courses have been accessible to students with less experience in these subject areas. “Flight and Floating” is likely to be offered again in 2013 and then on a two or three-year rotation, reduced to one intense Maymester course rather than a longer two-course sequence. “Exploring Mars” and “Flight and Floating” are unique, exciting, and valuable additions to the Ripon College curriculum.

### **References**

Desotell, Sarah J. *Flight, Floating, and Mars; New Courses at Ripon College*. Proceedings of the 20th Annual Wisconsin Space Conference: Dawn of a New Age. Unpaginated. August 19-20, 2010, UW Sheboygan, Sheboygan, WI.

*Drag Coefficient of Various Shapes*, Ford Motor Co. and the National Research Council of Canada, <<http://www.nosecone.com/table.htm>, accessed May 2011>.

Gommes, Cedric J. *A more thorough analysis of water rockets: Moist adiabats, transient flows, and inertial forces in a soda bottle*. *Am. J. Phys.* **78** (3), 236-243, 2010.

**A Celebration of Life!**  
**An African American Ethnic Academy &  
BioPharmaceutical Technology Center Institute  
Science Outreach Partnership**

Barbara Bielec

BioPharmaceutical Technology Center Institute

**Abstract**

The primary goal of “*A Celebration of Life*” is to support the continued development of African American and other students’ interest in science, and to assist in providing them with the tools for success in school. A long-term goal is to increase the number of minority students who successfully complete high school science courses and who choose to pursue STEM careers. In partnership with the African American Ethnic Academy, Inc. (AAEA), a Madison non-profit organization, the BioPharmaceutical Technology Center Institute (BTC Institute) offered “*A Celebration of Life XVI: Healthy Bodies on Earth and in Space!*” during summer 2011. Two week sessions for elementary and middle school students were held weekday mornings at the BioPharmaceutical Technology Center, in Madison, Wisconsin. These programs represent a 16-year collaboration between AAEA and the BTC Institute that prioritizes offering a rich range of hands-on science activities for students.

**Introduction**

The primary goal of “*A Celebration of Life*” is to support the continued development of African American and other students’ interest in science, and to help provide them with the tools for success in school. A long-term goal continues to be increasing the number of minority students who successfully complete high school science courses, and who may eventually choose to pursue science, technology, engineering and math (STEM) careers. Extensive efforts are made to ensure participation of students from economically challenged families through the provision of scholarships and transportation.

**Program Details**

The program theme for 2011 was *Healthy Bodies on Earth and in Space!* For both sessions, content was selected to emphasize how maintaining a healthy body is related to life on earth and to space exploration. Program activities reflect the Wisconsin Model Academic Standards for Science, which follow the form and content of the National Science Education Standards. Many of the educational activities were from the NASA Summer of Innovation project ([http://www.nasa.gov/offices/education/programs/national/summer/education\\_resources/lifescience\\_grades4-6/index.html](http://www.nasa.gov/offices/education/programs/national/summer/education_resources/lifescience_grades4-6/index.html), 2011).

The BTC Institute is pleased to acknowledge the Wisconsin Space Grant Consortium Special Initiatives Program for their financial support.

Over 90% of the student participants were African American. Many received scholarships and transportation to facilitate their participation in the program. A total of 33 students: 19 girls (58%) and 14 boys (42%), participated in developmentally appropriate learning.

Table 1: Gender of Participants in *A Celebration of Life XVI: Healthy Bodies on Earth and in Space!*

<b>Program</b>	<b>Total Participants</b>	<b>Girls</b>	<b>Boys</b>
Healthy Bodies 2011 Elementary	14	7	7
Healthy Bodies 201 Middle School	19	12	7
<b>Total</b>	<b>33</b>	<b>19</b>	<b>14</b>

All specific topics for both sessions of the summer 2011 *Healthy Bodies!* program were related to NASA’s goal of keeping astronauts healthy, and many of the educational activities used were designed by NASA to include the following content:

- a healthy diet and eating good foods
- keeping your heart and lungs healthy
- bones and the prevention of bone loss
- the nervous system and reaction time
- current NASA projects related to staying healthy in space
- historic and contemporary African American science, technology, engineering and math (STEM) professionals, including those affiliated with NASA

Each session also included a field trip and concluded with student presentations of selected activities to peers, family members and other adult guests on the last day of each session. Students also shared their posters of African American STEM Professionals. The program was covered by *The Wisconsin State Journal* (Pamela Cotant, August 1, 2011), and *The Madison Times* (David Dahmer, July 6, 2011).

### **Results**

Pretests and post-tests are administered as part of each program as one indicator of students’ learning. Overall, both elementary and middle school students showed an increased knowledge about health and African American STEM professionals. For example, on the pretest only 2/10 of the elementary students tested could name a single African American Scientist, Engineer or Mathematician, and answer “What do they do?” On the post-test all 11 elementary students tested could do so, and 8 of the 11 students could name 3 or more AA STEM professionals and correctly describe their contributions.

Scientific content knowledge can be measured by the pre- and post-tests, providing information regarding one aspect of program assessment. Another key indication of success is the number of

students who had participated in previous AAEA/BTC Institute programs, or who had family members who were previous participants. Of the 14 elementary students in 2011, 2 had attended previous AAEA/BTC Institute summer sessions, 2 had family members who had previously participated in the program, and 2 were in their first year of eligibility for the program (entering 3rd grade in Fall 2011). In addition, based on the successful reputation of the program, a new group of 4 students from the Boys and Girls Club of Dane County participated in the elementary program.

In 2011, 8 of the 19 middle school students had attended previous AAEA/BTC Institute summer sessions, 3 of the new middle school students had family members who had previously participated in the programs, and 4 of the new students were referred by the Boys and Girls Club of Dane County. Of the 2011 middle school students, 6 of the 19 (32%) had participated in the summer program at least three times. When students return for the third, fourth, fifth or sixth time, it is a strong indication of their interest in science programming. In addition, three of the young women who have participated for either five or six years, and are now headed to high school, have expressed interest in coming back next year to be assistants with the elementary program.

Table 2: Participants in *A Celebration of Life XVI: Healthy Bodies on Earth and in Space!*

<b>Program</b>	<b>Total Participants</b>	<b>Participants in Previous Programs</b>	<b>Have Family Members who have participated previously</b>	<b>First Year of Eligibility (Grade 3)</b>
Healthy Bodies 2011 Elementary	14	2	2	2
Healthy Bodies 2011 Middle School	19	8	3	NA
<b>Total</b>	<b>33</b>	<b>10</b>	<b>5</b>	<b>2</b>

### **Conclusion**

In a 2009 National Science Foundation (NSF) report, entitled *Women, Minorities, and Persons with Disabilities in Science and Engineering*, it was found that: “Underrepresented minorities (blacks, Hispanics, and American Indians/Alaska Natives) increased their share of S & E [Science and Engineering] graduate students somewhat from 1996 to 2006 (from 9% to 11%), but their overall participation remained low. Only in psychology and the social sciences did underrepresented minorities’ participation exceed 10% in either year. Participation rates in other fields ranged from a low of 5.8% in earth, atmospheric & ocean sciences to a high of 9.5% in the biological sciences. These graduate study participation rates are well below the 17% share of S & E baccalaureate degrees earned by underrepresented minorities in 2006.” Supporting

African American educational opportunities in science is essential to helping increase the number of African American students who will ultimately go into baccalaureate and graduate programs in science. (NSF, *Women, Minorities, and Persons with Disabilities in Science and Engineering: 2009*)

In the same report, Table 3-1 S&E [Science and Engineering] graduate students, by field, sex, and race/ethnicity: 2008; showed that there was a total of 529,275 graduate S&E students in the U.S. in 2008, only 28,680 (5.4%) of whom were listed as black. (NSF, *Women, Minorities, and Persons with Disabilities in Science and Engineering: 2009*)

In one study examining the influence of race and gender role models on young adolescents, the author found that “the availability of race- and gender-matched role models showed a strong relationship to the developing identities of young adolescents. The availability of a race- and gender-matched role model was significantly and consistently predictive of a greater investment in achievement concerns on the part of these young adolescents.” (Sabrina Zirkel, 2002). The AAEA/BTC Institute programs will continue to focus on African American STEM professional role models to help inspire students in these areas.

The exploration opportunities provided by "A Celebration of Life" enrich and enhance students' scientific knowledge and associated skills. Generating interest in science is crucial to creating a diverse work force of problem solvers, scientists, inventors and engineers for the future. It is also essential for students to see themselves in those roles. Learning about historic and contemporary African American STEM professionals ensures that they do so.

Finally, this approach is in alignment with the goals and objectives of the National Space Grant College and Fellowship Program:

- “**Mission Statement #1:** Using our national network of scientists, engineers, and educators, enable the development of a diverse workforce of future scientists, engineers, technology professionals, and educators. **Goal #3:** Model diversity in Space Grant leadership, programs, and activities.” AAEA/BTC Institute students learned about historic and contemporary African American Science, Technology, Engineering & Math (STEM) Professionals, featuring many who work for NASA.
- “**Mission Statement #3:** Cultivate a nationwide network of partners from universities, industry, museums, science centers, state and local agencies, to pursue state and national aerospace research, education, and economic development goals. **Goal #5:** Establish Space Grant as a viable state/national resource and catalyst for aerospace research, education, and economic development.” The BTC Institute has continued to collaborate with AAEA to encourage interest in aerospace education and careers in an underrepresented group.
- **Mission Statement #6:** Serve the general public by contributing to scientific literacy. **Goal #11:** Develop Earth, Air, and Space programs to enhance public scientific literacy and to complement community needs. **Goal #12:** Engage in all facets of the community in the excitement of scientific discovery using Science, Math, Engineering and Technology; (Edutainment, Process of Discovery).” (National Space Grant College and Fellowship Program Strategic Plan 2002-2006 Executive Summary) The AAEA/BTC Institute science programs were founded, in part, by the great need for quality scientific

programming that can engage minority students and strengthen their learning in STEM content. They include sharing this information with family members and others in the community.

## References

NASA Summer of Innovation, *Life Science Units and Lessons for Grades 4-6, 2011*. Available from [http://www.nasa.gov/offices/education/programs/national/summer/education\\_resources/lifescience\\_grades4-6/index.html](http://www.nasa.gov/offices/education/programs/national/summer/education_resources/lifescience_grades4-6/index.html)

Wisconsin State Journal, *School Spotlight: Summer program focuses on health, here and in space*. Cotant, Pamela; August 1, 2011.

The Madison Times, *Young scientists show off their nutritional knowledge*. Dahmer, David; July 6, 2011.

National Science Foundation, Division of Science Resources Statistics, *Women, Minorities, and Persons with Disabilities in Science and Engineering: 2009*, NSF 09-305 (Arlington, VA; Jan 2009). Available from <http://www.nsf.gov/statistics/wmpd>

Teachers College Record Volume 104, Number 2, *Is There A Place for Me? Role Models and Academic Identity among White Students and Students of Color*, Sabrina Zirkel, 2002, Teachers College, Columbia University.

National Space Grant College and Fellowship Program Strategic Plan 2002-2006 Executive Summary. Available from <http://www.uwgb.edu/wsgc/stratplan.aspx>

# Biotechnology Teacher Training

Barbara Bielec

BioPharmaceutical Technology Center Institute

## Abstract

An integral part of enhancing science education is training teachers in current content and techniques, and biotechnology is one of the technologies that will be needed to maintain living systems in space. The BioPharmaceutical Technology Center Institute (BTC Institute) offered two graduate education courses in biotechnology for teachers during summer 2011. Each weeklong course was held at the BioPharmaceutical Technology Center. *Biotechnology: The Basics* and *Biotechnology: Beyond the Basics* were designed and presented to provide teachers with training, background and curriculum materials (including information about NASA and biotechnology), so that they may implement hands-on biotechnology in their classrooms. Teachers of a wide variety of subjects with varied levels of experience were active participants in lab-based training.

## Introduction

*Biotechnology: The Basics* and *Biotechnology: Beyond the Basics* are week long summer courses that were offered by the Biotechnology Technology Center Institute (BTC Institute) in summer 2011. The primary goal of *Biotechnology: The Basics* and *Biotechnology: Beyond the Basics*, is to provide middle school and high school teachers with the training essential to implementation of a laboratory-based biotechnology curriculum. This goal served as the guide in designing and implementing each activity, as well as in structuring each course. Both courses were offered for graduate education credits through Viterbo University and Edgewood College. All three course instructors are experienced teachers of biotechnology at the secondary level.

The NASA Directorate for Space Operations is to: “Extend the duration and boundaries of human space flight to create new opportunities for exploration and discovery.”[1] NASA wisely recognizes the need for training throughout many scientific disciplines, and as plans are made for humans to travel and someday live in space, biotechnology joins other technologies to support these efforts. Often students and teachers in the life sciences do not fully realize how biotechnology relates to this directorate of NASA. Another goal of this project is to highlight how biotechnology is and will be used in space exploration. Biotechnology, along with other Science, Technology, Engineering and Math training is needed to help the secondary teachers who directly influence the Science, Technology, Engineering and Math (STEM) professionals of tomorrow.

The BTC Institute is pleased to acknowledge the Wisconsin Space Grant Consortium (Aerospace Outreach Program) for their financial support of 15 teacher scholarships for these courses in 2011. In addition, the 2011 courses received support for 10 teacher scholarships from the Wolbachia Project, a Howard Hughes Medical Institute Precollege Science Education Initiative sponsored by The Marine Biological Laboratory.

## Program Details

Both *Biotechnology: The Basics* and *Biotechnology: Beyond the Basics* were offered in summer 2011. Representing rural, urban, and suburban school districts, the attendees were teachers of a variety of subjects, including: middle school science, biology, biotechnology, genetics, agriculture, environmental science, anatomy and physiology, business, forensics and science outreach. Currently there is a strong encouragement from the state of Wisconsin for agricultural educators to receive more science training. They are teaching many of the Biotechnology courses throughout the state, and about one-third of our attendees were agriculture teachers.

Most participants (18/26) are high school teachers in Wisconsin, but one is a high school teacher in Illinois, one is a high school teacher in Indiana, four are middle school teachers (including one who teaches in Illinois), and two are science outreach educators (one from Wisconsin and one from South Korea). *Biotechnology: The Basics* 2011 had 18 attendees (12 women & 6 men) and *Biotechnology: Beyond the Basics* 2011 had 8 attendees (all women). As evidence of how teachers value these courses, 4 of the teachers took one of the courses previously in 2010, and several 2011 *Biotechnology: The Basics* attendees made inquiries about registering for *Biotechnology: Beyond the Basics* in 2012. Class participants included teachers who had no previous training in biotechnology, as well as very experienced secondary teachers looking to update their knowledge of scientific content and techniques. Some of the teachers currently teach an independent Biotechnology course; others incorporate biotechnology curricula within other life science or agriculture classes. Several teachers were looking for information to help them design and implement a Biotechnology course for the first time.

Table 1: Participants in *Biotechnology: The Basics* and *Biotechnology: Beyond the Basics* Summer 2011

<b>Teacher Course</b>	<b>Total Participants</b>	<b>High School Science Teachers</b>	<b>Agriculture Teachers</b>	<b>Middle School Science Teachers</b>	<b>Science Outreach Educator</b>
Biotechnology: The Basics 2011	18	6	7	4	1
Biotechnology: Beyond The Basics 2011	8	6	1	0	1

The healthy number of attendees for the 2011 courses was due to funding provided by a Wisconsin Space Grant Consortium-Aerospace Outreach Program grant which covered course fees for 15 teachers, and a Wolbachia Project grant which covered course fees for 10 teachers. Professional development funding is increasingly difficult for teachers to obtain, and the BTC Institute and the teachers who took the courses are very grateful for the scholarships.

Barbara Bielec (K-12 Program Director, BTC Institute, Peter Kritsch (Teacher, Oregon High School), and Kathryn Eilert (Teacher, Middleton-Cross Plains High School) worked together to plan and implement the courses. All three are experienced teachers of biotechnology at the secondary level. The BTC Institute course fee was \$500 in 2011. Both courses were offered for graduate education credits through Viterbo University (3 graduate credits for \$270) and Edgewood College (1-3 graduate credits for \$150/credit).

Topics and laboratory activities for *Biotechnology: The Basics* included:

- DNA Extraction
- Agarose Gel Electrophoresis
- Restriction Enzyme Digestion
- Polymerase Chain Reaction
- Bacterial Transformation
- Bioethics – use of Case Studies
- Genetic Counseling
- Developing Integrated Lab Activities using the Wolbachia Project
- Biotechnology and NASA

Topics and laboratory activities for *Biotechnology: Beyond the Basics* included:

- BioFuels and the Great Lakes Bioenergy Research Center
- Microarrays
- Bioethics - use of Case Studies
- Stem Cell Research - current issues, how to address in the classroom
- Genetic Identity Testing using Short Tandem Repeats (STRs)
- Protein Purification and Detection
- Immunology- Antibody isolation and detection
- Epigenetics
- Developing Integrated Lab Activities using the Wolbachia Project
- Troubleshooting Experiments
- Biotechnology and NASA

Implementation was consistently emphasized. How would teachers apply what they learned in their own classrooms? Resources included:

- A comprehensive course binder for each teacher
- Laboratory protocols, classroom activities and power point presentations on a flash drive for each teacher
- Special discounts and offers from Fisher Science Education, Promega, and Fotodyne, Inc.
- Resources from the Wolbachia Project, the Great Lakes Bioenergy Research Center, WiCell, and the Fotodyne/BTC Institute Equipment Loan Program
- Daily discussion and review of course topics
- Discussion of funding sources and tips for successful grant writing

Each day teachers wrote a reflection detailing how they would integrate material into their curriculum and the challenges that they might face, including the resources they would need.

These reflections were discussed the next day with the entire group. Additionally, as a final project, each teacher had to design and present a detailed and personalized curricular unit (lesson plan) for teaching the content learned.

## Results

Course evaluations were extremely positive. For *Biotechnology: the Basics* teachers wrote:

- “The course was well organized and much appreciated....This has to be one of the BEST hands on courses that I have taken in my 24 years of teaching- I have materials to take back and implement immediately.”
- “This was, by far, the best training/class I have taken since exiting college. I am so excited to finally do this in class. The two instructors...are absolutely top shelf teachers. Please do everything to keep them.”
- “I can’t tell you how wonderful this class was! It was very helpful & eye opening. I had biotech all around me & didn’t even know it!! Great class, great teachers, great information – best graduate class.”
- “At 50 years old, I went from being extremely uneducated to now possessing some level of comfort in genes, DNA, etc.”
- “I was not sure about taking this course because I thought I would not understand it. I realized on Monday already I was wrong. This was a great week and I’m excited about Biotechnology.”
- “I really like the set-up of this course. It is just the right amount of lecture and lab.”
- “I have already told other teachers to take it [the class] and am planning to block out a week for next year’s class.”

For *Biotechnology: Beyond the Basics*, teachers wrote:

- “Wonderful week! I learned so so [sic] much!!! I so appreciate all of the support”.
- “The presenters were great! Very knowledgeable & enthusiastic. I am amazed by all that we did.”
- “I appreciated the variety of topics covered and the flexibility of the instructors/presenters.”
- Excellent Group/Instructors/Facilities & Work.”

Course evaluations also offered suggestions to improve the courses:

- “Have a list of materials + catalogue #s of costs for materials for each section.”
- “Take time to absorb/reflect more often.”
- “I’m still searching for an activity to introduce my students to BLASTs...”
- “I would formally have a Wiki or twitter or web page for classes & a place for us to continue these discussions as we implement and try these things in our classroom.” (Note: one of the Basics course participants did start a Wiki to continue biotechnology exploration among the teachers).
- “Write up [a list] of career, education, money, etc.”
- “I would explain the real life references first, then go to trying to figure out and the inquiry...a list of vocab to brush up on before the class.”
- “Recommended readings ahead of time.”
- “I would add lessons that could be modified for the middle school level.”

- “Give a better preview/background information about the Wolbachia Project and its effects on humans & insects.”
- “Overall I would not change anything! A few of the labs that we did would have ‘easier’ to understand, if we knew the process that was going to happen before we went into the lab.”

For both courses, teacher participants were recruited through an electronic mailing to the BTC Institute’s teacher list; posting in the Wisconsin Society of Science Teachers (WSST) newsletter (print and online); electronic posting and email from the Wisconsin Educators Association Council (WEAC), the Wisconsin Dept. of Public Instruction (DPI), and the Illinois Science Teachers Association (ISTA); posting on the Wisconsin Science Network (WSN) and the Education Communication Board (ECB); flyers distributed at WSST and the National Association of Biology Teachers (NABT) ) conferences; email from the Wisconsin Association of Agriculture Educators (WAAE) electronic network; direct contact through the BTC Institute’s Biotechnology Field Trip Program and at the Wisconsin STEM Summit; direct recommendation from UW-River Falls Agriculture Education Professor Timothy Buttles; and course listings in the Viterbo University and Edgewood College summer catalogs.

According to data collected on the course evaluations, attendees found out about the course in a variety of ways that are summarized in the following table. The results speak to the strength of the formal and informal networks of Wisconsin agriculture teachers which are reflected in 38% of the responses (9/24), as well as to direct contact and experience with other BTC Institute programs – also 38% (9/24) of the responses.

Table 2: How Participants in *Biotechnology: The Basics* and *Biotechnology: Beyond the Basics* Summer 2011 Learned About BTC Institute Biotechnology Courses.

<b>How Participants Learned About BTC Institute Biotechnology Courses</b>	<b>Number of Responses (in order)</b>
Other Agriculture teachers and the WAAE network	5
BTC Institute direct contact (field trip)	5
BTC Institute email contact	3
BTC Institute direct contact at a conference or meeting	3
Ag. Education DPI List Serv	2
Dr. Tim Buttles UW-River Falls Ag. Ed. Professor	2
From a school district science coordinator/dept. chair	2
From another teacher	1
WSST website	1
Web page	1
Took previous BTC Institute course	1
<b>Total Responses</b>	<b>24</b>

## **Conclusion**

The enthusiasm demonstrated by our attendees is always inspiring. It consistently and clearly demonstrates the need for high quality graduate education courses that have immediate relevance to the classroom. As stated in a National Science Teachers Association (NSTA) Position Statement: "To be prepared for the 21st century it is critical that all students have sufficient knowledge of and skills in science. Studies suggest that high-quality teaching can make a significant difference in student learning...a high-quality science teacher workforce requires meaningful, ongoing professional development." [2] We plan to offer both courses in summer 2012, and are seeking grant opportunities that will enable us to fund teacher scholarships. As always, we will utilize previous course evaluations to improve our courses.

In 2011 one of the requirements to receive a Wisconsin Space Grant Consortium scholarship was to: "Submit a 2-3 page summary report to the BTC Institute, at the end of the 2011 or 2012 semester in which they implement discussion of NASA utilization of Biotechnology. This report should include: description of how a discussion of NASA utilization of Biotechnology was implemented, description and demographics of the course(s) in which the discussion took place, and student feedback on the discussion". We are looking forward to receiving these reports and learning how teachers use NASA research as a way to demonstrate the relevance of biotechnology content and techniques. We will incorporate the information we receive from teachers about their inclusion of NASA & Biotechnology content in future courses as well.

The support provided by the Wisconsin Space Grant Consortium to design and implement these courses is greatly appreciated. The donations of instructor time and materials from Fotodyne, WiCell, Promega, Fisher Science Education, Great Lakes Bioenergy Research, and the Wolbachia Project are also key to our success. These partnerships, along with the options to receive graduate education credits through Viterbo University and Edgewood College, ensure the continuation of these essential opportunities for professional development.

## **References**

1. NASA Directorate for Space Operations, <http://education.nasa.gov/about/nasaent/>, 2010
2. NSTA Position Statement, Professional Development in Science Education, <http://www.nsta.org/about/positions/profdev.aspx>, adopted May, 2006

## **Spaceflight Academy for CESA District #5**

Bradley J. Staats, President

Spaceflight Fundamentals, LLC  
New London, Wisconsin

### **Synopsis**

Spaceflight Academy for CESA District #5 was a teacher workshop<sup>1</sup> that focused on the history, math, science, and technology of spaceflight. This workshop offered a unique approach to teaching by incorporating “real world” applications into the classroom.

### **Goals and Project Value**

Spaceflight Academy for CESA District #5 was a one-day workshop that focused on STEM (Science, Technology, Engineering, and Math) related topics for spaceflight. The course offered a unique approach to teaching and answering the age old question “Why do I have to learn this?” by elegantly incorporating “real world” applications into the classroom. Instructors experienced a unique approach to teaching math, science, and technology standards by tackling real world issues in inspiring classroom experiences. Spaceflight Academy for CESA District #5 utilized award-winning approaches to advance an educator’s knowledge base by employing a fun, hands-on approach to learning.

For this year’s workshop, instructors in the Cooperative Educational Service Agency #5 district were the target audience. The workshop was setup to provide 20 instructors with a full day of instruction and over \$100 per person in materials and resources to take back to their respective classrooms. A lunch was also provided to all participants. After advertising extensively for this 3-12 workshop, a total of 21 instructors pre-registered for it. Four percent were elementary instructors; forty eight percent were middle level instructors while the remaining forty eight percent were high school instructors.

Due to the broad range of teaching levels present for this workshop, the workshop was broken into three basic segment/components - elementary, middle, and high school level topics. The workshop was co-facilitated. The AM sessions were devoted to elementary and middle level discussions while the PM session was devoted to high school topics. During these sessions the following topics/activities were covered: perception / paradigm shifts; center of gravity; Bernoulli implications; Newton’s universal law of gravitation; various orbital shapes (conic sections); circular orbits; geosynchronous orbits; elliptical orbits; spaceflight mathematics; history of human space exploration; and technologies of space exploration.

---

<sup>1</sup> The main financial support for this workshop was provided by the Wisconsin Space Grant Consortium. Additional support was provided by the following sponsors: Spaceflight Fundamentals, LLC; Science Kit & Boreal Labs; and the Wisconsin Dells School District.

## Evaluation Results

At the conclusion of this workshop, the following questions were asked on an evaluation form. The results, of this evaluation, are based on a 100-point scoring system with 100% = strongly agreeing with the provided statement, 80% = agreeing with the statement, and so on.

1. My exposure to this project has increased my knowledge/understanding in space, aerospace, space-related science, design, and technology. [Score = **88%**.]
2. Student exposure to this project could increase an interest in space, aerospace, space-related science, design, and technology. [Score = **91%**.]
3. The project has self-sustaining/replicable qualities due to the fact that the participants are trained and supplied with the basic materials to go out and duplicate in their classrooms the work that was incorporated in this workshop. [Score = **97%**.]
4. The project meets the goal of Teacher Training which is defined as successfully educating, training, and exciting teachers about the math, science, technology, and history pertaining to spaceflight. [Score = **92%**.]
5. The instructors were knowledgeable about the subject matter that was being taught. [Score = **97%**.]
6. The workshop was well organized. [Score = **97%**.]
7. The instructors' presentation style was well suited for the audience in attendance. [Score = **94%**.]
8. I am pleased with the information and materials that I received as part of this workshop. [Score = **96%**.]
9. What is the total number of students that you teach per day? [\*Based on the number of instructors present and their teaching assignments, a total of **1415 students** will be positively impacted by this workshop.]
10. How do you plan to implement this material into your classroom curriculum? [\*The following are highlights of responses to this question]

“As part of my space unit for grade 8 science and to share it with elementary teachers.”

“I teach a physical science class in which I will be incorporating most of these activities.”

“I have a project where these activities can be incorporated.”

“I plan to use a lot of the activities for building inquiry into my class.”

“I'm definitely going to use the constellation chart and the mind challenges.”

“I will use the celestial cylinder – Way better than a planisphere or other versions.”

“Add to our current unit of study – Gives us more hands-on activities.”

“Expand grade 6 space / astronomy unit. Fun ways to explore Bernoulli.”

“Use the software for our astronomy unit – Show the students different scenarios.”

“Complete the rocket project with our astronomy and physical science units.”

11. Please express any additional comments regarding the workshop and/or instructors.  
[\*The following are highlights of responses to this question]

“Very knowledgeable instructors.”

“This was a fantastic workshop. I have never had so much fun and had so many classroom applications!”

“Great workshop with wonderful ideas.”

“Well done and great hands-on activities for students to get them interested in space topics.”

“Super job – A rare workshop that allowed me to take many things with me to use in the classroom.”

“Well done! Great sense of humor! Thank you for your time and expertise. Nice freebies!”

“Loved the door prizes!”

“Very knowledgeable instructors – Enjoyable workshop.”

“Exceptionally well done!”

“Thanks, I loved it!”

“Loved this opportunity – So many wonderful ideas to use in many aspects of teaching. Thank you!”

“I found this course particularly useful because it included quick, very easy activities that I can readily incorporate into my curriculum.”

### **Evaluation Analysis**

Based upon the positive evaluations and comments of these grades 3-12 teachers, there should be a definite increase for interest in space, aerospace, space-related science, design, technology, and its potential benefits for their students in CESA District #5. Invariably, based on our evaluations, this project should allow secondary (pre-college) students the opportunity to increase their interest, recruitment, experience and training in the pursuit of space or aerospace related science, design, or technology in CESA District #5.

The project has self-sustaining/replicable qualities due to the fact that the instructors that were trained were supplied the basic materials to go out and duplicate the work that we incorporated in our workshop. The goal is for teachers to go back to their classroom and replicate this work to their students – The “multiplier effect” is then engaged. Through this effect, each teacher is able to provide their students with exposure to this exciting curricular approach. For the 2011-2012 school year, 1415 students will have the opportunity to be exposed to this worthwhile curriculum. Based upon the amount of grant money received from the Wisconsin Space Grant Consortium (WSGC) and the number of students each registered instructor has, it only cost WSGC an average of \$1.51 per student to run this workshop – This is an amazing investment!

The goal for this program is to have it ultimately offered throughout the state. Based upon the workshop’s evaluations, the project certainly met this year’s specific goal of Teacher Training. The whole purpose of the project is to educate, train, and excite teachers about the math, science, technology, and history pertaining to spaceflight – This workshop definitely and successfully accomplished this feat.

**Alignment with NASA Directorate, Center Goals, and/or Educational Standards Science Mission Directorate.** The scientific investigation of the Earth, Moon, Mars and beyond with emphasis on understanding the history of the solar system, searching for evidence of habitats for life on Mars, and preparing for future human exploration. This workshop definitely exposes and prepares the next generation of scientists to aerospace related fields. As we prepare for future human exploration, we will need many new scientists and engineers to accomplish this endeavor. Our project's goal was to train teachers who in turn can train these future scientists and engineers. Our proposal, therefore, provided assistance in this area.

**Space Operations Mission Directorate.** The three themes – The International Space Station, Space Shuttle Program and Flight Support provide critical enabling capabilities that make possible the science, research and exploration achievements for the rest of NASA. This workshop provided as part of its focus the ISS, Space Shuttle program and required Flight Support. This focus allowed the participants to better understand how they work together and provided enabling capabilities as a whole.

**Educational Standards.** The National Research Council's (NRC) Science Education Standards were addressed throughout the workshop. Special emphasis was put on the following Standards areas: The Teaching Standards: Guiding and Facilitating Learning & Building Learning Communities; The Professional Development Standards: Learning Science Content, Learning To Teach Science, & Learning To Learn; and The Content Standards: Scientific Inquiry, Technological Design, & Science and Technology.

**Participants.** The workshop was limited to 20 science and/or math instructors. It was made available on a first come, first serve basis. Once the 20 slots were filled, two additional registrations would also be accepted. Spaceflight Fundamentals, LLC fully complies with the Americans with Disabilities Act of 1990 (ADA), Section 504 of the Rehabilitation Act of 1973, and its amendments, all of which prohibit discrimination on the basis of disability in the admission, access to, or participation in programs or activities.

**Location of Project.** The workshop was advertised to science/math (Grades 3-12) teachers in the CESA #5 district (Wisconsin Dells area). The workshop was located at the Wisconsin Dells High School, 33 520 Race Street, Wisconsin Dells, WI. We coordinated the workshop advertisement with school districts in the Wisconsin Dells / CESA #5 area. The target audience was science / math classroom instructors (Grades 3 –12). Based upon future funding, follow-up (Part 2) workshops and additional initial (Part 1) workshops could be set around the state.

**Work Plan.** Our work plan involved an eight-hour workshop. In those eight hours, we focused on the concept of spaceflight via a variety of hands-on activities (labs, simulations, computations, etc.) and discussions. High emphasis was placed on cooperative work and constructivistic approaches being fueled through facilitator lead Socratic dialogue. The goal was to allow the instructors to have the chance to infuse their new knowledge into their respective curriculums with the hopes that a follow-up workshop can be funded in order to further our focus.

**General Information**

Spaceflight Fundamentals, LLC is a small but dedicated company to the advancement of aerospace in the classroom. For the past ten years, our company has been authoring and publishing educational materials on aerospace education in the state of Wisconsin. Also, in those ten years, we have had the opportunity to organize and instruct several teacher graduate course workshops. The workshops have always been well received and have made definite positive impacts in our state's classrooms. With that said, our hope is that workshops like these will allow further opportunities to educate and motivate the current and next generation of instructors/students on aerospace education in the state of Wisconsin. We look forward to creating future proposals / activities for teacher aerospace workshops and further broadening our ability to work with other state organizations with the same goals. We feel that the state of Wisconsin has benefited from our activities, and that we hope to continue being a positive force in the WSGC's community outreach efforts while helping to nurture and grow the aerospace industry in our state.

## Promoting the Computational Science Initiative (ProCSI)

Dan Melanz

University of Wisconsin – Madison

PROMoting the Computational Science Initiative (ProCSI) Summer Program is a six day pre-college engineering program for high school students who come from ethnic groups that are traditionally underrepresented in engineering. The ProCSI program is designed to attract outstanding high school students to the College of Engineering at UW Madison. Students become part of a pre-collegiate community that will explore the excitement and rigors of engineering and collegiate life through participation in hands-on labs, industry and undergraduate seminars, graduate research presentations, college preparation workshop, lab tours, undergraduate admissions presentations, and social activities. Students will go through a lab sequence focused on Mechanical Engineering, Applied Mathematics, Computer Science, Computational Science, and Engineering Applications, respectively.

### Sponsoring Organization Information

The sponsoring organization is the Simulation Based Engineering Laboratory (SBEL). Broadly speaking, the goals of this lab are (1) to investigate and develop computational tools and methods that help one understand how systems change in time, and (2) to use these tools and methods to gain insights into the dynamics of processes. Most of our effort is dedicated to understanding through simulation the time evolution of mechanical systems, a topic sometimes called **multibody dynamics simulation**. The primary focus of the lab is the simulation of classical multibody dynamics at macro and meso-scales. The idea here is to produce numerical algorithms that are capable of robustly and efficiently predicting the time evolution of a collection of mutually interacting elements, which can be rigid or flexible. The primary motivation underlying our research efforts is the simulation-based engineering concept, whose entire goal is that of replacing, whenever possible, hardware prototyping with virtual prototyping in design engineering. In a wider context, as members of the **Computational Science** community, we promote the idea of scientific discovery through advanced computing.

An important part of our mission in the Simulation Based Engineering Lab is to let other people learn about the potential of simulation, in particular, and Computational Science, in general. We believe strongly that there is a lot of merit in exposing to this emerging discipline groups of people that in their day-to-day life are very unlikely to get the chance to understand and see how computers are used in Science and Engineering. Belonging to a public education institution, we do this not only because we ought to, but because we truly believe that a career in Computational Science is an exciting and rewarding path to take at this time.



Figure 1. ProCSI 2008 recruiting, Milwaukee: African-American high school students of the Dream-Chasing non-profit organization, lab graduate students Yakira Braden and Justin Madsen, and PI Dan Negrut.

PROMoting the Computational Science Initiative (ProCSI) Summer Program is a six day pre-college engineering program for high school students who come from ethnic groups that are traditionally underrepresented in engineering. The ProCSI program is organized by the Simulation Based Engineering Lab in the Department of Mechanical Engineering with financial support from the National Science Foundation, and it is designed to attract outstanding high school students to the College of Engineering at UW Madison. Students become part of a pre-collegiate community that will explore the excitement and rigors of engineering and collegiate life through participation in hands-on labs, industry and undergraduate seminars, graduate research presentations, college preparation workshop, lab tours, undergraduate admissions presentations, and social activities. Students will go through a lab sequence focused on Mechanical Engineering, Applied Mathematics, Computer Science, Computational Science, and Engineering Applications, respectively.

### **Previous Funding**

Partial ProCSI funding for 2008 was secured through NSF project CMMI-0700191, and for 2009 to 2013 through NSF project CMMI-0840442. Additional funding was provided by an industry partner (BAE Systems).

### **Participants Anticipated**

The ProCSI Engineering Summer Camp has been host to several minority high-school students of African American, Hispanic, and Hmong descent from Wisconsin and Illinois. During ProCSI 2008, 13 African American High School Students from Milwaukee, WI participated. Of these 13 students, 5 were female. During ProCSI 2009, 9 students from varying ethnic backgrounds participated from both Wisconsin and Illinois. Of these 9 students, 2 were female. During ProCSI 2010, 14 students (4 female), also from varying ethnic backgrounds participated. It is expected that ProCSI 2011 will be composed of participants from similar underrepresented minority backgrounds. Attendance will be increased to 16 students total, with approximately a third of the group being female. ProCSI targets high school students finishing the 9<sup>th</sup> or 10<sup>th</sup> grade. This decision was reached after consultation with the Diversity Affairs Office (DOA) of the College of Engineering. Students are encouraged to apply if they are going into their junior or senior year of high school with selection being based on grade point average, transcripts, and recommendations.

## Metrics

In terms of *impact assessment*, the web-based Student Assessment of Learning Gains Instrument (SALGI), developed by the National Institute for Science Education (NISE) College Level One Team under NSF support at the University of Wisconsin, will be used for outcome control and implementation of a continuous improvement process, which also draws on exit interviews with the participants. A list of ProCSI alumni is available at <http://sbel.wisc.edu/Outreach/ProCSI/ProCSIalumni.htm>. All 2008 ProCSI alumni went on to college in Fall 2009 at University of Wisconsin-Madison, University of Wisconsin-Milwaukee, DePaul, Southern Illinois University-Edwardsville, and Howard University.



Figure 2. Students from ProCSI 2010.

## Ability to sustain and replicate

There are several requirements to fulfill in order to replicate this program. First of all, it is crucial to recruit students that want to learn about Computational Science. It is important that the students have a place to sleep during their stay. Transportation, food, and classrooms are also necessities to this program. Arguably the most important piece to ProCSI is providing the students with useful information about mechanical engineering, mathematics, and computer science and ensuring that the lecturers are knowledgeable about the topic that they are presenting. Based on the successful implementation of ProCSI 2008 and 2009, there is no doubt that this program can be sustained.

Assisting in the effort to sustain ProCSI is a similar program offered by the UW-Madison campus, called the Engineering Summer Program (ESP). ESP is a six-week residential program designed to attract future engineers to the University of Wisconsin-Madison College of Engineering. It has, on average, 20 participants each summer, 92 percent of whom represent underrepresented ethnic minority backgrounds. In recent years, ESP participants have made up 23 percent of all targeted underrepresented students graduating from UW-Madison with engineering degrees. The vision is for ProCSI to serve as a preamble to ESP for students entering the 11<sup>th</sup> and 12<sup>th</sup> grades. ProCSI and ESP thus cover the entire high school student population with interest in Math and Science; i.e., the likely candidates for future careers in Engineering.

## Budget

In conjunction with increasing the participation in the ProCSI programs by adding six additional high-school students, the PI requests \$3,000 for each of the three years of the project. This will cover the following expenses:

- ProCSI Housing; \$45/night for each of the six students in double occupancy rooms, for a total of \$1,350.
- ProCSI Meals; breakfast \$8, lunch \$9, dinner \$13 for six students: \$900.
- ProCSI Transportation; to/from Milwaukee, and local transportation.

## Project Description/Overview

The ProCSI program (from **P**romoting the **C**omputational **S**cience **I**nitiative, pronounced like “proxy”), introduces students to Computational Science through the use of examples drawing on physics-based models for computer games and virtual prototyping in ADAMS. The 2008 and 2009 ProCSI schedules are available along with more than 200 pictures at <http://sbel.wisc.edu/>. The participating minority high-school students (African American, Hispanics, and Hmong from Wisconsin and Illinois) are recruited through seminars given by lab members in Milwaukee and with assistance from the Diversity Affairs Office (DOA) of the College of Engineering (letter included from DAO Assistant Dean). The instructional segment of the program runs for approximately five hours daily with modules covering, in this order, Mechanical Engineering,

### DISCUSSION

### HANDS-ON

Day 1: Mechanical Engineering
<ul style="list-style-type: none"> <li>Experiments &amp; Measurements</li> <li>Newton's 2<sup>nd</sup> law</li> </ul>
<ul style="list-style-type: none"> <li>Experiments:               <ul style="list-style-type: none"> <li>free fall</li> <li>motion on incline</li> <li>mass-spring-damper systems</li> </ul> </li> </ul>



Day 2: Applied Mathematics
<ul style="list-style-type: none"> <li>Equations governing free fall and motion on incline</li> <li>Rate of change and Euler formula for handling equations with rate of change</li> </ul>
<ul style="list-style-type: none"> <li>ADAMS simulation:               <ul style="list-style-type: none"> <li>free fall</li> <li>motion on incline</li> <li>mass-spring-damper system</li> </ul> </li> </ul>



Day 3: Computer Science
<ul style="list-style-type: none"> <li>Computer Architecture</li> <li>Fast computers: Flop rates</li> <li>Computer Graphics: Pov-RAY</li> </ul>
<ul style="list-style-type: none"> <li>Pov-RAY generated animation of granular flow</li> </ul>



Day 4: Computational Science
<ul style="list-style-type: none"> <li>What/Why/How?</li> <li>Physics Based Gaming</li> <li>Computer Aided Engineering</li> </ul>
<ul style="list-style-type: none"> <li>Computer Game: Car Racing</li> </ul>



Day 5: Applications
<ul style="list-style-type: none"> <li>Feedback and evaluation</li> </ul>
<ul style="list-style-type: none"> <li>Computer Games: Race Day</li> <li>ADAMS HMMWV model, passenger car, tracked vehicle</li> </ul>

Applied Mathematics, Computer Science, CAD, and video gaming. The instructional segment is complemented with several other activities: university lab visits, round table discussion with current minority engineering students, meeting with Industry representatives, meeting with University of Wisconsin staff to discuss admissions and college preparation, three-on-three basketball tournaments, and live outdoor music at the Student Memorial Union.

In an effort to increase the interest and recruitment of the next generation of experts in the pursuit of space- or aerospace-related science, the ProCSI program incorporated a space module in 2010. The space module focused on simulations in low gravity, such as modeling the Mars Rover navigating through fine Martian regolith or a sieve that operates on the Moon. Additionally, ProCSI had Dr. Matt Melis, of the NASA Glenn Research Center, visit and talk to students to encourage space-related pursuits. During ProCSI 2009 and 2010, Dr. Melis presented his work on the investigation into the Columbia Shuttle Disaster. For the ProCSI 2011 session, Dr. Abhi Jain, a scientist from the NASA Jet Propulsion Lab will come to present his work on the use of simulations and computer modeling in space exploration.

In terms of *impact assessment*, the web-based Student Assessment of Learning Gains Instrument (SALGI), developed by the National Institute for Science Education (NISE) College Level One Team under NSF support at the University of Wisconsin, will be used for outcome control and implementation of a continuous improvement process, which also draws on exit interviews with the participants. All 2008 ProCSI alumni went on to college in Fall 2009 at University of Wisconsin-Madison, University of Wisconsin-Milwaukee, DePaul, Southern Illinois University-Edwardsville, and Howard University. Partial ProCSI funding for 2008 was secured through NSF project CMMI-

0700191, and for 2009 to 2013 through NSF project CMMI-0840442. Additional funding was provided by an industry partner (BAE Systems).

The 2011 goal of *teacher training* has been, and will continue to be achieved through graduate student members of the SBEL lab. They recruit, organize and teach a majority of the seminars for the ProCSI event. This teaching is new to all of these students and provides a valuable learning experience for both the participants of ProCSI and the graduate student teachers.

# Rocket Science for Educators; K-12 Techniques for Science Technology Engineering and Mathematics

Todd H. Treichel<sup>1</sup>

American Institute of Aeronautics and Astronautics and  
Orbital Technologies Corporation

The Wisconsin AIAA chapter has leveraged the talent of its members to provide a variety of outreach opportunities for precollege aged students. Hands-on demonstrations, visual aids, and real-life space flight examples provide a foundation for bringing pre-college aged students face-to-face with space-related science, designed hardware, technology, and potential benefits; increased interest in aerospace and space related fields that lead to study at the university level followed by career. The Rocket Science for Educators program consists of a workshop used to assist schools in implementing rocket science into respective math or science curriculums. Participating educators attend a weekend workshop and receive a set of rocket science materials that they may take back to their respective schools. This workshop is taught by aerospace professionals where they provide a unique opportunity for teachers to provide meaningful activities in their classrooms and improve student performance in the fields of science, technology, engineering, and mathematics.

## Nomenclature

<i>AIAA</i>	=	American Institute for Aeronautics and
<i>CG</i>	=	Center of gravity
<i>CM</i>	=	Center of mass
<i>G</i>	=	Acceleration force due to gravity
<i>HI-REL</i>	=	High reliability
<i>V</i>	=	Velocity
<i>RH</i>	=	Relative humidity
<i>NASA</i>	=	National Aeronautics and Space
<i>ORBITE</i>	=	Orbital Technologies Corporation
<i>STEM</i>	=	Science Technology Engineering and
<i>WSGC</i>	=	Wisconsin Space Grant Consortium

## Introduction

The Wisconsin section of AIAA is based in Madison, Wisconsin and has a current membership of approximately 80 members and has recently won the 2009 *Harry Staubs Pre-College Outreach Award*. The award is presented annually to sections that have developed and implemented an outstanding pre-college (k-12) outreach program that provides quality educational resources for teachers in science, technology, engineering, and mathematics (STEM) subject areas. In 2010 AIAA-Wisconsin was awarded an outreach grant from the Wisconsin Space Grant Consortium (WSGC) and successfully administered a *Rocket Science for Educators* workshop for K-12 educators in Madison, Wisconsin.

## Goals and Value of Project

A decline in both the quantity and quality of students pursuing careers in STEM is widely noted in policy reports, the press, education, and government. Fears of increasing global competition compound the perception that there has been a drop in the supply of high-quality students

<sup>1</sup> Systems Engineer, Space Center, 1212 Fourier Drive, Madison, Wisconsin, USA, AIAA Senior Member.

moving up through the STEM pipeline in the United States. A recent article published on February 12, 2010, by the Milwaukee Journal Sentinel, reveals the following (Miller, 2010):

*Grade school science teachers aren't doing the best job of informing their students about careers in science and engineering, according to a new survey of students from the American Society for Quality (ASQ). The survey of more than 1,110 students, which was done in December 2009, tried to discover how well teachers translate their knowledge and passion for science to getting children excited about engineering and science careers. It found that 63% of students think their teachers are not doing a good job of talking to them about engineering careers, and 42% said their teachers aren't good at showing them how science can be used in a career.*

*Among the survey's findings:*

- *85% of students said their teachers deserve at least a "B" grade when it comes to knowledge about science topics, and 55% gave them an "A."*
- *Nearly one third of students give their teachers a "C" or lower for making science more exciting and fun to learn and assigning fun hands-on projects in the classroom.*
- *Students in grades 3-6 rate their science teachers higher for making science exciting and hands-on than students in grades 7-12 rate their science teachers.*
- *72% of students in 3-12 grades think a person needs to do well in science and math to get a good paying job in the future.*
- *As students get older (7-12 grades) however, they are less likely to believe that science and math are necessary to getting a good paying job.*

The Wisconsin AIAA chapter has leveraged the talent of its members to provide a variety of outreach opportunities for precollege aged students. Hands-on demonstrations, visual aids, and real-life space flight examples provide a foundation for bringing pre-college aged students face-to-face with space-related science, designed hardware, technology, and the potential benefits; increased interest in aerospace and space related fields that lead to study at the university level followed by career. Section officers discussed and reviewed a compilation of various outreach projects summarizing a three year period covering 2006 – 2008. A survey form was constructed in an attempt to measure effectiveness of outreach efforts.

In 2009 the Wisconsin AIAA conducted a series of workshops on Physics of Propulsion and Space Flight. To test the effectiveness of these workshops, participants were asked to participate in a pre and post workshop survey. Survey results are summarized in Figure 1 where students sampled, grades six through eight, considered math and science important but only 60% were interested in STEM subjects.

At the conclusion of the workshop series, students again were surveyed where a 35% increase in STEM interest resulted.

Over the last century, America's economy has shifted from an agricultural and industrial focus to one that requires greater scientific and mathematical knowledge as well as technological expertise. According to the Bureau of labor Statistics, of the thirty fastest growing occupations projected for 2016, twenty-two of them are in STEM related fields. AIAA Wisconsin members and involved teachers were intrigued by these measureable results. Thus, causing the development of an educational outreach program that reaches out to K-12 teachers.

**WI AIAA 2009 Outreach Survey Results**  
(35 Students, 6<sup>th</sup> – 8<sup>th</sup> Grade)

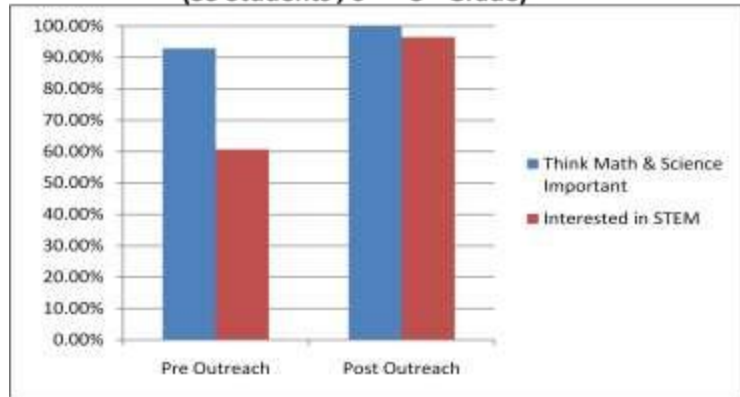


Figure 1, 2009 outreach survey summary.

The goal of the *Rocket Science for Educators* workshop is to assist schools in implementing rocket science into respective math or science curriculums. A proposal was submitted to the Wisconsin Space Grant Consortium (WSGC) to assist with funding the newly designed program. The *Rocket Science for Educators* workshop was designed specifically for educators from public and private institutions and those educators experienced with teaching math or science subjects. Participating educators attend a weekend and receive a set of rocket science materials that they may take back to the respective schools for use and implementation. A workshop taught by aerospace professionals provides a unique opportunity for teachers to provide meaningful activities in their classrooms and improve student performance in the fields of science, technology, engineering, and mathematics.

**Rocket Science for Educators**

In fall of 2010, a WSGC grant funded Rocket Science for Educators workshop was conducted in Madison, Wisconsin where a total of fourteen educators were recruited to attend a rocket science workshop at no charge. Workshop attendees consisted of math, science, art, and special needs teachers from K-12 institutions, primarily from the southern part of the state (see Figure 2). The workshop was conducted at Orbital Technologies Corporation (ORBITEC), located in Madison, Wisconsin. The workshop utilized aerospace topics to provide STEM education to educators for preparing today's students for tomorrow's jobs allowing them to be competitive in an increasingly global economy.



Figure 2. Geographical origins of 2010 workshop participants.

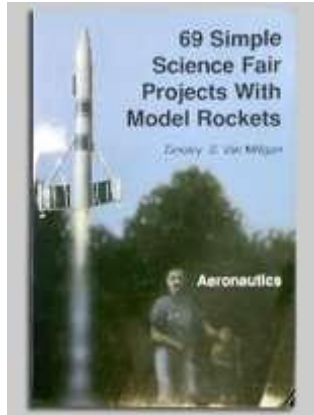


Figure 3. Rocket design simulation software and reference materials.

demonstrate participants' mastery of course subject matter. Educators were issued an achievement plaque and a set of materials that can be used for implementation into their respective math or science curriculums. Curriculum adaptable aerospace software license (see



Figure 4. Payload capable model rocket.

discouraged for reasons of safety. Extensive time was spent using RockSim design software to demonstrate rocket design techniques, 3D imaging, and flight simulation (see Figure 6) followed by construction and flight of a payload capable rocket. RockSim is a computer program that allows you to design any size rocket, and then simulate its flight to see how high, and how fast it will fly. Prior to teachers building their payload capable rockets, an analysis of various payload weights were conducted with different engine thrust parameters to determine if the actual flight would be stable and safe to launch. The purpose of lectures, demonstrations, and take-home materials was to provide educators with educational tools that:

1. Provide basic knowledge of aerospace engineering and rockets.
2. Provide rocket design and simulation software training and user license.
3. Ability to conduct flight experiments using an electronic altimeter.
4. Allows educator to have access to reference material for rocket propulsion.
5. Provide knowledge of how to build an electric powered launch pad.
6. Assure safety and enable educator with skills to properly conduct a rocket launch for educational groups.

Table 1 illustrates workshop topics and how each topic relates to an educational discipline. Lectures and hands on activities were conducted including design, construction, planned experimentation, altitude analysis and differential pressure, static rocket engine firing, and the launching of a payload capable rocket. At the close of the workshop, instructors provided

constructive feedback accompanied by a short competency quiz to

each participant completing the workshop. Highlights of the workshop consisted of a series of lectures which included demonstration (static) firing of potassium nitrate solid fuel, composite solid fuel, and hybrid rocket engines (see Figure 5). Safety rules for storage and handling of propellant materials was

discussed and making a science project out of home-made rocket engines was

7. Build interest and excitement about STEM.
8. Provide an opportunity for hands-on experiences with STEM subjects by designing, building, launching, and recovering payload capable rocket.
9. Raise student educational aspirations, knowledge of STEM, and interest in pursuing a career in aerospace.
10. Improve teaching of STEM subjects by collaborating with teacher preparation and professional development activities.

Table 1. Rocket science for educator’s workshop curriculum.

Education Module	Aerodynamics & Physics	Chemistry of Propulsion	Geometry & Measurement	Computer Aided Design	Design Simulation	Modeling	Electronics & Circuitry	Scientific Inquiry	Problem Solving	Communication	Graphic Design & Development
Newton’s Laws	X		X						X		
Principles of Flight	X		X	X	X						
Rocket Engines	X	X	X	X	X	X	X				
Rocket Stability	X	X	X	X	X	X					
Techniques of Rocket Design	X	X	X	X	X	X		X	X	X	
Payload Science	X	X	X	X	X	X	X	X	X	X	X
Recovery	X		X	X	X	X		X	X	X	X
Planned Experimentation	X	X	X	X	X	X		X	X	X	
Rocket Construction			X	X	X	X	X		X	X	X
Engineering Change Mgt.			X	X	X	X	X		X	X	X
Safety Procedures		X					X			X	
Weather	X				X			X	X	X	
Launch Pad & Controls	X		X				X			X	
Analysis & Reporting								X	X	X	X



Figure 5. Static firing of rocket engines

The purpose of workshop presentations was to give teachers a strong foundation in rocketry, understand the physics and science behind rocket propulsion, and bring a motivating set of materials and subject matter back to their classrooms. A particular emphasis on rocket propulsion and rocket stability was contained in take-home binder to accompany rocket propulsion discussions, talks about the physics, how rockets produce thrust, the types of propellants

used in rockets, characteristics of high and low thrust motors, the nomenclature

for rocket motors, the thrust curve, and how to select the best type of engine for a rocket and desired mission.

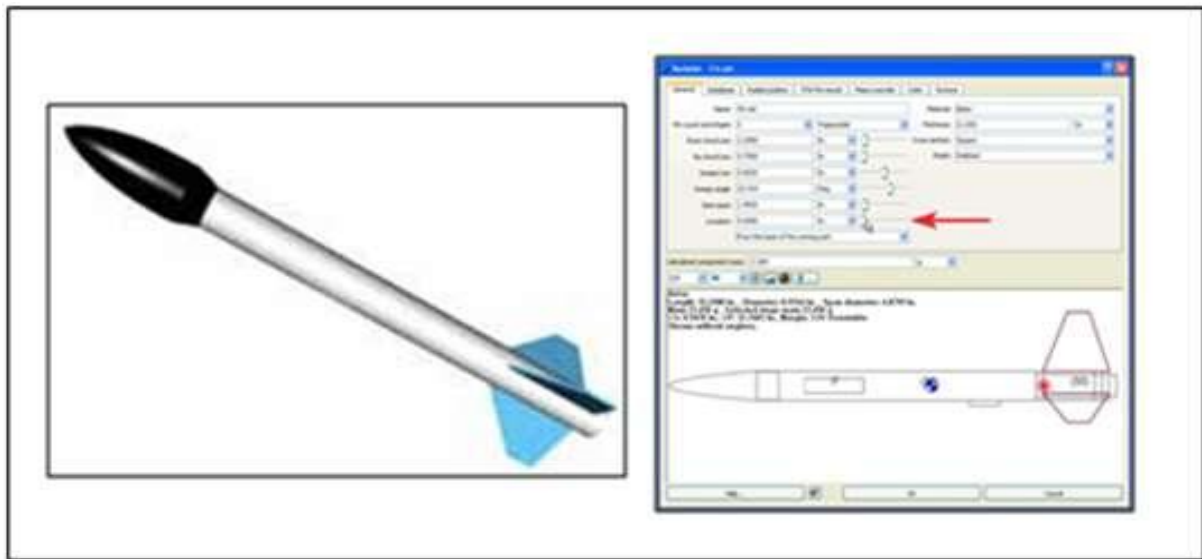


Figure 6. RockSim software design and simulation.

At the conclusion of launching the various payloads a post-launch review was conducted to discuss lessons learned and the process of corrective actions for improvement and future experimentation. Prior to adjournment, a survey was administered to test workshop effectiveness where each educator was asked to score the workshop for relevance and fit-for-use within their respective curriculums. The scoring scale was 1 – 10, where 1 indicates that they should have stayed home and 10 indicating that the workshop exceeded expectations). Workshop survey results are illustrated in Figure 7. An average score of 8.9 revealed a worthwhile effort and a desire among AIAA Wisconsin section members to pursue this type of outreach effort in the future. Figure 9 illustrates participants in a group photo at the conclusion of the educator workshop.

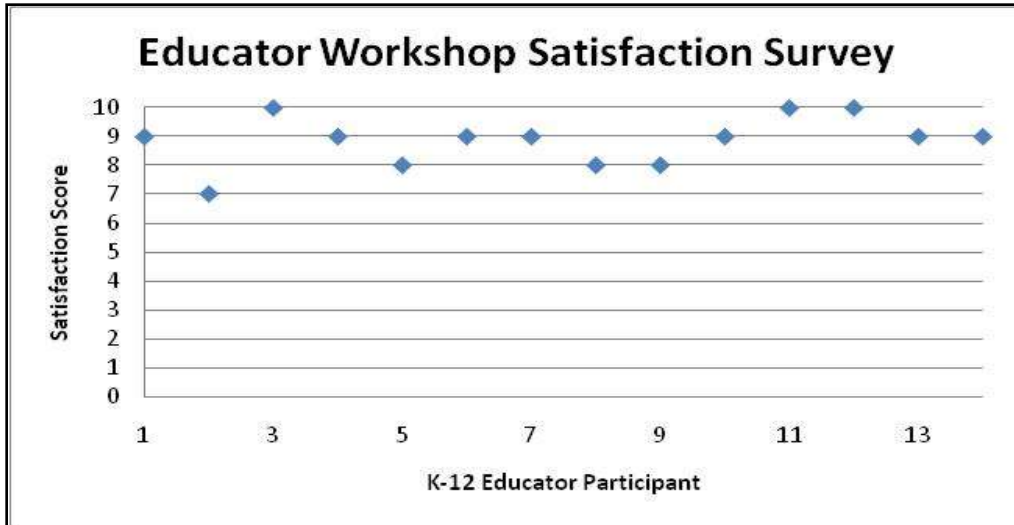


Figure 7. 2010 Rocket Science for Educators workshop survey results.

### Conclusion

In June 2011 the 14 educator workshop participants were contacted and asked to respond to five questions about their use of workshop materials and most importantly if respective activities improved student interest in STEM. Out of the 14 educators 11 responded to the survey and *yes* answers were recorded and are illustrated in Figure 8.

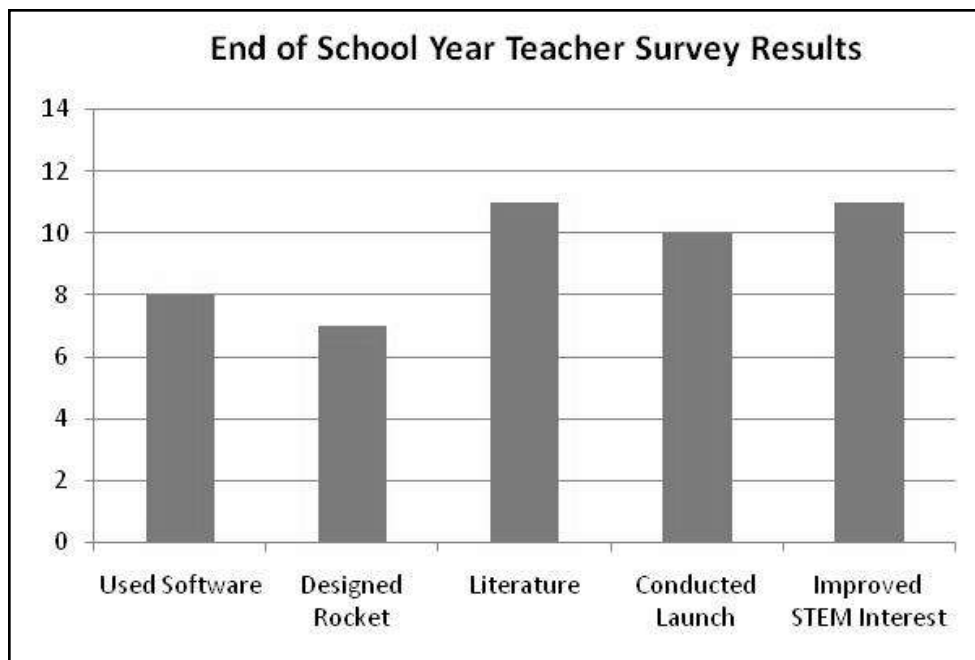


Figure 8. End of school year survey results from educators.

The following is one example cited from a workshop participant in the end of school year survey:

*I used the book and materials we were given to help me gain more confidence before I had my students assemble rockets for launching. I had never done this at school and had wanted to for a longtime. The experience with the rockets during the workshop really made me have enough knowledge to give it a try with my students.*

*I used the RockSim software with several classes. My advanced reading group read "Rocket Boys" (grade 7/8) and then launched rockets. We used RockSim to look at what would happen to the Rockets during flight. In both of my Earth Science classes (grade 7) we launched rockets in the spring, and again used RockSim to predict what would happen. It predicted that one of the rockets would launch and then crash to the ground nosecone first. That is what actually happened. Also several of my advanced science students spent time using the software on their own, it was very exciting for them and encouraged them to work on some rockets at home.*

*Building and launching rockets is always exciting for my students. This is a great science experience because we have successes and failures just like in all science experimentation! The students feel so empowered when they get a chance to make scientific decisions and then test what they build. We have great discussion about how scientists make building and experimentation decisions. Anytime students are actively building and experimenting they are inspired and ready to learn. Students that don't always show interest in science are active participants with hands-on activities like rocket building and launching.*



Figure 9. Educator workshop participants.

A simple, compelling philosophy drives AIAA Wisconsin's commitment to math, science, and technology education. Make it exciting, make it empowering, and make it fun. The Rocket Science for Educators workshop is a far-reaching program that targets precollege students, and the educators who inspire them. Learning starts with a teacher, a curious student, and fun in the classroom. The AIAA sponsored *Rocket Science for Educators* workshop provide educators with first-hand experience and training from real aerospace professionals that will spark students' excitement about machines ... space ... aviation ... how things work.... flying ... and why things happen. In short, all the facets of math and science. Please feel free to contact the author if you are interested in learning more about this STEM workshop.

## References

1. Chiaverini, M. J., Kuo, K. K. (2007). *Fundamentals of hybrid rocket combustion and propulsion*. Reston, VA: AIAA Press.
2. Fortescue, P., Stark, J., Swinerd, G. (2003). *Spacecraft systems engineering* (4<sup>th</sup> ed.). West Sussex, England: John Wiley and Sons Ltd.
3. Miller, S. A. (2010, February 14). Engineers step up for STEM next week. *Milwaukee Journal Sentinel*, pp. A37.
4. RockSim software. *Model rocket design and simulation software* (Ver. 9.0). Purchased from: [www.apogeerockets.com](http://www.apogeerockets.com).
5. Colorado Springs, CO: Apogee Components.
6. Van Milligan, T. S. (1995). *Developing Creativity Using Model Rockets to Teach the Techniques of Problem Solving*.
7. Colorado Springs, CO: Apogee Components.
8. Van Milligan, T. S. (2008). *Model rocket design and construction* (3<sup>rd</sup> ed.). Oregon, IL: Quality Books, Inc.

# Teaching Teachers about Astronomy

Coggin Heeringa

Crossroads at Big Creek

## Abstract

Crossroads at Big Creek, in collaboration with the Door Peninsula Astronomical Society, is dedicated to educational outreach in astronomy. We have had our best results by providing teacher education in the form of continuing education classes and workshops.

## Background

Crossroads at Big Creek, Inc. in Sturgeon Bay, Wisconsin is a learning preserve dedicated to life-long learning in science, history and the environment. The preserve includes an Astronomy Campus which includes the Leif Everson Observatory & StarGarden (owned by the School District of Sturgeon Bay) and the Ray and Ruthie Stonecipher Astronomy Center which houses an inflatable planetarium.

For more than a dozen year, in collaboration with the Door Peninsula Astronomical Society, Crossroads offered classes and events designed to introduce the public to astronomy and to interest young people in the STEM disciplines.

Through the years, Astronomy Days, night sky viewing, lectures, and youth programs were offered with limited participation. Those who did attend were predominantly families in which the parents had prior interest in astronomy. In short, we were “preaching to the choir.”

Unlike Baby Boomers, parents of today did not grow up during the Space Race. They did not cheer for Alan Shepard, pray for John Glenn, or thrill to the moon landings. They probably did not dream of growing up to be astronauts. To them, the term “rocket science” became a metaphor for something beyond comprehension. In short, as a group, they simply were not interested in space-related topics and consequently, did not bring their children to astronomy outreach activities.

Clearly, if our outreach efforts were to reach children, we would have to work through the elementary schools. But most teachers were in the same generation as the parents of their students and in too many [though, thankfully, not all] cases, were attracted to elementary education because science and math requirements were minimal.

Students become excited about topics presented by passionate teachers. If we could increase the content knowledge and enthusiasm for astronomy in elementary school teachers, we believed that they would inspire their students. Better than we could. After all, teachers really are the best teachers.

This project was underwritten with a grant from the Wisconsin Space Grant Consortium.

## **Methods**

The idea for reaching teachers occurred during a focus group trying to promote sustainability at Crossroads. A retired teacher made the offhand remark, “Teachers have to have continuing education, but the cost of graduate level courses is so excessive, they’ll sign up for any flying circus if they can get a credit cheaply.”

This was it! We could be the flying circus. If we would offer a generous scholarship stipend, teachers would sign up for a class in astronomy. Crossroads already had a working relationship with the University of Wisconsin-Green Bay Education Outreach program to offer graduate level methods classes and they approved the course “Teaching Astronomy in the Elementary School” and with the success of that added a second course, “Interactive Astronomy in the Elementary School.” A generous scholarship stipend (funded through WSGC) made these classes almost irresistible to teachers, many of whom had little or no prior interest in space education.

The plan worked. In fact, participating teachers went back to their schools and incorporated activities into their classes. Seeing their excitement, teachers who did not need credits asked if we could offer workshops as well.

Using funds from WSGC, we began offering workshops on astronomical topics: “The Real Stars of Harry Potter”; “Comets”; “Green Lasers and Lasagna”; “Night Sky Constellations”. We offered a free dinner, teaching materials and a stipend, and invited the teachers to bring their children and spouses along. The “bring the children” was included so teachers would not have to pay a babysitter, but it turned out to be the best part of the program. Teachers could observe how excited the children got while doing the activities.

Watching teachers leading children through hands-on activities spawned yet another idea. Teachers are great teachers. Why not hold our workshops immediately prior to outreach activities? Workshop participants could receive a small stipend for attending the training or a larger stipend if, after learning the activities, they would stay and become presenters at our outreach events.

## **Conclusions and Future Plans**

The best evaluation of our programs is the increase in astronomy-based school field trips to Crossroads and the increase prior knowledge the children have when they visit our planetarium. We can immediately recognize the student of teachers who have participated in our programs. We also have tripled our participation at outreach events. Apparently, teachers who will be presenting activities encourage their students to attend the events.

We will be offering a teacher workshop on exo-planets October 1 prior to our Family Astronomy Day and also offering a one graduate hour class “Teaching Astronomy in the Elementary School” through UW-Green Bay October 7, 8, and 15, 2011.

# Spanish Translation for Astronomy Outreach

James M. Lattis<sup>1</sup>

UW Space Place, Univ. of Wisconsin-Madison Dept. of Astronomy

## Introduction

Astronomy and space science outreach to the Hispanic community in Madison has taken many forms and presents many challenges. With support from WSGC, UW Space Place has experimented with a wide variety of Spanish-language outreach, including both bi-lingual (English presentation with simultaneous translation into Spanish) and Spanish-only interactive sessions, lectures in Spanish, star parties with Spanish interpreters present, community science “fairs” targeted for the Spanish-speaking community, and Spanish translations of exhibit materials. (See proceedings paper from last year.) In addition to the program development itself, each of these types of outreach requires Spanish-language promotional materials, support materials (e.g. agendas and event maps), and supplementary materials, such as take-home brochures. Thus, the simple-sounding process of translation itself arises constantly, although in different contexts, from beginning to end. I report here on the particular matter of translating outreach material of various sorts into Spanish. The appendix to this report contains examples of this translation work, funded entirely by WSGC.

## Types of Materials and Translators

When it comes to translation, there is an important distinction between promotional/support materials and the program content and take-home materials. The first rarely depend on any scientific content (except perhaps as illustrations) and are intended only to draw attention to the program, portray it as appealing, and make the logistics (such as place and time) clear. On the other hand, program content and supplementary materials are far more demanding of the writer or translator. As an educational enterprise, it is very important that a scientific discussion should introduce appropriate terminology in Spanish for the objects, processes, etc. that are part of the lesson. It is not hard to imagine how a simple dictionary lookup of technical terms could lead to Spanish expressions that diverge from what would be normal usage by Spanish-speaking scientists.

Items like advertisements and agendas, then, can be composed or translated into Spanish by nearly any competent writer with command of Spanish. But reliable scientific language requires a translator with some significant background in science, and they can be hard to locate.

## Recommendations

We have found that the talents of foreign graduate students and post-doctoral fellows in the University of Wisconsin System are a potentially excellent pool of scientifically literate native Spanish speakers who are often willing to do translation on a contract basis. A centralized registry to match up providers with those in need of such services could be a useful contribution to the science outreach community across the entire state.

---

<sup>1</sup> The author wishes to acknowledge the essential support of the Wisconsin Space Grant Consortium in carrying out the work described here.

Únase a nosotros para un día de

# Explorando las ciencias

Domingo, 14 de noviembre 12-4 pm

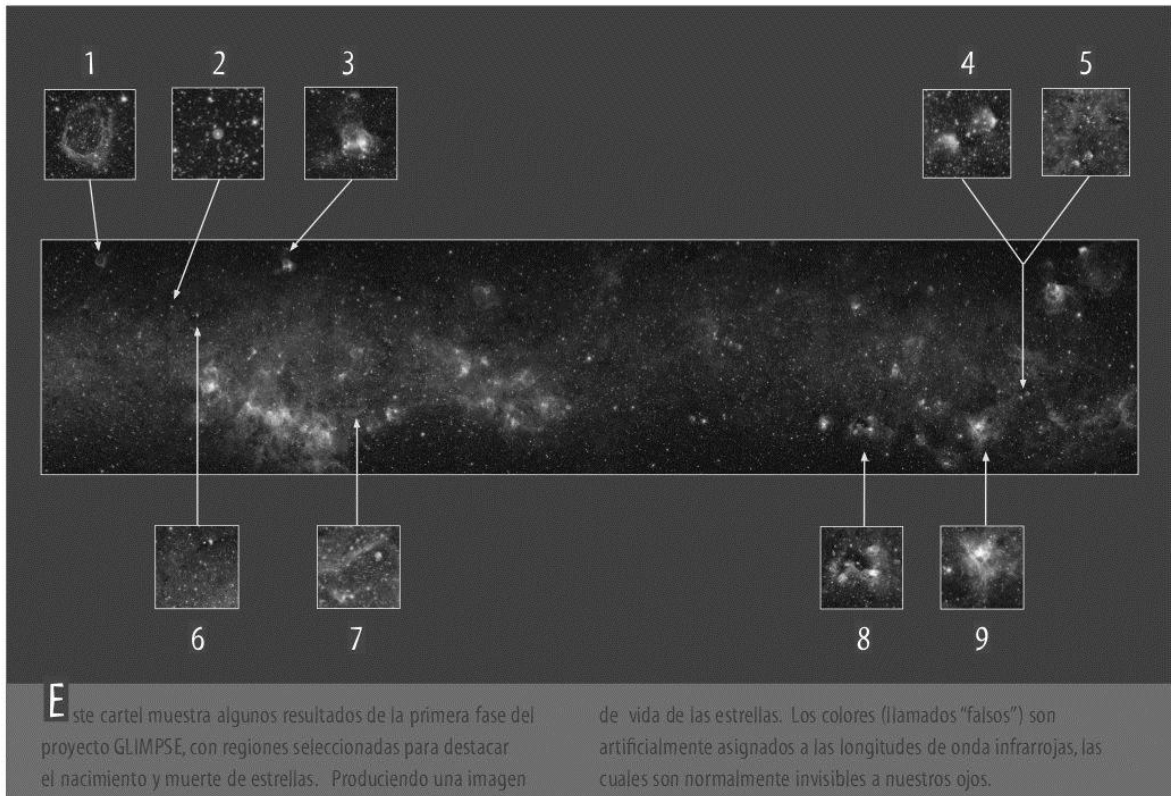


Explorando las Ciencias es un día para que toda la familia se divierta y aprenda acerca de las actividades científicas en la Universidad de Wisconsin. Habrá actividades prácticas para niños de todas las edades además de científicos que responderán a tus preguntas.

- Aprender a usar las herramientas científicas.
- Descubre cómo hacer que un centavo parezca plata.
- Mira un relámpago en una esfera de cristal.
- Hablar con científicos que construyeron IceCube, el telescopio bajo el hielo del Polo Sur.

**Space Place, en el Villager Mall, 2300 South Park Street**





**E**ste cartel muestra algunos resultados de la primera fase del proyecto GLIMPSE, con regiones seleccionadas para destacar el nacimiento y muerte de estrellas. Produciendo una imagen

de vida de las estrellas. Los colores (llamados "falsos") son artificialmente asignados a las longitudes de onda infrarrojas, las cuales son normalmente invisibles a nuestros ojos.



**1** Región HII (pronunciado "H-dos") - una nube de gases tibios y polvo del cual se forman las estrellas jóvenes. Esta imagen muestra que el gas es soplado para formar una burbuja. El soplo viene de los vientos estelares de una estrella masiva joven.



**2** Nebula planetaria - una bola creciente de gas expulsada por una estrella moribunda, cuya masa había sido similar a la de nuestro sol.



**3** Una región de formación de estrellas con una región asociada de HII.



**4** Una región de la Vía Láctea en la cual se están formando estrellas. El color rojo falso es causado por partículas de polvo "excitadas" por la luz ultravioleta emitida de estrellas masivas jóvenes.



**5** Nubes oscuras filamentosas, de las cuales se están formando estrellas. Regiones como ésta provocan preguntas importantes acerca de las condiciones (tales como la densidad, la temperatura y la presión) que inician el colapso de estas nubes para formar estrellas nuevas.



**6** Nubes oscuras filamentosas de gas y polvo de las cuales estrellas jóvenes se formarán eventualmente.



**7** Los restos de una estrella que explotó como una supernova.



**8** Otra del gran número de regiones donde estrellas se forman. En regiones donde estrellas se forman hay "protoestrellas" objetos que están creciendo y que pronto serán estrellas. Las protoestrellas generan efusiones supersónicas, las cuales empujan las nubes de gas y polvo alrededor. El color verde falso muestra esta interacción.

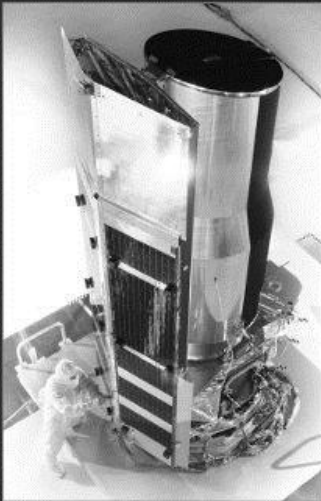


**9** Una región muy masiva de formación de estrellas.

## ¿Qué es GLIMPSE?

Los Astrónomos de la Universidad de Wisconsin dirigen el proyecto GLIMPSE (Estudio Extraordinario Legado Galáctico del Plano Medio por Infrarrojo), el cual usa el Telescopio Espacial Spitzer (TES) de NASA. Lanzado al espacio en 2003, el TES es la última nave espacial en el programa de Grandes Observatorios de NASA. El programa también incluye el Telescopio Espacial Hubble (TEH). El TES es diferente del TEH, porque observa por ondas infrarrojas del espectro, mientras el TEH observa por ondas visibles.

El TES es el telescopio infrarrojo más grande



que jamás se ha lanzado al espacio. Siendo que objetos tibios emiten mucha radiación infrarroja, se tomaron precauciones para proteger el TES de interferencia de ondas no deseadas. La nave espacial es enfriada a temperaturas que acercan al cero absoluto ( $-273^{\circ}\text{C}$  o  $-459^{\circ}\text{F}$ ), para que el telescopio no detecte su propia radiación. Lleva una cubierta grande para protegerlo del sol. El TES fue colocado en una órbita alrededor del sol para evitar otra fuente grande de radiación no deseada, es decir, la tierra.



# EL POZO de Gravedad



Pon una moneda en uno de los lanzadores.  
Intenta lanzar dos monedas de ambos lanzadores al mismo tiempo.

¿Siguen todas las monedas el mismo camino, y mueven a la misma velocidad? ¿Qué altera su manera de viajar?



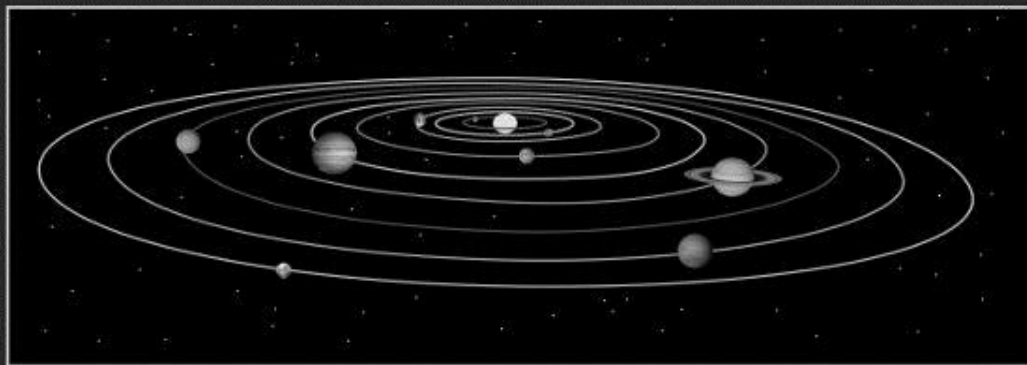
Cuando lanzas tu moneda, tu la pones en **moción**. Tu moneda quisiera viajar en una línea recta con una velocidad constante. Esto se llama la **INERCIA**.



Tu moneda no logra continuar en una línea recta. Esto resulta porque la **GRAVEDAD** ejerce su efecto en tu moneda. La gravedad es la fuerza que hace que los objetos caigan al piso.



Los efectos combinados de **INERCIA** y **GRAVEDAD** hacen que la moneda viaje en un camino casi elíptico alrededor del pozo.



La forma que tiene el Pozo de Gravedad imita el efecto de la gravedad del sol sobre un planeta en órbita alrededor del sol.

La fricción y la resistencia del aire hacen que las monedas en el Pozo de Gravedad pierdan energía con cada vuelta, causando que caigan al fondo. En el espacio, hay poca fricción para disminuir la velocidad de los planetas.

## Un Nuevo Departamento de Astronomía

Albert Whitford • Quinto Director  
1948-1958



Albert Whitford  
(1906-2002)  
inspecciona el espejo en  
blanco para el reflector  
de Pine Bluff de 90 cm.

Un nativo de Milton, Wisconsin, Whitford también tuvo fuertes conexiones previas con el observatorio. Mientras obtenía un doctorado en la física en la Universidad de Wisconsin, llegó a ser asistente de Joel Stebbins en 1931. El fue empleado como sucesor a Stebbins en 1948.

Whitford usó su entrenamiento en electrónicas avanzadas para mejorar los fotómetros fotodécimos de Stebbins. Como director de Washburn, Whitford continuó las investigaciones que él había comenzado con Stebbins sobre los colores de estrellas y galaxias.

Whitford transformó la astronomía en la Universidad de Wisconsin de una entidad propia dentro de la universidad a un departamento dentro del Colegio de Letras y Ciencias. El también reubicó a los astrónomos de un restringido local en Washburn al edificio Sterling.

Bajo la dirección de Whitford, la Universidad de Wisconsin edificó su primer telescopio nuevo de tamaño mayor en 70 años: el reflector de 90 cm en el observatorio de Pine Bluff (24 km al oeste de Madison), terminado en 1958. Whitford salió de Wisconsin ese año y llegó a ser el director del Observatorio Lick, siguiendo los pasos de Edward Holden.



El Observatorio de Pine Bluff

## Investigaciones del Espacio

Arthur Code • Sexto Director, 1958



Arthur D. Code  
(Nacido en 1923)

Code fue el último "Director del Observatorio de Washburn", aunque este título lo lleva nominalmente el presidente o presidenta actual del Departamento de Astronomía. El observatorio de Washburn llegó a ser anticuado para propósitos de investigaciones, pues el Observatorio de Pine Bluff fue el nuevo sitio del telescopio, y los astrónomos se habían mudado al edificio Sterling.

Primero, Code llegó a ser un miembro de la facultad de la Universidad de Wisconsin en 1951. El salió en 1953, pero retornó como director de Washburn en 1958. Después del lanzamiento de Sputnik I en 1957, Code y otros astrónomos quisieron poner instrumentos astronómicos en el espacio. Para lograrlo, Code fundó el Space Astronomy Lab (SAL) de la Universidad de Wisconsin en el 1959. El primer proyecto mayor de SAL fue el Paquete de Experimentos de Wisconsin para el Orbiting Astronomical Observatory (OAO).



Concepción artística del  
Observatorio  
Atomómico en Órbita en su  
cobertura espacial

Code llegó ser uno de los líderes de la astronomía en longitudes de onda ultravioleta (UV). Otro proyecto mayor en la astronomía ultravioleta fue el Wisconsin Ultraviolet Photo-Polarimeter

Experiment (WUPPE), para el cual Code fue el investigador principal.

Las investigaciones de Code, al igual que muchos otros astrónomos recientes de Wisconsin trabajando en las fronteras de la astronomía, están arraigadas en el conocimiento experto en fotometría, el cual se extiende atrás hasta 1920.

## Observatorio Washburn Hoy Día



El laboratorio Washburn ya no se usa para investigaciones, pero permanece como un sitio prominente histórico en el campus y un centro dedicado al alcance al público. Continuando la tradición comenzada por Edward Holden 1881, el observatorio se abre al público para observar los cielos en el primer y tercer miércoles de cada mes, si el cielo está despejado.

Para más información acerca de las noches cuando el público puede observar, visite el sitio web [www.astro.wisc.edu/Washburn](http://www.astro.wisc.edu/Washburn).

Space Place de la Universidad de Wisconsin, fundado en 1990, continúa esta tradición de educación y alcance al público.

Visite el sitio web  
**SPACEPLACE.ORG**  
para información sobre  
talleres de ciencia para la  
familia, noches públicas para  
observación astronómica,  
presentaciones por invitados,  
y más.

## Un Siglo de Astronomía

~ en la ~  
Universidad de Wisconsin  
1860-1960



El observatorio Washburn alrededor de 1880  
(Archivos Mary Lea Shane del Observatorio Lick)

Por más de 75 años el centro de astronomía en la Universidad de Wisconsin fue el Observatorio Washburn, uno de los observatorios más prominentes en los Estados Unidos. Esta exhibición presenta una historia del primer siglo de la astronomía en la Universidad de Wisconsin, desde la mitad de los 1850, a través de los años de Washburn, y entrando luego en la edad espacial.



UNIVERSITY OF WISCONSIN

## En el principio, 1854 - 1877



C.C. Washburn  
(1818-1882)

La astronomía fue una parte importante en la educación universitaria durante el siglo diecinueve. Comenzando en 1854, un poco después que la universidad de Wisconsin fue fundada, todos los estudiantes no licenciados fueron requeridos a completar por lo menos un término de astronomía. La universidad también esperó edificar un observatorio para ayudar en la enseñanza y realizar investigaciones, aunque no disponía de fondos.

En 1876, la legislatura de Wisconsin aprobó un proyecto de ley proveyendo fondos para un profesor de astronomía si alguien donaba un observatorio. Cadwallader C. Washburn dio el dinero en 1877. Un General en la Guerra Civil y Gobernador de Wisconsin entre 1874 y 1876, Washburn ganó su fortuna en la industria de molino. Más tarde su compañía de molino basada en Minneapolis llegó a ser General Mills.



El refractor Washburn de 40 cm, uno de los telescopios principales del observatorio. Cuando se instaló en 1879 fue el cuarto refractor más grande del mundo.

## Los Primeros Directores

### James Watson • Primer Director, 1879-1880



James C. Watson  
(1838-1880)

La construcción del observatorio de Washburn comenzó en 1878, y James Watson de la Universidad de Michigan fue empleado para ser el primer director. Watson era rico y contribuyó dinero para una adición al edificio principal y dos observatorios más pequeños: uno para estudiantes y el otro para encontrar "Vulcano" - un planeta hipotético que él creía que existía, pero que nunca fue encontrado. El murió en 1880.

### Edward Holden • Segundo Director 1881-1885



Edward S. Holden  
(1846-1941)

Edward Holden vino del Observatorio Naval de los Estados Unidos en Washington, D.C. en 1881. El supervisó la terminación de los edificios e instrumentos, comenzó observaciones, y estableció la revista Publicaciones del Observatorio Washburn, la primera revista de investigaciones de la Universidad de Wisconsin. Holden salió de Wisconsin, para llegar a ser el primer director del Observatorio Lick en California en 1885.

### Una Unión Hecha entre las Estrellas



Alice M. Lamb  
(1863?-1942)

Después de la partida de Holden, John Davies, un profesor de física, romo control del observatorio. Sin embargo la mayoría de las investigaciones fueron realizadas por dos asistentes: Alice Maxwell Lamb y Milton Updegraff. Lamb fue una de un grupo muy pequeño de mujeres en ese tiempo quienes llevaban a cabo investigaciones observacionales. Ella se casó con Updegraff y los dos salieron de Wisconsin en 1887.

## Un Tiempo de Estabilidad

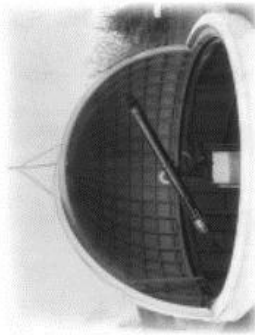
### George C. Comstock • Tercer Director 1889-1922



George C. Comstock  
(1855-1934)

Comstock fue el tercer director oficial de Washburn y un nativo de Madison quien regresó a Wisconsin para trabajar como un asistente en el Observatorio Washburn entre 1879 y 1885. Comstock llegó a ser subdirector de Washburn en 1887 y director en 1889. El se jubiló en 1922. La larga permanencia de Comstock como director trajo una estabilidad muy necesitada para el observatorio.

Comstock fue interesado principalmente en estudiar las posiciones y mociones de objetos celestiales - la astro nomía de posición. Uno de sus primeros proyectos fue un método novedoso de medir la distancia entre la tierra y el sol - llamado "la paralaje solar" - un valor muy importante para los astrónomos. Comstock también llevó a cabo investigaciones en el área nueva y creciente de la astrofísica, tales como una investigación de los colores de las estrellas. Además, él escribió varios papeles acerca de estructura de la Vía Láctea.



El observatorio de Washburn para situaciones con un arrefractor especial conectado al lado superior del telescopio. Comstock usó este arrefractor en su estudio novedoso de la paralaje solar.

## El Ojo Eléctrico en la Astronomía

### Joel Stebbins • Cuarto Director, 1922-1948



Joel Stebbins  
(1878-1966)

Stebbins estudió con Comstock como estudiante post graduado desde 1900 al 1901, obtuvo un doctorado en el Observatorio Lick en 1903, y entonces llegó a ser director del Observatorio de la Universidad de Illinois. Stebbins salió de Illinois y subsecuó a Comstock en la Universidad de Wisconsin en 1922. Stebbins se jubiló en 1948.

En Illinois, Stebbins llegó a ser un pionero astrónomíco de la fotometría electrónica (el estudio cuantitativo de la intensidad de luz). El siguió desarrollando los primeros métodos y tecnología cuando vino a la Universidad de Wisconsin, y fue el personaje principal en la fotometría por décadas. Los astrónomos usaban fotómetros electrónicos para distinguir cambios en la brillantez demasiado pequeños o rápidos para medir con otros métodos. Stebbins estudió primero las estrellas variables, incluyendo una investigación en los edipses de la estrella binaria Algol que abrió nuevos horizontes.

Stebbins trajo sus fotómetros a Madison en 1922 y realizó investigaciones tanto en Washburn como en el Observatorio de Mount Wilson en California. En los 1930, Stebbins continuó como pionero en la fotometría con sus estudios de la materia interestelar. Esta investigación condujo a un nuevo valor para el tamaño de la Vía Láctea. Su valor fue considerablemente más pequeño que el valor aceptado por astrónomos en aquel entonces y cerca al valor actualmente aceptado.



Joel Stebbins observado con un refractor en el Observatorio de Washburn de 15.6 pulgadas.

Peso y Masa:  
¿Cuál es la diferencia?

Masa es una medida de cuánta materia contiene un objeto. Si viajamos a otro planeta, todavía tenemos la misma cantidad de masa pero nuestro peso cambia.

Peso es una medida de la atracción de gravedad entre usted y el planeta en el que está parado. Su peso cambiará dependiendo de la masa del planeta y a qué distancia está usted del centro de dicho planeta.

## Su Peso en Otros Planetas

Mi peso en la Tierra es \_\_\_\_\_ lbs.

¿Qué sabe de cada uno de los planetas? ¿Qué tanta masa tiene y qué grande (qué distancia hay del centro del planeta a la superficie) es?

Prediga si su peso será mayor o menor en cada planeta. Luego haga los cálculos para cada planeta y vea si su predicción es correcta.

	Prediga (marque uno)	Real
MERCURIO	↑      ↓	
VENUS	↑      ↓	
LUNA	↑      ↓	
MARTE	↑      ↓	
JUPITER	↑      ↓	
SATURNO	↑      ↓	
URANO	↑      ↓	
NEPTUNO	↑      ↓	
PLUTON	↑      ↓	
¿Qué pasaría aquí? SOL	↑      ↓	

**21st Annual Conference  
Appendix A**

2011 Program

**Wisconsin Space Grant Consortium**

**&**

**University of Wisconsin-La Crosse**

*Present:*

**the Twenty-First Annual  
WISCONSIN SPACE CONFERENCE**

***“Seeing Farther from Space”***

University of Wisconsin-La Crosse  
La Crosse, Wisconsin

**Thursday, August 18 – Friday, August 19, 2011**

---

**CONFERENCE 2011 PROGRAM**

---

## Thursday, August 18, 2011

7:30-8:45 am	<b>Registration</b>	<b>Cartwright Center</b>	<b>Levee</b>
	<b>Continental Breakfast</b>		<b>CC337</b>
	<b>Poster Setup</b> (formal poster session at 2:45 p.m.)		<b>CC337</b>

### \*\*\* Plenary Session \*\*\*

8:45-9:00 am	<b>Welcome and Introductions</b>		<b>CC339</b>
	<b>Gubbi Sudhakaran</b> , Associate Director for Research, Wisconsin Space Grant Consortium, Chair of Physics Department, University of Wisconsin-La Crosse		
	<b>Joe Gow</b> , Chancellor, University of Wisconsin-La Crosse		
9:00-10:00 am	<b>Session 1: Keynote Address</b>		
	<b>Introduction of Keynote:</b>		
	<b>Gubbi Sudhakaran</b> , Associate Director for Research, Wisconsin Space Grant Consortium, Chair of Physics Department, University of Wisconsin-La Crosse		
	<b>Dr. Robert D. Gehrz</b> , Professor of Physics and Astronomy and Department of Astronomy Chair, University of Minnesota-Twin Cities, <i>Infrared Astronomy with NASA's New Spitzer Space Telescope</i>		
10:00-10:30 am	<b>Morning Break</b>		<b>CC337</b>

### \*\*\* Plenary Session \*\*\*

10:30-11:50 am	<b>Session 2: Other Student Programs</b>		<b>CC339</b>
	<b>Moderator: Tom Bray</b> , WSGC Associate Director for Special Initiatives and Dean of Applied Research and Grants, Milwaukee School of Engineering		
	<b>NASA Reduced Gravity Program:</b>		
	<b>Amber Bakkum</b> , <i>Fluid Volume Measurement Using Non-Invasive PZT Technology</i> , Undergraduate Student, Physics Department, Carthage College, Non-Presenting Team Members: Stephanie Finnvik, Isa Fritz, Bradley Frye, Cecilia Grove, Katelyn Hartstern, Samantha Kreppel, Emily Schiavone, KelliAnn Anderson, Erin Gross, Steven Mathe, Kimberly Schultz, Danielle Weiland		

**Benjamin Butler, Patrick Bersch**, *Zero Gravity Flight*, Undergraduate Students, Department of Engineering Mechanics and Astronautics, University of Wisconsin-Madison, Non-Presenting Team Members: Kevin Machstutis, Nathaniel Kainz, Samuel Marron, Marcus Fritz

***Senior Design Program:***

**Matthew Kallerud, Tim Paladin, Anthony Wilson**, *In-Situ Resource Utilization: Investigation of Melted Lunar Regolith Simulant JSC-1A*, Undergraduate Students, Department of Mechanical Engineering, Milwaukee School of Engineering, Non-Presenting Team Member: Brian Nguyen

**Derek Struck**, *Lunar Horizontal Axis Laundering System*, Undergraduate Student, Department of Mechanical Engineering, Milwaukee School of Engineering, Non-Presenting Team Members: Joseph Gnutek, Michael Swagger

11:50-1:00 pm **Lunch**

**Valhalla B**

**\*\*\* Concurrent Sessions -- Research Stream \*\*\***

1:00-2:45 pm **Session 3R: Physics and Astronomy**

**CC339**

**Moderator: Eric Barnes**, Assistant Professor, Physics Department, University of Wisconsin-La Crosse

**Sara Stanchfield**, *Optical Coupling of Radiation to Microwave Detectors*, Undergraduate Student, Department of Physics, University of Wisconsin-Madison

**Lou Nigra**, *Cancellation of Space-Based Interference in Radio Telescopes*, Graduate Student, Department of Astronomy, University of Wisconsin-Madison

**Sydney J. Chamberlin**, *Detection of Non-Einsteinian Gravitational Waves Using a Pulsar Timing Array*, Graduate Student, Department of Physics, University of Wisconsin-Milwaukee

**Benjamin D. Lackey**, *Determining the Neutron-Star Equation of State with Gravitational Waves*, Graduate Student, Department of Physics, University of Wisconsin-Milwaukee

**Victoria Hartwick**, *Identification of Crystallized Ice on Kuiper Belt Objects*, Undergraduate Student, Department of Astronomy, University of Wisconsin-Madison

**Ali M. Bramson**, *Using Networking Algorithms to Assess the Environment of Galaxy Groups*, Undergraduate Student, Department of Astronomy, University of Wisconsin-Madison

**Shauna Sallmen**, *Studying Interstellar Shells in our Milky Way Galaxy*, Associate Professor, Physics Department, University of Wisconsin-La Crosse

**\*\*\* Concurrent Sessions -- Education Stream \*\*\***

1:00-2:45 pm      **Session 3E: K-12 Education & General Public Outreach**      **CC332**

**Moderator: Daniel Bateman**, Director, Spaceport Sheboygan

**Sarah Desotell**, *Round 2: Flight, Floating, and Mars Courses*, Assistant Professor, Physics Department, Ripon College

**Barbara Bielec**, *Biotechnology Teacher Training*, K-12 Program Director, BioPharmaceutical Technology Center Institute

**Barbara Bielec**, *Healthy Bodies: On Earth and in Space!*, K-12 Program Director, BioPharmaceutical Technology Center Institute

**Brad Staats**, *Spaceflight Academy for CESA District #5*, CEO, Spaceflight Fundamentals, LLC

**Dan Melanz**, *Promoting the Computation Science Initiative (ProCSI) Summer Program*, Research Assistant, Department of Mechanical Engineering, University of Wisconsin-Madison

**Todd H. Treichel**, *Rocket Science for Educators (K-12)*, Senior Systems Engineer, American Institute for Aeronautics and Astronautics-Wisconsin

**Coggin Heeringa**, *Teaching Teachers about Astronomy*, Director, Crossroads at Big Creek, Inc.

2:45-3:00 pm      **Afternoon Break**      **CC337**

**\*\*\* Concurrent Sessions -- Poster Session \*\*\***

2:45-4:25 pm      **Session 4P: Posters**      **CC337**

**Facilitator: Marty Gustafson**, Chair, WSGC Advisory Council, Commercial Products Manager, Orbital Technologies, Inc.

**Nickolas Pingel**, *Magnetohydrodynamic Turbulence at High-Latitude Regions of the Milky Way*, Undergraduate Student, Department of Astronomy, University of Wisconsin-Madison

**Jane Kaczmarek**, *Three Dimensional Structure of the Coma-Abel 1367 Supercluster*, Undergraduate Student, Department of Astronomy, University of Wisconsin-Madison

**Melissa Wheeler**, *Toward Better Understanding of Dark Matter Halo Structures Around Galaxies*, Undergraduate Student, Physics Department, University of Wisconsin-La Crosse

**Michael Ramuta**, *Structure and Behavior of AWM and MKW Clusters*, Undergraduate Student, Department of Astronomy, University of Wisconsin-Madison

**Elizabeth Tennyson**, *Studying Neutral Hydrogen Shells in the Interstellar Medium*, Undergraduate Student, Physics Department, University of Wisconsin-La Crosse

**Kyle Kimminau**, *The Effect of Magnetic Defects on Domain Wall Motion in a Nanowire*, Undergraduate Student, Department of Physics, Marquette University

**Callie Kwiatkowski**, *Experimentation for Diagnostic Algorithm Benchmarking*, Undergraduate Student, Department of Mathematics, University of Wisconsin-Milwaukee

**Capri Pearson**, *Symbolic Computation Tools in Spacecraft Design Model*, Undergraduate Student, Department of Engineering Physics, University of Wisconsin-Madison

**Ben Oleson**, *Investigation of Annealed Multilayer Thin Oxide Films*, Undergraduate Student, Physics Department, University of Wisconsin-La Crosse

**Collin Bezrouk**, *Feathersail – The Next Generation Solar-Sail Satellite*, Undergraduate Student, Department of Engineering Mechanics and Astronautics, University of Wisconsin-Madison

**Matthew Kallerud, Tim Paladin, Anthony Wilson**, *In-Situ Resource Utilization: Investigation of Melted Lunar Regolith Simulant JSC-1A*, Undergraduate Students, Department of Mechanical Engineering, Milwaukee School of Engineering, Non-Presenting Team Member: Brian Nguyen

**Michael Czech**, University of Wisconsin-Milwaukee; **Patrick Johnson**, Carroll University; **Tyler Van Fossen**, University of Wisconsin-Madison; **Kelly Westphal**, Milwaukee School of Engineering, WSGC Balloon Launch Team

**\*\*\* Concurrent Sessions -- Research Stream \*\*\***

3:00-4:20 pm      **Session 4R: Engineering**      **CC332**

**Moderator: Eric Barnes**, Associate Professor, Physics Department, University of Wisconsin-La Crosse

**Seth King**, *Towards Cheaper Solar Cells: Developing ZnO Nanolaminates*, Assistant Professor, Physics Department, University of Wisconsin-La Crosse

**Devin Turner**, *Structural Dynamics of Aerospace Systems*, Undergraduate Student, Department of Mechanical Engineering, Marquette University

**Marco Lo Ricco**, *Impact Effects on Carbon-Fiber/Epoxy Laminates Subject to High-Strain Compression*, Graduate Student, Department of Civil Engineering and Applied Mechanics, University of Wisconsin-Milwaukee

**Stefanie Knauf**, *Experimental Determination of Flow and Heat Transfer Correlations for Passive Regenerators*, Research Assistant, Department of Mechanical Engineering, University of Wisconsin-Madison

**\*\*\* Concurrent Sessions -- Research Stream \*\*\***

3:00-4:20 pm      **Session 4SSI: Sounding Rocket Competition**      **CC339**

**Moderator: Bill Farrow**, WSGC Associate Director for Student Satellite Program, Assistant Professor, Milwaukee School of Engineering

**First Place – Non-Engineering Division – Team Falcon One**

**Wesley Barnes, Joey DeCarlo, Charlotte Evans, Glen Gregerson**, Undergraduate Students, Department of Physics, University of Wisconsin-River Falls

**Third Place – Engineering Division – Team Rocket Power**

**Brandon Jackson**, Undergraduate Student, Department of Mechanical Engineering, Milwaukee School of Engineering, Non-Presenting Team Members: Benjamin Steffes, Jonathon Slightam

**Second Place – Engineering Division – Team Rally Axe**

**Tyler Van Fossen, Alex Gonring**, Undergraduate Students, Department of Engineering Mechanics and Astronautics, University of Wisconsin-Madison

**First Place – Engineering Division – Team Jarts**

**Ryan May, Jacob Rice**, Undergraduate Students, Department of Electrical Engineering, Milwaukee School of Engineering, Non-Presenting Team Members: Cameron Schulz, Jordan Wagner

4:20-4:35 pm    **Afternoon Break**    **CC337**

**\*\*\* Plenary Session\*\*\***

4:35-5:20 pm    **Session 4R: Engineering (continued)**    **CC339**

**Moderator: Eric Barnes**, Associate Professor, Physics Department, University of Wisconsin-La Crosse

**Collin Bezrouk**, *Symbolic Computation Software: A Comparison Between Maple and Mathematica*, Undergraduate Student, Department of Engineering Mechanics and Astronautics, University of Wisconsin-Madison

**Matthew McKay**, *Developing Flight Applications of the Interplanetary Internet*, Undergraduate Student, Computer Science and Information Systems Department, University of Wisconsin-River Falls

**Mark Mahoney**, *Software Evolution and the Moving Picture Metaphor*, Associate Professor, Computer Science Department, Carthage College

**\*\*\* Adjourn for the Day \*\*\***

## Friday, August 19, 2011

8:00-9:00 am	<b>Registration</b>	<b>Cartwright Center</b>	<b>Levee</b>
	<b>Continental Breakfast</b>		<b>CC337</b>
8:00-8:45 am	<b>Undergraduate Workshop</b>		<b>CC332</b>

### \*\*\* Plenary Session \*\*\*

9:00-10:10 am	<b>Welcome and Introductions</b>		<b>CC339</b>
	<b>Bruce Riley</b> , Dean, College of Science and Health, University of Wisconsin–La Crosse		

#### **Session 5: Keynote Address**

##### **Introduction of Keynote:**

**Gubbi Sudhakaran**, Associate Director for Research, Wisconsin Space Grant Consortium, Chair of Physics Department, University of Wisconsin-La Crosse

**Dr. Jonathan P. Gardner**, Chief of the Observation Cosmology Lab, NASA Goddard Space Flight Center and Deputy Senior Project Scientist for the James Webb Space Telescope, *The James Webb Space Telescope*

10:10-10:25 am	<b>Morning Break</b>		<b>CC337</b>
----------------	----------------------	--	--------------

### \*\*\* Plenary Sessions\*\*\*

10:25-10:45 am	<b>Session 6: Student Satellite Program and Senior Design Program</b>		<b>CC339</b>
----------------	---	--	--------------

**Moderator: Bill Farrow**, WSGC Associate Director for Special Initiatives, Assistant Professor, Milwaukee School of Engineering

#### **Elijah High Altitude Balloon Program**

##### **Balloon Payload Team:**

**Amber Bakkum**, Carthage College; **Tyler Capek**, University of Wisconsin-River Falls; **Patrick Johnson**, Carroll University; **Aleysha Kobiske**, Carroll University; **Paul Nurczyk**, Milwaukee School of Engineering; **Richard Oliphant**, Milwaukee School of Engineering

10:45-11:15 am **Session 7: Biology**

**CC339**

**Moderator: Danny Riley**, Professor, Department of Cell Biology, Neurobiology, and Anatomy, Medical College of Wisconsin

**David Higgs**, *Optimization and Genetic Analysis of Lipid Accumulation in Algae as a Renewable Source for Biodiesel*, Associate Professor, Department of Biological Sciences, University of Wisconsin-Parkside

**Jonathan M. Van Dyke**, *Preserving Muscle Length Requires Simultaneous Stretch and Contraction*, Graduate Student, Department of Cell Biology, Neurobiology & Anatomy, Medical College of Wisconsin

11:15-12:00 pm **Group Photograph**

**As Directed**

12:00-1:00 pm **Awards Luncheon**

**Valhalla B**

1:00-1:55 pm **Awards Ceremony**

**Sharon D. Brandt**, Program Manager, Wisconsin Space Grant Consortium  
**WSGC Program Associate Directors**

1:55-2:00 pm **2012 Conference** – Kevin Crosby, Carthage College

2:00 pm **Conference Adjourned**

**\*\*\* Adjournment \*\*\***